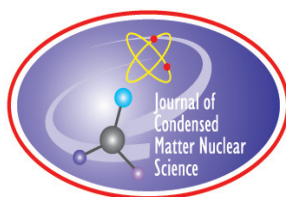


JOURNAL OF CONDENSED MATTER NUCLEAR SCIENCE

Experiments and Methods in Cold Fusion

VOLUME 6, February 2012



JOURNAL OF CONDENSED MATTER NUCLEAR SCIENCE

Experiments and Methods in Cold Fusion

Editor-in-Chief

Jean-Paul Biberian
Marseille, France

Editorial Board

Peter Hagelstein
MIT, USA

Xing Zhong Li
Tsinghua University, China

Edmund Storms
KivaLabs, LLC, USA

George Miley
*Fusion Studies Laboratory,
University of Illinois, USA*

Michael McKubre
SRI International, USA

Akito Takahashi
Osaka University, Japan

JOURNAL OF CONDENSED MATTER NUCLEAR SCIENCE

Volume 6, February 2012

© 2012 ISCMNS. All rights reserved.

This journal and the individual contributions contained in it are protected under copyright by ISCMNS and the following terms and conditions apply.

Electronic usage or storage of data

JCMNS is an open-access scientific journal and no special permissions or fees are required to download for personal non-commercial use or for teaching purposes in an educational institution.

All other uses including printing, copying, distribution require the written consent of ISCMNS.

Permission of the ISCMNS and payment of a fee are required for photocopying, including multiple or systematic copying, copying for advertising or promotional purposes, resale, and all forms of document delivery.

Permissions may be sought directly from ISCMNS, E-mail: CMNSEditor@iscmns.org. For further details you may also visit our web site: <http://www.iscmns.org/CMNS/>

Members of ISCMNS may reproduce the table of contents or prepare lists of articles for internal circulation within their institutions.

Orders, claims, author inquiries and journal inquiries

Please contact the Editor in Chief, CMNSEditor@iscmns.org or webmaster@iscmns.org



JOURNAL OF CONDENSED MATTER NUCLEAR SCIENCE

Volume 6

2012

CONTENTS

PREFACE

RESEARCH ARTICLES

- | | |
|--|----|
| When Bubble Cavitation becomes Sonofusion
<i>Roger S. Stringham</i> | 1 |
| Characterization of Neutrons Emitted during Pd/D Co-deposition
<i>Pamela A. Mosier-Boss, Frank E. Gordon and Lawrence P.G. Forsley</i> | 13 |
| Development of a High Temperature Hybrid CMNS Reactor
<i>Francesco Celani, O.M. Calamai, A. Spallone, A. Nuvoli, V. Andreassi, B. Ortenzi, F. Piastra, E. Righi, G. Trenta and E. Marano</i> | 24 |
| TOF-SIMS Investigation on Nuclear Transmutation from Sr to Mo with Deuterium Permeation through Multi-layered Pd/CaO
<i>A. Murase, N. Takahashi, S. Hibi, T. Hioki, T. Motohiro and J. Kasagi</i> | 34 |
| Modified Szpak Protocol for Excess Heat
<i>Dennis Letts and Peter L. Hagelstein</i> | 44 |
| Lochon-mediated Low-energy Nuclear Reactions
<i>K.P. Sinha and A. Meulenberg</i> | 55 |
| Effects of Self-poisoning of Pd on the Deuterium Permeation Rate and Surface Elemental Analysis for Nuclear Transmutation
<i>T. Hioki, N. Takahashi, J. Gao, A. Murase, S. Hibi and T. Motohiro</i> | 64 |
| The Open Gate Phenomenon: A New Energy Technology
<i>S.L. Taft and J. Marwan</i> | 77 |

Cryogenic Calorimetry of “Exploding” PdD _x Wires <i>F.L. Tanzella, J. Bao and M.C.H. McKubre</i>	90
Bose–Einstein Condensation Nuclear Fusion: Role of Monopole Transition <i>Y.E. Kim and T.E. Ward</i>	101
Nuclear Particles Generated by Electrolysis – a Review <i>R.A. Oriani</i>	108
Underlying Mechanism of the Nuclear of Implied by the Energy–momentum Conservation [I] <i>Tetsuo Sawada</i>	118
A Review on Nuclear Products Generated During Low-Energy Nuclear Reactions (LENR) <i>P.A. Mosier-Boss</i>	135
LANR Nanostructures and Metamaterials Driven at their Optimal Operating Point <i>M.R. Swartz</i>	149
Bird’s Eye View of Phonon Models for Excess Heat in the Fleischmann–Pons Experiment <i>P.L. Hagelstein</i>	169
Transmutation of Elements in Low-energy Glow Discharge and the Associated Processes <i>I.B. Savvatimova</i>	181
Experimental results on Excess Heat Power, Impurity Nuclides and X-ray Production in Experiments with a High-Voltage Electric Discharge System <i>A.B. Karabut and E.A. Karabut</i>	199
Spectral and Temporal Characteristics of X-ray Emission from Metal Electrodes in a High-current Glow Discharge <i>A.B. Karabut and E.A. Karabut and P.L. Hagelstein</i>	217
First-principles Studies of Electronic and Ionic Transport in Palladium Hy- drides/Deuterides <i>N. Luo and George H. Miley</i>	241

PREFACE

A brief history of New Energy Technologies (NET) symposia at the American Chemical Society (ACS) national meetings and associated events is provided. The ACS is the world's largest scientific society.

In 2007, the Division of Environmental Chemistry of the ACS allowed Jan Marwan, of Marwan Chemie, Research & Development, to organize a symposium on New Energy Technologies, which was to include Low Energy Nuclear Reactions (LENR). The first NET symposium occurred at the 233rd ACS National Meeting in Chicago, IL. The one-day symposium occurred on the last day of the meeting. There were two sessions in this historic symposium and presenters included Steve Krivit, Jan Marwan, Vladimir Vysotskii, George Miley, Mel Miles, and Pam Boss. Although attendance was light at this first NET symposium, the Environmental Chemistry Division did ask Jan Marwan to organize a proceedings book. Jan Marwan and Steve Krivit worked together to organize the Low Energy Nuclear Reactions Sourcebook, Fig. 1.

In August 2008, at the 236th ACS National Meeting in Philadelphia, PA, the Division of Environmental Chemistry allowed Jan Marwan to organize a second NET symposium. There were two sessions in this one-day symposium that occurred on the next to last day of the national meeting. Well-recognized researchers in the field of LENR presented at this second NET symposium. Presentations by Antonella De Ninno, Akito Takahashi, XingZhong Li, and Thorsten Ludwig gave the symposium an international flavor. This symposium resulted in the Low Energy Nuclear Reactions Sourcebook Volume 2, Fig. 2, which was edited by Jan Marwan and Steve Krivit.

The year 2009 marked the 20th anniversary of the Fleischmann-Pons announcement that their electrochemical cells were producing more heat than could be accounted for by chemistry. By happenstance, the 237th ACS National Meeting was being held in Salt Lake City, UT in March - where it all began. The third NET symposium had six sessions over three days. The symposium started on the first day of the national meeting. All six sessions were well attended. On March 23rd, the anniversary of the Fleischmann-Pons announcement, ACS held a press conference. Participants of this press conference were Jan Marwan, Steve Krivit, John Dash, Mahadeva Srinivasen, Antonella De Ninno, and Pam Boss. This press conference prompted the Discovery Science channel to run a short segment on the SPAWAR Systems Center results during their "BRINK" program that aired on March 27th.

As a result of the third NET symposium, Jan Marwan and Steve Krivit were invited to write a review article on LENR for the Journal of Environmental Monitoring (JEM). In this review article, which published in September 2009, they discussed the 1989 Fleischmann-Pons press conference and the events that preceded it, which culminated in that infamous press conference. They discussed the controversy resulting from the press conference and how, despite the manner in which LENR was announced, scientists world-wide went into their laboratories to replicate the effect. Marwan and Krivit summarized the 20 years of research in LENR as well as bubble fusion. They discussed both experimental work as well as efforts in developing theories to account for the observed reaction products. Kirk Shanahan, from the Savannah River National Laboratory in SC, wrote a lengthy critique of the Marwan-Krivit review paper. The editor of JEM gave the original authors of the work critiqued by Shanahan an opportunity to rebut his comments. Both the Shanahan critique and the LENR researchers rebuttal were published back-to-back in August 2010.

As it turns out, 2009 was one of the high points for LENR. On April 19, 2009, "60 MINUTES" aired a story on LENR profiling the research done by Energetics Technologies LLC as well as their collaborative work with SRI International and ENEA. CBS asked Robert Duncan, vice chancellor for research at the University of Missouri and an expert in low-temperature physics, to look into the LENR research. Duncan read some of the published papers and he met with researchers at the Energetics laboratory in Israel. He became convinced that the excess heat effects were real and on May 30, 2009, the University of Missouri hosted a LENR symposium that was webcast. On November, 2009,

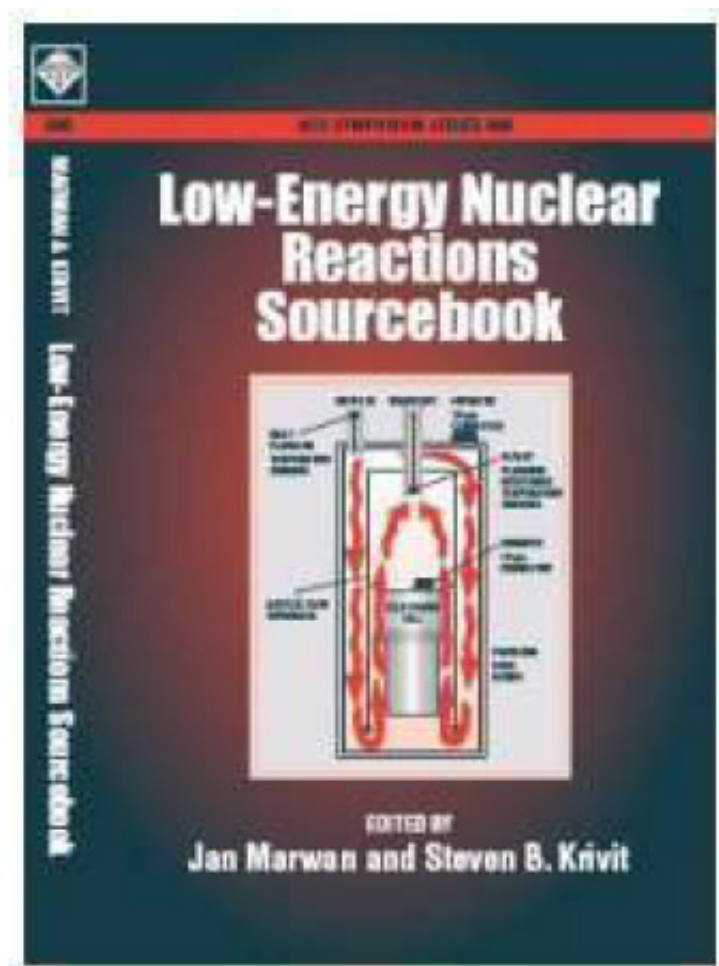


Figure 1. Cover of the ACS NET symposium book (Vol. 1).

the Defense Intelligence Agency (DIA) released a report on LENR warning US officials of the possibility of technology surprise.

In 2010, the fourth NET symposium was held in March at the 239th ACS National Meeting in San Francisco, CA. The symposium was scheduled for the first two days of the conference. There were four sessions over two days. Again the sessions were well attended. There was a second press conference in which the participants were Mel Miles, George Miley, Vladimir Vysotskii, Peter Hagelstein, Mike McKubre, and Jan Marwan.

After the third NET symposium, Marwan began to organize a symposium book to be published by the American Institute of Physics (AIP). The title of the book was "LOW ENERGY NUCLEAR REACTIONS: The Information Fundamental Source". At about the same time, ACS contacted Marwan about publishing a third volume of the LENR Sourcebook. The ACS papers had been submitted to Marwan and were under review when, in July 2010, ACS declined to publish Volume 3. The AIP book was ready for publication when, on October 5, 2010, Marwan was informed by AIP

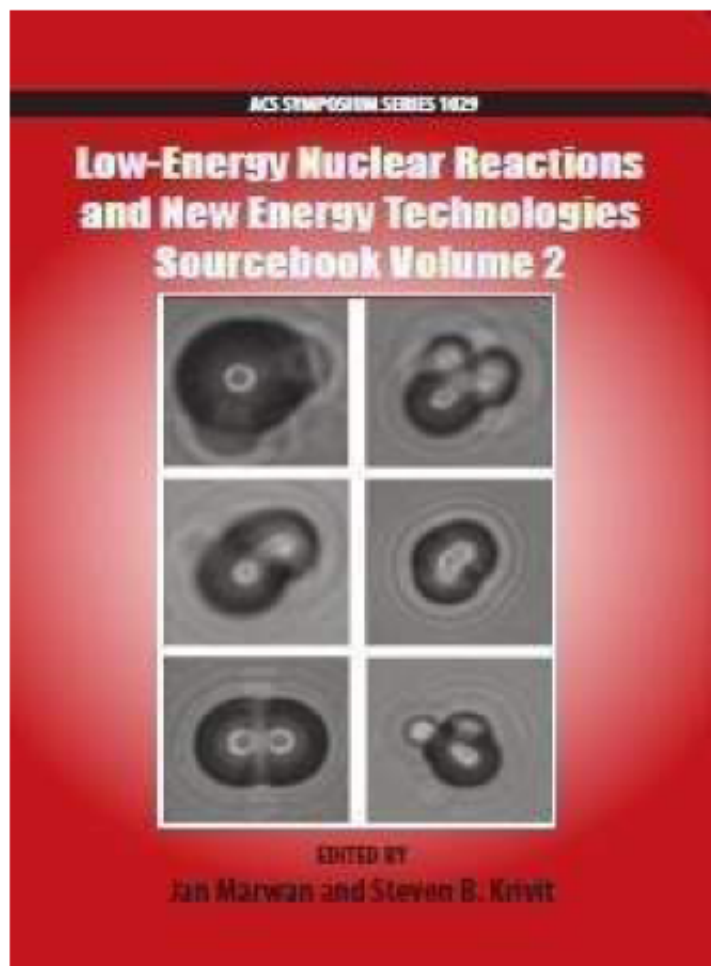


Figure 2. Cover of the ACS NET symposium book (Vol. 2).

that they were declining to publish the proceedings book. The papers for the AIP proceedings book were eventually published in Volume 4 of JCMNS. The papers of the ACS proceedings book are being published in this volume of JCMNS.

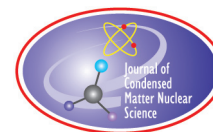
The fifth, and as it turns out final, NET symposium was held in March 2011 at the 241st ACS National Meeting in Anaheim, CA. The symposium was scheduled for the first two days of the conference. There were three sessions over those two days. The sessions were well attended, but were not accompanied by a press conference.

In July 2011, Jan Marwan indicated that he was unable, because of time constraints, to organize a sixth NET symposium for the 243rd ACS National Meeting that will be held in March 2012 in San Diego, CA. Those of us who participated in the first five NET symposia are grateful to Jan for organizing those symposia. When the call came from ACS for organizing a symposium, Fran Tanzella, of SRI International, gauged the CMNS community for interest in

presenting at a sixth NET symposium. The response was favorable. As a result, Fran Tanzella, Pam Boss, and Mel Miles agreed to work together to organize a sixth NET symposium. A NET symposium proposal was submitted to the Division of Environmental Chemistry of ACS and the request was rejected. The Environmental Chemistry Division said that, although the NET sessions were well attended, the attendees were primarily researchers in the LENR field. Fran Tanzella sent an E-mail indicating that, while that was true of the first two symposia, it was not true for the last three. At least half of the attendees at the last three symposia were not known researchers in the LENR field. Given this information, he then asked the Division to reconsider their rejection of a sixth NET symposium, but there was no reply.

As indicated above, the ACS is the world's largest scientific society, and it is noteworthy that they sanctioned five NET symposia and the publication of two symposia books. The purpose of this brief history was to document those symposia and events either directly or peripherally. In many ways, LENR is in the same position as Dan Shechtman was when he first discovered the icosahedral phase in 1982. This discovery opened the new field of quasi-periodic crystals and led to Shechtman's Nobel Prize in Chemistry in 2011. At the time, Shechtman's discovery was extremely controversial and he experienced several years of hostility. The head of his research group told him to "go back and read the textbook." Linus Pauling said, "There is no such thing as quasicrystals, only quasi-scientists." Despite the current set-back with the ACS, we believe that the future of LENR is bright. We believe that it is only a matter of time before we unlock the key interactions and move toward scaling up to become useful technology in the world of energy.

*Fran Tanzella
February 2012*



Research Article

When Bubble Cavitation becomes Sonofusion

Roger S. Stringham *

First Gate Energies, PO Box 1230, Kilauea, HI 96754, USA

Abstract

Experimentally, excess heat, Q_x , and ^4He are the measured fusion products of transient high-density sonofusion, SF. A possible path to DD fusion is explained by piezo driven cavitation bubbles, where the critical parameters are temperature, pressure, acoustic input, and frequency that control, for a picosecond, the low-energy nuclear reactions that produce DD fusion events. The electromagnetic, EM, pulse compressed deuteron clusters squeezing them into a Bose Einstein Condensate. The BEC cluster environment provides for the direct conversion of fusion energy into heat and ^4He . The continuous production of 10^{16} bubbles/sec produces radiation free usable heat as observed via ejecta site surveys.

© 2012 ISCMNS. All rights reserved.

Keywords: BEC, Charged-plasma, Clusters, High-density, Sonofusion

1. Introduction

The high transient density of inertial confined fusion, ICF [1,2] along with new astrophysical information and the ultra low-temperature bosons and fermions [3] are linked and can be applied to a sonofusion, SF, model by way of sub-nanometer deuteron clusters. The SF cluster systems are 1000 times faster and 10^{18} times smaller in volume, m^3 , and number of particles than the hot fusion ICF systems [4]. The SF model is a series of sequential steps where the cavitation and jet are already well established in mainstream science. The formation of transient clusters and their compression is more speculative. The determination of a heat source from ejecta site data is the logical interpretation of scanning electron microscopy, SEM, photos of ejecta site surveys on exposed target foils [5]. The products measured are ^4He and heat via mass spectroscopy and calorimetry. A tentative explanation of a path to the produced fusion products of heat, Q_x , and ^4He needed an explanation with the association of the collapsing bubble, the jet, the sonofusion deuteron cluster, the heat pulse, and the ejecta site [4,6].

2. Sonofusion Process

Some of the basic information on the well-documented cavitation processes that produce very high transient energy densities is reviewed [7]. Cavitation is known to be a destructive force but in sonofusion this force is turned around

*E-mail: firstgate@earthlink.net

to produce useful heat in a transient DD fusion environment via transient cavitation bubbles, TCBs, in circulating D₂O. A resonating piezo is the source of the sonofusion driven acoustic power. The feedback oscillator driven piezos produce a variable size bubble population where the natural individual resonance properties of a bubble couple with the parameters of pressure, temperature, and acoustic power of the cavitating D₂O. In recent years at higher frequencies of 1600 kHz, piezo resonance reduces the damage characteristics found using lower frequencies. The initial bubble passes through phases in a microsecond where its resonant radius of about 0.2 μm grows isothermally gaining mass and size to a maximum radius of about 2 μm immediately followed by its violent adiabatic collapse to its final radius of about 0.02 μm producing sonoluminescence, SL, and a high-density jet. At 1.6 MHz the volume increase in the one cc reactor volume of the D₂O will increase about 1%. This frequency will generation of 10^{10} of 4 μm diameter bubbles, maximum, in one acoustic cycle or $10^{16}/\text{s}$. This number of bubbles has the potential of producing 10^{17} clusters/s and 10^5 W. Experimentally for a 40 W Qx the 1.6 MHz system is working at an efficiency of $40/10^5 = 0.0004$.

During its collapse, a tremendous increase in the bubble's energy density occurs where the external pressure controls the initial energy density in the circulating D₂O. An adiabatic bubble collapse shows a one-hundred-fold decrease in the bubble radius and leads to about a 10^6 increase in energy density. Ideally this is the case but surface oscillations and shock waves are a reality and dampen the bubble's energy density during one acoustic cycle. The high-density jet produced at collapse has a structure of exterior sheath electrons transferred from the bubble's interface. These high velocity electrons are involved in an EM z-pinch compression of the jet's contents. The jet implants dense a plasma of electrons and deuterons into a target foil that immediately separate. The deuterons cluster as an EM picosecond pulse produces a cooling and compressing environment for BEC fusion that producing Qx, heat, and ⁴He.

3. Jet Formation and SL

The TCB bubble jet is formed by the violent implosion of the bubble in the cavitating D₂O acoustic field. The acceleration collapse process produces jets composed of dissociated D₂O, a partial plasma [4]. The jet's outer and inner surface is the stretched collapsing bubble surface, an electron sheath, enclosing a picosecond z-pinch deuterium plasma. The produced sonoluminescence has been used to monitor SF, and is a tool for looking at the plasma condition at that instant of photon emission measured with a photo-multiplier device. Managing the parameters of temperature, pressure, and acoustic input controls the plasma condition for a particular piezo frequency. The reactor sonoluminescence measurements relate the condition of implanting plasma into an accelerating projection of the bubble interface into the form of a jet. There are many more jets formed than are implanted into the target foil and there are other reactor geometries that may be superior, but for the present the ability to observe sonoluminescence with the disk configuration is necessary for control of sonofusion's intensity observation. Only those jets within a few μm of the target surface will implant. The transient change of the bubbles into jets has been photographed [5].

4. The Jet Squeeze of the High-Density Plasma Jet

The velocity of sheath electrons and the orientation of water's surface tension molecules provide for electromagnetic compression fields. The concentric layer model of the jet plasma and its high velocity sheath electrons make for a complex z-pinch of the jet's plasma contents and helps explain the jet's transient geometry. The jet is conical, construction consisting of a series of concentric layers starting with the outside water-deuteron interface, outer sheath electrons, the deuteron plasma, inner sheath electrons, and vacuum inner-core [4]. During the several picoseconds lifetime of the jet, it will implant the target foil before its natural z-pinch destruction. From the TCB metamorphosis, the jet's contents of deuterons and electrons are further compressed by electromagnetic, EM, pressures, via z-pinch forces, to higher densities in the order of 10^{32} D⁺/m³. The jet 20 Mach sheath electrons result from the final stage of the TCB [4] and the jet z-pinch. The total compression pressure's confinement of the jet contents is enhanced by

its passage through the cavitating D₂O dielectric. During this jet implantation the already dense plasma of the jet is further compressed. During this short time frame the jet will appear to be passing through a glass dielectric. The jet is on its way to a target implantation. The jet contents are implanted into the target foil lattice where the D⁺ and e⁻ are momentarily separated.

5. Implantation and Cluster Formation

Figure 1 shows the deuteron cluster compression pulse just after the jet implant into the target foil. The impulse pressure of the Coulombically attracted cluster's free electrons produce a picosecond implosive EM pressure pulse that exceeds the cluster's repulsion relatively constant Coulombic escape pressure. Deuterons and electrons enter as an implanted dense plasma jet with the high impact velocity of a meteor, 30 k/s. At the point of jet impact into the target foil the jet implant energy is about equal to a single DD fusion event. Those electrons loosely associated with the higher energy levels of the deuteron atom were stripped of their remaining electron via lattice stripping and are part of the populations of separated deuterons and free mobile electrons. During the following femtoseconds the surrounding mobile electrons are directed via Coulombic implosive forces that clump deuterons into nm spheres, forming the deuteron cluster before Coulombic forces separate the D⁺. The positive charge of the implanted deuterons attracts all surrounding free electrons to the cluster's center and can be compared with laser compressed 2 mm deuteron capsules, Inertial Confined Fusion [1]. During the picosecond EM compression pulse, the build up of compression heat is removed by cooling via evaporating surface deuterons of the BEC cluster contents. The energy of deuteron and electron recombination, 14.7 eV, occurs one nm away from the BEC cluster contents and produces a compression shock wave. The momentum exchange from the evaporation of cluster surface deuterons adds to the EM compression.

The BEC's high transition temperature, T_c , for clusters is based on its large energy gap between ε_0 and ε_1 that exist for the nuclear shell-model for deuterons in the picosecond EM pulse absence of electrons. Clusters cooled by evaporation should show a separation decrease associated with the de Broglie wave, λ_{Tc} , where a deuteron phase BEC may exist. D⁺ at ε_0 , the ground state, with the next energy level, with regard to its shell-model, of $\varepsilon_1 = 2.31$ MeV makes for a high T_c of millions of degrees for a picosecond for the cluster [8,9]. This is quite different from the electron shell energy level where one finds the next level above ground state about 0.06 eV.

The cluster is a squeezed BEC; for example, a 1 nm diameter of a million boson deuterium ions, or a smaller number, is cooled by the evaporation of its exterior cluster deuterons. In this example at 4000 K has a low T compared to the cluster's T_c . As the D–D cluster's separation decreases, the de Broglie wavelength over-lap increases. So the T/T_c ratio decreases improving the cluster's BEC character. It is important to keep the temperature, T , of the cluster low. The initial cluster radius of 0.5 nm is squeezed to 0.05 nm. There is a tendency for the cluster contents to heat as the cluster radius compresses to 0.1 radius. and the cluster volume approaches the density of muon fusion, 10^{36} D⁺/m³. The initial cluster density is 10^{30} to 10^{33} D⁺/m³. There is some evidence in Fig. 3(a) of super-dense transient clusters that fell through the Pd lattice target foil leaving gaping holes, perhaps initiated by tremendous transient cluster gravitational forces that broke out of the Pd lattice containment. A density of 10^{35} D⁺/m³ is 3.3×10^8 kg/m³ for a 1 nm cluster.

The Coulombic escape pressure of the cluster is much less than the implosive EM pressure pulse during the cluster's picosecond lifetime but is a constant force and after a picosecond the cluster will self-destruct through Coulombic repulsion pressures if no fusion occurs. The cluster coherence, superfluid properties, comes from the high-density low temperature of the cluster having a de Broglie deuteron wave much broader than the DD separation, $10^{-9} - 10^{-12}$ m, in the very dense cluster. The BEC nature of the cluster alters the path to the cluster's fusion event's products, which are heat, Qx , and ${}^4\text{He}$ with no gammas. If one compares muon fusion, MF, to SF, one finds the SF deuteron separation can be driven close to DD separation of MF. This path attempts to explain the products Qx and ${}^4\text{He}$, sonofusion's experimental measured results. The difference is the ability of the SF BEC deuteron cluster to absorb the fusion heat pulse before any gamma can be produced. This fusion environment is the result of the cluster's BEC nature. The cluster

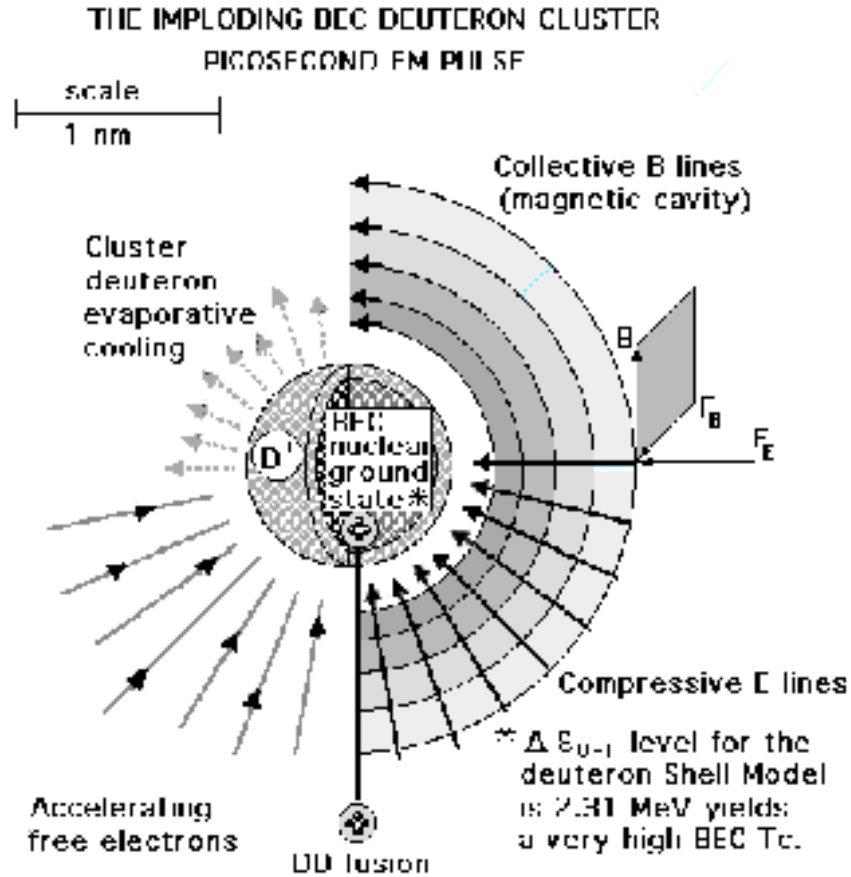


Figure 1. The spherical EM compressing E field and collapsing B field after the jet implantation creates a BEC D^+ cluster – a picosecond implosion pulse.

provides a large heat sink that immediately absorbs all the fusion $Q\alpha$ heat before other available paths such as the one oscillation required producing a 24 MeV gamma.

This is in contrast to muon fusion that has only two deuterons of mass, not enough to alter its fusion products of neutrons, gammas and helium, but can be viewed as a pseudo BEC phenomenon.

The implantation of jet electrons followed by deuterons produces clusters, schematically shown in Fig. 1. The figure shows a cluster with its EM compression pulse and the immediate neighborhood involving about a 3 nm volume with a 1 nm cluster volume. The clustered imploding picosecond EM pulse, divided into four over-lapping time phases, is shown during its BEC and fusion product formation. The one million deuteron clustered ions separation, $10^{-10} - 10^{-11}$ m, initial to a final diameter, 10^{-12} m, is squeezed by an EM compression pulse [11]. The simultaneous aspects are: lower right the compressive E field lines, black arrows; lower left the accelerating free electrons, gray arrows; upper left the surface deuterons evaporating from the cluster surface cooling the BEC contents, broken arrows; the upper right shows the spherical containment of the B magnetic lines that squeeze the cluster, progressive gray spheres.

The black arrows show the EM implosion compressing pulse where the perpendicular 3D E field is a squeezing

pulse. The curved black arrows parallel to the cluster surface show the spherical magnetic 3D B field that forms the magnetic cavity of cluster containment during the EM picosecond cluster squeezing process. The evaporative cooling deuterons, the broken gray arrows in the upper left, remove heat from the cluster and eventually may recombine with some of the free accelerating electrons, away from the BEC contents. Electrons compress the cluster with their picosecond E field pressure pulse that exceeds the cluster's continuous Coulombic repulsion for a picosecond before D^+ repulsion or a fusion event destroys the cluster. The surrounding EM B and F_B are spherical, at right angles, and parallel to the cluster surface squeezing collectively as accelerating electrons advance to the surface, shown in Fig. 1. These self-generated B field lines contain the cluster in a magnetic cavity. The F_B force and B field are not enough to deflect the electrons on their short path to the cluster center. The curvature of the electron path, gray arrows, influenced by F_B of the accelerating electrons is minimal. During this picosecond the cluster of deuterons has been squeezed to a BEC superfluid shown as the dark dots representing D^+ . The remaining interior deuterons are cooled by surface deuteron evaporation, one-half of the cluster's total deuterons, gray arrows, keep the BEC cool. Deuterons evaporated from the cluster's sphere surface may pick up an electron removing 14.7 eV away from the cluster. Fusion probably takes place near the cluster's surface, the four small spheres make an alpha. A spherical fusion heat pulse immediately fills the BEC, before any gamma formation, destroying the cluster and moving through the target lattice breaking the surface and escaping into the circulating D_2O releasing the Q_x heat and helium four.

6. Experimental Results

6.1. Heat pulse

There have been more than twenty years of cavitation experiments coupled to fusion products heat and ^4He . It was determined, in the last 5 years, that the driving piezo resonant acoustic frequency shows a connection to the extent of cavitation damage via ejecta site size and distribution in target foils. The lower the frequency the greater the observed damage to the target foils. At high frequencies, 1.6 MHz, the ejecta sites remain small and are basically limited to one 20 MeV fusion event. The 1.6 MHz bubble systems involve much smaller numbers of deuterons, smaller jets, and smaller clusters. The ejecta site SEM photos of 1.6 MHz experiments show mostly single fusion events where the lower frequencies show both single and multiple fusion events. The population of these low-frequency multiple fusion events may be as high as 10^6 events. These large ejecta sites produce extensive damage to the target foils.

The frequency changes the acoustic input as to bubble size, and implantation, but not the energy density at the final stage of the bubble collapse as measured by sonoluminescence. The amount of energy that forms the ejecta site in the target foil is a function of the ejecta site diameter. Small area target foil surveys of ejecta site diameter population distribution of typically exposed target foils at different frequencies are shown in Figs. 2(a)–(c). Three frequencies were used in the experiments of sonofusion systems, 20, 46, and 1600 kHz (A–C). These had different ejecta size population distributions. See Figs. 2(a) and (c). These target foil ejecta site distributions are related to their energy by the diameter size (volume of ejecta) of each observed ejecta site. In this model the 50 nm diameter ejecta site equates to 20 ± 10 MeV as the ejecta site depth varies with the cluster deuteron implantation depth. The volume was calculated as the depth $2 \times$ radius times the ejecta area. Of the three frequencies (A) at 20 kHz is the most destructive to the target foil. These ejecta sites had the highest bubble energy input, and produced the largest number of fusion events per cluster. The data for 20 kHz (A) systems was extrapolated from (B) and (C) population distributions because the SEM resolution at frequency (A) was low, around $0.3 \mu\text{m}$. The damage at (A) was too low a resolution to do a proper survey. See Figs. 2(c) (A) and 3(a) and (b). Frequency, (B), at 46 kHz and 20 nm field emission SEM resolution showed, via survey, a decided decline in the severity of ejecta damage of exposed foils and showed fewer multiple fusion events per cluster than (A), but made up this discrepancy with an increase in the number of bubbles that formed implanting jets. Frequency of 1.6 MHz, (C), shows almost no visible damage except for a slight color change to the target surface. SEM photo of (C) and Fig. 5(a) and (b) shows many small single ejecta sites, about 50 nm in diameter, and few double sites.

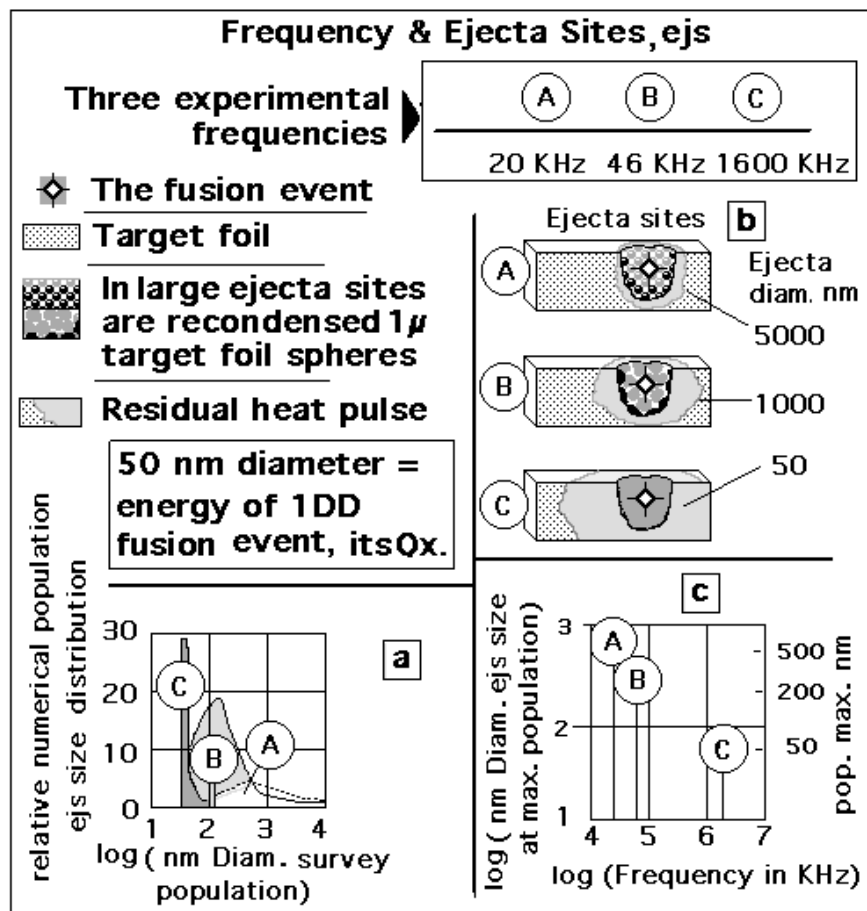


Figure 2. a, b, and c. The frequency influences the sizes of the cavitation bubble, the jet, the cluster, the heat pulse, and the ejecta sites. 2a is the ejecta site population distribution. 2b is the ejecta size. And 2c is the population distribution maximum. Ejecta volume is proportional to the cluster fusion events, single or multiple events.

At (C) the fusion event population was almost exclusively from single fusion events.

From surveys of the distribution of ejecta sites with respect to size (energy), Fig. 2(a), shows the dominance of small clusters at (C) resonance and their single fusion events. The lower resonance frequencies, (A) and (B), have fewer ejecta sites but show a majority of multiple fusion events.

Figure 2(b) shows the difference between the fusion energy in a single fusion event and multiple events originating in a cluster. The fact that the heat pulse ejects larger and more energetic clusters at lower frequency results in ejecta sites recondensed target foil spheres, 1 μ m in diameter, in and around the heat pulse's ejecta site. The energy densities of (A)–(C) show sonoluminescence. The 50nm diameter ejecta site (C) shows a population almost entirely of single fusion event clusters. If the location of the cluster is too deep in the lattice, below the lattice surface, there may not be enough energy in the heat pulse to reach the target foil lattice surface. The Q_x will be distributed in the foil where it is removed by the circulating D_2O . In this case a small amount of helium four will be captured in the lattice and will not

be collected as a gas for analysis. This helium is still in the foil and can be analyzed at a later date. The conditions, 1.6 MHz, of (C) make the Pd target much more suitable for commercial use. What (C) loses in number of fusion events per cluster it gains from the increased number of the much smaller transient cavitation bubbles and increased small cluster production in the target foil

Evidence of fusion events in Fig. 2(b) where ejecta volume of target foil vapors leaves behind 1 μm spheres of condensed Pd at the ejecta site at frequencies (A) and (B). The spheres are found imbedded on ejecta site walls and as free particles at the site. The target foils in the (C) system, 1.6 MHz, are free of the 1 μm particles as the particles are larger in diameter than the (C) ejecta site diameters. Note the residual heat pulse is distributed into the target foil lattice and remelts the adjacent lattice of earlier produced ejecta sites

Graph 2c for a given frequency shows that surveys of population of ejecta size diameters have a maximum number relating to cluster size. This population maximum size changes as the eject size distribution narrows with increasing frequency. The maximum ejecta size population is shown for each resonance frequency. The energy of the heat pulse from (A) and (B) destroys the target foil. In (C) there may not be enough energy to always break the surface of the foil. The foil may contain non-ejected ^4He as compared to a foil at (A) that shows little increase in ^4He residing in the target foil lattice as most is ejected into the D_2O . The magnitudes of chemical and nuclear events should be kept in mind.

6.2. Ejecta sites

Figures 3(a) and (b) are two SEM photos at 20 kHz (A) cavitation inputs exposing 100 μm thick Pd target foils to cavitating D_2O in Woodside Laboratory, CA in 1993. The damage to this foil was extreme showing large ejecta events shown in SEM photos 3(a) and 3(b), where 10 μm ejecta site with loose 1 μm spheres were piled up inside its rim. See Fig. 2(c) (A). Figure 3(a) shows the general Pd surface terrain that needs to be resolved to make the ejecta survey count. A straight-line extrapolation of (B) and (C) in Fig. 2(c) is the maximum population number for (A).

Figures 4(a) and (b) are two field emission SEM photos at 46 kHz (B) with cavitation inputs exposing 100 μm thick 50 cm^2 Pd target foil, which includes both sides from a run at Stanford Research International, SRI. There have been many such foils and all show this type of ejecta damage at (B). Only a few exposed target foils have been analyzed via SEM photos. About 50% of the target foil surface in the sonofusion reactor comes in contact with the intense cavitation field that produces transient cavitation bubbles. The surface here is typical of the Pd target foil surfaces that have been photographed, and run at frequency (B). See Figs. 2(b) and (c) (B). Figure 4(c) shows the general Pd surface terrain that is expanded to about 1 square μm , 3d, for the ejecta survey count at 46 kHz exposed Pd target foil surface. This survey includes 21 ejecta sites with a wide distribution of ejecta site volumes.

Figures 5(a) and (b) are two FE SEM photos at 1600 kHz (C) with cavitation inputs exposing 100 μm thick Pd target foil from the First Gate lab in Kilauea, HI. The 1.6 MHz reactors were about 20 g compared to 5 kg for the 46 kHz devices. The one square μm of the field emission SEM photo 3(f) was surveyed and a total of 30 sites were found with a very narrow population distribution that consisted of 29 50 nm diameter sites, single fusion events, and one multiple ejection sites of two or three fusion events. This surface is much different showing no visual damage, only the very small events that appear not to lose target foil mass. See Fig. 2(c) (C). Figure 5(a) shows the general Pd surface terrain that shows the close packed 50 nm ejecta sites and survey count for the 1600 kHz, (C), exposed Pd target foil surface.

The SEM photos of sonofusion target foils exposed to cavitating D_2O at different acoustic driving frequencies are shown in Figs. 3–5. These are the same frequencies described for Figs. 2(a)–(c) and represent typical SEM analysis photos and survey counts of ejecta sites. Ejecta site survey distributions in small typical areas of exposed target foil are from SEM photos, Figs. 3(b), (4b), and (5b). The SEM photos of these figures correlate with Figs. 2(a)–(c). Figures 3(a) and (b) were SEM photos by John Dash at Portland State University. The other SEM photos taken by Jane Wheeler of Charles Evans lab in Sunnyvale, CA, using a JOEL 6400 FE SEM with better resolution. SEM photos by Lorenza Moro at SRI, not shown, were of targets foils of different elements [11].

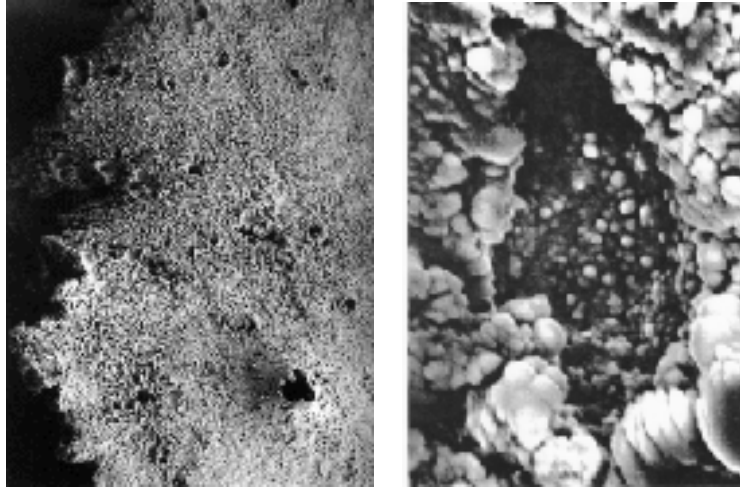


Figure 3. a SEM photo of a Pd target foil ejecta site at a frequency of 20 kHz shows the ejecta damage to the foil surface. (Maybe some high density gravitational effects) scale, 20 μm across. SEM photos 3(a) and (b), John Dash. (b) SEM photo of a detail of 3(a), a large ejecta site, in a Pd target foil exposed to 20 kHz cavitation shows one of the large multi-fusion events showing the 1 μm diameter sphere debris in the vent. Woodside, CA Lab. 1993.

There is a lot more analysis work to be done with 60 exposed target foils in storage. Only a few Pd foils are shown here but the sample is a good cross section for demonstrating the differences between acoustic frequency inputs. The damage done to the target foils varies and establishes a relation between cluster size and ejecta size, number of fusion events per ejecta, and the constant energy density of these sonoluminescence systems.

Calculating the heat pulse kinetic energy of the ejected target foil mass that is vaporized, Pd heat of vaporization is 377 J/kg°C, and ejecta mass velocity for a total of about 6×10^{-12} J for a single event. The volumes of ejected target lattice atoms, numbering 3×10^6 Pd atoms, are ejecta from a site at the resonant frequency of (C). See Fig. 5(b). The energy of one DD fusion event producing ^4He is about 4×10^{-12} J. The (C) cluster ejection sites of the surveyed foil surface found in a 1 μm^2 area are 30–50 nm in diameter and about equivalent to the energy of one DD helium fusion

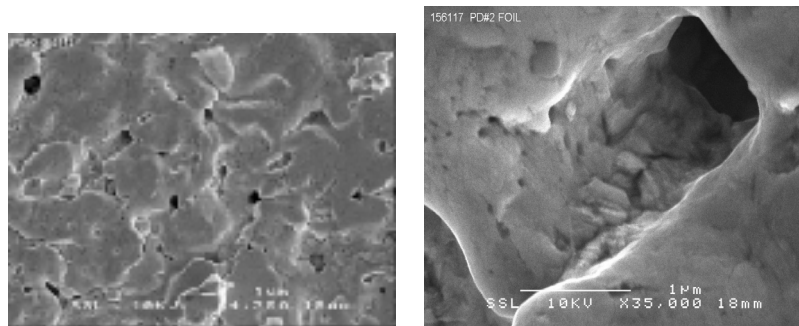


Figure 4. a) SEM photo of a Pd target foil ejecta sites at a frequency of 46 kHz shows the ejecta damage to the foil surface. Much milder damage than 20 kHz. SEM photos, Scale 1 cm = 4 μm (b) Detail from 4(a) SEM photo of several square μm of 4(a) Pd target foil exposed to 46 kHz cavitation shows the diversity of the ejecta population. Scale 1 cm = 1 μm . SEM photos, Jane Wheeler, Evans Lab., Sunnyvale CA. Foil from SRI, Menlo Pk. CA.

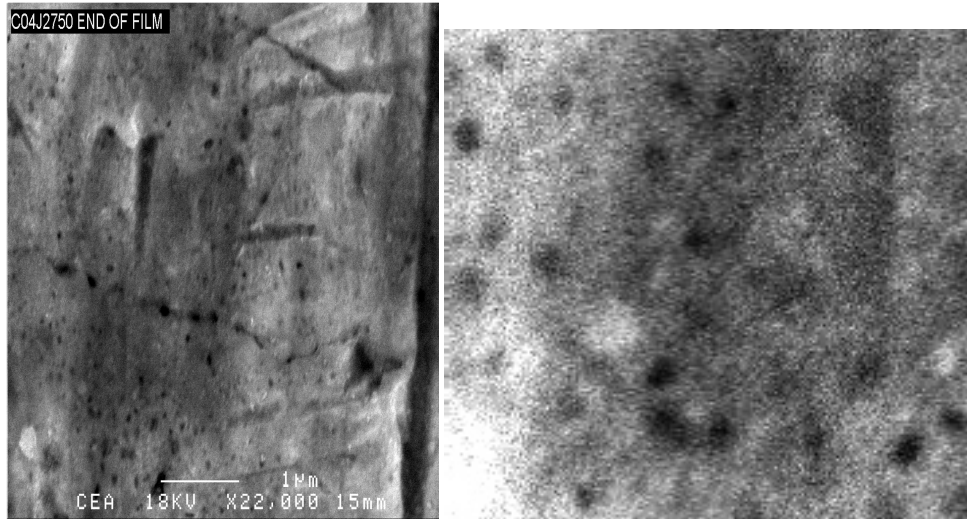


Figure 5. (a) SEM photo of a Pd target foil with ejecta sites at a frequency of 1600 kHz shows the ejecta damage to the foil surface. The damage is minimal to the exposed foil surface. Scale 1 cm = 1 μm . (b) Detail from 5(a) SEM photo of a square μm of 3e Pd target foil exposed to 1.6 kHz cavitation shows the uniformity of the ejecta population in the 50 nm diameter range. Scale 2 mm = 50 nm. Jane Wheeler, Evans Lab., Sunnyvale, CA. Foil from First Gate, Kilauea, HI.

event. (It is expected that the same results will be found in exposed target foils of other elements.) A spherical heat pulse expands through the Pd lattice until it reaches the foil surface where the heat pulse breaks the plane of the foil surface and ejects the contents of the ejecta site into the circulating D_2O at a velocity of about 3000 m/s. The fusion heat pulse starting a temperature of 10^9K expands its lattice volume spherically to 4000 K ejecta temperature. The instant the cavitation process is stopped the surface is frozen and allows for a leisurely SEM photo analysis of the foil surface. One often sees, via SEM, in the interior of the larger vent sites, 2000–10,000 nm in diameter, 1 μm and smaller diameter spheres of recondensed target foil that loosely coalesce in and on the target foil vent site surface, Fig. 2(b). The path from the jet plasma formation to the ejecta site is reasonable, but not the only path to DD fusion.

7. Discussion

Measured fusion heat and nuclear products show that a non-obvious path is necessary to explain experimental results. Calorimetry measures the excess heat, Q_x . The calorimetry used was the D_2O flow through type and is described in [4]. One measures ΔT of D_2O at measured flow rate F . The Joules of heat exiting, $\Delta T \times F \times 4.669 = Q_o$, are measured. The specific heat constant for D_2O of 4.669 J/(g K) is from [12]. The acoustic watts input are measured, Q_a . $Q_o - Q_a = Q_x$, the excess heat in watts, DD fusion heat, and is a product along with measured ^4He .

The nuclear products measured by mass spectroscopy from gases collected during experiments at 20 kHz (A) on Pd foil system by the DOE's Brian Oliver showed 452 ppm of ^4He in the 50 cm^3 sample volume [4,6]. Fusion products escaped the target lattice via the heat pulse ejecta into circulating D_2O where gases were collected and sampled. Also measured by mass spectroscopy were T and ^4He and ^3He from experiments with D_2O cavitation exposed Ti foil [11]. In earlier experiments in 1990, inductively coupled plasma MS measurements showed the presence of the lone isotope Cs 112 [13].

Nuclear products, gammas and/or neutrons associated with hot fusion, measured and not found. So, one must explain the measured ^4He production as originating in a piece of matter like a BEC cluster. Here is a dense environment

that produces ${}^4\text{He}$ and Qx before any other products can be formed. The result is usable energy without harmful long-range radiation.

The muon, μ , fusion of two deuterons, if thought of as a pseudo BEC, is a parallel to sonofusion. The overlap of the Boson $\text{DD}\mu$ at 10^{-12} m separation and the increasing fusion rate as the temperature is lowered, fit BEC muon fusion phenomena.

The environment of sonofusion is cavitated, Ar saturated, and reactor circulated D_2O . A target foil is carefully placed in the reactor. A cavitation produced transient deuteron cluster of BEC deuterons is implanted into the lattice, and serves as the containment for this sub-nano scale cluster. The initially dense cluster is further compressed and cooled by evaporative surface deuterons of the cluster. These interact with free electrons away from the cluster-forming deuterium atoms that surround the cluster. This leaves the cluster cooler but with fewer deuterons. These Coulombic accelerating free electrons produce an imploding spherical electromagnetic pulse that squeezes the cluster to fusion densities in less than a picosecond. These electrons are hot enough and will pass through the evaporative-formed deuteron ions to the fresh surface of the clustered deuterons to keep the implosion pulse compressing for about 0.1 ps. The compressing cluster approaches the density of muon ion $\text{DD}\mu^+$. The fusion event initiates a heat pulse destroying the cluster. The spherical heat pulse travels into and through the lattice to the target foil surface. There it erupts with lattice ejecta, Figs. 3–5, and fusion products ${}^4\text{He}$ and heat are ejected into the D_2O , and measured by mass spectroscopy and calorimetry. Left behind in the target foil are ejecta sites frozen in the target foil, easily analyzed by SEM, and their ejecta size relates to the number of fusion events per site via the energy of their ejecta volume.

An interesting comparison between SF and muon fusion are its density and BEC nature. In a conversation with Steve Jones, who was historically involved in early cold fusion, regarding his muon fusion experiments stated the colder the μ bombardment of liquid deuterium the faster the fusion rate. The de Broglie wave function overlap in the $\text{DD}\mu^+$ will increase at lower temperatures decreasing the T/T_c ratio, decreasing the amount of contact time needed per fusion event in that chain reaction. This is the case if the cluster density is $10^{36} \text{ D}^+/\text{m}^3$. Sonofusion may respond to the same lowering of the cluster temperature via recombination and a more favorable fusion environment.

The system of cavitating D_2O in a piezo-produced acoustic field creates cavitation bubbles as a precursor to high-density implanting plasma jets, Bose Einstein Condensate clusters, where fusion events occur. A good review of single bubble cavitation and densities produced during the collapsing bubble and other pertinent cavitation data about water bubbles in their final stages of collapse can be found in reference [4]. As the Mach 4 surface collapse of the cavitation bubble [14] terminates the bubble, an ejection of some of the collapsed bubble plasma contents compresses and dissociates D_2O , forming high density jet plasmas. The dense z pinch accelerating plasma jet is injected into the cavitating D_2O via the bubble collapse and implants into a target foil, where for a picosecond EM-squeezed and evaporated cooled BEC clusters fuse producing excess heat and ${}^4\text{He}$. The BEC fusion environment has a high ion density and is superconducting. Unique properties relate to BEC cluster MeV D^+ energy levels via its nuclear shell model. The fusion heat pulse that terminates the cluster explodes from the target foil surface as ejecta carries vaporized target foil and fusion products into the D_2O . All of the above can be found in my earlier papers and in references [4,6].

It is interesting that the visually observed Pd surface of an exposed 2-mm thick target did not show the damage found in the $100 \mu\text{m}$ Pd foils. The thin Pd foils show very obvious ejecta damage and also strong induced MHz standing wave forms in the (A) and (B) resonance system, Fig. 2 [11]. If one looks at the 4000 K of the cluster, the T/T_c ratio of 0.000002 should provide a good fusion environment for BEC fusion. It is the fusion in the transient BEC clusters contained in the $100\text{-}\mu\text{m}$ thick Pd target foil that produces target foil ejecta sites.

8. Summary

The system of cavitating D_2O in a piezo produced acoustic field creates cavitation bubbles as the Mach 6 surface bubble collapse terminates with the jet and sonoluminescence, and the sequence to fusion continues. High-density lattice

implanting z-pinch plasma jets provides a picosecond separation of deuterons and electrons. The accelerating free electrons trap some deuterons in an EM pulse forming 1 nm deuteron clusters. The picosecond EM pulse overwhelms the cluster's Coulombic repulsion squeezing deuteron Bose Einstein Condensate clusters. The pulse provides for dense and evaporative cooled environments for DD fusion events. The fusion heat, Q_x , produced a heat pulse that expels fusion products of Q_x and ^4He from the lattice. The escaping fusion heat pulse leaves SEM observable ejecta sites. This is the proposed sequential path to clean usable energy.

The normal BEC forms at ultra low temperatures because in ordinary matter, it includes electrons. The BEC exists only between the ground state and the next energy level, maybe 0.06 eV. However, in the deuteron cluster, for a picosecond, the next level above ground state is 2.32 MeV [9] as there are no electrons. The cluster EM compression pulse is stronger than the Coulombic repulsion for a picosecond. That is enough contact time for the BEC cluster fusion event to occur.

The BEC is composed of Bosons, even numbered spins (deuterium, ^4He , H_2 , H_2^{2+} , etc.). Fermions have an odd numbered spin like $1/2$ for electrons, protons, and neutrons, where two protons may form an electron free Boson cluster. The Fermion protons may assume a Boson mode by pairing, and for a picosecond have the properties of a BEC that leads to the observed lattice ejecta effects [15]. Fermions have the ability to couple, forming bosons and may explain their damaging effects in cavitating target foils in H_2O .

Acknowledgements

I would like to thank Julie Wallace, Jim Reiker, and Dick America for their support over many years of work, and also Dennis Letts, Fran Tanzella, Steve Krivit, Joe McDowell, Joel Garbon, Jan Marwan, Scott Chubb and many others for helping to put these ideas into the mainstream.

References

- [1] R.D. Petrasso et al., Proton radiography of inertial fusion implosions, *Science* **319** (2008) 1223–1225.
- [2] M.A. Liberman, J.S. De Groot, A. Toor and R.B. Spielman, *Physics of High-Density Z-Pinch Plasmas*, Springer-Verlag, NY, 1998, p. 19 and pp. 238–241.
- [3] T. Fukuyama and M. Morikawa, Relative BEC Model for Matter and Energy, ESO Astrophysics Symposia, *Relativistic Astrophysics and Cosmology- Einstein's Legacy*, Springer-Verlag, NY, 2007, p. 96.
- [4] R.S. Stringham, *Sonofusion, Deuterons to Helium Experiments*, ACS, LENR sourcebook, Vol. 2, Jan Marwan and Steve Krivit (ed.), 2009.
- [5] Y. Tomita and A. Shima, High speed photographic observations of laser induced cavitation bubbles in water, *Acoustica* **71** (1990) 161. M.P. Felix and A.T. Ellis, Laser-induced liquid breakdown – a step by step account, *Appl. Phys. Lett.* **19** (1971) 484. W. Lauterborn and J. Bolle, Experimental investigations of cavitation- bubble collapse in the neighborhood of a solid boundary, *Fluid Mech.* **723** (1975) 91.
- [6] R.S. Stringham, *Model for Sonofusion*, AIP Conference Proc., San Francisco, CA, LENR, Jan Marwan (ed.), 20–21 March 2010, To be published.
- [7] M.P. Brenner, S. Hilgenfeldt and D. Lohse, Single bubble sonoluminescence, *Rev. Modern Phys.* **74**(2) (2002) 425–484.
- [8] N.D. Cook, *ICCF-15 Proceedings*, Poster, V. Violante (ed.), Rome, Italy, 2009, to be published.
- [9] M. Ragheb, *Deuteron Disintegration in Condensed Matter*, 2007, <https://netfiles.uiuc.edu/mragheb/www/NPRE%20402%20ME%20405%20Nuclear%20Power%20Engineering/Deuteron%20disintegration%20in%20condensed%20matter.pdf>
- [10] S. Badiei, P.U. Andersson and L. Holmlid, Production of ultradense deuterium: A compact future fusion fuel, *Appl. Phys. Lett.* **96** (2010) 96, 124103-1
- [11] R.S. Stringham, *ICCF-15 Proceedings*, Poster, V. Violante (ed.), Rome, Italy, 2009, to be published.
- [12] M. Nakamura, K. Tamura, S. Murakami, Isotope effects on thermodynamic properties: mixtures of $x(\text{D}_2\text{O or H}_2\text{O}) + (1-x)\text{CH}_3\text{CN}$ at 298.15 K, *Thermochim. Acta* **253** (1995) 127–136.

- [13] R.S. Stringham, Fusion product analysis – ICP of Pd 108 \diamond Cs 112 by Samantha Tam, Balazs Laboratories, Sunnyvale, CA (1990). No other Cesium isotopes detected.
- [14] K.R. Weninger, P.G. Evans and S.J. Putterman, Time correlated single photon Mie scattering from a sonoluminescing bubble, *Phys. Rev. E* **61**(2) (2000) 1020.
- [15] Y. Kim, Theory of BEC mechanism for deuteron-induced nuclear reactions in micro/Nano-scale metal grains and particles, *Naturwissenschaften* **96** (2009) 803–811.



Research Article

Characterization of Neutrons Emitted during Pd/D Co-deposition

Pamela A. Mosier-Boss *

Research Laboratory of Electronics, MIT, Cambridge, MA 02139, USA

Frank E. Gordon †

Global Energy Corporation, Annandale, VA 22003, USA

Lawrence P.G. Forsley

JWK International Corp., Annandale, VA 22003, USA

Abstract

Experiments using CR-39 detectors have shown that energetic particles and neutrons are emitted during Pd/D co-deposition. Using 6 μm Mylar between the CR-39 and the cathode, it has been shown that the majority of the tracks formed have energies on the order of 1–3 MeV. This conclusion was supported by computer analysis of the pits using the 'Track_Test' program developed by Nikezic and Yu. In this communication, additional analysis of the detectors will be discussed. In particular, it will be shown that the size distribution of the neutron-generated tracks on the back side of the CR-39 detectors are consistent with the occurrence of DD and DT fusion reactions. This is supported by the presence of triple tracks in the CR-39 as well as the energies of the charged particles as determined in the Mylar experiments.

© 2012 ISCMNS. All rights reserved.

Keywords: Co-deposition, CR-39 detectors, Heterostructures, Photomicrographs, Triple tracks

1. Introduction

In the inertial confinement fusion (ICF) field, CR-39 is a solid state nuclear track detector (SSNTD) used to detect energetic particles such as alphas, protons, deuterons, and tritons as well as neutrons [1]. Because CR-39 is an allyl glycol carbonate plastic, it is not affected by the electromagnetic pulse (EMP) that disables electronic detectors in ICF experiments. When energetic charged particles travel into or through a CR-39 detector, they create along their ionization track a region that is more sensitive to chemical etching than the rest of the bulk. After treatment with an etching agent, tracks remain as holes or pits whose size and shape can be measured. The attributes that make CR-39

*E-mail: pboss@san.rr.com.

†Retired.

the detector of choice for ICF measurements also make it an ideal detector for detecting particle emissions in the Pd/D system. Also, since CR-39 detectors are examples of constantly integrating detectors, events are permanently stamped on and, in the case of neutrons, inside the detector. This is particularly important for systems, like Pd/D, that exhibit low flux rates and/or events that occur in bursts. Table 1 summarizes the strengths and weaknesses of SSNTDs [2].

Table 1. Strengths and Weaknesses of SSTDs [2].

Strengths	Weaknesses
Small geometry—trails of damage are nm/ μ m in diameter and length	Lack of real-time capability
Long history and selectivity of track recording – SSNTDs can retain a record of activity for billions of years	Poor charge and energy discrimination—track size/shape depends upon the charge and mass of the particles as well as the angle of incidence. There is significant overlap in the size distributions of the tracks due to energetic particles
Existence of thresholds for registration – SSNTDs can register particles only if their charge and LET value are above a threshold	Variability in SSNTDs – environmental conditions and manufacturing procedures results in problems of precision and reproducibility
Ruggedness and simplicity Inexpensive Integrating capability Can respond to both charged particles and neutrons	Lack of theoretical understanding – no theoretical work explains how certain properties of materials can predicate or ascertain a viable ability for track formation/retention

Investigators who have used CR-39 detectors in Pd/D electrolysis experiments include Oriani and Fisher [3], Roussetski [4], and Lipson et al. [5–7]. The experimental configurations employed and results are summarized in Table 2. Based upon the success of these earlier experiments, the use of CR-39 detectors in Pd/D co-deposition experiments was explored.

In the Pd/D co-deposition experiments, the tracks are concentrated in areas where the cathode was in contact with the CR-39 detector [8]. A comparison of tracks obtained from a known alpha source and those obtained as a result of Pd/D co-deposition is shown in Fig. 1. Figure 1(a) shows tracks obtained when a CR-39 detector is exposed to alphas from an ^{241}Am source. Tracks obtained as a result of Pd/D co-deposition are shown in Fig. 1(b). For the top images of Figs. 1(a) and (b), the microscope optics are focused on the surface of the detectors. The tracks are dark in color and either circular or oval in shape. When the microscope optics are focused on the bottom of the pits, bottom images of Figs. 1(a) and (b), a bright spot inside the track is observed. Tracks are conical in shape and the bright spot observed inside the track is due to the tip of the cone acting like a lens when the detector is backlit. As shown in Fig. 1, the features of the tracks obtained as a result of Pd/D co-deposition are consistent with those obtained for alpha-particle generated tracks. A series of control experiments were done that showed that the Pd/D co-deposition tracks were not due to radioactive contamination of the cell components nor to either chemical or mechanical damage [8]. Experiments were done placing 6 μ m thick Mylar between the CR-39 detector and the cathode indicating that the majority of tracks on the front surface have energies on the order of 1–3 MeV [9]. These conclusions were supported by track modeling and analysis using linear energy transfer (LET) curves.

Table 2. Summary of CR-39 Results obtained by other investigators.

Experimental configuration	Results
Pd sheet foil, electrolysis in Li_2SO_4 in D_2O , CR-39 placed above and below Pd cathode [3]	Track density of electrolysis experiments ($150\text{--}3760\text{ tracks cm}^{-2}$) greater than controls ($59\text{--}541\text{ tracks cm}^{-2}$)
Au/Pd/PdO heterostructures, load with D electrolytically, remove from cell and place in contact with CR-39, cycle temperature for 1 h [4]	Observed triple tracks due to the carbon breakup reaction. The number of tritons needed to create triple tracks greater than the yield of DD tritons.
Au/Pd/PdO heterostructures, load with D electrolytically, remove from cell and place in contact with CR-39, cycle temperature for 1 h [5]	Tracks detected in CR-39 that were consistent with 2.5–3.0 MeV protons and 0.5–1.5 MeV tritons
50 μm thick Pd foil, electrolysis in Li_2SO_4 in H_2O , CR-39 placed in contact with Pd cathode [6]	Tracks concentrated in areas where the cathode was in contact with the CR-39 detector
Thin Pd films, electrolysis in Li_2SO_4 in H_2O , Cu and Al spacers placed between CR-39 and Pd cathode [7]	Tracks in CR-39 detectors consistent with 11–16 MeV alphas and 1.7 MeV protons

In addition to tracks on the front surface of the CR-39 detectors, tracks have also been observed on the backside of the 1 mm thick detectors. In this communication, the nature of the tracks observed on the back surface of the CR-39 detectors are discussed.

2. Experimental Procedure

Cell assembly and experimental procedures have been described elsewhere [8,9]. In these experiments, the CR-39 detectors are placed in close proximity to the cathode, as illustrated in Fig. 2(a). This is due to the energy losses the particles sustain as they traverse through water. The deposit formed as a result of Pd/D co-deposition, Fig. 2(b), has a cauliflower-like morphology that traps pockets of water. Because of the morphology of the Pd deposit, the thickness of the water layer will vary. Linear energy transfer (LET) curves are used to determine how far an energetic, charged particle can travel through a medium of known composition and density. In this investigation LET curves were calculated using the SRIM-2003.26 code of Ziegler and Biersack [10]. This code can be downloaded from the <http://www.srim.org/> website. The LET curves, shown in Fig. 2(c), illustrate the impact a thin water film, of varying thickness, has on the energy of the charged particles.

Prior to using a CR-39 detector in an experiment, one corner on the side facing away from the cathode is exposed to an ^{241}Am source. This provides an internal standard that can be used to account for variability in the CR-39 detectors. By having an internal standard on the same detector used in an experiment assures that both sets of tracks experience identical experimental and etching conditions. The track images shown in Fig. 1 were from the same CR-39 detector. At the completion of the experiment, the cell was disassembled and the CR-39 detector was etched in 6.5 N NaOH solution for 6 h at 62–68°C. After etching, the CR-39 detector was analyzed using either a Nikon Eclipse E600 microscope or an automated track analysis system.

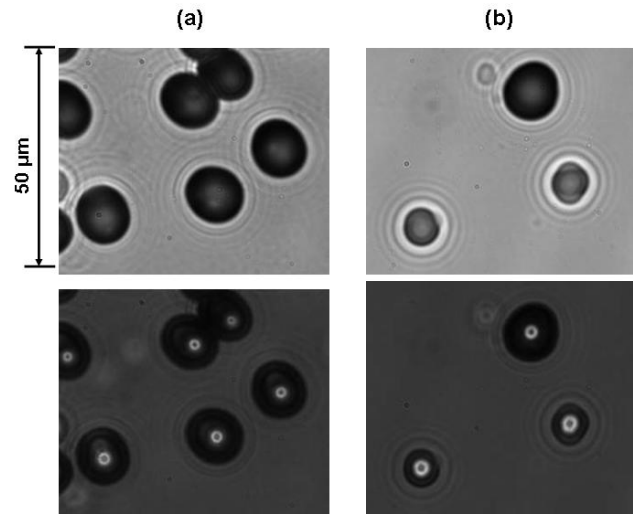


Figure 1. Images of tracks on CR-39 obtained (a) upon exposure to an americium-241 alpha source and (b) as a result of a Pd/D co-deposition experiment on a Au cathode. Both sets of tracks were on the same CR-39 detector. In the top images, the focus is on the surface of the CR-39 detector. The bottom images are an overlay of two images taken at two different focal lengths (top and bottom of pits).

3. Results and Discussion

3.1. Neutron interactions with CR-39 detectors

The possible interactions of DD neutrons (2.45 MeV) and DT neutrons (14.1 MeV) are described in Fig. 3(a). In the interaction shown in case 1, the DD and DT neutrons can scatter elastically, producing recoil protons, carbons, or oxygen nuclei in the forward direction. But DT neutrons can also undergo two inelastic (n,p) and (n, α) reactions with carbon or oxygen, cases 2 and 3, respectively, in Fig. 3(a). These inelastic reactions result in charged particles that can produce tracks on the front and/or the back surfaces of the CR-39 detector. Phillips et al. [11] have shown that neutron spectrometry can be done using CR-39. At low neutron energies (0.144 MeV), only recoil protons are seen and are observed as a peak at $\sim 10 \mu\text{m}$ neutron, Fig. 3(b). As the neutron energy increases, a broadening of the proton recoil peak at $\sim 10 \mu\text{m}$ is observed. At 1.2 MeV neutron energy, a second peak is visible at $\sim 25 \mu\text{m}$. This second peak is attributed to recoil carbon and oxygen atoms. For neutron energies between 1.2 and 8 MeV, the size distributions of tracks observed in the CR-39 detectors are roughly similar. In the CR-39 detector exposed to 14.8 MeV neutrons, a decrease in the proton recoil at $\sim 10 \mu\text{m}$ is observed, Fig. 3(b), and a peak is observed at $\sim 35 \mu\text{m}$ which is attributed to the three alpha particle reactions.

3.2. Characterization of tracks observed on the backside of the CR-39 detectors

Earlier it was reported that tracks had been observed on the backside of a CR-39 detector at the end of a Pd/D co-deposition experiment [13]. The CR-39 detectors used in these experiments are 1 mm in thickness. The LET curves

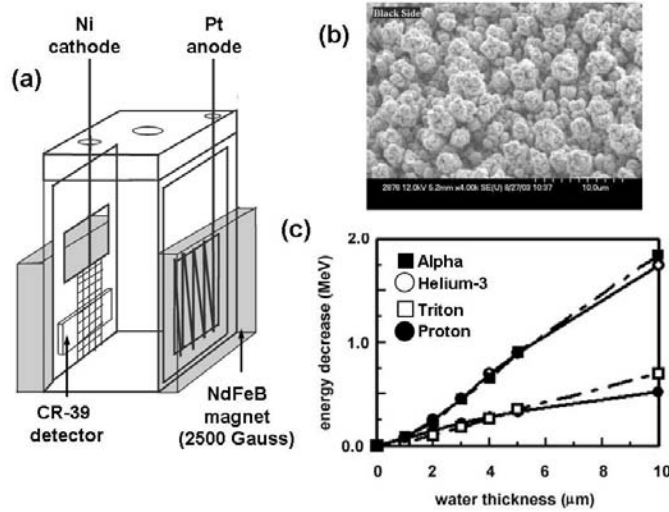
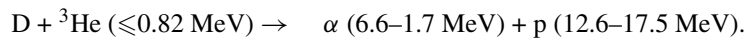
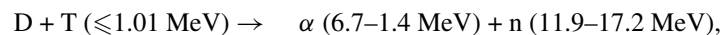


Figure 2. (a) Schematic of the cell showing the placement of the CR-39 detector. (b) SEM image showing the morphology of the Pd deposit created on a Au cathode as a result of Pd/D co-deposition. Reprinted with permission from *Eur. Phys. J. Appl. Phys.* [8]. (c) LET curves showing the decrease in energy of the charged particles as a function of water thickness.

indicate that the only particles that can traverse through 1 mm thick CR-39 are ≥ 40 MeV alphas, ≥ 10 MeV protons, and neutrons. Figure 4 shows the size distribution of the Pd/D generated tracks observed on the backside of the detector. The tracks range in size from 5 to 40 μm . A 40 MeV alpha would leave a ~ 5.5 μm diameter track on the front surface of the detector [6]. A 10 MeV proton would leave a ~ 1.7 μm diameter track on the front surface [14]. When a charged particle passes through a medium, it causes extensive ionization of the material [15]. The particle loses energy as it travels through the medium and eventually stops. As the particle loses energy and slows down, the extent of the damage caused by the ionization decreases. After etching, the resultant track has a conical shape. Consequently, the diameter of the track is largest on the surface where the particle entered the detector than inside where the particle stops. This indicates that the diameters of the 40 MeV alpha and 10 MeV proton generated tracks on the back surface of the CR-39 detectors will be significantly smaller than the diameters on the front surface. Since the track size distribution, shown in Fig. 4, ranges between 5 and 45 μm , it is unlikely that the observed tracks are due to ≥ 40 MeV alphas and ≥ 10 MeV protons.

In Fig. 4, the size distribution of the Pd/D generated tracks is overlaid with the size distributions of tracks obtained for CR-39 detectors exposed to 2.45 and 14.8 MeV neutrons. The peaks attributed to recoil protons, recoil carbon and oxygen, and carbon shattering are indicated. The 2.45 and 14.8 MeV neutrons are created by DD and DT fusion, respectively. The primary DD reactions and secondary DT and D^3He are:



As shown in Fig. 4, these neutrons can be differentiated simply by examining the size distribution of the tracks. Compared to DT fusion, the recoil proton peak observed for DD fusion is shifted to larger track size. The shift to larger track size is probably due to the fact that the DD neutrons are less energetic than the DT neutrons. The energy transferred to a proton is less when hit by a DD neutron than with a DT neutron. Less energy results in bigger tracks. For DT fusion, a peak is observed between 30 and 40 μm that is attributable to the carbon breakup reaction. This peak is absent in the DD fusion track size distribution. The size distribution obtained on the back side of a CR-39 detector that had been used in a Pd/D co-deposition experiment exhibits features consistent with both DD and DT fusion. Both the CR-39 track size distributions obtained for DT fusion and Pd/D co-deposition show tracks between 30 and 40 μm that are attributable to the carbon breakup reaction. This peak is absent in the DD fusion track size distribution. The recoil proton peak observed for the Pd/D co-deposition track size distribution has both a small track size (DT) and large track size (DD) contribution. These results suggest that both DD and DT fusion reactions are occurring. These conclusions are further supported by the Mylar experiments and the track modeling [16]. In these experiments a 6 μm thick Mylar spacer was placed between the CR-39 detector and the cathode. These experiments indicated that the majority of the charged particles leaving tracks on the front surface of the detector have energies on the order of 1–3 MeV. This energy range is consistent with the energies of charged particles formed as a result of the primary DD and secondary DT and D^3He reactions.

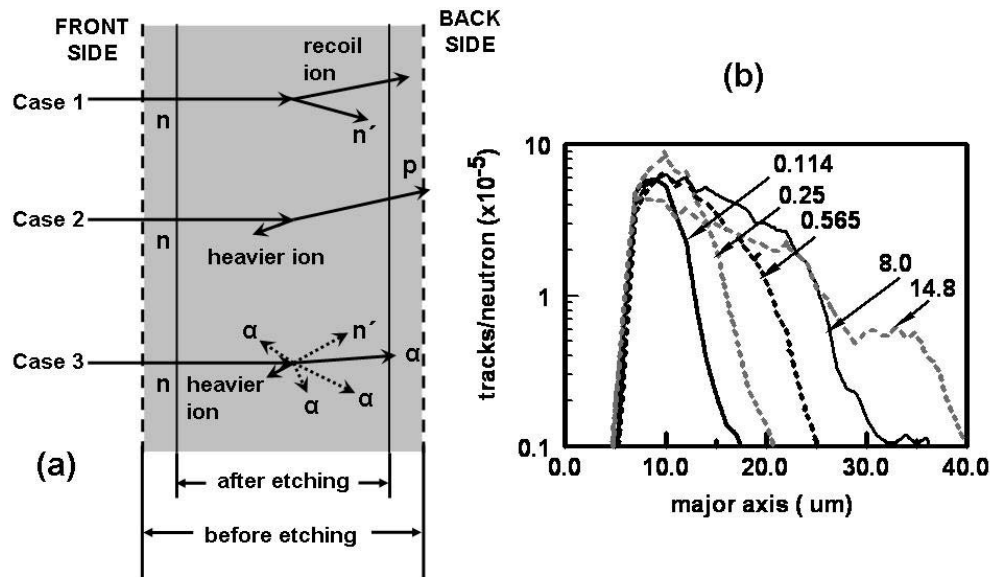


Figure 3. (a) Schematic drawing of the CR-39 track detector and the neutron interaction processes that can take place inside the plastic [12]. The drawing is not to scale. Case 1 summarizes the DD neutron interaction with CR-39. Cases 1–3 describe the DT neutron interactions with CR-39. Reprinted with permission from Naturwissenschaften [17]. (b) Track size distribution for CR-39 detectors that have been exposed to neutrons [11]. The energies of the neutrons, in MeV, are indicated.

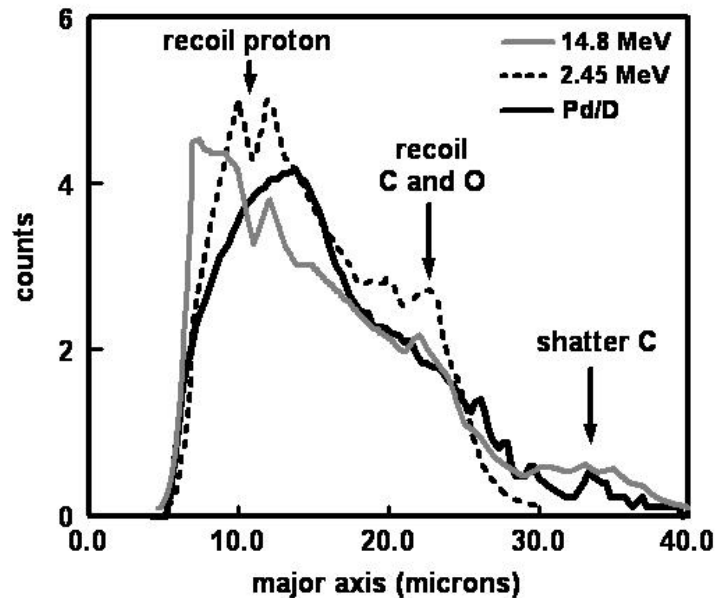


Figure 4. Track size distribution for CR-39 detectors that have been exposed to 2.45 and 14.8 MeV neutrons are overlaid with the track size distribution obtained on the backside of a CR-39 detector used in a Pd/D co-deposition experiment.

3.3. Visual comparison of Pd/D tracks with neutron generated tracks and the results of sequential etching

A photomicrograph of tracks observed on the backside of a CR-39 detector that was used in a Pd/D co-deposition experiment, Fig. 5(a), is compared with a photomicrograph of tracks resulting from exposure to a ^{238}PuO , broad-spectrum neutron source, Fig. 5(b). In both photomicrographs, it can be seen that the tracks are primarily circular in shape. However, some tracks are circular with a small tail, indicated by arrows in Figs. 5(a) and (b). These are recoil protons that have exited the CR-39 at an angle less than 90° . Small tracks are also observed in these photomicrographs. Some of these smaller tracks are indicated by a circle in Figs. 5(a) and (b).

As illustrated in Fig. 3(a), neutron interactions can occur anywhere throughout the CR-39 detector. These smaller tracks are attributed to tracks that are deeper inside the CR-39 detector. These latent tracks can become prominent with additional etching of the CR-39 detectors, as shown in Figs. 5(c) and (d). In Fig. 5(c), three very large tracks are observed. These tracks originally appeared on the surface of the detector after the first etch. After additional etching these three tracks got much larger. The lower two tracks have pear-like shapes with tails. These features indicate that the particles that created these tracks came in at an oblique angle. These two tracks are lighter in color than the top track. This indicates that the bottom two tracks are shallower than the top track. Again this indicates that the particles that created these tracks came in at an oblique angle. In contrast, the top track is circular in shape and is much darker in color than the other two surface tracks. These features are consistent with a particle entering the detector at a $\sim 90^\circ$ angle. To the left of this track, a much smaller track is observed that is elliptical in shape. This smaller track resulted

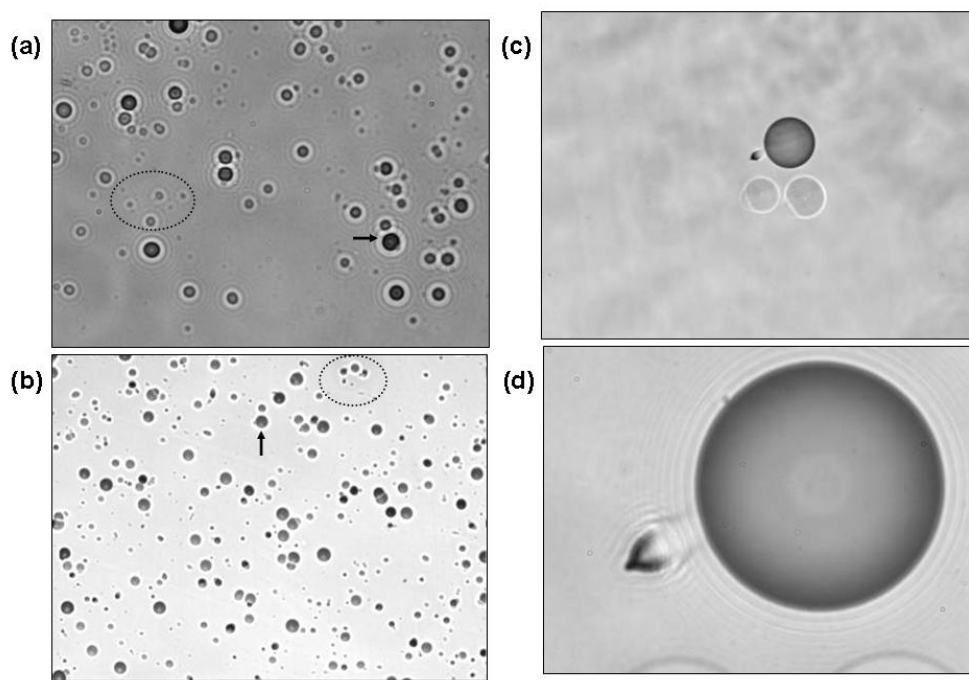


Figure 5. Photomicrograph of tracks observed (a) on the backside of a CR-39 detector used in a Ag/Pd/D co-deposition, magnetic field experiment and (b) on a CR-39 detector exposed to neutrons from a ^{238}PuO source (image supplied by Gary Phillips). Magnification $200\times$. Latent tracks are circled. Arrow indicates circular tracks with a small tail. Results of sequential etching of the CR-39 detector where (c) was taken at a magnification of $200\times$ and (d) was taken at a magnification of $1000\times$.

from a neutron hitting an atom deeper inside the detector. Given the size and shape of this track, it is most likely a recoil proton moving in the forward direction and resulted from the reaction shown in case 1 of Fig. 3(a).

3.4. Triple tracks—evidence of energetic neutrons

Figure 6(a) shows tracks obtained in a Pd/D co-deposition experiment in which a $60\ \mu\text{m}$ thick polyethylene film was placed between the cathode and the CR-39 detector. Besides neutrons, the LET curves indicate that $>2\ \text{MeV}$ protons and $>10\ \text{MeV}$ alphas can penetrate $60\ \mu\text{m}$ thick polyethylene. In Fig. 6(a), a triple track is observed among the solitary tracks. As the density of tracks in this region is low, it is unlikely that this triple track is due to overlapping tracks. Examination of the bottom of the track, Fig. 6(b), shows three individual lobes breaking away from a center point. It is unlikely that such a structure would be observed for three tracks that overlap randomly. A triple track, such as the one shown in Fig. 6, is indicative of a reaction resulting in the formation of three particles of equal mass and energy. This reaction is the carbon break up reaction illustrated in case 3 in Fig. 3(a) and provides additional evidence of the emission of neutrons by the Pd/D system [17]. In the carbon breakup reaction, an energetic neutron creates a metastable ^{13}C atom in the CR-39 detector, which then shatters into three alpha particles. The residuals of this reaction can be viewed in the CR-39 detector as a three-prong star where each prong represents each charged particle that occurs in the

decay [18].

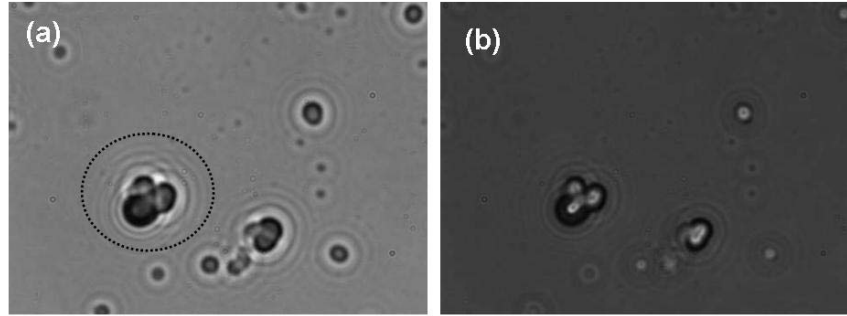


Figure 6. (a) Image of a triple track (circled) among solitary tracks on a CR-39 detector used in a Au–Ag–Pt three wire experiment done in the presence of a magnetic field. (magnification 1000×). In this experiment, a 60 μm thick piece of polyethylene was between the detector and the cathodes. This photomicrograph was obtained by focusing the optics on the surface of the detector. (b) Overlay of two photomicrographs taken at different focal lengths (surface and bottom of the pits).

Figure 7(a) shows another triple track. This triple track was created in a Pd/D co-deposition experiment in which the cathode was in direct contact with the CR-39 detector. Looking inside the track, Fig. 7(b), it can be seen that the alpha track designated α_3 is separated from the other two tracks. The threshold energy of the neutron required to shatter a carbon atom to form a three-prong star is 9.6 MeV [19]. Knowing the threshold energy needed to shatter a carbon atom and the distance each alpha particle of the triple track has traveled in the detector, the energy of the neutron that created that triple track can be estimated. The LET curve shown in Fig. 7(c) is used to determine the stopping distance of alphas in CR-39 as a function of alpha-particle energy. The energy of the neutron is given by the following relationship:

$$E_n = E_{\text{th}} + E_{\alpha 1} + E_{\alpha 2} + E_{\alpha 3}, \quad (1)$$

where E_n and E_{th} are the energy of the neutron causing the triple track and threshold energy required to shatter a carbon atom, respectively, and $E_{\alpha 1}$, $E_{\alpha 2}$, and $E_{\alpha 3}$ are the energies of the alpha particles. In Fig. 7(b), the distance between the center point and the prongs of the triple track are indicated. Using the LET curve, Fig. 7(c), these distances can be converted into energy. The energies of the alphas are therefore 0.6, 0.9, and 1.2 MeV. The threshold energy of a neutron to shatter a carbon atom is 9.6 MeV. Adding these energies together, the energy of the neutron that created the triple track shown in Fig. 7 is estimated to be 12.3 MeV. In DT fusion reactions, the neutron has an energy ranging between 11.9 and 17.2 MeV.

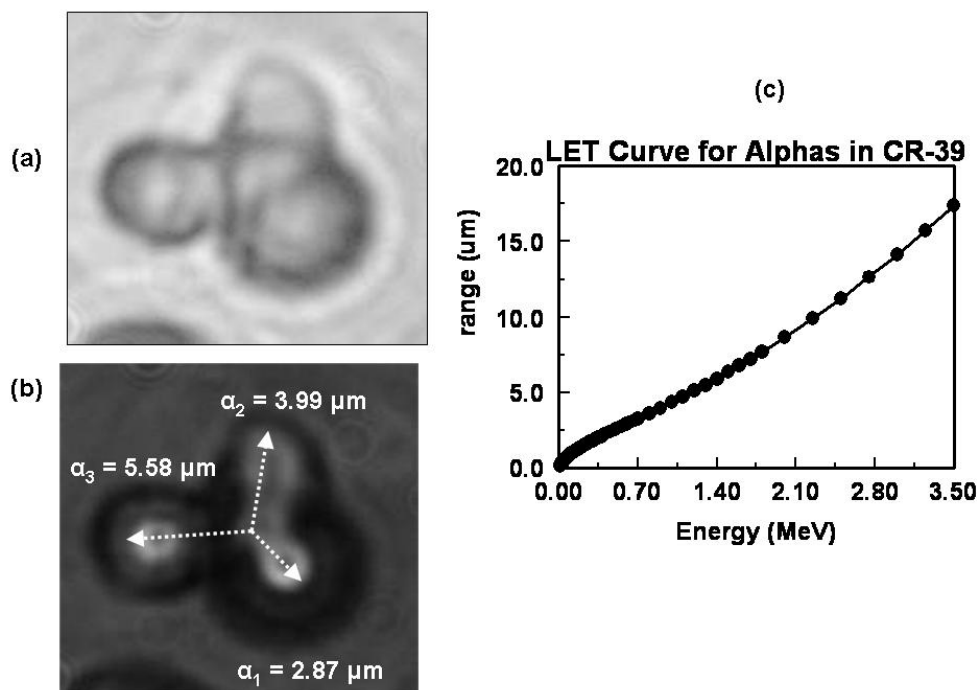


Figure 7. (a) Photomicrograph of a triple track obtained with the optics focused on the surface of the CR-39 detector. Reprinted with permission from Naturwissenschaften [17]. (b) Overlay of two photomicrographs taken at different focal lengths (surface and bottom of the pits). (c) LET curve for alphas in CR-39.

4. Conclusions

CR-39 detectors have been used to monitor the nuclear processes occurring inside the Pd lattice created as a result of the Pd/D co-deposition process. In these experiments, tracks have been observed on both the front and back surfaces of the CR-39 detectors. Mylar spacer experiments, track modeling, and LET curves indicate that the majority of the charged particles on the front surface have energies between one and three MeV. This energy range is consistent for charged particles produced as the result of DD primary fusion reactions. Sequential etching of the CR-39 detectors shows the presence of tracks deeper inside the plastic that are attributable latent tracks due to neutron interactions. Tracks on the backside of the CR-39 detectors range in size between five and forty microns. This size distribution is consistent with neutrons resulting from both DD primary and secondary fusion reactions. The presence of triple tracks, attributable to the carbon breakup reaction, provides additional evidence of neutrons with energies greater than 9.6 MeV. Such neutrons can be formed as the result of DT secondary reactions.

Acknowledgements

This work was funded by the Defense Threat Reduction Agency (DTRA) and JWK Corporation. The authors would like to thank Dr. Gary Phillips, nuclear physicist, retired from the Naval Research Laboratory, US Navy, Radiation

Effects Branch, for valuable discussions in interpreting the data. The authors acknowledge the contributions of Dr. Stanislaw Szpak, who pioneered the Pd/D co-deposition process.

References

- [1] B.G. Cartwright, E.K. Shirk and P.B. Price, A nuclear-track-recording polymer of unique sensitivity and resolution, *Nucl. Instru. Meth.* **153** 1978 (1978) 457–460.
- [2] S.A. Durrani, Nuclear Tracks today: strengths, weaknesses, challenges, *Rad. Measurements* **43** (2008) S26–S33.
- [3] R.A. Oriani and F.C. Fisher, Generation of nuclear tracks during electrolysis, *Jpn. J. Appl. Phys.* **41** (2002) 6180–6183.
- [4] A.S. Roussetski, Application of CR-39 plastic track detectors for detection of DD and DT-reaction products in cold fusion experiments, in *Condensed Matter Nuclear Science: Proceedings of the 8th International Conference on Cold Fusion*, Lerici, La Spezia, Italy, 2000.
- [5] A.G. Lipson, B.F. Lyakhov, A.S. Roussetski, T. Akimoto, T. Mizuno, N. Asami, R. Shimada, S. Miyashita and A. Takahashi, Evidence of low-intensity D–D reactions as a result of exothermic deuterium desorption from Au/Pd/PdO:D heterostructure, *Fusion Technol.* **38** (2000) 238–252.
- [6] A.G. Lipson, A.S. Roussetski, G.H. Miley and C.H. Castano, In-situ charged particles and X-ray detection in Pd thin film-cathodes during electrolysis in $\text{Li}_2\text{SO}_4/\text{H}_2\text{O}$, in *Condensed Matter Nuclear Science: Proceedings of the 9th International Conference on Cold Fusion*, Beijing, China, May 19–24, 2002; X.Z. Li (Ed.), Tsinghua Univ. Press, Beijing, 2002, pp. 218–223.
- [7] A.G. Lipson, A.S. Roussetski, G.H. Miley and E.I. Saunin, Phenomenon of an energetic charged particle emission from hydrogen/deuterium loaded metals, In *Condensed Matter Nuclear Science: Proceedings of the 10th International Conference on Cold Fusion*, Cambridge, MA, Aug. 24–29, 2003, P.L. Hagelstein and S.R. Chubb (Eds.), World Scientific, Singapore, 2006, pp. 539–558.
- [8] P.A. Mosier-Boss, S. Szpak, F.E. Gordon and L.P.G. Forsley, The use of CR-39 in Pd/D co-deposition experiments, *Eur. Phys. J. Appl. Phys.* **40** (2007) 293–303.
- [9] P.A. Mosier-Boss, S. Szpak, F.E. Gordon and L.P.G. Forsley, Reply to comment on the use of CR-39 in Pd/D co-deposition experiments: a Response to Kowalski. *Eur. Phys. J. Appl. Phys.*, **44** (2008) 291–295.
- [10] J.F. Ziegler and J.P. Biersack, *The Stopping and Range of Ions in Solids*, 1985.
- [11] G.W. Phillips, J.E. Spann, J.S. Bogard, T. VoDinh, D. Emfietzoglou, R.T. Devine and M. Moscovitch, Neutron spectrometry using CR-39 track etch detectors, *Radiation Protection Dosim.* **120** (2006) 457–460.
- [12] J.A. Frenje, C.K. Li, F.H. Séguin, D.G. Hicks, S. Kurebayashi, R.D. Petrasso, S. Roberts, V.Y. Glebov, D.D. Meyerhofer, T.C. Sangster, J.M. Soures, C. Stoeckl, G.J. Schmid and R.A. Lerche, Absolute measurements of neutron yields from DD and DT implosions at the OMEGA laser facility using CR-39 track detectors, *Rev. Sci. Instrum.* **73** (2002) 2597–2605.
- [13] P.A. Mosier-Boss, S. Szpak, F.E. Gordon and L.P.G. Forsley, Detection of energetic particles and neutrons emitted during Pd/D co-deposition, *Low-Energy Nuclear Reactions Sourcebook*, 2008.
- [14] F.H. Séguin, J.A. Frenje, C.K. Li, D.G. Hicks, S. Kurebayashi, J.R. Rygg, B.-E. Schwartz, R.D. Petrasso, S. Roberts, J.M. Soures, D.D. Meyerhofer, T.C. Sangster, J.P. Knauer, C. Sorce, V.Y. Glebov, C. Stoeckl, T.W. Phillips, R.J. Leeper, K. Fletcher and S. Padalino, Spectrometry of charged particles from inertial-confinement-fusion plasmas, *Rev. Sci. Instrum.* **74** (2003) 975–995.
- [15] D. Nikezic and K.N. Yu, Formation and growth of tracks in nuclear track materials, *Mat. Sci. Eng. R.* **46** (2004) 51–123.
- [16] P.A. Mosier-Boss, S. Szpak, F.E. Gordon and L.P.G. Forsley, Characterization of tracks in CR-39 detectors obtained as a result of Pd/D co-Deposition, *Eur. Phys. J. Appl. Phys.* **46** (2009) ????.
- [17] P.A. Mosier-Boss, S. Szpak, F.E. Gordon and L.P.G. Forsley, Triple tracks in CR-39 as the result of Pd-D co-deposition: evidence of energetic neutrons, *Naturwissenschaften* **96** (2009) 135–142.
- [18] B. Antolković and Z. Dolenec, The neutron-induced $^{12}\text{C}(n,n')^3\alpha$ reaction at 14.4 MeV in a kinematically complete experiment, *Nuclear Phys. A* **237** (1975) 235–252.
- [19] S.A.R. Al-Najjar, A. Abdel-Naby and S.A. Durrani, Fast-neutron spectrometry using the triple- α reaction on the CR-39 detector, *Nuclear Tracks* **12** (1986) 611–615.



Research Article

Development of a High Temperature Hybrid CMNS Reactor^{†,‡,§}

Francesco Celani,* O.M. Calamai, A. Spallone, A. Nuvoli, V. Andreassi, B. Ortenzi, F. Piastra, E. Righi, G. Trenta and E. Marano

National Institute of Nuclear Physics, Frascati National Laboratories, Via E. Fermi 40, 00044 Frascati (Rome), Italy

P. Marini, V. di Stefano, M. Nakamura and E. Purchi

ISC MNS, RomeNo. 1 Group, Via Lero 30, 00129 Rome, Italy

Abstract

We presents some improvements on the reactor presented at ICCF14 (Washington DC, August 2008): use of long-thin Pd wires with nano-coated surfaces by multi-layers of several elements, loading with D₂ at pressure <10 bar; wires temperatures >500°C; Stainless Steel (SS) reactor wall temperature <100°C; current density along Pd up to 45 kA/cm²; voltage drop along the Pd wire up to 70 V. Mainly, the Pd wire temperature was increased up to 750°C and was improved the temperature detection of anomalous excess heat, if any, using a SS shielded type-K thermocouple: it was put inside a small Cu tube, used as thermal equalizer, where, at the outer surface, both the “active” Pd wire and the “reference” Pt were twisted. The overall results were in agreement with that obtained in 2008 experiments and they confirm the positive effect of high temperatures in increasing the amount of anomalous energy gain. In both the experiments the fast and simple isoperibolic calorimetry was used. Main gas adopted were: He and He (60%)–Ar(40%) mixture, both for calibration purposes; D₂ and D₂(60%)–Ar(40%) as potentially active gas.

© 2012 ISCMNS. All rights reserved.

Keywords: Anomalous effects, Deloading, Hybrid, Isoperibolic calorimetry, Nano-particles

*E-mail: francesco.celani@lnf.infn.it

[†]Collaboration with:

1. F. Tarallo and G. Mariotti, Enel Eng. and Innov. SpA, Via A. Pisano 120, 56122, Pisa, Italy.
2. U. Mastromatteo, STMicroelectronics, Via Tolomeo 1, 20010 Cornaredo, MI, USA.
3. A. Mancini, ORIM SpA, Via Concordia 65, 62100 Macerata, Italy.
4. F. Falcioni, M. Marchesini, P. Di Biagio, and U. Martini, Centro Sviluppo Materiali, Via di Castel Romano 100, 00129 Roma, Italy.
5. L. Gamberale and D. Garbelli, Pirelli Labs, Viale Sarca 222, 20126 Milano-Italy.
6. G. Cappuccio and D. Hampai, INFN-LNF, Via E. Fermi 40, 00044 Frascati, Italy.

[‡]Work partially supported by Lam.Ba. SrL, Caluso (To)-Italy.

[§]Researchers involved: L. Barbero and A. Bassignana.

1. Introduction

In the framework of Condensed Matter Nuclear Science (CMNS), starting from 2004, we developed and used a specific procedure that sums together different methods proved to be beneficial to induce “anomalous heat release” in Palladium–Deuterium (Pd–D) systems. Recently, we started experiments also with Nickel–Hydrogen (Ni–H) systems.

Such procedure, that we called “hybrid”, couples the use of:

- a Nano-particles.
- b Multilayer nano-coating onto D (or H) absorbing materials, like Pd.
- c Flowing of large current into materials of b), shaped as thin and long wires, in order to exploit the *Preparata Effect* (voltage drop along wire up to 100 V/m in our experimental set up)..

We remind that the first Researcher, in the field of CMNS, who used concentrated Pd nano-particles, to increase the D/Pd ratio, was Prof. *Yoshiaki Arata* at Osaka University since 1993 [1]; the first one who developed multiple nano-layers of Pd–CaO was Dr. *Yasuhiro Iwamura* at Mitsubishi Heavy Industries, in Yokohama in 1999 [2]. Both used, de-facto, Deuterium gas loading.

As we have been experiencing since 1993, the so-called “anomalous effects” (thermal anomalies and/or some, few, nuclear particles generation) are detectable only when the system is under some *non-equilibrium condition*, spontaneous or forced. This seems to be a *necessary condition* to achieve some macroscopic evidence of the reactions but it’s absolutely not a sufficient one.

It has to be guaranteed, at the same time, a large amount of H or D inside the lattice of the active material or, at least, on its surface. It is therefore necessary to “flow” as much as possible gas (or, better to say, D^+) through the Pd (or Ni) lattice at a rate as fast as possible. It’s not important the direction of the flux: as consequence, fast loading and de-loading cycles have similar effects. Our forced loading procedure takes about 5–10 s using Pd (reaching a D/Pd ratio of around 0.75, obtained by R/R_0 measurement); putting enough gas in the lattice and the faster is the loading, the larger will be the results of anomalous heat production.

The specificity of excess heat, flowing the Deuterium *in any direction* (at 383°C, 13 atm), was first discovered at NASA (*Gustav C. Fralick* and others) on 1989. Because they were concentrated at that time only on neutron emission, they didn’t make deeper studies about, but just reported the effect in the framework of a Technical Memorandum [3] among others, very poorly diffused worldwide.

2. The Hybrid Procedure

In order to achieve both a high D/Pd ratio (or H/Ni ratio) and a “fast flowing” gas in the lattice, as stated above, we developed a hybrid procedure mainly based on the following effects:

(1) Electromigration (EM)

The EM effect was discovered and developed around 1929, in Germany, by several scientists. We started to use it feeding thin Pd wires (diameter $\Phi = 50 \mu\text{m}$, length = 50–100 cm) with large DC (i.e. steady state) current density (up to 40–50 kA/cm²) under electrolytic conditions and, in the more recent years, under gas loading. Previously (in electrolytic regimes), we even improved it since 1996 [4], introducing pulsed regimes of few μs of duration and peak current up to 150 A. The pulsing procedure allowed reaching a peak current density through the wires of up to 300 kA/cm² without largely increasing the mean power applied. Moreover, using proper repetition rates (5–33 kHz), the self de-loading of D_2 between pulses was kept under control [4].

The disadvantages of the pulsing procedure were: very complicate circuitry; complex evaluation of excess heat; quite frequent catastrophic failure of the electronics due to extremely large values of peak power.

(2) Large voltage drop



Figure 1. Wires braid inside the thermal insulation.

The large EM currents, the high resistivity of deuterated Pd and the high temperatures (around 500°C or higher in our most recent gas experiments) induce 50–100 V voltage drop along the Pd wire. According to *Giuliano Preparata's* (Milan University, 1995) theory [5], large voltage drops along Pd wires, together with other specific experimental conditions, have the peculiarity to increase the D/Pd ratio because of “coherence effects”. Preparata studied only electrolytic, not pressurized cells (with Pt anode and LiOD as electrolyte): maximum temperature of cathode Pd wire was $\ll 100^\circ\text{C}$. According to the theory, higher temperatures facilitate the growing of Pd–D γ phase (which formation is an endothermic process, while the formation of α and β phases are exothermic); this leads to an enhanced state of reaction due to a higher D/Pd loading.

(3) Use of Pd-based nano-particles

The effects of micro and nano-particles in CMNS experiments, from the point of view of increased Deuterium loading and generation of anomalous effects, were pioneered by *Yoshiaki Arata* (Osaka University, 1993) [1]. More recently (since 2005) Arata got anomalous heat in a fully reproducible way, for time as long as two days, using an innovative Pd–ZrO₂ system and D₂ gas pressurised at up to 60 atm [6].

Arata's experiments were independently reconfirmed (2008) by *Akito Takahashi* and *Akira Kitamura* group (Technova Inc., Kobe University collaboration, Japan) [7] even using “commercial” material: produced by Santoku Corporation (Kobe), a Company (since 1935) expert in Precious Metals and Rare Earths production/purification. This experiment was a milestone: it overcame the historical problem of *transferred irreproducibility* in CMNS experiments.

(4) Use of multi-layers

Since 2000 *Yasuhiro Iwamura* (Mitsubishi Heavy Industries, Yokohama, Japan) developed a suitable procedure to deposit two substances (CaO and Pd) in nano-metric layers on a bulk Pd plate [2].

The aim of the experiment was to demonstrate the transmutation of selected elements deposited in the outermost side of the multilayer into new ones: recently, from Sr, Cs and Ba they got respectively Mo, Pr and Sm. The effect is induced by the flowing of D₂ gas in a slightly pressurised chamber (max 2 atm) and by mild temperatures (up to 80°C). Iwamura (and Collaborators) used advanced ion beam technology for the multi-layer structure construction.

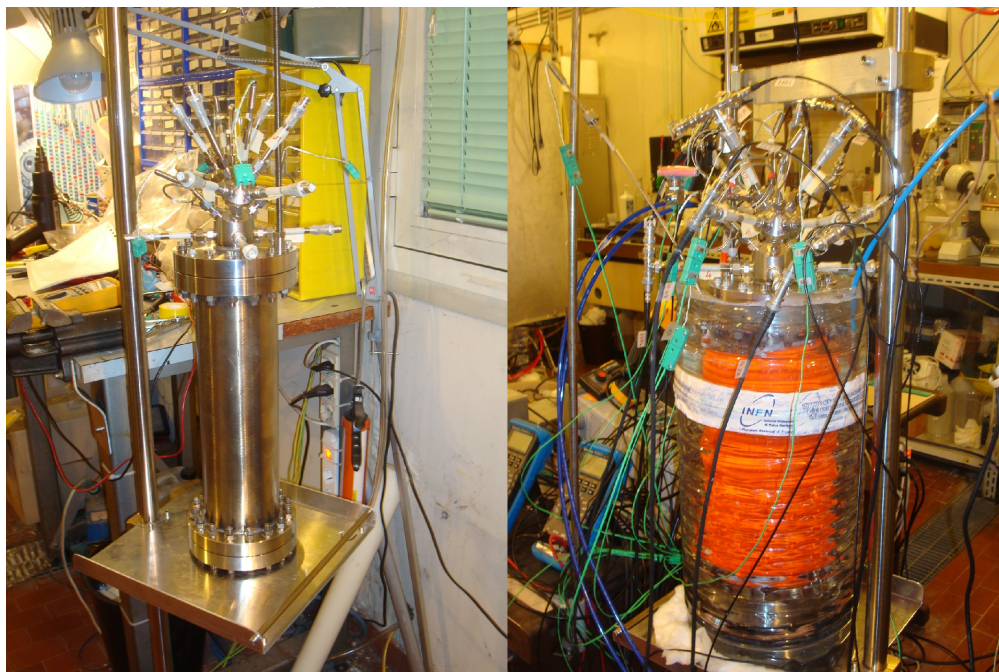


Figure 2. The apparatus mounted without and with the water bath.

(5) *Fractal nano-layer*

Since 1998 [8], we experienced that in electrolytic environment, using a mildly acid solution with innovative electrolytes (like salts of Ca, Sr, and Ba) at very low concentration (<0.1 mM), the Pd wire (typical diameter $100\mu\text{m}$) was sometimes covered by a sub-micrometric layer of several elements, including Pd itself, especially after several cathodic–anodic cycles.

After this spontaneous development of such porous and very thin layer (like a sponge), the characteristics of D_2 absorption changed dramatically and the loading time was reduced of several order of magnitude (from hours to minutes) especially at low current density of electrolysis (about $10\text{--}20$ mA/cm^2). Moreover, we observed that Pt deposition (present at anode) was usually deleterious to Deuterium absorption.

We observed correlations between the increasing of the amount of thermal effects and the arising of compositional anomalies (detected by SEM-EDAX and, later, by ICP-MS). We realised that the cause of anomalies arose from such “fractal/sponge” layers. We published several reports about such observations although the situation was quite frustrating: any attempt to build the layers on demand failed. In short words, the system was very delicate and easy to self-destruction.

Because of the uncontrolled growth of this spontaneous layer and its instability, we moved (since about 2004, as ancillary experiments at the beginning) from liquid electrolysis to gas environment where the fractal layer is more stable and can be used with larger success.

2.1. Fractal nano-layer construction

Using a gas environment avoids uncontrolled self-dissolution of the sponge layer due to electrolytes and large local pH changes due to cathodic and short time (if needed) anodic electrolytic regimes at the Pd surface.

We prepared the sponge material over the wire in an almost controlled way before inserting it in the reactor. Anyway, we point out that further experimental work is necessary to improve the quality/reproducibility of the coating.

The wire is made by an active support like Pd (or recently Ni) and it is coated with nano-materials (some used as anti-sintering agents) containing also Pd. The nominal dimension of the main nano-material is 6–9 nm.

The active support is a thin wire, $\Phi = 50 \mu\text{m}$ and length = 60–90 cm, coated by a total number of about 50 layers: the apparent increase of thickness of the wire is 1–2 μm . The procedure involves several high temperature cycling between 20 and 900°C, using Joule heating in air with several specific patterns in the timing of both the steady-state regime and transient one: we adopted current-controlled power supply with low values of output capacitors to avoid blowing of wire.

2.2. Characteristics of nano-coated Pd wires

As general behaviour, the loading time is a nice and simple indication of the coating quality. Usually it takes from 6 to 30 s to reach $R/R_0 = 2$, i.e. $D/Pd = 0.75$ using H_2 or D_2 gas at a pressure of 6.5 atm. The shorter is the loading time the better is the coating and the longer will be the deloading time. A couple of hours can be necessary for a full deloading of the loaded wire by putting the system under dynamic vacuum (usually 10^{-3} – 10^{-4} atm) at 350–400°C.

This is an important effect that we observed since 2002, even in electrolytic experiments. We named it the “Diode

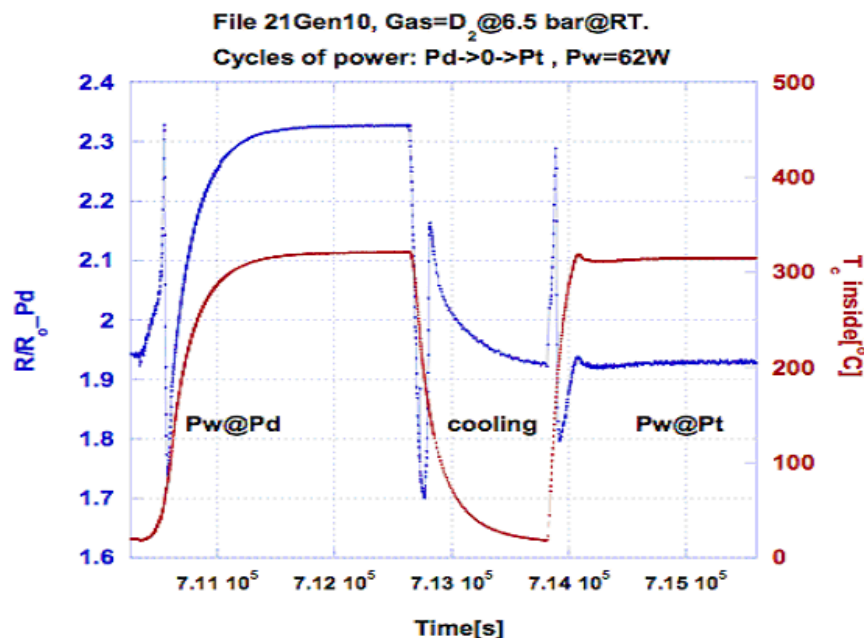


Figure 3. Behaviour of R/R_0 of Pd, changing the Power (Pw) from Pd to Pt wire. At the same temperature (red line) inside the Cu tube, the value of R/R_0 (blue line) is higher if the Pd wire is heated directly (Pw@Pd).

Effect”: the H_2 or D_2 gas can flow-in very easily and rapidly and on the contrary the flowing-out is very difficult.

3. Description of the New Experimental Set-up

The new experimental set-up is a development of the previous apparatus, presented at ICCF14 (August 2008, Washington D.C.) and at ICCF15 (October 2009, Rome). Basically, they are similar each other because the power measurements (and calibrations) are based on the comparison of results between a normal Pt wire, assumed to be inert under D_2 atmosphere, and an “active” Pd wire, i.e. a Pd wire with the above mentioned coating.

These wires are put singly inside an insulating sheath made of glass or quartz fiber and then twisted together to be very close each other. They are thermally insulated, from the stainless steel (SS) internal wall, by a high temperature (fibrous ceramic) wool, named SW607HT, (Fig. 1).

The procedure is based on feeding several different electric powers alternatively to Pd and Pt wires, before in “inert” gas (He) and later in “active” gas (D_2 , H_2). Equilibrium temperatures were recorded versus the different powers applied. The maximum internal temperature reached by the SS reactor wall is 110°C , avoiding the sulphur degassing problem from the wall, as pointed out by Prof. *Tatsumi Hioki* (Toyota Research Centre, Aichi-Japan) since 2007 at ICCF13 [9].

Main improvements were:

- The braids, made by the quartz sheaths allocating the Pd and Pt wires, were rolled up around a copper (3N purity) tube (4–6 mm inner-outer diameter; length 24 cm) in order to homogenize the temperatures. In the inner side of the tube, in the middle, was put a, high resolution, type K thermocouple (Tc) with insulated body (SS 316N against penetrating of the gas inside the thermocouple lattice; MgO as electrical insulator). In this way we realised a sort of furnace (the Cu is an excellent IR reflector), which is heated, alternatively, by the Pd and Pt wires.
- A second braid made of a couple of wires and a copper tube was prepared, but in this case both wires were made of Pt instead of Pd and Pt. This second set of wires was used as in situ and on-line cross-comparison of the behaviours of the reactor when changing the atmosphere (^4He , D_2 , D_2 -Ar mixtures, Ar, air, and vacuum).
- Both couples of braids were individually thermally insulated and put in the same pressurised SS cell. Finally the cell was put in a large water bath continuously and largely cooled (Fig. 2).

4. Methodology of Measurements

The procedure foresaw first of all a calibration test, made by using pure ^4He at 6.5 atm, and different wire temperatures due to proper powers applied along it. After that, the experiment was replicated in D_2 , Ar and air atmosphere and in vacuum. Using different atmosphere composition, it was possible not only to evaluate the effect of different gas on the anomalous heat release, if present, but also to change the regime temperature, due to the different thermal conductivity.

Each session included a series of runs; in each run an input power was selected and maintained until a thermally stationary regime was reached. At that time the key parameters (input power, temperature, R/R_0) were measured and labelled as *equilibrium values* for further analysis.

An additional session was performed in a mixture of D_2 (4.62 bar) and Ar (1.68 bar) to study the effect of a higher wire temperature due to the approximately seven times lower thermal conductivity of pure Argon in respect to pure Deuterium. The rationale for this test was that we thought that higher temperatures could be helpful for these specific reactions and that could compensate the lower pressure of active gas or may even improve the overall amount of anomalous excess heat production. A percentage of 24% of Ar in D_2 reduces the D_2 gas thermal conductivity of about 56%, i.e. from 151 to $96 \text{ mW}\cdot\text{m}^{-1}\cdot\text{K}^{-1}$ at 95°C .

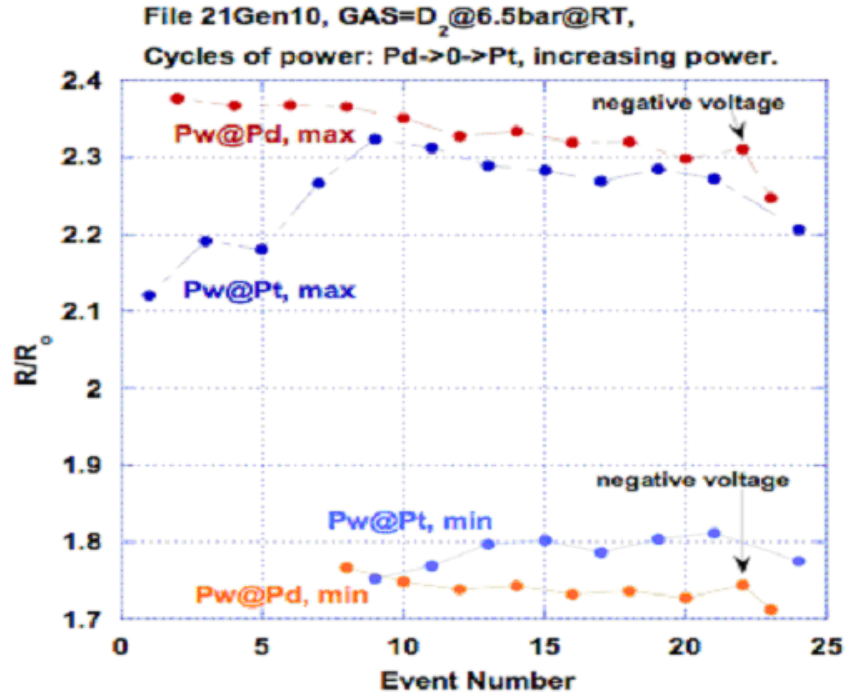


Figure 4. By feeding directly the Pd wire (Pw@Pd) the R/R_0 reaches both higher maximum and lower minimum in respect to indirect heating (Pw@Pt).

Eventually the test gave a positive answer to our expectations and the increase of temperature improved largely the anomalous heat production, overcoming the D₂ pressure reduction.

5. Main Results

This chapter presents the main results obtained with our experimental system between January and February 2010. Also some theoretical interpretations are formulated, but we want to underline that this is not the main purpose of the paper, which is mainly addressed to make our experimental results available for who wants to build a valid explaining theory.

Figure 3 is related to an experiment in atmosphere of pure Deuterium (6.5 bar at room temperature), with an external input power of 62 W. We can identify three different phases: in the first one the power is given directly to the Pd wire (by Joule effect), in the second one there is not external power (to allow system to cool down), in the third one the power is provided to the Pt wire. The figure shows that, even if the final (stationary) temperature in the system is the same, the ratio R/R_0 in the Pd wire is much higher in the first phase, leading to the conclusion that the presence of an electrical current plays a fundamental role in increasing the wire loading by Deuterium.

We consider this as a confirmation that the maximum R/R_0 of Palladium under direct heating (electro-migration) is always larger of any maximum that can be obtained with only high temperatures.

Some authors have interpreted this behaviour as an evidence of some kind of confinement of Deuterium inside Palladium due to the voltage drop along the thin and long Pd Wire (according to the Preparata Model).

Prof. Yeong E. Kim (Purdue University, USA) thinks this is as an evidence of the *Bose-Einstein Condensation Nuclear Fusion* (BECNF, Naturwissenschaften, 2009); he actually mentioned our ICCF-14 experiments as the first experimental proof of such model. Prof. Francesco Premuda (Bologna University, Italy) in 1993 [11] firstly formulated the hypothesis that several of CMNS effects could be explained as a special case of Bose–Einstein Condensation (BEC). Also Akito Takahashi (now at Technova Inc.) thinks BEC is a thoughtful concept to start to study the anomalous CMNS effects, and his TSC (Tetrahedral Symmetric Condensate) model is a special case of dynamic (transient) BEC [private communications during 239^oACS, March 2010].

Figure 4 shows the minimum and maximum values of R/R_0 achieved in a series of tests during which different amounts of power were provided alternatively to the Pd (Pw@Pd) and to the Pt (Pw@Pt) wires.

A series of observations are drawn in the following:

- I. The minimum values of R/R_0 in Pd/D system are always lower using direct feeding of the Pd wire instead of indirect heating. Such an effect was predicted by Prof. Premuda as a proof of presence of “islands” of superconductivity in D/Pd system (supposing the system in plasma regime).
- II. Using the Palladium–Hydrogen system in similar condition and with both direct and indirect heating we observed that the maximum values of R/R_0 are very similar to the Pd–D ones, but the minimum values are larger. This effect can also be explained according to the Premuda model, in this case we can’t get islands of superconductivity because there are fermions (H) and not bosons (D).
- III. Putting a negative voltage polarization on the Pd wire, respect to the grounded Pt wire at a 1 mm distance, shows a measurable increase of both R/R_0 maximum values and anomalous heat production (about +12%) when compared to the same operating condition but using a positive voltage. Moreover, the temperatures detected inside the copper tube at maximum and minimum R/R_0 are remarkably higher. We observed this effect since 1996 in electrolytic systems and discussed it in various conferences, but the high voltage discharge problems forced us to quit this method to increase the gain. We are developing a new version of reactor (#4) dedicated to study more deeply such phenomenon. We may speculate that the changing, at the proper low frequency, of the polarization of the voltage could stimulate the movement of deuterium between the surface and the Palladium bulk in both directions enhancing the anomalous reactions.
- IV. We observed that even Platinum absorbed some Deuterium at the level of 1–2% (estimated by R/R_0 measurements) when there is large (20–40 kA/cm²) electro-migration.
- V. We observed that Palladium can absorb He at 1–2% level under very large electro-migration ($J = 40 - 50$ kA/cm²).
- VI. We observed that an addition of Argon reduces strongly the possibility of He absorption by both Pd and Pt.
- VII. We had confirmation that the high temperature is one of the key parameter influencing the amount of anomalous heat generated in D/Pd systems. After Deuterium absorption inside Pd lattice was performed, adding about 40% of Ar in the cell atmosphere rises the temperature that can be reached by the wires due to the lower thermal conductivity of Ar in respect to D₂. In this case we noticed an increased heat surplus made by the Pd wire in respect to the Pt one.

6. Conclusions

It was experimentally proved that, under specific conditions, it is possible to generate anomalous excess heat at macroscopic levels (several Watt or up to 400 W/g of Pd, expressed as excess-power/g).

According to our experiments, in the Pd–D system, the key parameter controlling the amount of anomalous heat generated is the “motion” of deuterium between Pd bulk and/or the nano-coating (i.e. at the surface). In other words,

it is necessary to maximize the amount of moving Deuterium and its speed. Such an effect, although discovered by us since 1993 and roughly discussed [12], is quite difficult to be obtained in practical experiments.

The method of coating with some specific nano-materials (including Pd) over a long and thin palladium wire, to make it active from the point of view of deuterium absorption, seems a reliable procedure, at least at laboratory level, to fulfil the request for reproducible experiments.

We experienced that high temperature (of the order of 300°C and over) is a pre-condition to get some macroscopic effect even under mild pressures (4–8 atm).

We experienced that high temperature by itself increases the anomalous heat release, especially above 700°C. Such an effect was by us predicted and experimentally found.

We experienced that the electro-migration, especially at high current density ($>20 \text{ kA/cm}^2$) improves in the whole the anomalous effects.

Even if this subject is not specifically addressed in this paper, we experienced also that the coating of nano-materials is a procedure that allows, in an easier way, the detection of the anomalous effects, thermal included.

The power density (up to 400 W/g of Pd) and time duration (experienced by us of over 1 week) of anomalous heat generated pushed us to think that the origin of such anomalous heat is out of any known chemical reaction. Remarkably, the anomalous heat increased over a number of ON–OFF cycles, probably because in this way the quantity of fractals at the surface were increased with further reduction of dimensionality. This is due to the well-known phenomenon of both *embrittlement* of Pd (and of several other metals and alloys) and large changing of dimensionality (see our report at ICCF15) due to Hydrogen/Deuterium loading de-loading cycles. Drawback of such (simple) procedure is the possibility of the wire breakage, especially if it is thin. For this reason we made some specific “developments” to reduce such catastrophic final result. Another weak point of Pd is that it changes his dimensions after several loading–deloading cycles. In short, in the case of wire geometry, the length decreases and wide increases.

Further work, and sophisticated/expensive instrumentation, is necessary to identify clearly the supposed non-chemical origin of the phenomenon: e.g. detection of ^4He as nuclear ash.

The positive effect of a transversal electric field at Pd surface (i.e. negative voltage) was reconfirmed and opens the way to an experimental set-up that, in principle, can boost the anomalous heat production without increasing the input power.

If all the still remaining doubts will be (hopefully soon) fully clarified, the phenomenon under study can be the starting point for a new source of energy for practical purposes (like water boilers and even engines). We recall that, in our specific experiments, we can operate at quite large temperatures (about 700°C, i.e. at high intrinsic Carnot efficiency) and that the increasing of the temperature generally lead to an increase of the anomalous effects. In other words, we are in the lucky situation, from technological point of views, of *positive feedback*.

References

- [1] Y. Arata and Y.C. Zhang, *Proc. Japan Acad.* **70B** (1994) 106. See also: Yoshiaki Arata, *Toward the Establishment of Solid Fusion as a Perpetual Energy for Humankind*, ISBN 888-6062-066-X (2008). Translated from Japanese to English (by M. Nakamura).
- [2] Y. Iwamura and T. Itoh et al., *Jpn. J. Appl. Phys.* **41** (2002) 4642–4648.
- [3] Gustave C. Fralick, Arthur J. Decker and James W. Blue, Results of an attempt to measure increased rates of the reaction $2\text{D} + 2\text{D} \rightarrow 3\text{He} + \text{n}$ in a nonelectrochemical cold fusion experiment, *NASA Technical Memorandum* 102430, December 1989.
- [4] F. Celani and A. Spallone et al., *Phys. Lett. A* **214** (1996) 1–13. See also *proc. ICCF5* (Montecarlo, 1995), F. Celani et al. paper and registered discussion at Conference.
- [5] E. Del Giudice and G. Preparata et al., The Fleischmann–Pons effect in a novel..., *Proc. ICCF8*, (21–26 May 2000, Lerici-Italy). Edited by Italian Phys. Soc., **70**, pp. 47–54. ISBN 88-7794-256-8.
- [6] Y. Arata and Y. Zhang, The special report on research project forcreation of new energy, *J. High Temperature Soc.* No. 1, 2008.

- [7] Akira Kitamura and Akito Takahashi et al., Anomalous effects in charging of Pd powders, *Phys. Lett. A* **373** (2009) 3109–3112.
- [8] F. Celani et al., Thermal and isotopic anomalies when Pd cathodes are electrolysed in electrolytes, *Proc. ICCF10 (August 24–29, 2003) Cambridge, Massachusetts, USA. Condensed Matter Nuclear Science series, World Scientific*, pp. 379–398, ISBN 981-256-564-7.
- [9] Tatsumi Hioki, N. Takahashi and T. Motohiro, XPS study on surface layer elements of Pd/CaO multilayer complex with and without Deuterium permeation, *Proc. ICCF13 (June 25–July 1, 2007), Sochi-Russia*. pp. 518–528. ISBN: 978-5-93271-428-7.
- [10] Y.E. Kim, Theory of Bose–Einstein Condensation for deuteron-induced nuclear reactions in micro/nanoscale metal grains and particles, *Naturwissenschaften* **96** (2009) 803.
- [11] F. Premuda, Coulomb barrier total screening by Bose–Einstein-condensed deuterium in palladium blisters and reaction chains in high-density hysteresis, *Fusion Technol.* **33** (1998) 350.
- [12] F. Celani et al., High power ms pulsed electrolysis for high deuterium loading in Pd plates, *Trans. Fusion Technol.*, ISSN 0748-1896, **26** No. 4T, 127–137.



Research Article

TOF-SIMS Investigation on Nuclear Transmutation from Sr to Mo with Deuterium Permeation through Multi-layered Pd/CaO

A. Murase*, N. Takahashi, S. Hibi, T. Hioki and T. Motohiro

Toyota Central R & D Laboratories Inc., Nagakute, Aichi 480-1192, Japan

J. Kasagi

Research Center for Electron Photon Science, Tohoku University, Sendai 982-0826, Japan

Abstract

The selective nuclear transmutation from ^{88}Sr to ^{96}Mo reported by Iwamura et al. was investigated replacing electrochemical deposition with ion implantation for seeding $^{88}\text{Sr}^+$ and replacing a quadrupole mass spectrometer with a time of flight mass spectrometer for secondary ion mass spectrometry (TOF-SIMS) for analysis of possible transmuted products. At the surface of the Sr implanted Pd/CaO multilayer foil, Mo was clearly detected by X-ray photoelectron spectroscopy (XPS) after deuterium gas permeation. After the D_2 permeation, the sample was heat treated in the air to remove S which condensed at the surface during the permeation. After the successful removal of S, Mo could be clearly detected by XPS on the surface of the $^{88}\text{Sr}^+$ implanted Pd/CaO multilayer foil. The isotopic abundance ratio of the surface Mo measured by TOF-SIMS was similar to that of natural Mo. However, after the removal of the outermost surface layer with ion sputtering, the observed isotopic abundance ratio of Mo changed from that of natural Mo with an isolated strong peak at a mass close to ^{96}Mo . This result duly suggests that the transmutation from ^{88}Sr to ^{96}Mo had took place, although the peak of $m/z = 96$ might be also assigned to GaAl^+ , Ca_2O^+ or CaFe^+ , beside $^{96}\text{Mo}^+$. By further analyses of the TOF-SIMS data from the viewpoint of accurate masses, depth profiles and isotopic abundances, it was clarified that the peak of $m/z = 96$ was assigned to Ca_2O^+ originated from Pd/CaO multilayer.

© 2012 ISCMNS. All rights reserved.

Keywords: Deuterium permeation, Pd/CaO multilayer, Time of flight secondary ion mass spectrometry, Transmutation, X-ray photoelectron spectroscopy

1. Introduction

Nuclear transmutation with deuterium (D_2) gas permeation through a Pd/CaO multilayer foil has firstly been reported by Iwamura et al. [1]. Identifying the surface elements on the Pd foil covered with $(\text{Pd/CaO})_n$ multilayer film before and after the D_2 gas permeation over one week at a temperature as low as 343 K, they have given the evidences that

*E-mail: e0483@mosk.tytlabs.co.jp

electrochemically deposited Sr and Cs change to Mo and Pr, respectively. The isotopic abundance ratio for the induced Mo was quite different from that for natural Mo: this observation with secondary ion mass spectrometry by a quadrupole mass spectrometer has suggested that the change is caused by a nuclear process. By the D₂ gas permeation method, they have further found that Ba changes to Sm [2].

It is considered that these results are easily replicated in different laboratories. However, only a limited number of replication experiments have been reported so far [3–5]. One of the difficulties is to reproduce a condition of the high D₂ gas flow rate [6]. A D₂ gas flow rate through Pd is sensitive to the state of the surface. Therefore, appropriate pretreatments of Pd as well as clean experimental environment are required to realize a high D₂ flow rate. We have reported that commercially available Pd foils are often contaminated with S and a segregation of the S impurity on the surface during D₂ gas permeation results in a lowering of the flow rate [7–9]. Furthermore, if S is on the surface, it is difficult to examine the generation of Mo using X-ray photoelectron spectroscopy (XPS), because a S2s peak in the XPS spectrum overlaps with Mo 3d peaks [7]. In our previous paper, we reported that a small amount of S impurity in Pd concentrates and forms sulfuric compounds at the surface during D₂ permeation and the sulfuric compounds are removed by annealing in air at 1273 K for 10 min after the permeation [8,9].

The selective nuclear transmutation from ⁸⁸Sr to ⁹⁶Mo reported by Iwamura et al. has been investigated replacing electrochemical deposition with ion implantation for seeding ⁸⁸Sr⁺ without an implantation of any other isotopes and replacing a quadrupole mass spectrometer with a time of flight mass spectrometer for secondary ion mass spectrometry (TOF-SIMS), which has a great advantage in mass resolution, for analysis of possible transmuted products [9]. In this study, a more detailed TOF-SIMS study has been made in order to clarify the origin of the anomalous isotopic abundance ratio for the induced Mo. Pd foils with five sets of Pd/CaO layers were implanted with 65-keV ⁸⁸Sr⁺ ions, and were subjected to D₂ gas permeation treatment at 343 K same as Iwamura's report [1]. XPS and TOF-SIMS measurements were performed to examine the change of surface elements before and after the gas permeation. This paper reports the results of the TOF-SIMS investigation from the view point of accurate masses, isotope abundances and depth profiles on nuclear transmutation from Sr to Mo.

2. Experimental

2.1. Sample preparation

Pd foils of 50 μm (purity: 99.97%) in thickness were commercially obtained from the Nilaco Corporation. The as-purchased foils were first ultrasonically cleaned with ethanol and heat-treated in vacuum (5×10^{-5} Pa) at 1223 K for 5 h and subsequently in air at 873 K for 10 min. Layers of CaO and Pd were piled up alternately on the substrate Pd foils by the RF sputter deposition method. The structure of the multilayer was the same as reported by Iwamura et al.: Pd (40 nm) / CaO (2 nm) / Pd (18 nm) / CaO (2 nm) / Pd (18 nm) / CaO (2 nm) / Pd (18 nm) / CaO (2 nm) / Pd (18 nm) / CaO (2 nm) / Pd foil (50 μm). Then ⁸⁸Sr⁺ was implanted in the multilayer foil at 65 keV and a dose of 1×10^{16} ions/cm². Subsequently the foils were heat-treated in the air at 573 K for 10 min in order to remove carbonaceous materials deposited during the ion implantation. The samples were then subjected to D₂ gas permeation treatments at 343 K for about 10 days. The D₂ permeation system was the same with that reported by us previously [7,8,10]. The upstream side was filled with D₂ of 200 kPa. The purity of the D₂ gas was 99.995%. The downstream side was evacuated with a dry pump and a turbo molecular pump. The upstream side was connected with a reservoir tank of 1.0 L. The flow rate of D₂ was determined from the reduction of the pressure of the tank. A metal O-ring was used for the vacuum seal. An example of the relationship between permeation rate and time is shown in Fig. 1. After the permeation, the samples were annealed in the air at 1273 K for 10 min, in order to remove S, which had concentrated at the surface during D₂ permeation and disturbs the detection of Mo by XPS. The origin of the S contamination and the details of above procedure for removing the influences of S are described in a separate paper [11].

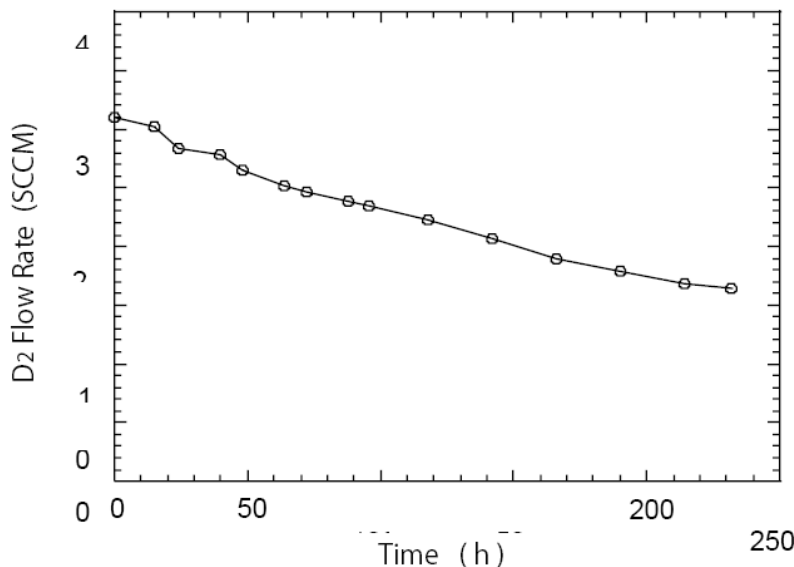


Figure 1. Variation of permeation rate with time for a $^{88}\text{Sr}^+$ implanted Pd/CaO multilayer sample.

2.2. Analysis

XPS measurements were performed with ULVAC-PHI Inc. “Quanterra SXM” (20 kV, 100 W): the X-ray used for excitation of photoelectrons was the monochromatic Al-K α line (1.438 keV). The size of the incident X-ray beam was $100 \times 1500 \mu\text{m}^2$ on the sample.

TOF-SIMS measurements were performed with ULVAC-PHI Inc. “TRIFT II” instrument. High mass resolution spectra of $M/\Delta M > 5000$ at m/z 27 (C_2H_3^+) were acquired using pulsed $^{69}\text{Ga}^+$ ion beam with an impact energy of 15 keV, an ion current of 2 nA for one pulse, a pulse width of 13 ns (700 ps after bunching) and a pulse frequency of 10 kHz. Total ion doses in these measurements were $< 1 \times 10^{12}$ ions/cm 2 . For the depth profiling with TOF-SIMS, continuous $^{69}\text{Ga}^+$ ion beam with impact energy of 15 keV was used for sputtering. The sputtering area was $300 \times 300 \mu\text{m}^2$, and the sputter rate was approximately 0.4 nm/60 s in the case of the (111) surface of crystal silicon.

3. Results and Discussion

3.1. XPS spectrum of surface after annealing in air

The XPS spectrum around Mo3d for a $^{88}\text{Sr}^+$ implanted Pd/CaO multilayer sample after D_2 permeation is shown in Fig. 2. This sample maintained a comparatively high permeation rate of 1.6 SCCM even at the permeation time of 230 h as shown in Fig. 1. The two peaks in the spectrum definitely correspond to Mo3d5/2 and Mo3d3/2, because (i) the intensity ratio is 3:2 and (ii) the energy difference between the two peaks is 3.13 eV. This spectrum was obtained when the sample was annealed in the air after the D_2 permeation treatment. The air annealing was conducted in order to remove S accumulated onto the surface of the sample during the D_2 permeation treatment. The influences of S on the permeation rate and elemental analysis with XPS are described in [10]. Then, TOF-SIMS analyses were performed

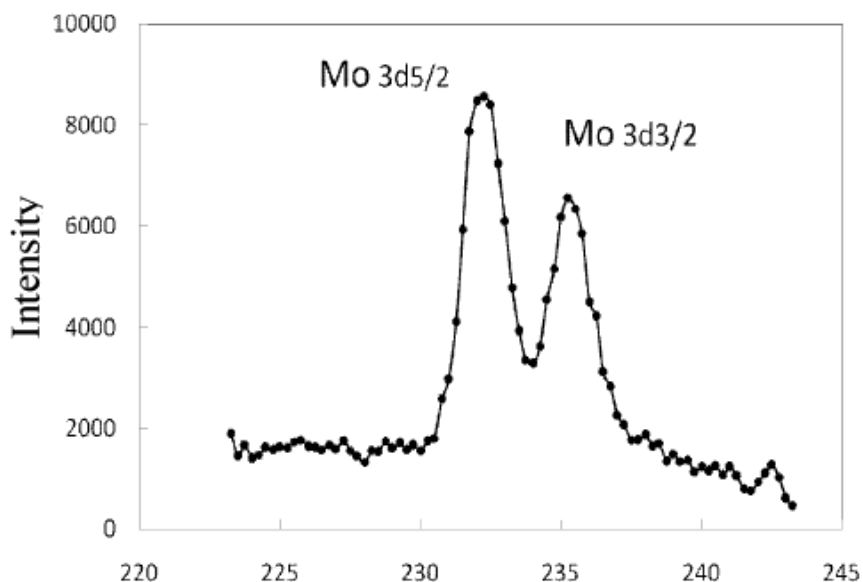


Figure 2. XPS spectrum around Mo_{3d} for $^{88}\text{Sr}^+$ implanted Pd/CaO multilayer sample after D_2 permeation followed by annealing in the air.

in order to clarify the origin of this Mo.

3.2. TOF-SIMS spectra of surfaces and sputtered surfaces

Figure 3 shows TOF-SIMS spectra of the Sr implanted Pd/CaO multilayer after D_2 permeation. On the surface, the existence of ^{88}Sr is confirmed by a peak of $m/z = 88$ in Fig. 3(a) and all the isotopes of natural Mo appear as shown in Fig. 3(b). The spectrum after removing an outermost surface layer by ion sputtering for 60 s (about 0.4 nm in depth), however, a stronger peak is observed at the mass of ^{96}Mo than peaks of other Mo isotopes as is shown in Fig. 3(c). This spectrum is similar to that reported by Iwamura et al. [1], suggesting the evidence of the transmutation from ^{88}Sr to ^{96}Mo .

Figure 4 shows the spectra before D_2 permeation. They were taken for the area where Sr^+ ions had not been implanted. On the surface, neither Sr nor Mo isotopes are observed as shown in Figs. 4(a) and (b), respectively. However, when the outermost surface layer is removed by sputtering for 60 s, a peak at a mass close to ^{96}Mo is observed as shown in Fig. 4(c). The peak cannot be due to ^{96}Mo of nature, because any other Mo isotopes, especially the most abundant ^{98}Mo , are not seen. This result indicates that the peak at a mass close to ^{96}Mo observed by TOF-SIMS after removing the outermost surface layer is not the ^{96}Mo generated by transmutation from ^{88}Sr . This peak was observed from all of the 60s sputtered surfaces of Pd/CaO multilayer samples before and after D_2 permeation. We refer to this peak as ^{96}X , here. Candidate materials for X are GaAl, Ca_2O and CaFe besides ^{96}Mo as shown in Table 1. Then, we attempted to narrow the possibilities of the candidates from accurate mass, isotope abundance and depth profiles obtained by TOF-SIMS measurements.

Table 1. Candidates for X.

Molecule	Mass	Source material
Ca ₂ O	95.920	Pd/CaO multilayer
GaAl	95.907	Ga: ⁶⁹ Ga ⁺ primary ion for TOF-SIMS Al: impurity in Pd
CaFe	95.898	Ca: Pd/CaO multilayer Fe: impurity in Pd
⁹⁶ Mo	95.905	

3.3. Accurate mass

The accurate mass of peaks at $m/z = 96$ read off from the spectra of Figs. 3(b), (c) and 4(c), and the deviation of each accurate mass from the mass of GaAl, Ca₂O, CaFe and ⁹⁶Mo are shown in Table 2. In this case, all the spectra were calibrated with the same ions; CH⁺, C₂H₃⁺, C₃H₅⁺, ⁴⁰Ca⁺ and ⁶⁹Ga⁺. The peak of $m/z = 96$ observed from the surface after D₂ permeation (Fig. 3(b)) can be assigned to ⁹⁶Mo⁺ originating from natural Mo because of its isotope abundance. On the other hand, the masses of the ⁹⁶X⁺ observed from sputtered surfaces both before (Fig. 4(c)) and after (Fig. 3(c)) D₂ permeation are shifting from that (Fig. 3(b)) of the surface after D₂ permeation and are rather closer to the mass of Ca₂O than to the mass of ⁹⁶Mo and GaAl. And this shift of mass with sputtering indicates that the ⁹⁶X⁺ observed on the sputtered surfaces cannot be assigned to ⁹⁶Mo⁺. CaFe is still less corresponding than other candidates. From these results, the highest possibility for the assignment of ⁹⁶X is considered to be Ca₂O among the candidates of ⁹⁶X listed in Tables 1 and 2.

3.4. Isotope abundance

Among the candidates of ⁹⁶X, Ca₂O has an isotope peak of ⁴⁴Ca⁴⁰CaO at $m/z = 99.9$ beside the main peak of ⁴⁰Ca₂O at $m/z = 95.9$, and the ratio of the peak intensity of $m/z = 99.9$ to that of $m/z = 95.92$ is approximately 1–25. From

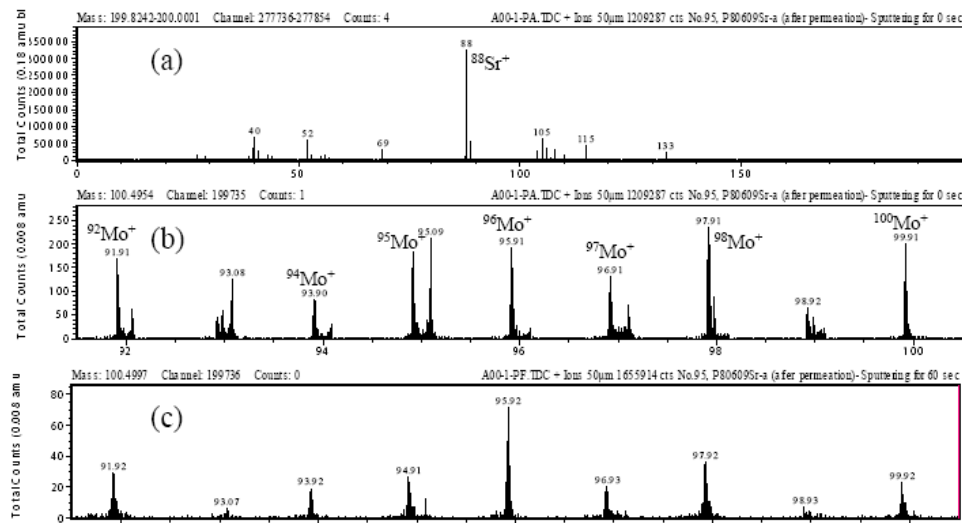


Figure 3. TOF-SIMS spectra for Sr implanted Pd/CaO multilayer after D₂ permeation; (a) spectrum in wide mass range at surface; (b) spectrum around Mo at surface; (c) spectrum around Mo after sputtering for 60 s.

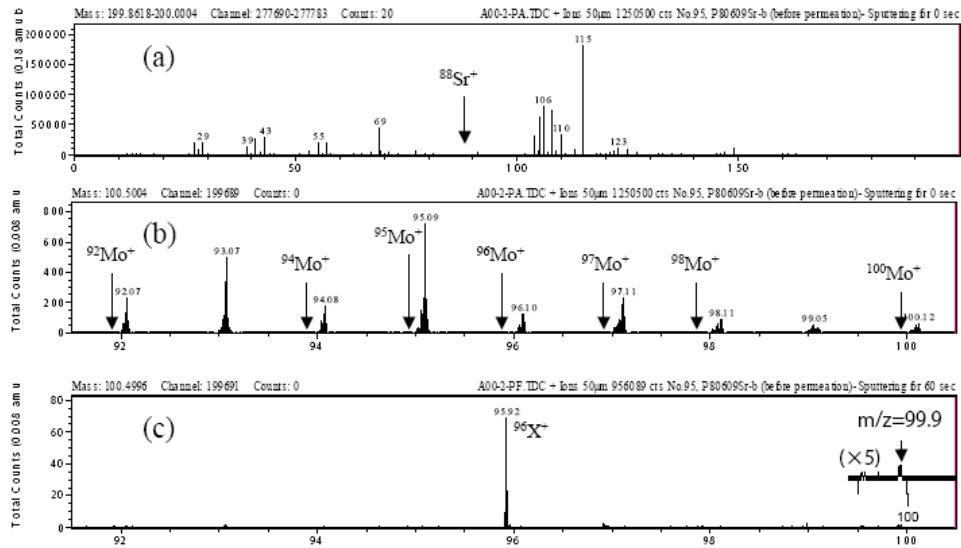


Figure 4. TOF-SIMS spectra for Pd/CaO multilayer (un-implanted area) before D_2 permeation; (a) spectrum in wide mass range at surface; (b) spectrum around Mo at surface; (c) spectrum around Mo after sputtering for 60 s.

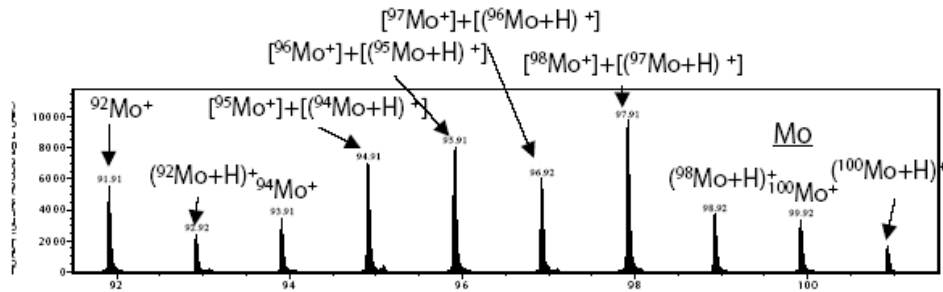


Figure 5. TOF-SIMS spectrum of the surface of Mo metal plate, and assignment of each peak.

Table 2. Accurate mass of the peak at $m/z = 95.9$ for each spectrum, and deviation from the theoretical mass of each candidate for ^{96}X .

Spectrum	Accurate mass (measured)	Deviation from the mass of each candidate			
		Ca_2O	GaAl	CaFe	^{96}Mo
Figure 3(b)	95.909	0.011	0.002	0.011	0.004
Figure 3(c)	95.916	0.004	0.014	0.018	0.011
Figure 4(c)	95.916	0.004	0.014	0.018	0.011

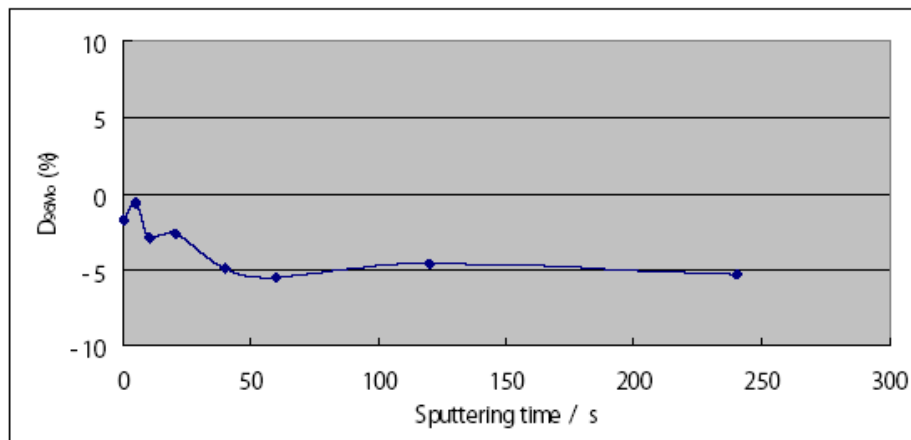


Figure 6. Relationship between deviations of measured intensities from theoretical intensity for $^{96}\text{Mo}^+$ calculated with Eq. (3) and sputtering time.

Fig. 4(c), a peak at $m/z = 99.9$ is observed. From Fig. 3(c), on the other hand, many peaks of natural Mo isotopes disturb the confirmation of the peak of $^{44}\text{Ca}^{40}\text{CaO}$. Therefore, Ca_2O is not negative for the candidate of ^{96}X .

On the other hand, ^{96}Mo or GaAl has no isotope ion. Therefore, the possibility of these for the candidates of ^{96}X cannot be evaluated by isotope abundance.

CaFe which was negative from accurate mass has an isotope of Ca^{54}Fe at $m/z = 93.9$ beside the main peak of Ca^{56}Fe at $m/z = 95.90$, and the ratio of the peak intensity of $m/z = 93.9$ to that of $m/z = 95.9$ is approximately 1–16. From Fig. 4(c), however, no peak at $m/z = 93.9$ is observed. Therefore, the possibility of CaFe is denied for the candidate of ^{96}X also from isotope abundance.

3.5. Depth profiles

By the evaluation with accurate mass and isotope abundance, as mentioned above, it was found that Ca_2O is the most probable for the candidate of ^{96}X and that ^{96}Mo or CaFe is negative. However, GaAl has not been completely denied yet, although its probability for the candidate of ^{96}X is lower than that of Ca_2O . Then, further investigation for the possibilities of these candidates was attempted by comparing the depth profiles of ions relating to the candidates. For this investigation, it is necessary to divide the peak of $m/z = 95.9$ on measured spectra into $^{96}\text{X}^+$ and $^{96}\text{Mo}^+$ of nature. For this purpose, the reliability of the peak intensity of $^{96}\text{Mo}^+$ of nature calculated from measured data was evaluated by comparing it with theoretical intensity of $^{96}\text{Mo}^+$ calculated from natural abundance and measured intensity as follows;

The peak intensity of $m/z = 95.9$ measured from a TOF-SIMS spectrum of a surface of natural Mo is not the intensity of $^{96}\text{Mo}^+$, because it consists of $^{96}\text{Mo}^+$ and $(^{95}\text{Mo}+\text{H})^+$, as shown in Fig. 5. Among the observed peaks, the measured peak intensities of $m/z = 91.9$, $m/z = 92.9$, $m/z = 93.9$, $m/z = 98.9$, $m/z = 99.9$, and $m/z = 100.9$ are those of $^{92}\text{Mo}^+$, $(^{92}\text{Mo}+\text{H})^+$, $^{94}\text{Mo}^+$, $(^{98}\text{Mo}+\text{H})^+$, $^{100}\text{Mo}^+$, and $(^{100}\text{Mo}+\text{H})^+$, respectively. Therefore, the ratio of intensities of $(\text{Mo}+\text{H})$ to Mo can be calculated from the ratio of peak intensities of $m/z = 92.9$ and $m/z = 91.9$, or $m/z = 109.9$ and $m/z = 99.9$. In this study, the ratio of $\text{Mo}+\text{H}$ to Mo was calculated by the measured peak intensities of $m/z = 92.9$ and $m/z = 91.9$. By this ratio, the intensity of $^{96}\text{Mo}^+$ ($I_{96\text{Mo}}$) can be calculated from measured peak

intensities as Eq. (1).

$$\begin{aligned}
 I_{96\text{Mo}} &= I_{95.9} - I_{(95\text{Mo}+\text{H})} \\
 &= I_{95.9} - (I_{92.9}/I_{91.9})I_{95\text{Mo}} \\
 &= I_{95.9} - (I_{92.9}/I_{91.9})[I_{94.9} - (I_{92.9}/I_{91.9})I_{93.9}],
 \end{aligned} \tag{1}$$

where, $I_{95.9}$, $I_{92.9}$, $I_{91.9}$, $I_{94.9}$, and $I_{93.9}$ represent the measured peak intensities of $m/z = 95.9$, $m/z = 92.9$, $m/z = 91.9$, $m/z = 94.9$, and $m/z = 93.9$, respectively.

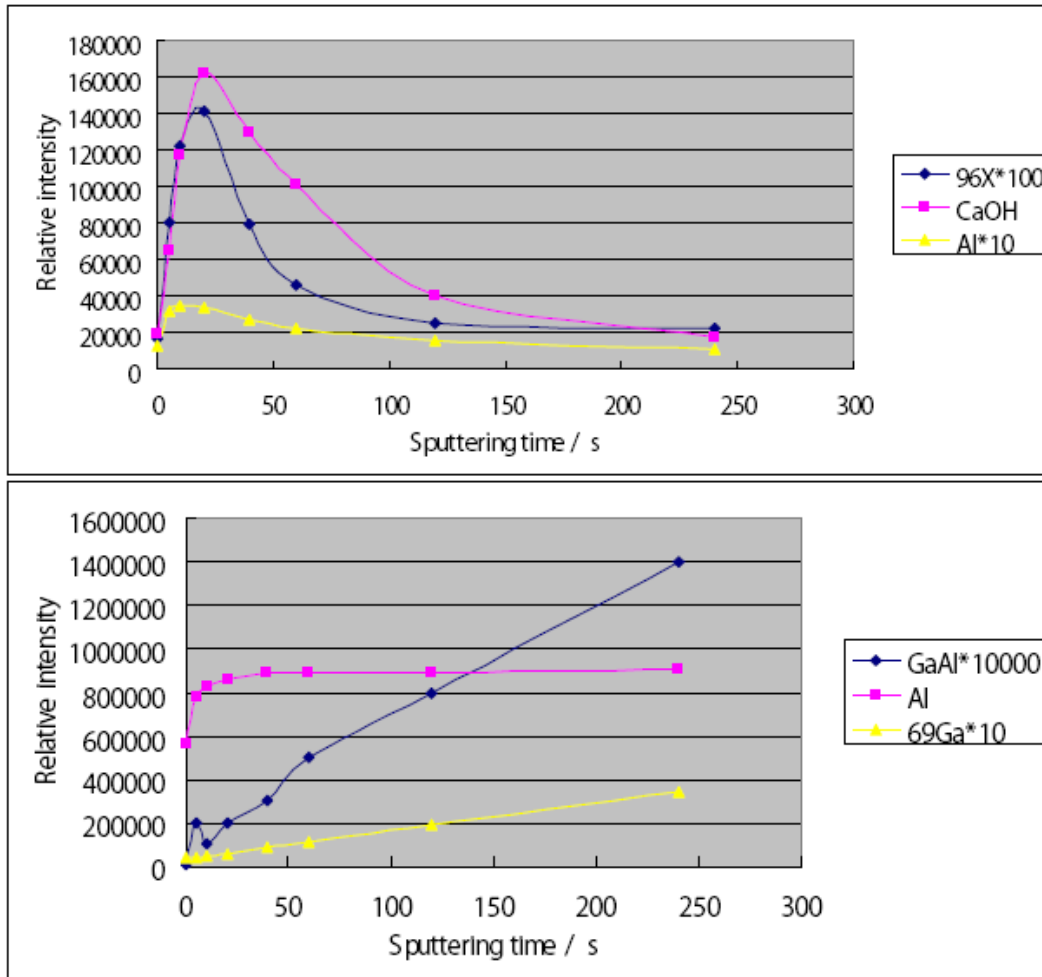


Figure 7. Depth profiles obtained by TOF-SIMS analysis; (a) $^{96}\text{X}^+$ (blue line), CaOH^+ (pink line), and Al^+ (yellow line) profiles for Sr implanted Pd/CaO multilayer after D_2 permeation; (b) GaAl^+ (blue line), Al^+ (pink line), and $^{69}\text{Ga}^+$ (yellow line) profiles for Al foil.

On the other hand, theoretical intensity of $^{96}\text{Mo}^+$ ($T_{96\text{Mo}}$) can be calculated by a natural abundance ratio of ^{96}Mo to ^{92}Mo , i.e. (16.68/14.84) and measured peak intensity of $^{92}\text{Mo}^+$ as Eq. (2).

$$T_{96\text{Mo}} = (16.68/14.84)I_{91.9}. \quad (2)$$

Then, we define a deviation of measured intensity from theoretical intensity as Eq. (3).

$$D_{96\text{Mo}} = 100(I_{96\text{Mo}} - T_{96\text{Mo}})/I_{96\text{Mo}}. \quad (3)$$

When TOF-SIMS measurements were performed on eight different positions of a pure Mo metal plate, all the $D_{96\text{Mo}}$ were within $\pm 4\%$. And when the measurements were performed with sputtering, the $D_{96\text{Mo}}$ were approximately -5% , independently of sputtering time after 50 s as shown in Fig. 6. From above results, it was confirmed that the peak intensity of $^{96}\text{Mo}^+$ calculated with Eq. (1) is reliable within $\pm 5\%$ in the case of depth profiling, and that the intensity of $^{96}\text{X}^+$ can be calculated from the measured peak intensities of $m/z = 95.9$ and $m/z = 91.9$ as Eq. (4).

$$\begin{aligned} I_{96\text{X}} &= I_{95.9} - T_{96\text{Mo}} \\ &= I_{95.9} - (16.68/14.48)I_{91.9}. \end{aligned} \quad (4)$$

Figure 7 shows depth profiles of $^{96}\text{X}^+$ using the data calculated by the Eq. (4) with those of peaks relating to Ca_2O and GaAl . From Fig. 7(a), the profiles of CaOH^+ originating from CaO are rather similar to that of $^{96}\text{X}^+$. This result is compatible to the results of the investigation from accurate mass and isotope abundance. On the other hand, the profile of Al^+ is not so similar to that of $^{96}\text{X}^+$ as CaOH^+ . Furthermore, from Fig. 7(b), the intensity of GaAl^+ is four orders of magnitude smaller than that of Al^+ at the surface after 120 s sputtering in the case of an Al foil, whereas the intensity of $^{96}\text{X}^+$ is only one order of magnitude smaller than that of Al^+ at 120 s sputtered surface. This result indicates that GaAl is negative as the candidate of ^{96}X .

From the above results of TOF-SIMS investigation, it was clarified that the peak of $m/z = 96$ observed on the sputtered surfaces is not $^{96}\text{Mo}^+$, GaAl^+ or CaFe^+ , but Ca_2O^+ originated from Pd/CaO multilayer. This conclusion is supported by the fact that Ca_2O^+ is detected from surface region of a Pd/CaO multilayer not implanted with $^{88}\text{Sr}^+$ as shown in Fig. 8.

4. Conclusions

From the surface of the $^{88}\text{Sr}^+$ ion implanted Pd/CaO multilayer, Mo was clearly detected by XPS after D_2 permeation. However, this Mo was found to be a natural Mo from the isotope abundance obtained by TOF-SIMS.

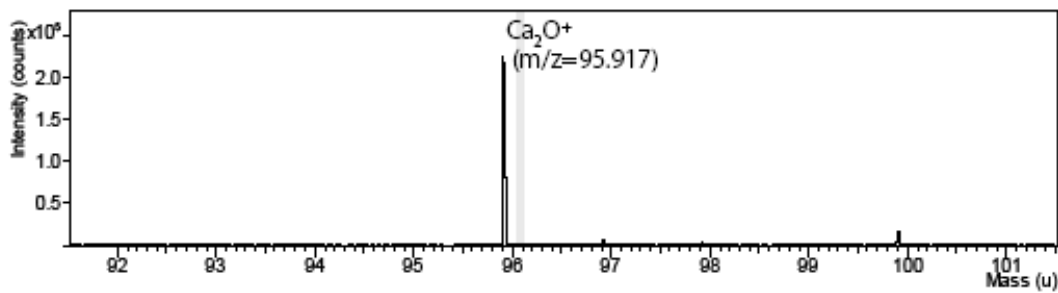


Figure 8. TOF-SIMS spectrum of Pd/CaO multilayer without Sr implanting. The integral of spectra from surface to about 5 nm depth by O_2 sputtering.

By TOF-SIMS analysis after removing the outermost surface layer containing natural Mo with ion sputtering, a strong peak at a mass close to ^{96}Mo was observed, which might be assigned to GaAl^+ , Ca_2O^+ or CaFe^+ , beside $^{96}\text{Mo}^+$.

By analyses of the TOF-SIMS data from the viewpoint of accurate masses, depth profiles and isotopic abundances, it was clarified that the peak of $m/z = 96$ was assigned to Ca_2O^+ originated from Pd/CaO multilayer.

Acknowledgments

The authors would like to thank Dr. Y. Iwamura of Mitsubishi Heavy Industries Inc. for useful discussions, also thank Drs. J. Gao, H. Azuma, and A. Ito for helpful discussions.

References

- [1] Y. Iwamura, M. Sakano, and T. Itoh, *Jpn. J. Appl. Phys.* **41** (2002) 4642–4648.
- [2] T. Iwamura et al., *Proc. ICCF11*, Marseilles, France, 31 October–5 November, 2004, pp. 339–350.
- [3] T. Higashiyama et al., *Proc. ICCF10*, Cambridge, USA, 24–29 August, 2003, pp. 447–454.
- [4] A. Kitamura et al., *Proc. ICCF12*, Yokohama, Japan, 27 November–2 December, 2005, pp. 272–277.
- [5] F. Celani et al., *Proc. ICCF10*, Cambridge, USA, 24–29 August, 2003, pp. 379–397.
- [6] Y. Iwamura et al., *Proc. ICCF10*, Cambridge, USA, 24–29 August, 2003, pp. 435–446.
- [7] T. Hioki, N. Takahashi and T. Motohiro, *Proc. ICCF13*, Sochi, Russia, June 25–July 1, 2007, Y. Bazhutov (Ed.), Publisher Center MATI, Moscow, Russia, 2008, pp. 518–528.
- [8] J.S. Gao et al., *J. Vac. Sci. Technol.* **A28**(1) (2010) 147–151.
- [9] T. Hioki et al., *Proc. ICCF14*, Washington DC, USA, 10–15 August, 2008, pp. 203–211.
- [10] T. Hioki et al., *J. Condensed Matter Nucl. Sci.*, to be published.



Research Article

Modified Szpak Protocol for Excess Heat

Dennis Letts *

12015 Ladrado Lane, Austin, TX 78727, USA

Peter L. Hagelstein †

Research Laboratory of Electronics, MIT, Cambridge, MA 02139, USA

Abstract

In recent theoretical work, vacancies in PdD have been shown to be able to host molecular D₂, which is conjectured to be necessary for excess heat in Fleischmann–Pons experiments. Vacancies in the original Fleischmann–Pons experiment are proposed to be created through inadvertent codeposition at high loading. This suggests that a better approach should be to focus on experiments in which Pd codeposition is controlled, such as in the Szpak experiment. Unfortunately, the Szpak experiment has proven difficult to replicate, and we conjecture that this is due to low D/Pd loading. A modified protocol has been tested in which codeposition is carried out at higher current density with a lower PdCl₂ concentration. Positive results have been obtained in all of the tests done with this protocol so far.

© 2012 ISCMNS. All rights reserved.

Keywords: Codeposition, Deuterium, Excess power, Palladium, Seebeck calorimetry, Vacancies

1. Introduction

Fleischmann, Pons, and coworkers first claimed to observe large amounts of excess energy in heavy water electrolysis experiments in early 1989 [1]. Controversy followed, as could have been expected due to the nature of the claims. Probably the biggest issue was that it was argued that the effect was nuclear, yet there were not energetic particles commensurate with the energy produced that would be expected if any known exothermic nuclear reaction were responsible. Also at issue was whether the experiment could be replicated, since in the months following the initial announcement a great many negative results were reported.

Over the many years that have ensued, enough positive results have been reported that those working in the field are sure that there is an excess heat effect associated with the Fleischmann–Pons experiment. There is not agreement on the physical mechanism responsible, but it is clear that the effect is new. One picture widely held by the researchers

*E-mail: lettslab@sbcglobal.net

†E-mail: plh@mit.edu

is that in the new physical process, two deuterons interact in some new way to make ^4He , with the reaction energy converted to condensed matter degrees of freedom prior to thermalization.

An effort was made by McKubre and coworkers to identify the necessary conditions required to see the effect, which allows a better understanding of why so many negative results were obtained early on [2]. In the SRI experiments it was found that cathodes that had not loaded to a peak D/Pd loading of about 0.95 were unlikely to produce an excess heat effect. As a separate requirement, the D/Pd loading needed to exceed about 0.85 during an excess heat event, since the excess power seemed to be roughly parabolic in loading above this threshold. Also, there was observed a requirement on the time during which the cathode was loaded prior to the observation of excess heat; typically a cathode would need to be loaded for 2–4 weeks before excess heat could be seen. These requirements generally were not met in essentially all of the early experiments where no excess heat was seen.

2. Vacancies

It seems reasonable to ask why such requirements on D/Pd loading and loading time are important in the Fleischmann–Pons experiment. In one line of argument, the issue has to do with arranging for two deuterons to come together to make D_2 inside the cathode. The basic problem is that the electron density is too high in PdD for D_2 to form. When the electron density is 0.06 electrons/ \AA^3 or higher, there is significant occupation of the antibonding orbitals, which results in a large separation between the deuterons. The lowest electron density in PdD due to the Pd occurs at the octahedral sites, where the electron density is near 0.08 electrons/ \AA^3 . For a molecule to form, by analogy with sigma-bonded Pd: D_2 , the electron density due to the Pd should be near 0.033 electrons/ \AA^3 [3]. It has been conjectured that such a low electron density can occur in the vicinity of a Pd vacancy, and recent density functional theory calculations suggest that sigma-bonded D_2 should be reasonably tightly bound near an O-site next to a vacancy where the other O-sites are occupied by deuterium atoms [4].

Given such an argument, we are motivated to consider the problem of vacancy formation in PdD. Vacancies are unstable in pure Pd, as it requires on the order of 1 eV to produce a Pd monovacancy in crystalline Pd. Adding H or D to Pd leads to a stabilization of the vacancies (see Figure 1), so that by the time the D/Pd loading reaches 0.95, the lattice near room temperature would be able to find a lower energy if it could rearrange into a different phase with on the order of 25% Pd vacancies. Fukai and coworkers took advantage of this effect to produce $\text{Pd}_{0.75}\text{H}$ in a superabundant vacancy phase where one out of every four Pd atomic sites was vacant [5].

Consistent with this line of reasoning is to associate the requirement in the SRI experiments that the cathode reach a D/Pd loading of 0.95 with the loading required to stabilize vacancies in PdD. In essence, we need the vacancies so that we can form D_2 inside the cathode, and to do so we need for the cathode to reach a loading of 0.95 so that the vacancies can form. We might imagine that when the D/Pd loading reaches 0.95, that vacancies might be able to diffuse inward from the surface or from internal voids. Unfortunately, the atomic self-diffusion rate of Pd is very low; we would expect essentially no diffusion of Pd over the course of the experiment near room temperature.

So, at a D/Pd loading of 0.95, vacancy formation is favored thermodynamically, but the cathode seems to be restricted in its ability to make the needed vacancies. In the analysis of the elemental composition of cathodes used in Fleischmann–Pons experiments it has been noticed that a variety of elemental impurities appear in the outer 100–300 nm of the cathode, including Pt which is presumed to come from the Pt anode. This motivates us to consider the possibility that the Pt and other impurities were codeposited during electrolysis. Since considerable Pd is present in the outer layer, it follows that it too was most likely codeposited. This is significant since if this codeposition takes place at a loading of 0.95 or higher, then this codeposited layer should have superabundant vacancies. In this picture, the excess heat would result from reactions associated with D_2 formation in these vacancies. This is consistent with observations of ^4He in the gas phase associated with excess heat production, since had the helium been created in the bulk deeper than 1 micron it would have remained in the lattice since the diffusion coefficient is small.

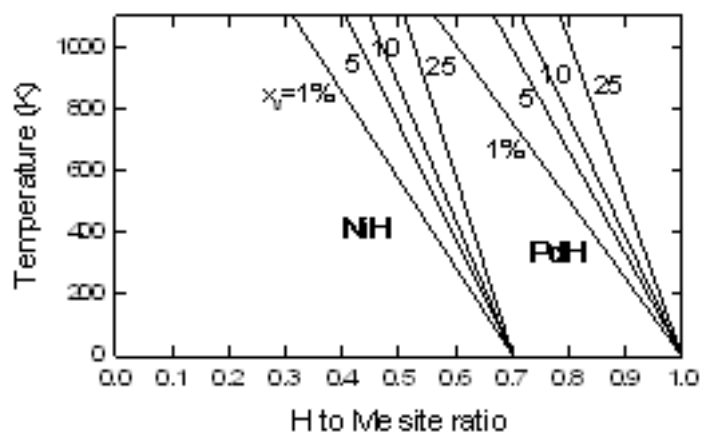


Figure 1. Estimated vacancy fraction in NiH and PdH as a function of loading and temperature. In PdH the maximum vacancy concentration at equilibrium is obtained at a loading near 0.95 at 300 K.

3. Codeposition and the Szpak Experiment

In view of the above arguments, we might consider the Fleischmann–Pons experiment to be a “bad” experiment in the sense that it works only because of a critical inadvertent and uncontrolled codeposition that takes a very long time (2–4 weeks) to occur. Since reasonably heroic electrochemical efforts are required to reach and sustain a loading near 0.95, we can begin to understand why the Fleischmann–Pons experiment has been so difficult to master over the years.

These arguments motivate us to consider the Szpak experiment, in which palladium is added to the electrolyte as PdCl_2 , and codeposited on a copper substrate [6]. According to the ideas outlined above, this experiment has the potential to improve on the Fleischmann–Pons experiment since the Pd codeposition is now a key step in the experimental protocol, rather than occurring inadvertently. Rather than waiting for 2–4 weeks, we might expect excess power to be observed as soon as the Pd is codeposited in the Szpak experiment. This is consistent with observations in successful Szpak codeposition experiments.

However, the D/Pd loading in the Szpak experiment is uncontrolled, which is of concern to us given the requirement that we need the D/Pd loading to be at or above 0.95 in order for the vacancies to be favored thermodynamically. That this is an issue in the Szpak experiment is reflected in the literature in the relative absence of replications showing excess heat.

From our perspective, this is perhaps simple to understand. The equilibrium loading in PdD depends on current density, and higher loading tends to occur at higher current density (certainly in the Volmer–Tafel regime). We would expect that the D/Pd loading relation will likely be different in a codeposition experiment than in a Pd rod or foil experiment, since the latter probably are dominated by internal Tafel losses that are probably absent in the codeposition experiment. Nevertheless, based on the arguments given above, we would ideally like to see codeposition run at a high current density to help ensure reaching a D/Pd loading of 0.95.

Unfortunately, codeposition at high current density is problematic in the Szpak experiment, primarily since an adhesion problem occurs when the Szpak experiment is run with too high of a current density [7]. If so, then there is a

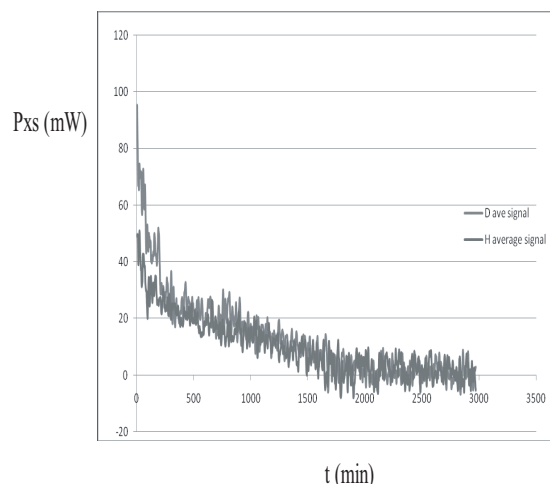


Figure 2. Excess power as a function of time for the Szpak experiment (courtesy of D. Cravens); comparison between heavy water cell result (D_2O) and light water control (H_2O). Pd was codeposited on polished copper in 0.3M LiCl in D_2O with 0.03 M $PdCl_2$; the current density used for codeposition was 1 mA/cm² for 8 hours, then 3 mA/cm² for 8 hours, then 5 mA/cm² for 8 hours.

subtle difficulty built into the Szpak experiment. To get it to work, the D/Pd loading has to be very high at low current density; and if it happens not to be high enough, then large numbers of vacancies can't be created, and no excess heat will be seen. Although there have been many attempts to replicate the Szpak experiment, the number of confirmations is low, suggesting that this D/Pd loading issue may be important. Based on the discussion above, only those groups who are able to achieve very high loading at low current density have reported success in the Szpak experiment; the others have not obtained positive results (see the results in Fig. 2).

4. Modified Szpak Protocol at High Current Density

The original Szpak protocol uses LiCl at a concentration of 0.30 M and $PdCl_2$ at 0.05 M [6]. In [7], the current density is raised in steps to 1.3, 2.6, and 6.3 mA/cm². A low current protocol was used successfully by Miles, who used 6 mA of electrochemical current for 48 h, then 100 mA for another 48 h [8]. In our tests, this protocol did not produce excess power, which motivated us to explore modifications of the protocol. In an initial effort to produce more vacancies, we started our experiments at 6 V, 500 mA/cm², and it was observed (as others have found) that the adhesion of the codeposited Pd was poor; excessive palladium accumulation on the cathode caused bridging between the anode and cathode.

To address the adhesion and bridging problems, codeposition was attempted at high current density with a reduced concentration of Pd in the electrolyte. The resulting codeposited Pd layer had much improved adherence, and we observed excess power in all experiments with the modified protocol. In our modification of the Szpak protocol, we begin by plating a bare copper cathode with gold, typically for 5 min at 3 V and 200 mA/cm². The plating solution we used was obtained from GoldTouch Inc., TivaGlo 24 kt, stock number GLO1Q. The gold plating was applied to the copper substrate ($5 \times 10 \times 0.6$ mm) in a separate beaker before beginning the calorimetric part of the experiment. When plating was complete, the cathode was rinsed in tap water and dried. Our electrolyte was mixed using 100 g of 99.9% D_2O from Aldrich, 0.15M LiCl and 0.44 g palladium (II) chloride solution, 5 wt.% solution in 10 wt.% HCl. Our chemical concentration was nominally 50% less than the original Szpak protocol; however, the actual concentration of palladium was 0.00125 M, or 1/40-th of Szpak's original concentration of palladium. This drastic reduction of

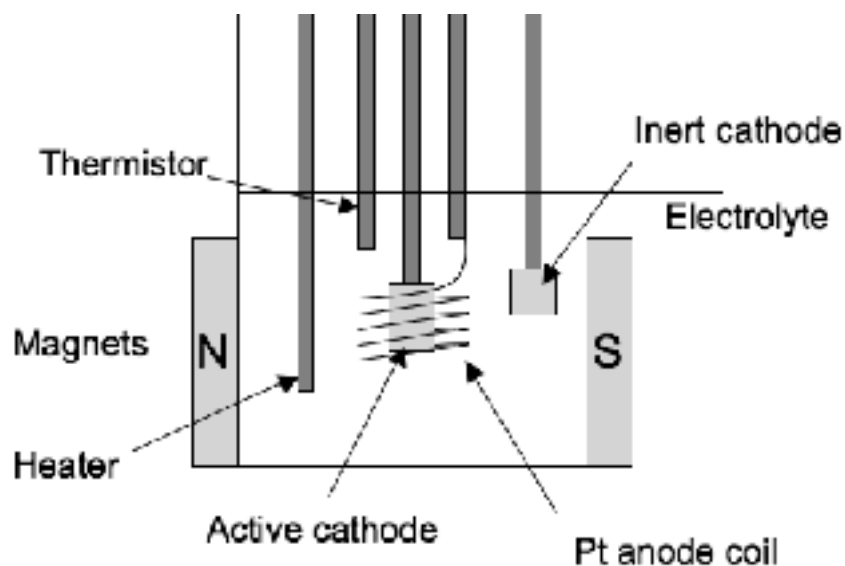


Figure 3. Schematic of the cell used in our experiments.

concentration allowed us to reduce the rate at which palladium is deposited on the cathode, which we reasoned might allow improved Pd adhesion at higher current densities. Codeposition was done at about 500 mA/cm^2 , and the solution clears in a couple of hours.

5. Experimental Set-up

The electrochemical cell contains the codeposition cathode (described above) surrounded by a spiral Pd anode, as depicted in Fig. 3. Also shown is a second "dead" (Ti) cathode which was used for calibration. Temperature sensors are indicated, and an immersion heater was used to set the cell temperature. External magnets were used in these experiments, as we have found in earlier work that they seem to help. A siphon (not shown) is located in the rear of the cell to allow replacement of the electrolyte during the experiment. All cells were closed and gases recombined using 1/8 inch alumina pellets coated with 0.5% platinum reduced (Alpha Aesar, #89106). The recombiner pellets were supported by a Teflon post attached to the cell lid as shown in Fig. 4. The recombiners worked well as long as cell temperature was maintained between 45 and 50°C. A bubbler containing spent electrolyte was used to monitor recombiner activity. In personal communications, Miles has reported that closed cells prevent the removal of H_2O impurity during electrolysis. The first author saw this confirmed using NMR analysis in 2004, so it is interesting that the presence of a small amount of H_2O does not seem to inhibit the heat producing effect during codeposition.

6. Calorimeter

Calorimetry at 1% level of precision using was done using a Seebeck calorimeter constructed using thermoelectric devices (TEC's) epoxied to a rectangular glass vessel with Duralco 128 thermal epoxy. The approach used in this study relies on air coupling to keep the cool side of the TEC's at a constant temperature. A schematic of the calorimeter is shown in Fig 5. A laser view port is visible, which provides access for cathode inspection and laser stimulation. The



Figure 4. The electrode holders and thermistor probes are 5 mm diameter sealed glass tubes. Hook up wire is 0.5 mm platinum wire spot welded to copper wire sealed inside the glass tubes. The platinum wire is sealed against the soft glass tubing making an airtight seal. Recombiner pellets are also shown.

area of the view port is $\sim 4\%$ of the total surface area of the calorimeter. A strong airflow up the axis of the heat sinks is provided by a 4 inch brushless DC fan. Two thermistors are secured in the aluminum trough to provide feedback for controlling air temperature to within $\pm 0.02^\circ\text{C}$. Highly conductive thermal epoxy (Duralco 128) provides good thermal transfer, but is not electrically conductive.

The core of the calorimeter is a rectangular piece of borosilicate glass 15 cm long and 45 mm on each side (Friederich & Dimmock, #BST45-200, Fig. 5). The wall thickness is 2 mm. A square-to-round Teflon lid provides sealing for the electrochemical cell and support for up to six electrode holders/thermistor probes. The Teflon lid provides six pass through holes for one thermistor (Digi-Key, 2250 Ω , #615-1000-ND), an immersion heater, a gas vent tube, an anode, a main cathode, a calibration cathode or a siphon tube so that the electrolyte can be changed during operation without loss of precision. The lid also supports the recombiners as shown in Fig. 4.

Two Cu plates are epoxied to the outside of the cell wall; magnets are epoxied to the Cu plates; and TEC's are epoxied to the magnets. The Cu plates provide an optional high voltage electric field; the two magnets provide a 500 G magnetic field at the cathode (United Nuclear, two 2" \times 1/4" plate magnets). The copper plates are electrically insulated by the Duralco 128 epoxy. A 25 \times 50 mm viewport provides visual and laser access to the cathode during operation without loss of calorimetric precision (Fig. 5). The 50 \times 50 mm TEC's (Thermal Enterprises, eBay store, #TEC310117657888) are epoxied directly to the electrochemical cell except the area containing the copper plates and magnets, providing for rapid heat transfer and thermal equilibration. The thermal epoxy used was Duralco 128 with 10% flexibilizer (Cotronics Corp., # 105RF-1) to avoid thermal expansion damage.

7. Calorimeter Performance

The Seebeck calorimeter was typically run in a controlled temperature enclosure capable of holding the ambient temperature at a set point ranging from 15 to 35°C; $25 \pm 0.02^\circ\text{C}$ was the preferred temperature set point. Calibration checks were run before each experiment using a titanium cathode which is known to be inert in LiCl, PdCl₂, and D₂O

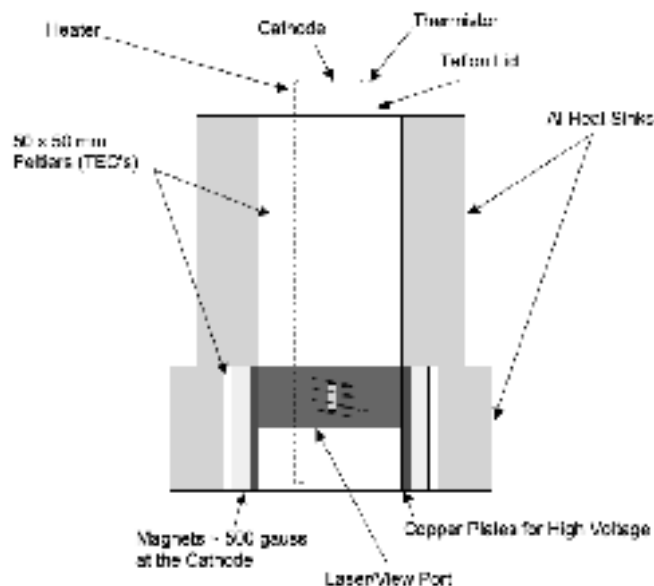


Figure 5. Schematic of the Seebeck calorimeter.

electrolyte. The anode was a coil of platinum wire with an inside diameter of 12 mm and 5 turns over the cathode length. An immersion heater was in the cell and provided constant DC power at 11 W to keep the cell temperature about 45°C so the recombiners would work properly in the chloride environment. A calibration was typically performed before each experiment over the power range to be tested (11–14 W). The immersion heater provided a constant 11 W and the electrolysis power was varied over 0.5–3.5 W. The cell was closed and recombination of the gases was provided by alumina pellets coated with 0.5% platinum. The cell was not mechanically stirred, although the external magnetic field provided some degree of stirring.

The fitting coefficients of the calorimeter vary slightly depending on how the lid pass-throughs are configured for the experiment, which is the motivation to perform a calibration check before each experiment. However, once calibrated for a particular experiment, the Seebeck calorimeter retains the calibration coefficients even if the calorimeter is opened for maintenance. The Seebeck produces a good calibration plot over a wide range of power. As long as 0.5 W of electrolysis is provided for stirring, heater power can be substituted for electrolysis power for on-the-fly calibration checks (Fig. 6).

8. Experiment 684d

Experiment 684d was designed to permit changing or repositioning of the electrodes and removal/replacement of the electrolyte while the experiment is running. This can be done without changing calorimeter performance or calibration. The cathode used for 684d was a $4 \times 10 \times 0.6$ mm Cu substrate plated with Au for 5 min at 3 V, 200 mA. The anode coil was 0.999 Pt wire with an ID of 12 mm. The electrolyte was 0.15 M LiCl and nominally 0.025 M palladium (II) chloride solution, 5 wt.% in 10 wt.% HCl, in 100 mL of 99.9% D₂O. The actual concentration of palladium was 0.00125 M as mentioned above, which was 1/40-th of the original Szpak concentration. A 5 mm glass tube 16 cm long was located in the rear of the cell to remove/replace electrolyte during the experiment. The cathode width was

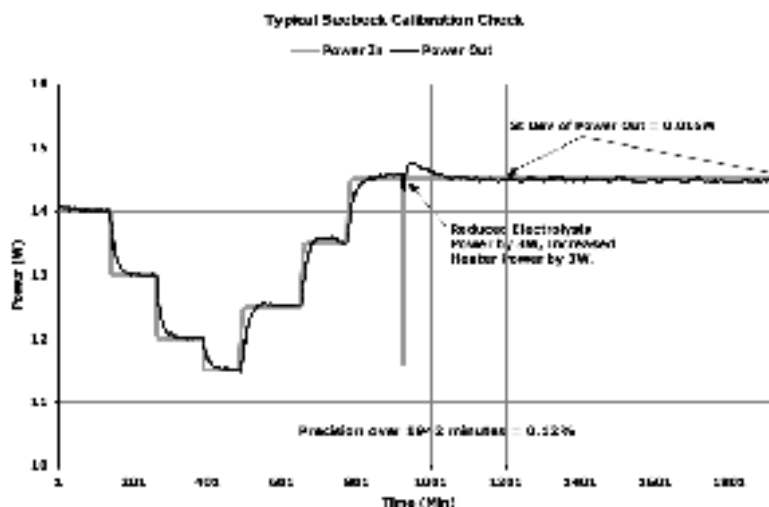


Figure 6. Results from calibration test which shows that calibration provides for a good input/output power balance over the tested range of 11.5–14.5 W ($P_{out} - P_{in}$)/ P_{in} at $\sim 0.12\%$ over the entire range tested.

reduced from previous experiments so the cathode could be withdrawn through the 5 mm lid pass-through during the experiment.

Results from this experiment are shown in Fig. 7. Up to point 800, the “dead” Ti cathode was electrolyzed at 3 W outside of the anode coil (see Fig. 3); the cell during this time was in power balance to within 1%. At point 800, electrolysis was diverted to the gold plated copper cathode inside the Pt anode coil. An excess power signal of 250 mW appeared very quickly and cell temperature increased at the same time by 4–5°C. The excess power signal and cell temperature remained elevated, producing ~ 7 kJ of excess energy. At point 1100, a pump was activated to remove the deuterium-based electrolyte and replace it with hydrogen-based electrolyte of identical volume and concentration as that used at the start of the experiment. As seen in Fig. 7, the excess power signal declined over a nine-hour period after replacing D_2O with H_2O .

9. Experiment 685

Experiment 685 was similar to 684d: the cathode was gold plated copper, $5 \times 10 \times 0.6$ mm, plated with gold for 5 min at the same current. The electrolyte was fresh for 685, while 684d ran with electrolyte that had been used once previously (the freshness of the electrolyte may be a factor). The “dead” Ti cathode was electrolyzed over points 0 - 1100 and appeared to produce about 100 mW of excess power (no excess power was expected since Ti seemed to be inactive in previous work we have done). At point 1100 of Fig. 8, electrolysis power was switched to the active gold-plated copper cathode and a very robust excess power signal appeared immediately, recovering 110 kJ of excess energy. The signal showed no signs of diminishing over 60 h.

10. Experiments 690a and 691d

These experiments were performed as a matched pair with one using a heavy water electrolyte, and one using a light water electrolyte as a control. During the first four hours of these two experiments, the cells were electrolyzed using

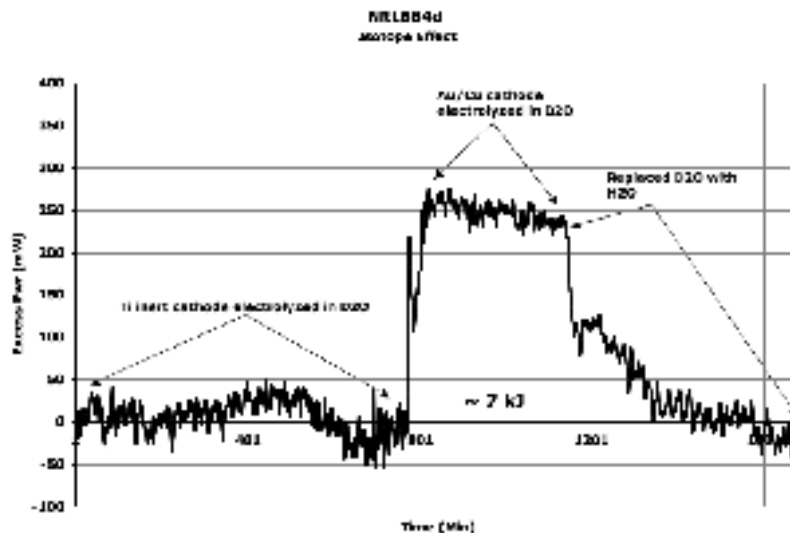


Figure 7. Excess power as a function of time for 684d. From minute 0 to minute 800 the cell was run using the "dead" Ti cathode; between 800 and 1100 the Pd/Au/Cu cathode was used and excess heat was seen; after 1100 the D₂O electrolyte was replaced by H₂O and the system returned to power balance.

LiCl as a salt. After the cells were in thermal equilibrium at minute marker 240, palladium chloride was added to the cells. As can be seen from the data shown in Fig. 9, the two cells responded very differently. Experiment 690a (D₂O) produced a robust exothermic response, recovering almost 4 kJ of excess energy over 4 hours. In contrast, 691d (H₂O) produced a slightly endothermic response from H₂O based electrolyte, absorbing approximately 529 J of energy. In both experiments, 0.44 g of palladium (II) chloride solution, 5 wt.% solution in 10 wt.% HCl was added to the electrolysis cell. The endothermic response observed in this experiment could have been due to calorimeter error, high loading of the palladium, or chemical reactions producing a net absorption of energy. We discounted calorimeter error because the instrument was well calibrated before experiment 691d and a post-experiment test was made of the calorimeter, which showed the instrument remained in good calibration. We also discounted the possibility of endothermic high loading because the amount of palladium on the cathode was too small to produce the observed 529 J endotherm. In a personal communication, Dr. Melvin Miles suggested that the reaction $\text{HCl} + \text{H}_2\text{O} \rightarrow \text{HClO} + \text{H}_2$ forming hypochlorous acid would be a good candidate. Dr. Miles estimated the net enthalpy change to be +332.1 kJ/mol. We estimated that the amount of chlorine available for this reaction was 0.0016 mol from adding 0.44 g of PdCl₂ solution and from the existing LiCl in the cell at the time of the addition. The palladium chloride solution was weighed on an inexpensive lab scale with an accuracy estimated at 5%. So, the calculated net enthalpy change was in the range of 503–555 J and agreed with the observed value of +529 J within experimental accuracy.

11. Discussion

The experiments reported here began as part of a program focused on the Szpak experiment as a possible cold fusion "lab rat" experiment. One motivation for this has been the difficulties over the years in obtaining Pd cathodes which are capable of attaining a high D/Pd loading and giving high levels of excess power. Recent advances at ENEA Frascati have improved the situation, but issues remain. However, if it is the case that the important thing that is going on in the

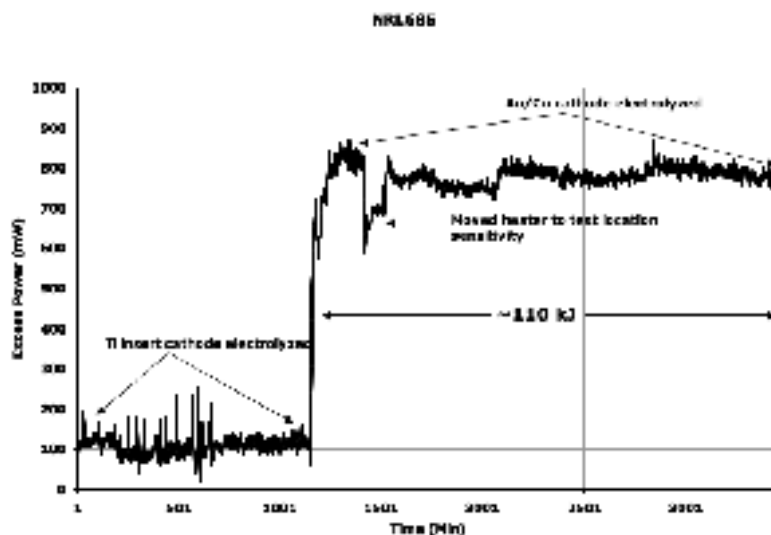


Figure 8. Excess power as a function of time for experiment 685. Between minute 1 and minute 1100 the "dead" Ti cathode was electrolyzed; after 1100 electrolysis was switched to the Pd/Au/Cu cathode with an associated increase in the excess power. A variation in the excess power is noted at a time when the immersion heater location was changed.

Fleischmann–Pons experiment is the creation of vancancies in the outer 100–300 nm of the surface through inadvertent codeposition, then we should be able to do better pursuing codeposition experiments.

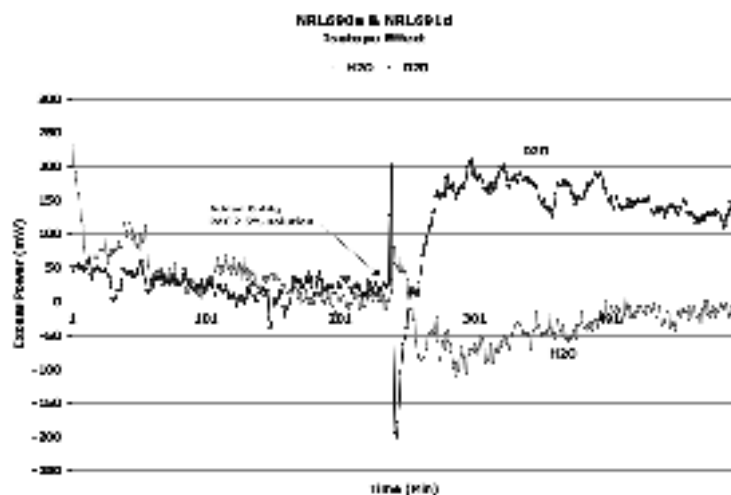


Figure 9. Excess power as a function of time for the heavy water cell (690a) and a matched light water cell (691d). The cells were run to near power balance up to 240 min, where PdCl_2 was added.

The best known codeposition experiment is the Szpak experiment, which has so far given positive excess heat results in the hands of only a few groups. In light of the ideas discussed above, codeposition experiments should probably play a much bigger role in the field. So, the obvious question is: what makes the Szpak experiment so difficult to replicate? If it is vacancy production, then the clear answer is that the loading needs to be higher during Pd codeposition, which suggests that the weak link in the Szpak protocol is the relatively low current density. Low current density is needed so that the Pd adheres; at higher current densities the Pd does not adhere well at a PdCl_2 concentration of 0.05 M.

We encountered this problem, and in response, we explored a modification of the Szpak protocol where the PdCl_2 concentration is reduced, which allows the Pd to stick even when the codeposition is done at much higher current density. Positive excess heat results were obtained in all experiments we have done using this protocol so far.

In the recent SPAWAR codeposition experiments that focus on energetic particles, the current density is low during codeposition, which in our view results in fewer vacancies. In codeposition excess heat experiments carried out in 1990, the cell was run in a potentiostatic mode with a stepped protocol: 30 min at -0.5 V (-5.5 mA), then 2 h at -2.0 V (-25 mA to -40 mA); then 16 h at -2.5 V (-78 mA at the end); excess heat was sought after the Pd plated out with -190 mA [9]. The copper substrate in this case started out roughly 1 inch square, and sufficient Pd codeposited so that the cathode was approximately spherical with a 1 inch diameter (100 mL electrolyte was used) at the end of codeposition. Note that we used a higher current density than was used in this older experiment.

Acknowledgment

We are grateful to DTRA for partial support (contract N0 017308P2015), and to Breed and Harvel for contract management. We are also grateful to Dr. Melvin Miles, Rick Cantwell and Dr. Pam Boss for shaping the discussion about potential endothermic reactions.

References

- [1] S. Pons, M. Fleischmann and M. Hawkins, *J. Electroanal. Chem.* **261** (1989) 301.
- [2] M. McKubre, presented at ICCF15, 2009.
- [3] P.L. Hagelstein and I.U. Chaudhary, Arguments for dideuterium near a monovacancy in PdD, *Proc. ICCF15* (in press).
- [4] L. Dechiaro, private communication.
- [5] Y. Fukai and N. Okuma, *Phys. Rev. Lett.* **73** (1994) 1640.
- [6] S. Szpak, P.A. Mosier-Boss and J.J. Smith, *J. Electroanal. Chem.* **302** (1991) 255.
- [7] P.A. Mosier-Boss, S. Szpak, F.E. Gordon and L.P.G. Forsley, *Eur. Phys. J. Appl. Phys.* **40** (2007) 293.
- [8] M.H. Miles, private communication.
- [9] P.A. Mosier-Boss, private communication.



Research Article

Lochon-mediated Low-energy Nuclear Reactions

K.P. Sinha

Department of Physics, Indian Institute of Science, Bangalore 560012, India

A. Meulenberg *

NAv6 Centre of Excellence, Universiti Sains Malaysia, 11800 Penang, Malaysia

Abstract

In heavily hydrogenated (deuterated) palladium crystals, the crystallinity is degraded. This non-uniformity results in phonon modes that are localized and of higher frequency than for unloaded lattices. These modes create dynamic electrostatic fields that couple strongly with both bound and free electrons and the hydrogen (H and D) sub-lattice. A consequent potential inversion leads to the formation of “lochons” (local-charged bosons—electron pairs in the singlet state) and results in H^- or D^- ions in the sub-lattice. The nuclear-Coulomb repulsion between colliding $D^+ D^-$ ion pairs in the sub-lattice is considerably reduced by the resultant “strong screening” and “lochon-drag” effects. Furthermore, work is done, by the bound lochon in a D^- ion attracting an adjacent D^+ ion. This results in reductions: of the deuteron’s electron-orbital radii, as the ion pair approaches; of the mass deficit between the deuteron pair and a ^4He atom (or a proton pair and a $^2\text{He}/^2\text{H}$ atom); and finally of the Coulomb repulsion between nuclear protons in a helium nucleus. Thus, the end product of such a deuteron-pair fusion is an excited-helium nucleus ($^4\text{He}^*$) with lower energy relative to that resulting from energetic deuteron collisions. This reduced energy of the excited nucleus may be lower than its new fragmentation levels. The effect of lochon mediation, to alter the nuclear potential-well and fragmentation energies, allows decay to the ^4He ground states to be free of particulate radiation. This decay process, of “neutral” ^2He (from p+p) or ^4He excited nuclei, is also a basis for observed transmutation.

© 2012 ISCMNS. All rights reserved.

Keywords: Deep orbital, Fragmentation, LENR, Lochon, Strong screening

1. Introduction

It is now established by sustained experimental work that low-energy nuclear reaction (LENR) occurs in PdD_x or PdH_x after considerable loading when x attains a minimum value ($x > 0.8$) [1]. However, this heavy-loading process results in the degradation of crystallinity [2]. For this situation one has to consider the newly created interface-phonon modes. The solutions correspond to localized (longitudinal optical, Fig. 1) phonon modes near the interface. With particular

*E-mail: mules333@gmail.com

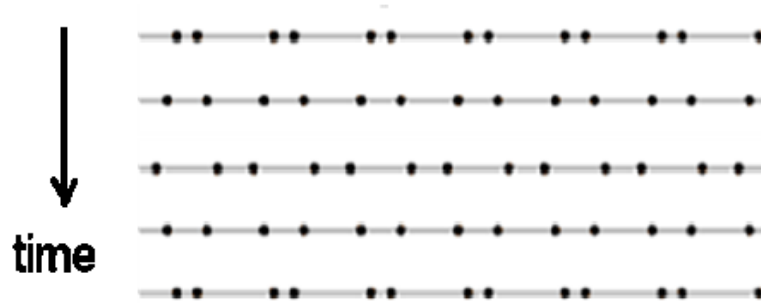


Figure 1. Longitudinal optical modes where adjacent lattice atoms/ions move in opposite directions along a common axis.

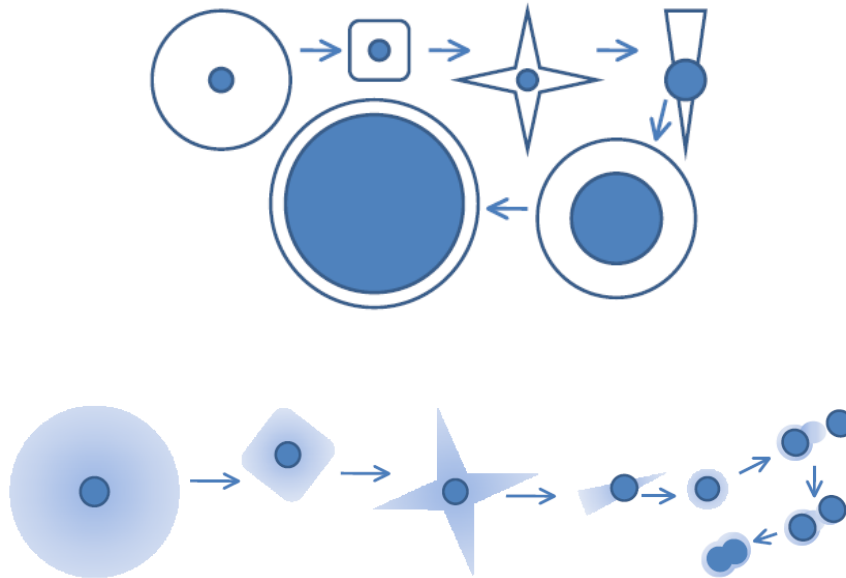


Figure 2. Schematic representation of the electron distribution (size) relative to that of a nucleus (at 1000× magnification relative to electron orbit) as a hydrogen atom moves within its PdD_x sub-lattice site (see text).

interface orientations, the major phonon modes are reduced from three dimensions to one. Further, the frequency (ω) of the localized mode is above that of the highest phonon mode of the bulk PdD lattice.

The expectation value of the number of such local phonons $\langle n_{q\omega} \rangle$ and the expectation value of their amplitude $\langle A_{q\omega} \rangle$ are related by $\langle n_{q\omega} \rangle = 2M\omega\langle A_{q\omega} \rangle^2/\hbar$, where M is the mass of the D atom (ion) and \hbar is the Planck constant divided by 2π . With $M = 3.34 \times 10^{-24}$ g, $\omega \sim 5 \times 10^{14}$ per second, and $A = 3 \times 10^{-8}$ cm, the number of phonons is of the order of a few thousands. The total energy of the local phonons could thus be in the multi-eV range.

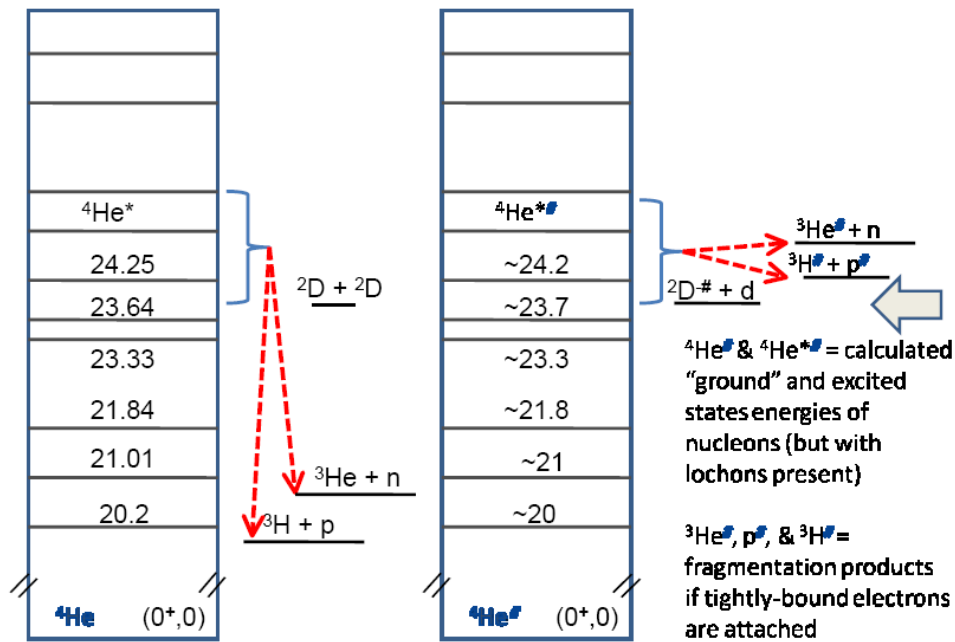


Figure 3. Energy levels for ^4He with normal atomic electrons (left side) and with tightly-bound electrons (right side).

These modes, in an ionized lattice or sublattice, create electrodynamic fields that are strongly coupled with electrons confined in the layer. This coupling and the disorder due to degradation of crystallinity lead to a localization of the electrons on some D^+ ions. The concomitant potential inversion makes it possible to produce electron pairs (in the singlet state; local charged bosons, acronym “lochons”) at some deuterons to give D^- ions [3,4]. The lochons formed by this mechanism and by phonon-induced charge polarization provide strong screening for the static and dynamically induced ion pairs D^-D^+ . As the deuterons approach each other closely and penetrate the distributed-electron Coulomb field, the residual proton–proton repulsive barrier is considerably reduced in height as well as in length by this strong screening.

The presence of lochons results in enhanced barrier-penetration probability [4] and it has been shown in our earlier papers that fusion is possible [3,4]. However, dictated by mass deficit ($Q = 23.8$ MeV), the resultant excited nuclear state, $^4\text{He}^*$, will emerge above the fragmentation levels at 20.6 and 19.8 MeV above the ^4He ground state. Thus, $^4\text{He}^*$ will likely fragment into energetic particles rather than decay to the ^4He ground state. The work done by the bound lochon, in a D^- ion attracting an adjacent D^+ ion during a phonon cycle, results in reductions of the deuteron’s electron-orbital radii, as the ion pair converges. If the lochon remains attached during a collision/fusion process, this reduced orbit lowers the mass deficit and raises the energy required for fragmentation. Thus, the lochon-modified $^4\text{He}^*$ can emerge below one, or both, of the fragmentation levels. The present work addresses this problem. The resulting extended “lochon” model may thus explain all the major observations of LENR.

2. Lochon Model and Strong Screening

Consider a chainlet of deuterons surrounded by an equal number of electrons in the interface regions of PdD_x . The Hamiltonian for this system $[H = H_e + H_L + H_{eL} + A]$ will comprise the electronic part H_e , the sub-lattice H_L of D^+ ions that execute Einstein oscillations, and an electron–phonon interaction H_{eL} . “ A ” is a constant negative energy due to space charge in the channel. After a suitable unitary transformation (diagonalizing the matrix and thus establishing the system resonances), one gets a displaced harmonic oscillator and a reduced on-site electron energy, a hopping integral, and an enhanced effective mass (by being dressed with a large number of phonons – details are given in [3,4]).

The enhanced effective mass of the electron (m^*), resulting from the interaction of an electron with the phonon field, may be critical to the present argument.

$$m^* = m_e \exp(E_d/\hbar\omega_D) = m_e \exp(g^2), \quad (1)$$

where the contribution from a single electron is $E_d = g^2\hbar\omega_D$, $\hbar\omega_D$ is the energy of the Einstein oscillator of deuteron; and g is the dimensionless electron–phonon coupling constant. The on-site electron energy is $E_m^* = E_m - E_d$ (the bare electron energy as modified by the phonon field). For the case of two electrons in a site, the Coulomb repulsion between a pair of electrons, U_e , is similarly modified (but now with $2E_d$).

$$U_e^* = U_e - 2E_d. \quad (2)$$

We see that for $U_e < 2E_d$, U_e^* becomes negative and there is potential inversion (e.g., a pair of electrons in the singlet state and localized at a D^- ion). Note that in such a lattice, a D^- state will be more stable and will have lower energy than a neutral D atom. Thus one can visualize the existence of $\text{D}^+ \text{D}^-$ pairs in the PdD_x system. Under the influence of phonon fields, such pairs may undergo dynamical oscillations in which lochons will hop from one to the other deuteron, $\text{D}^- - \text{D}^+ \leftrightarrow \text{D}^+ - \text{D}^-$ dragging each other to closer proximity. This will result in considerable reduction in the Coulomb repulsion between the two nuclei. The screened effective potential is now described by

$$U_{dd}^* = (e^*)^2/r = (e^2)(1 - \exp(-a_s/\lambda_L))/r, \quad (3)$$

where e^* is the effective charge, a_s is the strong-electron screening length, $\lambda_L = \hbar/m_L * v_L$ is the effective lochon dimension (orbit radius from the deBroglie wavelength), m_L^* its effective mass, and v_L its speed. The screening produced by lochons (bound-electron pairs) extends to short range and is much more effective in reducing the repulsive Coulomb potential between reacting nuclei (deuterons) relative to the screening effect of itinerant electrons of the system that can be ignored [5]. An important point to note is that the barrier to the penetration by quantum mechanical tunneling is associated with composite units in which not only the bare deuterons but the lochons are involved.

In the low-energy situation (e.g., LENR), the low orbital angular momentum state ($l = 0$) of the nuclei contributes most. The tunneling factor for $l = 0$, turns out to be

$$P(0, E_a) = (e^{*2}/R) \exp(-e^{*2}/\hbar v_r)/E_a, \quad (4)$$

v_r being the relative velocity and E_a the total energy; R is the effective radius of the nuclear well.

The d–d fusion reaction rate per unit area on a surface or in a defect-plane is given by [4]

$$R_{dd} = r_{dd}^* k_B T \lambda_L (N_s^2/\hbar) (e^{*2}/\hbar v_r) \exp(-e^{*2}/\hbar v_r), \quad (5)$$

where $r_{dd}^* = \hbar^2/2M_N e^2$ is the nuclear Bohr radius of a deuteron; $M_N \approx 1.66 \times 10^{-24}$ g, the mass per nucleon, k_B the Boltzmann constant, T the absolute temperature, and N_s is the number of deuterons per unit area. The calculation of the reaction rate as a function of internuclear distance is given in [4].

3. Lochons: Deepening on the Atomic Potential Well

The crucial point is that the lochon formation (D^-) and the presence of D^-D^+ pairs with attractive interaction provide a mechanism for energy transfer at the atomic level [9]. The lochon drag, involved in the movement of D^+ and D^- toward each other, results in work done and transfer of corresponding potential energy from lochons to D^+ deuterons. Since the ground-state electrons (lochon) have inadequate angular momentum to form photons, this energy loss required for them to move to deeper levels in a conventional manner must result from doing work rather than by radiation.

Figure 2 gives a symbolic representation of the electron size and distribution relative to that of the nucleus. The nucleus has been scaled at $1000\times$ that of the electron to better represent the change in size of the electron orbit. The left-most pictogram represents the electron distribution for an atom in free space. The electron distribution, as seen by a slow-moving nucleus, is that of the whole spherical s-orbit. Therefore, the electron “size” is represented by the Bohr radius determined from the deBroglie wavelength divided by 2π ($= \lambda_{dB}$). A fast-moving electron (free or bound) sees the fluctuating electric dipole of the electron–proton pair. The electron “size” is therefore strongly dependent on the observer. What does a tunneling proton see? How is this vision shaped by the environment which affects the electron distribution?

Starting as it is seen in free space, the electron ‘size/shape’ progresses to that: as confined in a Pd-interstitial site, as modified by the sub-lattice phonon field, as constricted during passage between lattice sites, as having done work greatly-in-excess of lattice-barrier height, as moving toward a nought orbit and to a nought-orbit molecule.

The square distribution symbolically represents the effects of the bound Pd-lattice electrons on confining the hydrogen-bound electron cloud. The star-shaped distribution represents the effects (on the bound-electron distribution) of 3-dimensional, phonon-induced, motion of the hydrogen atom within its sub-lattice site and of the phonon electric fields. Given the proper lattice parameters, standard quantum mechanics can represent these electron distributions.

The wedge-shaped pictogram represents the shrinking and oriented electron distribution as the atom moves into the denser Pd-electron clouds of the Pd-lattice barrier region. Next, with work being done in overcoming the barrier and bringing the D^-D^+ pair closer together, the D^- electron orbit shrinks further and becomes deep enough that it is no longer influenced by the lattice. Since these and the succeeding conditions are not average, a Born–Oppenheimer approximation must be used to determine the electron distributions, in steps, as the D^- mounts the lattice barrier and moves closer to the approaching D^+ .

The last three pictograms represent the successive distortion of the D^- electron distribution toward the D^+ ion on which it is working. This distortion (increasing the electron probability between the protons) and eventual overlap has an important effect on the D–D tunneling probability (enhancement is not calculated here). Remembering that the figure has amplified the nucleus size by $1000\times$, the electron EM-field distribution in the final stages is representative of the nought-orbit size (see Appendix). D–D tunneling probability is already high at this point; but the possibility of sharing the lochon between the nucleons and forming a molecule (based on the nought orbit) is real. This possibility is particularly important for collisions that are not truly $l = 0$. Forming the nought-orbit molecule in collisions that otherwise might not result in fusion greatly enhances the total LENR-fusion cross section. The nature of the fusion process from direct tunneling and that from the nought molecule is still to be described.

Note that at a finite temperature, the tunneling rate between lattice sites is enhanced by thermal fluctuation arising from the presence of damping in imperfect solids due to defects. The enhancement is proportional to T^2 for ohmic damping [6]. In contrast, for undamped systems, the enhancement is exponentially weak [6]. Another important enhancement of the tunneling and subsequent reaction is caused by the laser stimulation of LENR in which the system PdDx has a layer of gold film on top of it. This leads to the formation of surface plasmon polariton modes particularly in the surface region [7]. The optical potential is enhanced by several orders of magnitude. The situation is similar to surface-enhanced Raman scattering [8].

4. Lochons: Nuclear Potential Well and Fragmentation Energy

As colliding deuterons move closer together, the D^-D^+ Coulomb potential grows and the merger of a D^-D^+ pair is accelerated. As the pair comes closer yet, the D^-D^+ potential dominates the lattice barrier and the merging velocity increases. The fall of an electron pair into the Coulomb well of a deuteron causes its orbit to shrink. The field energy of the electron pair (and its centre of “mass”) eventually concentrates within tens to hundreds of Fermi of the nucleus. The cancelled charge far-field energy will be replaced by near-field electrostatic and electromagnetic energy. The source of this work, the lochon, moves deeper into the D^- Coulomb potential well. The cancellation of electric fields of electrons by protons reduces the total field energy (potential energy). This will result in a change of the mass of nuclear particles [10].

Once the D^-D^+ pair gets close enough to fuse (tunneling the last distance), then we can calculate the energy levels of the resultant excited compound atom. Let us consider the standard D–D reaction (no lochon) to give ${}^4\text{He}^*$ (where * indicates an excited state). The left-hand side of Fig. 3 shows the normal transition to excited states with total energy (above the ${}^4\text{He}$ ground state) equal to the kinetic energy (bracket) of the colliding pair plus $Q = 23.8$ MeV (broad arrow). This Q value corresponds to the energy equivalent of the mass difference between a D–D pair and the ${}^4\text{He}$ atom (same as between ${}^4\text{He}^{++}$ and 2d). These excited states are above the fragmentation levels ~ 20.6 and 19.8 MeV and will decay preferentially via these paths (dashed arrows).

Experimentally, energetic fragments from both these levels have been reported in LENR experiments. However, the excess heat observed is much greater than would be indicated by the radiation levels seen if fragmentation occurs. Furthermore, the measured amount of ${}^4\text{He}$ has been found to be orders of magnitude higher than expected from standard nuclear physics theory. More recently, nuclear transmutation of heavier nuclei has also been seen [11]. Clearly, something else must be going on.

These anomalies can be accounted for within the extended lochon model [10]. This is realized by a non-fragmentation mechanism that does not depend on new states below 20 MeV. The mechanism of tightly-bound electron pairs (lochons) shifts the ${}^4\text{He}^{++}$ nuclear level down by reducing the nuclear-proton repulsion. By the same mechanism, the fragmentation levels are also shifted up in energy. (With less Coulomb repulsion, the nucleon kinetic energy must be greater to overcome the now more-attractive nuclear potential.) In addition, both the lochon and protons have had mass converted into EM-field and kinetic energy. The right side of the figure indicates the change when the extended lochon model is introduced. The D^-D^+ mass at fusion is the same as the D–D mass. The difference is that the mass energy of the electrons (as a lochon) is greater than that of atomic electrons and the deuteron nuclei are correspondingly lighter. The Q value gives a common starting point for the two pictures. The nuclear energy levels are perturbed by the presence of the lochon. However, much of the reduction in nuclear potential is compensated by the extra energy in the lochon. Thus, most of the energy levels in both pictures are close. The major difference is in higher fragmentation levels.

With reduced repulsion between the protons, the nuclear wave functions are more concentrated within the nuclear potential well. This increases the effective depth of the well. Since the nucleons are closer together and the protons have less repulsion for each other, more kinetic energy is required to cause fragmentation and those levels go up.

The levels shown on the right side of the figure include the energetic electrons in the fragmentation product energies. For LENR, with only thermal energies on the input, the energy possible for excited states from D^-D^+ fusion is below the fragmentation levels. If these energetic electrons were “lost,” or replaced by normal electrons, the fragmentation energies would be reduced by 1–2 MeV. Thus, if the lochon breaks up before or during the tunneling process, fragmentation becomes a real decay channel again. It is apparent that LENR products (in the Extended Lochon Model) can range from full fragmentation to no fragmentation at all. Fusion at sub-fragmentation energy allows heat-only decay to the ${}^4\text{He}$ ground state (via near-field coupling to Pd electrons by the tightly bound lochon). Another ramification is that fusion at sub-fragmentation energy (e.g., with lochon intact) provides a neutral “nucleus” during the “slow” decay to

ground state. Thus, this model permits transmutation via neutral, internally energetic nuclei.

5. Lochons: Nuclear Decay and Transmutation

If the fusion product ${}^4\text{He}^*$ is below the fragmentation level, then the only place it can go is to the ${}^4\text{He}$ ground state. There are not likely to be any excited states below the new fragmentation levels that have allowed gamma transitions to the ground state. But, nuclear-energy loss to and through the tightly bound electrons would be a steady process.

Protons do not radiate well because they are too massive for the large radiative effects that electrons display. Nevertheless, when energetic and confined in the nucleus, they do radiate (in the form of gamma rays – when allowed). Furthermore, a high energy-transfer rate is possible between very-close charge dipoles. The effective interaction of the dipoles drops off as the sixth power of the separation, R_{ij} , and with the sum of the transition energies [12]:

$$[U_{\text{NF}}(R_{ij})]^{(2)} \approx -\frac{2}{3} \frac{|\mu_{mn}(2)|^2 |\mu_{mn}(1)|^2}{R_{ij}^6 [E_{mn}(1) + E_{mn}(2)]}, \quad (6)$$

where μ_{mn} are the matrix elements of the transition-dipole moments.

At nuclear separation, despite the small dipole moments of the protons and tightly bound electrons, a steady energy transfer from protons to these electrons prevents the establishment of any nuclear energy “level.” These electrons, if provided with angular momentum from the protons will, in turn, radiate. And, because of the proximity effect, they will radiate preferentially to the adjacent Pd electrons. The separations between the tightly bound H electrons and the Pd electrons are larger than the Fermi distances of the nucleus. Nevertheless, radiation from the MeV-level electrons will be much higher than that from the protons and the dipole moments of the Pd electrons will be much higher than that of the tightly bound electrons. Following the energy consideration in the denominator of Eq. (6) and the higher number of outer-orbit Pd electrons, low-energy transfer will dominate. However, any resonance effects of the energetic tightly bound electrons with the high-energy inner Pd electrons might make the latter preferred “targets.” A range of X-rays has been measured in LENR experiments [13]. This observed radiation, while informative, does not appear adequate to account for the expected levels of Pd atomic-electron excitation. It may be that these electrons are only a transfer medium between the deep electrons and the phonon field.

The means of decay from ${}^4\text{He}^*$ to ${}^4\text{He}$ without particulate radiation is clear. A similar path for ${}^2\text{He}^*$ to ${}^2\text{He}$ (from p–p fusion) might be possible. However, a competing path is likely. The three-body reaction, $\text{p–e–p} \rightarrow \text{d}^+ + \nu$ (where ν is a neutrino), in solar physics is well known [14]. In the sun, it is not a major fusion pathway ($\text{p–p} \rightarrow \text{d}^+ + \text{e}^+ + \nu$ dominates). However, in stars, the protons and electrons are not nearly as close as in our model and there is never a *pair* of electrons in a tight cluster. If a coupled-electron pair (lochon) is present, the $\text{p–2e–p} \rightarrow \text{d}^+ + \text{e} + \nu$ or $\text{p–2e–p} \rightarrow \text{d}^+ + \text{e}$ reactions should be even faster. How fast they are, relative to the decay to the unstable ${}^2\text{He}$, determines whether the reaction is one of fusion or of scattering.

Both ${}^2\text{He}^*$ and ${}^4\text{He}^*$ display non-resonant decay paths. This means that the neutral ‘atom,’ with its tightly bound lochon is ‘free’ (and has time) to drift through adjacent electron and nuclear potentials with impunity. If it enters another nucleus, then the decay may be instantaneous and the decay products predictable. LENR data indicate the possibility of transmutation with the preferential addition of two and four nucleons to native elemental concentrations in active PdD lattices.

6. Summary

A lattice-specific model has been proposed whereby, negative hydrogen ions attract positive ions rather than experience the normal Coulomb barrier considered to be a major argument against low-energy nuclear reactions. The negative ions are a result of electron–phonon coupling that makes a lattice ion with an electron pair (a localized, doubly charged,

boson – lochon) more probable than neutral atoms (those having only a single electron) in the sub-lattice. Specific phonon modes (most likely at linear-defect sites or at interfaces and surfaces) induce near collisions of the D^-D^+ pairs at a high rate ($>10^{14}$ /s per pair). As an attractive element in the pair, the lochon does work during collision and falls deeper into its Coulomb-potential well, becoming even more stable in this phonon phase.

If the collision process proceeds far enough that the attractive potential is greater than the lattice barrier, then the D^-D^+ pair continues to converge, the lochon continues to fall deeper into its potential well, and the conditions for the final tunneling and fusion of the deuteron pair is established. As the lochon is spin-paired electrons in a filled orbital, there is no spinflip possible to provide angular momentum to generate photons. Therefore, this excess energy may be converted into work and lochon KE that could be on the order of MeV. Thus, up to the point of fusion, this is a reversible process – even though the deuterons may end up in other than their original lattice sites.

After fusion, when a deuteron is inside the D^- Coulomb barrier with a MeV-type lochon present, the situation is quite different from the normal d–d nuclear scattering with no, or only a single eV-range, bound atomic electron. In the usual d–d scattering of nuclear physics, the mass difference between ^4He and $2D$ is involved. In the present case, the electrons exist in shrunken orbits for the tightly bound paired state in D^-D^+ and, after fusion, in the excited $^4\text{He}^*$. The Coulomb far field of these electrons is negligible as it has been compensated by a comparable amount extracted from that of the protons. The far-field energy has been converted into more intense near-fields and kinetic energy. This reduces the apparent size of an electron to that of the shrunken orbit for slow motions and to the classical-electron radius for fast motions (e.g., tunneling). As a consequence of the reduced Coulomb repulsion within the nucleus, the effective depth of the nuclear potential well is increased. The ground and excited state energies become lower; but the fragmentation levels go up.

The tightly bound electron pairs (lochons) increase the lattice and Coulomb barrier penetration probability necessary for D^+D^- fusion. The bound-electron pairs may remain intact in the tunneling process. The above considerations lead to a conclusion that the energy of the excited state $^4\text{He}^*$ nucleons could be less than 20 MeV. If so, and/or if the fragmentation level is raised above the excited states, no fragmentation is probable. The slower decay process to the ground state proceeds via radiative proximity coupling of the nuclear potential energy, between the protons and tightly bound electrons and then between the tightly bound electrons and the adjacent Pd electrons. This process provides both a path for conversion of the nuclear energy to thermal energy and, for a brief period, a small, neutral, internally energetic body that can drift (at thermal velocities) into adjacent nuclei during the decay.

The extended lochon model thus is capable of explaining: the realistic probability of low-energy nuclear reactions, normal D–D fusion decay paths with energetic fragments, the existence of a path from hydrogen collision (H^+H^- or D^+D^-) to a ground state (D or ^4He) without energetic particles, and a basis for the transmutation products observed in some LENR experiments.

Appendix: Deep Atomic Orbitals

A few remarks regarding a recent reference to the Klein–Gordon (K–G) equation applied to lochons (which have bosonic character) for describing a very small atomic orbital on D^- [10] may be in order. For the K–G equation, the energy states for a singly charged boson are given by (see Naudts) [14]

$$E_n = (n + \gamma^2)m_{\text{eff}}c^2/\sqrt{n^2 + \gamma^2(2n + 1)}, \quad (\text{A.1})$$

where the binding energy of the orbit is $m_{\text{eff}}c^2 - E_n$ and $\gamma > \alpha/\sqrt{f}$, $\alpha > 1/137$, and $f > 1$,^a or ~ 0 . The orbit

^aNaudts uses l for this dummy variable, but we use f to avoid confusion with the angular momentum used in this paper.

radius is

$$r_n = \hbar \sqrt{n^2 + \gamma^2(2n+1)/m_{\text{eff}} c \alpha} . \quad (\text{A.2})$$

The $f > 1$ state is normally rejected as being non-physical, e.g., not observed. But, for the unique $n = 0$, $f > 1$ (or nought orbit) state,

$$E_0 > \alpha m_{\text{eff}} c^2, \quad (\text{A.3})$$

$$r_0 = \hbar/m_{\text{eff}} c \sqrt{f} > \hbar/m_{\text{eff}} c. \quad (\text{A.4})$$

Thus, r_0 is essentially the Compton radius and, for lochons with $q_{\text{eff}} = 2q_0$ and $m_{\text{eff}} = 2m_0$, $r_0 \sim 2 \times 10^{-11}$ cm.^b With a binding energy perhaps close to 1 MeV, we have a very energetic and shrunken orbital for lochons in H^- or D^- . This orbital will produce the same fusion as does a muonic-hydrogen atom. Even if not stable, it could be considered a resonance, rather than a state, and still have a major impact on fusion rates.

Considering the means of attaining this nought orbit, it seems likely that a nought-orbit molecule would form in the process. Depending on the angular momentum of the collision (nominally $l = 0$), the lifetime of the molecule is limited by the fusion of the nuclei or by electron capture by one of the protons. Thus, LENR results may provide support for the existence of a deep atomic orbital that is still controversial and, furthermore, the extended lochon model would suggest that a nought molecule could form as an intermediate step prior to fusion or electron capture.

This deep orbit (\sim MeV level, achieved by the work done in bringing the deuterons together) completes the pre-fusion orbit-shrinkage story of Fig. 2 begun with the Pd-lattice confinement of the hydrogen atom, continued as shown earlier [3,4] with the enhanced mass of lochons, and extended further by the reduced dimensionality of the lattice-barrier region being penetrated by colliding hydrogen.

References

- [1] M.C.H. McKubre, 4th Int. New Energy Technology 239th ACS Meeting, San Francisco, CA, March 2010.
- [2] Manika Khanuja et al., *J. Appl. Phys.* **106** (2009) 093515.
- [3] K.P. Sinha, *Infinite Energy* **29** (2000) 54.
- [4] K.P. Sinha and A. Meulenberg, Proc. ICCF-14, Int. Conf. Condensed Matter Nuclear Science, Washington DC, 2008.
- [5] S. Ichimaru, in *Statistical Plasma Physics*, Vol. II, Condensed Plasmas, Addison-Wesley, 1994.
- [6] U. Weiss, in *Quantum Dissipative Systems* (World Scientific, Singapore, 1999).
- [7] K.P. Sinha and A. Meulenberg, *Current Sci.* **96** (2006) 907.
- [8] S.A. Maier and H.A. Atwater, *J. Appl. Phys.* **98** (2005) 011101.
- [9] T. Bernard, Private Communication.
- [10] A. Meulenberg and K.P. Sinha, textit Proc. of the 15th Int. Conf. on Cond. Matter Nuclear Science, Rome, Italy, October, 2009, *J. Condensed Matter Nucl. Sci.*, **4** (2011) 241.
- [11] For example, Y. Iwamura, M. Sakano and T. Itoh, *Jap. J. Appl. Phys.* **41** (2002) 4642.
- [12] Proximity radiative coupling (including the non-resonant component that dominates here) of dipoles is the starting point of this citation. K.P. Sinha and A. Meulenberg, arXiv:0902.0682 (accessed 30 June 2010). Basis in Power, E.A.; Thirunamchandran, T. *Phys. Rev. A* **51** (1995) 3660 and *Chem. Phys.* **171** (1993) 1.
- [13] S. Szpak, P.A. Mosier-Boss and J.J. Smith, *Phys. Lett. A* **210** (1996) 382–390.
- [14] http://en.wikipedia.org/wiki/Proton%E2%80%93proton_chain_reaction#The_pep_reaction (accessed 23 Sept 2011).
- [15] J. Naudts, <http://arxiv.org/abs/physics/0507193> (accessed 30 June 2010).

^bThese values are only approximated because of the charge and nature of the lochon. The effects of a doubly charged, compound boson are not analyzed here because of the complications resulting from the internal-charge repulsion and the uncertainty in its distribution in space and time.



Research Article

Effects of Self-poisoning of Pd on the Deuterium Permeation Rate and Surface Elemental Analysis for Nuclear Transmutation

T. Hioki *, N. Takahashi, J. Gao, A. Murase, S. Hibi and T. Motohiro

Toyota Central Research and Development Laboratories Inc., Nagakute, Aichi 480-1192, Japan

Abstract

Factors affecting the deuterium permeation rate through Pd foils at a temperature as low as 70°C have been studied using X-ray photoelectron spectroscopy. It has been demonstrated that the surface segregation of S from the interior of Pd bulk during the permeation process causes a significant lowering of permeation rate with increasing permeation time, although the concentration of S impurity in Pd bulk is probably less than 10 ppm. The surface accumulated S during D₂ permeation also gives rise to a difficulty in detecting small amount of elements on the surface of Pd after deuterium permeation treatment. For selected nuclear transmutation from Sr to Mo reported by Iwamura group, we have successfully observed Mo on the surface of Sr ion-implanted Pd after a deuterium permeation treatment, by adding a process that removes the sulfur accumulated on the surface of the Pd foil. A time-of-flight secondary ion mass spectroscopy (TOF-SIMS) study on the origin of the observed Mo will be described in a separate paper.

© 2012 ISCMNS. All rights reserved.

Keywords: Deuterium permeation, Pd metal, Poisoning, S impurity, Transmutation, X-ray photoelectron spectroscopy

1. Introduction

Deuterium permeation through palladium has been employed as an effective tool to induce low energy nuclear phenomena in condensed matter, although the typical phenomenon of excess heat has been intensively studied using the electrochemical method.

Arata and Zhang invented a double-structure reactor (DS-reactor), in which a nano-Pd sample is loaded with deuterium by gas permeation through the wall of a palladium vessel [1]. They reported that, using the DS-reactor, the existence of cold fusion or excess heat has been verified with efficiency good enough to be utilized as a practical reactor. Modifications of this type of reactor have been made by several research groups to study quantitatively the excess heat effect using the gas loading method [2–4]. It has been suggested that the surface modification of the Pd vessel is an important factor to generate the excess heat effect [3].

*E-mail: hioki@mosk.tytlabs.co.jp

Table 1. Impurities in Pd

Impurity	Concentration (ppm)
Pt	210
Ru	24
Ag	21
Rh	21
Fe	11
Si	11

Iwamura et al. have intensively used deuterium permeation through nanostructure layers of Pd and CaO, to induce the selective nuclear transmutation from Sr to Mo [5], Cs to Pr [5–7], and Sm to Ba [8]. They have claimed a high reproducibility of these nuclear transmutation phenomena, and quite a few reproduction experiments have been reported so far [9–14]. For nuclear transmutation from Cs to Pr, Iwamura et al. [6] have shown that the conversion rate is roughly proportional to the average deuterium gas permeation rate, and that about 50% of Cs atoms deposited on the multi-layer system convert to Pr atoms when the average deuterium permeation rate is about 2 sccm (Standard Cubic Centimeter per Minute). The permeation rates used by the Iwamura group seem to be considerably higher than those reported in the literature [15,16], and the conditions for permeation are not exactly the same.

The hydrogen permeation rate through Pd is known to be strongly affected by surface contamination [17]. In many past studies, because of the practical use of hydrogen purification, hydrogen permeation measurements have largely been conducted at high temperatures greater than a few hundred °C, at which point the effect of surface contamination is comparatively small [18]. Nuclear transmutation experiments by the Iwamura group have been performed at a temperature as low as 70°C.

In the present study, the effects of surface contamination on the deuterium permeation rate through Pd foils at 70°C have been examined using X-ray photoelectron spectroscopy (XPS). It has been demonstrated that the surface segregation of sulfur during the deuterium permeation is the main cause of the observed decrease in the permeation rate with increasing permeation time. A pre-heat treatment to suppress the degradation of the permeation rate is presented. The effects of the surface-segregated sulfur on surface elemental analysis for nuclear transmutation is discussed and a procedure to avoid the effects of sulfur on elemental analysis is also demonstrated for nuclear transmutation from Sr to Mo.

2. Experimental

2.1. Sample preparation

Foil samples of Pd with a purity of 99.97% and thickness of 50 μm were obtained from the Nilaco Corporation. The impurities and their concentrations determined by the supplier are shown in Table 1.

Table 2. Heat treatments before deuterium permeation.

Sample number	Vacuum annealing	Air annealing
No. 1	No	300°C \times 10 min
No. 2	No	500°C \times 10 min
No. 3	No	1000°C \times 10 min
No. 4	No	950°C \times 120 min
No. 5	950°C \times 120 min	No
No. 6	950°C \times 120 min	1000°C \times 10 min
No. 7 (^{88}Sr ion implanted)	950°C \times 300 min	600°C \times 10 min

Table 3. Impurities in D₂ gas.

Impurity gas	Concentration (ppm)
Oxygen	< 5
Nitrogen	< 5
Carbon monoxide	< 1
Carbon dioxide	< 1
Total hydrocarbon	< 1
Water	< 5

The as-received foils were ultrasonically cleaned in alcohol and dried. They were then heat-treated before deuterium permeation as shown in Table 2.

2.2. Deuterium permeation

The deuterium permeation system was the same as that reported by us previously [13]. The upstream side was filled with deuterium at 100–300 kPa. The deuterium gas with purity more than 99.995% was obtained from Takachiho Chemical Industrial Co. Ltd. The impurities and their concentrations in the gas determined by the supplier are shown in Table 3. The concentrations were less than 5 ppm for oxygen, nitrogen and water, and less than 1 ppm for others.

The downstream side was evacuated with a dry pump and a turbo molecular pump. The upstream side was connected with a reservoir tank of 1.0 L. The deuterium flow rate was determined from the reduction of the pressure in the reservoir tank. A metal O-ring was used for the vacuum seal.

2.3. Surface elemental analysis

XPS was used to analyze the surface layer elements of the samples. The instrument was a Quantera SXM (ULVAC-PHI INC., 20 kV, 100 W) with a monochromatic Al(K α) X-ray source (1.438 keV). The size of the incident X-ray beam was $100 \times 1500 \mu\text{m}^2$.

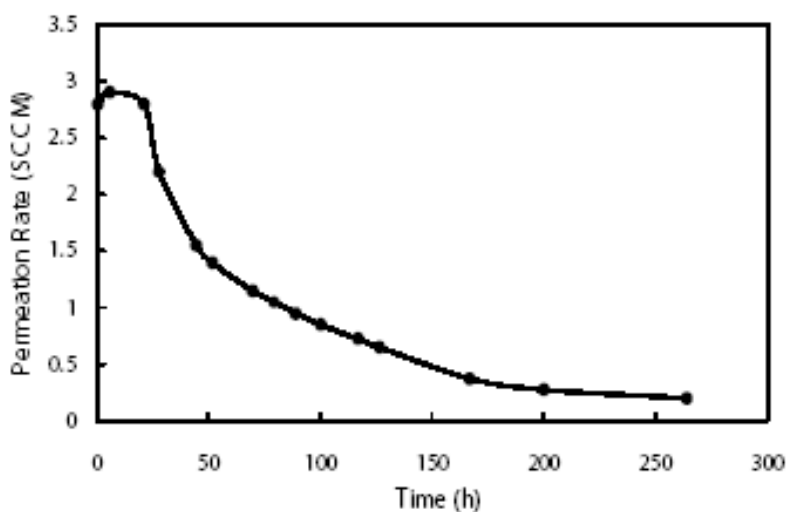


Figure 1. Variation of permeation rate with time for the Pd foil pre-heat treated in air at 300°C for 10 min (No. 1 sample).

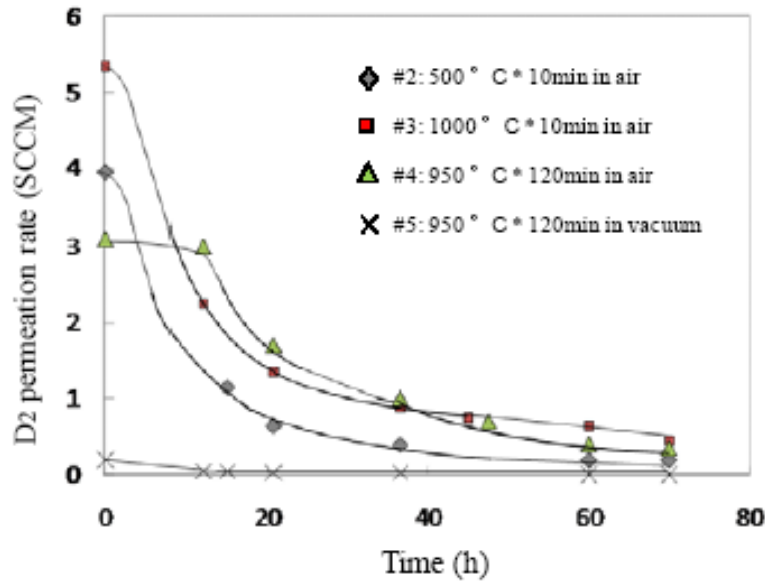


Figure 2. D₂ permeation rate at 70°C as a function of time for foils pre-heat treated in air or in vacuum at various temperatures and periods. The solid lines simply connect the experimental points smoothly.

3. Results and Discussion

3.1. Variation of deuterium permeation rate with time

An example of the deuterium permeation rate as a function of time is shown in Fig. 1. As a pre-heat treatment, this sample (No. 1) was annealed at 300°C in air for 10 min. The pressure of the up stream side was 275 kPa and the temperature of the sample was 70°C.

As seen in the figure, the permeation rate is high at the initial stage of permeation, but it decreases gradually with time. The initial value of the permeation rate and the degree of its decrease with time varied from sample to sample when as-received foils without any pre-heat treatment were used. It has been reported by Yamakawa et al. that the surface impurities that suppress hydrogen permeation through Pd are carbon atoms which may come from hydrocarbons [19]. They have also demonstrated that the contaminants are quickly removed from the Pd surface by heat treatment around 200–300°C in air [18]. The heat treatment of No. 1 sample was conducted following Yamakawa method. As seen in Fig. 1, the initial permeation rate is higher than 2 sccm which is a value expected to induce nuclear transmutation at a high efficiency of ~50% [6]. The initial high permeation rate is considered to result from the pre-heat treatment removal of hydrocarbons adsorbed on the Pd surface. However, the permeation rate decreases gradually with time and finally reaches a value of about 1/10 of the initial value.

In order to investigate the mechanism of the decrease in the permeation rate with increasing permeation time, Pd foils were pre-heat treated in air or in vacuum at different temperatures and the surface elements were examined with XPS for the foils before and after D₂ permeation. Figure 2 shows the permeation rate as a function of permeation time for foil Nos. 2–5. The pressure of the upper stream side was 0.275 MPa, and the sample temperature was 70°C.

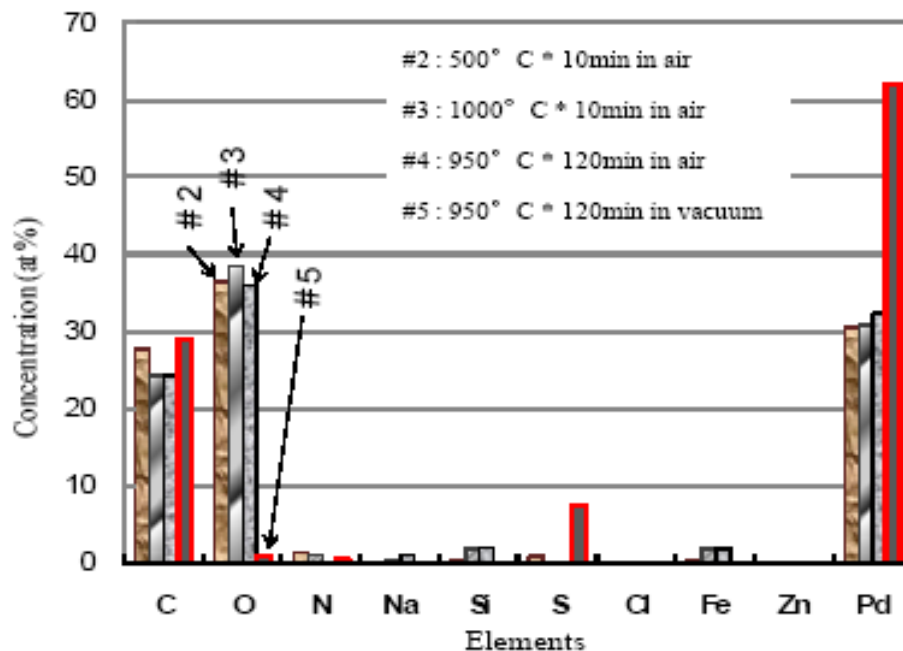


Figure 3. Elemental concentration on the surface layer of Pd after heat treatments.

It is seen in Fig. 2 that: (i) all the foils heat treated in air show high initial permeation rates larger than 2 sccm, while the foil heat treated in vacuum shows almost no permeation from the beginning of permeation. (ii) The permeation rates of the foils with high initial rates decrease with increasing permeation time and reaches a value less than ~ 0.5 sccm at a permeation time of 70 h.

3.2. XPS analysis on Pd surface

Figure 3 compares the concentrations of the elements observed on the surface of Pd foils just after the various heat treatments using XPS. The main elements on the surface layer shallower than about ~ 1 nm are Pd, O and C. As impurities, N, Na, Si, S, Cl, Fe and Zn are detected. From Fig. 3, it is seen that the foils annealed in air have high concentrations of O and comparatively lower concentrations of Pd, indicating that the surface layer of Pd is oxidized with the annealing in air. It is noted that the concentrations of C are similar and relatively high for all the samples. Therefore, the existence of C is not the reason why only the vacuum annealed sample shows an extremely low initial permeation rate. What is most remarkable in Fig. 3 is that the concentration of S is significantly high for only the foil sample annealed in vacuum. The concentration of S on the surface reaches a value of 7.5 at.% for the vacuum annealed sample, while it is less than ~ 1 at.% for the air annealed samples. Therefore, it is suggested that a surface concentration of S as high as ~ 10 at.% results in the extremely low permeation rate for the vacuum annealed sample, as reported by us previously [20]. Sulfur has been known as a poisoning element for the catalytic activities of Pd, i.e., it works to prevent dissociative adsorption of hydrogen molecules on the Pd surface.

Figure 4 compares the XPS spectra around S 2p and Pd 3d between the samples annealed in air and in vacuum. The intensity of the S 2p peak for the vacuum annealed sample is much stronger than those of the samples annealed in

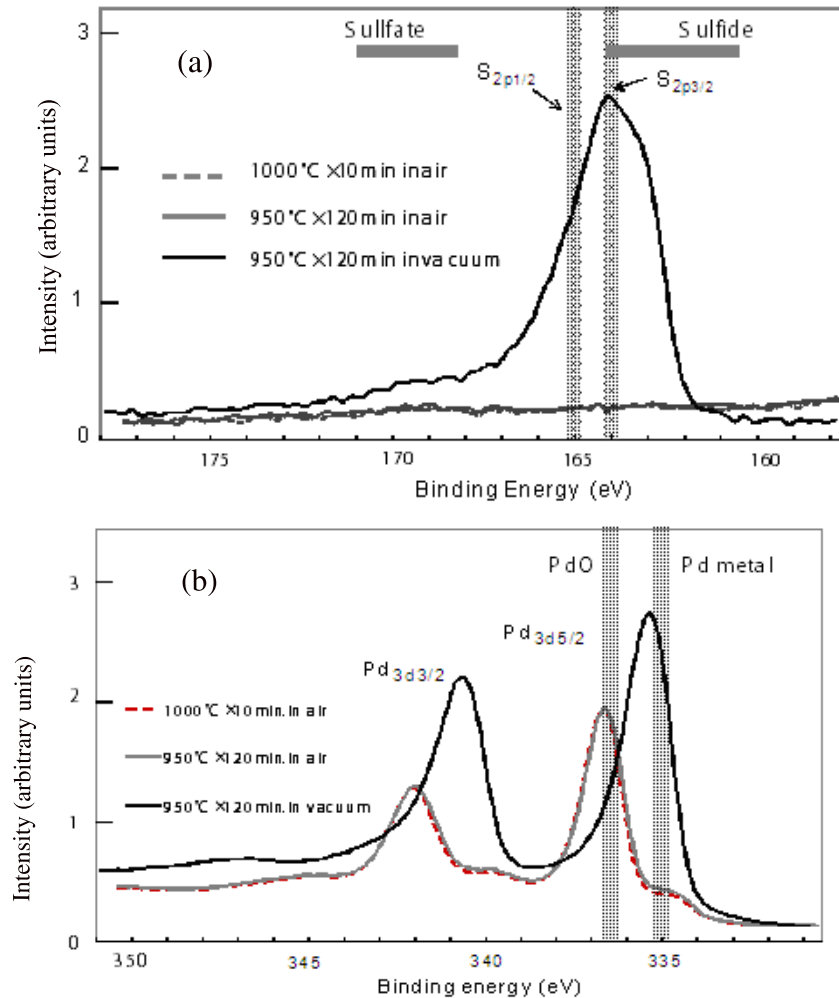


Figure 4. XPS spectra (a) around S 2p and (b) around Pd 3d for foil samples annealed in air (No. 3, No. 4) and in vacuum (No. 5).

air. The observed high concentration of S is considered to result from the surface segregation of S during annealing at 950 °C in vacuum. The sulfur probably exists in the Pd bulk as an impurity with a concentration of ~ 10 ppm or less. Sulfur does not form a solid solution with Pd even at a concentration close to zero [21]. Therefore, even a very small amount of S impurity in Pd bulk is considered to concentrate on the surface of Pd up to ~ 10 at.% with annealing in vacuum at the temperature of 950 °C. It is also suggested in Fig. 4 (a) that the chemical form of S is a sulfide.

From the Pd 3d spectra in Fig. 4 (b), it is clearly seen that the surface layer is metallic for the foil annealed in vacuum, while it is oxidized for the foils annealed in air. Since the foils annealed in air have high initial permeation rates as shown in Fig. 2, it is apparent that the formation of PdO in the surface layer of Pd hardly affected the deuterium permeation rate of Pd.

Figure 5 compares the changes in the concentrations of surface elements with the deuterium permeation

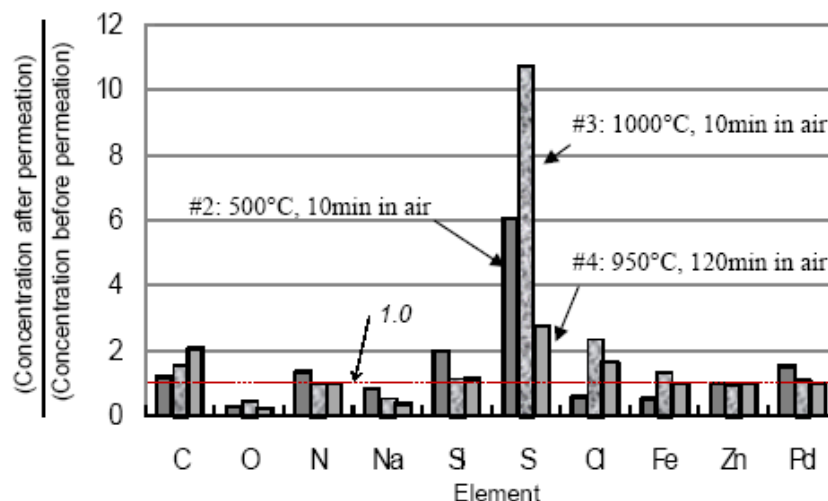


Figure 5. The ratio of the elemental concentration after D₂ permeation to that before D₂ permeation.

at 70°C for a period of 70 h for the foil samples annealed in air. From this figure, it is seen that the only element which is remarkably increased with the deuterium permeation is S, while the only element which is remarkably decreased is O. The observed increase in the surface concentration of S suggests that S impurities in the Pd bulk migrates and concentrates onto the surface during deuterium permeation at a temperature as low as 70°C. Since all the foils annealed in air show high initial permeation rates as shown in Fig. 2, it is strongly suggested that the decrease in the permeation rate with increasing permeation time is due to surface segregation of S during deuterium permeation. The remarkable decrease of O after the deuterium permeation indicates that the oxidized surface layer of Pd is reduced by deuterium permeation at 70°C.

Figure 6 compares the XPS spectra around Pd 3d before and after the deuterium permeation. It is clearly seen that the surface layer is initially PdO while it is metallic after the deuterium permeation at a temperature as low as 70°C.

3.3. Improving the degradation of permeation rate

From the results shown above, it has been demonstrated that surface segregation of S strongly affects deuterium permeation through the Pd foil. The surface segregation of S is caused either (i) by annealing in vacuum at a temperature as high as ~950 °C or (ii) by deuterium permeation for a long time at a temperature as low as ~70°C. It has also been indicated that the surface concentration of S is small for Pd foils annealed in air at a temperature in the range of 500–1000°C. The surface sulfur seems to evaporate as SO_x. As a result, the initial permeation rate of the foils pre-heat treated in air is higher than 2 sccm. Therefore, in order to keep a high permeation rate for a long period of permeation, it is required to suppress the surface segregation of S impurity in Pd or to decrease the concentration of S impurity in Pd.

As a trial to decrease S impurity in Pd bulk, we have tried to intentionally segregate S on to the surface by annealing in vacuum at 950°C for a long time (e.g., 2 h or 5 h), followed by annealing at 1000°C in air for a short time (10 min) to burn the S concentrated onto the surface. Figure 7 compares the permeation behavior for the sample (No. 6)

heat treated with a combination of vacuum-annealing and air-annealing to that for the sample (No. 3) heat treated only with an air-annealing.

It is noted that sample No. 6 maintained a high permeation rate larger than 2 sccm even at a permeation time of 45 h, while the permeation rate of sample No. 3 becomes lower than 2 sccm at a permeation time of 12 h. Figure 8 shows the XPS spectra around S2p for sample No. 6 after the vacuum annealing at 950°C and after the subsequent air annealing at 1000°C. It is confirmed that the intensity of S 2p is very strong just after the vacuum annealing but it becomes almost zero after the subsequent air annealing.

It may be worth mentioning that the S concentrated on the surface during deuterium permeation comes from the interior of the Pd bulk (self-poisoning) and not from the environment, e.g., the deuterium gas. The deuterium gas used in this study is a high purity one and it is not contaminated by any gaseous species containing S as shown in Table 3. If the deuterium gas used in this study contained a very small undetectable amount of S and accumulated on the Pd surface during deuterium permeation, the amount of the accumulated S would have been larger for a foil showing a higher permeation rate. For example, in Fig. 7, the total amount of D₂ passing through the foil of sample No. 6 is about 13 L, while that of sample No. 3 is 5.5 L. Therefore, the amount of S deposited on the Pd surface of the upper stream side of sample No. 6 should be larger by 2.4 times than that of sample No. 3, and the decrease in the permeation rate for sample No. 6 should have been larger than that for sample No. 3. That effect is contrary to the experimental result, as shown in Fig. 7.

3.4. Influence of surface segregated S on surface elemental analysis

As demonstrated by the Iwamura group, XPS is a useful tool for studying nuclear transmutation [5]. This analysis technique has also been employed in the reproduction experiments by a couple of research groups [12,13]. However, as reported by us previously [13] in examining the transmutation from Sr to Mo, it is difficult to detect Mo clearly by XPS, if S atoms exist on the surface of Pd. This is because the peak energy of S 2s comes close to that of Mo 3d and the spectra are composed of a few peaks with different intensities. In Fig. 9, an example of such experimental spectrum (the curve: raw data) obtained for sample No. 7 is shown.

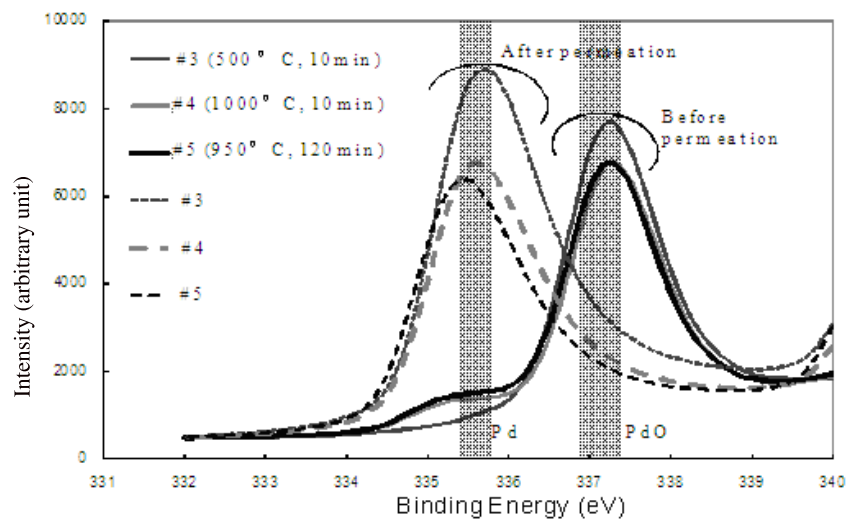


Figure 6. XPS spectra around Pd 3d_{5/2} before and after deuterium permeation for samples pre-heat treated in air.

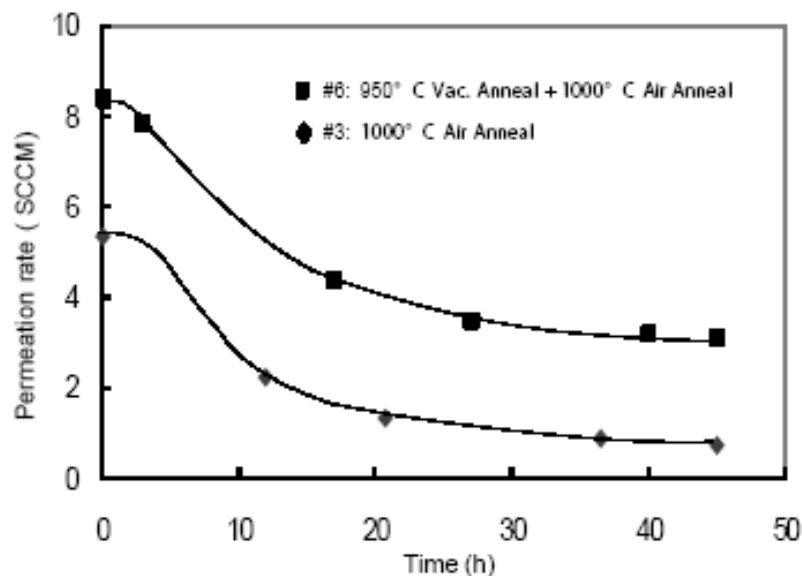


Figure 7. Comparison of the variations of permeation rate with time for samples Nos. 6 and 3.

This sample was implanted with ^{88}Sr ions and subsequently treated with D_2 permeation at 70°C for ~ 11 days. As seen in Fig. 9, the experimental spectrum apparently shows two large peaks with an energy difference of ~ 7 eV which is different from the energy difference between $\text{M d}3\text{d}5/2$ and $\text{Mo }3\text{d}3/2$ (3.13 eV). The two large peaks are considered to arise from compounds of sulfur. Actually, as shown in Fig. 10, the experimental spectrum around S 2p for the same sample shows a similar line shape to the raw data in Fig. 9. The experimental spectrum in Fig. 10 is assumed to be composed of four sulfuric compounds: a sulfide, a sulfate, and two other sulfuric compounds. As seen in Fig. 10, the experimental spectrum for S 2p can be well reproduced assuming these four compounds.

Therefore, the experimental spectrum around Mo 3d should also be well reproduced if the spectrum is only composed of S 2s peaks of the four sulfuric compounds. However, as seen in Fig. 9, a small difference is observed between the raw data and the total curve composed of the four S 2s lines calculated from the simulated results in Fig. 10.

This difference may mean that Mo atoms exist on the surface after the permeation treatment. However, it is difficult to definitely conclude the existence of Mo from this analysis. This difficulty arises from S which is segregated onto the surface during the deuterium permeation for a long period.

3.5. Removing S after the deuterium permeation process

As discussed above (Section 3.3), the sulfur concentrated on the surface of Pd can be removed by annealing in air. Therefore, if the sample after deuterium permeation is again heat treated in air at a temperature of $500\text{--}1000^\circ\text{C}$ for a short time, the sulfur on the surface may be removed and the elements buried under the over layer of sulfuric compounds may be detected. As shown in Fig. 11, this procedure has proven useful for detecting Mo which emerges on the surface of Sr-implanted Pd after the deuterium permeation process.

The energy difference between the two peaks in Fig. 11(c) is 3.13 eV and the intensity ratio of the two peaks is close to 3:2. Therefore, these peaks definitely indicate that Mo atoms are observed on the surface of Pd after the deuterium permeation process.

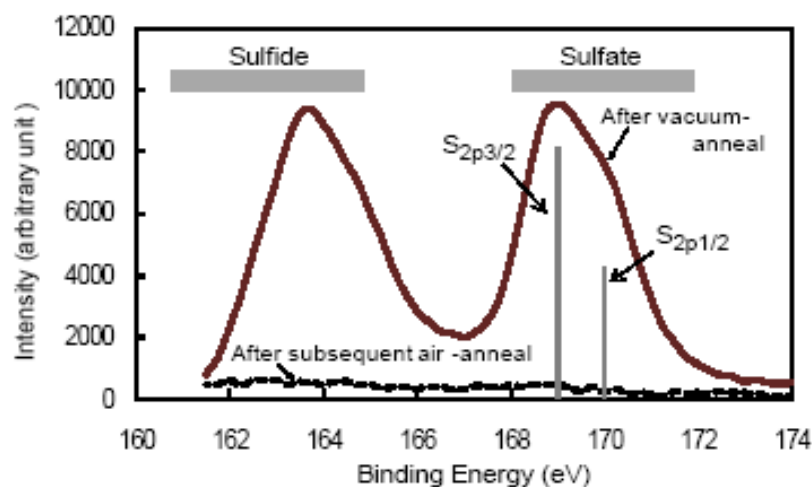


Figure 8. XPS spectra around S 2p for the sample (No. 6) just after annealing in vacuum at 950°C for 2 h and after subsequent annealing in air at 1000°C for 10 min.

Similarly, as reported by us previously, Mo has also been detected after deuterium permeation for Pd foils with multi-layers of Pd/CaO being deposited with ^{88}Sr by ion implantation [14]. Whether the observed Mo is a nuclear transmuted one or not is an important problem to be carefully examined as a next step. As reported by Iwamura et al., to study the isotopic abundance ratio of the observed Mo seems to be useful to identify the origin of the Mo. The TOF-SIMS technique is a powerful tool to measure the isotopic abundance ratio for an atom. We have applied the technique

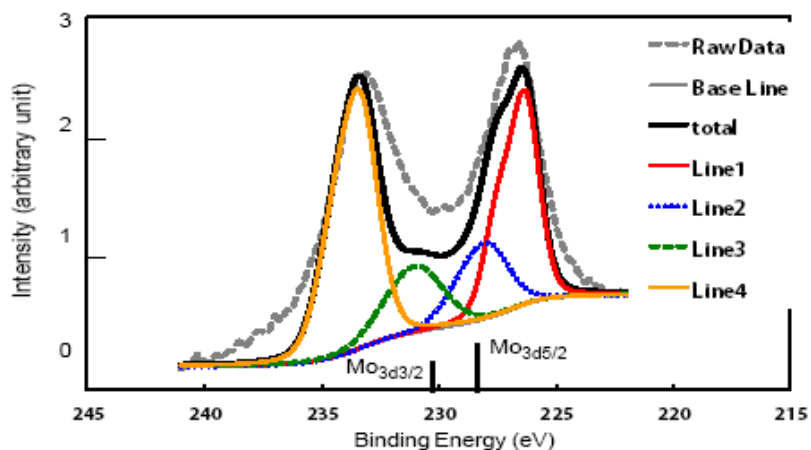


Figure 9. XPS spectrum around Mo 3d for sample No. 7. Raw Data: experimental spectrum; Line 1: S 2s from a sulfide; Line 2: S 2s from a sulfur compound; Line 3: S 2s from a sulfur compound; Line 4: S 2s from a sulfate.

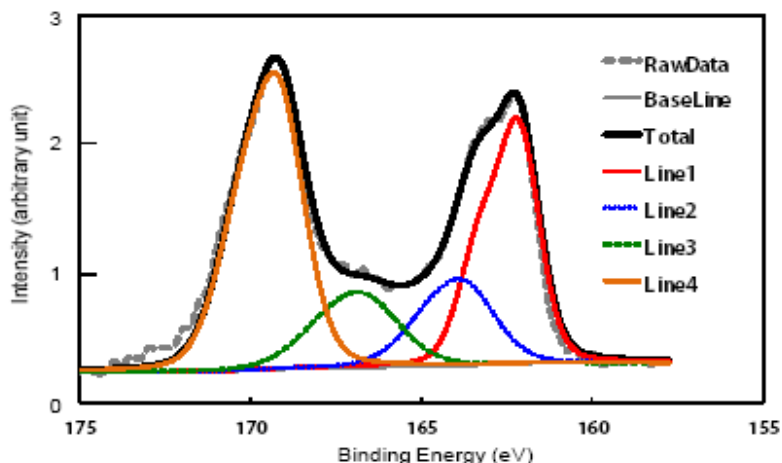


Figure 10. XPS spectrum around S 2p for sample No. 7. Raw Data: experimental spectrum; Line 1: S 2p from a sulfide; Line 2: S 2p from a sulfur compound; Line 3: S 2p from a sulfur compound; Line 4: S 2p from a sulfate. The total line shape composed of the four S 2p lines corresponding to the assumed four sulfuric compounds well simulates the raw data.

to measure the isotopic abundance ratio of the Mo atoms which emerge in the surface layer of Sr ion-implanted Pd/CaO multi-layer system after deuterium permeation [14]. A more detailed TOF-SIMS study on the origin of the emerged Mo will be published in a separate paper [22].

4. Conclusions

Palladium is often contaminated with a small amount of S. It has been demonstrated that:

- (i) S in the Pd bulk segregates on the surface with annealing in vacuum at a high temperature around 950°C.
- (ii) The deuterium permeation rate at 70°C is drastically lowered if the surface concentration of S is ~10 at.%.
- (iii) The surface segregation of S also occurs with the deuterium permeation process at a temperature as low as 70°C.
- (iv) The lowering of the deuterium permeation rate with increasing permeation time is due to the surface accumulation of S coming from the interior of Pd bulk (self-poisoning).
- (v) To maintain a high permeation rate for an extended period of time, pre-heat treatment of Pd in vacuum at a high temperature around 950°C followed by annealing in air at 500–1000°C has been proved effective.
- (vi) The sulfur accumulated on the surface during deuterium permeation covers the surface of Pd and makes it difficult to detect surface elements of small concentrations with surface analytical methods like XPS.
- (vii) By removing the surface-accumulated S by annealing in air at a temperature of 600–1000°C, Mo has been detected clearly on the surface of Sr-ion implanted Pd foils after deuterium permeation treatments.

Acknowledgements

We are grateful to Dr. Y. Iwamura of Mitsubishi Heavy Industries Ltd. and Prof. J. Kasagi of Tohoku University for discussions.

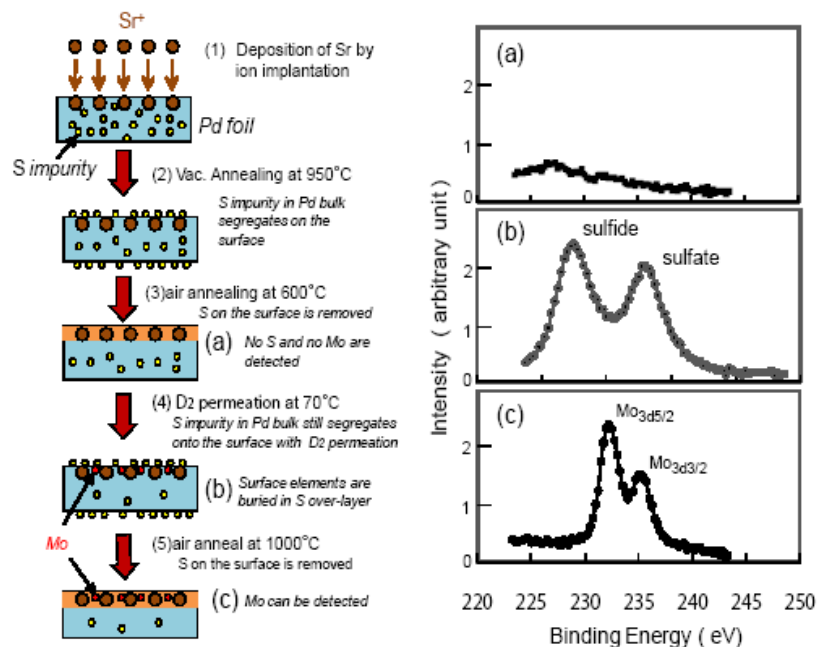
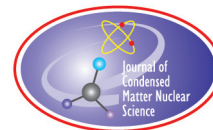


Figure 11. Schematics of the processes to detect Mo on the surface of Sr-ion implanted Pd after the deuterium permeation process, and XPS spectra around Mo 3d, (a) before D₂ permeation, (b) just after D₂ permeation treatment, (c) after adding an air-annealing at 1000°C to the D₂ permeated sample.

References

- [1] Y. Arata and Y. Zhang, Development of “DS-reactor” as the practical reactor of “cold fusion” based on the “DS-Cell” with “DS-cathode”, in, *Condensed Matter Nuclear Science: Proceedings of 12th International Conference on Cold Fusion*, Yokohama, Japan, Nov. 27–Dec. 2, 2005; A. Takahashi, K.-I. Ota and Y. Iwamura (Eds.), World Scientific, Singapore, 2006, pp. 44–54.
- [2] V.A. Kirkinskii and A.I. Khmel'nikov, Setup for measuring of energy balance at interaction of metals and hydrogen isotopes gas at high temperatures and pressures, in, *Condensed Matter Nuclear Science: Proceedings of 13th International Conference on Cold Fusion*, Sochi, Russia, June 25–July 1, 2007, Y. Bazhutov (Ed.), Publisher Center MATI, Moscow, Russia, 2008, pp. 43–46.
- [3] J.P. Biberian and N. Armanet, Excess heat during diffusion of deuterium through palladium, in, *Condensed Matter Nuclear Science: Proceedings of 13th International Conference on Cold Fusion*, Sochi, Russia, June 25–July 1, 2007, Y. Bazhutov, (Ed.), Publisher Center MATI, Moscow, Russia, 2008, pp. 170–180.
- [4] F. Celani et al., High temperature deuterium absorption in palladium nano-particles, in, *Condensed Matter Nuclear Science: Proceedings of 13th International Conference on Cold Fusion*, Sochi, Russia, June 25–July 1, 2007, Y. Bazhutov (Ed.), Publisher Center MATI, Moscow, Russia, 2008, pp. 181–201.
- [5] Y. Iwamura, M. Sakano and T. Itoh, Elemental analysis of Pd complexes: effects of D₂ gas permeation, *Jpn. J. Appl. Phys.* **41** (2002) 4642–4648.
- [6] Y. Iwamura et al., Low energy nuclear transmutation in condensed matter induced by D₂ gas permeation through Pd complexes: correlation between deuterium flux and nuclear products, in *Condensed Matter Nuclear Science: Proceedings of 10th International Conference on Cold Fusion*, Cambridge, MA, Aug. 24–29, 2003, P.L. Hagelstein and S.R. Chubb (Eds.), World Scientific, Singapore, 2006, pp. 435–446.

- [7] Y. Iwamura et al., Observation of surface distribution of products by X-ray fluorescence spectrometry during D₂ gas permeation through Pd complexes, in *Condensed Matter Nuclear Science: Proceedings of 12th International Conference on Cold Fusion*, Yokohama, Japan, Nov. 27–Dec. 2, 2005, A. Takahashi, K.-I. Ota and Y. Iwamura (Eds.), World Scientific, Singapore, 2006, pp. 178–187.
- [8] Y. Iwamura et al., Observation of nuclear transmutation reaction induced by D₂ gas permeation through Pd complexes, in *Condensed Matter Nuclear Science: Proceedings of 11th International Conference on Cold Fusion*, Marseilles, France, Oct. 31–Nov. 5, 2004, J.P. Biberian (Ed.), World Scientific, Singapore, 2006, pp. 330–350.
- [9] T. Higashiyama, H. Miyamaru and A. Takahashi, Replication of MHI transmutation experiment by D₂ gas permeation through pd complex, in *Condensed Matter Nuclear Science: Proceedings of 10th International Conference on Cold Fusion*, Cambridge, MA, Aug. 24–29. 2003, P.L. Hagelstein and S.R. Chubb (Eds.), World Scientific, Singapore, 2006, pp. 447–454.
- [10] F. Celani et al., Thermal and isotopic anomalies when Pd cathodes are electrolyzed in electrolytes containing Th–Hg salts dissolved at micro molar concentration in C₂H₅OD/D₂O mixtures, in *Condensed Matter Nuclear Science, Proceedings of 10th International Conference on Cold Fusion*, Cambridge, MA, Aug. 24–29. 2003, P.L. Hagelstein and S.R. Chubb (Eds.), World Scientific, Singapore, 2006, pp. 379–397.
- [11] H. Yamada et al., Producing transmutation element on multi-layered Pd sample by deuterium permeation, in *Condensed Matter Nuclear Science, Proceedings of 12th International conference on Cold Fusion*, Yokohama, Japan, Nov. 27–Dec. 2, 2005, A. Takahashi K.-I. Ota and Y. Iwamura (Eds.), World Scientific, Singapore, 2006, pp. 196–205.
- [12] A. Kitamura et al., in situ accelerator analyses of palladium complex under deuterium permeation, in *Condensed Matter Nuclear Science, Proceedings of 12th International conference on Cold Fusion*, Yokohama, Japan, Nov. 27–Dec. 2, 2005, A. Takahashi, K.-I. Ota and Y. Iwamura (Eds.), World Scientific, Singapore, 2006, pp. 272–277.
- [13] T. Hioki, N. Takahashi and T. Motohiro, XPS study on surface layer elements of Pd/CaO multilayer complex with and without deuterium permeation, in *Condensed Matter Nuclear Science: Proceedings of 13th International conference on Cold Fusion*, Sochi, Russia, June 25–July 1, 2007, Y. Bazhutov (Ed.), Publisher Center MATI, Moscow, Russia, 2008, pp. 518–528.
- [14] T. Hioki et al., in *Condensed Matter Nuclear Science: Proceedings of 14th International conference on Cold Fusion*, Washington DC, Aug. 10–15, 2008, D. Nagel et al. (Eds.), New Energy Foundation Inc., Concord, NH, 2010, pp. 203–211.
- [15] S.A. Koffler et al., Hydrogen permeation through alpha–palladium, *Trans. Metallurgical Soc. AIME* **245** (1969) 1735–1740.
- [16] R.E. Buxbaum and A.B. Kinney, Hydrogen transport through tubular membranes of palladium-coated tantalum and niobium, *Ind. Eng. Chem. Res.* **35** (1996) 530–537.
- [17] R.G. Musket, Effects of contamination on the interaction of hydrogen gas with palladium: a review, *J. Less-Common Metals* **45** 1976, 45, 173– 183.
- [18] K. Yamakawa et al., Hydrogen permeability measurement through Pd, Ni and Fe membranes, *J. Alloys and Compounds* **321** (2001) 17–23.
- [19] K. Yamakawa et al., Surface adsorbed atoms suppressing hydrogen permeation of Pd membranes. *Journal of Alloys and Compounds* 2003, 352, 57–59.
- [20] J.S. Gao et al., Influences of sulfur segregation to permeability in Pd–D₂ permeation system, *J. Vac. Sci. Technol. A* **21**(1) (2010) 147–151.
- [21] H. Okamoto, in *Desk Handbook: Phase diagrams for binary alloys*, ASM international, Materials Park, OH, 2000, p. 657.
- [22] A. Murase et al., TOF-SIMS investigation on nuclear transmutation from Sr to Mo with deuterium permeation through multi layered Pd/CaO, *J. Condensed Matter Nucl. Sci.*, to be published.



Research Article

The Open Gate Phenomenon: A New Energy Technology

Susan L. Taft

Flowing Water Consulting, P.O. Box 709, Geneva, OH 44041 USA

Jan Marwan *

Dr Marwan Chemie, Rudower Chaussee 29, 12489 Berlin, Germany

Abstract

The Open Gate Phenomenon is a unique solid-state mechanism that results in a significant and sustained electron transfer from an n-type semiconductor to Schottky metal particles that are *grown from* the semiconductor substrate itself. This results in a unique interface that acts as a one-way (rectifying) open gate. First identified in reduced polycrystalline titanium dioxide (an n-type semiconductor) to Group VIII metal particles, the interface significantly affects the Schottky barrier height resulting in electron flow into the metal particles from the reduced titanium dioxide (TiO_2) based on their respective work functions. The result is a negative charge on the metal particles which is of sufficient magnitude and duration to provide cathodic protection of the metal particles from surface oxidation. In essence, the metal particles behave as a negatively charged electrode without an externally supplied power source.

© 2012 ISCMNS. All rights reserved.

Keywords: Microspheres, Pechini process, Polycrystalline, Submonolayer, X-ray photoelectron spectroscopy

1. Introduction

The data supporting the hypothesis of the Open Gate Phenomenon was collected thirty years ago where extremely unusual negative binding energy shifts below zero valence energies were observed for rhodium ($\text{Rh}3d_{5/2}$) on reduced titanium dioxide (TiO_2) using X-ray photoelectron spectroscopy (XPS). The discovery of the unusual negative binding energy shifts was the result of the initial failure to make a rhodium-doped TiO_2 material ($\text{Ti}_{0.99}\text{Rh}_{0.01}\text{O}_2$) to reduce the band gap for a TiO_2 -based photoelectrochemical material using the Pechini process [1] to substitute Rh into the TiO_2 lattice. After formation of the resin intermediate from the Pechini process, the materials were subjected to high temperature oxidation and reduction, in excess of 1400°C . X-ray photoelectron spectroscopy (XPS) analysis was chosen to help verify Rh substitution by identifying its oxidation state. The binding energies for $\text{Rh}3d_{5/2}$ for materials prepared at three different temperatures (1400°C , 1600°C and 1650°C) were consistently far below the reference of

*E-mail: info@marwan-chemie.fta-berlin.de

307.2 eV for Rh^0 [2] (301.2, 302.2, and 202.6 eV, respectively). This corresponds to negative binding energy shifts of 6.0, 5.0, and 4.6 eV below the reference for Rh^0 , an extremely unusual occurrence. The binding energies for $\text{Ti}2p_{3/2}$ did not exhibit the same negative binding energy shifts. Subsequent scanning electron microscopy (SEM) examination using energy dispersive X-ray (EDX) analysis found that rhodium was observed in discrete particles on the surface of the crystalline TiO_2 material, *grown from* the TiO_2 substrate. The particles were both regularly and irregularly shaped microspheres from approximately 1–10 μm in size.

A subsequent literature search at the time (1981–1982) found three instances where negative binding energy shifts of metals were observed: (1) surface atom core-level shifts (SCLS), both positive and negative, relative to bulk [3], (2) metal alloys [4], and (3) submonolayer thin film coverage and small clusters [5–7]. In the case of SCLS, Johansson and Martensson [4] attributed the shifts to the difference in potential experienced by surface atoms relative to bulk due to the lower coordination number. Their calculated shifts indicated negative shifts on the order of 0.3 eV for iridium and platinum. Kleiman et al. [5] studied binding energy shifts by XPS for various ratios of Pt–Cu alloys and found that while Cu $2p$ shifted up to -0.7 eV, no shift was observed for Pt $4d$ lines. In regard to submonolayer thin film coverage and small clusters, both positive and negative binding energies shifts were observed relative to bulk materials. Both Mason and Baetzold [6] and Takasu et al. [4] measured positive shifts for small clusters, 2.5 eV for silver on carbon, and 1.6 eV for palladium on amorphous silver, respectively. Oberli et al. [8] measured negative binding energy shifts of 0.7 eV for the smallest gold clusters on carbon. It was concluded that none of these instances provided an explanation owing to the significant differences in material preparation and material–particle morphology. Additionally, the most significant of the binding energy shifts exceeded other reported shifts, often by more than a full order of magnitude.

The literature review also found reports of negative binding energy shifts for Group VIII metals on reduced TiO_2 catalyst supports during investigations of unusual catalytic activity attributed to strong metal support interactions (SMSI). While some of the early XPS studies of SMSI materials in the early 1980s reported negative binding energy shifts of the supported metal particles, none reported shifts below referenced metals zero valence energies. Fung [8], one of the first to report a negative binding energy shift for platinum on TiO_2 (Pt/TiO_2), reported a 1.6 eV negative binding shift for $\text{Pt}4f_{7/2}$. A closer review of the data shows that the negative shift was not below the energy of Pt^0 . Instead, the negative shift was based on a comparison of binding energies obtained from vacuum deposition of platinum as a thin film (approximately one atom thick) compared to a thick film produced during typical of catalyst preparation. Chien et al. [9] reported a negative shift of 0.2 eV for $\text{Rh}3d_{5/2}$ during their investigation of Rh/TiO_2 . This was also based on relative measurements between materials prepared as rhodium evaporated as a thin film on single crystals of rutile and catalyst samples prepared by impregnation. Again, the binding energies did not shift below metallic rhodium, Rh^0 , the lowest valence state energy. In both instances, the negative shifts are more consistent with those observed with submonolayer coverage cited previously [5–7].

While there did not appear to be a direct correlation with SMSI investigations (the bulk of the high temperature reduction temperatures rarely exceeded 500°C since high temperatures are contra-indicated for maintaining optimal surface area for catalysis), the similarity of materials was intriguing. Information from the SMSI helped to steer a series of follow-on experiments to further elucidate the similarities in materials and differences as it related to obtaining negative binding energy shifts. Additionally, one of the proposed mechanisms to explain SMSI was based on the n-type semiconductivity (electrical conductivity) of reduced TiO_2 [4]. This was also one of the key understandings regarding the basis for the highly unusual binding energy shifts that evolved during the investigation.

This article reviews the original series of experiments designed to elucidate the cause of the unusual negative binding energy shift. We will also review and re-evaluate data from the original experiments with more recent information obtained from the literature to provide the basis for the hypothesis of the Open Gate Phenomenon. We will also show that others inadvertently overlooked data that supports the hypothesis.

2. Experimental

The materials (Rh, Pt, and Ir in TiO_2) were prepared using two different processes prior to high temperature oxidation and reduction. The initial series of materials were prepared using the Pechini process which is based on U.S. Patent 3,330,697. Materials were prepared following Example I of the patent by adding the desired amount of Group VIII metal (Rh, Pt, and Ir), from 1 to 2% mole percent ($\text{Ti}_{100-x}\text{M}_x\text{O}_2$), to prepare the resin intermediate which was calcined in air in temperatures ranging from 400 to 500°C. The subsequent material was ground with a mortar and pestle to obtain a powder which was then subjected to high temperature oxidation (100% O_2) and reduction (1% H_2 and 5% H_2 in Ar) in a mullite tube furnace.

A metal salt impregnation–evaporation process was also used as a substitute for the Pechini process step prior to high temperature oxidation and reduction following the procedure for catalyst preparation outlined by Tauster et al. [12], the researchers who first identified SMSI. The materials were prepared by impregnating TiO_2 with metal salt solutions (0.5 wt.%), followed by air drying prior to high temperature oxidation and reduction. In all instances, the substituted materials were subsequently stored in plastic or glass vials under normal atmospheric conditions with no special handling precautions to maintain an inert environment prior to XPS and/or SEM/EDX analysis.

SEM analysis was performed on a JEOL JSM-35C scanning electron microscope equipped with a solid-state backscatter electron detector and Princeton Gamma-Tech X-ray detector. The samples were mounted using a conductive carbon paint/paste. A conductive carbon coating (via carbon evaporation) was not applied prior to analysis since the materials were generally sufficiently conductive to eliminate charging. SEM microprobe X-ray analysis and backscattered electron imaging using Z-contrast (imaging based on percentage of backscattered electron relative to atomic number) provided the ability to identify the location of Group VIII metals relative to TiO_2 .

Two different XPS spectrometers were used for analysis. Spectrometer A was a PHI (Physical Electronics, Eden Prairie, MN) spectrometer with Auger and XPS capabilities. Spectrometer B was a Varian (Varian Analytical Instrument Devices, Palo Alto, CA) spectrometer. XPS data was typically collected within a few days of material preparation. Charge correction was based on adventitious carbon ($\text{C}1s$) at 284.6 eV. Except where noted, ion (Ar) sputtering was not employed prior to analysis. In order to obtain in-house reference data to compare to the PHI Handbook Data [2], XPS data was measured on pure foil and powders obtained from Alpha Products post ion sputtering.

3. Results

3.1. Initial “first incidence”

The unusual XPS data was initially observed for $\text{Rh}3d_{5/2}$ in a material (Sample 1-0) prepared with high temperature (1400°C) oxidation and reduction post-preparation of a Pechini resin intermediate to obtain a 1 mole percent rhodium substitution for TiO_2 ($\text{Ti}_{0.99}\text{Rh}_{0.01}\text{O}_2$). Upon observing the initial raw data, the spectrometer was recalibrated and the sample was ion sputtered for five minutes before the second set of data was obtained and which again, confirmed the original highly unusual negative binding energy shift below the reference of 307.2 eV for Rh^0 (Table 1).

With instrument error ruled out, the issue of charge correction presented two possible options. The first used adventitious $\text{C}1s$ for correction (284.6 eV) which resulted in lower than expected reference $\text{Ti}2p_{3/2}$ energies of 458.7 eV [2]. Given the high temperature reduction, the presence of reduced species of Ti were possible which would result in a lower binding energy. Using the second option, a correction based on $\text{Ti}2p_{3/2}$, was also problematic because of the distinct possibility of reduced species. However, regardless of which charge correction was used, the magnitude of the negative shifts for $\text{Rh}3d_{5/2}$ far exceeded either charge correction option. With that in mind, electrodes (powder compressed into pellets) from the next series of materials (1600°C, and 1650°C oxidation and reduction) were analyzed by SEM prior to testing in a photo-electrochemical cell in order to determine the morphological nature of the materials.

Table 1. “First Incidence” initial data

Sample 1–0 1400°C (oxidation & reduction)	Uncorrected/corrected eV (pre-sputter)	Uncorrected/corrected eV (post-sputter)
C1s	286.7/284.6	284.9/284.6
Rh3d _{5/2}	303.3/301.2	303.0/302.7
Ti2p _{3/2}	458.7/456.6	NM
Ti2p _{1/2}	464.6/462.5	NM
NM: Not Measured		

SEM examination using EDX and backscattered imaging revealed that rhodium did not appear to be substituted within the rutile structure. Instead, it was observed and detected as discrete regularly and irregularly shaped microspheres, often observed at the grain boundaries, on the surface of the TiO₂. The particles were approximately 1–10 μm in size and the irregular shape was often due to the presence of a flat surface facet interposed onto the more-or-less spherical particles. The unexpected presence of platinum with rhodium in the particles was the result of contamination from the platinum boat used to contain the material during oxidation and reduction. The temperature was sufficient for platinum to migrate and alloy with the rhodium particles. (*Note:* this practice was subsequently discontinued with future material preparations.) Subsequent XPS analysis of non-sputtered materials again confirmed substantial negative binding energy shifts for rhodium and platinum, alloyed together in the metal particles (Table 2). The data was also consistent for the presence of mixed species of titanium, Ti⁴⁺ and Ti³⁺.

It is also interesting to note the presence of oxidized species of Rh³⁺ present in Sample 1–2 which was tested in a cell prior to XPS analysis in addition to a spectral line indicating a negative binding energy shift for Rh⁰ (assumed species). This further confirmed the validity of the data that indicated negative binding energy shifts. It also indicated the possible presence of two different particles on the surface, those with oxidized rhodium (Rh³⁺) and those with Rh⁰ exhibiting the negative shifts. A summary of the data for the binding energy shifts of the the initial three samples is found in Table 3.

3.2. Follow-on experiments

The variables explored during the follow-on experiments were designed to understand the preparation conditions that result in negative binding energy shifts including comparable material preparation conditions to those reported for SMSI. The variables were concentrated in three areas: (1) oxidation and reduction temperature range, (2) use of a metal salt impregnation–evaporation process for the initial intermediate preparation (a replacement for the Pechini process), and

Table 2. Initial confirming data.

	Sample 1-1 1600°C (oxidation and reduction) (eV)	Sample 1-2* 1650°C (oxidation and reduction)
Rh3d _{5/2}	302.2	302.6 eV (Rh ⁰) 308.3 eV (Rh ³⁺)
Rh3d _{3/2}	308.6	312.7 eV (Rh ³⁺)
Pt4f _{7/2}	62.2	NM
Pt4f _{5/2}	61.1	NM
Ti2p _{3/2}	458.0	458.0 eV
Ti2p _{1/2}	463.5	463.6 eV

*Post-cell testing

References [2]: Rh⁰ – 3d_{5/2} is 307.2 eV and 3d_{3/2} is 311.9 eV.

Pt⁰ – 4f_{7/2} is 71.1eV and 4f_{5/2} is 74.3 eV.

Ti⁴⁺ (TiO₂) – 2p_{3/2} is 458.7 eV and 4f_{5/2} is 764.4 eV.

Table 3. Summary of initial binding energy data.

Sample	Binding energy shift from Rh ⁰ 3d _{5/2} (eV)	Binding energy shift from Pt ⁰ 4f _{7/2}
1-0	−6.0	NM
1-1	−5.0	−8.9
1-2	−4.6	NM

(3) substitution of other Group VIII metals, specifically platinum and iridium. Tables 4 (Pechini process preparation) and 5 (metal salt impregnation–evaporation process) provide a summary of data from the follow-on rhodium substitution experiments including varying oxidation and reduction temperatures and reduction environments ranging from 100% Ar (considered mildly reducing) to 5% H₂ in argon (the most severe).

One of the critical factors was determined to be the combination of reduction temperature and environment. Even 100% Ar at sufficiently high temperatures produced the conditions necessary for binding energy shifts. Reducing temperatures as low as 800°C were also sufficient with the more severe reduction environment (5% H₂).

The larger the microsphere, on the order of 10–20 μm and larger, the greater the propensity for irregularly shaped microspheres with angular crystal facets protruding from the relative spherical shape.

Materials were also prepared for iridium and platinum substitution (0.5 wt.%) based on the oxidation and reduction conditions required to obtain negative binding energy shifts for rhodium using the metal salt impregnation–evaporation process. Table 6 provides a summary of the experiments which resulted in negative binding energy shifts. Aside from the unusual negative shifts, consistent negative shifts without the formation of surface oxides were also observed weeks after material preparation. This was also considered highly unusual without special handling and storage of the materials.

Table 7 provides the data obtained from an experiment to illustrate the effects of high temperature oxidation and reduction on rhodium powder.

As expected, the experiment confirmed: (1) presence of surface oxides on pure rhodium metal powder without special storage, (2) high temperature exposure in air oxidizes rhodium metal powder to Rh³⁺ (Rh₂O₃), (3) high temperature

Table 4. Summary of experiments based on Pechini preparation.

No.	Substitution (mol%)	Preparation	BE shift*	Comments (XPS and SEM)
2-1	1% Rh	1650°C/O ₂	2.2	Spectrometer B: Rh is oxidized which is consistent with preparation.
2-2	1% Rh	Same as 2-1 and 600°C/H ₂	0.3	Spectrometer B: Rh is reduced metal with surface oxidation.
3-1	2% Rh	Same as 2-1	2.0	Same as 2-1
3-2	2% Rh	Same as 2-2	0.4	Same as 2-2
4-0	1.7% Rh	1650°C/O ₂ only	1.4 and 2.0	Spectrometer B: Two distinct species of oxidized Rh. Large particles up to 20 μm in size.
4-1	1.7% Rh	Same as 4-0 and 1500°C/Ar	−1.2	Spectrometer A: Smaller regular and irregular microspheres to 1 μm at grain boundaries.
4-1			−0.6	Spectrometer B: Three weeks post preparation.
4-2	1.7% Rh	Same as 4-0 and 1400°C/Ar	−0.5	Spectrometer B: Numerous regular and irregular microspheres to 1 μm at grain boundaries.

*Pure rhodium foil reference: Rh⁰ − 3d_{5/2} is 307.1 eV.

Table 5. Summary of experiments based on metal salt preparation.

No.	Substitution (wt.%)	Preparation	BE shift	Comments (XPS and SEM)
5-1	0.5% Rh	800°C/O ₂ , 1150°C/1% H ₂	−0.7	Spectrometer B Microspheres approx. 0.2 μm and less
5-1			−0.6	Spectrometer B: over a month post preparation
5-1			−1.0	Spectrometer A: two months post preparation
5-1			−0.9	Spectrometer B: four months post preparation
5-1			ND	Spectrometer B: over six months post preparation
5-2	0.5% Rh	Same as 6-1 and 800°C/1% H ₂	−0.7	Spectrometer B
5-3	0.5% Rh	Same as 6-1 and 850°C/1% H ₂	−0.7	Spectrometer B Microspheres are less than 1 μm in size
5-3			−0.6	Spectrometer B: over one month after initial testing
5-4	0.5% Rh	450°C/O ₂ , 850°C/1% H ₂	ND	Spectrometer B: Insufficient temps for oxidation and reduction.
5-5	0.5% Rh	600°C/O ₂ , 800°C/1% H ₂	1.2	Spectrometer B: Rhodium in oxidized state-insufficient temps for oxidation and reduction.
5-6	0.5% Rh	Salt prep and 800/O ₂ , 800°C/1% H ₂	1.1	Spectrometer B: Rhodium in oxidized state-insufficient temps for oxidation and reduction.
5-7	0.5% Rh	1000/O ₂ , 800°C/5% H ₂	−0.3	Spectrometer B
5-8	0.5% Rh	500°C/O ₂ , 800°C/5% H ₂	−0.8	Spectrometer B
5-8			−0.7	Spectrometer B: six days after initial testing
5-9	0.5% Rh	500°C/O ₂ , 1000°C/5% H ₂	−0.4	Spectrometer B

*Rh foil reference: Rh⁰ − 3d_{5/2} is 307.1 eV and 3d_{3/2} is 311.8 eV

ND- not detected.

exposure to a reducing environment removes surface oxides as does ion sputtering prior to XPS analysis, and (4) surface oxides readily form on metal powder within days of exposure to air without special storage and handling precautions. The experiment also illustrated that the high temperature oxidation and reduction required to produce negative binding energy shifts in rhodium substitute TiO₂ do not produce the same shifts in rhodium powder alone. More importantly, surface oxidation of rhodium particles does not occur when negative binding energy shifts are observed.

Overall review of the SEM and XPS data resulted in seven key observations in order to obtain negative binding energy shifts and are summarized in Table 8. It should be noted that due to the spatial resolution (area) of the XPS spectrometers, an assumption was made that the XPS data provided a representative sampling of particle sizes for the sample. This was further supported by the fact that size was generally consistent (within a relative range) for a given material preparation. Materials with small particles (in the less than 1 μm range) did not also have particles in the 10 μm and higher range.

Table 6. XPS Data for Pt and Ir substitution.

No.	Substitution	BE shift (4f 7/2)*	BE shift (4d 5/2)*	Comments
6-0	Pt	−0.3	NM	Spectrometer B
6-1	Pt	−0.7	NM	Spectrometer B
7-0	Ir	−0.7	−1.0	Spectrometer B
		−0.7	NM	Spectrometer A: 2.5 months post-preparation

*Pt foil reference: Pt⁰ − 4f_{7/2} is 71.1 eV.

Ir powder reference: Ir⁰ − 4f_{7/2} is 60.9 eV, and 4d_{5/2} is 297.0 eV.

Table 7. Rhodium powder surface oxidation.

No.	Preparation	Rh3d5/2 (eV)*	BE shift	Comments
A	As Received	307.5	0.4	Spectrometer B: not ion sputtered
B	900°C/air	308.5	1.4	Spectrometer B: not ion sputtered. Analyzed next day after preparation.
C	800°C/1%H ₂	307.1	0.0	Spectrometer B: not sputtered. Analyzed next day after preparation
C		307.4	0.4	Analyzed (not sputtered) four days after initial analysis. No special handling or storage conditions.
C		307.1	0.0	Ion sputtered.

*Rh³⁺ – 3d_{5/2} is 308.2 eV [13].

4. Discussion

4.1. Then (1982)

The three most significant observations regarding the metal particles on reduced TiO₂ (the negative binding energy shifts, the morphological shape as microspheres, and resistance to surface oxidation) indicates electron transfer from the reduced TiO₂, an n-type semiconductor, to the metal particles. This is sufficient to provide a negative charge on the particles which imparts cathodic protection from the formation of surface oxides as illustrated in Fig. 1. The transfer of electrons appeared to initiate during high temperature reduction resulting in morphological changes to the metal particles that were initially formed during high temperature oxidation. Two possible explanations for the formation of microspheres were proposed. The first was due to Gauss' law whereby the preferred shape for a point charge is a sphere to equalize charge interaction. The second derives from minimizing surface tension effects at the elevated temperatures by agglomeration.

An on-going review of the literature failed to provide any answers to explain the observations and while there appeared to be a linkage to SMSI investigations at that time due to the similarity of materials, differences in material preparation remained the critical difference, particularly in regard to the temperatures for oxidation and reduction. However, Meriaudeau et al. [10] and Chen and White [11] were some of the first to propose an electron conduction mechanism based on reduced TiO₂ as an n-type semiconductor. This supported a key understanding that evolved during the original investigation, that the fundamental mechanism for the negative binding energy shifts was associated with electron transfer from the reduced TiO₂ as n-type semiconductor to the metal particles.

The purpose of the follow-on investigation was to understand the general material preparation required to reproduce the negative binding energy shifts, and that indeed, the shifts were reproducible. No attempt was made to investigate

Table 8. Key observations.

1	Group VIII metal segregation into crystalline particles occurs during high temperature oxidation, primarily at TiO ₂ grain boundaries and presumed defect sites
2	Reduction temperature and environment (in excess of 800°C) is critical to materials which exhibit binding energy shifts
3	Morphological transformation occurs from crystalline particles to microspheres during high temperature reduction of materials which exhibit binding energy shifts
4	Large microspheres on the order of 10–20 μm and larger are irregularly shaped with crystal faces protruding from the relatively spherical shape
5	Smaller binding energy shifts are observed with materials prepared with the metal salt encapsulation-evaporation process and which also produces smaller microsphere sizes
6	Binding energy shifts are observed for more than 4 months without preferential storage conditions of the materials

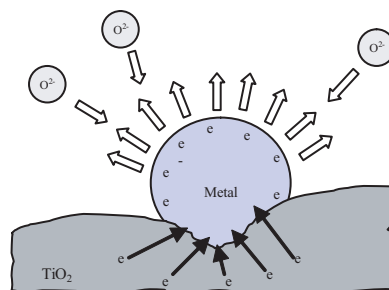


Figure 1. Cathodic protection.

any other aspect of the data, including the particle size relationship to the magnitude of the shifts and many questions remained unanswered when the investigation ended in 1982.

4.2. Now (present)

The original investigation and data was revisited more than thirty years later along with a review of the literature since that time. There is now considerably more information available concerning TiO_2 owing to its applications as a catalyst support, and in particular, as a photocatalyst. With one exception, the literature still does not show any instances of similar experimentation and data. However, a review of the literature provides information which further contributes to an understanding of the original investigation.

One area of interest is specifically related to the anatase-rutile transformation temperature for TiO_2 . The threshold temperature of approximately 800°C was determined to be the lower threshold to produce the negative shifts which was lower than the presumed (in 1982) threshold of approximately 1000°C for the anatase-rutile transformation. A more recent paper by Gouma et al. [14] studying anatase-rutile transformation referenced research dating back 50 years to a paper by Shannon and Pask [15] with data that indicated that the transformation can occur as low as 400°C depending upon the synthesis method, the atmosphere, and the presence of other ions. They noted that reduction increases the rate and lowers the transformation temperature due to oxygen vacancies. This confirmed a study by Iida and Ozaki [16], where rutile transformation was enhanced by a reducing environment (argon, hydrogen, and vacuum). Their studies also found that additions of transition metals can promote the transformation at lower temperatures. Therefore, although the specific causal link is not currently understood, the threshold temperature required to obtain negative shifts is linked to the transformation to the rutile TiO_2 .

Based on this information, a clearer understanding evolved for the conditions required to prepare materials which exhibit negative binding energy shifts: (1) material preparation that contributes to intimate mixing of metal oxides with TiO_2 and subsequent mobility that accompanies high temperature oxidation, (2) sufficient reduction of TiO_2 to an n-type semiconductor, and (3) transformation of TiO_2 to the rutile structure. The high temperature oxidation allows the metal to grow from the TiO_2 substrate (regardless of the initial pre-oxidation preparation) as opposed to a deposition onto a TiO_2 support. This implies an inherent difference between a metal-substrate interface as opposed to a metal-support interface. Herein is a key to understanding the basis for the mechanism that results in negative shifts. With this in mind, a review of SMSI-related literature also provides information which further supports the original investigation.

SMSI-related research exploded in the mid-1980s beyond the original catalysis investigations. This included experiments designed to test for electron transfer of metals deposited onto single crystal TiO_2 using surface analysis techniques as well as investigations into other reducible oxides and the use of dopants to explore the semi-conductor properties of reduced TiO_2 . Unfortunately, no single electronic-based hypothesis could explain the often mixed and

confusing results with the widely ranging materials preparations from real-catalyst to single crystal in-situ preparations. An alternative explanation evolved based on data that indicated encapsulation of the metal particles by a TiO suboxide layer which, with a few exceptions, is currently the preferred explanation for SMSI. However, a few more recent catalysis studies, including gold on reduced TiO₂, also continue to provide additional support to the original SMSI investigations of real catalysts where an electronic basis was first postulated.

In a study of real Au/TiO₂ catalysts (prepared using a metal salt impregnation–evaporation process, not single crystal in-situ preparations) in 2001, Akita et al. [17] found preferential nucleation of gold clusters on rutile structures prepared at different calcination temperatures. Their data indicated preferential nucleation of Au particles at grain boundary interfaces and that it initiates during calcination (high temperature oxidation). They also noted a “significant difference between catalyst prepared by deposition precipitation [polycrystalline] and a model catalyst made by evaporation of gold onto the surface of a single crystal of rutile.”

In 2003, Eider and Kramer [18] investigated the structural and electronic effects of high reduction temperatures of real Pt/TiO₂ catalysts. The reduction temperatures for this study ranged up to 800°C, higher than many previous studies and which is a temperature sufficient for complete transformation to rutile. Their findings were significant in regard to the effects of temperature on grain size, surface area, and conductivity. They concluded that the “higher density of charge carriers causes a narrowing of the space charge region at the metal support phase boundary” and that the “charge transfer necessary to align the Fermi levels of the two phases becomes larger which most likely affects the catalytic properties of these catalysts.”

In 2005 paper, Iddir et al. [19], also studying real Pt/TiO₂ catalysts observed an “unexpected” preferential nucleation for Pt particles on rutile over anatase with reduction and that the distribution of Pt seemed independent of surface orientation of TiO₂ particle with a higher concentration at the TiO₂ particle edges. They also observed a “nearly perfect spherical shape and thus has a point-like contact with titania [TiO₂]” which as they explained “shows the complex interdependence between the Pt particle shape, Pt–TiO₂ interface extent, TiO₂ phase, surface crystallographic orientation, and possibly the local density of oxygen vacancies.” Although their investigation did not include any XPS analysis, their results support the effects of charge transfer on the morphology of the supported metal particles. Micrographs using Z-contrast (backscattered electron imaging) are particularly reminiscent of observations in the original investigation.

All of these papers concur with the findings of this paper and reinforces the complexity of polycrystalline TiO₂. However, a paper published in 1986 provided data that directly supported the original negative shift investigations. Spichiger-Ulmann et al. [20] prepared Pt/TiO₂ catalyst materials for XPS analysis using salt impregnation–evaporation of thick films (10–15 μm) of TiO₂ followed by air calcination and reduction in argon. Subsequent XPS analysis reported negative binding energy shifts from 0.2 to 0.6 eV for Pt particles (less than 1 μm) below their Pt⁰ reference (prepared as a thick film on titanium). Additionally, the negative binding energy shifts were “persistent even after exposure of the samples to air for several days” and in one sample, up to four months before a positive shift back to a binding energy relative to the standard. Their findings correlate well with the original investigations presented in this paper and are also expected given their material preparation and calcination (oxidation) and reduction temperatures (up to 550°C).

They recognized the earlier work of Meriaudeau et al. and Chen and White in regard to the shifts explained in terms of Fermi energy adjustment between the reduced TiO₂ and metal resulting in the formation of a Schottky barrier. However, they considered this assumption problematic owing to the size of the particles on the surface and the assumption, in principle, of a region of less than 0.5 nm in which a significant change of electron density would be expected. The size of the particles were too large relative to the assumed size and nature of the space charge layer of the barrier. They concluded that encapsulation could just as easily be an explanation.

It is important to consider the general assumptions of the time in order to understand the context of their assumptions. This paper was first presented in 1985 at a symposium sponsored by the American Chemical Society during the height of investigations into an electronic hypothesis but also during the earliest hypotheses of encapsulation. Additionally, the assumptions about Schottky barriers was (and is) based on a metal deposited onto a semiconductor, not grown from

the semiconductor itself. Understanding this difference is one of the key elements to understanding the cause of the negative shifts, and more importantly, the cause and underlying mechanism.

4.3. Open gate hypothesis

In metal–semiconductor contact theory, thermodynamic equilibrium assumes that the electrochemical potential is uniform throughout the system. A potential forms at the junction of a metal and semiconductor, a Schottky barrier, based on their respective differences in electrochemical potentials. The ideal barrier height is determined by

$$\phi_B = \phi_M - \chi_S,$$

where ϕ_M is the work function of the metal and χ_S is the electron affinity of the semiconductor. As contact is made, electrons will flow initially to the material with the smaller potential. However, as the barrier forms, the flow of electron slows and eventually stops due to the formation of a depletion (of charge) zone, the charge neutral layer (CNL). In traditional semiconductor fabrication and applications, the presence of a thin layer of interfacial oxides is also a significant factor determining the actual barrier height.

Additional factors are taken into consideration with metal–semiconductor contacts in regard to Group VIII metals. For Rh, Ir, and Pt in contact with TiO_2 , the contact potential is the difference in work functions: 4.6 eV [21] for reduced TiO_2 , 4.98 eV for Rh, 5.61 eV for Ir (average for 100, 110, and 111 crystal planes) and 5.64 eV for Pt [22]. This results in electrons transferred to the metal particles. For TiO_2 which is a strongly ionic semiconductor, the Schottky barrier height will be equal or proportional to the difference in work functions. In regard to the amount of charge transferred, it is assumed to be significant since TiO_2 has a very high static dielectric constant and that there will be a strong dipole at the metal– TiO_2 interface. It is also assumed that while the affected volume of charge depletion in TiO_2 will be substantially larger (on the order of 10^6), the charge in the metal will remain at the interface due to the effective screening of metal electrons ([23] and references therein). In the case of small metal particles, the electric field will be dependent upon the metal–particle diameter. Nevertheless, the charge at the free metal surface will be negligible. Herein is the apparent departure from traditional metal–semiconductor assumptions for the Open Gate hypothesis.

Three elements are key to understanding the underlying mechanism of the negative shifts. The first is that although Group VIII metals on reduced TiO_2 are Schottky metals on an n-type semiconductor, the metal–semiconductor interface is not the same in the traditional sense of a fabricated Schottky diode. The metal particles coalesce from the TiO_2 substrate thereby providing a very different interface than metallization applied to a semiconductor support during diode fabrication.

The second element is that the negative shifts occur in polycrystalline materials. Polycrystalline materials have grain boundaries and defect sites which affect electrical properties relative to a single crystal. While no metal was detected within the rutile lattice, this was not confirmed using another more precise analytical technique and therefore some level of metal doping of the rutile lattice may also contribute to the mechanism. Taken altogether, this adds to the complexity of understanding electron transport and conductivity of reduced TiO_2 .

However, what is consistent with metal–semiconductor theory is that the junction is rectifying. The electrons flow one-way from the n-type semiconductor into the Schottky metal. This is the third element and critical piece in understanding the cause of the negative shifts. The shifts are caused by an isolated (one-way) negative charge on the metal particles. This is best understood by understanding what affects binding energies and how binding energies are measured in an XPS spectrometer.

The binding energy of an electron depends on the energy level from which it originates (1s, 2s, $2p_{3/2}$, etc. ...) but also on the oxidation state of the atom as well as the local chemical and physical environment. The binding energies derived from measurements in a spectrometer are based on the following:

$$E_{\text{binding}} = E_{\text{photon}} - E_{\text{kinetic}} - \phi,$$

E_{photon} is the energy of the excitation radiation and ϕ is the work function of the spectrometer (not the material/sample analyzed). The key assumption is that both the sample and the spectrometer are at the same potential (grounded to one another). However, if an external voltage is applied to a sample which was isolated (not at ground with the spectrometer), then the binding energies of the isolated sample shift relative to the applied voltage. Herein is the explanation for the negative binding energy shifts. The metal particles are isolated from the TiO_2 substrate and therefore from the spectrometer due the rectifying interface between reduced TiO_2 and the metal particles. The negative binding shifts are the result of the local environment alone created by the transfer of electrons from reduced TiO_2 (n-type semiconductor) and the metal particles (Schottky metal). The negative charge on the particles is the local environment and explains why corresponding shifts were not observed for titanium binding energies.

It would initially appear that the observations for negative shifts observed in the iridium substitution material (Sample 7-0) are not consistent because of the difference in the magnitude of the binding energy shifts for the energies for $\text{Ir}4f_{7/2}$ and $\text{Ir}4d_{5/2}$ (0.7 eV versus 1.0 eV). This difference, however, may be attributed to the differences in the shielding effects related too the relative radius differences of the electron orbitals [24]. This may also be a factor in the difference in shifts observed in Sample 1-1 between $\text{Rh}3d_{5/2}$ and $\text{Pt}4f_{7/2}$ where the metals are alloyed in the same microspheres.

However, the electron flow and resultant negative charge on the metal particles is also not the result of X-ray photon excitation during the XPS examination. The flow of electrons from TiO_2 into the metal is established during high temperature reduction and is of sufficient magnitude to affect morphological changes in the particles exhibiting the negative charge. Due to Gauss' law, the preferred shape is a sphere for a point charge to equalize charge interaction. The metal microspheres are therefore a conducting sphere where the charge resides on the surface, instead of only at the interface. However, at a given magnitude of charge on a microsphere relative to its size (radius), the energy balance tips in favor of the crystal lattice structure. This explains the observations of crystal facets and edges protruding from some of the very large microspheres. While this implies a limiting factor as to the size of the charge on the particles-microspheres, the charge is also of sufficient durability to provide cathodic protection from surface oxidation of the metal particles over an extended period of time.

In the material (Sample 5-1) where the negative shift was observed at 4.5 months, no rhodium was detected after 6 months (Table 5). This along with other anomalous data suggested a carbon-based surface contamination on the sample, perhaps plasticizer from the plastic vial. Unfortunately, this was at the end of the investigation and no further experimentation was performed to resolve the inconclusive results. However, in the Spichiger–Ulmann study, a positive shift relative to the reference value for Pt^0 was observed in the sample after four months of air exposure indicate. This is understood to indicate a loss of the negative charge on the metal particles.

It is therefore proposed that the underlying mechanism for the Open Gate Phenomenon is based on a unique metal–semiconductor interface that results from metal particles grown from the semiconductor itself. The interface significantly affects the Schottky barrier height and CNL resulting in a one-way open gate for electron flow from the reduced TiO_2 to the metal particles based on their difference in work function. The result is a significant and durable negative charge (electron transfer) to the metal particles.

Any conjecture beyond this basic hypothesis is difficult. Many questions remain unanswered. Assuming that there are factors which limit the negative charge on the metal particles, is it based on metal particle size or, something associated with the reduced TiO_2 itself? Is there a charge–discharge cycle associated with it? Is the loss of cathodic protection from surface oxidation attributed to the loss of conductivity of the TiO_2 with its re-oxidation during air exposure, or is there another mechanism involved?

Of course, the most important unanswered question revolves around what initiates and maintains the charge. Is it possible that the electron flow into the metal particles is as simple as that work function equilibrium is not attained? Why not? Is the source of electrons only those contained within the materials? Depending upon the answers to these questions, the Open Gate Phenomenon has the potential to become the foundation of a new energy technology.

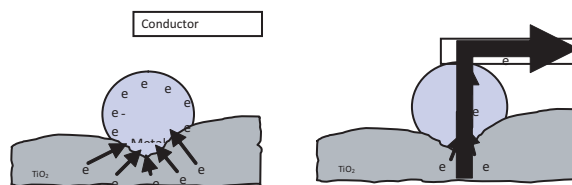


Figure 2. Current (electron flow) to a conductor.

From an application standpoint for a new energy technology, the behavior of metal microspheres may be comparable to miniaturized Van de Graff generators. Borrowing on the concept that Van de Graff generators are a nearly ideal current source derived from an electrostatic generator, the metal microspheres may also provide for direct electrical energy generation. Figures 2 and 3 illustrate this concept based on a series of connected parallel plates on which a thick-film of an Open Gate Phenomenon-based metal oxide is prepared with a metal (ground support) and conductive over-layer providing a connection to the negatively charged microspheres. However, unlike with an electrochemical-based battery, connecting to ground (a source of free electrons) does not short-out the device because of the inherent one-way gate (diode) of the interface. The black box is an internal circuit that may be required if the mechanism has a charge–discharge cycle associated with it.

5. Conclusions

The Open Gate hypothesis is based on readily observable and reproducible experimental results. Additional in-depth research is required to investigate the full nature of the interface and mechanism that results in the unusual negative charge on Group VIII metal particles grown from reduced rutile TiO_2 . Once this is more fully understood, the Open Gate Phenomenon may be applicable to other appropriate metal–reducible oxides and mixed metal oxides. Based on the preliminary findings, the Open Gate Phenomenon has the potential to become the foundation for a new technology with direct and indirect energy applications including catalysts and electrocatalysts, particularly for fuel cells.

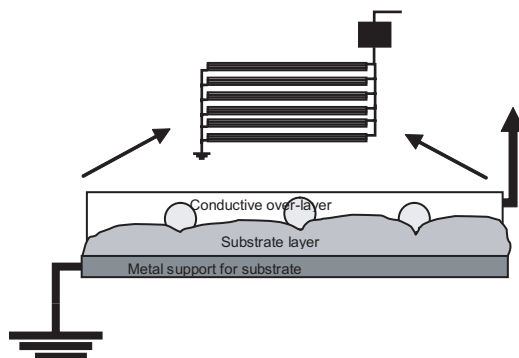


Figure 3. Concept of a device for direct electrical energy generation.

References

- [1] U.S. Patent 3,330,697; Maggio Pechini, inventor; Method of Preparing Lead and Alkaline Earth Titanates and Niobates and Coating Method using the Same to Form a Capacitor. July 11, 1967.
- [2] *Handbook of X-Ray Photoelectron Spectroscopy*, Perkin Elmer Corporation, Physical Electronics Division, Eden Prairie, MN, USA, 1979.
- [3] B. Johansson and N. Martensson, Core-level binding energy shifts for the metallic elements, *Phys. Rev. B* **21** (1980) 4427.
- [4] G.G. Kleiman, V.S. Sundaram, C.L. Barreto and J.D. Rogers, ESCA determination of the electronic structure of Pt–Cu alloys, *Solid State Communications* **32** (1979) 919.
- [5] M.G. Mason and R.C. Baetzold, ESCA and molecular orbital studies of small silver particles, *J. Chem. Phys.* **64** (1976) 271.
- [6] Y. Takasu, B. Unwin, B. Tesche and A.M. Bradshaw, Photoemission from palladium particulate arrays on an amorphous silica substrate, *Surface Sci.* **77** (1978) 219.
- [7] L. Oberli, R. Monot, H.J. Mathieu, D. Landolt and J. Buttet, Auger and X-ray photoelectron spectroscopy of small Au particles, *Surface Sci.* **106** (1982) 301.
- [8] S.C. Fung, XPS studies of strong metal-support interactions (SMSI)–Pt/TiO₂, *J. Catal.* **76** (1982) 225.
- [9] S.H. Chien B.N. Shelimov, D.E. Resasco, E.H. Lee and G.L. Haller, Characterization of the interaction between Rhodium and titanium oxide by XPS, *J. Catal.* **77** (1982) 301.
- [10] O. Meriaudeau, O.H. Ellestad, M. Dufaux and C. Naccache, Metal–support interaction: catalytic properties of TiO₂–supported platinum, iridium, and rhodium, *J. Catal.* **75** (1982) 243.
- [11] B.H. Chen and J.M. White, Properties of platinum supported on oxides of titanium, *J. Phys. Chem.* **86** (1982) 3534.
- [12] S.J. Tauster, S.C. Fung and R.L. Garten, Strong metal support interactions, group 8 noble metals supported on TiO₂, *J. Catal.* **100** (1978) 170.
- [13] Y. Okamoto, N. Ishida, T. Imanaka and S. Teranishi, Active states of rhodium in rhodium exchanged Y zeolite catalysts, *J. Catal.* **58** (1979) 82.
- [14] P.I. Gouma, M.J. Mills and G.S. Rohrer, Anatase-To-rutile transformation in titania powders, *J. Am. Ceramic Soc.* **284** (2001) 619.
- [15] R.D. Shannon and J.A. Pask, Kinetics of the anatase-rutile transformation, *J. Am. Ceramic Soc.* **48** (1965) 391.
- [16] Y. Iida and S. Ozaki, Grain growth and phase transformation of titanium oxide during calcination, *J. Am. Ceramic Soc.* **44** (1961) 120.
- [17] T. Akita, L. Ping, S. Ichikawa, K. Tanaka and M. Haruta, Analytical TEM study on the dispersion of Au nanoparticles in Au/TiO₂ catalyst prepared under various temperatures, *Surf. Interface Anal.* **31** (2001) 73.
- [18] D. Eder and R. Kramer, Stoichiometry of “Titanium Suboxide”: Part 2. Electric properties, *Phys. Chem. Chem. Phys.* **5** (2003) 1314.
- [19] H. Iddir, M.M. Disko, S. Ogut and N.D. Browning, Atomic scale characterization of the Pt/TiO₂ interface, *Micron* **36** (2005) 233.
- [20] M. Spichiger-Ulmann, A. Monnier, M. Koudelka and J. Augustynski, *Spectroscopic and Electrochemical Study of the State of Pt in Pt–TiO₂ Catalysts, Strong Metal Support Interactions*, R.T.K. Baker, S.J. Tauster and J.A. Dumesic (Eds.), American Chemical Society Washington, DC, 1986, p. 212.
- [21] Y.W. Chung, W.J. Lo and G.A. Somorjai, Low energy electron diffraction and electron spectroscopy studies of the clean (110) and (100) titanium dioxide (rutile) crystal surfaces, *Surface Sci.* **64** (1977) 588.
- [22] *CRC Handbook of Chemistry and Physics*, David R. Linde (Editor-in-Chief), CRC Press, Boca Raton, FL, 2008, pp. 12–119.
- [23] X.E. Verykios, Support Effects on Catalytic Performance of Nanoparticles. Catalysis and Electrocatalysis at Nanoparticle Surfaces, A. Wieckowski, E.E. Savinova and C.G. Vayenas (Eds.), Marcel Dekker, New York, 2003, p. 745, and references herein.
- [24] Carlson Thomas A., *Photoelectron and Auger Spectroscopy*, Plenum Press, New York, 1975.



Research Article

Cryogenic Calorimetry of “Exploding” PdD_x Wires

F.L. Tanzella *, J. Bao and M.C.H. McKubre

SRI International, Menlo Park, CA 94025, USA

Abstract

Reports in the literature have shown that thin PdD_x structures have yielded anomalous effects (heat and nuclear products) when stimulated by different forms of electro diffusion. We have designed, constructed, and operated a calorimeter operating at 77 K with a minimum detectability of less than 0.1 J and an accuracy of less than 0.06 J, which utilizes an “exploding wire” technique to examine the effect of a destructive electro-diffusion on a highly loaded PdD_x wire. We have shown, using a very thin Pd wire cathode and a thin Pt wire anode, that highly loaded PdD_x wires can be formed using high-voltage electrolysis of very high-purity D₂O. Highly loaded PdD_x wires can disintegrate (“explode”) to form microscopic particles when subjected to high current density pulses at 77 K. Under certain conditions PdD_x wires can yield excess energy when subjected to high-current density pulses at 77 K. © 2012 ISCMNS. All rights reserved.

Keywords: Cryogenic calorimetry, Deuterium loading, Electrochemical, Detectability, Exploding wires

1. Introduction

Several groups [1,2] have reported anomalous effects (heat and nuclear products) in thin PdD_x materials stimulated by different forms of electro diffusion. We have extrapolated this technology to the electrical heating of thin PdD_x wires, which resulted in destructive high-speed melting, i.e., “exploding wires.” Nairne reported using exploding wire techniques over 225 years ago [3]. Over 150 years ago Faraday reported using exploding wire technology to produce fine metal particles [4]. Celani et al. [5,6] have reported the electrochemical loading of thin Pd wires to approximately 1:1 and the electrochemical sealing of their surface. Such sealed wires can be immersed in liquid nitrogen (LN) and analyzed for anomalous effects at those temperatures or soon after warming up, according to Tripodi [7]. Celani et al. [8] reported using pulsed microsecond electrolysis to induce excess power. We hypothesized that electrically exploding highly D-loaded Pd wires immersed in LN should release the deuterium and cause the evolution of gaseous N₂ equal to the electrical energy passed through the wire due to the enthalpy of vaporization of LN.

Since a correlation between the rates of excess heat and ³He and ⁴He production has been reported [9,10], we will analyze the off-gases for excess He and non-natural isotopic He ratios.

*E-mail: francis.tanzella@sri.com

2. Experimental

2.1. Electrochemical methods

We have adapted the original H₂O high-loading/sealed-cathode techniques of Celani and Tripodi to D₂O. This is not a trivial effort, since the loading process requires ultra-clean materials and ultra-pure reagents. Unfortunately, most available D₂O is chemically impure when compared to 18 M Ω -cm deionized H₂O. We have been using high-purity D₂O (Sigma–Aldrich #P192341), which also provides the high isotopic purity necessary to yield high D loading. To maintain this isotopic purity, all transfers are performed under dry N₂ or Ar.

To achieve high electrochemical loading of deuterium (D/Pd ratio \gg 0.9), cleanliness of all materials is of the utmost importance. Figure 1 is a diagram of the electrochemical cell used for loading the Pd. The specifics of the electrochemical cell have been reported elsewhere [11]. In the present work, a 5–6 cm length of 99.9% Pd wire (Goodfellow, Oakdale, PA), 50 μ m in diameter, is attached to four lengths of 0.25 mm Pt lead wires in the center of the cell. This allows for in situ accurate 4-wire resistance measurements of the Pd cathode. The anode is a 30-cm-long, 1-mm-diameter Pt wire, wound helically around the Pd wire, and fixed by a cage made of six quartz pillars forming a cylinder of \sim 2 cm in diameter.

After the wire is spot welded, the whole cell and the quartz cylinder are immersed in ethyl alcohol held in an ultrasonic bath, followed by sonication in 18.3 M Ω -cm deionized water and oven drying. The Pd cathode is then annealed by applying a series of current steps that resistively heat the cathode until it ultimately is red-hot, then slowly cooled by reducing the current in steps. This procedure is repeated until the Pd resistance does not change upon annealing. This final resistance is considered R_0 . Annealing can reduce the wire's internal stress and the number of grain boundaries. Grain boundaries are where H/D recombination can occur to yield H₂/D₂ gas and provide a conduit for the gas to diffuse out. After annealing, the cell is again cleaned and dried.

The electrolyte solution used in the experiments (0.5×10^{-4} M SrSO₄) is prepared from D₂O (inside a glove bag filled with N₂ or Ar and sealed) or H₂O and stirred overnight. The starting electrolytic current is 2–3 mA, equivalent to 200–300 mA/cm², low enough to minimize crack formation. To determine the stoichiometric ratio of H/D atoms dissolved into the Pd cathode during the electrochemical loading process, in situ four-probe resistance measurements of the Pd cathode are performed using a Hewlett Packard 4338A milliohmeter. The relative ratio of the resistance of the loaded Pd wire to the initial Pd wire is known to be a function of the average stoichiometric ratio of H/D to Pd, as has been shown in previous publications [12]. After a stable resistance value is obtained at this low current, the current is increased to 5.0 mA.

After achieving the maximum possible loading, Hg in the form of a 2.5×10^{-4} M Hg₂SO₄ solution is added to the electrolyte. Hg is reduced cathodically on the Pd surface and forms a nearly homogeneous amalgam bond. The presence of Hg atoms at the surface poisons the recombination of D atoms, thus reducing the formation of D₂ gas and in turn inhibiting de-loading of the Pd wire. Hg₂SO₄ solution is added, 1 ml at a time, until the resistance stops decreasing. As the Hg is added, the current is reduced in an attempt to maintain the loading at reduced current. After the loading is stabilized even at a minimal current (such as 1 mA), the electrolysis is stopped, and the wire is immediately transferred to the cryogenic calorimeter filled with LN.

2.2. Cryogenic calorimetry

Figure 2 shows a schematic layout of the cryogenic calorimeter designed at SRI, which comprises a stainless steel (SS) dewar, a silicone rubber gasket, a DelrinTM adapter and thick DelrinTM cap for good insulation, a 1/4" opening for boiling off N₂ gas, and two copper current rods and blocks to fix the loaded Pd wire for the excess heat measurement. The gas outlet is sent to an Aalborg GFM-17 0–5 l/min calibrated mass flow-meter with a 0–5 V analog output. The Dewar flask is filled with a certain amount of LN. The copper rods and gas outlet are exposed to the environment to be

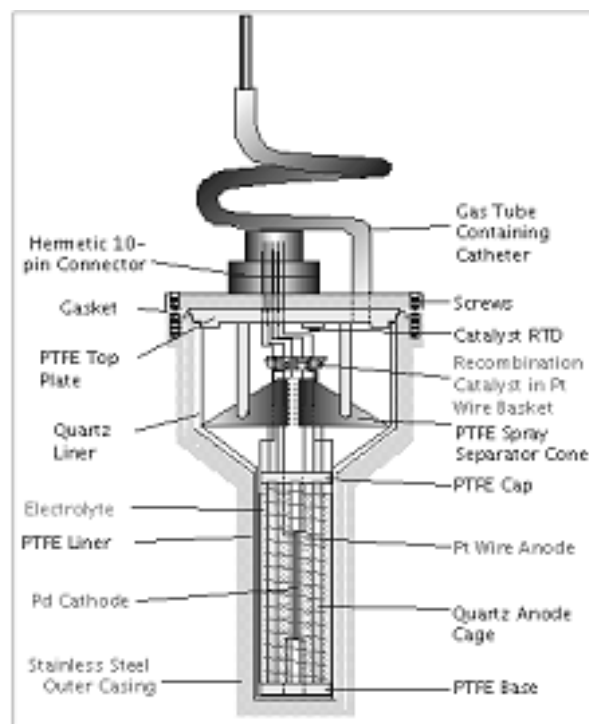


Figure 1. Degree of loading cell used to load and seal thin wires.

connected to the electrical cables and gas mass flow meter. The parts exposed to the room temperature environment can transfer heat to the LN, especially through the copper rods (which is a good current conductor and also a good heat conductor), so that the LN boils off at a certain rate. An integration of the mass flow rate gives the total amount of N_2 gas evolved. The whole system is placed inside a cylindrical acrylic shield to minimize the ambient environmental fluctuation.

Since the LN inside the Dewar flask is continuously boiling off without further replenish, an absolute steady state base flow rate cannot be reached. Instead, the flow rate decreases very slowly (the decay rate is less than 2 ml/min or 0.03 ml/s when the base flow rate is below 1.8 l/min). However, within a short time, a quasi-steady state is reached. Theoretical base and details will be published elsewhere. When a high-voltage pulse of less than 0.1 s is provided, the system responds to the input heat by the boiling off of excess N_2 gas, which can be seen as a sharp pulse in the flow rate of less than 1.5 s duration. An integration of this pulse after baseline subtraction gives the total excess gas volume evolved by the pulse. The input energy is provided by a 50 V, 8 A, four-quadrant power supply (Kepco BOP 50-8, Flushing, New York). The power supply is triggered using software developed using the Labview[®] (National Instruments, TX) development system, which also is used to collect the current, power, and flow rate data.

National Instruments PCI-6173 and PCI-6143 cards are used to both initiate the output pulse and collect data. The current, voltage, and flow rate, which are measured at a sampling rate of $10,000\text{ s}^{-1}$, are used to calculate both the energy input to the calorimeter and the volume of N_2 evolved by the pulse. From the heat of vaporization of LN at 77 K, 5.56 kJ/mol, equivalent to 4.32 mL/J at room temperature, the evolved excess N_2 gas after the pulse could be compared with the theoretical value calculated from the input energy. We calibrated the volume of N_2 evolved at different input

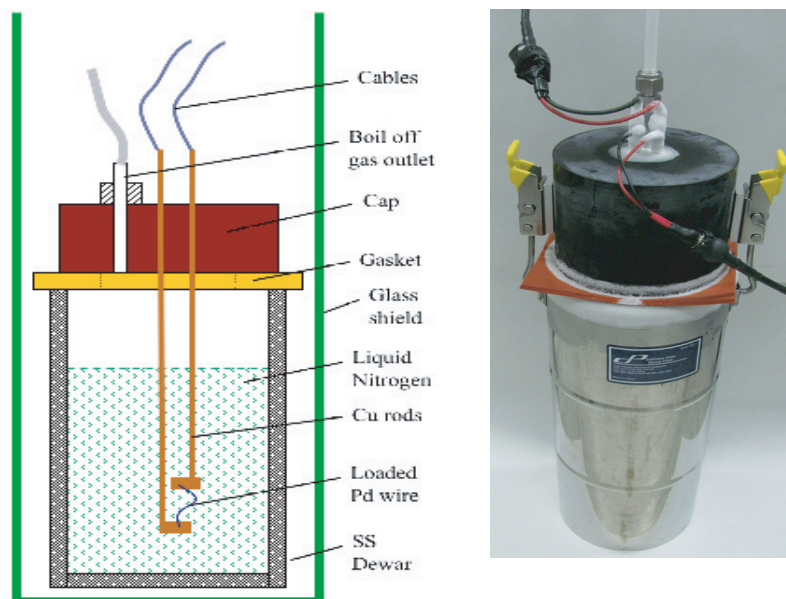


Figure 2. Schematic diagram and photograph of the cryogenic calorimeter.

energies by using different length pulses and current levels into a current shunt immersed in the LN calorimeter, in that way, the input energy could be controlled. We also calibrated the system by stimulating at least nine blank Pd wires, and calculating the output energy from the increased volume of N_2 gas evolved.

3. Results and Discussion

3.1. Calorimeter calibration

Figure 3 shows five typical behaviors for the base flow rates of boiled-off nitrogen gas from the LN in the Dewar flask. The data are collected every 5 ms until 50 s and after 52 s, and at every 0.1 ms in the interval from 50 to 52 s, during which the pulse is applied and excess gas volume is measured. The flow rate usually fluctuates around an average rate with a standard deviation of about 0.013–0.014 l/min, except for baseline 3, which has a standard deviation of 0.02 l/min. Note that the high-frequency fluctuation comes from electronic noise. The stability of the system is very important, and shielding from the environmental perturbation is also recommended.

However, deviations from the quasi-steady state are also seen as thermal fluctuations and slight baseline drifts. The thermal fluctuation usually starts and ends in about 20–30 s, which is seen as a rise/drop in flow rate and then a return to the average. From the base flow rate collected before and after the application of the pulse, we are able to locate the position of the excess flow peak, whether it is collected when the system is steady, on a rising/decreasing wave, or drifting to another baseline. The nearest few seconds should be used as the baseline for the later cases, and the error will still be minimal, since the response to the pulse only lasts for 1.1–1.2 s. In extreme cases, where sharp rises/drops (~ 1 s) are concurrent with a thermal fluctuation wave, the error could be as high as ± 0.25 ml (which was obtained by picking a high peak, calculating the difference with the nearest low average, then integrating for 1.2 s). Otherwise, the difference is usually between 0.1 and 0.2 ml if fluctuation occurs. The error percentage is obviously less at higher input energies. Therefore, upper and lower bounds of 0.25 ml from the theoretical value are considered the absolute limits of

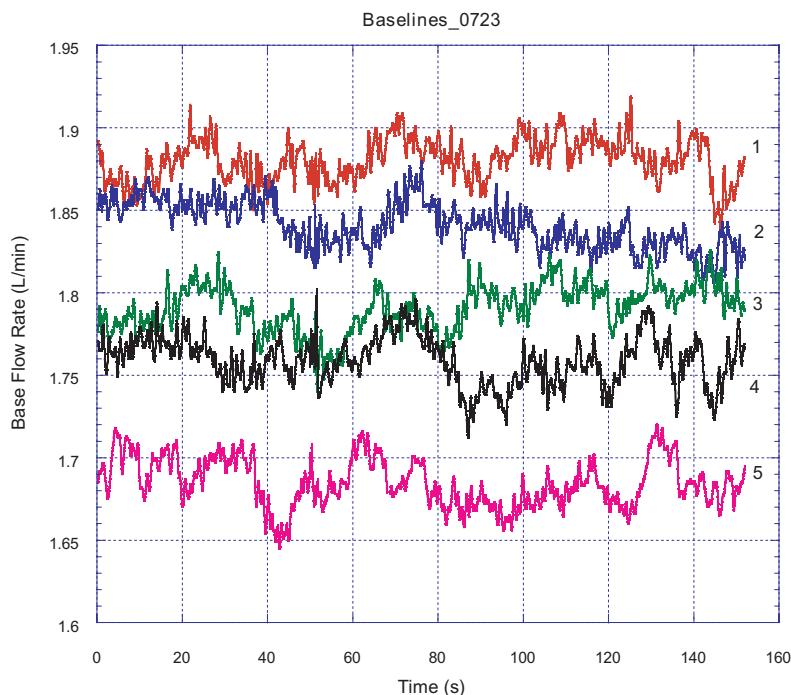


Figure 3. Typical base flow rate variation with time measured by the cryogenic calorimeter.

error. If the measured (and calculated) excess gas volume is obviously much more than 0.25 ml, it is clear that excess heat has been generated. If the excess gas volume is approximately 0.25 ml or less, excess energy is difficult to prove.

Calibration of the cryogenic calorimeter was carried out using both a 10 Ω resistor and blank (as received) Pd wires. We applied a series of current pulses of 0.3–2 A for durations of 100–500 ms to the 10 Ω resistor and measured the evolved gas volume. Each experiment was operated three times to determine the statistical error. This calibration method provides a wide range of input energy, and the results are presented in Fig. 4. The measured gas volume at each input energy level lies very close to the theoretical line and well within the limits of error. The response time of the calorimeter is ~ 3 s after the input stimulation pulse, which is found to be significantly different from that of the calorimeter using thin wires (1.1–1.2 s). A high current pulse is applied and the power generated is usually over several hundred watts, which can momentarily heat up the wire causing the thin wires to break in a few milliseconds. Therefore, we performed calibrations with thin pure Pd wires. Figure 5 shows the measured gas volume for each of the 9 blank wires tested, and its corresponding theoretical gas volume. It is seen that the measured/calculated gas volumes are very close to the theoretical values (within ± 0.25 ml). These data confirm that no excess heat was generated with blank Pd wires, and that the calorimeter yields repeatable results. With this calibration method, the maximum input energy is limited by the energy needed to break or melt the thin wire. Using heat capacity data from HSC[®] software by Outokumpo, we calculated that only 0.75 J is required to melt a 5 cm long Pd wire of 50 μm diameter in LN, if heat conduction is neglected. For a 6 cm long wire, the energy needed is 0.9 J. In many cases, the wire breaks at a weak point, so the input heat is far less than the energy needed to melt the whole wire.

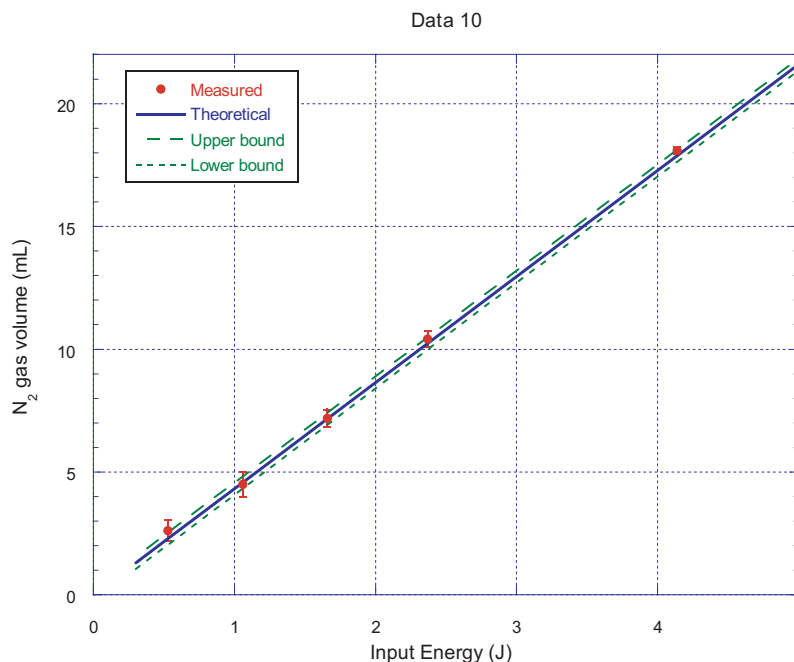


Figure 4. Calibration of the calorimeter using a series of electrical pulse across a 10 Ω resistor.

3.2. Electrochemical results

Figure 6 shows a typical annealing curve and a photograph of the Pd wire during this annealing process.

Low-molarity Pd/SrO₄/D₂O electrolysis experiments were performed using 50 μ m wires. These wires were then sealed electrolytically using Hg₂SO₄. A typical cell response to current steps and Hg₂SO₄ additions is shown in Fig. 7. R/R_0 (the ratio of the instantaneous Pd resistance to its starting resistance) went through a maximum very quickly, as was expected for such a thin wire. Then, small amounts of Hg₂SO₄ were added to enhance the loading and seal the wire. Finally, the current was reduced in steps with minimal loss of loading. These wires were then successfully transferred to a cryogenic calorimeter without loss of loading.

In addition to the input pulse, the gas volume measured may be affected by the enthalpy of melting/volatilizing the wire as well as the gas evolution from the desorption of any hydrogen/deuterium. For these reasons, the results from PdD_x wires will be compared with the energy released from pure Pd or Pt wires as well as the results from PdH_x.

3.3. Calorimetry results

Figure 8 shows typical calorimetric responses to current pulses being sent through a PdD_x wire and a 10 Ω resistor.

The average response time for blank Pd wires is 1.22 s, with a standard deviation of 0.035 s. Therefore, response time of 1.2 s is used for the calculation of PdD_x wires for ease of calculation and also to minimize the error. For the 10 Ω resistors, the response time is around 2.9 s. There are always two major peaks seen in the flow rate of the evolved gas after the pulse (in some cases, the second peak is finely divided into two peaks) with pure Pd wires, PdD_x wires, and calibration resistors.

For the resistors, the first rise is possibly related to the copper rods, which are very good heat conductors that almost

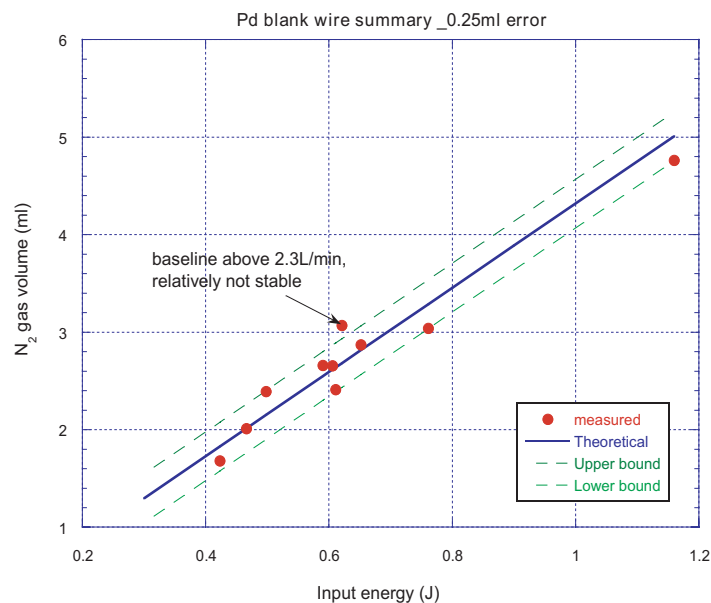


Figure 5. Calibration of the cryogenic calorimeter using blank Pd wires.

immediately transfer the heat to the liquid nitrogen. The second rise is then related to the heat conducted from the heated resistor to the liquid nitrogen. For the wires, the faster response is probably due to direct heating of the liquid nitrogen after the wire disintegrates, together with the heating of the copper rods. The second peak is probably the heat released from the wire itself. Since the wire has faster heat conductance than the resistor, the temporal separation between the two peaks is less. Also, because the current is applied for 100 ms for the 10 Ω resistors, while it only lasts about 3–5 ms for the thin wires, the half-height-widths of the peaks are larger for the resistor calibration pulses.

Table 1 summarizes the calorimetric results for PdH_x and PdD_x wires for which the calorimeter showed a stable baseline. It is interesting to point out that after a large amount of testing with thin Pd wires, it seems that whether the wire would completely disintegrate into fine powders or simply break is determined by the nature of the wire itself, and possibly has nothing to do with loading and generation of excess energy. If the wire has defects, it would break at the weakest point(s). Otherwise, the wire would completely disintegrate, whether it is loaded or blank. If the defect is very weak, then the input pulse energy is also very low, as the input energy is an indication of the energy to break the wire. It is also interesting to note that the wire with the highest deuterium loading was very brittle. When transferring it to the calorimeter, it broke several times near the point fixed to the calorimeter, and finally became too short to measure. Whether it is due to the high loading impairing the crystallographic structure or the intrinsic defects within the wire is unknown. It only happened in this one occasion.

None of the blank wires showed any excess heat. Among the three wires loaded with H, two didn't show any excess heat significantly greater than the input energy. One showed relatively high excess heat, but with an unstable baseline. Therefore, with limited data points in the present work, it is difficult to conclude whether PdH_x wires generate significant amount of excess heat. Whereas among the seven wires loaded with deuterium, five showed the generation of excess energy significantly higher than the error range. The amount of excess energy varies from $18.4 \pm 8\%$ to $51.9 \pm 7\%$ (excluding wire #8, which has an excess percent of $499.5 \pm 100\%$ due to the low energy input, but the baseline is over 2 l/min). Figure 9 clearly illustrates which wires generated excess energy. Three wires are within the error range, but

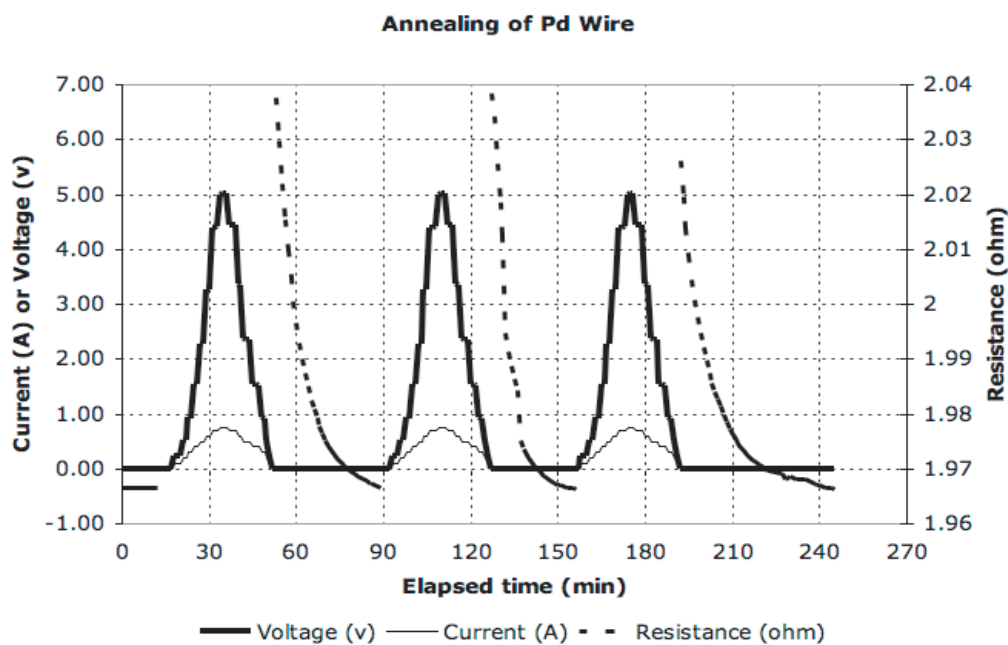


Figure 6. Plot of R/R_0 , current, and voltage during Pd wire annealing.

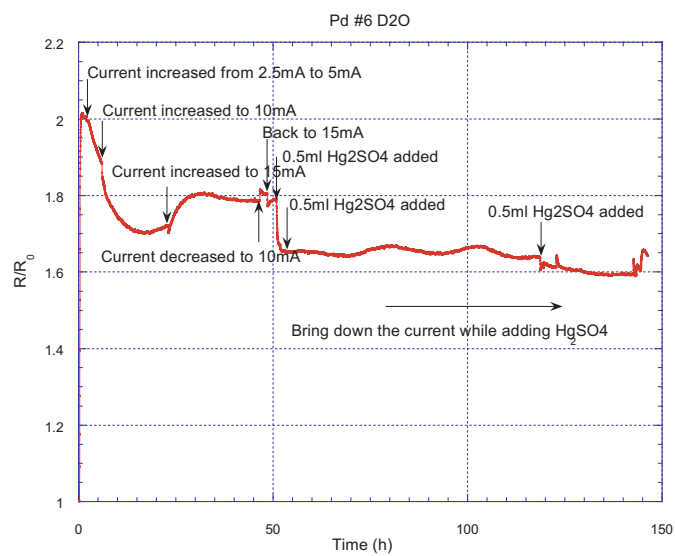


Figure 7. Plot of R/R_0 for D loading of Pd wire.

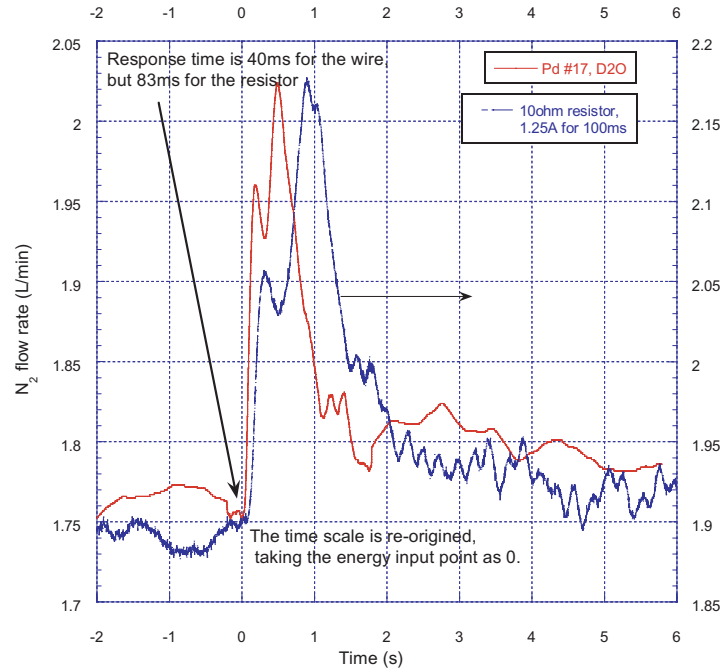


Figure 8. Typical calorimetric response to a current pulse through a PdD_x wire and a 10 Ω resistor.

Table 1. Cryogenic calorimeter results summary.

Exp.	Material	<i>x</i>	Energy input (J)	Energy output (J)	% Excess energy*	Comments
8	PdD _x	0.88	0.12	>=0.69	500 ± 100%	Unstable baseline
9	PdH _x	~ 1.0	0.68	0.74 ± 0.12	8.2 ± 18	Unstable baseline
10	PdH _x	> 1.0	0.64	0.96 ± 0.12	47 ± 19	Unstable baseline
11	PdH _x	> 1.0	0.37	0.49 ± 0.06	32.5 ± 16	
e 12	PdD _x	0.98	0.71	0.84 ± 0.06	18.4 ± 8	
13	PdD _x	0.93	0.94	1.22 ± 0.06	29.7 ± 6	
14	PdD _x	0.95	0.63	0.70 ± 0.06	11.7 ± 10	
15	PdD _x	0.96	0.53	0.51 ± 0.06	-3.5 ± 11	
16	PdD _x	0.97			-	Too brittle to measure
17	PdD _x	0.97	0.50	0.70 ± 0.06	40 ± 12	Wire disintegrated
18	PdD _x	0.90	0.82	1.25 ± 0.06	51.9 ± 7	

*Note: The error percentage is calculated by dividing the inherent system error range, 0.06 J, by the input energy of that specific wire.

the other seven wires show measured energy clearly greater than the error range. Although no obvious correlation can be made between excess energy production and loading level, the amount of excess energy generated by the stimulation of PdD_x is generally much more than that generated by PdH_x wires.

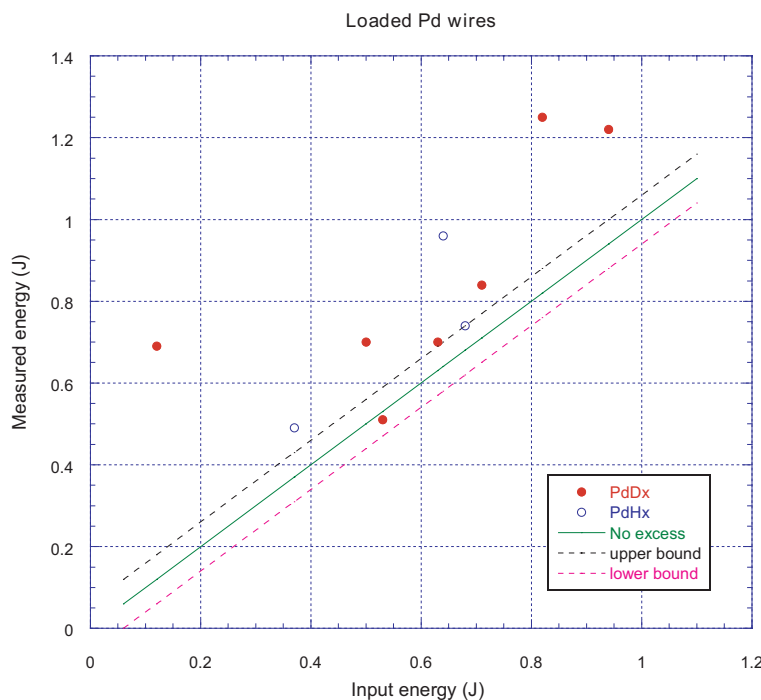


Figure 9. Input energy and measured energy for all the Pd wires loaded with H or D.

4. Conclusions and Future Work

We have shown that the Tripodi technique for electrochemically forming highly loaded 50- μm -diameter PdH_x wires can be extended to PdD_x wires. We have designed, built, and operated a cryogenic calorimeter with a minimum detectability of less than 0.1 J and accuracy of less than 0.06 J. Under certain conditions when passing high current density pulses through highly loaded PdD_x wires, output energies as high as 150% of input energies have been measured. We have shown that PdD_x wires can disintegrate (“explode”) when high current density pulses are passed through them at 77 K. In all cases seen so far, this disintegration leads to excess energy. No correlation can yet be made between the average deuterium loading level and excess energy.

We will collect gas from the calorimeter headspace during these “exploding wire” pulses and use mass spectroscopy to measure He isotope concentration in these gases. We will also use a metal vaporization inlet furnace to the He isotope mass spectrometer to analyze any Pd fragments for anomalous He isotopic ratios. We must measure more highly loaded PdH_x wires using a stable calorimetric baseline in order to develop a statistically significant comparison.

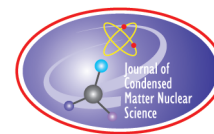
Pd (and other metal and alloy) wires subjected to He insertion will be loaded and subjected to high current density pulses using the techniques described above in an attempt to maximize the excess energies. He insertion will be used to form defects in the Pd cathodes, which we feel should facilitate anomalous effects.

Acknowledgments

We gratefully acknowledge the support of the Basic Research Program of the U.S. Defense Threat Reduction Agency (DTRA).

References

- [1] E. Del Giudice, A. De Ninno, A. Frattolillo, G. Preparata, F. Scaramuzzi, A. Bulfone, M. Cola and C. Giannetti, The Fleischmann–Pons effect in a novel electrolytic configuration, in *Proceedings of the 8th International Conference on Cold Fusion*, The Italian Physical Society, Vol. 70, 2000, pp. 47–54.
- [2] C. Manduchi, S. Salviato, C. Ciricillo, E. Milli, G. Zannoni, G. Mengoli and M. Fabrizio, Electric-field effects on the neutron emission from Pd deuteride samples, *Nuovo Cimento Soc. Ital. Fis. A* **108A**(10) (1995) 1187–205.
- [3] E. Nairne, Electrical Experiments by Mr. Edward Nairne of London, Mathematical Instrument-Maker, Made with a M... *Phil. Trans. Royal Soc. (London)* **64** (1774) 79–89.
- [4] M. Faraday, Experimental relations of gold (and other materials) to light, *Phil. Trans. Royal Soc. London* **147** (1857) 145–181.
- [5] F. Celani, A. Spallone, P. Marini, V. Di Stefano, M. Nakamura, A. Mancini, S. Pace, P. Tripodi, D. Di Gioacchino, C. Catena, G. D'Agostaro, R. Petraroli, P. Quercia, E. Righi and G. Trenta, High hydrogen loading into thin palladium wires through precipitate of alkaline-earth carbonate on the surface of cathode: evidence of new phases in the Pd–H system and unexpected problems due to bacteria contamination in the heavy water, in *Proceedings of the 8th International Conference on Cold Fusion*, Italian Physical Society, Vol. 70, 2000, pp. 181–190.
- [6] F. Celani, A. Spallone, P. Tripodi, A. Petrocchi, D. Di Gioacchino, M. Boutet, P. Marini, V. Di Stefano, M. Diociaiuti and W. Collis, Reproducible D/Pd ratio > 1 and excess heat correlation by 1-micro s-pulse, high-current electrolysis, *Fusion Technol.* **29**(3) (1996) 398–404.
- [7] P. Tripodi, M.C.H. McKubre, F.L. Tanzella, P.A. Honnor, D. Di Gioacchino, F. Celani and V. Violante, Temperature coefficient of resistivity at compositions approaching PdH, *Phys. Lett. A* **276**(1–4) (2000) 122–126.
- [8] F.S. Celani, A. Spallone, P. Tripodi, A. Petrocchi, D. Di Gioacchino, P. Marini, V. Di Stefano, S. Pace and A. Mancini, Deuterium overloading of palladium wires by means of high power μ s pulsed electrolysis and electromigration: suggestions of a "phase transition" effect, *Phys. Lett. A* **214** (1996) 1–13.
- [9] Y. Arata and Y.-C. Zhang, Definitive difference between [DS-D₂O] and [Bulk-D₂O] cells in "deuterium-reaction", *Proc. Jpn. Acad. Ser. B* **75B**(4) (1999) 71–75.
- [10] D. Gozzi, P.L. Cignini, R. Caputo, M. Tomellini, G. Balducci, G. Gigli, E. Cisbani, S. Frullani and F. Garibaldi et al., Experiments with global detection of cold fusion byproducts, in *Front. Sci. Ser.*, H. Ikegami (Ed.), Universal Academy Press, Tokyo, Vol. 4, 1993, pp. 155–164.
- [11] M. C. H. McKubre, R.C. Rocha-Filho, S. Smedley, F. Tanzella, J. Chao, B. Chexal, T. Passell and J. Santucci, Calorimetry and electrochemistry in the deuterium/palladium system, in *Proceedings of the First Annual Conference on Cold Fusion*, F. Will (Ed.), NCFI, Salt Lake City, 1990, pp. 20–31.
- [12] M. C. H. McKubre, F. Tanzella, P.L. Hagelstein, K. Mullican, M. Trevithick, The need for triggering in cold fusion reactions, in *Condensed Matter Nuclear Science, Proceedings of the International Conference on Cold Fusion*, P.L. Hagelstein and S.R. Chubb (Eds.), World Scientific, Singapore, 2006, pp. 199–212.



Research Article

Bose–Einstein Condensation Nuclear Fusion: Role of Monopole Transition

Yeong E. Kim *

Department of Physics, Purdue University, West Lafayette, IN 47907, USA

Thomas E. Ward

Techsource Inc., 20251 Century Blvd., Suite 440 Germantown, MD 20874, USA

Abstract

Based on a single conventional physical concept of Bose–Einstein condensation of deuterons in metal, theory of Bose–Einstein condensation nuclear fusion (BECNF) has been developed to explain many diverse experimental results. We investigate the role of monopole transition in BECNF theory, assuming a collective monopole vibrational excited nuclear state in ^4He . Using the threshold resonance reaction mechanism, we derive formulae for S -factor, which can be used in BECNF theory to obtain the nuclear reaction rate. We find the reaction rate for this reaction is far greater than other exit reaction channels. The proposed monopole transition mechanism is capable of dissipating fusion energy into vibrational (phonon) energies in metal. Experimental tests of the monopole transition mechanism are proposed.

© 2012 ISCMNS. All rights reserved.

Keywords: Bose–Einstein condensation, Monopole, Nuclear fusion

1. Introduction

Recently, a consistent conventional theory of Bose–Einstein condensation nuclear fusion (BECNF) [1,2] has been developed for explaining the anomalous results observed for deuteron-induced nuclear reactions in metal at ultra low energies [3–6]. The BECNF Theory [1,2] is based on a single conventional physical concept of Bose–Einstein condensation of deuterons in metal. The theory is capable of explaining most of the experimental observations [3–6] and also provides theoretical predictions which can be tested experimentally [2]. In this paper, we give a brief summary of derivation of the BECNF theory and then introduce the collective monopole transition mechanism into the theory. Theoretical derivation of the reaction rate and S -factor for the monopole transition mechanism will be presented in terms of a threshold resonance reaction. The theory is then applied to describe the BECNF processes. We describe theoretical predictions, which can be tested experimentally. Finally, summary and conclusions will be described.

*E-mail: yekim@Purdue.edu

2. Summary of Derivations of BECNF Theory

In developing the BEC theory of deuteron fusion in metal, one basic assumption was made that mobile deuterons in a micro/nano-scale metal particle form a BEC state. The validity of this assumption is to be verified by independent experimental tests suggested in this paper. Because of the above assumption, the theory cannot be applied to deuterons in bulk metals, which do not provide well-defined localized trapping potentials for deuterons.

For applying the concept of the BEC mechanism to deuteron fusion in a micro/nano-scale metal particle, we consider N identical charged Bose nuclei (deuterons) confined in an ion trap (or a metal grain or particle). Some fraction of trapped deuterons are assumed to be mobile as discussed above. The trapping potential is 3-dimensional (nearly-sphere) for nano-scale metal particle, or quasi 2-dimensional (nearly hemi-sphere) for micro-scale metal grains, both having surrounding boundary barriers. The barrier heights or potential depths are expected to be an order of energy (≤ 1 eV) required for removing a deuteron from a metal grain or particle. For simplicity, we assume an isotropic harmonic potential for the ion trap to obtain order of magnitude estimates of fusion reaction rates.

Experimental values of the conventional hot-fusion cross section $\sigma(E)$ for reaction $D(d,n)^3\text{He}$ or $D(d,p)\text{T}$ have been conventionally parameterized as

$$\sigma(E) = \frac{S(E)}{E} \exp(-2\pi\eta) = \frac{S(E)}{E} \exp[-(E_G/E)^{1/2}] \quad (1)$$

with $\eta = Z_1 Z_2 e^2 / \hbar v$. $\exp(-2\pi\eta)$ is known as the “Gamow factor”, and E_G is the “Gamow energy” given by $E_G = (2\pi\alpha Z_D Z_D)^2 M c^2 / 2$ or $E_G^{1/2} \approx 31.39 \text{ (keV)}^{1/2}$ for the reduced mass $M \approx M_D/2$. The value E is measured in keV in the center-of-mass (CM) reference frame. The S -factor, $S(E)$, is extracted from experimentally measured values of the cross section $\sigma(E)$ for $E \geq 4$ keV and is nearly constant; $S(E) \approx 55 \text{ keV-barn}$, for reactions $D(d,n)^3\text{He}$ or $D(d,p)\text{T}$ in the energy range of interest here, $E \leq 100$ keV. The S -factor is known as “astrophysical S -factor” [7].

The N -body Schrödinger equation for the system is given by

$$H\Psi = E\Psi \quad (2)$$

with the Hamiltonian H for the system given by

$$H = \frac{\hbar^2}{2m} \sum_{i=1}^N \Delta_i + \frac{1}{2} m \omega^2 \sum_{i=1}^N r_i^2 + \sum_{i < j} \frac{e^2}{|\mathbf{r}_i - \mathbf{r}_j|}, \quad (3)$$

where m is the rest mass of the nucleus. Only two-body interactions (Coulomb and nuclear forces) are considered since we expect that three-body interactions are expected to be much weaker than the two-body interactions.

Electron degrees of freedom are not explicitly included, assuming that electrons and host metal atoms provide a host trapping potential. In presence of electrons, the coulomb interaction between two deuterons can be replaced by a screened coulomb potential in Eq. (3). Hence, Eq. (3) without the electron screening effect represents the strongest case of the reaction rate suppression due to the coulomb repulsion.

The approximate ground-state solution of Eq. (2) with H given by Eq. (3) is obtained using the equivalent linear two-body method [8,9]. The use of an alternative method based on the mean-field theory for bosons yields the same result (see Appendix in [10]). Based on the optical theorem formulation of low energy nuclear reactions [11], the ground-state solution is used to derive the approximate theoretical formula for the deuteron–deuteron fusion rate in an ion trap (micro/nano-scale metal grain or particle). The detailed derivations are given elsewhere including a short-range nuclear strong interaction used [10,12].

Our final theoretical formula for the nuclear fusion rate R_{trap} for a single trap containing N deuterons is given by [1]

$$R_{\text{trap}} = 4(3/4\pi)^{3/2} \Omega S B \frac{N^2}{D_{\text{trap}}^3} \propto \Omega \frac{N^2}{D_{\text{trap}}^3}, \quad (4)$$

where N is the average number of Bose nuclei in a trap/cluster, D_{trap} is the average diameter of the trap, $B = 2r_B/(\pi\hbar)$, $r_B = \hbar^2/(2\mu e^2)$, and S is the S -factor for the nuclear fusion reaction between two deuterons, as defined by Eq. (1). $B = 1.4 \times 10^{-18} \text{ cm}^3/\text{s}$ with S in units of keV-barn in Eq. (3). $SB = 0.77 \times 10^{-16} \text{ cm}^3/\text{s}$ for $S = 55 \text{ keV-barn}$. Unknown parameters are the probability of the BEC ground state occupation, Ω , and the S -factor, S , for each exit reaction channel. We note that $\Omega \leq 1$.

The total fusion rate R_t is given by

$$R_t = N_{\text{trap}} R_{\text{trap}} = \frac{N_D}{N} R_{\text{trap}} \propto \Omega \frac{N}{D_{\text{trap}}^3}, \quad (5)$$

where N_D is the total number of deuterons and $N_{\text{trap}} = N_D/N$ is the total number of traps. Equation (5) shows that the total fusion rates, R_t , are very large if $\Omega \approx 1$.

The total reaction rate R_t for each exit reaction channel can be calculated for given values of Ω and S , using Eqs. (4) and (5). The S -factor can be either inferred from experimental data or can be calculated theoretically using Eq. (12) shown later. The branching ratio between different two-exit reaction channels can be obtained as the ratio between two S -factors.

Equations (4) and (5) provide an important result that nuclear fusion rates R_{trap} and R_t do not depend on the Gamow factor in contrast to the conventional theory for nuclear fusion in free space where it must be included. This could provide explanations for overcoming the Coulomb barrier and for the claimed anomalous effects for low-energy nuclear reactions in metals. This is consistent with the conjecture noted by Dirac [13] and used by Bogoliubov [14] that boson creation and annihilation operators can be treated simply as numbers when the ground state occupation number is large as in the case of a Bose–Einstein condensate. This implies that for large N each charged boson behaves as an independent particle in a common average background potential and the Coulomb interaction between two charged bosons is suppressed. This provides an explanation for the Gamow factor cancellation. There is a simple classical analogy of the Coulomb field suppression: for a uniform charge distribution in a sphere, the electric field is a maximum at the surface of the sphere and decreases to zero at the center of the sphere.

3. Monopole Transition Mechanism

For the monopole transition mechanism, we assume a threshold resonance state, ${}^4\text{He}^*(0^+, \text{TR}, 23.85 \text{ MeV})$, which is a nuclear vibrational “phonon” state with a monopole vibration (density fluctuation). BEC collective nuclear phonon states exist as excited states of many nuclei. ${}^4\text{He}^*(0^+, \text{TR}, 23.85 \text{ MeV})$ state is assumed to decay with a decay width of $\Gamma \sim \hbar\omega \sim 6 \text{ eV}$ corresponding to free electron plasma frequency of $\omega \sim 1 \times 10^{16}/\text{s}$.

As shown in Fig. 1, $\text{D} + \text{D}$ in the BEC state proceeds with the threshold resonance reaction {1} to form ${}^4\text{He}^*(0^+, \text{TR}, 23.85 \text{ MeV})$ state.

$$\{1\} (\text{D} + \text{D}) \text{ in BEC} \rightarrow {}^4\text{He}^*(0^+, \text{TR}, 23.85 \text{ MeV}), Q = 0.$$

Since $Q = 0$, the momentum is conserved for reaction {1}. The ${}^4\text{He}^*(0^+, \text{TR}, 23.85 \text{ MeV})$ can now decay to the ${}^4\text{He}$ ground-state by two exit reaction channels, {1a} and {1b}:

$$\begin{aligned} \{1a\} {}^4\text{He}^*(0^+, \text{TR}, 23.85 \text{ MeV}) &\rightarrow {}^4\text{He}(0^+, \text{g.s.}, 0.0 \text{ MeV}) + \text{phonons}, Q = 23.85 \text{ MeV} \\ \{1b\} {}^4\text{He}^*(0^+, \text{TR}, 23.85 \text{ MeV}) &\rightarrow {}^4\text{He}(0^+, \text{g.s.}, 0.0 \text{ MeV}) + e^+e^- \text{ pair} \end{aligned}$$

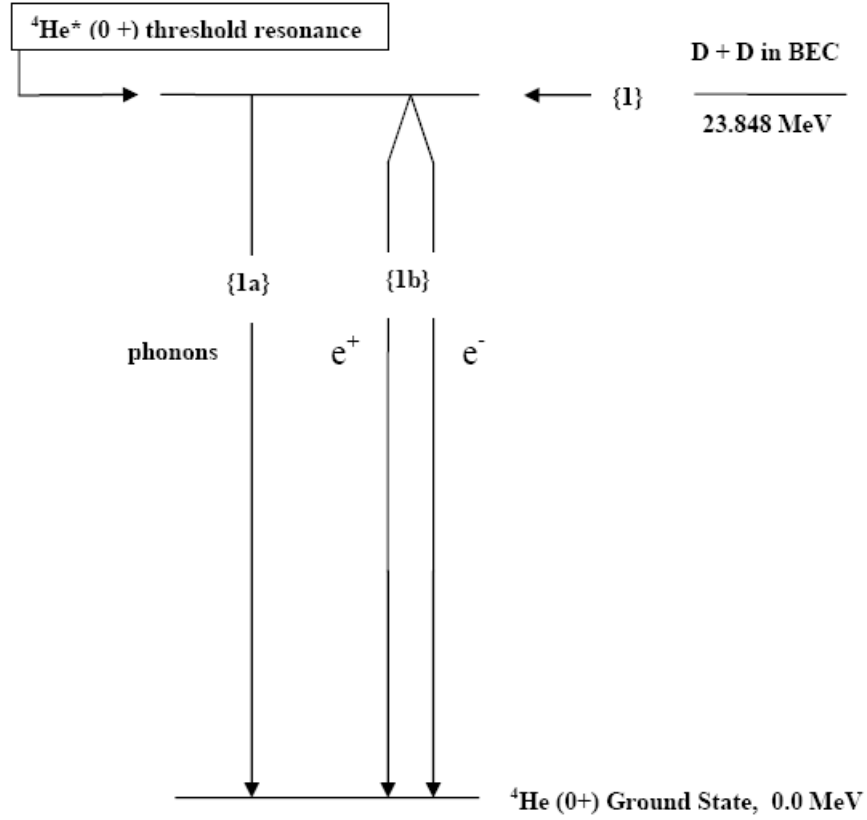


Figure 1. Entrance and exit reaction channels for the threshold resonance reaction in Bose–Einstein condensation nuclear fusion for deuterons in metal.

For the exit reaction channel {1a}, collective vibrations of electrons (and deuterons) in the deuteron BEC state leads to the free electron plasma oscillation in metal with $\omega \sim 1 \times 10^{16}/\text{s}$. This in turn leads to the metal lattice vibrations (lattice phonons) producing heat in metal.

3.1. Determination of S -factor and reaction rates

The $S(E)$ factor for the resonance reaction can be written as [15,16]

$$S(E) = E \exp(2\pi\eta) \pi \lambda^2 w \frac{\Gamma_{i,\ell}(E) \Gamma_f}{(E - E_R)^2 + (\Gamma/2)^2}, \quad (6)$$

with

$$\Gamma_{i,\ell}(E) = \frac{2\hbar}{R_n} \left(\frac{2E}{\mu} \right)^{1/2} P_\ell(E, R) \theta_\ell^2, \quad (7)$$

where R_n is the nuclear radius, μ is the reduced mass, and w is a statistical factor.

The penetration factor $P_\ell(E, R_n)$ in Eq. (7) is given by

$$P_\ell(E, R_n) = \frac{1}{F_\ell^2(E, R_n) + G_\ell^2(E, R_n)}, \quad (8)$$

where F_ℓ and G_ℓ are regular and irregular Coulomb wave functions [17].

For the s-wave ($\ell = 0$) formation of the compound nucleus at energies E near zero, we have $F_0(E, R_n) \approx 0$ and

$$G_0(E, R_n) \approx 2e^{\pi\eta} \left(\frac{\rho}{\pi}\right)^{1/2} K_1(x), \quad (9)$$

where $x = 2\sqrt{2\eta\rho}$, $\rho = \sqrt{\mu E} R_n / \hbar$ and $K_1(x)$ is the modified Bessel function of order one [18]. The argument x is given by $x = (8Z_1 Z_2 e^2 R_n \mu / \hbar^2)^{1/2} = 0.525(\mu Z_1 Z_2 R_n)^{1/2}$, and μ is the reduced mass in units of atomic mass unit (931.494 MeV).

The penetration factor for $\ell = 0$, $P_0(E, R_n)$, is then given by

$$P_0(E, R_n) \approx \frac{1}{G_0^2(E, R_n)} = \frac{\pi}{4\rho K_1^2(x)} e^{-2\pi\eta} \quad (10)$$

and the compound nucleus formation width, $\Gamma_{i,0}(E)$, is

$$\Gamma_{i,0}(E) = \frac{\pi \hbar^2}{2\mu R_n^2} \frac{1}{K_1^2(x)} \theta_0^2 e^{-2\pi\eta}. \quad (11)$$

From Eqs. (6)–(11), we obtain the $S(E)$ factor near zero energy for the $\ell = 0$ state as

$$S(E) = \frac{\pi^2 \hbar^4}{4\mu^2 R_n^2} \frac{1}{K_1^2(x)} w \theta_0^2 F_{BW}(E), \quad (12)$$

with

$$F_{BW}(E) = \frac{\Gamma_f}{(E - E_R)^2 + (\Gamma/2)^2}. \quad (13)$$

Equations (12) and (13) show that the $S(E)$ factor has a finite value at $E = 0$ and drops off rapidly with increasing energy E . θ_i^2 is the reduced width of a nuclear state [19], representing the probability of finding the excited state in the configuration i , and the sum of θ_i^2 over i is normalized to 1. θ_i is the overlap integral between the initial and final nuclear states, $\langle \psi_{\text{final}} | \psi_{\text{initial}} \rangle$. The dimensionless number θ_i^2 is generally determined experimentally and contains the nuclear structure information.

Equations (12) and (13) were used extensively in analysis of (p, γ) reactions involved in nucleosynthesis processes in astrophysics [7,16,20–22].

Once $S(E)$ is calculated using Eqs. (12) and (13), the reaction rates can be calculated from Eqs. (4) and (5), using the calculated values of $S(E)$.

For the case of $0^+ \rightarrow 0^+$ transition {1a}, we obtain $S\{1a\} \approx 0.45 \times 10^8 \theta\{1\}^2$ keV-barn calculated from Eqs. (12) and (13) using $\Gamma \approx \Gamma_f \approx 6$ eV and other appropriate inputs.

For the decay channel {1b} ($0^+ \rightarrow 0^+$ transition), γ -ray transition is forbidden. However, the transition can proceed via the internal e^+e^- pair conversion, {1b}, in addition to {1a}. The transition rate for the internal electron pair conversion is given by

$$\omega = \frac{1}{135\pi} \left(\frac{e^2}{\hbar c}\right)^2 \frac{\gamma^5}{\hbar^5 c^4} R_n^4, \quad R_n^2 = \left| \langle \psi_{\text{exc}} | \sum_i r_i^2 \psi_{\text{g.s.}} \rangle \right| \approx R_n^2 \phi, \quad (14)$$

where γ is the transition energy, R_n is the nuclear radius, and $\phi = \langle \psi_{\text{exc}} | \psi_{\text{g.s.}} \rangle$ which is the overlap integral between the initial and final nuclear states. Equation (14) was derived by Oppenheimer and Schwinger [23] in 1939 for their theoretical investigation of $0^+ \rightarrow 0^+$ transition in ^{16}O . The rate for the internal electron conversion is much smaller by many order of magnitude.

For our case of $0^+ \rightarrow 0^+$ transition {1b}, we obtain $\omega \approx 1.75 \times 10^{13}/\text{s}$, and $\Gamma_f = \hbar\omega \approx 1.15 \times 10^{-2}$ eV, using appropriate inputs in Eq. (14). Using $\Gamma_f = \Gamma\{1b\} = 1.15 \times 10^{-2}$ eV in Eq. (13), we find that the S -factor for decay channel {1b} calculated from Eq. (12) is $S\{1b\} \approx 0.86 \times 10^5 \theta\{1\}^2 \phi\{1b\}^2$ keV-barn for $E \approx 0$.

Using $S\{1a\} \approx 0.45 \times 10^8 \theta\{1\}^2$ keV-barn, we obtain a branching ratio, $R\{1b\}/R\{1a\} = S\{1b\}/S\{1a\} \approx 2 \times 10^{-3} \phi\{1b\}^2$. Experiments are needed for testing this predicted branching ratio.

4. Experimental Tests of Assumptions and Predictions

For the monopole transition mechanism, described in this paper, we assume existence of an excited vibrational “electric monopole photon” nuclear state, $^4\text{He}^*(0^+, \text{TR}, 23.85 \text{ MeV})$, at 23.85 MeV above the ^4He ground state with a resonance width of $\Gamma \approx 6$ eV. We note that $^4\text{He}^*(0^+, \text{TR}, 23.85 \text{ MeV})$ state cannot be observed by deuteron beam experiments. It could be observed from inelastic electron scattering, $^4\text{He}(e, e')^4\text{He}^*$.

Nuclear phonon states exist as excited states in many other nuclei, and are often observed when the ground states of nuclei are excited by high-energy γ -rays. However, the electric monopole vibrational state, $^4\text{He}^*(0^+, \text{TR}, 23.85 \text{ MeV})$, cannot be reached by γ -ray excitation. Therefore, we propose to carry out inelastic electron scattering, $^4\text{He}(e, e')^4\text{He}^*$ to measure both the width of the $^4\text{He}^*$ state and its decay mode, e^+e^- pair production {1b}.

For experimental tests of theoretical predictions, we propose to measure the predicted branching ratio, $R\{1b\}/R\{1a\} = S\{1b\}/S\{1a\} \approx 2 \times 10^{-3} \phi\{1b\}^2$, by detecting both ^4He production rate and the e^+e^- production rate. For $\phi\{1b\}^2 \approx 10^{-2}$, we expect $R\{1b\}/R\{1a\} \approx 2 \times 10^{-5}$.

5. Summary and Conclusion

Based on the assumption that a monopole vibrational “phonon” nuclear state, with a vibrational frequency of the metal free electron plasma, exists as an excited state of ^4He ground state, we have calculated the reaction rates for the Bose–Einstein condensation nuclear fusion (BECNF) processes for $\text{D} + \text{D}$ reaction in metal. There are two exit reaction channels, {1a} and {1b}, both involving $0^+ \rightarrow 0^+$ monopole transitions. From calculated reaction rates, we obtain the branching ratio of $R\{1b\}/R\{1a\} \approx 2 \times 10^{-3} \phi\{1b\}^2$ where $\phi_2 = |\langle \psi_{\text{final}} | \psi_{\text{initial}} \rangle|^2$ is the probability of overlap between initial ($^4\text{He}^*$) and final (^4He) nuclear states.

We propose experimental tests of both (1) the assumption of $^4\text{He}^*$ monopole phonon nuclear state and (2) the predicted branching ratio. For (1), inelastic electron scattering from ^4He is proposed, while for (2) we propose to measure the reaction products and rates of the exit reaction channels {1a} and {1b}: ^4He for {1a} and e^+e^- pair production for {1b}.

References

- [1] Y.E. Kim, Theory of Bose–Einstein condensation mechanism for deuteron-induced nuclear reactions in micro/nano-scale metal grains and particles, *Naturwissenschaften* **96** (2009) 803 and references therein.
- [2] Y.E. Kim, Theoretical interpretation of anomalous tritium and neutron productions during Pd/D co-deposition experiments, *Euro. Phys. J. Appl. Phys.* **52** (2010) 31101.
- [3] M. Fleischman and S. Pons, Electrochemically induced nuclear fusion of deuterium, *J. Electroanal. Chem.* **261** (1989) 301; Errata, *J. Electroanal. Chem.* **263** (1989) 187.
- [4] P.L. Hagelstein et al., New physical effects in metal deuterides, *Proc. ICCF-11*, Marseille, France, Condensed Matter Nuclear Science, World Scientific, Singapore, 2006, pp. 23–59, and references therein.

- [5] Y. Arata and Y.C. Zhang, *J. High Temp. Soc.* **34**(2) (2008) 85.
- [6] A. Kitamura et al., *Phys. Lett. A* **373** (2009) 3109, and references therein.
- [7] W.A. Fowler, G.R. Caughlan and B.A. Zimmermann, Thermonuclear reactions rates, *Annu. Rev. Astron. Astrophys.* **5** (1967) 525; see also Thermonuclear reaction rates II, *Annu. Rev. Astron. Astrophys.* **13** (1975) 69.
- [8] Y.E. Kim and A.L. Zubarev, Ground state of charged bosons confined in a harmonic trap, *Phys. Rev. A* **64** (2001) 013603-1.
- [9] Y.E. Kim and A.L. Zubarev, Equivalent linear two-body method for Bose–Einstein condensates in time-dependent harmonic traps, *Phys. Rev. A* **66** (2002) 053602-1.
- [10] Y.E. Kim and A.L. Zubarev, Ultra low-energy nuclear fusion of Bose nuclei in nano-scale ion traps, *Italian Phy. Soc. Proc.* **70** (2000) 375.
- [11] Y.E. Kim, Y.J. Kim, A.L. Zubarev and J.H. Yoon, Optical theorem formulation of low-energy nuclear reactions, *Phys. Rev. C* **55** (1997) 801.
- [12] Y.E. Kim and A.L. Zubarev, Nuclear fusion for Bose nuclei confined in ion traps, *Fusion Technol.* **37** (2000) 151.
- [13] P.A.M. Dirac, *The Principles of Quantum Mechanics*, Second edition, Clarendon Press, Oxford Chapter XI, Section 63, 1935, pp. 235.
- [14] N. Bogoliubov, On the theory of superfluidity, *J. Phys.* **11** (1966) 23–29.
- [15] J.M. Blatt and V.F. Weisskopf, *Theoretical Nuclear Physics*, Wiley, 1952, 8th Printing, 1972.
- [16] C.E. Rolfs and W.S. Rodney, *Cauldrons in the Cosmos: Nuclear Astrophysics*, University of Chicago Press, 1988, chapter 4.
- [17] Y.E. Kim and A.L. Zubarev, Coulomb barrier transmission resonance for astrophysical problem, *Modern Phys. Lett.* **B7** (1993) 1627; Improved Coulomb barrier transmission coefficient for nuclear fusion cross-sections, *Fusion Technol.* **25** (1994) 475.
- [18] M. Abramowitz and I.A. Stegun (Eds.), *Handbook of Mathematical Functions with Formulas, Graphs, and Mathematical Tables*, National Bureau of Standards Applied Mathematics Series 55, August 1966.
- [19] R.G. Thomas, On the determination of reduced widths from the one-level dispersion formula, *Phys. Rev.* **81** (1951) 148; An analysis of energy levels of the mirror nuclei, C^{13} and N^{13} , *Phys. Rev.* **88** (1952) 1109.
- [20] C. Rolfs and A.E. Litherland, *Nuclear Spectroscopy and Reactions*, Part C, J. Cerny (Ed.), Academic Press, New York, 1974, p. 143.
- [21] C. Rolfs and H. Winkler, The 2425 keV state in ^{21}Na as a subthreshold resonance in $^{20}Ne (\rho, \gamma)^{21}Na^*$, *Phys. Lett.* **52B** (1974) 317.
- [22] C. Rolfs, W.S. Rodney, M.H. Shapiro and H. Winkler, Hydrogen burning of ^{20}Ne and ^{21}Ne in stars, *Nucl. Phys. A* **241** (1975) 460.
- [23] J.R. Oppenheimer and J.S. Schwinger, *Phys. Rev.* **56** (1933) 1066.



Research Article

Nuclear Particles Generated by Electrolysis – a Review

R.A. Oriani*

University of Minnesota, Minneapolis, MI 55455, USA

Abstract

CR39 plastic detectors for nuclear particles are employed to demonstrate that a nuclear reaction can accompany electrolysis, an electrochemical process. Detectors placed within or above the electrolyte display statistically greater numbers of nuclear pits than do detectors used as controls. Placing the cathodes in contact with Mylar-covered detectors is the basis for a technique that reproducibly generates evidence for a nuclear reaction during electrolysis. Nuclear pits are produced in plastic detectors exposed to the oxygen evolved at the anode, as well as to the hydrogen evolved at the cathode. Nuclear damage trails are found that are initiated within the 0.83 mm thickness of the plastic detectors. These phenomena clearly show that a nuclear reaction of as yet unknown nature can be generated during electrolysis.

© 2012 ISCMNS. All rights reserved.

Keywords: CR39 detectors, Damage trails, Electrolysis, Etch pits, Nuclear particles, Nuclear reactions

1. Introduction

In 1989 Fleischmann and Pons [1] presented calorimetric evidence that during electrolysis with lithium sulfate dissolved in heavy water and palladium as the cathode more thermal energy is produced than the electrical energy provided. Because the magnitude of the excess energy was much larger than could be accounted for by any conceivable chemical reaction the excess energy was attributed to an accompanying nuclear reaction. The calorimetric finding has been verified many times [2,3] but the claim that a nuclear reaction is the responsible agent remains repugnant to the majority of the nuclear physics community. It would be useful, therefore, to apply a technique that is more direct, simpler, and more transparent than calorimetry to confirm that a nuclear reaction can accompany electrolysis.

This paper is a review of the author's work since 2000 with plastic detectors applied to electrolysis. Energetic nuclear particles and very energetic neutrons can be detected and recorded by a high-polymeric material designated as CR39 that has been used by nuclear physicists [4] for many years. Upon entering the plastic, a nuclear particle produces a trail of disrupted chemical bonds which are more easily chemically attacked than undamaged material. The pit that results from etching the material in hot, concentrated alkali solution is unambiguous evidence that a nuclear reaction has taken place because the energies required to break the chemical bonds are much larger than can be provided by any chemical reaction.

*E-mail: orian001@umn.edu

2. Experimental Procedure

The CR39 plastic used in this research was purchased with both sides covered by adhering plastic films designed to prevent the formation of nuclear tracks by air-borne radon. To prepare the CR39 for use in the experiments the desired chip sizes are obtained by scoring the plastic on one side with a sharp blade, and then cracking the plastic. Very small holes are drilled through the plastic-protected chips to enable their suspension within the electrolysis cell and also subsequently within the etching solution. If necessary, identifying characters are scratched on the chips through the protective film, which is removed just before mounting in the electrolysis cell.

The experiments consist in determining the number density of tracks that are produced in the electrolysis-exposed chips and comparing with the number densities produced in the chips used as controls. For this purpose, the experimental (active) and the control chips are etched together in stirred 6.5 N KOH or NaOH solution at 60–80°C for 6–24 h depending on the etchant temperature. After rinsing off the alkaline solution and drying, the etched chips are protected against radon either by covering with adhering Scotch tape or by tight wrapping in aluminum foil until examination under the microscope. The chips are examined immediately after cleaning, done by scrubbing with a small, soft brush in a detergent solution, rinsing under tap water, and drying in warm air. This procedure was found superior to ultrasonic cleaning.

To aid in the identification of nuclear-caused pits, experience was gained by examining etch pits caused by exposure to radiation from pitchblende and to ^{241}Am . Defects produced during the manufacture of the CR39 plastic can make it difficult to discriminate between nuclear pits and artifacts. The polymerization process can leave poorly polymerized regions. Such regions will etch more rapidly than does well polymerized material and pits will result. However, these pits are usually small, circular, and shallow, and can be distinguished from nuclear pits by the much darker appearance of the latter when examined under a microscope employing illumination from above. Features of dubious identity are not counted as nuclear pits.

Scratches and other mechanical insults to the detector chips can also cause etch pits. This problem was examined by a series of experiments in which various mechanical forces were applied to the chips, followed by etching and microscopic examination. Light scratching produces linear arrays of pits, usually of uniform diameter. For this reason, pits in linear arrays are disregarded. Etch pits are not caused by high pressure against the chip surface by the points of metal tweezers or by the handle of an Exacta knife. However, pressure with the point of an Exacta blade produces a very dark etch pit. Rubbing with a plastic rod has no effect, but rubbing with a metal spatula leaves a faint trace after etching, and rubbing with the points of tweezers produces an etchable trail. Grasping a detector chip with metal tweezers exerting a considerable force does not produce any effects.

The electrolysis apparatus consisted of a cylindrical glass tube of about 15 mm internal diameter whose lower end terminates in a flanged joint between whose O-rings can be clamped a cathode plate or a CR39 detector chip. For all of the experiments here reported, the electrolyte is a solution of lithium sulfate in either D_2O or distilled H_2O , the anode is a spiral of platinum wire, and the cathode is made of palladium, nickel, or platinum. The detector chips are examined at 100 \times and 500 \times magnification, and the etch pits are photographed in some of the experiments and are counted for all of the experiments. The details of cell design and operation differ between the types of experiments; these are presented in the sections below.

3. Electrolyses with Immersed Detectors

The electrolysis cell employs a platinum wire the upper end of which is spot-welded to a tungsten wire, and the lower end is fashioned into a spiral to serve as the anode. The palladium cathodes are 25 \times 25 mm sheets of 1 mm thickness obtained from Dr. E. Storms, Los Alamos Laboratory (retired). They are sanded and washed before being clamped between the Viton O-rings of the glass flanged joint. The nickel cathodes are of 99.9% purity and are of about 0.2 mm thickness. The electrolytes are a solution of 0.025 g of Li_2SO_4 per ml of D_2O or distilled H_2O . The electrolyses are

Table 1. Results of the Mann–Whitney analysis applied to the data for the immersed detectors

System	<i>P</i> -value
Pd/D ₂ O	2.5×10^{-5}
Pd/H ₂ O	1.2×10^{-6}
Ni/D ₂ O	5.5×10^{-4}

Note: *P* is the probability that the data for the active and for the control chips belong to the same population.

carried out with current densities between 0.1 and 0.37 A/cm² for two or three days with the evolved gases evolved into the environment. Chips of detector plastic are suspended within the electrolyte by platinum wires both above and below the anode spiral. To serve as controls one or two detector chips are immersed in electrolyte solution contained in bottles open to the air during the duration of the electrolysis, and are etched along with the active chips. These controls account for the exposure of all the detector chips to environmental radon during handling, etching, washing, and microscopic examination. Because bubbling within the electrolyte might increase the number of nuclear tracks caused by radon, additional non-electrolysis tests were performed in which D₂ gas bubbles, produced by forcing the gas through a fine fritted glass tube inserted in the solution, impinged upon detector chips suspended in the solution. The impingement of bubbles was found not to increase the number density of nuclear tracks over the number density found in chips kept in quiescent solution. Prior to use in the experiments, the chips are etched and various areas of the chips are photographed at 100× magnification. After their use the chips are again etched and the same areas are again photographed and the etch pits are counted. The difference between the numbers of etch pits before and after use are divided by the areas photographed to yield the number densities of nuclear pits produced by electrolysis or, in the case of the controls, by immersion in the bottled electrolyte solution.

Experiments of this type were carried out with Pd cathodes and D₂O/Li₂SO₄ as the electrolyte [5], with Pd cathodes and H₂O/Li₂SO₄ as the electrolyte [6,7], and with Ni cathodes and D₂O/Li₂SO₄ as the electrolyte [6,7]. In all instances there is some overlap between the number density of nuclear tracks produced by electrolysis and those produced in the controls. Some electrolyses produced as few tracks as did some of the controls. Hence, a careful statistical analysis must be applied to the data. A conservative analysis is that of Mann and Whitney [8]. It has the considerable merit of not being dependent on the data having a Gaussian distribution. The results of this analysis are presented in Table 1, in which *P* is the probability that the data for the active chips and those for the controls constitute a single population. The analysis shows that the data for the active chips are a distinct and significantly different population from that of the control data. One can conclude with a very high confidence level that the excess track densities in the active chips are caused by a physical agent associated with electrolysis. The agent can not be nuclear particles originating at the electrode because the distance through the solution covering the electrode is much larger than the mean free path of charged particles through the solution. It must be concluded that the nuclear particles are generated close to the surfaces of the detector chips immersed in the solution.

4. Detector Chips above the Electrolyte

The electrolysis cell was modified to provide for detector chips suspended in the vapor above the level of the electrolyte. To mitigate the accumulation of liquid water on the chips, the vapor space of the cell is surrounded by a heating coil to maintain a temperature of about 60°C, and a closely fitting nickel disc is placed between the surface of the electrolyte and the chips hanging on hooks. For controls, detector chips are suspended above electrolyte solution in closed bottles, without electrolysis. In this instance investigation of the effect of bubbling within the solution upon the control chips was deemed not necessary because the nickel disc interposed between the solution surface and the suspended chips in

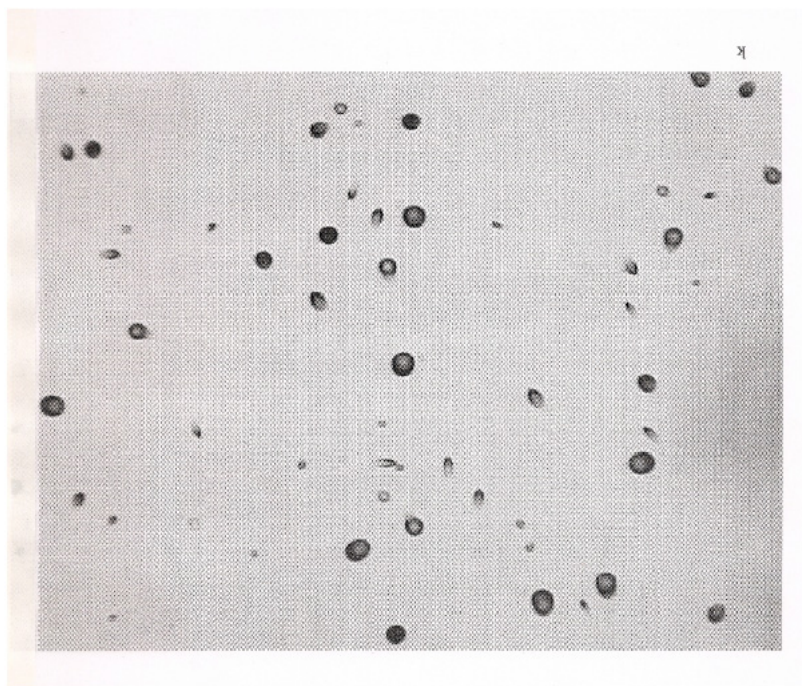


Figure 1. Nuclear pits produced on a CR39 chip suspended during electrolysis in the vapor above the solution of Li_2SO_4 in D_2O .

the electrolysis cell effectively prevented any effects from bubbling during electrolysis.

With either Pd or Ni as the cathode material and Li_2SO_4 in distilled H_2O as the electrolyte, most electrolyses produced number densities of nuclear pits exceeding the densities on the control chips [9]. The result of the Mann–Whitney test applied to the active and the control chips is $P = 3 \times 10^{-10}$, so that there is only a vanishingly small probability that the two sets of data constitute a single population. One may therefore conclude that electrolysis can generate nuclear particles by some kind of nuclear reaction that takes place in the vapor phase.

In some experiments very large numbers of nuclear pits were recorded. An example of what can be called showers is shown in Fig. 1. In one particularly interesting experiment, detector chips that during electrolysis had been suspended fairly close together in the vapor developed enormous numbers of nuclear tracks on the chip surfaces that had faced each other, and smaller numbers on their opposite sides. The etch pits on one side of these chips were laboriously counted to a total of about 33,000. From the shapes of the pits, and the angles and senses of the impingements of the responsible nuclear particles, the location of the point of origin of the nuclear particles was deduced to have been at about 2 mm from the chip surface in the vapor between the two chips.

5. Detectors Proximate to the Cathodes

It has been shown that detector chips immersed in, or suspended above, the electrolyte during electrolysis frequently develop many more nuclear tracks than do the control chips. However, not every experiment yields such pit densities. Hence it would be highly desirable to devise an experimental technique that yields a nuclear signature every time that the experiment is performed. Placing the detector chip very close to the cathode is the strategy adopted to try to achieve

Table 2. Summary of consecutive electrolysis experiments.

Exp. No.	Cell	Current (mA)	Duration (h)	Tracks/cm ²	
				Front	Rear
1 ^a	S	0.2–25	168	284	150
2 ^a	S	0.1–45	120	156	160
3 ^b	S	12–100	102	—	—
4	S	70–143	67	352	16
5	S	30–75	96	393	498
6	S	50	97	76	74
7	S	5–50	96.5	71	96
8	S	10–100	94	80	70
9	S	300	65	D	D ^c
10	B	10, 25	98	98	40 ^c
11	S	12, 28	97	229	48 ^c
12	S	20	95	38 ^c	167
13	B	27	95	193 ^c	298
14	S	20	94	11	81
15	B	19	94	195	49
16	S	40	94	36 ^c	9 ^c , 103 ^h
17	B	39	94	127	9 ^{c,h} , 32 ^h
18	S	60	93	28	102
19	B	60	93	47	35
20	S	80	117	72	41
21	B	80	117	60	132
22	S	100	93	426	207
23	B	101	93	62	51
24	S	50	96	102	38
25	B	50	96	26	344

^aThe electrolyte in these two experiments was LiCl plus PdCl₂ in D₂O with Ag as cathode material.

All the other experiments used Li₂SO₄ in H₂O with Ni as cathode.

^bThe detector chip of Exp.3 was lost before a careful count of the clearly large number of tracks could be made.

^cThe chip area counted had been covered during electrolysis by the manufacturer-supplied blue plastic film.

Track counting was done over the chip area subtended by the O-ring, 3.5 cm², except for items marked h, for which counting was over half of the 3.5 cm² area.

^dSignifies that the number of tracks was so large that counting was impractical.

replicability. However, direct contact of the cathode with the detector runs the risk of chemical attack of the plastic by the hydroxyl ions produced by the reduction of water at the cathode. To preclude chemical attack, Mylar foil of 6 μ m can be interposed between the electrolyte and the detector chip. Preliminary experiments were done to make sure that radiation from pitchblende can traverse the Mylar film. In the configuration adopted, a CR39 plate overlain by Mylar film is clamped between the O-rings of the glass ball joint and the lower end of the cathode rests upon the Mylar. The electrolyses usually employed a platinum anode and an electrolyte of lithium sulfate in distilled ordinary water. The electrolyses are followed by etching the active and the control chips and then counting the nuclear pits. For the actives the counting is restricted to the area circumscribed by the O-rings to avoid chip areas that might have been affected by radon during the electrolyses. Two different cells of identical design were employed for the 25 consecutive electrolyses, each of which lasted from two to four days.

The results of these experiments are presented in Table 2. The counts of nuclear tracks per unit area, either on the Mylar-covered surface (the front surface) or on the opposite surface, or on both surfaces, are always considerably

Table 3. Results of control experiments (Tracks/cm²)

CR39 configuration	First CR39 sheet			Second CR39 sheet		
	<i>N</i>	Mean value	σ	<i>N</i>	Mean value	σ
Wrapped in Mylar	16	26.4	12.1	13	13.6	6.8
With new O-rings				10	16.2	6.0
In stock solution				14	5.9	2.7
In new cell				6	16.5	5.2

Notes: *N* is the number of tests. σ is the standard deviation

greater than the counts on the control chips. The control experiments were of four kinds, each lasting two to four days. Some chips were wrapped in Mylar film, some immersed in electrolyte solution in which the working electrolyte had been stored, other chips were pressed against as-received O-rings and wrapped in aluminum foil, and other chips were mounted in a newly constructed cell fitted with unused electrodes, electrolyte, Mylar film and stoppers but without electrolysis. The results of the four kinds of controls using chips cut from two different CR39 sheets are presented in Table 3. A comparison of the active chips with the controls leads to the conclusion that a nuclear reaction of an unknown kind is consistently generated in the course of electrolysis. The many instances of nuclear tracks on the rear surfaces of the detector plates is particularly significant because it is strong evidence that ordinary radionuclides contaminating the electrolyte can not have been responsible for the observed tracks. This is because charged particles of 15 MeV or less can not traverse the plastic of 0.83 mm thickness.

It is worth remarking that the nuclear pits often appear in two distribution modes. One is a random scatter over the surface of the detector chip. The other mode is that of a cluster of nuclear pits surrounded by areas relatively devoid of pits. The clusters themselves are of two kinds: one in which the pits are randomly distributed as to position and shape, and the other in which the elliptical or conical axes of the pits are radially distributed. Figure 2 shows an example of the latter kind of cluster that indicates that the nuclear particles that produced the cluster originated at a common point. Clusters of two to five tracks diverging from one point also sometimes appear. These track patterns should prove helpful in the elucidation of the phenomena here described.

6. Internal Tracks

The finding of nuclear tracks on the rear surfaces of detector chips held between the O-rings of the electrolysis cell led to investigating whether or not nuclear tracks can be initiated totally within the thickness of the plastic. This question was addressed by the simple technique of repeated etching [10]. The first etching after electrolysis reveals the nuclear tracks generated by nuclear particles that entered through the original surface of the plastic. If a second etching removes a thickness of the plastic greater than the mean free paths of the nuclear particles and many new tracks are thereby revealed, more than can be accounted by radiation from radon in the air, then one can conclude that the majority of the second set of tracks was initiated within the original thickness of the detector. The effect of radon can be evaluated by conducting suitable controls, namely, counting the pits after the first and then after the second etching of chips never exposed to electrolysis.

Table 4 collects the results of the re-etching of detector chips that had been covered with Mylar and that had been clamped between O-rings during electrolysis. The increments in number densities of tracks after the second etch are to be compared with the results from the controls: an average of 5.6 new tracks per cm² after the second etch, ranging between 0 and 21 per cm²; this reflects only the effect of air-borne radon. Thus, the electrolysis chips contain damage trails that begin below the depth in the plastic reached by the first etch after electrolysis. This is about 30 μ m. These

nuclear pits could not have been the result of contaminating radionuclides external to the chip. The pits that appear only after the second etching of the electrolysis-exposed chips exhibit distributions of size and shape different from those that appear after the first etch.

7. Detectors in the Anode Compartment

The conventional thinking in the field of low energy nuclear reactions is that the reaction is produced at the cathode where deuterium from the electrolysis of heavy water dissolves at very high concentration in the palladium cathode. Of importance in the elucidation of the mechanism of the nuclear reaction that can accompany electrolysis would be the establishment of whether or not the cathodic reaction is essential. This question can be examined by placing CR39 detectors in the anode compartment of an electrolysis cell constructed in the form of a U in which platinum spirals in each leg of the U serve as the electrodes. The electrolyte of Li_2SO_4 in distilled H_2O is contained in the lower portions of the U-tube, the liquid extending sufficiently high into each leg so that the gases produced at the electrodes can not mix with each other. Detector chips are suspended above the liquid level in the anode compartment where they are maintained at about 60°C by an external Nichrome wire heater. Prior to electrolysis the detector chips are etched and examined for pre-existing nuclear tracks. Electrolysis with $0.1\text{--}0.4\text{ A/cm}^2$ is done for two or three days, after which the chips are again etched and examined. For controls, detector chips are suspended above bottled electrolyte solution for two to four days without electrolysis. An additional precaution was to ascertain that holding detector chips in oxygen at 60°C does not damage the detectors.

Tracks were produced on chips held in the vapor in the cathode compartment. But more to the point, tracks were

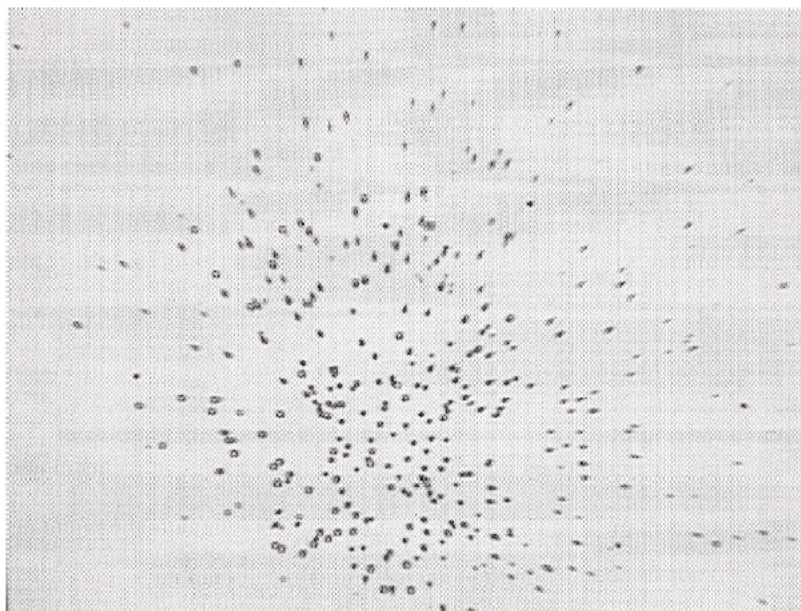


Figure 2. A cluster of nuclear pits formed on the rear surface of a CR39 chip. The angular shape of the pits and their distribution indicate that the nuclear particles that produced the nuclear tracks originated at a common point.

Table 4. Change of track count (tracks/cm²) upon re-etching

After first etch	After re-etch	Increment	<i>D</i> (μm)
82	160	78	—
71	75	4	—
147	151	4	—
55	TL	TL	—
48	TL	TL	—
22	56	34	—
8	194	186	—
38	295	255	60
64	70	6	60
49	121	72	135
53	TL	TL	70
11	700	690	50
17	53	36	45
44	551	515	75
19	41	22	—
50	86	36	—
52	620	568	70

Notes: TL signifies that the number of tracks was so large that counting was impractical. *D* is the depth of recession of the chip surface from its original position caused by the etchings.

also produced on the CR39 chips suspended in the oxygen-water vapor mixture in the anode compartment. Fig. 3 shows an example of these nuclear pits. Table 5 summarizes the U-cell experiments that resulted in number densities of nuclear tracks much greater than those produced in the control chips. An equal number of U-cell experiments produced track densities comparable to the results with the control chips. These unsuccessful experiments provide assurance that ordinary physico-chemical phenomena associated with the moving oxygen gas are not responsible for the large track densities listed in Table 5. It is clear from these experiments that hydrogen-producing cathodic processes are not essential for causing the nuclear reaction that the CR39 plastic records.

8. Discussion

The relatively simple and transparent technique of using CR39 detectors has clearly shown that nuclear reactions of currently unknown mechanism can be produced during electrolysis. An experimental protocol has been developed that

Table 5. Detectors in the anode vapor space

Experiment	Front surface (tracks/cm ²)	Rear surface (tracks/cm ²)
1	253	349
2	306	250
3	272	301
4	258	307
5	612	385
6	238	200
7	326	228
8	300	245

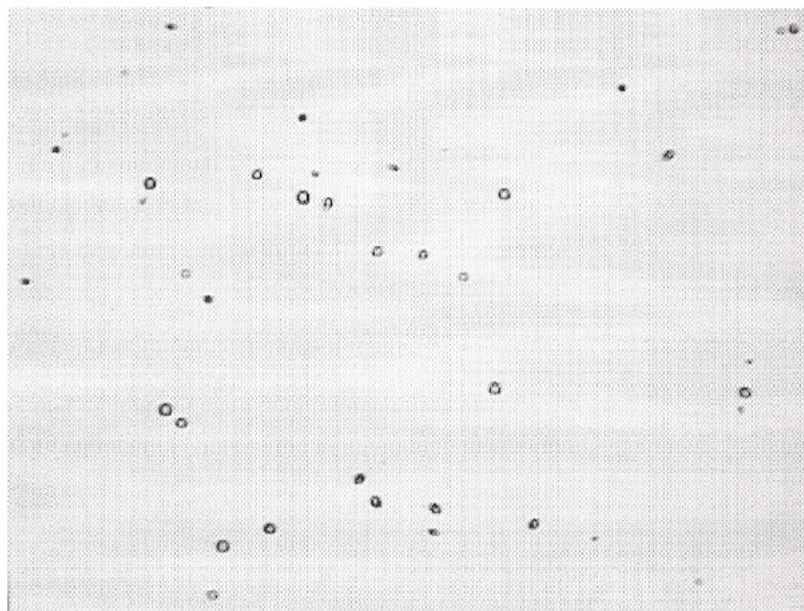


Figure 3. Pits formed on a chip suspended during electrolysis in the vapor in the anode compartment of the electrolysis cell where only oxygen is evolved.

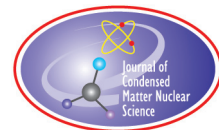
is able reproducibly to generate the nuclear reaction. However, what specific feature of electrolysis is responsible for making the nuclear reaction possible is not at all clear. It has been shown that the use of heavy water with palladium as the cathode is not essential. Using light water and nickel cathodes is virtually equally effective, but what ions in the electrolyte are necessary is not known. Nuclear particles that leave damage trails in the detector plastic can be produced within the electrolyte, and in the vapor space that contains either hydrogen and water vapor or oxygen plus water vapor. More surprising is that nuclear particles can be generated within the thickness of the plastic. Any attempt to develop the mechanism of the nuclear reaction involved should take the phenomena here described into consideration. At present there is nothing in nuclear physics as currently understood that can account for these experimental facts. It is clear that the nuclear reaction that produces the tracks recorded by the CR39 detectors is not the cause of the anomalous excess energy that has been measured calorimetrically by many investigators beginning with Fleischmann et al. [1]. Nevertheless the mechanism of the track-producing nuclear reaction needs to be understood in order to progress towards developing a much needed non-polluting source of nuclear energy.

Acknowledgment

Much appreciation is expressed for valuable discussions with John C. Fisher, whose theoretical developments [11] inspired and supported some of the experimental work here described.

References

- [1] M. Fleischmann, S. Ponnus and M. Hawkins, *J. Electroanal. Chem.* **261** (1989) 301.
- [2] R.A. Oriani, J.C. Nelson, Lee Sung-Kyun and J.H. Broadhurst, *Fusion Technol.* **80** (1990) 652.
- [3] E. Storms, *Proc. 8th Intern. Conf. Cold Fusion*, 2000, p. 55.
- [4] R.L. Fleischer, P.B. Price and R.M. Walker, *Tracks in Solids*, University of California Press, Berkeley, CA.
- [5] R.A. Oriani and J.C. Fisher, *J. Jpn. Appl. Phys. Part 1* **41**(10) (2002) 6180; Erratum, *ibid.* **42**(3) (2003) 149.
- [6] R.A. Oriani, *Trans. Amer. Nucl. Soc.* **88** (2003) 640.
- [7] R.A. Oriani and J.C. Fisher, *Proc. 10th Intern. Conf. Cold Fusion*, 2006, p. 577.
- [8] F. Mosteller and R.E.K. Rourke, *Sturdy Statistics: NonParametric Order Statistics*, Addison–Wesley, Reading, MA, 1975 .
- [9] R.A. Oriani and J.C. Fisher, *Proc. 10th Intern. Conf. Cold Fusion*, 2006, 567.
- [10] R.A. Oriani and J.C. Fisher, *Proc. 11th Intern. Conf. Cold Fusion*, 2006, 295.
- [11] J.C. Fisher, *Fusion Technol.* **34** (1992) 66.



Research Article

Underlying Mechanism of the Nuclear of Implied by the Energy–momentum Conservation [I]

Tetsuo Sawada*

Institute of Quantum Science, Nihon University, Tokyo 101-8308, Japan

Abstract

By studying the conservation of energy and momentum, it is found that in the nuclear cold fusion, existence of the localized external potential is necessary to absorb the large momentum transfer. We can narrow down the candidate of the required external field to the magnetic field produced by the magnetic monopole. The roll of the magnetic monopole in lowering the repulsive Coulomb barrier when two deuterons come close and fuse is considered.

© 2012 ISCMNS. All rights reserved.

Keywords: Charge–monopole system, Coulombic field, d–d Reaction, Momentum conservation, Momentum transfer

1. Introduction

The conservation laws of the energy and the momentum are the most important thing to obey when we study the nuclear reaction for example. As Noether's theorem taught us, the conservation law appears from the symmetry of the system. In particular, the translational invariance in time implies the energy conservation, whereas the momentum conservation arises from the homogeneity of the space.

The final states of the d–d reactions in vacuum at low energy are $t + p$ and ${}^3\text{He} + n$ with 50% each in the branching ratio. In the c.m. system, the produced energy Q is shared by the two final state particles by $Q = \vec{p}^2/2m_1 + (\vec{p}')^2/2m_2$. On the other hand, in the nuclear CF, the reaction changes to $d + d \rightarrow {}^4\text{He}$. When we examine the conservation laws in the center of mass system, from the momentum conservation the momentum \vec{q} of ${}^4\text{He}$ must be zero, whereas the energy conservation requires $q = \sqrt{2M_4Q}$, where M_4 is the mass of ${}^4\text{He}$. Therefore, two conservations are not compatible. We know that the homogeneity of the space is often destroyed when the external field exists. Since $Q = 23.9$ MeV, the momentum transfer becomes $q = 422$ MeV/c. In the potential scattering we know the scattering amplitude is the Fourier transformation of the external potential $V(r)$: $a(q) = -(2m/4\pi\hbar) \int d^3r' \exp[i\vec{q} \cdot \vec{r}'] V(r')$. Since $|a(q)|^2$ is the probability of the momentum transfer, the spread of the potential Δr must be very small in order to produce such a large momentum transfer. They are related by the uncertainty relation $q \cdot \Delta r \sim \hbar$, which means $\Delta r = 0.47$ fm. in our case.

*E-mail: sawadaphys@hotmail.com

The candidates of the source X of the external field are severely restricted. The external fields, to which the nucleus can respond, must be either electric or magnetic. However, X cannot be the electric charge. This is because the electron cloud cannot become as small as $\Delta r = 0.47$ fm., since the size of the electron cloud must be larger than its Compton wave length, which is around 400 fm. Another candidate of X is the magnetically charged particle (magnetic monopole), since the nuclei with the non-zero magnetic moment can respond to the magnetic field. Because of the charge quantization condition of Dirac, the magnetic field of the magnetic monopole is super-strong, namely $*e^2/\hbar c = 137/4$. The interaction potential between the nucleon and the magnetic monopole is $V(r) = -\kappa_{\text{tot}}(e/2m_p)*e - \vec{\sigma} \cdot -\vec{r}/r^3$. This strong potential serves to form the bound states of the monopole and the nucleons or small nuclei. For example, the binding energy of the $*e - d$ system is around 2.3 MeV. Therefore, if the d-d reaction proceeds after two deuterons are trapped by the magnetic monopole, it is energetically impossible to become the (t+p) or ($^3\text{He} + n$) states. This is because the binding energy of t and ^3He is 8.5 and 7.7 MeV, respectively. The only allowed final state is ^4He , however it must leave the monopole, because the spin of ^4He is zero and there is no bound state of the monopole and ^4He .

In this way, when the reaction proceeds under the influence of the magnetic monopole, the channels (t + p) and ($^3\text{He} + n$) are energetically closed. On the other hand, the reaction of (two-body \rightarrow one-body) type such as (d+d \rightarrow ^4He) becomes possible. In Section 2, how the external potential, whose existence destroys the homogeneity of the space, can “absorb” the momentum transfer will be explained. Since the magnetic monopole plays the central role in the nuclear cold fusion, the brief review of the theory of the magnetic monopole will be given in Section 3. In Section 4, the Schrödinger equation in the external magnetic Coulomb field is solved. Existence of the magnetic monopole can change the purely repulsive Coulomb potential between deuterons to a potential which enables for the two zero-incident energy deuterons to approach to the fm region. In Section 5, the mechanism of the change of the potential will be discussed along with the evaluation of the penetration factor. Other characteristic feature of the nuclear cold fusion is the sporadic property in starting the reaction. This phenomenon does not occur on demand, but some kind of probability comes into the scene. The magnetic monopole, which is the rare particle, plays the role of the “one-particle catalyst” of the nuclear CF reaction. In Section 6, the meaning of the lack of the reproducibility is considered.

2. Energy–momentum Conservation

The most important difference of the very low energy (d + d) reaction in vacuum and that of the nuclear cold fusion is that although the former reaction is the (two-body \rightarrow two-body) type, the latter reaction is the (two-body \rightarrow one-body) type. In fact, the final states of reactions in vacuum are (p+t), ($n + ^3\text{He}$) or ($^4\text{He} + \gamma$). On the other hand, in the nuclear CF the final state is ^4He . Let us examine the conservation laws in the center of mass system. The momenta of the final state particles, whose masses are m_1 and m_2 , are \vec{p}' and $(-\vec{p}')$, respectively. The energy conservation of the zero-incident energy becomes

$$Q = \frac{(\vec{p}')^2}{2m_1} + \frac{(-\vec{p}')^2}{2m_1}, \quad (1)$$

where Q is the energy produced in the exothermal reaction. The equation indicates that the energy Q is shared by the two particles with proportional to the inverse of the masses. For example, in the (d+d \rightarrow p + t) reaction 75% of the energy is taken by the proton and 25% goes to the triton.

For the case of (d + d \rightarrow $^4\text{He} + \gamma$) reaction, small modification is necessary because the photon γ is the relativistic particle and whose energy is $p'c$, the energy conservation becomes

$$Q = \frac{(\vec{p}')^2}{2M_4} + p', \quad (2)$$

where M_4 is the mass of ^4He , and the natural units $c = \hbar = 1$ are adopted. Since numerically $Q = 23.9\text{MeV}$ and $M_4 = 3732\text{MeV}$, by solving Eq. (2) we obtain $p'/Q = 0.99682$, which means that 99.682% of the energy is taken

away by the γ ray and only 0.318% becomes the kinetic energy of ^4He . These sharings of the energy Q are confirmed by the experiments of d+d reactions at very low energy.

On the other hand, in the (two-body \rightarrow one-body) reaction, the energy conservation and the momentum conservation can not be compatible. This is because in the c.m. system, the momentum of the final state particle p' must be zero from the momentum conservation. However, the energy conservation requires $p' = \sqrt{2M_4 Q}$. Therefore, for exothermal reaction: $Q > 0$, the two conservations are not consistent.

It is well-known from Noether's theorem that the translational invariance of the nuclear system in vacuum is responsible for the momentum conservation. Since the Lagrangian of the nuclear system has the form

$$L = \sum_i \left(-\frac{1}{2m_i} \right) \nabla_i^2 - \sum_{i>j} V_{ij}(\vec{r}_i - \vec{r}_j), \quad (3)$$

L does not change when we shift all the coordinates \vec{r}_i by \vec{a} , namely $(\vec{r}_i \rightarrow \vec{r}'_i = \vec{r}_i + \vec{a})$. In the new coordinate \vec{r}'_i , L remain the same. So the homogeneity of the system in space direction is responsible for the momentum conservation. Likewise the homogeneity in the direction of time is the cause of the energy conservation.

On the other hand, such a homogeneity in space is destroyed when the external potential exists at the specified point in space. As is well-known in the problem of the scattering by the potential, the momentum is transferred to the external potential $V(r)$ with the scattering amplitude $a(q)$ introduced by

$$a(q) = -(2m/4\pi\hbar) \int d^3r' \exp[i\vec{q} \cdot \vec{r}'] V(r'), \quad (4)$$

and the probability of the occurrence of such a momentum transfer is $|a(q)|^2$. In our case of d+d \rightarrow ^4He , the momentum transfer is $q = \sqrt{2M_4 Q} = 422 \text{ MeV}/c$, which corresponds to the wave length $\lambda = 2\pi\hbar/q = 3.0 \text{ fm}$. Large value of the momentum transfer q means the very localized potential, whose spread Δr is related to q by the ‘‘uncertainty relation’’ $q \cdot \Delta r \sim \hbar$, when the functional form of $V(r)$ is Gaussian. In this way we can conclude that the nuclear CF can progress under the influence of the external potential whose locality is the order of fm.

We can narrow down the underlying mechanism of the nuclear CF, further. In general the nucleon can respond only to the two types of external fields, which are the electric field and the magnetic field. In fact the electric charges of protons interact with the electric field, whereas the magnetic dipole moments of nucleons interact with the magnetic field. Let us introduce the source particle X of the external field. Such a source particle X must attract fuel deuterons to fuse, so the candidate is the electron when the external field is electric. However, this does not work well, since the lower bound of the size of the wave packet of the electron is limited by its Compton wave length, which is around 400 fm, and so it cannot produce the sharply localized potential $V(r)$ with 1 fm in size. On the other hand if the source X is the magnetically charged particle (magnetic monopole), it attracts the nucleus when the tail of the magnetic moment orients to the direction of the magnetic monopole. Since the magnetic Coulomb field $*e\vec{r}/r^3$ accompanies the magnetic monopole, the interaction potential of the magnetic moment of the nucleon is

$$V_m(r) = -\kappa_{tot} \frac{*ee}{2m_p} \frac{(\vec{\sigma} \cdot \vec{r})}{r^3} F(r), \quad \text{with} \quad F(r) = 1 - e^{-ar} (1 + ar + a^2 r^2/2), \quad (5)$$

where $F(r)$ is the form factor of the nucleon, and numerically $a = 6.04\mu\pi$. If we substitute $V_m(r)$ of Eq. (5) into Eq. (4), we shall find that the scattering amplitude $a(q)$ has appreciable value at the required value of q , and which means that the momentum transfer to the external field in the d+d \rightarrow ^4He goes smoothly. Moreover the potential $V_m(r)$ has the strength of the strong interaction. In the next section we shall see that the Coulomb field of Dirac's magnetic monopole is super-strong, namely $*e^2/\hbar c = 137/4$, which is the magnetic counterpart of the ordinary fine structure constant $e^2/\hbar c = 1/137$. Therefore, the coefficient $(*ee)$ of Eq. (5) is $1/2$.

In this way we found that the reaction $(d+d \rightarrow {}^4\text{He})$, which is forbidden in the nuclear physics in vacuum, can occur if the reaction progress under the influence of the external field produced by the magnetic monopole. In Section 3, a brief review of the magnetic monopole will be given.

3. Brief Review of the Theory of the Magnetic Monopole

It is well-known that the Maxwell equations in vacuum are symmetric under the duality transformation, which interchange the electricity and the magnetism. On the other hand, the full Maxwell equations with the source and current terms do not have such a symmetry, and therefore the electricity and the magnetism are not treated on the same footing. For example, although \vec{D} has source ρ , \vec{B} does not have.

3.1. Maxwell equations with dual symmetry

In 1931, Dirac proposed to modify the Maxwell equations to restore the duality symmetry, which are:

$$\begin{aligned}\text{div } \vec{D} &= 4\pi\rho, \\ \text{div } \vec{B} &= 4\pi^*\rho\end{aligned}\tag{6}$$

and

$$\begin{aligned}\text{rot } \vec{H} - \frac{1}{c} \frac{\partial \vec{D}}{\partial t} &= \frac{4\pi}{c} \vec{i}, \\ \text{rot } \vec{E} + \frac{1}{c} \frac{\partial \vec{B}}{\partial t} &= -\frac{4\pi}{c} {}^*\vec{i}.\end{aligned}\tag{7}$$

It is not difficult to examine the invariance of the equations under the following duality transformations.

$$\begin{aligned}\vec{D} &\rightarrow \vec{B}, \\ \vec{B} &\rightarrow -\vec{D}, \text{ etc.}\end{aligned}\tag{8}$$

and

$$\begin{aligned}\rho &\rightarrow \rho \\ {}^*\rho &\rightarrow -\rho, \text{ etc.}\end{aligned}\tag{9}$$

Once such a modification is done, we can consider a system in which the electric charge and the magnetic charge coexist. In the next subsection we shall see that, in such a system, an extra angular momentum emerges in addition to the ordinary orbital angular momentum.

3.2. Extra angular momentum characteristic to charge–monopole system

In order to see the existence of the angular momentum ${}^*QQ/c$, let us consider monopole with magnetic charge *Q is fixed at the origin, and a particle of mass M and electric charge Q is moving in the magnetic Coulomb field produced by the magnetic monopole. The equation is

$$M\ddot{\vec{r}} = (Q/c)\dot{\vec{r}} \times \vec{B}, \quad \vec{B} = {}^*Q \frac{\vec{r}}{r^3},\tag{10}$$

and as in the case to prove the conservation of the angular momentum, we make the vector product $\vec{r} \times$ of the equation of motion

$$M \frac{d}{dt}(\vec{r} \times \dot{\vec{r}}) = \left(\frac{{}^*QQ}{c} \right) \frac{\vec{r} \times (\dot{\vec{r}} \times \vec{r})}{r^3}. \quad (11)$$

Because of $\vec{a} \times (\vec{b} \times \vec{c}) = \vec{b}(\vec{a} \cdot \vec{c}) - \vec{c}(\vec{a} \cdot \vec{b})$, we obtain

$$M \frac{d}{dt}(\vec{r} \times \dot{\vec{r}}) = \left(\frac{{}^*QQ}{c} \right) \left(\frac{\dot{\vec{r}}}{r} - \frac{\vec{r}\vec{r} \cdot \dot{\vec{r}}}{r^3} \right) = \left(\frac{{}^*QQ}{c} \right) \frac{d}{dt} \left(\frac{\vec{r}}{r} \right). \quad (12)$$

The same extra angular momentum is also obtained if we integrate the angular momentum density $\vec{r}' \times \epsilon \mu \vec{S}(\vec{r}')$ stored in space, in which \vec{S} is Poynting vector. Therefore, what is conserved in time is $M\vec{r} \times \dot{\vec{r}} - ({}^*QQ/c)\hat{r}$.

3.3. Charge quantization condition

Since in quantum mechanics a component of the angular momentum can assume only the integer multiple of $\hbar/2$, we can derive the charge quantization condition of Dirac[?]

$$\frac{{}^*QQ}{2} = \frac{\hbar}{2}n, \quad n = 0, \pm 1, \pm 2, \dots \quad (\text{Dirac}). \quad (13)$$

On the other hand, Schwinger claims that the component of the extra angular momentum assumes not $\hbar/2$ but $\hbar n$ as in the case of the orbital angular momentum, because the term $-({}^*QQ/c)\hat{r}$ is obtained classically. Since we are going to consider both cases, let us introduce a number D and assign $D = 1$ for Dirac and $D = 2$ for Schwinger, and write the charge quantization as

$$\frac{{}^*QQ}{\hbar c} = \frac{D}{2}n, \quad n = 0, \pm 1, \pm 2, \dots \quad (14)$$

If we write the non-zero smallest magnetic charge as *e , Q becomes

$$Q = \frac{\hbar c}{{}^*e}n, \quad n = 0, \pm 1, \pm 2, \dots \quad (15)$$

This equation indicate that the electric charge Q is discrete and is integer multiple of $(\hbar c/{}^*e)$. Moreover we can understand the equality of the electric charges of the electron and proton up to the sign, on the other hand experimentally the equality has been known with extremely high relative accuracy 10^{-22} .

3.4. Magnetic counterpart of the fine structure constant

For the non-vanishing smallest charges e and *e , the charge quantization condition becomes ($n = 1$)

$$\frac{{}^*ee}{\hbar c} = \frac{D}{2}. \quad (16)$$

If we combine it with the value $e^2/\hbar c = 1/137.036$, the “fine structure constant” of the magnetic charge becomes

$$\frac{{}^*e^2}{\hbar c} = 1/137.036 \frac{D^2}{4}. \quad (17)$$

Therefore, the Coulomb force between the magnetic monopole is super-strong, and if we compare it with the Coulomb force between the electric charges it is stronger by 4,695 times for Dirac’s case ($D = 1$) and 18,780 times for Schwinger’s case ($D = 2$).

Since the magnetic Coulomb field is super-strong, we may expect the anomalous magnetic moment of a nucleus is attracted to the monopole and forms the bound states. This is in fact the case, since the potential of such an interaction is

$$V_m(r) = -\left(\frac{\kappa_{\text{tot}} e}{2m_p}\right) \vec{\sigma} \cdot \vec{B}(r) \quad \text{with} \quad \vec{B} = *eD \frac{\hat{r}}{r^2}, \quad (18)$$

which is valid in the region of $r \gg r_A$, where r_A is the radius of the nucleus. From the charge quantization condition

$$V_m(r) = -\left(\frac{\kappa_{\text{tot}} D}{4m_p}\right) \frac{\vec{\sigma} \cdot \hat{r}}{r^2} \quad (19)$$

Therefore, when $\kappa_{\text{tot}} > 0$, the spin state belongs to the eigenvalue $(\vec{\sigma} \cdot \hat{r}) = +1$ becomes attractive, and the strength V_m is nearly the same as that of the nuclear potential. For example, for proton the potentials V_m are -9.3 MeV and -2.33 MeV at $r = 1.41$ fm. and at $r = 2.82$ fm. respectively (for $D = 1$).

4. System of the Nucleus and the Magnetic Monopole

In order to understand the roll of the magnetic monopole as the catalyst of the nuclear fusion reaction, we must solve the Schrödinger equation in the external magnetic Coulombic field. We shall set the mass of the magnetic monopole to infinity, although Schwinger estimated its mass was 8 GeV. Such an approximation must be useful in understanding the effect of the magnetic monopole on the small nuclei ($A < 5$), qualitatively. To include the magnetic field into the Schrödinger equation, the standard procedure is to make the replace $-i\nabla j \rightarrow (-i\nabla j - (Ze/c)A_j)$, in which \vec{A} is the vector potential whose rotation is the magnetic Coulomb field. However, such a procedure does not work well, because $\text{div}(\text{rot } \vec{A}) = 0$ for the regular function \vec{A} . In the next subsection a method to circumvent this difficulty will be explained.

4.1. The vector potential of magnetic Coulomb field

The magnetic Coulombic field \vec{B} origin satisfies produced by a magnetic monopole $*Q$ fixed at the

$$\text{div} \vec{B} = 4\pi *Q \delta^3(\vec{r}) \quad (20)$$

and if we substitute $\vec{B} = \text{rot} \vec{A}$ we obtain a contradictory equation, because $\text{div}(\text{rot } \vec{A})$ is identically zero if \vec{A} is regular. On the other hand, a vector potential

$$\vec{A}^{(a)} = *Q \frac{(1 - \cos \theta)}{r \sin \theta} \hat{\phi}, \quad \text{north} \quad (21)$$

or

$$\vec{A}^{(b)} = -*Q \frac{(1 + \cos \theta)}{r \sin \theta} \hat{\phi}, \quad \text{south} \quad (22)$$

becomes the magnetic Coulomb field when we compute its rotation. These \vec{A} 's have singularities on the negative and positive z -axis, respectively, and whose rotation become strings (Dirac string) on the half z -axis.

Wu and Yang proposed to use $\vec{A}^{(a)}$ in the north hemisphere and $\vec{A}^{(b)}$ in the south hemisphere as the vector potential. On the overlapping region around the equator, these potentials are related by the gauge transformation, because

$$\vec{A}^{(a)} - \vec{A}^{(b)} = -\left(\frac{2*e}{r \sin \theta}\right) \hat{\phi} = \nabla(-2*e\phi). \quad (23)$$

It is well-known that the change of the gauge of $\vec{A}^{(a)}$ results in only the change of the phase of the wave function Ψ . In the next subsection, we shall see this property explicitly.

4.2. The monopole harmonics $Y_{q,l,m}(\theta, \phi)$

If $\vec{L} = M\vec{r} \times \dot{\vec{r}} - q\hat{r}$, where q is the magnitude of the extra angular momentum, the eigen-function of \vec{L}^2 and Lz is the monopole harmonics $Y_{q,l,m}(\theta, \phi)$, [?] and which reduces to the ordinary spherical harmonics $Y_{q,l,m}(\theta, \phi)$ when $q = 0$. If we write $Y_{q,l,m}(\theta, \phi) = e^{\pm iq\phi} e^{im\phi} \Theta(\theta)$, where \pm of the exponential corresponds to the northern and the southern hemisphere, respectively, $\Theta(z)$ must satisfy

$$[l(l+1) - q^2]\Theta = -(1-z^2)\Theta'' + 2z\Theta' + \frac{(m+qz)^2}{1-z^2}\Theta. \quad (24)$$

The explicit form of $Y_{q,l,m}(\theta, \phi)$ is

$$Y_{q,l,m}^{(n)}(\theta, \phi) = \sqrt{\frac{2l+1}{4\pi}} e^{+iq\phi} d_{-q,m}^{(l)}(\theta) e^{+im\phi} \quad \text{in } R_n \quad (25)$$

and

$$Y_{q,l,m}^{(s)}(\theta, \phi) = e^{-2iq\phi} Y_{q,l,m}^{(n)}(\theta, \phi) \quad \text{in } R_s, \quad (26)$$

where R_n and R_s is the northern and southern hemispheres of the sphere, respectively, $d_{m',m}^{(l)}(\theta)$ is Wigner's d-function of rotation[?] which is widely used in the nuclear physics.

4.3. The equation of the monopole-nucleus of spin-0

It is instructive to start from the simplest problem of the motion of the single charged particle such as ^4He in the magnetic Coulomb field, whose Hamiltonian is

$$H_0 = \frac{1}{2m_A} \left(\vec{p} - \frac{Ze}{c} \vec{A} \right)^2. \quad (27)$$

The radial function $R(r)$, introduced by

$$\psi = R(r) Y_{q,l,m}, \quad (28)$$

satisfies the following equation:

$$\left[-\frac{1}{2m_A r^2} \frac{d}{dr} \left(r^2 \frac{d}{dr} \right) + \frac{l(l+1) - q^2}{2m_A r^2} - E \right] R(r) = 0. \quad (29)$$

The solution, which does not blow up at $r = 0$, is the J-Bessel:

$$R(r) = \frac{1}{\sqrt{kr}} J_{\mu} kr, \quad (30)$$

where

$$\mu = \sqrt{l(l+1) - q^2 + 1/4} = \sqrt{(l+1/2)^2 - q^2} > 0 \quad \text{and} \quad l = |q|, |q| + 1, |q| + 2, \dots \quad (31)$$

For $E < 0$, there is no meaningful solution, and therefore there is no bound state.

4.4. Angular function of spin 1/2 particle in the monopole field

For the spin-0 particle, we know the monopole harmonics $Y_{q,l,m}$ is the angular function. For the spin-1/2 particle, we can construct the state of the total angular momentum (j, m) by combining spin-up and spin-down states with the monopole harmonics $Y_{q,l,m}$, in which the Clebsch–Gordan coefficients appear. In general, for given j there are two states

$$\begin{aligned}\Phi_{j,m}^1 &= \sqrt{\frac{j+m}{2j}} Y_{qj-1/2,m-1/2} \begin{bmatrix} 1 \\ 0 \end{bmatrix} + \sqrt{\frac{j-m}{2j}} Y_{qj-1/2,m+1/2} \begin{bmatrix} 0 \\ 1 \end{bmatrix} \\ &= \begin{bmatrix} \sqrt{\frac{j+m}{2j}} Y_{qj-1/2,m-1/2} \\ \sqrt{\frac{j-m}{2j}} Y_{qj-1/2,m+1/2} \end{bmatrix}\end{aligned}$$

and

$$\begin{aligned}\Phi_{j,m}^2 &= -\sqrt{\frac{j-m+1}{2j+2}} Y_{qj+1/2,m-1/2} \begin{bmatrix} 1 \\ 0 \end{bmatrix} + \sqrt{\frac{j+m+1}{2j+2}} Y_{qj+1/2,m+1/2} \begin{bmatrix} 0 \\ 1 \end{bmatrix} \\ &= \begin{bmatrix} -\sqrt{\frac{j-m+1}{2j+2}} Y_{qj+1/2,m-1/2} \\ \sqrt{\frac{j+m+1}{2j+2}} Y_{qj+1/2,m+1/2} \end{bmatrix}\end{aligned}$$

except for the smallest j , namely for $j = |q| - 1/2$. After Wu and Yang we shall call the (j, m) state with $j \geq |q| + 1/2$ type-A, to which two states $\Phi_{j,m}^1$ and $\Phi_{j,m}^2$ belong.

On the other hand, the state of $j = |q| - 1/2$ is the type-B and to which only one state j, m belongs. Since the ground state appears in the type-B state, we shall write it explicitly:

$$\eta_m \begin{bmatrix} -\sqrt{\frac{|q|-m+1/2}{2|q|+1}} Y_{q,|q|,m-1/2} \\ \sqrt{\frac{|q|+m+1/2}{2|q|+1}} Y_{q,|q|,m+1/2} \end{bmatrix}, \quad (32)$$

in which $l = |q|$ and $j = |q| - 1/2$.

4.5. The eigenvalue problem of the proton–monopole system

The equation to be solved is

$$\left[\frac{1}{2M} (-i\vec{\nabla} - e\vec{A})^2 + V(r) - \frac{1}{r^2} \frac{b(r)}{2M} (\vec{\sigma} \cdot \hat{r}) \right] \psi = E\psi, \quad (33)$$

where

$$b(r) = \bar{b} \left(1 - e^{ear} \left(1 + ar + \frac{a^2 r^2}{2} \right) \right) \quad (34)$$

with

$$\bar{b} = \kappa_{\text{tot}} q = 2.7928, \quad q = D/2 \quad \text{and} \quad a = 6.04\mu\pi. \quad (35)$$

If we remember

$$\vec{L} = \vec{r} \times (\vec{p} - e\vec{A}) - q\hat{r} \quad \text{with} \quad q = D/2 \quad (36)$$

and

$$(\vec{p} - e\vec{A})^2 = \frac{1}{r^2} \frac{d}{dr} \left(r^2 \frac{d}{dr} \right) + \frac{1}{r^2} (\vec{L}^2 - \vec{q}^2) \quad (37)$$

for the type-B amplitude

$$\psi = \frac{1}{r} g(r) \eta m \quad (38)$$

the Schrödinger equation of the radial function becomes

$$\left[\frac{d^2}{dr^2} + 2M(E - V(r)) - \frac{R}{r^2} \right] g(r) = 0 \quad (39)$$

with

$$R = (j + 1/2)(j + 3/2) - q^2 - b(r)q/|q| = |q|(1 - b(r)/q). \quad (40)$$

When $V(r) = 0$, the equation is

$$\left[\frac{d^2}{dr^2} - \kappa - \frac{1}{r^2} (|q| - b(r)) \right] g(r) = 0 \quad \text{with } \kappa^2 = -2ME \quad (41)$$

For $ar \gg 1$, the solution, which damps for large ar , is the K-Bessel:

$$g(r) = \sqrt{\kappa r} K_{i\mu}(\kappa r) \quad \text{with } i\mu = \sqrt{|q|}(1 - \kappa_{tot}) + 1/4. \quad (42)$$

Since in small ar region the regular solution is determined by the index equation:

$$g(r) = c_1(ar)^\alpha \quad \text{with } \alpha = 1/2 + \sqrt{|q|} + 1/4, \quad (43)$$

we can solve the equation numerically and match to the logarithmic derivative of the Bessel function at $ar = x_m \gg 1$.

We can see that there are infinitely many energy levels which shrink exponentially to $\kappa = 0$. Since for pure imaginary index $i\mu$, the asymptotic form of the K-Bessel is

$$K_{i\mu}(x) = \frac{\pi}{\sin h\pi\mu} \sin(\mu \log x/2)[1 + o(x)], \quad (44)$$

the logarithmic derivative reduces to

$$r \frac{d}{dr} \log(\sqrt{\kappa r} K_{i\mu}(\kappa r)) = \frac{1}{2} + \mu \cot(\mu \log \frac{\kappa r}{2}). \quad (45)$$

The periodicity of \cot implies the eigenvalues appear in the way that $\mu \log(\kappa/a) = -\pi n' + \text{const.}$ with the integer n' . In terms of the binding energy $-E$,

$$-E_n = \frac{\kappa_n^2}{2M} = C_\infty \exp \left[-\frac{2\pi}{\mu} (n - 1) \right], \quad (46)$$

where n is the principal quantum number.

4.6. Binding energy of magnetic monopole and nuclei of spin 1/2

The binding energies of the spin 1/2 nuclei can be estimated in the same way as the proton, by simply changing the mass, charge, κ_{tot} and the parameter a of the form factor, as long as the deformations of the nuclei in the magnetic Coulomb field are negligible. Following table is the first few binding energies $-E_n$ of the Dirac's magnetic monopole ($D = 1$) with p, t and ${}^3\text{He}$ along the the parameters μ and C_∞ of Eq. (46) along with the orbital radius of the ground state \bar{r}_1 .

	Proton	Triton	${}^3\text{He}$
$D = 1$	$-E_1 = 0.1882 \text{ MeV}$	$-E_1 = 1.516 \text{ MeV}$	$-E_1 = 0.2434 \text{ MeV}$
	$-E_2 = 76.046 \text{ eV}$	$-E_2 = 58.085 \text{ keV}$	$-E_2 = 2.7413 \text{ keV}$
	$-E_3 = 0.0307 \text{ eV}$	$-E_3 = 2.226 \text{ keV}$	$-E_3 = 30.047 \text{ eV}$
	\vdots	\vdots	\vdots
	$C_\infty = 0.1884 \text{ MeV}$	$C_\infty = 1.516 \text{ MeV}$	$C_\infty = 0.2502 \text{ MeV}$
	$\mu = 0.8040$	$\mu = 1.9263$	$\mu = 1.3921$
	$\bar{r}_1 = 11.00 \text{ fm}$	$\bar{r}_1 = 3.820 \text{ fm}$	$\bar{r}_1 = 7.371 \text{ fm}$

When the magnetic monopole is the Schwinger type $D = 2$, the binding energies are:

	Proton	Triton	${}^3\text{He}$
$D = 2$	$-E_1 = 2.4065 \text{ MeV}$	$-E_1 = 4.366 \text{ MeV}$	$-E_1 = 1.063 \text{ MeV}$
	$-E_2 = 15.457 \text{ keV}$	$-E_2 = 0.5479 \text{ MeV}$	$-E_2 = 51.115 \text{ keV}$
	$-E_3 = 98.231 \text{ eV}$	$-E_3 = 57.766 \text{ keV}$	$-E_3 = 2.3239 \text{ keV}$
	\vdots	\vdots	\vdots
	$C_\infty = 2.4322 \text{ MeV}$	$C_\infty = 5.4085 \text{ MeV}$	$C_\infty = 1.1259 \text{ MeV}$
	$\mu = 1.2421$	$\mu = 5.7697$	$\mu = 2.0312$
	$\bar{r}_1 = 3.666 \text{ fm}$	$\bar{r}_1 = 2.779 \text{ fm}$	$\bar{r}_1 = 4.596 \text{ fm}$

4.7. Binding energy of the magnetic monopole and the deuteron

The hamiltonian of the deuteron and the magnetic monopole system H^*_{e-d} is

$$H^*_{e-d} = H^*_{e-p} + H^*_{e-n} + V_{p,n}, \quad (47)$$

where $V_{p,n}$ is the nuclear potential of p and n. The hamiltonians of the magnetic monopole and the nucleons are

$$H^*_{e-p} = \frac{1}{2m_p} (-i\vec{\nabla} - e\vec{A})^2 - \kappa_{\text{tot}}^{(p)} D \frac{ee}{2m_p} \frac{(\vec{\sigma} \cdot \hat{r})}{r^2} F(r) \quad (48)$$

and

$$H^*_{e-n} = \frac{1}{2m_n} (-i\vec{\nabla})^2 - \kappa_{\text{tot}}^{(n)} D \frac{ee}{2m_p} \frac{(\vec{\sigma} \cdot \hat{r})}{r^2} F(r), \quad (49)$$

where the form factor function $F(r)$ is common to the proton and the neutron, and

$$F(r) = (1 - \exp[-ar](1 + ar + \frac{a^2}{2}r^2)) \quad \text{with} \quad a = 6.04\mu\pi, \quad (50)$$

in which a is related to the radius of the nucleon \bar{r} by $a = \sqrt{12}/\bar{r}$, and numerically $\bar{r} = 0.81 \text{ fm}$.

We searched for the energy level of the ground state of the ${}^*e - d$ system by the variational calculation, namely minimizing $\langle \Psi | H_{*e-d} | \Psi \rangle / \langle \Psi | \Psi \rangle$ by changing the trial function Ψ , which is the function of \vec{r}_p and \vec{r}_n including spin. We restrict the trial function to the type-B spin-angular function of Eq. (38) for proton, and for $(\vec{r}_n - \vec{r}_p)$ the two S-waves are retained, namely both the spin-singlet and the spin-triplet are included. Concerning the radial part, the prescription of the Gauss expansion method (GEM) is applied, namely the radial trial function is the sum of the Gauss functions whose range parameters are the “geometric series”. The numerical result obtained is $E = -4.5\text{MeV}$ in which the energy level of the state, where the three particles separate infinitely, is chosen as zero. Therefore, since the binding energy of the deuteron is $B_d = 2.2\text{MeV}$, we may say that the binding energy of $({}^*e - d)$ is $B_{d+*e} = 2.3\text{MeV}$.

This value of the binding energy leads to an important consequence that the two deuterons trapped by the same magnetic monopole is energetically impossible to decay to $(t+p)$ or $({}^3\text{He} + n)$ state since the binding energies are 8.5 and 7.7 MeV, respectively for t and ${}^3\text{He}$, while the binding energy of $d - {}^*e - d$ state is 9.0 MeV for $D = 1$ and 14.0 MeV for $D = 2$ magnetic monopoles. Since our calculation is variational, there remains some possibility for the binding energy of the deuterons with *e to increase slightly. In the next Subsection, we shall consider this important phenomenon characteristic to the nuclear cold fusion that the main channels $(t+p)$ or $({}^3\text{He} + n)$ are energetically closed in some detail.

4.8. Mechanism to close the $d + d \rightarrow (t + p)$ and $(n + {}^3\text{He})$ channels in CF

Since the most important feature of the nuclear CF reaction is the change of the open channels of the final states of the $d+d$ reaction, it is interesting to see whether a “theory” can successfully explain such a change. It is experimentally well-known that the final states of the low energy $d+d$ reaction in vacuum are $(t + p)$ and $({}^3\text{He} + n)$ with momentum conservation and the isotopic invariance. On the other hand, in the nuclear cold fusion (CF), the process becomes $d + d + {}^4\text{He}$, namely (two-body) \rightarrow (one-body) type. As explained in Section 2, the momentum conservation of the such a system is not satisfied, and so in order to restore the momentum conservation, we need the external (namely, outside of the nuclear system) potential to absorb the momentum transfer \vec{q} . Numerically in our case of the ${}^4\text{He}$ production, the magnitude of the transferred momentum is $q = \sqrt{2M_4Q} = 422\text{MeV}/c$, where M_4 is the mass of α -particle and $Q = 23.9\text{MeV}$. However, a soft and spread external potential $V(r)$ cannot do the job to absorb such a large momentum transfer q , instead we can estimate spacial size Δr of the external potential by using the relation $q\Delta r \sim \hbar$. We obtain $\Delta r \approx 0.45\text{fm}$. We can narrow down the type of the external field further. In order to obtain the external potential, the external field must interact with the nucleons. We know that the nucleon has two attributes, namely the electric charge and the magnetic dipole moment. Therefore, the candidate of the external field is either the electric field or the magnetic field. However, if we remember that the electron cloud spreads too widely and cannot produce the localized electric field, the only candidate of the external field becomes the magnetic field whose source particle is the magnetic monopole. Because of the charge quantization condition of Dirac, $*ee/\hbar c = 1/2$, the magnetic monopole is accompanied by the super-strong magnetic Coulomb field, which attracts surrounding nucleons or small nuclei with non-zero magnetic moment, and forms the bound state. In Section 4.6, the energy levels of the bound states are shown along with the orbital radius \bar{r}_1 of the ground state. Since the orbital radius is several fm, when two deuterons are trapped by the same magnetic monopole, it is expected that the nuclear reaction starts to occur and become the more stable particle ${}^4\text{He}$. When the binding of the deuterons to the magnetic monopole are too deep, we can expect such a state cannot energetically transit to the continuous states of $(t+p)$ and $(n + {}^3\text{He})$. Let us consider such closing of the t or n channels in more detail.

It is important to understand how the main channels $(t + p)$ and $(n + {}^3\text{He})$ of the $d + d$ reaction are closed when the nuclear reaction starts after the two deuterons are trapped by the same magnetic monopole *e . The energy level of the starting state E_{ini} is

$$E_{ini} = -2(B_{d+*e} + B_d), \quad (51)$$

in which the zero of the energy level is chosen where all the particles, namely the nucleons and the magnetic monopole, separate infinitely. In Eq. (51), B_A is the binding energy of the nucleus A, and numerically they are $B_d = 2.2$, $B_t = 8.5$, $B_{^3\text{He}} = 7.7$ and $B_{^4\text{He}} = 28.3\text{MeV}$, respectively. B_{*e-d} is the binding energy of the $d - *e$. If we remember that the continuous spectrum of the (t + p) system appears in $E \geq -B_t$, from the energy conservation initial state cannot become (t + p) as long as $E_{\text{ini}} < -B_t$. Therefore, from Eq. (51) the condition of the closing of the (t + p) channel is:

$$B_{d+*e} > \left(\frac{B_t}{2} - B_d\right) = 2.05 \text{ MeV} \equiv B^{\text{critical}}(\text{t} + \text{p}). \quad (52)$$

Likewise the continuous (n + ^3He) channel is closed when

$$B_{d+*e} > \left(\frac{B_{^3\text{He}}}{2} - B_d\right) = 1.65 \text{ MeV} \equiv B^{\text{critical}}(\text{n} + ^3\text{He}). \quad (53)$$

is satisfied. However, from the variational calculation given in Section 4.7, we know $B^*e - d = 2.5 \text{ MeV}$, and which means both of (t + p) and (n + ^3He) channels are closed which agrees with the observations of the CF experiments.

Concerning the one particle ^4He state, since the binding energy of ^4He is very large, namely $B_{^4\text{He}} = 28.3\text{MeV}$, the ^4He channel stays open as long as

$$B_{d+*e} > \left(\frac{B_{^4\text{He}}}{2} - B_d\right) = 11.95 \text{ MeV} \equiv B^{\text{critical}}(\text{n} + ^4\text{He}). \quad (54)$$

is satisfied. Therefore, the only open channel is ^4He . Since α -particle is spin-0, it is not attracted by the magnetic monopole, so it must be emitted by the monopole.

5. Penetration factor

5.1. Penetration factor in vacuum

The most disturbing mystery of the nuclear cold fusion is why the two positively charged nuclei of zero-incident energy can come close to the fm region. The standard argument against such a phenomenon is to calculate the penetration factor T by using the WKB approximation:

$$T = e^{-2\tau} \quad \text{with} \quad \tau = \int_a^b \sqrt{2m_{\text{red}}(V(x) - E)} dx / \hbar, \quad (55)$$

where the domain of penetration is $[a, b]$, and numerically we shall put $a = 1\text{fm}$ and $b = 1\text{\AA}$, since nucleus is shielded by the atomic electron. m_{red} is the reduced mass of the system. We shall consider the penetration of the (electric) Coulomb barrier of t+p and d+d system in the low energy limit $E \rightarrow 0$. Since $V_C(x) = +e^2/x$, τ becomes

$$T = \int_a^b \sqrt{2m_{\text{red}}e^2/x} dx = \sqrt{4m_{\text{red}}e^2}(\sqrt{b} - \sqrt{a}). \quad (56)$$

Therefore, numerically $T = 6.78 \times 10^{-92}$ for t+p system, whereas for the system of d+ d, $T = 5.33 \times 10^{-106}$. These extremely small values of T mean that such phenomena “never” occur.

5.2. Change of the penetration potential

Let us consider the case of t + p reaction. In the last section, we saw that a proton can form the bound state with the magnetic monopole $*e$, whose orbital radius is several fm. If the second nucleus, in our case it is the triton t, approaches to the bound state ($*e - p$), the potential felt by the incoming second particle is the sum of the repulsive Coulomb potential and the interaction between the magnetic monopole and the magnetic dipole of the triton. When the direction

of the magnetic moment of the triton orients to the opposite to the location of the magnetic monopole, the interaction becomes attractive, namely the sum of the potentials becomes

$$V_1(x) = +e^2/x - \kappa_{\text{tot}} \frac{D^* e e}{2m_p} \frac{1}{x^2}. \quad (57)$$

It becomes easier for the triton to penetrate to the region of the composite system $^*e - p$. In this way two nuclei p and t are trapped by the same magnetic monopole *e .

Since t and p are confined in the few fm region, it is unstable and fuses to become more stable particle ^4He . Since the spin of ^4He is zero, it cannot form a bound state with *e , and the energetic ^4He is emitted from the magnetic monopole. There remains a fresh magnetic monopole, and it starts to attract the surrounding nuclei anew. In this way, the magnetic monopole plays the roll of the catalyst of the nuclear cold fusion reaction $t + p \rightarrow ^4\text{He}$. Likewise $d + d \rightarrow ^4\text{He}$ of zero-incident energy must also occur.

If we compute the penetration factor T by using the new potential $V_1(x)$ of Eq. (53), although the value of T is improved, it is not sufficient to cause the expected nuclear cold fusion. However, in the electron rich environment, the magnetic monopole is shielded by an electron cloud whose radius is around the electron Compton wave length $\hbar/m_e c = 386.2$ fm. In the next subsection, we shall show that the Dirac equation of the electron in the external magnetic Coulomb field has such a solution which was found by Kazama and Yang.[?] Therefore, the pure repulsive (electric) Coulomb term $+e^2/x$ of Eq. (53) is modified to $+(e^2/x) \exp[-2m_e x]$.

5.3. Dirac equation in the external magnetic Coulomb field

The equation to solve is obtained by making the standard gauge substitution $\vec{p} \rightarrow \vec{p} - (Ze/c)\vec{A}$ of the free Dirac equation, where \vec{A} is the vector potential whose rotation is the magnetic Coulomb field of strength *eD and which is given in Eqs.(21) and (22). If we choose the representation of the 4×4 Dirac matrices $\vec{\alpha}$ and β as,

$$\vec{\alpha} = \begin{bmatrix} 0 & \vec{\sigma} \\ \vec{\sigma} & 0 \end{bmatrix} \quad \text{and} \quad \beta = \begin{bmatrix} I_2 & 0 \\ 0 & -I_2 \end{bmatrix}, \quad (58)$$

the Hamiltonian becomes

$$H = \vec{\alpha} \cdot (-i\vec{\nabla} - e\vec{A}) + \beta M - \frac{\kappa_a q}{2MR^2} \begin{bmatrix} \vec{\sigma} \cdot \hat{r} & 0 \\ 0 & -\vec{\sigma} \cdot \hat{r} \end{bmatrix}, \quad (59)$$

where the last term is the Pauli term, and in which κ_a is the anomalous magnetic moment of the electron in the unit of the Bohr magneton $e^2/2M$, whose value is 0.00116, or 2.13 in the unit of the nuclear magneton $e^2/2m_p$.

Since t and p are confined in the few fm region, it is unstable and fuses to become more stable particle ^4He . Since the spin of ^4He is zero, it cannot form a bound state with *e , and the energetic ^4He is emitted from the magnetic monopole. There remains a fresh magnetic monopole, and it starts to attract the surrounding nuclei anew. In this way, the magnetic monopole plays the roll of the catalyst of the nuclear cold fusion reaction $t + p \rightarrow ^4\text{He}$. Likewise $d + d \rightarrow ^4\text{He}$ of zero-incident energy must also occur.

If we compute the penetration factor T by using the new potential $V_1(x)$ of Eq. (53), although the value of T is improved, it is not sufficient to cause the expected nuclear cold fusion. However, in the electron rich environment, the magnetic monopole is shielded by an electron cloud whose radius is around the electron Compton wave length $\hbar/m_e c = 386.2$ fm. In the next subsection, we shall show that the Dirac equation of the electron in the external magnetic Coulomb field has such a solution which was found by Kazama and Yang.[?] Therefore, the pure repulsive (electric) Coulomb term $+e^2/x$ of Eq. (53) is modified to $+(e^2/x) \exp[-2m_e x]$.

Let us consider an eigen-value problem $H\psi = E\psi$. In particular, the type-(B) solution has the form:

$$\psi_m^{(B)} = \begin{bmatrix} f(r)\eta_m \\ g(r)\eta_m \end{bmatrix}, \quad (60)$$

where η_m is the hedgehog solution of the spin 1/2 particle given in Eq. (32), and which is the eigen-function of $(\vec{\sigma} \cdot \hat{r})$ with eigen-value +1. By substituting this form into the eigen-value equation, we obtain

$$[M - E - \kappa_a |q| (2Mr^2)^{-1}] f(r) - iq|q|^{-1} (\partial_r + r^{-1}) g(r) = 0 \quad (61)$$

and

$$-iq|q|^{-1} (\partial_r + r^{-1}) f(r) - [M + E - \kappa_a |q| (2Mr^2)^{-1}] g(r) = 0. \quad (62)$$

If we introduce $F(r)$, $G(r)$ by

$$f(r) = \frac{\kappa_a q}{|\kappa_a q|} \frac{F(r)}{r} \quad \text{and} \quad g(r) = -i \frac{G(r)}{r}. \quad (63)$$

Equations (61) and (62) become

$$\frac{dG}{dr} = \left[-\frac{(E - M)\kappa_a}{|\kappa_a|} - \frac{|\kappa_a q|}{2Mr^2} \right] F(r), \quad (64)$$

$$\frac{dF}{dr} = \left[\frac{(E + M)\kappa_a}{|\kappa_a|} - \frac{|\kappa_a q|}{2Mr^2} \right] G(r). \quad (65)$$

Furthermore, if we introduce a new independent variable ρ by $r = |\kappa_a q| \rho (2M)^{-1}$, the equations change to the simpler form:

$$\frac{dG}{d\rho} = \left(A - B - \frac{1}{\rho^2} \right) F \quad (66)$$

$$\frac{dF}{d\rho} = \left(A + B - \frac{1}{\rho^2} \right) G, \quad (67)$$

where

$$A = \frac{\kappa_a |q|}{2} \quad \text{and} \quad B = \frac{\kappa_a |q|}{2M} E \quad (68)$$

By changing the energy variable B , we must find the eigen-functions, which satisfy the boundary conditions that for $\rho \rightarrow \infty$ they must damp, and at $\rho = 0$ they must vanish: $F(0) = 0$ $G(0) = 0$. The solution which satisfies the requirements is

$$B = 0, \quad F(\rho) = -G(\rho) = \exp[-A\rho - 1/\rho]. \quad (69)$$

In terms of the former variable r , the eigen-value and the wave function is

$$E = 0, \quad F = -G = \exp[-Mr - \kappa_a |q| / (2Mr)]. \quad (70)$$

The requirement $\kappa_a > 0$ is necessary for the wave function to vanish at $r = 0$. However, in QED we know that the first term of the perturbation of κ_a is the Schwinger term $\kappa_a = e^2/2\pi = 0.00116$ and so it is positive.

The form of Eq. (70) of the eigen-function indicates that the radius of the orbit of the wave function is $r = 1/M$, the electron Compton wave length. Therefore, a magnetic monopole or the ($e^+ - p$) system is shielded by the electron cloud whose size is the Compton length of the electron $1/Mc$. This fact makes it much easier for the second nucleus

t to penetrate to the region of the composite particle (${}^*e - p$). In the next subsection, we shall see the drastic change of the numerical value the penetration factor T of (${}^*e - p$) – t in the electron-rich environment. Since the (electric) Coulomb potential is shielded, the penetration potential becomes

$$V_2(x) = +(e^2/x) \exp[-2Mx] - \kappa_{\text{tot}} \frac{D^*e e}{sm_p} \frac{1}{x^2}, \quad (71)$$

where M is the mass of the electron.

5.4. Penetration factor T of the (t+p) and (d+d) systems

In this subsection, we shall give the table of the penetration factor T for the d+d and p+t process when the penetration potential of the incoming second nucleus $V_2(x)$ of Eq. (67) is used in the WKB calculation of Eq. (51). We shall use the notation such as (${}^*e - p$) – t, which means that firstly the magnetic monopole *e traps the proton p and a composite particle (${}^*e - p$) is formed, and then the second nucleus t approaches to the composite particle (${}^*e - p$). In the process (${}^*e - t$) – p, the roll of p and t is interchanged. Numerical values of τ and T of Eqs. (52) and (51) are

	(${}^*e - t$) – p	(${}^*e - p$) – t	(${}^*e - d$) – d
$D = 1$	$\tau = 7.52$ $T = 2.93 \times 10^{-7}$	$\tau = 3.76$ $T = 5.39 \times 10^{-4}$	$\tau = 9.45$ $T = 6.22 \times 10^{-9}$
$D = 2$	$\tau = 4.51$ $T = 1.22 \times 10^{-4}$	$\tau = 2.41$ $T = 8.01 \times 10^{-3}$	$\tau = 7.88$ $T = 1.42 \times 10^{-7}$

These values of the penetration factor T should be compared with T in the vacuum

t+p	D+D
$\tau = 104.96$	$\tau = 121.20$
$T = 6.78 \times 10^{-92}$	$T = 5.33 \times 10^{-106}$

Therefore, in the framework of the ordinary nuclear physics, in which the constituent particles are proton and neutron, the nuclear reaction of the zero incident energy can- not occur. This is what almost all the nuclear physicists claim. On the other hand, if we extend the nuclear physics to include the magnetic monopole as an additional ingredient, the nuclear cold fusion reaction occurs rather freely. Since the Hamiltonian of such a system is known as given in Eq. (47), it is not difficult to construct the world in which *e , p and n are the ingredients, because from 1990s we have developed the techniques to treat the few-body system by solving honestly the simultaneous Schrödinger equations.

6. Problem of the Reproducibility of Nuclear Cold Fusion

The last mystery of the nuclear cold fusion is that such a reaction does not start on demand. It is said that we have to wait at least a few weeks before the heat generation starts anew. This sporadic nature of the nuclear cold fusion is the main obstacle in understanding the phenomenon as the scientific fact, or in applying it to the practical use. It is believed that when we reuse the successful cathode, the probability of starting of the heat generation increases. It is interesting to consider how to understand the sporadic nature, when the magnetic monopole plays the roll of the catalyst of the nuclear fusion reaction.

6.1. “One-particle catalyst”

We saw that if a magnetic monopole $*e$ exists in the domain of the high density deuteron, it forms the bound state ($*e-d$) and sometimes forms the doubly bound state ($d-*e-d$). However, since the size of the orbits of the deuterons at $*e$ is around a few fm, ($d-*e-d$) is unstable and two deuterons become a more stable ${}^4\text{He}$. Since the spin of ${}^4\text{He}$ is zero, there is no attractive potential between ${}^4\text{He}$ and $*e$, ${}^4\text{He}$ must be emitted with energy 23.8 MeV. Since we rely on the magnetic monopole floating in nature, which is the rare particle, nothing occurs until a magnetic monopole moves into and stops in the region where the density of the deuteron is high. In this way the probability comes into the scene. We need not worry about the apparent sporadic nature of the phenomenon when the physical law of the underlying mechanism is understood well.

In order to understand the non-reproducibility, it is useful to introduce the concept of the “one-particle catalyst”. In the ordinary catalyst, although the number of the catalyst particle $\langle N_c \rangle$ is much small compare to the particle number of the reactant $\langle N_r \rangle$, the value of $\langle N_c \rangle$ is still macroscopic number. Let us consider the case where $\langle N_c \rangle$ decreases to a finite number. Number $\langle N_c \rangle$ must be different from experiment to experiment and fluctuate around the average value $\langle N_c \rangle$ with the spread $\sqrt{\langle N_c \rangle}$. If the average $\langle N_c \rangle$ decreases further and becomes much smaller than 1, we must encounter the non-reproducibility. In decreasing $\langle N_c \rangle$, we must increase the strength of each catalyst particle properly.

The length of the track of the emitted α is around 0.1 mm, the energy of the α is transferred to the electron and then to the lattice in the neighborhood of the trapped magnetic monopole, which is the one-particle catalyst. Since, as we shall see in the next subsection, the trapping potential of the magnetic monopole is proportional to $1/T$, where T is the temperature of the place of $*e$, the magnetic monopole must hop to the neighboring cooler place. In fact Szpak and Mosier-Boss [?] observed by using the infrared camera, the discrete hot-spots are spreading in the cathode.

6.2. Energy of the magnetic monopole in the lattice

Let us consider a medium lattice, which consists of atoms with the magnetic dipole moment κ in the unit of the Bohr magneton $e/2m_e$. Suppose that at first the directions of the magnetic dipoles fixed on the lattice points are random, and consider what happen when a magnetic monopole of the strength $*eD$ moves into and stops in the lattice. The dipoles of the atoms must align and the energy of each dipole is $\Delta V = -\kappa(e/2m_e)(*eD)/r^2$, where r is the distance of the magnetic dipole from the magnetic monopole $*e$. Because of the thermal agitation, whose energy is $k_B T/2$, there is a sphere of radius R determined by the temperature T , and outside of which the directions of the dipoles are random. R is determined by

$$\kappa(e/2m_e)*eD/R^2 = \frac{k_B T}{2}. \quad (72)$$

The trapping energy of the magnetic monopole is the sum of the alignment energy in the sphere R , namely

$$V = -\frac{4\pi}{a^3} \int_0^R r^2 dr \kappa(e/2m_e)*eD/r^2, \quad (73)$$

where a is the lattice constant.

Because of the charge quantization condition $*ee = 1/2$, the numerical values of V and R become for the lattice constant 1\AA

$$V = -\left(\frac{\kappa D}{2}\right)^{3/2} \frac{14.24 \text{ keV}}{\sqrt{T}} \text{ and } R = \sqrt{\frac{\kappa D}{2}} \frac{2.97 \times 10^{-6} \text{ cm}}{\sqrt{T}}. \quad (74)$$

Therefore, for $T = 300^\circ$, $|V|$ is several keV and R is few nm in size.

6.3. Energy loss of the magnetic monopole in matter

If the magnetic monopole plays the roll of the catalyst of the nuclear fusion reaction, we must understand its behavior in the medium. The stopping power of a charged particle ze is given by the Bethe–Bloch's equation:

$$-\frac{dE}{dx} = \frac{K Z_{\text{med}} \rho_{\text{med}}}{A_{\text{med}}} \left(\frac{z}{\beta} \right) \left[\log \left(\frac{2m_e \gamma^2 \beta^2 c^2}{I} \right) - \beta^2 - \delta - \frac{C}{z_{\text{med}}} \right], \quad (75)$$

where $K = 4\pi N_A r^2 m_e c^2 = 0.3070 \text{ MeV cm}^2 / \text{g}$. Here Z_{med} and A_{med} are the charge and mass numbers of the medium and ρ_{med} is the mass density of the medium. δ and C are frequently small function and I is the order of the binding energy of the electrons in the medium.

Because the force between the incoming magnetic charge $*eD$ and the electron is the Lorentz force, we must change to $ze \rightarrow *eD\beta$ in Eq. (71) to get the stopping power of the magnetic monopole in a medium. There is another source to lose the energy of the magnetic monopole. The loss of the energy by the radiation is given by the Larmor's formula $dE/dt = -(2/3)e^2|a|^2$ where $|a|$ is the acceleration. The radiation loss of the magnetic monopole is

$$-\frac{dE}{dt} = -\frac{2}{3}(*eD)^2|\vec{a}|^2. \quad (76)$$

Since on the surface of the medium the trapping potential V changes, the acceleration becomes non-zero. Because of the large value of the magnetic “fine structure constant” $*e^2$, the radiation loss of the magnetic charge must be very large. In particular, when the medium is the collection of the nano-particle, the magnetic monopole passes through the surfaces many times and it loses energy effectively and trapped by the medium.

References

- [1] P.A.M. Dirac, *Proc. R. Soc. London A* **133** (1990) 60; J. Schwinger, *Science* **165** (1969) 757; A.O. Barut, *Phys. Rev. D* **3** (1973) 1747; T. Sawada, *Phys. Lett. B* **43** (1973) 517.
- [2] T.T. Wu and C.N. Yang, *Nucl. Phys. B* **107** (1976) 365.
- [3] J.J. Sakurai, *Modern Quantum Mechanics*, Benjamin Publishing Company Inc., 1983.
- [4] T. Sawada, *Found. Phys.* **23** (1993) 291.
- [5] S. Szpak and P.A. Mosier-Boss, *Phys. Lett. A* **221** (1996) 141.
- [6] Y. Kazama and C.N. Yang, *Phys. Rev. D* **15** (1977) 2300.



Research Article

A Review on Nuclear Products Generated During Low-Energy Nuclear Reactions (LENR)

Pamela A. Mosier-Boss *

Research Laboratory of Electronics, MIT, Cambridge, MA 02139, USA

Abstract

Given the response to the Fleischmann–Pons news conference in 1989, it became clear to many researchers in the field that excess heat was not convincing enough evidence to prove that nuclear processes were occurring inside a metal lattice. Skeptics attributed the excess heat to recombination of deuterium and oxygen gases and/or poor calorimetry, despite the fact that control experiments showed that this was not the case. Consequently, a number of researchers redirected their efforts from measuring heat to looking for nuclear products such as neutrons, charged particles, X- and gamma rays, and transmutation. The results of these efforts are discussed in this communication.

© 2012 ISCMNS. All rights reserved.

Keywords: Charged particles, Helium-4, Neutrons, Transmutation, X- and gamma rays

1. Introduction

When Stanley Pons and Martin Fleischmann held their press conference on March 23, 1989, the only evidence they had that nuclear processes were occurring inside the palladium lattice was excess heat. Their electrochemical cells were producing more heat than could be accounted for by chemical means. The lack of collaborating nuclear products, particularly neutrons, outraged many scientists. But that did not stop many scientists world wide from going into their laboratories to replicate the Fleischmann–Pons experiment and to look for evidence that the effect had a nuclear origin. Many of these efforts failed and the reasons for the failures are now understood. They include improper cell configurations causing inhomogeneous deuterium loading of the palladium, cracks in the palladium rods used in the experiments which impeded deuterium loading, and the lack of recognition that there was an incubation time needed to load the palladium rods with deuterium. In each of these instances, the experimental conditions used failed to achieve the high deuterium loadings and flux inside the lattice needed to initiate the effect. Since the Fleischmann–Pons announcement, continuing research, using a wide variety of techniques from electrolysis, gas loading, to glow discharge, has yielded evidence that supports the nuclear nature of the effect. Nuclear products that have been observed include tritium, neutrons, charged particles, gamma and X-rays, transmutation, as well as helium-4. A brief discussion

*E-mail: pboss@san.rr.com

of the experiments performed and their results follows. It is by no means complete. Yet it does illustrate the number of techniques and approaches that have been taken to measure LENR nuclear products. The fact that these different approaches yield similar results strengthens the validity of those results.

2. Neutrons and Tritium

In the March 23, 1989 press conference, Pons claimed that they had “established a sustained nuclear fusion reaction by means which are considerably simpler than traditional techniques.” He further claimed that the deuterium is driven inside a metal rod to such an extent that fusion between the deuterons occurs. Because of these claims, researchers conducted experiments looking for DD fusion products.

In thermonuclear fusion, the DD fusion reactions are:



In thermonuclear fusion, the branching ratio for reactions (1) and (2), n/T, is 1. That is, 50% of DD fusion follows reaction (1) and 50% follows reaction (2). Reaction (3) occurs 10^{-6} of the time and is negligible. If deuteron fusion reactions were occurring inside the palladium lattice and if those reactions were similar to what was observed in plasma fusion, expected products would include tritium and neutrons. Because of these expectations, early investigators focused on detecting tritium and 2.45 MeV neutrons.

When researchers at India's Bhabha Atomic Research Center (BARC) heard the Fleischmann–Pons announcement, they began to conduct electrolysis experiments using a Milton-Roy electrolytic cell, Fig. 1(a) [1]. The cathode area was 300 cm^2 and the cells could operate up to 100 A current. During electrolysis, the cell was monitored using two different kinds of neutron detectors – BF_3 counters embedded in paraffin blocks for thermal neutron detection and proton recoil plastic scintillator counters for fast neutron detection. The background was monitored using ${}^3\text{He}$ counters embedded in paraffin. At the same time they recorded cell current, voltage, and temperature, and they collected samples for tritium analysis. Figure 1(b) shows the results of the BF_3 and proton recoil neutron detectors during the first run in April of 1989. Clearly the detectors track one another. As the current was slowly increased to 100 A, the cell overheated which caused the trip circuit to turn off cell power. This was followed by a burst of neutrons that was approximately two orders of magnitude larger than background levels over a 2 min interval. Of the 11 cells, six saw a neutron signal within 9 h of operation, one within 24 h, and two showed a neutron signal after 2 weeks. The neutron emissions were observed to stop after continued electrolysis. It was also observed that high D/Pd loadings were not required to obtain a neutron emission. But more importantly, it was observed that, although neutrons and tritium were produced simultaneously, the branching ratio (n/T) was not 1 as observed in thermonuclear fusion. For the Pd/D system, the n/T ratio was measured to be $\sim 10^{-7}$.

Iwamura et al. [2] of Mitsubishi Heavy Industries gas-loaded palladium foils with deuterium to a D/Pd loading of 0.66. Once loaded, the deuterated foils were sealed with either a thin aluminum or gold film. The samples were then placed in a vacuum chamber and set on a heater. The chamber was equipped with two ${}^3\text{He}$ neutron detectors, a NaI scintillator detector for gamma-ray spectroscopy, and a high-resolution quadrupole mass spectrometer for gas analysis. The samples were heated to 400 K causing the release of deuterium. During deuterium gas desorption from the samples, they observed the emission of neutrons and tritium as well as charged particles. No gamma rays were detected using these palladium structures.

A consortium of scientists from the Russian Academy of Sciences, Hokkaido University, New Hydrogen Energy Laboratory in Sapporo Japan, and Osaka University conducted experiments using Au/Pd/PdO heterostructures [3].

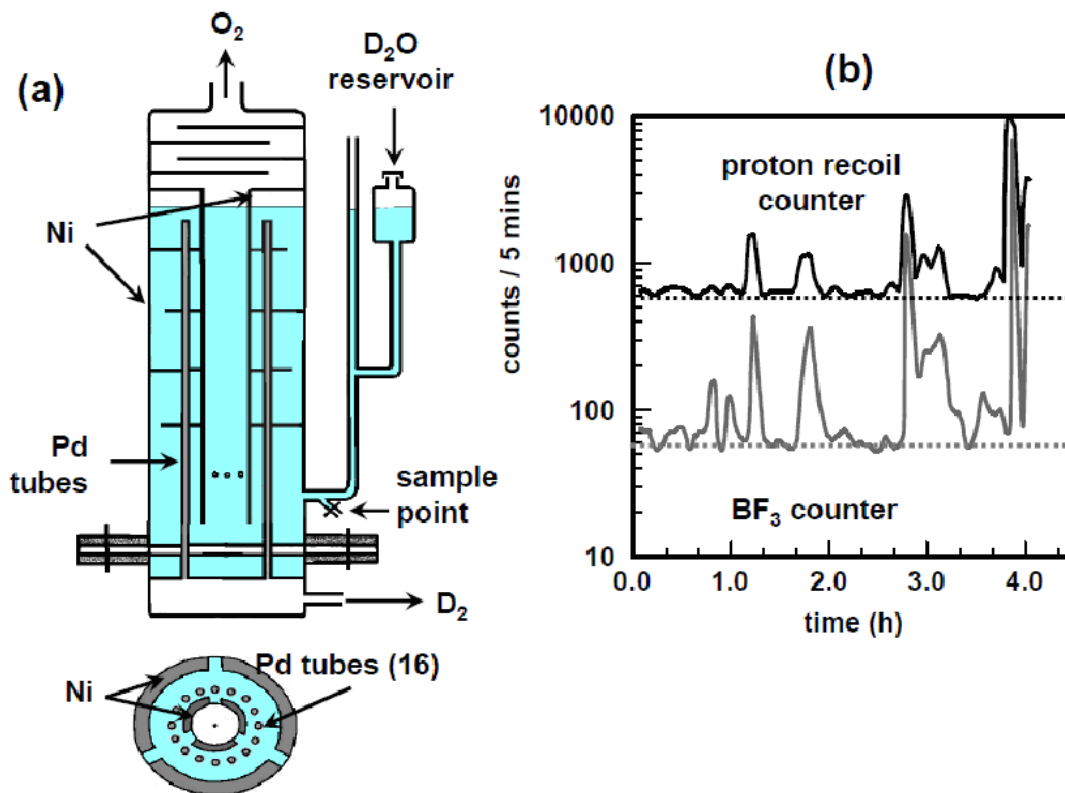


Figure 1. (a) Schematic of a Milton-Roy electrolytic cell used in the BARC experiments. AgPd tubes are 200 mm in height and 3 mm in diameter. (b) Neutron counts measured as a function of time using a proton recoil counter (top) and a BF₃ counter (bottom). Dotted lines indicate background count rates for both detectors. Reproduced with permission from Srinivasen

These heterostructures possess high deuterium loading capacity, high mobility of deuterium at the Pd–PdO interface, and a screening potential, U_S , of 600 eV. After electrochemically loading the Au/Pd/PdO heterostructures with deuterium, they took the samples out of the electrolyte and monitored the exothermic desorption of deuterium using a detection system based upon a liquid scintillator that responds to neutrons and gamma rays, a silicon surface barrier detector that detects energetic particles, and CR-39 detectors that responds to both charged particles (alphas, protons, and tritons) and neutrons. Using this array of detectors, they saw charged particles with energies between 1 and 3 MeV and neutrons between 2.4 and 2.8 MeV. They concluded that the energies of the charged particles and neutrons were consistent with those resulting from DD fusion reactions, (1) and (2). However, they were not able to determine the branching ratios of those reactions.

Other researchers who have measured tritium in electrolytic cells include Ed Storms [4] of Los Alamos National Laboratories, John Bockris [5] of Texas A&M State College, and Szpak et al. [6] of SPAWAR Systems Center Pacific. Storms measured tritium, in both the gas and liquid phases, during electrolysis using palladium and palladium alloys with lithium, carbon, sulfur, boron, and beryllium. In these studies, excess tritium was observed in $\sim 10\%$ of the cells. No excess tritium was measured for the Pd alloys, which were prepared by arc-melting Pd powder with the other element under an argon atmosphere. Storms also looked at the effect of various surface treatments on the production of

tritium. He showed that palladium heated in dihydrogen sulfide to form a sulfide layer did not produce excess tritium while some cells using palladium heated in paraffin vapor did show excess tritium. Of the solution additives examined (thiourea, wheat flour, iron, silver, mercury, uranium-238, lithium sulfide, arsenic trioxide, and silver sulfide), only wheat flour and arsenic trioxide sometimes gave excess tritium.

John Bockris [5] also measured tritium in both gas and liquid phases. Out of 58 experiments using bulk palladium cathodes, 18 showed tritium production. He showed that the tritium production occurred in bursts and that the tritium did not correlate, either temporally or quantitatively, with the heat production. These experiments showed that the measured tritium was less than 0.1% of that needed to produce the observed heat, assuming DD reaction (1) is the heat producing channel.

Szpak et al. [6] used the palladium/deuterium co-deposition process in their experiments. Instead of bulk palladium electrodes, they started with a solution of palladium ions. When a current is applied, palladium plates out onto a cathode in the presence of evolving deuterium gas. Measurements were made of both the gas and the liquid. Out of ten experiments, six gave excess tritium. The tritium production was observed to occur in bursts. John Bockris replicated the co-deposition process and saw excess tritium in six out of nine cells. While the co-deposition process produced tritium more reliably than bulk palladium, the amount of tritium produced using the co-deposition process was orders of magnitude less than what had been observed for those bulk palladium cathodes that did produce tritium.

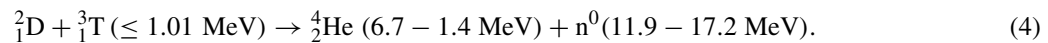
Claytor et al. [7], of Los Alamos National Laboratories, have shown tritium production from a low-voltage deuterium discharge on palladium and other metals. In their procedure, a wire is oriented perpendicular to and a few millimeters above a circular plate. Deuterium gas is added to the chamber and the wire is then pulsed negatively with currents between 2 and 5 A (voltages varied between 1500 and 2500 V) to create a light blue plasma (D^{2+}) with areas of pink (D^{3+} or D^{+}). Tritium concentration in the gas was monitored continuously using a Femtotech tritium gauge. At the end of the experiment, the tritium concentration was verified by collecting the gases, running them through a recombination chamber to convert the tritiated deuterium gas into tritiated heavy water. The tritium content of the resultant liquid was then determined using a liquid scintillator. The real-time measurements showed no tritium production when platinum wires were used in both hydrogen and deuterium gas discharges. No tritium was observed for the palladium/hydrogen gas system. However the palladium/deuterium gas system produced tritium at rates of 0.1–0.2 nCi/h (background is 0.002–0.01 nCi/h). It was found that the tritium output depended upon the temperature, pressure, and current applied to the cells. It was also sensitive to the purity and metallurgical condition of the palladium used in the experiments.

Neutrons have been measured by Mizuno et al. [8] of Hokkaido University, Francesco Scaramuzzi [9,10] of ENEA in Italy, Roussetski [11] of the P.N. Lebedev Physical Institute in Russia, and Mosier-Boss et al. [12,13]. In their experiments, Mizuno et al. [8] used three ^3He neutron detectors placed 50 cm above and apart from the cell. To reduce noise, the detectors were covered with an electromagnetic shield. Neutron emissions were detected by the coincidence and the anti-coincidence method with one detector that was covered with a cadmium film. The palladium wire cathodes used in these experiments were 3 cm long and 1 mm in diameter. After first loading the palladium wires in a heavy water electrolyte for 3 h, they were placed in a light water electrolyte and the cell voltage was increased from 30 to 85 V. With this voltage change, seven out of ten cells gave bursts of neutrons that lasted between 2.6 and 200 s. Total neutron counts during these bursts ranged from 25,800 to 1,573,800.

Shortly after the 1989 Fleischmann–Pons announcement, Scaramuzzi et al. [9,10] began to conduct deuterium gas-loading experiments of titanium shavings. Like palladium, titanium also absorbs hydrogen isotopes. A BF_3 neutron detector was used to monitor the gas loading. After immersion in a liquid nitrogen Dewar for a short period of time, the stainless steel chamber containing the deuteriated titanium was taken out of the Dewar to warm up and to create non-equilibrium conditions. Two events of neutron bursts were observed. The first event lasted for forty hours. However, the reproducibility of these experiments was very poor. In 2003, Keeney et al. [14] reported on similar gas loading experiments using titanium foil. They used ^3He neutron detectors. The reproducibility of their experiments was 40%. They also looked at electrolytic loading of the titanium foils. Although neutron emissions were observed,

the reproducibility was much less than that observed for the gas loading experiments.

In 2000, Roussetski [11] prepared PdO/Pd/PdO and PdO/Pd/Au samples that were electrochemically deuterated. After electrolysis, each sample was placed on CR-39, a solid state nuclear track detector (SSNTD), and the sample was heated to $\sim 50^\circ\text{C}$ to stimulate desorption of deuterium. This process was repeated a number of times. Analysis of the detectors showed tracks consistent with DD reaction products as well as triple tracks that are diagnostic of the carbon shattering reaction, $^{12}\text{C}(n,n')3\alpha$, caused by $a \geq 9.6$ MeV neutron. In plasma fusion, one potential source of these neutrons is the DT thermonuclear fusion reaction:



However, Roussetski found that the mean DT neutron flux emitted from the deuterated samples was higher than the yield of tritons from DD fusion reaction (1), suggesting that there was either another source of fast tritons or fast neutrons. This was the first evidence suggesting that both primary and secondary fusion reactions were occurring in the palladium/deuteride system.

Mosier-Boss et al. [12,13] have been monitoring their palladium/deuterium co-deposition experiments using CR-39. Using these detectors, they have observed tracks on both the front and the backsides of the detectors. The only particles that can traverse through 1 mm thick CR-39 detectors are ≥ 40 MeV alphas, ≥ 10 MeV protons, or neutrons. The size distribution of the tracks on the backside of the CR-39 detectors was consistent with the energy of protons and neutrons observed in DD fusion reactions (1) and (2), respectively, and of neutrons that are observed in DT fusion reaction (4). They also observed triple tracks [12] in the CR-39 detectors, like those shown in Fig. 2(a). In Fig. 2(a), the right hand images, which are an overlay of an image taken with the microscope optics focused on the surface of the detector and another taken with the optics focused on the bottom of the track, clearly show three particles breaking away from a center point. Very few of these triple tracks, usually between five and ten, are observed in the CR-39 detectors used in the co-deposition experiments. These triple tracks have been observed on both the front and backsides of the detectors. Figure 2 compares DT fusion generated triple tracks, with the palladium/deuteride generated triple tracks. It can be seen that the features of the palladium/deuteride generated triple tracks, Fig. 2(a), are indistinguishable from those of DT fusion generated triple tracks, Fig. 2(b).

3. Charged Particles

If DD fusion reactions were occurring inside the palladium lattice as conjectured by Pons and Fleischmann in their March 23, 1989 press conference, these reactions should produce charged particles in addition to neutrons. Techniques used to measure these charged particles include silicon surface barrier detectors, solid state nuclear track detectors such as CR-39, and scintillating detectors.

Shortly after the Fleischmann–Pons announcement, Ed Cecil [15] of the Colorado School of Mines implanted deuterium in a $6 \mu\text{m}$ thick palladium film. When an electric current was passed through the thin film, 5 MeV charged particles were detected using a silicon surface barrier detector. The same experiments using thin deuterated titanium films gave similar results. George Chambers [15] of NRL bombarded titanium foils with 350 eV deuterons and detected 4.9 MeV charged particles. Of 13 experimental runs, four produced charged particles and five did not. In four of the null experiments, the titanium foil delaminated from the base thereby voiding the run. Iida et al. [16] of Osaka University also conducted deuteron implantation experiments on titanium foils. When titanium foils with an aluminum oxide layer were bombarded with 243 eV deuterons, peaks in the 5–12 MeV range were observed. These peaks were attributed to alpha particles resulting from multibody fusion reactions as proposed by Takahashi, also of Osaka University. In 2003, Keeney et al. [17] reported on gas loading experiments on titanium foils. Using a PMT/dual scintillator system, they were able to detect 2.6 MeV protons.

In 1990, Li et al. [18] of Tsinghua University in China were the first to use CR-39 SSNTDs to detect charged particle emission in palladium. In these experiments, palladium foil was in direct contact with the CR-39 detector. The

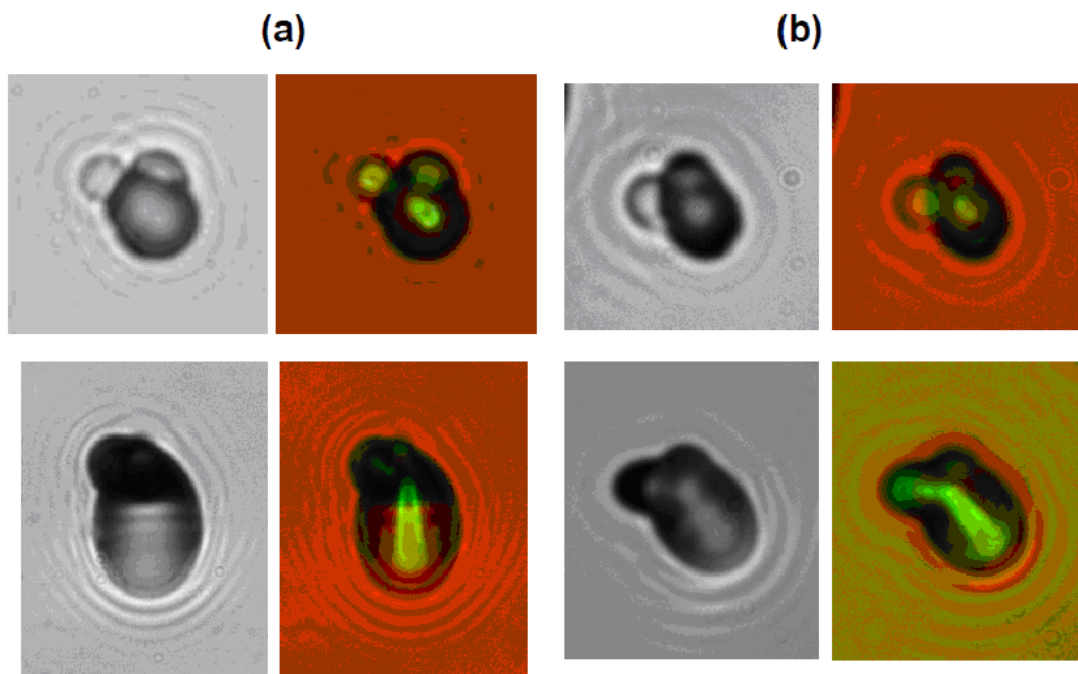


Figure 2. Photomicrographs of (a) Pd/D co-deposition generated and (b) DT neutron generated triple tracks. In (a) and (b), the left-hand images were taken with the microscope optics focused on the surface of the detectors. The right-hand images are an overlay of two images taken at two different focusing depths (surface and bottom of the tracks). Reproduced with permission from Mosier-Boss.

palladium was then gas loaded with either hydrogen or deuterium. No tracks were observed for the hydrogen loading experiments. However, a large number of tracks in the CR-39 were obtained as a result of the palladium/deuteride experiment. It was found that when palladium was cleaned in aqua regia, no tracks were obtained. Li et al. concluded that the aqua regia treatment poisoned the surface of the palladium. From these results Li et al. concluded that the observed nuclear effects were related to some surface phenomenon.

The $Y_1Ba_2Cu_3O_{7-8}$ (YBCO) high temperature super conductor has the ability to absorb hydrogen. Pellets or powders of $Y_1Ba_2Cu_3O_{7-8}$ were placed in contact with CR-39 detectors. The pellets/powders were then gas loaded with deuterium. After a one to two days exposure to the deuterated $Y_1Ba_2Cu_3O_{7-8}$ pellets/powders, the CR-39 detectors were etched. Microscopic examination of the detectors showed tracks with a density of $\sim 3 \times 10^5$ tracks cm^{-2} [19].

As discussed vide supra, Lipson et al. [3] used CR-39 detectors to detect charged particles emitted from the deuterated Au/Pd/PdO heterostructures. In these experiments, the heterostructures were electrochemically loaded with deuterium. Once loaded, the heterostructures were placed in contact with the CR-39 detectors and the temperature was cycled to induce desorption of deuterium. Tracks consistent with 2.5–3.0 MeV protons and 0.5–1.5 MeV tritons were observed in the CR-39 detectors.

In 2002, Oriani and Fisher [20] were the first to report the use of CR-39 detectors in an electrolysis experiment. They placed the detectors above and below the Pd foil cathode so as to not impede uniform loading of the cathode with deuterium. Because charged particles cannot travel far in an aqueous medium (10 μm of water slow alpha particles by 2 MeV), this is not the optimum geometry to detect charged particles. During each run, control detectors were immersed in bottled electrolyte solution. Track densities ranged between 59 and 541 tracks cm^{-2} for the control detectors and

156–3760 tracks cm^{-2} for detectors used in active cells. They concluded that the reactions responsible for the particles causing the tracks did not occur at the distant cathode but most likely occurred in the electrolyte very close to the plastic surface. Their more recent experiments involving sequential etching of the detectors show additional tracks deeper inside the plastic. The tracks could either be due to recoils from neutrons or from ≥ 10 MeV protons.

Also in 2002, Lipson et al. [21] at the University of Illinois began to conduct in situ electrolysis experiments in which the CR-39 detectors were in direct contact with palladium foils. They observed tracks due to charged particles in the detectors and concluded that the cathode was the source of those particles. Using Cu spacers between the cathode and the detector, they were able to identify the particles as being 11–16 MeV alphas and ~ 1.7 MeV protons.

Mosier-Boss et al. [22,23] have used CR-39 detectors in their palladium/deuterium co-deposition experiments. Track density was highest where the cathode had been in contact with the detector indicating that the source of the tracks is the cathode. The distribution of tracks along the cathode was inhomogeneous indicating that some Pd sites were more active than others. Control experiments showed that the tracks were not due to radioactive contamination of the cell components; nor were they due to impingement of the deuterium gas bubbles on the surface of the detector; nor were they the result of chemical attack by D_2 , O_2 , or Cl_2 gases; nor were they due to the metal dendrites of the palladium deposit piercing into the plastic. Spacer experiments indicated that the charged particles formed had energies on the order of 1–3 MeV.

Karabut et al. [24] of the Scientific Industrial Association LUTCH in Russia have conducted glow discharge experiments using palladium in deuterium gas. They used both silicon surface barrier and CR-39 detectors in these experiments. The silicon surface barrier detectors measured charged particles up to 18 MeV in energy. Tracks were observed in the CR-39 detectors. The measured track density was on the order of 2×10^5 tracks cm^{-2} .

4. Gamma/X-rays

The first evidence of gamma/X-ray emission is shown in Fig. 3(a). At the end of a deuterium plasma loading experiment, Srinivasan [25] of BARC placed the titanium rod on a sheet of Polaroid paper. Figure 3(a) is the positive image of the Polaroid negative. Dark areas are regions of greater activity. Srinivasan attributed the observed image to be due to X-rays from tritium generated in the titanium rod. This same electrode was repeatedly autoradiographed over a one-year period, revealing the same pattern.

Knowing of the BARC results, McKubre [26] of SRI took a palladium cathode that had produced excess heat and placed it between two layers of Polaroid film for 12 days. The negative image is shown in Fig. 3(b). Fogging of the film was observed indicative of some type of ionizing radiation. The points of light with diffuse halo exposure suggest that some of the radiation may be coming from point sources within the metal and being scattered by the lattice structure.

At the end of a palladium/deuterium co-deposition experiments on a silver disk, Szpak [22] placed a plastic sheet over the cathode and a piece of photographic film on top of that. After a week, the film was developed and the positive image is shown in Fig. 3c. The one aspect that all three images have in common is that the emission of X-rays is inhomogeneous and that some sites are more active than others. Measurements of co-deposition experiments using high purity germanium (HPGe) and lithium-doped silicon detectors showed that the emission of radiation was sporadic and of limited duration [27]. They also showed that the energy distribution was broad with the occasional emergence of peaks near 20 and 8–12 keV.

Miles [28] of China Lake placed dental film around his calorimeter cells using bulk palladium cathodes. He also observed fogging of the film. The film closest to the cathode showed the greatest exposure. Karabut et al. [24] also reported on the emission of 200 keV gamma rays in their glow discharge experiments.

Violante et al. [29] of ENEA and SRI conducted electrolysis experiments using thin films of copper and/or nickel or palladium. The experiments were monitored using a HPGe detector optimized for the 2–22 keV energy range. The copper/palladium cathodes gave signals significantly above background in the energy range where the palladium X-ray

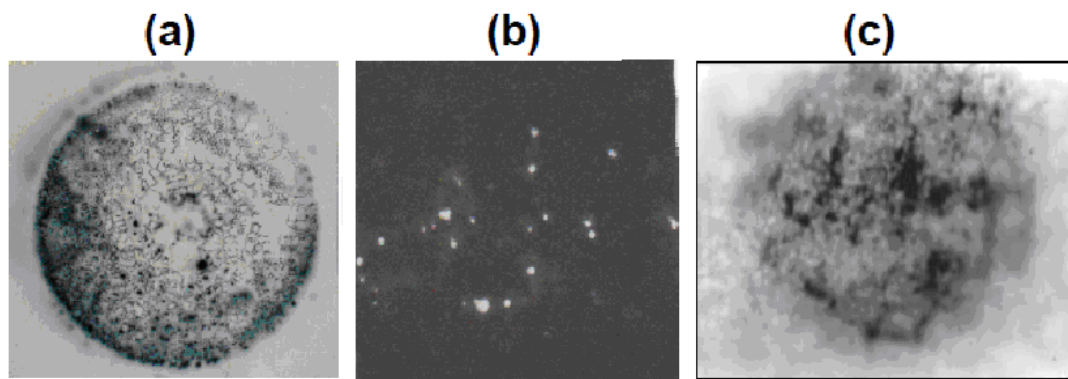


Figure 3. Autoradiographs of cathodes used in LENR experiments. These autoradiographs were obtained by placing photographic film in contact with the cathode over a period of 7–12 days. In the positive images, dark areas show greater activity while the reverse is true for negative images. (a) Positive image of a titanium rod that has been plasma loaded with deuterium. Reproduced with permission from Srinivasan. (b) Negative image of a bulk palladium cathode that had produced excess heat for SRI. Reproduced with permission from McKubre. (c) Positive image of a cathode used in a palladium/deuterium co-deposition experiment. A 100 μm thick plastic sheet separated the cathode from the photographic film. Reproduced with permission from Mosier-Boss.

lines occur. For the copper/nickel cathodes, X-ray emissions and a change in the copper-63/copper-65 isotopic ratios were observed after the deuterium-loaded cathodes had been irradiated with a HeNe laser for 3 h.

Prelas et al. [30] of the University of Missouri used a Maxwellian plasma and sub-atmospheric deuterium gas to load palladium metal. The experiments were monitored using both a BF_3 neutron detector as well as a sodium iodide (NaI) gamma-ray detector. In these experiments, it was observed that an increase in the neutron counts and gamma-ray readings occurred whenever the deuterium plasma was formed. The NaI detector showed a mysterious, broad gamma-ray peak at 8.1 MeV.

5. Transmutation

Kevin Wolf [31] of Texas A&M State College was electrolyzing three palladium cathodes simultaneously. The experiment was monitored using both a neutron and a gamma ray detector. During the electrolysis, the neutron counts increased from a background of 24 counts/h up to 150 counts/h, then leveled off to 100 counts/h over a 21 h period. During that time interval, the gamma ray counts stayed at background levels. After 21 h, the neutron counts dropped back to background, but the gamma ray counts increased. Upon termination of the experiment, it was found that all three cathodes had become mildly radioactive. Gamma ray spectra of the cathodes obtained using a germanium detector showed the presence of isotopes of rhodium, silver, and ruthenium that had not been present prior to the experiment.

John Bockris [32] analyzed his bulk palladium cathodes before and after his electrolysis experiments. The analysis of the cathode was done at 1 μm in depth. He observed the production of magnesium, silver, silicon, calcium, titanium, iron, copper, zinc, and platinum. Similar results were reported by Mizuno [33]. In addition to the elements Bockris had observed, Mizuno also detected chromium. He also showed that the new elements accumulated in holes and cracks on the bulk palladium cathode which formed during electrolysis. Also some of the new elements had isotopic distributions different from the natural ones, with the largest deviations found within the outermost 1 μm layer of the cathode. Using thin palladium films, Miley et al. [34] of the University of Illinois observed significant shifts in isotope ratios from natural abundance of a number of elements.

John Dash [35] of Portland State University conducted electrolysis experiments using titanium cathodes. Excess

heat was produced at the rate of about 1.2 W during electrolysis of heavy water. Analysis of the electrodes before and after electrolysis with a scanning electron microscope (SEM) and an energy dispersive spectrometer (EDS) revealed that new surface topographical features with concentrations of unexpected elements (V, Cr, Fe, Ni, and Zn) formed during electrolysis. He also did palladium/deuterium co-deposition experiments on bulk palladium foils. These experiments showed that co-deposition enhanced the production of excess enthalpy. SEM-EDS analysis of the cathodes showed the presence of silver.

Szpak et al. [36] performed palladium/deuterium co-deposition experiments on gold foil in the presence of either an external electric or magnetic field. Upon termination of the experiments, the cathodes were subjected to SEM analysis. Fractal structures, craters, and micro-volcano like features were observed in the SEMs. These features are suggestive of localized melting of the palladium deposit. Elemental analysis of these features using EDS showed the presence of new elements such as silicon, aluminum, calcium, magnesium, iron, zinc, chromium, and nickel. The distribution of these new elements on the surface of the cathodes was not uniform indicating that their presence could not be the result of contamination.

A consortium of Italian scientists did hydrogen and deuterium gas loading of palladium samples [37–39]. Once loaded, these samples were irradiated with either a HeNe or a 308 nm excimer laser. SEM analysis of the palladium showed the formation of small craters and caverns. Associated with these craters were the following new elements: aluminum, silicon, sulfur, chlorine, iron, cadmium, platinum, chromium, magnesium, titanium, and zinc.

Glow discharge experiments done by Karabut [40] and others also yielded new elements. The new elements obtained are the same as those obtained in the electrolysis experiments described above.

Iwamura et al. [41] observed transmutation that was induced by deuterium gas permeation through palladium complexes. A schematic of their experimental set-up is shown in Fig. 4(a). Figure 4(b) shows a schematic and an SEM of one of their palladium complexes. When the source metal is cesium, in situ X-ray photoelectron spectroscopy (XPS) measurements showed a decrease in the cesium peaks with a simultaneous emergence of peaks due to praseodymium as deuterium permeated through the sample. This was confirmed by ex situ X-ray fluorescence (XRF) measurements of the samples. When the source metal was strontium, gas permeation studies showed a decrease in strontium with a simultaneous increase in molybdenum. Secondary ion mass spectrometry (SIMS) analysis showed significant changes in the isotopic ratios of the molybdenum, as shown in Fig. 4(c).

6. Helium-4

In 1991, Miles et al. [42] showed that helium-4 production temporally correlated with the excess heat production. In these experiments, the gases evolved during electrolysis were collected and were sent away for analysis using a high resolution mass spectrometer. Helium-4 was observed in those samples collected when the cell was giving off excess heat.

In 1991, Bockris et al. [43] terminated an electrolysis experiment in which the palladium cathode was producing tritium. The cathode was removed from the cell and immersed in liquid nitrogen for a week to prevent helium from permeating out of the cathode. The cathode was then cut up into smaller pieces, packed in dry ice, and sent away for analysis by high resolution mass spectrometry. To determine the helium-4 content, the sample was melted in a resistance-heated tungsten-wire crucible in the mass spectrometer's high temperature vacuum furnace. Excess helium-4 was observed in nine out of the ten pieces of this tritium-producing cathode. The amount of helium-4 in these nine pieces varied between 1.7 and 166.8 billion helium-4 atoms. Background samples contain 0.5 billion helium-4 atoms. The majority of the helium-4 was found in the near-surface regions of the cathode and not within the bulk. No helium-4 was observed above background in the non-electrolyzed palladium from the same virgin stock or in that platinum anode material. Because earlier helium-4 claims suffered from the criticism of possible permeation through the glass cells, this was the first substantiated report of the production of helium-4.

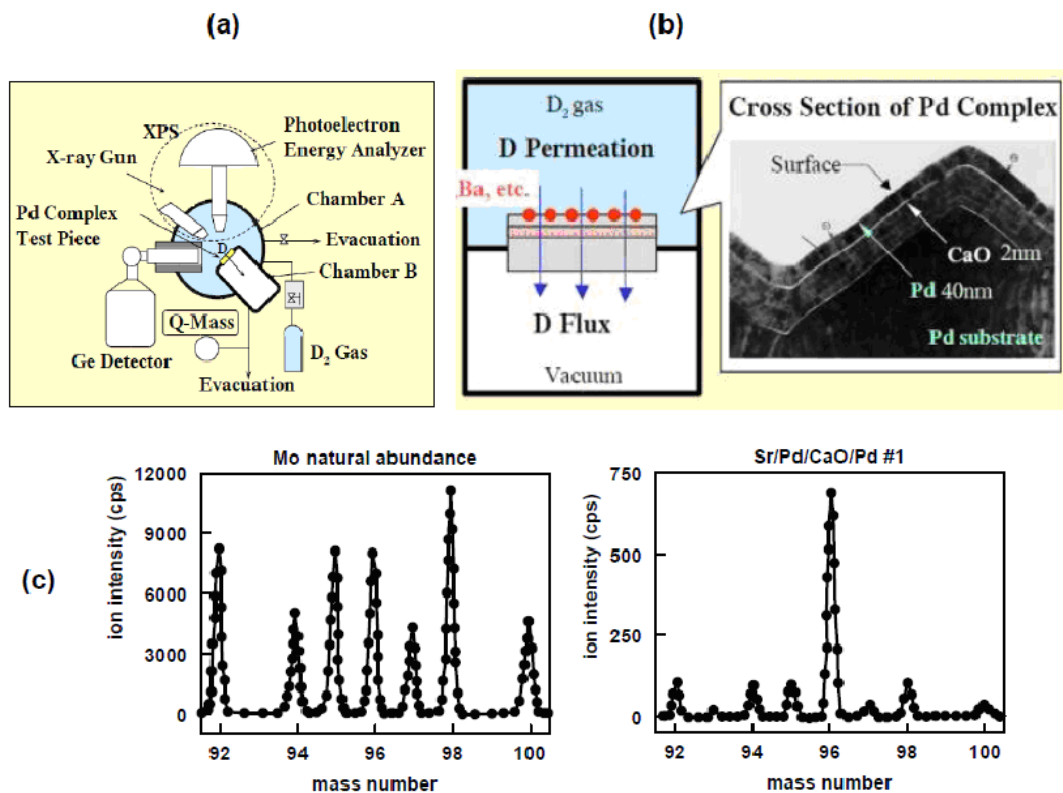


Figure 4. (a) Schematic of the Iwamura deuterium gas permeation experiment. (b) Structure of the palladium complex comprised of M/Pd (400 Å) /CaO and Pd (1000 Å) / Pd (0.1 mm), where M = Cs, Sr, and Ba. (c) Comparison of the natural molybdenum (left) with that observed in the palladium complex (right). Reproduced with permission from Y. Iwamura.

In 1998, McKubre et al. [44] of SRI reported that they had completed a replication of Miles' results. They conducted open cell electrolysis in metal sealed cells incorporating active exclusion of helium-4. The evolving gases were likewise collected in metal vessels and were analyzed by high-resolution mass spectrometry. In three instances when excess power was measured, helium-4 was found in the electrolysis gases. If the helium-4 results from reaction (3), the helium-4 found in the gases constituted only 76% of expectation. However, the results of Bockris et al. [43] showed that helium can be trapped inside the palladium. McKubre et al. [44] concluded that, if helium-4 is produced in association with excess power, it is not released to the gas phase immediately, or completely.

Following the Miles' replication, McKubre et al. [44] conducted electrolysis experiments in a closed cell system using bulk palladium. The cell was leak tight and was designed to allow sampling of the gases in the headspace. During a period of excess power, the gas phase contained only 62% of the helium-4 expected if reaction (3) was the source of the helium-4. The remainder of the helium-4 was retained in the cathode as was determined, in situ, by subjecting the cathode to an extended period (~200 h) of compositional and thermal cycling by varying the current density in both anodic and cathodic directions. The high anodic currents used in this process increased the temperature of the palladium electrode by ~30°C and caused microcracks to form. Both the temperature increase and anodic current drove deuterium out of the lattice thereby quenching the nuclear processes occurring inside. The microcracks formed

in the cathode provided a means for helium-4 to escape. This was the first quantitative correlation between heat and helium-4.

De Ninno et al. [45] of ENEA in Italy sputtered palladium on an inert surface, wound in a ‘bustrophedic’ geometry. The resultant cathode is 100 cm long, 50 μm wide, and 2 μm thick. The cathode was loaded with deuterium electrolytically. The gases evolved during the experiment were collected in a storage vessel. A 6.29% aliquot of this gas was periodically sent to a high resolution mass spectrometer for analysis. Excess heat was measured using a Peltier element that was in good thermal contact with the cathode. Whenever the cathode temperature increased, helium-4 in the gases was measured. As the amount of excess power increased, localized melting of the palladium cathode occurred which caused the experiments to terminate. Because of the extended damage in many separated subsections, it is highly unlikely that the melting of palladium was due to the Joule effect.

In 1998, Gozzi et al. [46] built a calorimetric system, with a recombiner, that allowed online sampling of the residual gases for detection of helium-4 using a high resolution mass spectrometer. Measurements of helium-4 were not performed in a continuous mode. Consequently, a significant volume of the electrolysis gas mixture is lost without being analyzed. Despite that, they noticed that helium-4 in the gas stream temporally correlated with the excess heat. However, the amount of helium was less than the amount predicted if it was produced by reaction (3). At the end of the experiment, the cathode was cut up into smaller segments. Each segment was heated to melting while under high-vacuum pumping. The evolved gases were then analyzed, using the mass spectrometer, for helium-4. Unlike Bockris [43] and McKubre et al. [44], Gozzi et al. [46] did not find any helium-4 inside the palladium cathode. Although helium-4 diffuses slowly through palladium, the presence of micro-cracks in the palladium would cause helium-4 to be released more readily into the atmosphere. It should be noted that, unlike Bockris et al. [43], Gozzi et al. [46] did not immerse the cathode in liquid nitrogen prior to analysis which would have prevented the release of helium-4 through micro-cracks.

In 1998, Lester Case [47] of Fusion Power Inc. had claimed to see excess heat and helium-4 when palladium on a carbon supported catalyst was gas loaded with deuterium. McKubre et al. [44] conducted a series of experiments to verify the Case results. In these experiments, the catalyst was placed in a stainless steel vessel that was connected to a steel manifold. Periodic measurements of helium-4 were made by direct connection to a high resolution mass spectrometer. Hydrogen gas loading showed no excess heat or helium-4. In contrast, both heat and helium-4 were observed to correlate with deuterium gas loading.

Arata and Zhang [48] of Osaka University had reported on obtaining large quantities of excess heat using a ‘double structured’ cathode comprised of a palladium tube filled with palladium black. McKubre et al. [44] replicated the heat results of Arata and Zhang. Post analysis of the cathodes showed the presence of both helium-4 and helium-3.

In 2008, Arata and Zhang [49] reported on heat and helium-4 production as a result of deuterium gas loading of palladium/zirconium oxide nanopowders. No heat or helium-4 were observed in the hydrogen loading experiments. The heat effects have been replicated by Kitamura et al. [50] of Kobe University.

7. Conclusions

Since the announcement by Pons and Fleischmann in 1989, researchers worldwide have conducted experiments to detect nuclear ash to show that nuclear processes are occurring inside the metal lattice. Methods to load hydriding materials, such as Pd, Ti, and YBCO, with deuterium included electrolysis, gas loading, and glow discharge. Both real-time nuclear diagnostics and constantly integrating detectors have been used in these experiments. Regardless of the method or the analytical technique used, the following nuclear emissions have been observed: gamma and X-rays, energetic charged particles and neutrons, and transmutation. These nuclear emissions are consistent with those observed for primary and secondary fusion reactions. Taking all of the data together, there is compelling evidence that nuclear reactions can and do occur inside a metal lattice once the appropriate conditions to initiate those reactions have been

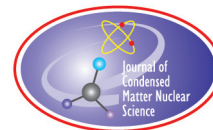
achieved.

References

- [1] M. Krishnan, S. Malhotra, D. Gaonkar, M. Srinivasen, S. Sikka, A. Shyam, V. Chitra, T. Iyengar and P. Iyengar, Cold fusion experiments using a commercial Pd–Ni electrolyser, *BARC Studies in Cold Fusion*, P. Iyengar and M. Srinivasen (Eds.), Bhabha Atomic Research Centre, Trombay, Bombay, India, 1989, A1, pp. 1–10.
- [2] Y. Iwamura, T. Itoh and I. Toyoda, Observations of anomalous nuclear effects in D₂–Pd system, *Proc.: Fourth Int. Conf. on Cold Fusion*, Vol. 3, *Nuclear Measurements Papers*, Lahaina, Maui, Hawaii. Dec. 6–9, 1993, T.O. Passell (Ed.), Electric Power Research Institute, Palo Alto, CA, 1994, pp. 12.1–12.9.
- [3] A. Lipson, F. Lyakhov, A. Roussetski, T. Akimoto, N. Asami, R. Shimada, S. Miyashita and A. Takahashi, Evidence for low-intensity D–D reaction as a result of exothermic deuterium desorption from Au/Pd/PdO:D heterostructure, *Fusion Sci. Technol.* **38** (2000) 238–252.
- [4] E. Storms and C.L. Talcott, Electrolytic tritium production, *Fusion Technol.* **17** (1990) 680–695.
- [5] J. Bockris, C.-C. Chien, D. Hodko and Z. Minevski, Tritium and helium production in palladium electrodes and the fugacity of deuterium therein, *Frontiers Sci. Series No. 4, Proc. of the Third Int. Conf. on Cold Fusion*, Nagoya, Japan, October 21–25, Nagoya Japan, H. Ikegami (Ed.), Universal Academy Press, Tokyo, Japan, 1993, p. 231.
- [6] S. Szpak, P. Mosier-Boss, R. Boss and J. Smith, On the behavior of the Pd/D system: evidence for tritium production, *Fusion Sci. Technol.*, **33** (1998) 38–51.
- [7] T. Claytor, J. Jackson and D. Tuggle, Tritium production from a low-voltage deuterium discharge on palladium and other metals, *J. New Energy* **1**(1) (1996) 111–118.
- [8] T. Mizuno, T. Akimoto, T. Ohmori, A. Takahashi, H. Yamada and H. Numata, Neutron evolution from a palladium electrode by alternate absorption treatment of deuterium and hydrogen, *Jpn. J. Appl. Phys.* **40** (2001) L989–L991.
- [9] A. De Ninno, A. Frattolillo, G. Lollobattista, L. Martinis, M. Martone, L. Mori, S. Padda and F. Scaramuzzi, Emission of neutrons as a consequence of titanium–deuterium interaction, *Il Nuovo Cimento, note brevi* **101** (1989) 841.
- [10] A. De Ninno, A. Frattolillo, G. Lollobattista, L. Martinis, M. Martone, L. Mori, S. Padda and F. Scaramuzzi, Evidence of emission of neutrons from a titanium–deuterium system, *Europhys. Lett.* **9** (1989) 221–224.
- [11] A.S. Roussetski, Application of CR-39 plastic track detector for detection of dd and DT-reaction products in cold fusion experiments, *Proc. 8th Int. Conf. on Cold Fusion*, May 21–26, 2000, Lerici (La Spezia), Italy, Italian Physical Society, Bologna, Italy.
- [12] P. Mosier-Boss, S. Szpak, F. Gordon and L. Forsley, Triple tracks in CR-39 as the result of Pd–D co-deposition: evidence of energetic neutrons, *Naturwissenschaften* **96** (2009) 135–142.
- [13] P. Mosier-Boss, S. Szpak, F. Gordon and L. Forsley, Detection of energetic particles and neutrons emitted during Pd/D co-deposition, *Low-Energy Nuclear Reactions Sourcebook*, J. Marwan and S. Krivit (Eds.), American Chemical Society, Washington, DC, 2008, p. 311.
- [14] F. Keeney, S. Jones, A. Johnson, P. Hagelstein, G. Hubler, D. Buehler, F. Cecil, M. Scott and J. Ellsworth, Neutron emissions from metal deuterides, *Condensed Matter Nucl. Sci.: Proc. Tenth Int. Conf. on Cold Fusion*, Aug. 24–29, 2003, Cambridge, MA, P. Hagelstein and S. Chubb (Eds.), World Scientific, New Jersey, 2006, p. 525.
- [15] C. Beaudette, *Excess Heat: Why Cold Fusion Research Prevailed*, Oak Grove Press, LLC, South Bristol, Maine, 2002, 280–282.
- [16] T. Iida, M. Fukuhara, Sunarno, H. Miyamaru and A. Takahashi, Deuteron fusion experiments with Ti and Pd foils implanted with deuteron beams II, *Proc. Fourth Int. Conf. on Cold Fusion*, Vol. 3, *Nuclear Measurements Papers*, Lahaina, Maui, Hawaii, Dec. 6–9, 1993, T.O. Passell (Ed.), Electric Power Research Institute, Palo Alto, CA, 1994, pp. 13.1–13.8.
- [17] F. Keeney, S. Jones, A. Johnson, P. Hagelstein, G. Hubler, D. Buehler, F. Cecil, M. Scott, J. Ellsworth, Charged-particle emissions from deuterided metals, *Condensed Matter Nucl. Sci., Proc. Tenth Int. Conf. on Cold Fusion*, Aug. 24–29, 2003, Cambridge, MA, P. Hagelstein and S. Chubb (Eds.), World Scientific, New Jersey, 2006, p. 509.
- [18] X. Li, S. Dong, K. Wang, Y. Fang, L. Chang, C. Luo, R. Hu, P. Zhou, D. Mo, Y. Zhu, C. Song, Y. Chen, M. Yao, C. Ren and Q. Chen, The precursor of “cold fusion” phenomenon in deuterium/solid systems. Anomalous nuclear effects in deuterium/solid systems, “AIP Conference Proc. 228”, 1990, Brigham Young Univ., Provo, UT, American Institute of Physics, New York.

- [19] S. Jin, F. Zhan and Y. Liu, Deuterium absorbability and anomalous nuclear effect of YBCO high temperature superconductor, *Proc. Fourth Int. Conf. on Cold Fusion*, Vol. 3, *Nuclear Measurements Papers*, Lahaina, Maui, Hawaii, Dec. 6–9, 1993, T.O. Passell (Ed.), Electric Power Research Institute, Palo Alto, CA, 1994, pp. 4.1–4.3.
- [20] R.A. Oriani and J.C. Fisher, Generation of nuclear tracks during electrolysis, *Jpn. J. Appl. Phys. A* **41** (2002) 6180–6183.
- [21] A. Lipson, G. Miley, A. Roussetski, E. Saunin, Phenomenon of an energetic charged particle emission from hydrogen/deuterium loaded metals, *Condensed Matter Nucl. Sci., Proc. Tenth Int. Conf. on Cold Fusion*, Aug. 24–29, 2003, Cambridge, MA, P. Hagelstein and S. Chubb (Eds.), World Scientific, New Jersey, 2006, p. 539.
- [22] P. Mosier-Boss, S. Szpak, F. Gordon and L. Forsley, Use of CR-39 in Pd/D Co-deposition experiments, *Eur. Phys. J. Appl. Phys.* **40** (2007) 293–303.
- [23] P. Mosier-Boss, S. Szpak, F. Gordon and L. Forsley, Characterization of tracks in CR-39 detectors obtained as a result of Pd/D co-deposition, *Eur. Phys. J. Appl. Phys.* **46** (2009) 30901: 1–12.
- [24] A.B. Karabut, Y.R. Kucherov and I.B. Savvatimova, Nuclear product ratio for glow discharge in deuterium, *Phys. Lett. A* **170** (1992) 265.
- [25] M. Srinivasen, Personal communication.
- [26] M. McKubre, *Development of Advanced Concepts for Nuclear Processes in Deuterated Metals*, TR-104195, 1994, Electric Power Research Institute.
- [27] S. Szpak, P. Mosier-Boss and J. Smith, On the behavior of the cathodically polarized Pd/D system: search for emanating radiation, *Phys. Lett. A* **210** (1996) 382–390.
- [28] M. Miles, R. Hollins, B. Bush, J. Lagowski and R. Miles, Correlation of excess power and helium production during D₂O and H₂O electrolysis using palladium cathodes, *J. Electroanal. Chem.* **346** (1993) 99.
- [29] V. Violante, G. Mazzitelli, L. Capobianco, M. McKubre, F. Tanzella, F. Sarto and E. Santoro, Search for nuclear ashes in electrochemical experiments, *Condensed Matter Nucl. Sci., Proc. of the Tenth Int. Conf. on Cold Fusion*, Aug. 24–29, 2003, Cambridge, MA, P. Hagelstein and S. Chubb (Eds.), World Scientific, New Jersey, 2006, 405.
- [30] M. Prelas, F. Boody, W. Gallaher, E. Leal-Quiros, D. Mencin and S. Taylor, Cold fusion experiments using Maxwellian plasmas and sub-atmospheric deuterium gas, *J. Fusion Energy* **9** (1990) 309–313.
- [31] C. Beaudette, *Excess Heat: Why Cold Fusion Research Prevailed*, Oak Grove Press, LLC, South Bristol, Maine, 2002, pp. 264–265.
- [32] J. Bockris and Z. Minevski, Two Zones of “Impurities” observed after prolonged electrolysis of deuterium on palladium, *Infinite Energy Magazine* Nos. 5 and 6 (1995) 67.
- [33] T. Mizuno, T. Ohmori and M. Enyo, Isotopic changes of the reaction products induced by cathodic electrolysis in Pd, *J. New Energy* **1**(3) (1996) 31–47.
- [34] G.H. Miley and J. Shrestha, *Transmutation Reactions and Associated LENR Effects in Solids*, in *Low-Energy Nuclear Reactions Sourcebook*, J. Marwan, and S. Krivit (Eds.), Oxford University Press, 2008, p. 173.
- [35] J. Dash and S. Miguët, Microanalysis of Pd cathodes after electrolysis in aqueous acids. *J. New Energy* **1**(1) (1996) 23–27.
- [36] S. Szpak, P. Mosier-Boss, C. Young and F. Gordon, Evidence of nuclear reactions in the Pd lattice, *Naturwissenschaften* **92** (2005) 394–397.
- [37] A. Lorusso and V. Nassisi, Pd systems loaded with D₂ and H₂ gases and irradiated by laser beams, *Cold Fusion: The History of Research in Italy*, S. Martellucci, A. Rosati, F. Scaramuzzi, V. Violante (Eds.), ENEA, 2009, p. 155.
- [38] A. Battaglia, L. Daddi, S. Focardi, V. Gabbani, V. Montalbano, F. Piantelli, P.G. Sona and S. Nesi, Neutron emission in Ni–H systems, *Nuovo Cimento* **112A** (1999) 921–931.
- [39] E. Campari, S. Focardi, V. Gabbani, V. Montalbano, F. Piantelli and S. Veronesi, Overview of H–Ni systems: old experiments and new setup, *5th Asti Workshop on Anomalies in Hydrogen- /Deuterium-Loaded Metals*, Asti, Italy, 2004.
- [40] A. Karabut, Production of excess heat, impurity elements, and unnatural isotopic ratios in high-current glow discharge experiments, *Condensed Matter Nucl. Sci., Proc. Tenth Int. Conf. on Cold Fusion*, Aug. 24–29, 2003, Cambridge, MA, P. Hagelstein and S. Chubb (Eds.), World Scientific, New Jersey, 2006, p. 99.
- [41] Y. Iwamura, M. Sakano, T. Itoh, Elemental analysis of Pd complexes: effects of D₂ gas permeation, *Jpn. J. Appl. Phys.* **41** (2002) 4642–4650.
- [42] B.F. Bush, J.J. Lagowski, M.H. Miles and G.S. Ostrom, Helium production during the electrolysis of D₂O in cold fusion experiments, *J. Electroanal. Chem.* **304** (1991) 271–278.

- [43] C.-C. Chien, D. Hodko, Z. Minevski, J.O'M. Bockris, On an electrode producing massive quantities of tritium and helium, *J. Electroanal. Chem.* **328** (1992) 189–212.
- [44] M. McKubre, F. Tanzella, P. Tripodi and P. Hagelstein, The emergence of a coherent evaluation for anomalies observed in D/Pd and H/Pd systems: evidence for ^4He and ^3He production, *Proc. 8th Int. Conf. on Cold Fusion*, May 21–26, 2000, Lerici (La Spezia), Italy, Italian Physical Society, Bologna, Italy.
- [45] A. De Ninno, A. Frattolillo, A. Rizzo, E. Del Giudice and G. Preparata, *Experimental Evidence of ^4He Production in a Cold Fusion Experiment*, ENEA, 2002.
- [46] D. Gozzi, F. Cellucci, P.L. Gignini, G. Gigli, M. Tomellini, E. Cisbani, S. Frullani and G.M. Urciuloi, X-ray heat excess and ^4He in the D/Pd system, *J. Electroanal. Chem.* **452** (1998) 251–271.
- [47] C. Beaudette, *Excess Heat: Why Cold Fusion Research Prevailed*, Oak Grove Press, LLC, South Bristol, Maine, 2002, pp. 239–241.
- [48] Y. Arata and Y. Zhang, Solid-state plasma fusion (“cold fusion”), *J. High Temp. Soc.* **23** (1997) 1–56.
- [49] Y. Arata and Y. Zhang, The establishment of solid nuclear fusion reactor, *J. High Temp. Soc.* **34** (2008) 85–93.
- [50] A. Kitamura, T. Nohmi, Y. Sasaki, A. Taniike, A. Takahashi, R. Seto and Y. Fujita, Anomalous effects in charging of Pd powders with high density hydrogen isotopes, *Phys. Lett. A*, **273** (2009) 3109–3112.



Research Article

LANR Nanostructures and Metamaterials Driven at their Optimal Operating Point

Mitchell R. Swartz *

JET Energy Inc. Wellesley, MA, USA

Abstract

In lattice-assisted nuclear reactions (LANR, or LENR), the size and structural metamaterial shape of Pd–D nanostructures, and the deuterium flux through them all play decisive roles. The spiral Phusor®-type cathode system with open helical cylindrical geometry in a high electrical resistance solution is a LANR metamaterial design creating an unusual electric field distribution and requisite intrapalladial deuteron flow. Optimal operating point (OOP) technology allows improved and more reproducible operation. LANR power gain can be considerable. In situ imaging has revealed that the excess power gain is linked to non-thermal near-IR emission when the LANR devices are operated at their OOP.

© 2012 ISCMNS. All rights reserved.

Keywords: Deuterium, Lattice-assisted nuclear reactions, Loading flux, Metamaterials, Nanostructures, OOP manifolds, Optimal operating point, Palladium

1. Impact of Nanostructure, Size and Shape

Lattice assisted nuclear reactions (LANR) use hydrogen-loaded alloys to enable near room temperature deuterium fusion and other nuclear reactions [1–49] and nanostructures, metamaterials, and controlled operation are required for success. This paper will review the astounding range of LANR nanostructures is observed, including some generated within palladium and others created on its surface. Such Pd–D nanostructures are needed for successful LANR generated excess heat (XSH). Table 1 lists the LANR nanostructure issues covered in this paper and their impact on LANR.

LANR's generated excess heat is a response to relatively low energy initiation to produce excess power densities ranging from ~ 7 (1989 announcement) to $80\text{--}10,000\text{ W/cm}^3$, today. This magnitude of excess energy, in the absence of sufficient thermal relaxation times, yields significant heat and even changes which are wrought upon the electrode as volcano-like pits [8,18,19]. At LANR's "core" are deuterons which are tightly packed into binary ("highly loaded") metals and metallic nanostructures by an applied electric field or elevated gas pressure which supply deuterons in heavy water or gaseous deuterium.

*E-mail: mica@theworld.com

Table 1. LANR structure, shape, and priming for LANR Success

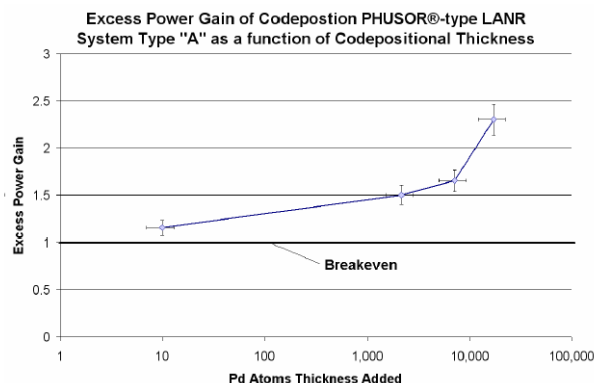
Size of nanostructure	Increased XSH if $> \sim 7$ nm
Purity of LANR structure	LANR quenched by contamination
Control of deuterium flow	Requisite for, and increases, XSH
Metamaterial shape	4–14 dB power gain in XSH
OOP control	8–25 dB power gain in XSH
Near IR emission at OOP	Confirmation of XSH
Multisystem calorimetry	Confirmation of XSH

Proof that nanostructures are important in LANR include codeposition, the diversity of LANR structure (Section 2), and non-thermal near IR emissions [25,34], and other recent data, such as shown in Fig. 1. The curve in Fig. 1 might be some of the first experimental evidence that LANR excess heat is correlated with the size of the Pd–D nanostructures. It shows a monotonic increase in excess heat from LANR as the codepositional layer was increased in size.

These relevant LANR nanostructures are discussed regarding the local and regional structure in Sections 3 and 4. The methods of driving LANR are discussed in Sections 5 and 6, both theoretically and experimentally, and some of the results are shown in Section 4. High impedance metamaterial nanostructured LANR devices have shown power gains more than 200% and short term power gains to $\sim 8000\%$ [1,2], compared to input energy and to input energy transferred to conventional dissipative devices. The excess energies observed with LANR are greater than any known chemical reaction. They are also increasingly studied. By the end of this chapter, the reader should understand the breadth of Pd–D nanostructures, how the nanostructure size correlates to the 'excess heat' observed in successful LANR systems (Fig. 1), and how the additional LANR operating condition requirements can be satisfied using metamaterials (Fig. 3) and the secondary deuterium flux (Fig. 4), in combination with optimum operating point driving (Fig. 5).

2. Lanr Nanostructure Diversity

The nanostructures arise, in part, because of the unique complex behavior of palladium and its binary alloy with hydrogen. It will be demonstrated in this section that LANR reactions are generated in one of three types of sites within, or upon, the deuterium-loaded, palladium ([50,51], Fig. 2). Each location has its own, characteristic production

**Figure 1.** Excess heat in LANR is correlated with palladium codeposition thickness

rate of excess heat, tritium, and helium, each characterized by a different optimal operating point (OOP) manifold [52–57], and they are both heterogeneous and diverse. This occurs because palladium is a unique metal [50,51,58,59] with one-of-a-kind properties. Many of them involve the incredible solubility of D and H in Pd. The binary alloy, hydrogen–palladium, is perhaps the most studied hydrogen system. Two solid solutions exist under normal conditions. The lattice parameter increases with hydrogen content, increasing from 3.891 Å for pure Pd to 3.902 Å for the saturated alpha phase. In some crystals, the Pd^{2+} ion occurs, such as in PdF_2 , and is paramagnetic. But, in aqueous solution, the $[\text{Pd}(\text{H}_2\text{O})_4]^{2+}$ diamagnetic ions [60] form complexes (“chelates”) which are square or 5-coordinate.

Relevant to LANR, palladium nanostructures include nanoparticles, nanowires, nanocrystals, nanoclusters, dendrimers, higher polymer aggregates, organic Pd hybrids, vacancy state materials, and many types of shaped alloys. They usually range in size from 2 to 200 nm. Palladium nanoparticles and nanowires are created by electrochemical deposition, usually on a carbon surface. They often have a vacancy in their center [61]. Similarly, LANR nanostructures include vacancies within them. In the alloys, they must drift into the bulk from the surface. This diffusion is slightly facilitated by the loading itself [1,2]. Swartz and Hagelstein have made Pd–D vacancies with electron beam irradiation [62]. Jan Marwan has improved the field by generating new methods of making additional “vacancies” with nanolipids and dyes [63].

Pd nanoparticles made on a gold surface show proton reduction catalytic activity enhanced by more than two orders of magnitude, as the diameter of the palladium particles decreases from 200 to 6 nm [64]. Pd nanoparticles can be made by poly(ethyleneglycol) (PEG) and $\text{Pd}(\text{OAc})_2$, where PEG is both reducing agent and stabilizer. The reduction of Pd^{2+} to nano Pd is sensitive to the chain length of the PEG, with larger chain lengths improving performance [65]. Larger spherical Pd nanoparticles, ~70 nm, are made with palladium acetate and octa(3-aminopropyl)octasilsesquioxane octahydrochloride [66].

Wire-shaped Pd nanoparticles, 5 nm in diameter and 1000 nm long are synthesized using poly(methacryloyloxyethyl dimethylbenzylammonium chloride and Si-wafers [67]. Colloidal Ni/Pd nanoclusters are made using ethylene glycol and *N*-vinyl-2-pyrrolidone with a molar ratio of Ni : Pd = 2 : 3. They exhibit 3.5 times greater activity than typical colloidal palladium catalysts [68]. Nanocrystalline palladium has been made by inert gas condensation and compaction with grain, crystallite, sizes ranging from 5 to 50 nm [69]. Palladium nanodendrimers of ~ 300 Pd atoms in a metallic core of 2.0 nm diameter are also fabricated [70]. Nearly 90% of the metal nanoparticle surface is unpassivated and available for catalysis. The dendrons inhibit metal agglomeration without adversely affecting chemical reactivity [71].

Some dynamically formed Pd D nanostructures in LANR are even more complicated. The nature of activation and energy transfer processes in LANR are debated, but the diversity of LANR sites of varying sizes and locations are not. A variety of LANR regions are involved upon -and within- the deuteron-loaded Pd lattice. Figure 2 shows some of these diverse LANR sites - which include the deep and superficial lattice, and above-surface structures generated during codeposition. Three different physical locations [material types] are distinguished [50,51]. Each location has distinctive rates of excess heat, and tritium and helium product generation, each controlled by a different OOP manifold. Each location is a compartment of LANR active sites which can be distinguished by calorimetry and spectroscopy, including by near infrared (IR) emission [34].

Experimental evidence for (at least) three different LANR regions include the two types of time constants associated with “heat after death” (HAD) and the monotonic increase of excess heat observed in LANR systems with increase of loaded depth. Region 1 refers to the most superficial portions of the palladium, including surface dendrites and a variety of micro- and nanoparticles, that characterize electrodeposits by codeposition. This involves at least several atomic layers. These surface sites, generated via codeposition and conventional LANR produce tritium. At the top left,

Figure 1 shows supra-surface palladium surface globules (Image A) produced during palladium codeposition upon a copper cathode at SPAWAR [19,20]. Codeposition efforts, including these at SPAWAR, produce subsurface reactions, involving at least several atomic layers. Palladium rods are shown which develop from the globules (Image B), produced after additional applied electric field; one of several morphologies generated. The volcanic-like burst changes in Pd

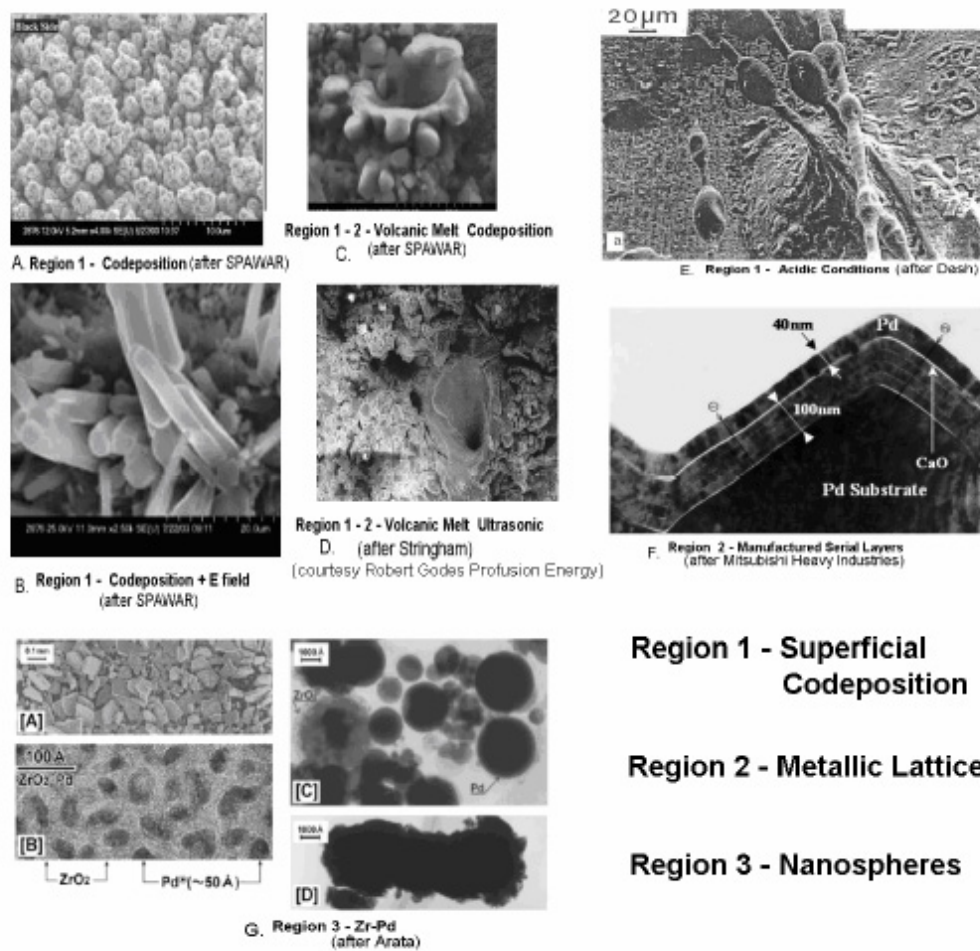


Figure 2. Three types (“regions”) of palladium LANR

seen with SPAWAR codeposition and cavitation LANR in thin Pd foils loaded by “sonofusion” [23] suggest melting and subsequent re-solidification of molten metal, reminiscent of nuclear fission fuel metal damage (spontaneous Californium “spike damage”). The top middle image shows the occasional local melting of the palladium surface (C), presumably from the desired reactions. Below it, in the center is a Pd melt cavity produced by cavitation LANR reactions (D)[23]. To the top right, Fig. 1 shows morphologies (Image E) generated by acidic electrolysis generating nanotubes [8].

Located deeper in the metal, subsurface Region 2 in LANR yields heat and helium production and transmutation products. It includes the metallic lattice physically located beneath Region 1, existing as a thin rim under the surface in the range of 40 microns to millimeters. Subsurface sites (Region 2) yield heat and helium production and transmutation products. Below on the right side bottom of Fig. 1 are detailed Pd fabrication layers (Image F), 40–100 nm wide with a thin CaO layer intercalated [10].

Region 3 is a special state and size of nanostructures which are typically of width 7–30 nm and which efficiently

yield heat and helium production. These are found in deuterided palladium-black, palladium-black dual cathode [3], and glass ZrO palladium-black systems. Below on the left side bottom of Fig. 1 are Prof. Y. Arata's [3] nanomaterials (Image G) made from zirconium, leading to spherules [50,51].

3. Metamaterials in LANR

LANR devices can be greatly expanded by metamaterial shape which adds incredible properties beyond those of the material itself (definition of a 'metamaterial'). Metamaterials, through their unique, novel structures, can make previously "impossible" effects occur. Metamaterials [32,72–90] change the properties of materials by specific, precise, shapes; their stereoconstellation. Then, metamaterials have surprising, physical characteristics that defy earlier expectations, yet each produce solid, indelible experimental results. Metamaterials create negative refractive index materials [72,73], electromagnetic cloaking (and not just screening) [74], a simultaneous negative phase and group velocity of light [75], anomalous reflections and excitations of surface waves [76], isotropic lenses [77], and soliton decoherence [78]. Metamaterials come in arrays [81,82] and sol-gel composites [83] and are useful as novel antennae, filters, waveguides, and artificial magnetic media [82].

As Table 1 shows, consideration of metamaterial shape can improve excess heat power gain by 4–14 dB. This improvement in power gain results directly from the fact that the metamaterial shape changes where the steady state electric field distribution ends up; inside the LANR material resulting in a continual hydrogen flux.

Years of experimental suggests that metamaterials are critical for successful LANR. Over 20 years, well-controlled experiments using certain D-loaded devices have yielded impressive energy gain with fairly good reproducibility in time-integrated runs producing excess power gains in Pd/D₂O/Pt, Pd/D₂O/Au, and Ni/H₂O_xD₂O_{1-x}/Pt LANR systems. Specifically, the uniquely shaped spiral Phusor®-type cathode, located opposite a platinum anode, has stood out for reproducibility, activity, power gain, and excess heat in this type of LANR system [32]. Its arrangement and stereoconstellation of electrodes appears to be one of the better arrangements for a LANR system, measured by activity and power gain [1–4,32]. Studies of more than a decade indicate a 4–14 dB gain from metamaterial technology. However, what was not clear until recently was why this occurs. It has been discovered that the spiral Phusor®-type cathode system with open helical cylindrical geometry in a high electrical resistance solution is a LANR metamaterial design which creates a unique and unusual electric field distribution, resulting in superior performance. To do this, Swartz and Verner used computed simulations based upon experimental findings to examine the impact of Phusor®-type LANR setups. Examined were geometric and other parameters of both the wire-wire and wire-Phusor system (Fig. 3) upon the electrical field distribution.

Dimensional (2D) vector electric field distributions are shown in Fig. 3 with the first case being that of two parallel, infinitely long, wire electrodes (anode at the top, and cathode below). The second case is a wire-Phusor system. In cross-section, the complex structure is approximated. The anode is at the top, and the cathode in each pair is located below it. Each cathode is electrically polarized against, and physically located opposite, an anodic wire of platinum. In a 2D view around a simple cathode wire, there is a near isotropic distribution of the E-field (Fig. 3). However, with the Phusor, there is a distinguishing electric field distribution different from customary wire-wire and plate-plate systems. The important secondary result is that when the Phusor®-type LANR metamaterial structure alters the electric field distribution, it produces continuous deuteron flux within the loaded palladium. The portion of the cathode vicinal to the anode has a higher than normal internal electric field intensity within its bulk volume. This does not characterize the two wire situation.

With the metamaterial LANR cathode configuration, there is an intrapalladial deuteron flow ("flux"), in addition to – and after – deuteron loading through portions of the cathode. The intraelectrode deuteron flux is through the metal, itself. This is reasonable because real palladium is not a perfect conductor, and in four terminal measurements of this sensors demonstrates resistances ranging from 40 to ~ 120 mΩ. Most relevant to LANR, this intrapalladial deuteron

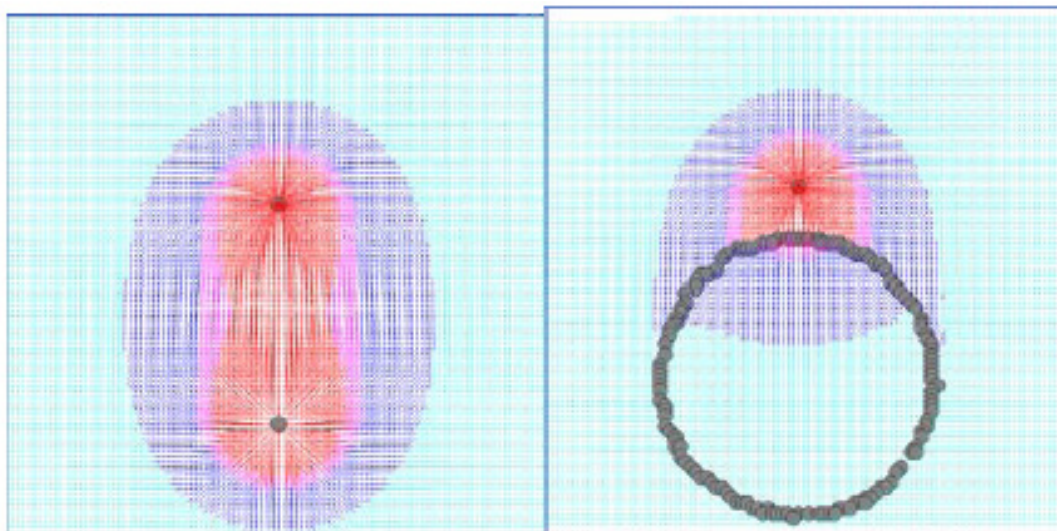


Figure 3. Phusor LANR Cathode in High Electrical Resistance Solution Left - 2-D vector electric-field distribution for two wire electrodes. Right - 2-D vector E-field distribution for PHUSOR®-type LANR system.

flow continues at equilibrium, similar to the microscopic semiconductor flux of holes and electrons at a p-n junction. We suspect that this additional type of deuteron flow is critical and enabling to LANR results. The results here support this, as do those of Violante [48] and Iwamura [10].

4. Deuteron Flux in LANR

Deuteron flux is key in LANR and there are two important points. First, metamaterials change the location of the flux, and second, mathematical solution requires the differential equations of continuum electromechanics. Nernst calculations of the activities of electrolyte [91,92] adjacent to a metal electrode have been applied to LANR to derive distributions of deuterium in the palladium and solution. However, because these LANR systems are not at equilibrium, the Nernst

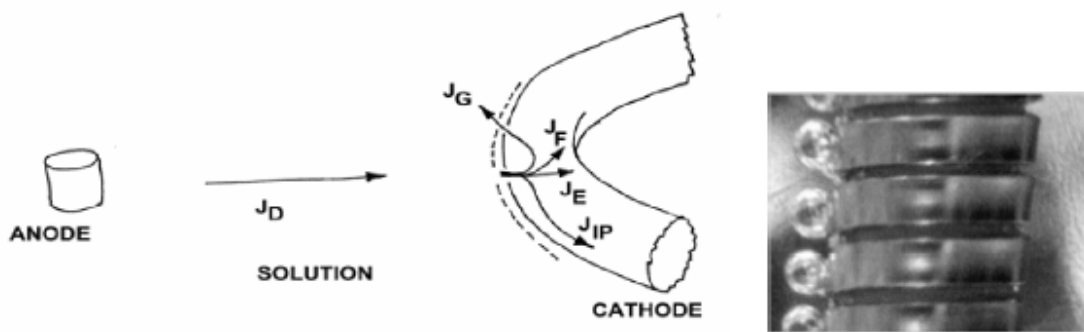


Figure 4. Metamaterial E-Field Distribution. (a) Left – Schematic of electrochemical loading, showing the fluxes of deuterons. (b) Right – Close-up of cathode showing asymmetric bubbling.

calculations are not applicable [52,53]. By contrast, and unaffected by non-equilibrium, the quasi-1- dimensional (Q1D) model of deuteron loading [52] analyzes the deuteron populations and the deuteron flow. It has foundation in the complex dielectric properties of materials [93] and continuum electromechanics [94]. Here, it has generated the deuteron-flux equation which explains some of the reasons for the difficulty in achieving LANR success. In the Q1D model, the different deuteron populations, their fluxes, and their locations (changed by the metamaterial shape) must be distinguished. They are seen in Fig. 4. On the left of Fig. 4 is a schematic representation of the anode, solution, and a portion of the cathode along with five types of deuteron fluxes involved in LANR. The deuteron fluxes are deuteron cationic flow in the solution (J_D), and the four types of deuteron flux in and near the loaded palladium cathodic metal lattice (J_E , J_G , J_F , and J_{IP}). The fluxes of deuterons in the metal include entry into the metal (“loading”, J_E), gas (D_2) evolution (“bubble formation”, J_G), intrapalladial deuteron flux (J_{IP}) flow through the metal, and an extremely tiny loss by fusion reactions (J_F). The continuous, equilibrium, flux of deuterons within the cathode (J_{IP}), produced by LANR metamaterials, is heralded by an observed unusual bubbling pattern, with spatial anisotropy, and synchronous with the excess heat. Referring to Fig. 4, this is shown on the right hand side.

Cationic deuteron flux (J_D) brings deuterons to the cathode surface. It begins far from the cathode surface, in the deuterium oxide (heavy water) located between the electrodes, where the deuterons are tightly bound to oxygen atoms as D_2O .

$$J_D = -B_D \frac{d[D(z, t)]}{dz} - \mu_D [D(z, t)] \frac{d\Phi}{dz} \quad (1)$$

In the absence of significant solution convection, the flux of deuterons (J_D) results from diffusion down concentration gradients and electrophoretic drift by the applied electric field [93–96]. J_D in the heavy water includes D-defects [95,96] driven by the applied electric field intensity to create a cathodic fall and double layer before the electrode surface. J_D depends on deuteron diffusivity (B_D) and electrophoretic mobility (μ_D), and the applied electric field intensity. Φ is the potential, the spatial gradient of which produces the electric field intensity. At any molecular site across the heavy water solution, the applied electrical energy is a tiny fraction compared to k_B^*T , so the deuterons migrate by drift ellipsoids of L– and D-deuteron defects in the applied electric field creating a ferroelectric inscription [95,96]. This D-defect conduction/polarization process augments other charge carriers, ionic drift, space charge polarization, and clathrates. The resultant D-defect migration produces a “cathodic fall” of deuterons and a E-field contraction so that most of the voltage drop is at the interface in front of the electrode surface. This concentration polarization may produce very large local electric field intensities, possibly ranging from 10^4 to 10^7 V/cm, resulting in a very large electrical potential drop across a small distance vicinal to the cathode.

Just beyond that, at the inner boundary of the double layer, intermolecular deuteron transfer from the heavy water solution to the metal surface, controlled by electron- limited transfer, leaves an atomic deuteron on the metal surface. This leaves an atomic deuteron attached to the metal surface, with its next transfer controlled by the metallurgy of the thin interfacial region possibly a few Angstroms thick, by the applied electric field intensity, and by the local concentrations of deuterons and quenching materials. The entry mechanisms to the palladium surface are driven by infrared vibrations and microwave rotations [95], creating a solution photosensitivity which produces a photoactivated increase of excess energy and loss of power gain [33].

At the surface of the low hydrogen-overvoltage palladium, there exist surface atomic (D) and diatomic (D_2) deuterons and some which also enter (‘load’) the bulk metal [52,53,1–3,32] or transit through the metal by intrapalladial deuteron flow if a metamaterial is used under select conditions. The gas bubbles (D_2) are undesirable producing low dielectric constant layers in front of the electrode, obstructing the electrical circuit. Any deuterons which enter the metal are electrically neutralized (‘dressed’) by a partial electronic cloud, shielding their charge (in a Born–Oppenheimer approximation) [38]. The deuterons drift along dislocations, and through the lattice and its vacancies as interstitials, falling from shallow to more deeply lying (energetically) binding sites. The deuteron drift is obstructed by ordinary hydrogen

and other materials blocking key interfacial sites and grain boundary dislocations.

It is the deuteron flow equations which explain the loading, the codeposition, the quenching effects, the metamaterial effects, and the optimal operating point manifolds. Numerically dividing each deuteron flux (J_E , J_G , and J_F) by the local deuteron concentration yields the first-order deuteron flow rates, k_E , k_G , and k_F (with units of cm/s, respectively). At the surface of the loading metal, using conservation of mass, Eq. (1) becomes Eq. (2), the deuteron flux equation of LANR.

$$\kappa_e = (\mu_D \mathbf{E}) - (\kappa_g + \kappa_f). \quad (2)$$

Equation (3) can be modified to Eq. (3) by substituting the Einstein relation.

$$k_e = \frac{B_D q V}{L [k_B T]} - (\kappa_g + \kappa_f). \quad (3)$$

Equation (3) is the modified deuteron loading rate equation, derived from geometric and material factors. B_D is the diffusivity of the deuteron. $k_B T$ is Boltzmann's constant and temperature. q is the electronic charge, and V is the driving applied voltage. There are many important lessons for LANR. First, dominating everything is the first term which now has the ratio of two energies (the applied electric energy organizing the deuterons divided by $k_B T$, thermal disorder). This energy ratio is decisive in controlling the deuteron loading flux in palladium. Successful LANR reflects the 'war' of organization by the applied electric field intensity which is organizing the deuterons versus their randomization by thermal disorder.

Second, the second term heralds that competitive gas evolving reactions at the metal electrode surface can destroy (quench) the desired reactions. Note that the first order loading flux rate constant (k_E) is dependent upon the applied electric field intensity minus the first order gas loss rate constant resulting from gas (D_2) evolution at the cathode (k_G). This implication is exactly opposite conventional "wisdom" that LANR is 'fusion by electrolysis' [1–4].

Third, detailed further analysis of Eq. (3) also suggests that LANR can be missed by insufficient loading, contamination (effecting k_E , by protons or salt), and by the evolution of D_2 gas, which all inhibit ("quench") the desired LANR reactions [3,4].

5. Optimal Operating Points In LANR

Success of LANR requires multiple factors including loading, adequate confinement time (sometimes weeks), loading rate, prehistory with careful preparation including absence of contamination and avoidance of materials which quench performance. We have reported that anomalous energy gain in metal deuterides became a more reproducible phenomenon as optimal operating point (OOP) understanding and technology [52–55] has been applied to LANR (JET Energy, 1–4; JWK, 57; Innoventek) [56]. Optimal operating points, and OOP manifolds, appear when the calibrated output data of an LANR device (producing amplified heat, excess power gain, de novo incremental helium-4 or tritium production) is presented as a function of the input electrical power (Fig. 5).

Figure 5 shows three LANR Optimal operating point (OOP) manifolds presenting power gain and *de novo* helium-4 and tritium production for conventional, high- impedance, codeposition and palladium-black nanomaterial LANR systems. The horizontal axis is the electrical power input (log watts). The vertical axis is uncalibrated and linear. The optimal operating point (OOP) is the relatively narrow peak of the biphasic LANR production curve when viewed as a function along the electrical input power axis. From an operational point of view, during situations in which excess power is generated from an active LANR sample or device, large changes in LANR output, such as excess power gain, are observed as the input power is varied over a relatively small range.

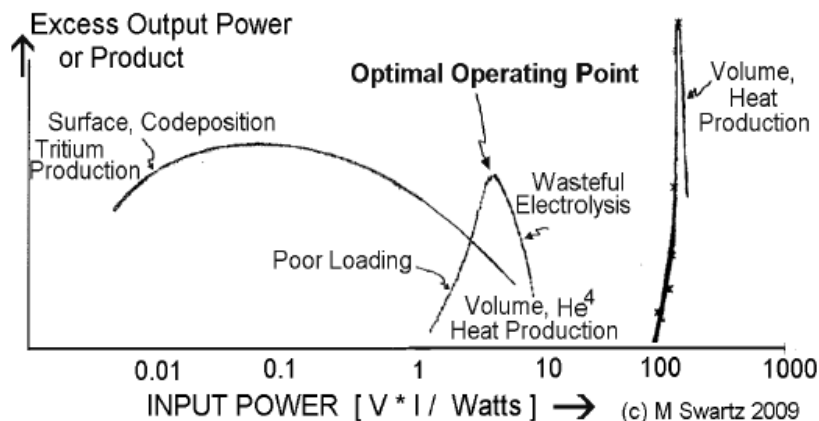


Figure 5. Three LANR optimal operating point (OOP) manifolds.

In Fig. 5, the central OOP manifold (curve) is for a Pd Phusor®-type LANR device, and has general overlap with the He^4 production curve [1,2,1,55–57]. The excess heat amounts to hundreds of thousands of joules of ‘excess heat’ per day [1,2]. The helium nuclei are generated in their first excited state, He^{4*} , which provides the lattice heating as the helium nucleus returns to its ground state in reactions which are consistent with nuclear [97–102], solid state [102–110], Mossbauer [111–113], and radiation physics [34,114]. The other two curves in Fig. 5 show how this LANR Optimal Operating Manifold compares to two other independent investigator setups involving nanomaterials (after Arata and Zhang) and tritium (after Szpak, Gordon, and Mosier-Boss). Charged particles, tritium [22,41,46,49], and low levels of particles and radiation [19,20,40] have been detected in some systems. Srinivasan from BARC (India) reported tritium and neutrons in 1989. John Bockris (Texas A&M) reported tritium in bursts, not accompanied by measurable heat. Szpak (SPAWAR) reported tritium in some codeposition systems. Miles and Srinivasan independently used dental X-ray films outside of their LANR to demonstrate fogging consistent with low energy x-ray production. Li (Tsinghua U), Larry Forsley (JWK International) and Mosier-Boss (SPAWAR) have used CR-39 to detect energetic charged particles, including D–D and D–T reactions [19,20].

OOPs and their manifolds are important for several reasons. First, organized this way (by input electrical power), the data formidably dispels the LANR “irreproducibility” myth. OOP manifolds make salient why LANR was so difficult to achieve in the first place. The optimal operating point is but one focus at which the system can be driven. The rest of the foci, other possible points at which the system can be driven, are the “optimal operating point manifolds”.

OOP manifolds provide important information, and understanding, about LANR system response as input power is changed. In heat-producing LANR experiments, at lower values of the input power, he said the reaction rates of the desired reactions vanish or are low (usually because the loading is inadequate). At higher values of input power (associated with the region located to the right of any of the OOP manifold peaks), the output power is reduced for several reasons. These include losses in output energy from a reduced number of reactions, a secondary effect associated with gas bubble formation, and the combined effect of both sources of energy loss on the system. Driving with electrical input power beyond the peak optimal operating point (OOP) does not improve the production of the desired product, but instead yields a falloff of the production rates despite increasing input power. Many negative LANR reports occur due to a failure to operate the LANR system at, or near, the optimal operating point.

Second, LANR is better controlled. OOP operation allows control, better understanding, more reproducible operation, and much improved success of LANR systems with what preliminary studies indicate a 8–25 dB or more gain [1–4].

Third, OOP understanding enables one to standardize examination of specimens and materials, normalizing treatment of samples. OOP characterization allows determination of maximal sample activity (MSA).

Fourth, control of OOP manifolds have shown their worth by being proven useful to maximize and control secondary LANR effects including “heat after death” [30,31], the response to incident coherent optical radiation [33], and non-thermal near IR emission [34].

Fifth, OOPs and OOP manifolds are universal in LANR systems. OOPs characterize Pd-heavy water LANR induced incremental helium and tritium production, and the generated excess heat production, including for conventional and high impedance Pd/D₂O/Pt and Pd/D₂O/Au LANR systems and Phusor®-type LANR devices, and for Ni/H₂O_xD₂O_{1-x}/Pt and Ni/H₂O_xD₂O_{1-x}/Au LANR devices, and for codeposition systems and codeposition LANR devices, and for tritium generated from codeposition and conventional heavy water systems for excess heat and helium production in palladium-black systems for excess heat in light water nickel systems [1,55–57].

Sixth, slightly different OOP manifolds characterize each type of nanostructures ([50,51], called “3RH”). This group segregation is consistent with the complex behavior of palladium (Section 2), and a growing set of LANR experimental data [1–51], including ‘heat-after-death (HAD) excess heat’ evanescent decay kinetics [30,31].

6. Building LANR Nanostructures

Nanostructure preparation, assembly, and driving are very complicated and described elsewhere [1–4,35,38]. However, when the correct nanostructure is combined with the correct deuteron flux, and the system driven at the OOP, there is a higher likelihood of LANR success. Beneath the complicated generated nanostructures are very pure materials. In these group of experiments, the cathodes were prepared from 99.98 + % Pd (Alfa Aesar, Ward Hill, MA), 1.0 mm diameter, ~4–7 turns on a spiral of ~1.3 cm diameter, with a gap separation from the anode arranged in a Pd/D₂O/Pt or Pd/D₂O/Au configuration (Pt 99.998%). The cathodes have four leads, supporting in situ four terminal electrical conductivity measurement. The solution is very low electrical conductivity heavy water (deuterium oxide, low paramagnetic, 99.99%, Cambridge Isotope Laboratories, Andover MA) with no additional electrolyte. The low electrical conductivity water bathed the spiral cathode. Contamination remains a major problem, with excess heat devastatingly quenched by increasing electrical conductance of the solution [2–4] and effects on the cathode. Contaminants appear from both electrode and container degradation and leeching, from atmospheric contamination, and after temperature cycling. These all inexorably, unintentionally, add to the electrolytic solution decreasing the level of deuteron loading achieved, the rate of loading as well, and the maximum heat producing activity. The heavy water is hygroscopic, therefore kept physically isolated from the air by seals, including several layers of Parafilm M (American National Can, Menasha, WI) and paraffin. We continue to avoid chlorine or chloride because of possible explosions. This is due to visible light ignition susceptibility, which results because the activation energy with chlorine is only ~17 μJ.

The loading of the palladium from the heavy water, and driving of the reactions through the two electrodes within the reaction container was obtained by controlled electric current source, or a Keithley 225 at low input, with ±1% accuracy. Electrical voltage sources included HP/Harrison 6525A for transsample potentials up to 3000 V (~ ±0.5% accuracy). All connections isolated, when possible, with Keithley electrometers for computer isolation. For 4-terminal intra-electrode Palladium electrical conductivity measurements, a first Keithley 225 electric current source was used to drive the cell, and load the Phusor. A second Keithley 225 electric current source was used to drive the electrical current portion of the four terminal electrical conductivity measurement of the palladium. All leads near the solution were covered with electrically-insulating tubes (medical grade silicone, Teflon, or proprietary materials) used to electrically isolate wires.

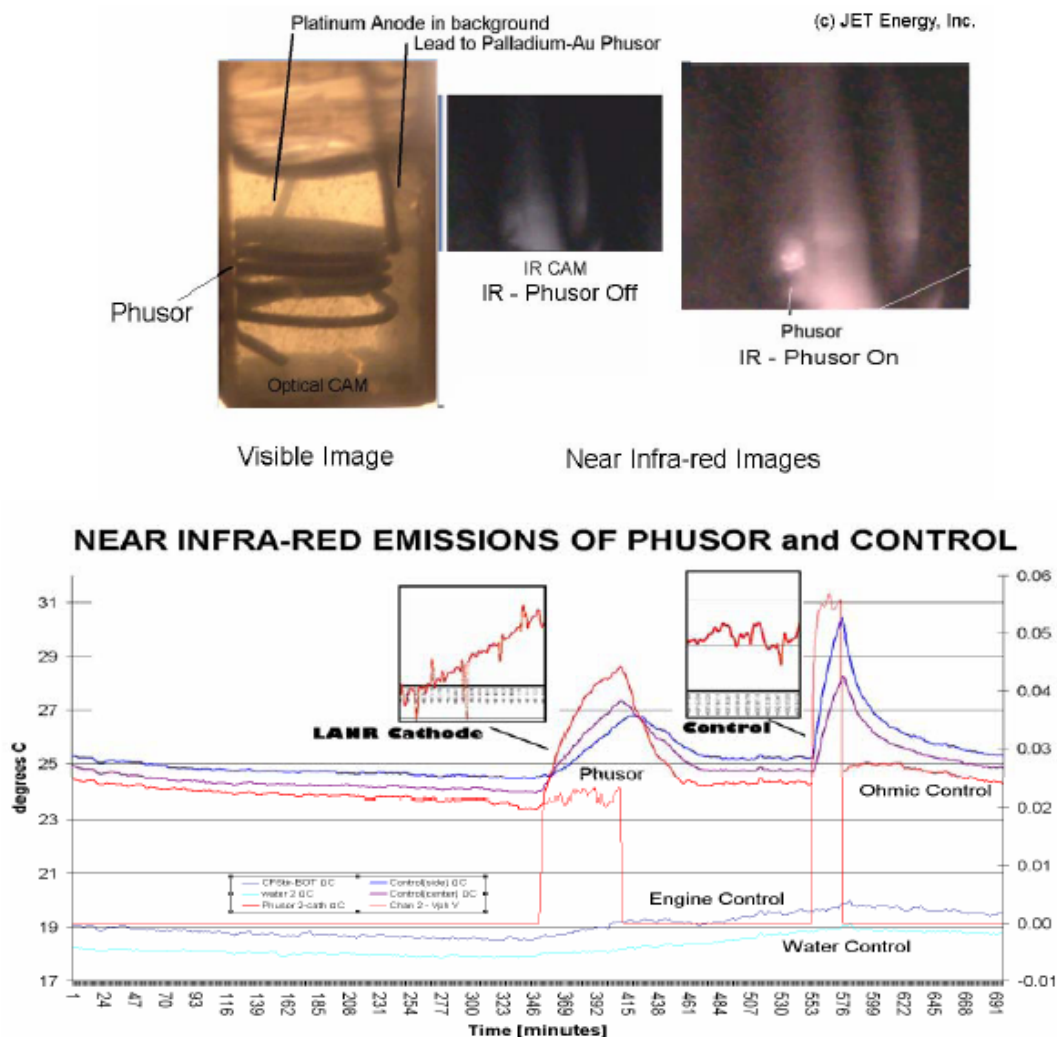


Figure 6. (above) Visible and IR Images of DAP LANR Cell, Before and After Activation

The data from voltage, current, temperatures at multiple sites of the solution, and outside of the cell, the 4-terminal measurement of the cathode's internal electrical conductivity, additional calibration thermometry and other measurements were sampled at 0.20 Hz, usually 1 Hz, 22+ bits resolution (Omega OMB-DaqTemp (Omega; voltage accuracy 0.015 ± 0.005 V, temperature accuracy $< 0.6^\circ\text{C}$) and recorded by computed DAQ. To minimize quantization noise, 1 min moving averages were sometimes made. The noise power of the calorimeter is in the range of $\sim 1\text{--}30$ mW. The noise power of the Keithley current sources is ~ 10 nW. Input power is defined as $V \cdot I$. There is no thermo-neutral correction in denominator. Therefore, the observed power is a lower limit. The instantaneous power gain (power amplification factor(non-dimensional)) is defined as $P_{\text{out}}/P_{\text{in}}$, as calibrated by at least one electrical joule control [ohmic

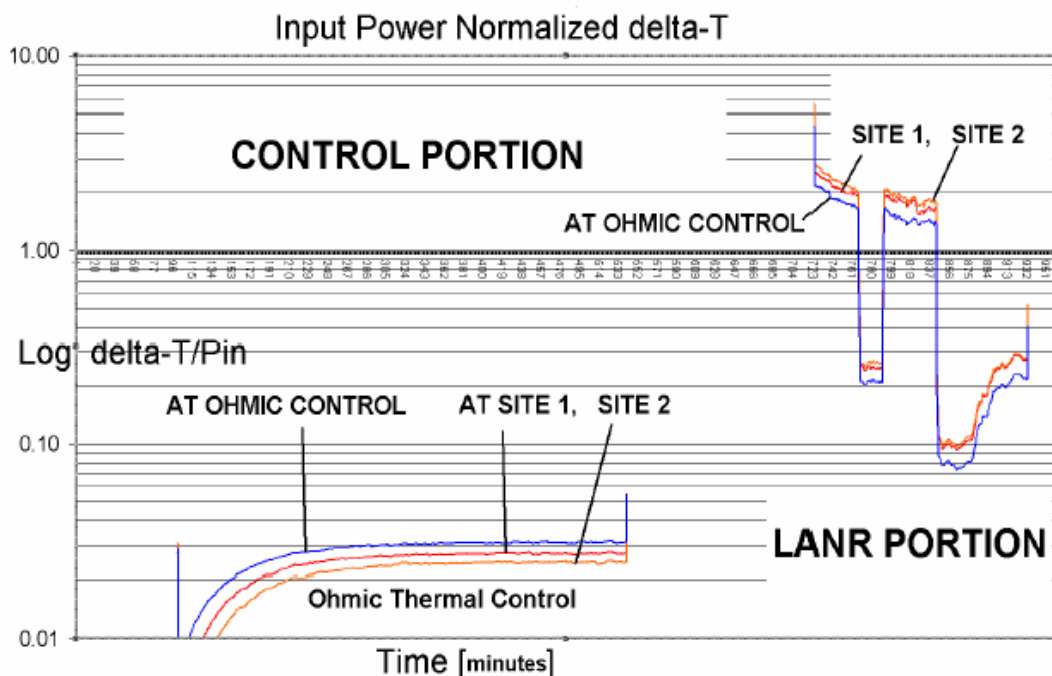


Figure 7. Input power normalized delta-T curves for DAP Phusor® LANR

resistor] and time integrated for validation. The excess energy, when present, is defined as $(P_{\text{output}} - P_{\text{input}}) \times \text{time}$. The amount of output energy is interfered from the heat released producing a temperature rise, which is then compared to the input energy.

The codepositional high impedance devices and the DAP (Dual anode Phusor®- Type LANR device; Pd/D₂O, Pd(OD)₂/Pt – Au) were generated as discussed elsewhere [2–4,34]. For the DAP Phusors, palladium is laid down from a sacrificial anode upon the surface of a virgin palladium cathode. Then, the palladium anode is removed, and replaced by a gold wire anode to stop the further laying down of further palladium nanostructure upon the palladium cathode. Interestingly, we have reported a new phenomenon during codepositional layering of the DAP Phusor cathode. This consists of a dynamic instability, observed as an oscillation, heralding an electrohydrodynamic Rayleigh–Taylor or Bernard instability which is associated with the layering. The time constant was circa 15 min per cycle, but this was irregularly irregular, with three to five cycles occurring in a 60 min period.

For Figs. 6 and 7, Pd and D were electrodeposited and the excess heat was measured when the thickness was circa 17,000 atoms deep over the deposited area, with a total area of 2.57 cm². At that time, the solution was 7.7 mmol Pd(OD)₂, and the open circuit voltage, V_{oc} , used to determine the effectivity of LANR [2,3], was 1.46 V. The Pd*/D₂O–Pd(OD)₂/Au Phusor®-type system has an initial cell resistance of circa 868 kilohms. During development of the nanostructure this falls to circa 48.3 kΩ and less.

Temperature measurements are made by specialized electrically -insulated thermocouples (accuracy ± 0.8 K, precision ± 0.1 K), RTD and other sensors. Probes were calibrated by Omega IcePoint Cell and core temperatures were maintained by feedback control using a Yellow Spring Thermal Controller Model 72 (bandwidth of 0.2 K) within a Honeywell water circulation zone controlled room (± 2.5 K). Thermocouples and other temperature sensors decorated

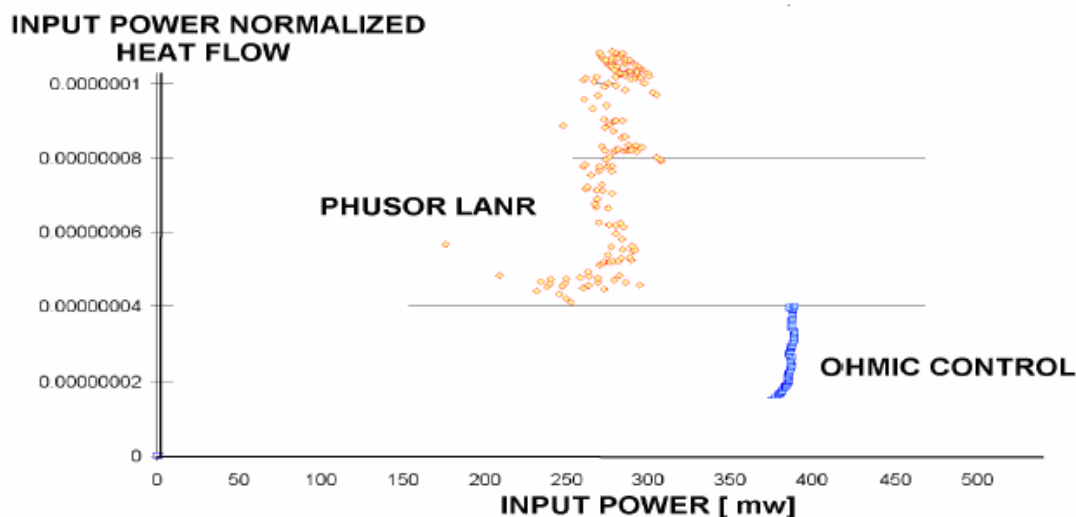


Figure 8. DAP LANR Device Heat Flow Output

the periphery of the cell, and a multicompartiment calorimeter was used. There was an additional heat-flow probes at the periphery outside of the core. To minimize contamination, the majority of temperature measurements were outside of the inner core container. Calorimetry is augmented by heat flow measurement, electricity production using thermoelectrics, and LANR-driven motors. Outputs are calibrated by ohmic (thermal) controls, and dual ohmic (calorimeter) controls, to evaluate, and certify possible excess heat. Additional calibration has included adequate Nyquist sampling, time-integration, thermal ohmic controls, waveform reconstruction, noise measurement, and other techniques [2–4].

The near IR Imaging is complicated. Dr. Stan Szpak (SPAWAR) et alia reported the emission of infra-red from LANR codeposition devices. However, they did not use a control, and there have been questions concerning both the linearity and calibration of their single effort. SPAWAR and JET Energy have investigated the physical changes, the excess heat generation, hot spots with additional controls by JET Energy demonstrating non-thermal near IR emission (Fig. 5). We have examined the impact of laser irradiation on LANR cathodes, and reported in 2003 that part of the impact is due to reflection off of the cathode back into the double layer. There, deuteron injection into the palladium increases (activation energy of ~ 14 kcal/mol) from microwave rotation and IR vibration for the intermolecular transfer of deuterons to the Pd [33]. Hagelstein, Letts and Cravens [11,12] have reported both single and dual photon impacts on cathodes.

In our near IR (NIR) LANR studies, we initially, incorrectly, thought a single control (vs. Szpak et al. who had used no controls) would be needed. It was soon discovered that two controls are needed. Thereafter, calibration included normalization of NIR emission intensities to both non-energized environmental and to ohmic control areas, supplementing semiquantitative calibration against an ohmic thermal control. NIR data capture was by slow scan near-IR and visible videocam (~ 1 Hz). Thereafter information was obtained by analysis using semiquantitative computed measurements of collected NIR output, integrated over both the DAP cathode, the ohmic thermal control, and their environment as they were each activated or not. The integrated NIR output of serial computed images of the DAP Phusor® and ohmic control were compared by normalization to the controls, and examined as a function of time.

Matched arrays of solar cells integrated the recorded near-IR emissions of the DAP device, the thermal control, and the control areas over time.

7. NT-NIR and XSH from LANR Nanostructures

Correctly driven, LANR nanostructures fabricated as LANR metamaterials exhibit significant excess heat, excess heat flow, and non-thermal near infrared (NT-NIR) emission linked to both. Figure 6 shows three visible and near-infrared (NIR) views of a DAP codeposition Phusor®-type LANR device in heavy water. The platinum anode is seen in the background. The DAP Phusor® is located in both images (~ 7.7 mmol Pd(OD)₂). The first view is in ordinary light, the other two (from a slightly different angle of observation) are in the near infrared (NIR). The two images on the left precede (controls, “off”), and the one on the right is after, activation and generation of excess heat. As in other experiments involving a variety of LANR metamaterial spiral-wound and other Phusor®-type lattice assisted nuclear reaction (LANR) systems, including high impedance palladium (Pd/D₂O/Pt, Pd/D₂O/Au), codepositional (Pd/Pd(OD)₂/Pt) heavy water, and nickel (Ni/H₂O_xD₂O_{1-x}/Pt, Ni/H₂O_xD₂O_{1-x}/Au) light water Phusor-type LANR devices [34], there is a linkage of excess power gain and heat flow with simultaneous NT-NIR emission. (below) Non-Thermal Near IR Emission at the Optimal Operating Point during Excess Heat Generation

There are several important findings and secondary implications. First, the emission of near-IR from the electrodes when excess heat is only observed when active electrodes operated at their optimal operating point, and then NT-NIR is linked and specific to the LANR devices’ excess heat production and not its physical temperature. The estimate of the color temperature during NT-NIR of for these LANR devices, driven at their optimal operating point and input power drive levels, was estimated at ~ 500 – 1000 K.

Second, these findings confirm the Bremsstrahlung-shift hypothesis [114] which states that in LANR, distinct from hot fusion, there is a temperature-related shift from hot fusion’s penetrating ionizing radiation to LANR’s skin-depth-locked infrared radiation. Simply put, unlike hot fusion or plasma systems, bremsstrahlung radiation in LANR systems cannot dissipate fusion derived excess power through penetrating radiation. The Bremsstrahlung radiant power density falls from 0.05–0.28 (hot fusion) to 1.4 – 8.1×10^{-10} for LANR. The delivered X-ray dose at 1 m decreases by 11–18 to 23 orders of magnitude, saving the graduate students, from 3.1×10^{19} Grays (hot fusion) to 1.4 – 3.3×10^{-4} Grays for LANR. This is consistent with the relative absence of ionizing emissions from most cold fusion systems, except for a few reports looking in the ~ 6 – 20 keV region. In addition, the temperature difference also causes the output spectrum of the Bremsstrahlung radiation to be shifted to the near infra-red, consistent with the NIR emission of LANR systems at their OOP.

Third, with control of LANR by precise material fabrication, metamaterial shape selection using high impedance (“High-Z”) Phusor®-type LANR devices in very low electrical conductivity D₂O, control of D-flux and post D-loading flux, there is a higher likelihood of achieving LANRs impressive energy gain with fairly good reproducibility. Such high impedance LANR devices have shown power gains 200–400%, and higher, compared to input energy and to input energy transferred to conventional dissipative devices.

Figure 7 shows the ephemeral superlative output of one DAP Phusor(R) type LANR device. The graph shows the input power-normalized change in temperature (degrees centigrade, delta-T) for both the ohmic thermal control and the DAP Phusor. When activated, the DAP (Pd*/D₂O – Pd(OD)₂/Au Dual Anode Phusor®-type), the peak power gain was circa 8000% (Fig. 6) which led to damage of the leads of the cell (Fig. 7).

Figure 8 shows the output for a heat flow sensor arranged to receive some of the heat output from both the DAP Phusor and the ohmic control. The data is the electrical output of the heat flow sensor normalized by the input electrical power. It can be seen that the DAP Phusor produced more heat flow normalized for power for input power, then did the ohmic thermal control. Excess power gain was $\sim 500\%$ based on the heat flow sensors.

In the future, LANR will become an energy multiplier because the energy density of LANR reactions is ten million

times that of gasoline. Given the prevalence of the fuel, and the incredible efficiency, LANR will play a critical role in all future technologies with potential revolutionary applications to all energy issues – robotics, transportation, electricity production, and space travel.

Acknowledgments

The author thanks Gayle Verner for her meticulous help in manuscript and idea development, and also Jeffrey Tolleson, Alex Frank, Alan Weinberg, Allen Swartz, Charles Entenmann, Frank Gordon, Larry Forsley, Pamela Mosier-Boss, Brian Ahern, Jeff Driscoll, Peter Hagelstein, Robert Smith, Jan Marwan, and the late Scott Chubb for their helpful conversations, and JET Energy and New Energy Foundation for the support. PHUSOR® is a registered trademark of JET Energy, Incorporated. PHUSOR®-technology is protected by U.S. Patents D596724, D413659 and Patents pending. © 2011 JET Energy, Incorporated

References

- [1] M.R. Swartz, Survey of the observed excess energy and emissions in latticeassisted nuclear reactions, *J. Scientific Exploration* **23**(4) (2009) 419–436.
- [2] M.R. Swartz, Excess power gain and tardive thermal power generation using high impedance and codepositional phusor type LANR devices, in *ICCF-14 Int. Conf. on Condensed Matter Nuclear Science*, Washington, DC, 10–15 August 2008, David J. Nagel and Michael E. Melich (Eds.), ISBN: 978-0-578-06694-3, 123, 2010.
- [3] M. Swartz, G. Verner, Excess heat from low electrical conductivity heavywater spiral-wound Pd/D₂O/Pt and Pd/D₂OPdCl₂/Pt devices, *Condensed Matter Nuclear Science, Proc. of ICCF-10*, P.L. Hagelstein, S. Chubb (Eds.), World Scientific, NJ, ISBN 981-256-564-6, 29-44; 45-54 (2006).
- [4] M. Swartz, Consistency of the biphasic nature of excess enthalpy in solid state anomalous phenomena with the quasi-1-dimensional model of isotope loading into a material, *Fusion Technol.* **31** (1997) 63–74.
- [5] Y. Arata and Y.C. Zhang, Anomalous Production of Gaseous ⁴He at the Inside of DS-cathodedDuring D₂-electrolysis, *Proc. Jpn. Acad. Ser. B*, **75**, p. 281 (1999); Y. Arata and Y.C. Zhang, Observation of anomalous heat release and helium-4 production from highly deuterated fine particles, *Jpn. J. Appl. Phys. Part 2*, **38** (1999) L774; Y. Arata and Y. Zhang, The establishment of solid nuclear fusion reactor, *J. High Temp. Soc.* **34**(2) (2008) 85.
- [6] F. Celani et al., Deuteron electromigration in thin pdwires coated with nano-particles: evidence for ultra-fast deuterium loading and anomalous, large thermal effects, in *ICCF-14 Int. Conf. on Condensed Matter Nuclear Science*, Washington, DC, 2008.
- [7] I. Dardik and H. Branover, A. El-Boher, D. Gazit, E. Golbreich, E. Greenspan, A. Kapusta, B. Khachatorov, V. Krakov, S. Lesin, B. Michailovitch, G. Shani and T. Zilov, Intensification of low energy nuclear reactions using superwave excitation, *Proc. 10th Int. Conf. on Cold Fusion* (2003).
- [8] J. Dash and D.S. Silver, Surface studies after loading metals with hydrogen and/or deuterium, 13th Conf. CMNS 2007, Sochi, Russia; J. Dash and S. Miguet, Microanalysis of Pd cathodes after electrolysis in aqueous acids, *J. New Energy* **1**(1) (1996) 23.
- [9] M. Fleischmann and S. Pons, Electrochemically induced nuclear fusion of deuterium, *J. Electroanal. Chem.* **261**, 301–308, erratum **263** (1989) 187; M. Fleischmann and S. Pons, Some comments on the paper Analysis of experiments on calorimetry Of LiOD/D₂O electrochemical cells, R.H. Wilson et al., *J. Electroanal. Chem.* **332** (1992) 1?, *J. Electroanal. Chem.* **332** (1992) 33–53, M. Fleischmann, and S. Pons, Calorimetry of the Pd–D₂O system: from simplicity via complications to simplicity, *Phy. Lett. A* **176** (1993) 118–129, M. Fleischmann, S. Pons, M. Anderson, L.J. Li and M. Hawkins, Calorimetry of the palladium–deuterium-heavy water system, *Electroanal. Chem.* **287** (1990) 293.
- [10] Y. Iwamura, M. Sakano and T. Itoh, Elemental analysis of Pd complexes: effects of D₂ gas permeation. *Jpn. J. Appl. Phys. A* **41** (2002) 4642, Y. Iwamura et al., Observation of surface distribution of products by X-ray fluorescence spectrometry during D₂ gas permeation through Pd complexes, in *12th Int. Conf. on Condensed Matter Nuclear Science*, 2005, Yokohama, Japan.
- [11] D. Letts and D. Cravens, Laser stimulation of deuterated palladium: past and present, *Proc. 10th Int. Conf. on Cold Fusion*, Cambridge, MA, 2003.

- [12] D. Letts and P.L. Hagelstein. Stimulation of optical phonons in deuterated palladium, in *ICCF-14 Int. Conf. on Condensed Matter Nuclear Science*, 2008, Washington, DC, D. Letts, D. Cravens and P.L. Hagelstein, *Thermal Changes in Palladium Deuteride Induced by Laser Beat Frequencies*, in Low-Energy Nuclear Reactions Sourcebook, J. Marwan and S. Krivit (Eds.), 2008
- [13] M. McKubre, F. Tanzella, P.L. Hagelstein, K. Mullican and M. Trevithick, The need for triggering in cold fusion reactions, *Proc. 10th Int. Conf. on Cold Fusion*, Cambridge, MA, 2003.
- [14] M.H. Miles, R.A. Hollins, B.F. Bush, J.J. Lagowski and R.E. Miles, Correlation of excess power and helium production during D_2O and H_2O electrolysis, *J. Electroanal. Chem.* **346** (1993) 99–117.
- [15] M.H. Miles and B.F. Bush, Heat and helium measurements in deuterated palladium, *Trans. Fusion Technol.* **26** (1994) 156–159.
- [16] M.H. Miles et al., Calorimetric analysis of a heavy water electrolysis experiment using a Pd–B alloy cathode, Naval Research Laboratory Report NRL/MR/6320-01-8526, 155 pp., March 16, 2001.
- [17] G.H. Miley, G. Narne and T. Woo, Use of combined NAA and SIMS analyses for impurity level isotope detection, *J. Radioanal. Nucl. Chem.* **263**(3) (2005) 691–696, G.H. Miley and J. Shrestha, Transmutation Reactions and Associated LENR Effects in Solids, in *Low-Energy Nuclear Reactions Sourcebook*, J. Marwan and S. Krivit (Eds.), Oxford University Press, Oxford, 2008.
- [18] P.A. Mosier-Boss and S. Szpak, The Pd/nH system: Transport processes and development of thermal instabilities, *Il Nuovo Cimento* **112A** (1999) 577–585.
- [19] P.A. Mosier-Boss, S. Szpak, F.E. Gordon and L.P.G. Forsley, Use of CR-39 in Pd/D co-deposition experiments, *Euro. Phys. J. Appl. Phys.* **40** (2007) 293–303.
- [20] P.A. Mosier-Boss, S. Szpak, F.E. Gordon and L.P.G. Forsley, Triple tracks in CR-39 as the result of Pd–D co-deposition, evidence of energetic neutrons, *Naturwissenschaften* **96** (2008) 135–142.
- [21] S. Pons, and M. Fleischmann, Heat after death, *Proc. ICCF-4*, Maui, EPRI TR104188-V2, 2, 1994, pp. 8-1, **Trans. Fusion Technol.** **26**(4T), Part 2 (1994) 87.
- [22] M. Srinivasan et al., Tritium and excess heat generation during electrolysis of aqueous solutions of alkali salts with nickel cathode, *Frontiers of Cold Fusion*, H. Ikegami (Ed.), *Proc. Third Int. Conf. on Cold Fusion*, October 21–25, 1992, Universal Academy Press, Tokyo, pp. 123–138.
- [23] R. Stringham, Cavitation and fusion, *ICCF-10*, 2003, Cambridge, MA.
- [24] M. Swartz, Can a Pd/D₂O/Pt device be made portable to demonstrate the optimal operating point? Condensed Matter Nuclear Science, *Proc. Of ICCF-10*, Peter L. Hagelstein and Scott R. Chubb (Eds.), World Scientific, NJ, ISBN 981–256–564–6, 29–44; 45–54, 2006.
- [25] M. Swartz, Codeposition of palladium and deuterium, *Fusion Technol.* **32** (1997) 126–30.
- [26] M. Swartz, Noise Measurement in cold fusion systems, *J. New Energy* **2**(2) (1997) 56–61.
- [27] M. Swartz, Patterns of failure in cold fusion experiments, *Proc. 33rd Intersociety Engineering Conf. on Energy Conversion*, IECEC-98-I229, CO, Aug. 1998.
- [28] M. Swartz, Patterns of success in research involving low-energy nuclear reactions, *Infinite Energy* **31** (2000) 46–48.
- [29] M. Swartz, The Impact of heavy water (D_2O) on nickel-light water LANR systems, *Proc. 9th Int. Conf. on Cold Fusion*, Beijing, China, Z. Xing and X. Li (Eds.), May 2002.
- [30] M. Swartz and G. Verner, Dual ohmic controls improve understanding of 'heat after death', *Trans. Amer. Nucl. Soc.* **93** (2005) 891–892. ISSN:0003-018X.
- [31] M. Swartz, and G. Verner, Two sites of cold fusion reactions viewed by their evanescent tardive thermal power, Abstract, ICCF-11 (2004), M. Swartz (Ed.), *Kinetics and Lumped Parameter Model of Excess Tardive Thermal Power*, Mitchell Swartz, APS, 2005.
- [32] M. Swartz, G. Verner, Metamaterial Function of Cathodes Producing Hydrogen Energy and Deuteron Flux, *Proc. 14th Int. Conf. Condensed Matter Nucl. Sci. and the 14th Int. Conf. Cold Fusion (ICCF-14)*, 10–15 August 2008, Washington, DC, David J. Nagel and Michael E. Melich (Eds.), ISBN: 978-0-578-06694-3, 458, 2010.
- [33] M. Swartz and G. Verner, Photoinduced excess heat from laser-irradiated electrically-polarized palladium cathodes in D_2O , Condensed Matter Nuclear Science, *Proc. ICCF-10*, Peter L. Hagelstein and Scott Chubb (Eds.), NJ, ISBN 981-256-564-6, 213-226, 2006.
- [34] M. Swartz and G. Verner, A. Weinberg, Non-thermal near-IR emission linked with excess power gain in high impedance and

- codeposition phusor-LANR Devices, in *Proc. 14th Int. Conf. Condensed Matter Nucl. Sci. and the 14th Int. Conf. Cold Fusion (ICCF-14)*, 10–15 August 2008, Washington, DC, David J. Nagel and Michael E. Melich (Eds.), ISBN: 978-0-578-06694-3, 343, 2010.
- [35] M. Swartz, Improved electrolytic reactor performance using pi-notch system operation and gold anodes, *Trans. Amer. Nucl. Assoc.*, Nashville, Tenn Meeting, ISSN:0003-018X publisher LaGrange, Ill, 1998, pp. 78, 84–85.
 - [36] M.R. Swartz, Breakeven from LANR phusor device systems: relative limitations of thermal loss in feedback loop, in *Proc. 14th Int. Conf. Condensed Matter Nucl. Sci. and the 14th Int. Conf. Cold Fusion (ICCF-14)*, 10–15 August 2008, Washington, DC, David J. Nagel and Michael E. Melich (Eds.), ISBN: 978-0-578-06694-3, 689, 2010.
 - [37] S. Szpak and P.A. Mosier-Boss, On the behavior of the cathodically polarized Pd/D system: a response to Vigier's comments, *Phys. Lett. A* **221** (1996) 141–143.
 - [38] S. Szpak, P.A. Mosier-Boss, S.R. Scharber and J.J. Smith, Cyclic voltammetry of Pd+D codeposition, *J. Electroanal. Chem.* **380** (1995) 1–6.
 - [39] S. Szpak, P.A. Mosier-Boss and J.J. Smith, Deuterium uptake during Pd–D codeposition, *J. Electroanal. Chem.* **379** (1994) 121–127.
 - [40] S. Szpak, P.A. Mosier-Boss and F.E. Gordon, Further evidence of nuclear reactions in the pd/d lattice: emission of charged particles, *Naturwissenschaften* **94** (2007) 511–514.
 - [41] S. Szpak, P.A. Mosier-Boss, C. Young and F.E. Gordon, Evidence of nuclear reactions in the Pd lattice, *Naturwissenschaften* **92** (2005) 394–397.
 - [42] S. Szpak, P.A. Mosier-Boss, S.R. Scharber and J.J. Smith, Charging of the Pd/nH system: role of the interphase, *J. Electroanal. Chem.* **337** (1992) 147–163.
 - [43] S. Szpak, P.A. Mosier-Boss, M.H. Miles and M. Fleischmann, Thermal behavior of polarized pd/d electrodes prepared by co-deposition, *Thermochim. Acta* **410** (2004) 101–107.
 - [44] S. Szpak, P.A. Mosier-Boss and J.J. Smith, On the behavior of the cathodically polarized Pd/D system: search for emanating radiation, *Phys. Lett. A* **210** (1996) 382–390.
 - [45] S. Szpak, P.A. Mosier-Boss and J.J. Smith, On the behavior of pd deposited in the presence of evolving deuterium, *J. Electroanal. Chem.* **302** (1991) 255–260.
 - [46] S. Szpak, P.A. Mosier-Boss, R.D. Boss and J.J. Smith, On the behavior of the pd/d system: evidence for tritium production, *Fusion Technol.* **33** (1998) 38–51.
 - [47] S. Szpak et al., The effect of an external electric field on surface morphology of co-deposited Pd/D films, *J. Electroanal. Chem.* **580** (2005) 284–290.
 - [48] V. Violante, E. Castagna, C. Sibilia, S. Paoloni and F. Sarto, Analysis of Mi-hydride thin film after surface plasmons generation by laser technique, *Proc. 10th Int. Conf. on Cold Fusion*, Cambridge, MA, 2003.
 - [49] F.G. Will, K. Cedzynska and D.C. Linton, Tritium generation in palladium cathodes with high deuterium loading, *Trans. Fusion Technol.* **26** (1994) 209–213; Reproducible tritium generation in electrochemical cells employing palladium cathodes with high deuterium loading, *J. Electroanal. Chem.* **360** (1993) 161–176.
 - [50] M. Swartz, Three physical regions of anomalous activity in deuterided palladium, *Infinite Energy* **14**(61) (2008) 19–31.
 - [51] M. Swartz and R., Optimal operating point manifolds in active, loaded palladium linked to three distinct physical regions, in *Proc. 14th Int. Conf. Condensed Matter Nucl. Sci. and the 14th Int. Conf. Cold Fusion (ICCF-14)*, 10–15 August 2008, Washington, DC, David J. Nagel and Michael E. Melich (Eds.), ISBN: 978-0-578-06694-3, 639, 2010.
 - [52] M. Swartz, Quasi-one-dimensional model of electrochemical loading of isotopic fuel into a metal, *Fusion Technol.* **22**(2) (1992) 296–300.
 - [53] M. Swartz, Isotopic fuel loading coupled to reactions at an electrode, *Fusion Technol.* **26**(4T) (1994) 74–77.
 - [54] M. Swartz, Optimal operating point characteristics of nickel light water experiments, *Proc. ICCF-7*, Vancouver, Canada, 1998, pp. 269.
 - [55] M. Swartz, Generality of optimal operating point behavior in low energy nuclear systems, *J. New Energy* **4**(2) (1999) 218–228.
 - [56] R.W. Bass and M.R. Swartz, Empirical system identification (ESID) and optimal control of lattice- assisted nuclear reactors, in *Proc. 14 Int. Conf. on Condensed Matter Nuclear Science*, DC, 2010.
 - [57]] M. Swartz and L. Forsley, Analysis of superwave-as-transitory-OOP-peak hypothesis, in *Proc. 14, Int. Conf. On Condensed Matter Nuclear Science*, DC, 2008.

- [58] C.A. Hampel, *Rare Metal Handbook*, Reinhold, NY, 1954.
- [59] M. Hansen and K. Anderko, *Constitution of Binary Alloys*, McGraw-Hill, NY, 1958.
- [60] F.A. Cotton and G. Wilkinson, *Advanced Inorganic Chemistry*, Interscience, NY, 1972.
- [61] L. F. Allard, E. Voelkl, D. S. Kalakkad and A. K. Datye, Electron holography reveals the internal structure of palladium nano-particles, *J. Materials Sci.* **29**(21) (1994) 5612–5614.
- [62] M. Swartz, P.L. Hagelstein, G. Verner and K. Wright, Vacancy phase states in nickel cathodes, *Proc. of the Seventh International Conference on Cold Fusion (ICCF-7)*, Vancouver, Canada, 1998, p. 137.
- [63] Jan Marwan has improved the field by generating new methods of making additional vacancies with nanolipids and dyes.
- [64] J. Meier J. Schiøtzb, P. Liub, I.J.K. Nørskovb and U. Stimminga, Nano-scale effects in electrochemistry ?, *Chem. Phys. Lett.* **390**(4–6) (2004) 440–44.
- [65] Chengcai Luo, Yuhong Zhang and Yanguang Wang, Palladiumnanoparticles in poly(ethyleneglycol): the efficient and recyclable catalyst for Heck reaction, *J. Mol. Catalysis A: Chemical* **229**(1–2) (2005) 7–12.
- [66] Kensuke Naka, ? Hideaki Itoh and Yoshiki Chujo?, Self-organization of spherical aggregates of palladium nanoparticles with a cubic silsesquioxane, *Nano Lett.* **2** (11) (2002) 1183–1186.
- [67] Anton Kiriy, SergiyMinko, ? Ganna Gorodyska, Manfred Stamm and Werner Jaeger, palladiumwire-shaped nanoparticles from single synthetic polycation molecules, *Nano Lett.* **2**(8) (2002) 881–885.
- [68] Ping Lu, Toshiharu Teranishi, Kiyotaka Asakura, MikioMiyake and Naoki Toshima?, Polymer-protected Ni/Pd bimetallic nano-clusters: preparation, characterization and catalysis for hydrogenation of nitrobenzene, *J. Phys. Chem. B*, **103** (44) (1999) 9673–9682.
- [69] P. G. Sandersa, J.R. Weertman and J.G. Barker, Structure of nanocrystalline palladium and copper studied by small angle neutron scattering, *J. Mater. Res.* **11** (1996) 12.
- [70] Young-Min Chung and Hyun-Ku Rhee, *J. Catalysis Lett.* **85**(3–4) (2003) 159–164, Pt–Pd bimetallic nanoparticles encapsulated in dendrimer nanoreactor, Young-Min Chung1 and Hyun-Ku Rhee1, *J. Catalysis Lett.* **85**(3–4)(2003) 159–164.
- [71] Karical R. Gopidas, James K. Whitesell, ? and Marye Anne Fox ?, synthesis, characterization and catalytic applications of a palladium–nanoparticle-cored dendrimer, *Nano Lett.* **3**(12) (2003) 1757–1760.
- [72] D.R. Smith, J.B. Pendry and M.C.K. Wiltshire, Metamaterials and negative refractive index, *Science* (2004), sciencemag.org.
- [73] Experimentalverification of backward-waveradiation from a negative refractive indexmetamaterial, *J. Appl. Phys.* (2002) [waves.utoronto.ca].
- [74] D. Schurig, J.J. Mock, B.J. Justice and S.A. Cummer, Metamaterial electromagnetic cloak at microwave frequencies, *Science* (2006) sciencemag.org.
- [75] G. Dolling, C. Enkrich, M. Wegener, C.M. Soukoulis, Simultaneous negative phase and group velocity of light in a meta material, *Science* (2006). sciencemag.org.
- [76] G. Brodin, M. Marklund, L. Stenflo and P.K. Shukla, Anomalous reflection and excitation of surfacewaves in meta materials, *Phys. Lett. A* **367**(3) (2007) 233–236.
- [77] E. Verney, B. Sauviac and C.R. Simovski, Isotropic metamaterial electromagnetic lens, *Phys. Lett. A* **315** (2004) 332.
- [78] M. Marklund, P.K. Shukla, L. Stenflo and G. Brodin, Solitons and decoherence in left-handed metamaterials, *Phys. Lett. A* **341** (2005) 231–234.
- [79] H. Chen, T-junction waveguide experiment to characterize left-handed properties of metamaterials, *J. Appl. Phys.* (2003). ceta-p6.mit.edu.
- [80] J. Pendry et al. Defense advanced research projects agency, <http://physics.ucsd.edu/~drs>, Air Force Office of Scientific Research (AFOSR).
- [81] R.A. Shelby, D. R. Smith and S. Schultz, Experimental verification of a negative index of refraction, <http://physics.ucsd.edu/~drs>, Appearing in the April 6, 2001 issue of Science.
- [82] <http://www.ee.duke.edu/Academics/Undergraduate/IndStudy03/ScottC2003.html>, Towards Negative Index Material: Magnetic Response.
- [83] J.E. Kielbasa, J. Liu, K.B. Ucer, D.L. Carroll and R.T., Sol-gel nanocomposites as metamaterials: preparation and optical measurements, *J. Materials Sci.: Materials Electronics* (2007).
- [84] W. Wu, E. Kim, E. Ponizovskaya, Y. Liu, Z. Yu and N. Fang, Optical meta materials at near and Mid- IR range fabricated by nanoimprint lithography, *Appl. Phys. A: Materials Sci. Processing* **87** (2007) 143–150.

- [85] W. Wu, Z. Yu, S.Y. Wang, R.S. Williams, Y. Liu and C. Sun, Mid-infrared metamaterials fabricated by nanoimprint lithography, *Appl. Phys. Lett.* (2007). link.aip.org...mat/pdf/0508/0508307.pdf; R. Marques, F. Medina and R. Rafii-El-Idrissi.
- [86] D. Korobkin, Y.A. Urzhumov, B. Neuner III, C. Zorman, Mid-infrared metamaterial based on perforated Sic membrane: engineering optical response using Z..., *Appl. Phys. A: Materials Sci. Processing* **88**(4) (2007) 605–609.
- [87] C. Caloz and H.V. Nguyen, Novel broadband conventional-and dual-composite right/left-Handed (C/D-CRLH) meta materials, *Appl. Phys. A: Materials Sci. Processing* **87**(2) (2007) 309–316.
- [88] Q. Wu, P. Pan, F.Y. Meng, L.W. Li and J. Wu, A novel flat lens horn antenna designed based on zero refraction principle of metamaterials, *Appl. Phys. A Materials Sci. Processing* (2007).
- [89] M.W. Klein, C. Enkrich, M. Wegener and S. Linden, Second-harmonic generation from magnetic metamaterials all 4 versions, *Science* (2006). sciencemag.org
- [90] S. Linden, C. Enkrich, M. Wegener, J. Zhou and T. Koschny, Magnetic response of metamaterials at 100 THz, *Science* (2004). sciencemag.org.
- [91] H.H. Uhlig, *Corrosion and Corrosion Control*, 2nd Edition, Wiley, New York, 1971.
- [92] J.O'M Bockris and A.K.N. Reddy, *Modern Electrochemistry*, Plenum Press, 1970.
- [93] A. Von Hippel, *Dielectric Materials and Applications*, MIT Press, Cambridge, 1954.
- [94] J.R. Melcher, *Continuum Electromechanics*, MIT Press, Cambridge, 1981.
- [95] A. Von Hippel, D.B. Knoll and W.B. Westphal, Transfer of protons through pure ice 1 h single crystals, *J. Chem. Phys.* **54** (1971) 134, 145.
- [96] M. Swartz, Dances with protons—ferroelectric inscriptions in water/ice relevant to cold fusion and some energy systems, *Infinite Energy* **44** (2002) 64–71.
- [97] P.L. Hagelstein et al., A theoretical formulation for problems in condensed matter nuclear science. in ICCF-14 Int. Conf. on Condensed Matter Nuclear Science, 2008, Washington, DC, P.L. Hagelstein and I. Chaudhary, Models Relevant to Excess Heat production in Fleischmann–Pons experiments, in *Low-Energy Nuclear Reactions Sourcebook*, J. Marwan and S. Krivit (Eds.), Oxford University Press, Oxford, 2008.
- [98] M. Rabinowitz et al., Opposition and support for cold fusion, in *Fourth Int. Conf. on Cold Fusion*, Lahaina, Maui: Electric Power Research Institute, CA 94304, 1993.
- [99] X.Z. Li et al., the precursor of cold fusion phenomenon in deuterium/solid systems. in anomalous nuclear effects in deuterium/solid systems, *AIP Conf. Proc.* **228**, 1990, Brigham Young Univ., Provo, UT, American Institute of Physics, New York.
- [100] A. Takahashi and N. Yabuuchi, Study on 4D/TSC condensation motion by non-linear Langevin equation, in *Low-Energy Nuclear Reactions Sourcebook*, J. Marwan and S. Krivit (Eds.), 2008, Oxford University Press, Oxford, A. Takahashi, Dynamic mechanism of TSC condensation motion, in *ICCF-14 Int. Conf. on Condensed Matter Nuclear Science*, 2008, Washington, DC.
- [101] M. Swartz, Possible deuterium production from light water excess enthalpy experiments using nickel cathodes, *J. New Energy* **3** (1996) 68–80.
- [102] M. Swartz, Positrons in nuclear reactions in solids, *Fusion Technol.* **31** (1997) 228–236.
- [103] S.R. Chubb and T.A. Chubb, The role of hydrogen ion band states in cold fusion. *Trans. Fusion Technol.* **26**(4T) (1994) 414.
- [104] T.A. Chubb and S.R. Chubb, Ion band states: what they are and how they affect cold fusion, in *Cold Fusion Source Book*, *ibid.* **75** (1994).
- [105] M. Swartz, Catastrophic Active medium hypothesis of cold fusion, Fourth Int. Conf. On Cold Fusion, sponsored by EPRI and the Office of Naval Research (1994); M. Swartz, Hydrogen redistribution by catastrophic desorption in select transition metals, *J. New Energy* **1**(4) (1977) 26–33.
- [106] D.A. Papaconstantopoulos, B.M. Klein et al., Band structure and superconductivity of PdDx and PdHx, *Phys. Rev.* **17**(1) (1977) 141–150.
- [107] E. Wicke and H. Brodowsky, *Hydrogen in Palladium and Palladium Alloys*, *Hydrogen in Metals II*, G. Alefield and J. Volkl (Eds.), Springer, Berlin, 1978.
- [108] H. Teichler, Theory of hydrogen hopping dynamics including hydrogen-lattice correlations, *J. Less-Common Metals* **172–174** (1991) 548–556.
- [109] B.M. Klein and R.E. Cohen, Anharmonicity and the inverse isotope effect in the palladium–hydrogen system, *Phys. Rev. B*

- 45** (1992) 21, 405.
- [110] R.W. Bussard, Virtual-state internal nuclear fusion in metal lattices, *Fusion Technol.* **16** (1989) 231–236.
 - [111] T.C. Gibb, *Principles of Mossbauer Spectroscopy*, Chapman and Hall, London (1974).
 - [112] D.P.E. Dickson and F. Berry, *Mossbauer Spectroscopy*, Cambridge University Press, Cambridge, 1983.
 - [113] U. Gonser, *Mossbauer Spectroscopy*, Springer, NY, 1975.
 - [114] M. Swartz and G. Verner, Bremsstrahlung in hot and cold fusion, *J. New Energy* **3**(4) (1999) 90–101.
 - [115] M.R. Swartz, Excess heat and electrical characteristics of type B anode-plate high impedance phusor-type LANR devices, *J. Scientific Exploration*, American Chemical Society, Salt Lake City, UT, *J Scientific Exploration* **23**(4) (2009) 491–495.



Research Article

Bird's Eye View of Phonon Models for Excess Heat in the Fleischmann–Pons Experiment

Peter L. Hagelstein *

Research Laboratory of Electronics, Massachusetts Institute of Technology, Cambridge, MA 02139, USA

Abstract

Over the past several years, we have been developing models relevant to excess heat in the Fleischmann–Pons experiment. Here we review some of the key issues, and give an account of some of the progress that we have made. The excess heat effect is prodigious, and ^4He seems to be correlated with the energy, but there are no energetic particles seen in amounts commensurate with the energy. This motivated us to seek models which fractionate a large energy quantum, and the lossy spin–boson model appears to do the job. Coherent energy exchange in the fractionation limit and excitation transfer are the mechanisms required which allow us to describe a new set of reactions and associated models which seem to be relevant to the experiments. The resulting models allow us to develop interpretations for numerous experimental observations.

© 2012 ISCMNS. All rights reserved.

Keywords: Excess heat, Coherent energy exchange, Fleischmann–Pons effect, Theory

1. Introduction

It has been more than two decades since the announcement of the excess heat effect in the Fleischmann–Pons experiment [1]. In our view, much progress has been made over these many years, and it seems appropriate here to review some of the ideas and approaches that we have been pursuing seeking a coherent theoretical explanation.

On the one hand, a great many experimental results have been put forth which seem inconsistent with what one finds in the nuclear physics and condensed matter physics textbooks. These results have been largely ignored by the mainstream scientific community, probably for several reasons; nuclear physics and condensed matter physics are mature areas of research, and present understanding in both areas appear to rule out the new effects; the effort required to sort through the associated chaff is very large, and the reward that awaits the scientist who puts the effort in is very likely the destruction of his or her career.

On the other hand, the excess heat effect is a very large effect that has been seen a great many times. One would not expect such a strong effect to occur without a good physics reason, which suggests that something very fundamental must be going on. Hence, by all rights we should be able to understand the physical mechanisms involved, and in doing

*E-mail: E-mail: plh@mit.edu

so we should expect that known physical law should apply pretty much throughout, perhaps in ways that we had not anticipated. In what follows, we consider a selection of the basic issues that arise in the development of a theoretical model for excess heat.

2. Absence of Energetic Particles

The Fleischmann–Pons experiment as initially described is an electrochemical experiment with a Pd (rod) cathode in D_2O with 0.1 M LiOD, and a Pt anode. Electrolysis has the effect of loading deuterium into the palladium, and a high D/Pd loading is important to see the excess heat effect [2,3]. In some experiments where excess heat is seen, the energy produced is prodigious; if we reference the energy produced to the number of atoms in the cathode, we find results reported in the range of hundreds to tens of thousands of eV per Pd atom. There is no evidence of associated chemical reactions which could produce so much energy, which led Fleischmann and coworkers to conjecture that the effect was nuclear. However, there is no evidence of energetic nuclear products in amounts commensurate with the energy produced. Known exothermic nuclear reaction processes release energy through energetic reaction processes, and the absence of commensurate energetic particles rules out such reactions. Skeptics have made use of this point to cast doubt on positive experimental results, and on the competence of those working on the problem.

From our perspective, there have been more than enough replications of the excess heat effect by different groups using different methods that we are sure that the effect is real. Hence, whatever physical mechanism is responsible for the excess energy must be something new. Since it is new, the best route forward initially is probably to focus on the body of experimental work to try to understand what it is and how it works. The early studies of Miles, Bush and coworkers [4] correlated excess 4He in the gas with the excess energy produced. The ratio of excess energy generated to 4He produced was found to be near 24 MeV [5] (a conclusion which continues to generate controversy even now). This result already allows us to reach a rather strong conclusion about the new physical mechanism.

If the energy produced in a conventional nuclear reaction occurs as energetic particles, and if 4He is involved in the new reaction process, we can ask how much energy the 4He particle is born with. To address this, we note that energetic 4He will occasionally collide with the deuterons in PdD (a picture of one billiard ball hitting another is useful here), producing an energetic deuteron which may collide with another deuteron to produce a fusion reaction. With a neutron detector it is possible to see whether such reactions occur; using textbook results for energy loss rates and deuteron fusion cross sections we can interpret the experimental result in terms of the energy of the 4He particle. What we find from such a study is that from theory fast 4He particles produce secondary neutrons readily even when their energy is modest (this effect has been seen in the experiments of Ref. [6]), and that hardly any neutrons were seen in experiments producing excess energy. We can conclude from such studies that the 4He atom must be born with less than 20 keV of the 24 MeV energy we might associate with the reaction process [7,8].

3. Two-laser Experiment

In conventional nuclear reactions the energy produced appears as energetic particles. The new process associated with excess heat in the Fleischmann–Pons experiment clearly doesn't work this way, which motivates us to ask where the reaction energy goes.

This question is important, and highly nontrivial. On the one hand, there are a great many possible energetic particles in principle that we might look for (photons, electrons, neutrons, nuclei, and more exotic particles), so we need to be sure that none were missed. On the other hand, if not energetic particles, then what should we look for (since we have no previous experience with a process like this in nuclear physics or condensed matter physics)? Although the energy is seen ultimately as thermal energy, intuitively we would expect that the nuclear energy should first be converted into an intermediate form of energy prior to thermalization. Candidates for this include phonons and plasmons.

Indirect evidence supporting the conversion of nuclear energy to optical phonon excitation comes from the two-laser experiment. It was found that excess heat in a Fleischmann–Pons cell could be stimulated with a single weak diode laser [9], but generally the excess heat did not persist once the laser was turned off. Excess heat was found to be stimulated by two weak diode lasers [10], and in this case the excess heat seemed to respond to the difference frequency, and generally persist after the lasers were turned off.

This behavior is consistent with a picture in which the laser stimulation excites (hybrid plasmon-optical phonon) modes which allow the new process to go, and in the single laser experiments the modes are lossy so that the excitation doesn't persist once the lasers are turned off. In the two-laser experiment, strong responses seem to be correlated with compressional optical phonon modes with zero group velocity. Since the effect persists after the lasers are turned off, it may be that some of the energy from the nuclear process is being channeled into these modes, and sustaining the excess heat effect [10].

4. Fractionation of a Large Quantum

In the experiments discussed above combined with the interpretations that we have given, there emerges a rather fundamental issue that pertains to the new physical mechanism. In a conventional deuteron–deuteron fusion reaction, we picture the two deuterons tunneling together, and then reacting to produce $p + t$ or $n + {}^3\text{He}$ as reaction products which push off each other converting reaction energy to kinetic energy. In such a picture, energy and momentum conservation local to the deuterons dictates that the reaction energy goes into the kinetic energy of the products, and even tells us what fraction of the energy goes to each particle. In the new physical process under discussion, the experiments seem to point to a new picture in which: the two deuterons tunnel together; a nearly stationary ${}^4\text{He}$ nucleus is produced; the 24 MeV reaction energy goes elsewhere, some of it ends up as optical phonon excitation (in the two-laser experiment); and then the energy is thermalized.

Note that this is not inconsistent with the observation of ${}^4\text{He}$ in the gas phase, since helium can diffuse to the surface in a few hours if created within a few thousand Angstroms of the surface. In some experiments the excess power is found to increase as the operating temperature increases [11]. The temperature dependence is similar to that of helium diffusion in Pd [12], which suggests the interpretation that excess power is limited by helium clogging up the active vacancy sites, which is cleared out by diffusion.

This picture motivates us to ask about a theoretical issue involving the fractionation of a quantum: is it possible for some kind of coherent process to take a very large 24 MeV quantum and split it up into an enormous number of quanta with much smaller (10s of meV) energy. If we take 23.85 MeV and convert it into optical phonon modes at 15.1 THz (63 meV), then we would have to produce about 3.78×10^8 quanta. There is no precedence for such an effect. However, if such an effect existed, then it would become possible to understand the new physical mechanism of the Fleischmann–Pons effect, and obtain a reconciliation with nuclear and condensed matter physics.

5. Energy Exchange between Two-level Systems and an Oscillator

These arguments above motivate us to consider simple models in which two-level systems are coupled to an oscillator. The idea here is that the math associated with a complicated quantum system tends to be a real mess, so that if we replace the complicated quantum system by a simple idealization, then we have the possibility of being able to work the math and gain some understanding of the physical effects under study. So, instead of starting with the complicated physical system that has a four-nucleon nuclear physics problem coupled to a PdD lattice with optical phonon modes and plasmon modes, we abstract the nuclear system into a two-level system, and abstract the condensed matter system into a harmonic oscillator. In the end, our two-level system stands in for any transition in any nuclear system (not just the four-nucleon system), and our oscillator stands in for any optical phonon mode, acoustical phonon mode, plasmon

mode, or hybrid optical phonon and plasmon mode. We are interested in whether a large quantum can be fractionated at all, independent at this point of what particular system can do the job.

Before rolling up our sleeves to analyze the problem, our intuition suggests that we should be able to exchange energy well if the transition energy of the two-level system were matched to the oscillator energy. For example, if an atom absorbs a photon we expect the excitation energy to be matched to the phonon energy; otherwise, probably energy exchange does not happen. But then we consider that there are nonlinear process that can occur. There are reports of rare gas atoms being excited in intense laser beams when several photons combine to produce the energy of the excited state. So, in some sense, the question seems to be whether it is possible to exchange lots of quanta efficiently between the oscillator and two-level systems while remaining coherent.

If we assume linear coupling in our model, we find the resulting model outlined in this discussion is one equivalent to one very well known in the physics literature [13] (the spin-boson model); it is written as

$$\hat{H} = \frac{\Delta E}{\hbar} \hat{S}_z + \hbar\omega_0 \hat{a}^\dagger \hat{a} + V \frac{2\hat{S}_x}{\hbar} (\hat{a}^\dagger + \hat{a}). \quad (1)$$

This model has been analyzed in a very large number of papers, and people have found that the model is capable of reasonably efficient coherent energy exchange between the two systems as long as the number of quanta exchanged is not too large (less than 50). We are pleased that there exists in the physics literature a model that shows coherent energy exchange with some fractionation, but it is clear that the spin-boson model will never exchange enough quanta to account for excess heat in the Fleischmann-Pons experiment.

6. Lossy spin-boson Model and Coherent Energy Exchange

So, what limits coherent energy exchange in the multiphoton limit in the spin-boson model? Why can we not fractionate a large quantum, and exchange energy coherently between two-level systems with MeV energy and an oscillator with meV energy?

Well, if we make use of perturbation theory, we can show quickly that what limits the rate for coherent energy exchange in the spin-boson model is destructive interference. Indirect coupling between distant states that are resonant proceeds through all possible pathways, and when we sum the contribution from all the different pathways we find that the cancellation is almost perfect. So, if we would like for a model to have a much larger rate of coherent energy exchange, we need to eliminate this destructive interference.

The simplest generalization of the spin-boson model in which this destructive interference is removed is a lossy generalization of the spin-boson model, where we assume that the oscillator sees loss at the transition frequency of the two-level system [14–17]; the associated Hamiltonian can be written as

$$\hat{H} = \frac{\Delta E}{\hbar} \hat{S}_z + \hbar\omega_0 \hat{a}^\dagger \hat{a} + V \frac{2\hat{S}_x}{\hbar} (\hat{a}^\dagger + \hat{a}) - \frac{i\hbar}{2} \Gamma(E). \quad (2)$$

It is not difficult for a physical system to work this way in general. In the coupled nuclear and optical phonon system, we would want to see a nuclear transition mediated by phonon exchange as the basis of the spin-boson part of the model; and then we would want to see phonon exchange to a lossy nuclear or atomic system (where the nucleus disintegrates, or an atomic system in which an electron is ejected, when large quantum is transferred to it). We have analyzed coherent energy exchange in the lossy-spin boson model using different approaches and approximations. It is clear that such models give very strongly enhanced energy exchange rates. We can see this using perturbation theory [18], and using brute force diagonalization of the associated Hamiltonian [19]. We have developed simplified versions of the model

that we can analyze in the strong coupling limit [20], and we can evaluate how fast coherent energy exchange occurs when a large quantum is fractionated into however many smaller quanta that we like [21].

The results of these studies so far tell us that it is possible to fractionate a large quantum, and to do it efficiently. The model says that the coupling needs to be very strong to get a fast coherent energy exchange rate for a large fractionation. The coupling strength in this model depends (linearly) on a local phonon exchange matrix element; it depends (square root) on how highly excited the oscillator is; and it depends (roughly linearly) on the number of two-level systems involved as long as each of them interact in the same way with the oscillator. The leverage in this case is in having a lot of two-level systems working together; on the one hand it is impossible within the models to fractionate a large quantum without a very much larger number of two-level systems (two to three orders of magnitude less than the square of the number of oscillator quanta) [21]; and on the other hand if enough two-level systems are involved then it does not seem to be a particularly difficult thing to do.

7. Excitation Transfer

The existence of the lossy spin–boson model tells us that a large quantum can be fractionated such that efficient coherent energy exchange is possible. The model describes a new physical mechanism in which a very large nuclear quantum can be fractionated into a large number of oscillator quanta of an optical phonon mode. But we still have work to do connecting things to a physical picture.

The problem is that there is a substantial Coulomb barrier between the two deuterons so that the associated coupling matrix element is going to be extremely small, so small that no reasonable amount of enhancement by having a lot of them is going to get us into the strong coupling regime enough to fractionate a 24 MeV quantum.

In response, we have been interested in models in which the excitation from an initial set of two-level systems (that are weakly coupled to the oscillator) is transferred to a second set (that are strongly coupled to the oscillator); it is this second set of two-level systems that fractionate the large quantum. Such a model can be written as

$$\hat{H} = \frac{\Delta E_1}{\hbar} \hat{S}_z^{(1)} + \frac{\Delta E_2}{\hbar} \hat{S}_z^{(2)} + \hbar \omega_0 \hat{a}^\dagger \hat{a} + V_1 \frac{2\hat{S}_x^{(1)}}{\hbar} (\hat{a}^\dagger + \hat{a}) + V_2 \frac{2\hat{S}_x^{(2)}}{\hbar} (\hat{a}^\dagger + \hat{a}) - \frac{i\hbar}{2} \Gamma(\hat{E}). \quad (3)$$

For this to work, we need an excitation transfer mechanism. Excitation transfer occurs in the context of spin–boson type models where there are two sets of two-level systems, but the effect requires precise resonances, and the associated rate is slow. However, when such models are augmented with loss, the rates are very much faster [21], and in the case that the second set of two-level systems are very strongly coupled with the oscillator then it is possible to make up quite a large energy mismatch [22].

8. Connection with the Physical System I

If coherent energy exchange between such strongly mismatched systems is predicted by the lossy spin–boson model, one might reasonably ask whether such an effect might be demonstrated by itself in an experiment. For example, suppose we wished to demonstrate coherent energy exchange from an excited lattice to a nucleus, then probably we would want to work with the lowest nuclear transition energy from a ground state. A list of the lowest energy transitions in the stable nuclei is given in Table 1. We see that the lowest energy transition occurs at 1565 eV in ^{201}Hg . If the vibrational excitation were uniform over the sample (e.g., the lowest vibrational mode in some orientation), then we might expect the nuclei to be excited in phase, with the resulting X-ray emission collimated due to a phased-array effect. Such an effect has been observed. In an experiment reported by Karabut, collimated X-ray emission is observed near 1.5 keV in connection with the termination of the discharge current in a glow discharge experiment [24–27]. In light of the

Table 1. Low-energy nuclear transitions from the ground state of stable nuclei, from the BNL online NUDAT2 table.

Nucleus	Excited state energy (keV)	Half-life	Multipolarity
²⁰¹ Hg	1.5648	81 ns	M1+E2
¹⁸¹ Ta	6.240	6.05 μ s	E1
¹⁶⁹ Tm	8.41017	4.09 ns	M1+E2
⁸³ Kr	9.4051	154.4 ns	M1+E2
¹⁸⁷ Os	9.75	2.38 ns	M1(+E2)
⁷³ Ge	13.2845	2.92 μ s	E2
⁵⁷ Fe	14.4129	98.3 ns	M1+E2

comments above, we view the discharge termination as providing a substantial pressure change that excites the lowest compressional mode of the sample (with a frequency in the MHz range). We propose that some of the vibrational energy is coherently exchanged to excite the 1565 eV transition of ²⁰¹Hg (which we imagine is deposited by the discharge, where mercury is assumed to be an impurity).

Within the framework of the theory outlined above, there are three different models that might be considered. We might take the 1565 eV transition as the two-level system, and then estimate the phonon exchange matrix element to see whether coherent energy exchange might occur. Assuming electric quadrupole (E2) or magnetic dipole coupling with electronic transitions, the resulting phonon exchange matrix element is too small by orders of magnitude to do the job. We might focus on the stronger electric dipole (E1) coupling to more highly excited nuclear states resulting in indirect coupling to the 1565 eV transition. To pursue this we developed a three-level generalization of the lossy spin–boson model and analyzed it in the strong coupling limit (so far not published). The coupling is much stronger in this case, and the analysis that results suggests that a much bigger experiment could be done in which coherent energy exchange would be predicted; however, it is clear that the Karabut experiment does not work in this way.

The third approach is to make use of the donor–receiver model formulation described in [23]; assume that the ²⁰¹Hg transition is weakly coupled to the phonon mode, and assume that a different and much stronger transition is present and couples to the oscillator. By matching the predictions of such a model with the Karabut experiment, we are able to develop a constraint on the ratio of the product of the zero-phonon and one-phonon exchange matrix elements to the transition energy. To be consistent, this ratio must be on the order of 5 keV or greater if the phonon exchange fraction of the interaction is low.

So, we face the question of what transition can couple so strongly. We have put in much effort to quantify electron–nuclear coupling, and by now we know that it falls short by orders of magnitude. Much stronger coupling is possible in the case of electronic (polarization) transitions, and we have begun to examine such transitions. From preliminary computations, it seems that the strongest of these gives a ratio near 0.1 eV. Our model would predict coherent energy exchange in a Karabut experiment in this case for much higher energy acoustic phonons (in the meV) range, but not for vibrations in the MHz range.

The only possible transition that is consistent with our interpretation of the Karabut experiment, within the framework of the model, is phonon exchange associated with configuration mixing of the nuclear states. This would be expected to occur due to the mass shift of the excited state configurations, as long as the phonon mode were sufficiently highly excited. Such an effect would require a generalization of the lossy spin–boson model so that phonon exchange with the strongly coupled system occurs through a mode rearrangement effect; the associated Hamiltonian would be of the form

$$\begin{aligned} \hat{H} = & \frac{\Delta E_1}{\hbar} \hat{S}_z^{(1)} + \frac{\Delta E_2}{\hbar} \hat{S}_z^{(2)} + \hbar \omega_0 (\hat{S}_z^{(2)}) \hat{a}^\dagger \hat{a} + V_1 \frac{2\hat{S}_x^{(1)}}{\hbar} (\hat{a}^\dagger + \hat{a}) \\ & + V_2 \left(\frac{\hat{S}_+^{(2)}}{\hbar} e^{i\hat{S}_D} + \frac{\hat{S}_-^{(2)}}{\hbar} e^{-i\hat{S}_D} \right) - \frac{i\hbar}{2} \Gamma(\hat{E}). \end{aligned} \quad (4)$$

The oscillator frequency and phonon modes structure change due to the mass shift in such a model, as indicated by the dependence of the frequency on the \hat{S}_z operator, and the presence of Duschinsky operators.

9. Connection with the Physical System II

We have put in much effort over the years trying to understand the excess heat effect in the Fleischmann–Pons experiment in terms of lossy spin–boson models and their generalizations. A direct connection can be made with the donor–receiver model described in [23] assuming that the $D_2/{}^4\text{He}$ transition is the weakly coupled donor transition. The hard part of the problem has always been the identification of the receiver system. There seem to be two basic approaches to the problem, based on how the models work. Two-level systems that are long-lived work a bit differently than two-level systems that decay rapidly.

Consider two-level systems that are long-lived first. In this case, the donor–receiver model allows the subdivision of the large donor quantum into many receiver excitations, which are converted into oscillator quanta. Metastable nuclear states are very long-lived, but couple poorly with the lattice as equivalent two-level systems. In this case, we have found that the generalization to the lossy three-level system has many of the same properties, so that we expect to be able to couple indirectly to metastable states. In this approach, metastable states with indirect transition energies from the ground state that are most nearly a submultiple of the donor transition energy are favored.

If the upper state of a two-level system decays rapidly, then there is no way to accumulate any real excitation, and hence there is no way to subdivide a donor transition. In this case one can think of the two-level system as being essentially adiabatically polarized by coupling with the oscillator, but deviations from adiabaticity leads to a mixing of the oscillator and two-level system degrees of freedom. It is possible for the strongly coupled two-level system with the short lifetime to mix with the oscillator in such a way that essentially no net excitations occur, but the mixing can allow efficient coherent energy exchange with a lower energy two-level system that is weakly coupled to the oscillator. This is the situation which seems to be the case in the Karabut experiment, but it should be able to work for energy production on equal footing.

All of these lead to the following pictures for excess heat production. In the simplest version of the model for $D_2/{}^4\text{He}$ transitions, the strongly coupled transition would be associated with configuration mixing of the deuteron ${}^3\text{S}$ and ${}^1\text{D}$ states (which have different masses), with phonon exchange taking place for sufficiently highly excited (Γ -point or L -point) optical phonon modes. Strong mixing of the phonon and nuclear degrees of freedom can result in energy exchange between long-lived states that are weakly coupled to the oscillator, such as the $D_2/{}^4\text{He}$ (or $\text{HD}/{}^3\text{He}$) transition. The reaction energy ends up in the oscillator, and the host nuclei of the lattice largely do not participate.

In the next simplest version of the model, the lattice has impurity nuclei with metastable transitions that are well matched as a submultiple of the $D_2/{}^4\text{He}$ (or $\text{HD}/{}^3\text{He}$) transition energy. The coupling to these states is much weaker, so we still require a strong configuration mixing transition (such as deuteron S/D mixing) to mix the nuclear and phonon degrees of freedom. But now most of the energy ends up going through the metastable transitions. In this case, we might expect to see a small fraction of the energy as gamma emission from the metastable state.

In a light water system, there is much less deuterium, so that the strong configuration mixing based coupling with the oscillator is more likely to be associated with the host nuclei. In this case, acoustic phonon mode excitation would be expected to be more important. The mixing of the nuclear and phonon degrees of freedom once again would allow

for the $D_2/{}^4\text{He}$ (or $HD/{}^3\text{He}$) transition energy to be coupled to the lattice. The same basic model applies. However, the strong acoustic mode excitation in such a model would allow coherent energy exchange with long-lived states generally in the host lattice nuclei. Some of these long-lived states may involve deformed nuclei that have slow fission decay channels. In this case one might expect to see a “lattice-induced” disintegration effect that would favor fission channels with minimum kinetic or excitation energy [28]. Finally, we might expect the subdivision route involving metastable transitions to be allowed in the case of an excited acoustic mode and host nuclei configuration based mixing with the phonons.

Tritium production can fit in nicely in such a picture. Suppose that we have strong optical phonon mode excitation with a metal deuteride, so that mixing between the deuteron S and D states couples with the excited phonon mode. However, suppose the phonon mode is insufficiently excited to allow for a 24 MeV energy exchange, but excited sufficiently to allow for a 4 MeV energy exchange. In this case the $D_2/{}^4\text{He}$ transition cannot go freely, but a slightly more complicated $D_2/{}^4\text{He}/\text{HT}$ transition would be allowed.

10. Connection with the Physical System III

In the analysis of the lossy spin–boson model, we focused on the limit where things work well, which is the situation after things start up. However, the models also talk about the regime where things just get started, which is interesting in its own right.

In the regime where excess heat production works well, there are lots of basis states available to the coupled quantum systems, so that if some are very lossy the system avoids them in favor of less lossy ones. As a result, the model works very efficiently, with little loss. The situation is very different when it first starts up. In this case, there are far fewer states available, and the system is unable to avoid lossy states and their associated decay channels (we noted this in Section 3.4 of [19]).

We might well expect loss from the $p + t$ and $n + {}^3\text{He}$ channels of deuteron–deuteron fusion in association with the two deuterons getting close to each other in the process of coherently reacting to produce ${}^4\text{He}$. Note that the coherent rate associated with the physical mechanism under discussion is linear in the Gamow factor, so it can be orders of magnitude faster than the incoherent fusion process. However, if the coherent process is not working very well, with a slow associated rate, then we might expect the deuteron–deuteron fusion products to show up as part of an expected decay channel at low level. Excitation transfer of the 24 MeV excitation energy from the $D_2/{}^4\text{He}$ transition in the case of acoustic mode excitation would be expected to go into producing real excitation of the very lossy host nucleus excited state. In the case of Pd, we might expect that alpha ejection might result. If it could be observed, it would support the conjecture that excitation transfer occurs in the way we were imagining (which was the reason we encouraged Lipson to see whether low-level energetic alphas could be observed along with the deuteron–deuteron fusion products). Energetic alphas were observed [29] in the 10–15 MeV region. If we think of this excitation transfer process as being something like gamma absorption, then we would imagine that a Bohr state might be formed (as in gamma absorption in Pd near 24 MeV), which would decay through all available channels. The alpha spectrum that results from 24 MeV gamma absorption in Pd looks similar to Lipson’s alpha spectrum from PdD. The Bohr state in Pd produces fast protons and neutrons more efficiently than alphas, so we have been interested in energetic proton and neutron emission which should accompany the Lipson energetic alphas. The first sign that the energetic neutrons in the right energy range might be present came from experiments reported by Roussetski [30] in which neutrons near 14 MeV were seen with CR-39 in amounts inconsistent with what was possible for secondary DT reactions. Remaining to be clarified is the situation in regard to energetic proton emission above 10 MeV, which seem not to be present in Lipson’s experiments.

A modification of this picture is in order based on Lipson’s observations of fast alphas from light water experiments, where excitation transfer of the 24 MeV quantum would not be expected from the $HD/{}^3\text{He}$ system. The resolution in this case is that the mixing of the phonon and nuclear degrees of freedom occasionally spreads the oscillator distribution

sufficiently that energy can be absorbed due to electron–nuclear coupling (involving an outer orbital that is sensitive to vibrational excitation), where the strongest coupling occurs with the giant dipole resonance. Such a mechanism would yield fast alphas on an equal footing with heavy and light water experiments, consistent with Lipson’s observations.

11. Connection with the Physical System IV

We discussed a route for tritium production that involved a $D_2/{}^4\text{He}$ transition and $HT/{}^4\text{He}$ transition, both of which are weakly coupled to the lattice, that could allow for tritium production as a favored coherent pathway if there were not enough mixing with the phonons to transfer 24 MeV of energy. This notion motivates us to think about the ${}^4\text{He}/n+{}^3\text{He}$ channel in analogy with the ${}^4\text{He}/HT$ channel. In previous years, we dismissed the ${}^4\text{He}/n+{}^3\text{He}$ channel in connection with excitation transfer and energy exchange mechanisms since the neutron is free. However, the more significant issue is how long the system remains localized. If we suppose for discussion that the relative energy is near zero, then there seems to be no reason that a neutron channel couldn’t exist similar to the tritium channel. We are tempted to think of the Wolf experiment in connection with this conjecture [31,32]. The Wolf experiment is interesting in particular since the current density was much lower than for excess heat production, but also low relative to experiments where tritium production was observed (but higher than Wolf had used earlier for neutron measurements).

For completeness we note that $p + t/{}^4\text{He}$ and $t + t/{}^6\text{He}$ have the potential to be source transitions in place of $d + d/{}^4\text{He}$ and $p + d/{}^4\text{He}$ discussed above. Given the difficulty of working with tritium in such experiments, these are probably of academic interest only.

12. D_2 and Vacancies

In the new reaction schemes discussed above, the starting point is molecular D_2 or molecular HD in the lattice. The notion of molecular D_2 in PdD is controversial even today, and there are as yet no observations of which we are aware. It has been argued over the years that the electron density is too high in bulk PdD for D_2 to occur, and we are in agreement. If so, then our focus should be on defects, where the electron density can be lower. The simplest example is a monovacancy, and this has been the focus of our attention recently [33].

One can verify that the electron density at the Pd vacancy location is on the order of a factor of two below what is needed for D_2 to form. In principle we then have a solution. However, the situation is more complicated. Unfortunately, D_2 near a monovacancy is unstable if there are any unoccupied octahedral sites surrounding the Pd monovacancy. The configuration with five occupied O-sites and a D_2 molecule seems to be favored, and a recent DFT computation [34] has shown that a caging effect favors a strongly bound D_2 in a relatively high electron density region.

We have proposed the connection of this problem with the observed excess power as a function of loading in the Fleischmann–Pons experiment [33]. Until the D/Pd loading reaches more than 0.80, one would not expect much D_2 in the monovacancies. The D_2 occupation in our initial version of a statistical calculation seems to go up faster at higher loading than the excess power versus loading curve. This is thought to be due to the omission of the eight deuteron configuration in the vacancy. In this configuration, there are six deuterons in octahedral sites, and a D_2 molecule at lower electron density. The conjecture (to be tested) is that the molecular D_2 in this configuration is effectively inert since there is much less screening. If so, then a revised computation of the 7-deuteron configuration D_2 occupation should be much closer to a match for the excess power versus vacancy curve.

So, if vacancies are so important, then how are they produced? In unloaded Pd, it takes on the order of 1 eV to make a vacancy, but adding H or D stabilizes the vacancies. At very high loading (above 0.95) the vacancies become preferred thermodynamically [35]. Unfortunately, the diffusion rate is very slow, so that diffusing even one lattice constant within a month is unlikely near room temperature.

We have conjectured that vacancies form in the Fleischmann–Pons experiment through inadvertent codeposition. Some of the Pd dissolves off of the cathode surface into the electrolyte, and then it codeposits back on over the course

of the experiment. Lithium from LiOD in the electrolyte is absorbed into the near surface region [37–42], which may make dissolution of the Pd more likely [43] under anodic polarization (which is sometimes used as part of the loading protocol). Evidence in support of Pd codeposition in the Fleischmann–Pons cathodes comes from observations of Pt on the outer surface layer along with Pd [36]. If the loading happens to be 0.95 or higher, then this codeposition should produce superabundant vacancies [35]. As a result, we would expect the active region in the Fleischmann–Pons experiment to be the outer 100–300 nm of the cathode. If so, then we should re-think codeposition experiments, or seek other materials in which molecular D_2 forms naturally without such heroic requirements.

13. Making Phonons

In the mechanisms reviewed above for $D_2/{}^4\text{He}$ transitions, the generalized lossy spin–boson models indicate that little excess heat is expected until the oscillator is very highly excited. We note that the thermal excitation of the oscillator is insufficient to promote the new process. So, how can we excite the optical phonons?

In the Fleischmann–Pons experiment, the thought is that when deuterium fluxes through the codeposited region near the surface, that the hopping associated with the diffusion is efficient at generating optical phonons. We would expect such a source to be nonspecific in that pretty much all of the phonon modes would be excited, and probably only a small (per cent) fraction of this excitation will be suitable for our needs. Excess heat has been seen to increase roughly linearly above a threshold in many different Fleischmann–Pons experiments, a behavior consistent with how we expect the models to work. A key goal of our modeling effort is to compute the threshold current density directly from the model, but this has not yet been done. As noted above, excess heat was seen to be stimulated in single laser experiments, which we interpret as producing a weak excitation of hybrid plasmon/optical phonon modes. Probably the nuclear energy in these experiments go into these modes, but the modes are likely too lossy to be self-sustaining near 500 THz. In the two-laser experiments, the optical phonon modes are stimulated [9,10]. Excess heat is often seen to persist after the lasers are turned off, which is consistent with the lower loss near 8, 15 and 21 THz. In both single-laser and two-laser experiments, the laser polarization is p-polarization, resulting in the stimulation of compressional modes [44].

Direct stimulation using THz radiation has been discussed but not tried yet. A barrier in electrochemical experiments is that THz radiation is strongly absorbed by the electrolyte. A much needed experiment is one in which the relative strength of the Raman sidebands are detected during excess power production in a two-laser experiment. If the nuclear energy goes into these modes, we should be able to see it in such a Raman experiment.

14. Getting the Helium Out

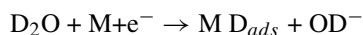
If ${}^4\text{He}$ is made as part of the new mechanism, then we would expect helium to accumulate in the monovacancies, reducing the efficiency of D_2 formation. Helium diffusion is slow, so that if the codeposited layer in the Fleischmann–Pons experiment is sufficiently thin then it can diffuse away. If we take the observed profile of codeposited Pt as a indicative of the thickness of the codeposited layer, and use the diffusion coefficient of helium in Pd as representative, we can get a consistency check that much of the helium should diffuse out into the gas within a few hours of having been produced.

However, in experiments where helium accumulation is an issue, we would like to find a way to get it out more rapidly. The largest available leverage in this case is through increasing the diffusion coefficient, by increasing the temperature. Fleischmann and Pons introduced the notion of positive feedback [45,46], wherein a heat pulse associated with calibration was seen to raise the level of excess power. If the temperature increase resulted in enhanced helium diffusion, then we might interpret the effect as simply activating more monovacancy sites.

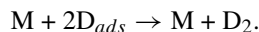
Storms reported a measurement of the increase in excess power with temperature leading to an activation energy of 670 meV (see [11]), which is essentially the same as the activation energy for helium diffusion in Pd [12].

15. Modeling

A major goal of our research effort is to develop a numerical simulation model for the Fleischmann–Pons experiment. Based on the discussion above, all of the various pieces seem to be available for such a modeling effort. It seems useful to consider briefly what might go into such a model. To begin with, we require an electrochemical model and deuterium diffusion model to account for the loading. One can find such a model in what is termed the hydrogen-evolution-reaction (HER) model, variants of which have been applied to the Fleischmann–Pons experiment. Loading occurs through the Volmer reaction



and deloading occurs through the Tafel reaction



So, increasing current leads to more loading, and when the loading increases the chemical potential increases, raising the rate of outgassing. At high current density, the loading is seen to drop in the experiments, which has been accounted for by the Heyrovsky reaction. Unfortunately, there is no experimental evidence that this mechanism occurs in the Fleischmann–Pons electrochemistry, and models which include the reaction are inconsistent with experimental observations of very high loading [47]. As a result, new models are needed. The situation is complicated by the large number of impurities that accumulate on the electrochemical surface. There are also complications in the diffusion coefficient, which is moderately high in the alpha phase, very low in the mixed phase region, and very high in the beta phase.

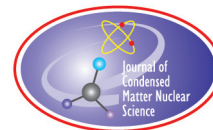
To model the Pd dissolution and subsequent inadvertent codeposition is largely problematic, since the dissolution and codeposition rates have not been studied in the experiment. However, reasonable models for the vacancy fraction can be developed as a function of the loading and temperature. Since numerous impurities are codeposited with the Pd, the situation is ultimately more complicated (a cleaner system would be a Pd codeposition system, or a different host that allowed D₂ occupation directly).

Some modeling of the phonon modes has been done, and crude models for the excitation of the optical phonon modes have been studied. Phonon exchange matrix elements have been formulated, but so far only a brute force computation of the D₂/⁴He matrix element has been attempted so far. Dynamical equations for excitation transfer and coherent energy exchange have been developed and studied, leading to models that behave something like experiment. However, at present an effort is underway to develop a new set of self-consistent models.

References

- [1] S. Pons, M. Fleischmann and M. Hawkins, *J. Electroanal. Chem.* **261** (1989) 301.
- [2] M.C.H. McKubre, S. Crouch-Baker, A.M. Riley, S.I. Smedley and F.L. Tanzella, *Proc. ICCF3* (1993) 5.
- [3] M.C.H. McKubre, Cold fusion LENR; One perspective on the state of the science, *Proc. ICCF15* (in press).
- [4] M. Miles, R.A. Hollins, B.F. Bush, J.J. Lagowski and R.E. Miles, *J. Electroanal. Chem.* **346** (1993) 99.
- [5] P.L. Hagelstein, M.C.H. McKubre, D.J. Nagel, T.A. Chubb and R.J. Hekman, *Proc. ICCF11* (2004) 23.
- [6] V.V. Gann and G.D. Tolstolutskaia, *Nucl. Instr. Meth. Phys. Res. B* **266** (2008) 3365.
- [7] P.L. Hagelstein, *Naturwissenschaften* **97** (2010) 345.
- [8] P.L. Hagelstein, *J. Cond. Mat. Nucl. Sci.* **3** (2010) 41.
- [9] D. Letts and D. Cravens, Laser stimulation of deuterated palladium: past and present, *Proc. ICCF10* (2003) 159.
- [10] P.L. Hagelstein, D. Letts and D. Cravens, *J. Cond. Mat. Nucl. Sci.* **3** (2010) 59.
- [11] E. Storms, *Proc. ICCF4* **2** (1993) 4-1.
- [12] J. Xia, W. Hu, J. Yang, B. Ao and X. Wang, *Phys. Stat. Sol. B* **243** (2006) 579.
- [13] C. Cohen-Tannoudji, J. Dupont-Roc and C. Fabre, *J. Phys. B: At. Mol. Phys.* **6** (1973) L2148.

- [14] P.L. Hagelstein, A unified model for anomalies in metal deuterides, *Proc. ICCF9* (2002) 121.
- [15] P.L. Hagelstein and I.U. Chaudhary, Progress on phonon exchange models for excess heat in metal deuterides, *Proc. ICCF13* (2007) 590.
- [16] P.L. Hagelstein and I.U. Chaudhary, Models relevant to excess heat production in Fleischmann–Pons experiments, *Low-energy nuclear reactions sourcebook* ACS Symposium Series **998** (2008) 249.
- [17] P.L. Hagelstein and I.U. Chaudhary, Excitation transfer and energy exchange processes for modeling the Fleischmann–Pons excess heat effect, *Proc. ICCF14* (2008) 579.
- [18] P.L. Hagelstein and I.U. Chaudhary, *J. Cond. Mat. Nucl. Sci.* **5** (2011) 52.
- [19] P.L. Hagelstein and I.U. Chaudhary, *J. Cond. Mat. Nucl. Sci.* **5** (2011) 87.
- [20] P.L. Hagelstein and I.U. Chaudhary, *J. Cond. Mat. Nucl. Sci.* **5** (2011) 102.
- [21] P.L. Hagelstein and I.U. Chaudhary, *J. Cond. Mat. Nucl. Sci.* **5** (2011) 116.
- [22] P.L. Hagelstein and I.U. Chaudhary, *J. Phys. B: At. Mol. Phys.* **41** (2008) 135501.
- [23] P.L. Hagelstein and I.U. Chaudhary, *J. Cond. Mat. Nucl. Sci.* **5** (2011) 140.
- [24] A.B. Karabut, X-ray emission in the high-current glow discharge experiments, *Proc. ICCF9* (2002) 155.
- [25] A.B. Karabut and S.A. Kolomeychenko, Experiments characterizing the X-ray emission from a solid-state cathode using a high-current glow discharge, *Proc. ICCF10* (2003) 585.
- [26] A.B. Karabut, Research into characteristics of X-ray emission laser beams from solid state cathode medium of high-current glow discharge, *Proc. ICCF11* (2004) 253.
- [27] A.B. Karabut, Study of energetic and temporal characteristics of X-ray emission from solid state cathode medium of high-current glow discharge, *Proc. ICCF12* (2005) 344.
- [28] E. Campari, G. Fasano, S. Focardi, G. Lorusso, V. Gabbani, V. Montalbano, F. Piantelli, C. Stanghini and S. Veronesi, *Proc. ICCF11* (2004) 405.
- [29] A.G. Lipson, G.H. Miley, A.S. Roussetsky and E.I. Saunin, Phenomenon of an Energetic Charged Particle Emission From Hydrogen/Deuterium Loaded Metals, *Proc. ICCF10* (2003) 539.
- [30] A.S. Roussetsky, *Proc. ICCF8* (2000) 253.
- [31] K. Wolf, unpublished technical material (unstable isotope distributions, gamma spectra, initial analysis) from the Sept. 7, 1992 event that produced activation of three Pd cathodes.
- [32] T.O. Passel, Radiation data reported by Wolf at Texas A&M as transmitted by T. Passell *EPRI report* (1995) (unpublished, but posted on the LENR-CANR website).
- [33] P.L. Hagelstein and I.U. Chaudhary, Arguments for dideuterium near monovacancies in PdD, *Proc. ICCF15* (in press).
- [34] L. Dechiaro, private communication.
- [35] D. Letts and P.L. Hagelstein, Modified Szpak protocol for excess heat, *J. Cond. Mat. Nucl. Sci.* (in press).
- [36] D.R. Coupland, M.L. Doyle, J.W. Jenkins, J.H.F. Notton, R.J. Potter and D.T. Thompson, *Proc. ICCF1* (1990) 299.
- [37] F. Dalard, M. Ulmann, J. Augustynski and P. Selvam, *J. Electroanalyt. Chem.* **270** (1989) 445.
- [38] S. Guruswamy and M.E. Wadsworth, *Proc. ICCF1* (1990) 314.
- [39] M. Nakada, T. Kusunoki, M. Okamoto and O. Odawar, *Proc. ICCF3* (1993) 581.
- [40] H. Uchidaa, M. Sato, W. Cui, T. Tabata, M. Kumagai, H. Takano and T. Kondo, *J. Alloys and Compounds* **30** (1995) 293.
- [41] O. Yamazaki, H. Yoshitake, N. Kamiya and K.-I. Ota, *J. Electroanalyt. Chem.* **390** (1995) 127.
- [42] Y. Oya, M. Aida, K. Iinuma and M. Okamoto, *Proc. ICCF7* (1998) 302.
- [43] E. Storms, private communication.
- [44] M. Apicella, E. Castagna, L. Capobianco, L. D'Aulerio, G. Mazzitelli, F. Sarto, A. Rosada, E. Santoro, V. Violante, M. McKubre, F. Tanzella and C. Sibilia, *Proc. ICCF12* (2005) 117.
- [45] M. Fleischmann and S. Pons, *Proc. ICCF3* (1993) 47.
- [46] M. Fleischmann, More about positive feedback, *Proc. ICCF5*, 1995, p. 140.
- [47] P.L. Hagelstein, M.C.H. McKubre and F.L. Tanzella, Electrochemical models for the Fleischmann–Pons experiment, *Proc. ICCF15*, in press.



Research Article

Transmutation of Elements in Low-energy Glow Discharge and the Associated Processes

I.B. Savvatimova *

Podolsk, Moscow Region, Russia

Abstract

The review of the main transmutation results in palladium and tungsten after the exposure to deuterium Glow Discharge (GD) measured by different Mass Spectrometry (MS) and Gamma-Spectrometry (GS) methods is given. The registered structure and isotopic ratio change alongside with formation of additional elements were accompanied by gamma and X-ray emission. The registered isotopic ratio change ranged within 2–1000 times, the quantity of additional elements undetected before varying within one tenth to dozens percents in Pd and Pd alloys. The isotopes with masses less than and exceeding those of the cathode material were measured in most of the experiments. The MS revealed that the tungsten isotopes transmuted into elements lighter than tungsten, higher post-experimental intensity of mass numbers 169, 170, 171, 178 and 180 being observed. The mass spectra peaks magnituded for isotopes lighter than W isotopes increased by factors ranging from 5 to 400. The registered increase varied from 5–50 cps in the original foils to 100–20 000 cps after the exposure to deuterium GD. Lighter isotopes in tungsten and tantalum foils placed on the GD cathode after deuterium GD exposure were identified using high resolution gamma/X-ray spectrometry. The comparison of thermal ionization mass-spectrometry (TIMS) data and data of gamma-spectra energy peaks allowed to assume that the peaks series observed in gamma spectra belong to the following isotopes: $^{169}_{70}\text{Yb}$, $^{170}_{72}\text{Hf}$, $^{171m}_{70}\text{Yb}$, $^{172}_{72}\text{Hf}$ and $^{178}_{70}\text{Yb}$. Correlation of TIMS and Gamma spectrometry data leads to the assumption that the appearance of light isotopes in tungsten resulted from the low-energy decay process initiation caused by deuterium GD.

© 2012 ISCMNS. All rights reserved.

Keywords: Isotopic ratio change, Low-energy gas glow discharge, Mass-spectrometry, Palladium, Transmutation, Tungsten

1. Introduction

The review of numerous GD experimentation results during and after the irradiation by GD ions starting 1989 and up to the present time is given. The analysis of structure, elemental and isotopic ratio change in the materials exposed to low-energy ions irradiation upon the GD cathode is carried out. Changes in elemental composition, quantity and places of concentration of the newly formed impurity elements depends upon the GD parameters, type of ions (H, D, and Ar), kind of current (direct or pulsed) and the presence of impurities in the cathode. The gamma emission intensity

*E-mail: isavvatim@mail.ru



Figure 1. The gas glow discharge setup with CdTe detector location: 1- CdTe gamma and X-ray detector.

registration was carried out during the GD ions exposure and after GD current switch off outside the GD chamber. Post-experimental direct measurements of the emission from the cathode material in contact with a gamma-detector were made. Post-experimental changes in an alpha-, beta-, and gamma-intensity in the cathode materials uranium exposed to hydrogen and deuterium ions bombardment, and also the change in the isotopic content and elements composition were observed. The results obtained show that the GD ions low-energy influence stimulates the registered nuclear processes.

In our previous papers [1,2,8], we described elemental and isotopic change in palladium and titanium. Weak gamma-emission, brief neutron bursts [5–7,9], changes of surface structure and of the elemental and isotopic composition in the Pd cathode were observed. The increase in Pd impurities (undetected in the original material) ranged 0.5–5% (an increase by 100–10 000 times).

Post-experimental local blackening of X-ray films placed in contact with Pd, Ti and Ag foils was observed [3,7,8]. Local blackening was also observed [3,9] in X-ray films placed both inside and outside of the GD chamber stainless steel wall. Results of Pd foils radiographic analysis showed presence of high-energy and low-energy components [6] in the films contacting the foils after the exposure. The observed effects are explained by the fusion–fission reaction on the cathode materials (mostly foils), by the interaction between the Pd lattice and Deuterium and by the subsequent decay into lighter elements. The majority of the post-experimental impurities were found in certain local zones (“hot spots”) [1–3,8]. Post-experimental impurity elements (with various content) such as Sc, Ti, V, Ag, Cd, In, P, Cl, Br, Ge, As, Kr, Sr, Y, Ru, and Xe were discovered in the Pd material after the exposure to all types of ions (D, H, Ar, and Ar + Xe). The estimated correlation of the integral sum of all impurity elements in Pd samples after the bombardment by D, H, and Ar ions showed 10:(2 or 3):1, respectively [9]. Considerable change in the isotopic ratios in Pd foils for $^{10}\text{B}/^{11}\text{B}$; $^{12}\text{C}/^{13}\text{C}$; $^{60}\text{Ni}/^{61}\text{Ni}/^{62}\text{Ni}$; $^{40}\text{Ca}/^{44}\text{Ca}$, and $^{90}\text{Zr}/^{91}\text{Zr}$ was registered by different mass-spectrometry methods [6]. Changes in the isotopic ratios for $^{109}\text{Ag}/^{107}\text{Ag}$ ranged from the initial Pd ratio of 1/1 to 3/1 and 9/1 after the GD exposure (described in [5,9]).

Weak gamma-emissions, short-term neutron bursts, neutron and gamma energy-spectra were registered. This data

Table 1. Changes in the isotopic shift and elemental composition of the impurity atoms upon Pd surface after the exposure to D ions bombarding (SIMS) [6].

No.	Mass	Element	Content (arb. units)				
			Before experiment	After experiment			
				Exposed side	Unexposed side	Increase factor	
						Exposed	Unexposed
1	6	Li*	0.02	1.00	0.15	50	7.5
2	7	Li*	0.02	9.00	0.28	450	14
3	10	B*	0.01	0.01	0.01	1	1
4	11	B*	0.10	7.00	0.01	70	0.1
5	51	V*	0.30	30.00	0.20	100	0.7
6	53	Cr	0.60	96.00	1.00	160	1.4
7	54	Fe	2.20	15.00	2.00	6.8	0.9
8	56	Fe	22.20	55.00	20.00	2.5	0.9
9	57	Fe	11.00	45.00	12.00	4.0	1.1
10	60	Ni	0.10	3.00	0.20	30	2
11	61	Ni	0.20	10.00	0.20	50	1.0
12	63	Cu	1.40	60.00	1.00	42.85	0.7
13	87	Sr*	0.10	1.00	0.10	10	1
14	88	Sr*	0.50	0.10	0.20	0.2	0.4
15	90	Zr*	0.01	57.00	0.01	5700	1
16	91	Zr*	0.10	34.00	0.10	340	1

The observed increase in content of chemical elements in: Li by factor of 50–450, ^{11}B by a factor of 70, Zr by a factor of ~ 5700 , V by a factor of 100, Cr by a factor of 160, Fe by a factor of 2–7, and Ni by a factor of 5–30.

1. The analyzed layer depth ~ 100 .

2. Li, B, V, Sr, and Zr were not present in the GD chamber earlier.

3.*The source of possible impurity is absent.

were published in previous papers [1,2]. Neutrons with energies up to 17 MeV were detected. We also observed an anomalous intensity ratio ranging 2.45 MeV/14 MeV in the neutron groups. This is an evidence of an anomalous type of nuclear reaction [1,2]. The Post-experimental blackening of X-ray films in contact with Pd, Ti, and Ag foils was observed [3–6].

Uranium radioactivity change was also observed after the exposure to D and H GD [7–9]. Post-experimental increase (by four times) in alpha emissions was registered in D discharge after 500 h exposure (for the exposed and unexposed sides). The increase in beta and gamma emissions intensity showed no more than 60% as compared to alpha emissions. The comparison of energy peaks intensity in the gamma spectra evidences that the isotopic ratio intensity (counts per second is cps) of thorium and uranium in energy peaks was changed [10]. Post-experimental changes in uranium alpha, beta and gamma emissions were detected for both sides of the 0.2 mm thick uranium (irradiated and back side) [10,11].

This paper contains a short review of transmutation results in gas GD cathode materials and the accompanying processes [13]. The paper describes isotopic and elemental changes, the associated gamma emissions. The possible mechanism is proposed.

The article presents post-experimental registration lighter isotopes in tungsten and tantalum foils (after the exposure to deuterium GD) using X-ray/gamma spectrometry. Two series of experiments with W foils are described in this review. The first set includes the results of Thermal Ionization Mass Spectrometry (TIMS) analysis, which started ~ 80

Table 2. Dose versus additional atoms quantity upon Pd surface after exposure to Deuterium GD (EDA) [6]

No.	The additional atoms	Atom number	Dependence of additional atoms quantity on dose $\times 10^{-2}$ at. %	
			4 h	40 h
1	Na	11	7.0 ± 0.3	3.0 ± 0.3
2	Mg	12	1.0 ± 0.3	2.0 ± 0.3
3	Al	13	4.0 ± 0.3	2.0 ± 0.3
4	Si**	14	1.5 ± 0.3	< 0.3
5	Ca	20	4.0 ± 0.3	3.0 ± 0.3
6	Ti*	22	1.0 ± 0.3	1.5 ± 0.3
7	Br*	35	3.0 ± 0.6	2.0 ± 0.6
8	Sr*	38	7.0 ± 0.6	6.0 ± 0.6
9	Y*	39	40.0 ± 1.0	20.0 ± 1.0
10	Mo**	42	15.0 ± 1.0	40.0 ± 1.0
11	Tc*	43	20.0 ± 1.0	10.0 ± 1.0

EDA is SEM “HITACHI-800” with “Link Analytical” device.
Probe diameter of analyzed place was $\sim 1 \mu\text{m}$.

*Source of impurity is absent.

**Sources of possible impurity are the parts of the of discharge chamber.

min after the GD current switch off (there was a 15-minute interval between each analysis). The second set of results included W foils analysis after 3–5 months after the experiment.

2. Methods

2.1. Experimental method

Deuterium discharge was experimental method of low-energy nuclear reaction initiated. The experimental setup is shown in Fig. 1.

The glow discharge apparatus was made with double quartz tubes (as the wall of the discharge chamber) with cooling water between these quartz tubes. The anode and cathode were cooled with flowing water also. The sequence of operations before discharge experiments was as follows: vacuum degassing to 10^{-3} Torr, followed by deuterium loading to between 3 and 10 Torr. Molybdenum was used as the anode. The used foil was placed on the cathode. The foil $\sim 100 \mu\text{m}$ thick and ~ 20 mm in diameter. The installation had a vacuum discharge chamber with a cathode and an anode. Deuterium, hydrogen, argon, xenon were used as working gases. Samples were irradiated with gas ion current density of $10\text{--}200 \text{ mA/cm}^2$ and with discharge voltage of $50\text{--}1200$ V. The discharge burning exposure was $1\text{--}40$ h, diameter of the used foils ~ 20 mm, thickness $\sim 100 \mu\text{m}$, the irradiated area about 1 cm^2 .

2.2. Methods of the analysis

The examinations procedure in detail is described in [3,4]. The analytical methods included: secondary ions mass spectrometry (SIMS), secondary ions mass spectrometry with additional ionization of the neutral pattering particles (SNMS), spark mass-spectrometry (SMS), thermoionization mass spectrometry (TIMS), energy dispersive analyses (EDA) and high resolution gamma-spectrometry. Changes in the element composition were analyzed with EDA methods and the isotope composition was analyzed with mass spectrometry. The elemental composition of the cathode

materials was studied on scanning electronic microscope Hitachi S-840 with Link Analytical LS-5 and JEOL JSM 6460-LV using INCA for X-ray spectral analysis.

The analyzed zone size was about $1 \mu\text{m}^2$ for the probe analysis in point, and up to $\sim 250 \times 200 \mu\text{m}^2$ the scanning area. Sensitivity of the method was $\sim 10^{-2}$ atom.%. Depth of an analyzed layer about 1 mk was used. Concentration of the impurity (“additional”) elements was determined using the majority of main lines of the characteristic X-ray spectrum. Initial samples and samples after experiments in gas glow discharge are analyzed. Places with structural defects and new formations such as swellings (blisters), craters, areas of micromeltings, needle structures, and sites of surface without special changes after and before irradiation in glow discharge plasma were explored.

2.2.1. Characterization of TIMS analysis

The isotope composition of the foils at high temperature was determined with TIMS using mass-spectrometers “Finnigan”-262 and Thermo Finnigan “Triton”. The most detailed analyses were performed in the range of mass numbers 166–206. The temperature between Re ionizer and analyzed foils was $\sim 1800^\circ\text{C}$ [1–4]. The majority of complex compounds should break up (dissociate) at such a temperature while the secondary ionic mass spectrometry can give many composite complexes. The analyzed tungsten strip had the width ~ 1 mm, the length ~ 20 mm and the thickness $\sim 100 \mu\text{m}$. The strip was cut off from the central part of W or Ta foils, irradiated by deuterons. The analyzed zone included the unirradiated part of W foil as well as irradiated parts, which led to a reduced contribution by more light isotopes. The spectra of minimal intensity (CPS) were removed from the table of TIMS data. The data regarding to mass numbers 185 and 187 corresponding to rhenium (Re) isotopes were removed from the table data as well, because Re was used as mass-spectrometer cathode. Two W foils layers were placed on the cathode of gas discharge device. The side of the foil irradiated with deuterium ions was analyzed.

3. Results

The analysis of metal foils after the exposure to GD low-energy ions by SIMS, TIMS, SNMS has shown sharp deviations in isotopic ratio ranging 2–10 times, changes in the elemental content (impurity yield increase, occurrence of additional elements), structural changes (formation of new structures, traces of micro-explosions, melting, occurrence of “hot points”), excess heat production, change in gamma-, alpha- and beta-emissions, neutron bursts [1–13].

3.1. Dependence of “Additional” elements quantity upon ions type

The dependence of quantity and variation in different additional elements in Pd foils after the exposure to Deuterium, Hydrogen and Ar + Xe was established [5]. It was shown, that the maximum quantity of additional elements occurs after the exposure in Deuterium GD. The ratio may be presented as D: H: (Ar + Xe) = 10: (2–3):1, correspondingly [5].

3.2. Dependence of “Additional” elements quantity upon in the ion dose, current type, place and method of analysis.

3.2.1. Dependence of “Additional” elements quantity upon the ion dose, and method of analysis

All the characteristic spectra peaks of Ti, Br, Sr, Y, and Tc were observed. Ti, Br, Sr, Y, and Tc were no observed in the discharge chamber before the exposure. The decrease in Na, Mg, and Ca after the 40-hour experiment with EDA method can be explained by participation of these elements in secondary transmutations or by lighter elements sputtering.

Table 3. “Additional” atoms quantity versus ions dose upon Pd surface after exposure to deuterium GD (SMS) [6].

Mass	Element	Before $\times 10^{-4}$ at.%, ($\times 100$ ppm)	Additional element in Pd for different ex- posure time $\times 10^{-4}$ at. %				Mass	Element	Before, 10^{-4} at. % \times 100 ppm	\times Additional element content in Pd for different ex- perimental time $\times 10^{-4}$ at. %			
			4 h							4 h			
			Upper	Lower	Upper	Lower				Upper	Lower	Upper	Lower
6	Li	0.06	0.15	0	0	0	49	Ti*	1.30	680.00	3.25	28	115
7	Li	0.06	0.33	0.40	0.90	0.50	50	Ti*	1.70	0	3.40	130.0	
10	B	0.07	0	0.15	0	0	78	Se*	0.23	0.23	0.20	0.20	4.00
11	B	0.07	0.30	0.20	0.20	0.70	80	Se*	0.30	0.20	0.20	0.20	33.00
23	Na	0.44	4.40	1.00	2.00	6.00	85	Rb*	< 0.03	0.01	0.05	90.00	51.00
27	Al	6.00	96.00	10.00	300.0	25.00	90	Zr*	< 0.05	25.00	0.05	60.00	0.22
28	Si**	9.00	18.00	9.00	0	3.00	91	Zr*	< 0.05	50.00	< 0.05	61.00	0
29	Si**	7.00	21.00	11.00	0	10.00	93	Nb*	< 2.00	40.00	2.00	7200	4.00
30	Si**	6.00	18.00	4.50	15.00	66.00	98	Mo**	0.40	0	0	0	3.00
32	S	7.00	14.00	2.00	3.50	2.00	100	Mo**	1.80	4500.0	1.80	2880	0
39	K	3.00	9.00	0	12.00	4.50	103	Rh*	7.00	21.00	21.00	25.00	7.00
41	K	3.00	12.00	1.00	18.00	9.00	107	Ag*	1.00	63.00	3.00	1.00	3.20
47	Ti*	1.20	1.80	60.00	0	0	109	Ag*	1.00	50.00	1.50	0	2.50
48	Ti*	1.40	580.0	2.50	0	3.50	115	In*	< 0.04	0.48	0.04	0.80	0.16

Table 4. Change of Ag quantity in Pd glow-discharge cathode at various ions density (SMS) [7].

No.	Current (mA)	Type of ions	Analyzed layer *	Isotope mass		The factor of increasing (after/initial)
				107	109	
Initial	0		1	17	22	
1666	35	D	1	5000	5200	~ 250
			2	2100	2200	~ 100
			3	<	<	-
1667	35	H	1	15	5	
			2	110	77	~ 4
			3	<	<	-
1668	25	H/D	1	20	20	
			2	570	560	~ 25
			3	690	740	~ 35
1670	25	H	1	120	130	~ 5
			2	1000	1000	~ 50
			3	450	450	~ 20
1671	25	D	1	2600	2700	~ 120
			2	1800	1900	~ 9.0

1, 2, 3 are the first, the second and the third analyzed 10 μm -thick layers.

1 is the first upper 10 μm -thick layer of exposed side of the Pd foil.

2 is the second (next) 10 μm -thick layer of exposed side of the Pd foil.

3 is the first layer of the back unexposed side of the Pd foil.

The analyzed layer depth was $\sim 10 \mu\text{m}$. Sensitivity of the method was $\sim 10^{-6}$ at.%. ^{80}Se content increases by ~ 100 times. 1000-fold increase in Zr and 3000-fold increase in Rb content is shown. Ag content increased by 50 times. ^{11}B increased by a factor of 10; In increased by a factor 10–20.

3.2.2. Ag content in post-experimental Pd versus kind of ions

The maximum Ag content increase in the near-surface layer is 5–100 times bigger in deuterium GD than in hydrogen GD for the same current density.

3.2.3. “Additional” elements quantity in Pd versus type of current

The increase in isotopes with lighter masses is more noticeable. The light isotopes sputtering can change the isotopic ratio by percents, but the isotopic ratio change that we observed amounted to ~ 10 –100 times. A considerable increase in ^{57}Fe content is also observed.

Table 5. Isotopic and elemental composition in Pd after the exposure to direct current Deuterium GD (TIMS) [2]

Mass	Element	Natural (%)	CPS1 1610/1	CPS2 1610/2	CPS1–CPS2	Mass	Element	Natural(%)	CPS1 1610/1	CPS2 1610/2	CPS1–CPS2
14	N	90.6	–	–		45	Sc	100	1.2×10^3	95	$+1.1 \times 10^3$
15		0.37	20	–	+ 20	46	Ti	8.0	50	65	–15
16	O	99.8	–	–		47		7.3	30	55	–25
18		0.20	10	–	+10	48		73.8	1.2×10^2	4×10^2	-2.8×10^2
22	Ne	9.32	60	10	+ 50	49		5.5	10	45	–35
24	Mg	78.99	10	38	– 28	50	Ti, Cr	5.4, 4.3	4.6×10^2	2×10^2	$+2.6 \times 10^2$
25		10	–	10	– 10	51	V	99.8	4.6×10^2	5×10^2	– 40
26		11	–	–		52	Cr	83.8	1×10^4	3.4×10^3	$+6.6 \times 10^3$
27	Al	100	1×10^3	1×10^4	$+9 \times 10^3$	53		9.5	7×10^2	3×10^2	$+4 \times 10^2$
28	Si	92.23	2.5×10^2	10	$+2.4 \times 10^2$	54	Fe, Cr	5.8; 2.37	2×10^3	2.6×10^2	$+1.74 \times 10^3$
29		4.68	–	1.5×10^2	-1.5×10^2	55	Mn	100	4×10^3	30	$+3.97 \times 10^3$
30		3.09	–	30	– 30	56	Fe	91.7	1.5×10^4	2.5×10^3	$+1.25 \times 10^4$
42	Ca	0.65	1.8×10^3	1.5×10^2	$+1.65 \times 10^3$	57		2.2	1.5×10^3	55	$+1.45 \times 10^3$
43		0.14	4.3×10^3	1.5×10^2	$+4.15 \times 10^3$	58		0.28	3.8×10^2	30	$+3.5 \times 10^2$
44		2.09	10	6×10^2	-5.9×10^2	59	Co	100	3.8×10^2	20	$+3.6 \times 10^2$

1610 (1) is exposed Pd foil; 1610, (2) shows screened Pd foil located under the exposed one (both are 100 μm -thick). There is no reason for the formation of Sc, Cr, Co, and Fe in the upper Pd foil facing the GD. It is suggested that the formation of Sc, Co, and Mn, the increase in Fe, Cr, and Al content in upper Pd foil results from the transmutation. It should be noted that the presence of masses with numbers 22, 45, 55 and 59 in the post-experimental Pd exposed to D GD is observed almost in all the experiments (CPS-count per second).

Table 6. Change in Fe, Cr, and Ti isotopic ratio in Pd exposed to direct current GD by TIMS in cps [2].

Mass	Element	Natural abundance (%)	Before CPS	After (CPS*)	exper.	Isotopic ratio, natural (N_n)	Isotopic ratio after experiment (N_{after})	N_n / N_{after}	CPS ratio after/ before
24	Mg	78.99	8	$50/8 \times 10^2^*$		24/25–8	24/25–12	$\sim 7 \times 10^{-1}$	6–100
25		10	8	0/67		25/26–1	25/26–1/0.5*	2×10^0	0–~8
26		11	8	0/38		24/26–8	24/26–1/0.5*	1.6×10^1	0–~5
28	Si	92.23	8	$1 \times 10^2 / > 1 \times 10^2^*$		28/29–20	28/29–0.16	1.25×10^2	~ 12
29		4.67	8	$6.3 \times 10^2 / 1 \times 10^3^*$					78–125
30		3.1	8	$2.2 \times 10^2 / 5 \times 10^2^*$		28/30–30	28/30–0.5	$\sim 6 \times 10^1$	27–62
40	Ca	96.86	8	1×10^6		40/44–50	40/44–5	$\sim 1 \cdot 10^1$	$\sim 1 \times 10^5$
42		0.6	3×10^3	2×10^5		44/42– 3	44/42–2.5×10^2	8×10^1	~67
43		0.15	2×10^2	$\sim 4 \times 10^3$		44/42 ~13.3	44/42– 1.25	$\sim 1 \times 10^{-1}$	20
44		2.0	1×10^3	$\sim 5 \times 10^3$					5
45	Sc	100	8	2×10^2		–	–	–	25
46	Ti	8	65	1.3×10^3		48/46–6.2	48/46–5.46	$\sim 9 \times 10^{-1}$	20
47		7.3	95	0					0
48		73.8	1×10^3	7×10^3					7
56	Fe	91.7	2.8×10^3	4.5×10^3		56/57–41.7	56/57–18	$\sim 2.3 \times 10^0$	~ 1.6
57		2.2	50	2.5×10^2					5
59	Co	100	8	1.5×10^3		–	–	–	~ 187

*x/y stands for the measured spectrum (first spectrum CPS /2-nd spectrum CPS). N_n/N_{after} is the isotopic ratio change.

Table 7. The isotopic ratio change in “additional” elements in Pd exposed to pulsed-current GD (TIMS) [2].

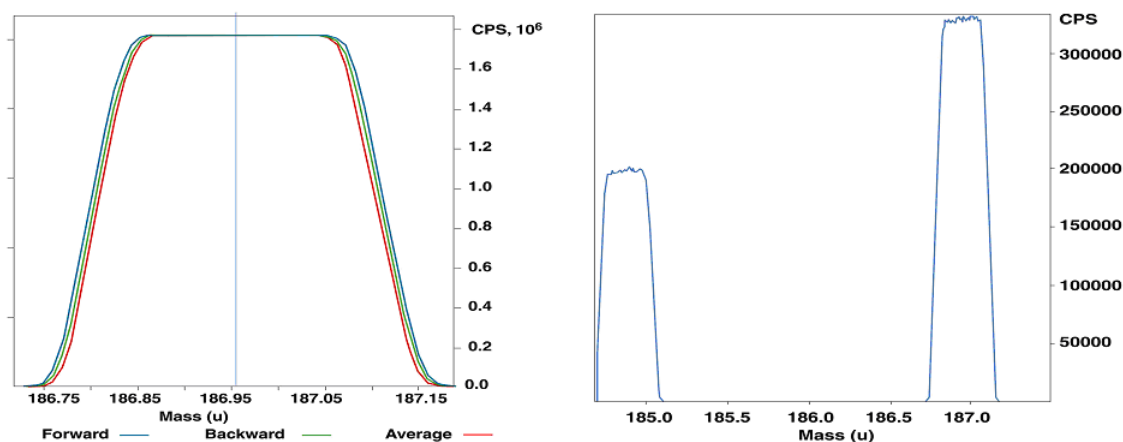
Element	Isotopic ratio	Natural isotopic ratio (N_n)	Ratio after experiment (N_{after})	N_n / N_{after}
Si	28/29	93.2/4.7 = 22.6	10/75 = 0.13	1.73×10^2
	28/30	93.2/3.1 = 29.8	10/20 = 0.5	5.96×10^1
Ne	20/21	90.5/0.27 = 33.5	20/30 = 0.67	5.0×10^1
	20/22	90.5/9.3 = 29.7	20/50 = 0.4	$7 \times 4 \cdot 10^1$
Ni	58/60	68.1/26.2 = 2.6	$1.5 \times 10^2 / 6.5 \cdot 10^2 = 0.23$	1.1×10^1
	58/61	68.1/1.25 = 55	$1.5 \times 10^2 / 3 \times 10^1 = 5$	1.1×10^1
	58/62	68.1/3.6 = 19	$1.5 \times 10^2 / 1.3 \times 10^2 = 1.15$	1.65×10^1
Fe	56/57	91.2/2.2 = 41.45	$1.6 \times 10^2 / 4 \times 10^3 = 0.04$	1.036×10^3
Cr	52/53	83.8/9.5 = 8.82	$4.8 \times 10^2 / 4.5 \times 10^2 = 1.066$	8. 26
Ti	48/47	73.8/8 = ~9	$2 \times 10^2 / 10 = 20$	0. 5
Ba	138/137	71.7/11.3 = 6.35	$3 \times 10^3 / 1.9 \times 10^2 = 15.8$	0. 4
	138/136	71.7/7.85 = 9.13	$3 \times 10^3 / 120 = 25$	0.36
	138/135	71.7/6.6 = 10.8	$3 \times 10^3 / 2.2 \times 10^2 = 13.63$	0.80
	138/134	71.7/2.4 = 29.8×10^3	$3 \times 10^3 / 2.5 \times 10^2 = 12$	2.5
Pb	208/207	52.3/22.6 = 2.31	$1 \times 10^2 / 48 = 2.0$	1.1
	208/206	52.3/23.6 = 2.22	$1 \times 10^2 / 40 = 2.5$	0.9

The isotopic deviation after the exposure to direct-current GD amounted to 10–100 times. While the isotopic content of ^{57}Fe after the exposure to pulsed-current GD increased by 1000.

3.3. Post-experimental “Hot” Spots

It is very important to note that the “hot” spots appeared after the exposure to D and H glow discharge:

- The segregations points of Zn, Co, Br, and Mg, were observed mostly on the boundary and sub-boundary of grains with density $\sim (1-10) \cdot 10^6 \text{ cm}^{-2}$. Segregation points of $\text{Zn} \sim (1-2) \cdot 10^6 \text{ cm}^{-2}$ and $\text{Br} \sim (2-4) \cdot 10^6 \text{ cm}^{-2}$ on the surface of Pd were registered with the help of microprobe EDX method [6].
- Partial local blackening of X-ray films was observed in places of contact with Pd, Ti, and Ag foils after the exposure in Deuterium GD [6].

**Figure 2.** Calibration of TIMS spectra on isotopes of Rhenium (a).

- Local blackening occurred in X-ray films placed both inside and outside the GD chamber stainless steel wall [6].
- The results of radiography analysis of X-ray films in contact with Pd cathode radioactive isotopes showed the availability of low-energy and high-energy component [6].
- The majority of “additional” elements, formed after the exposure to GD, were found in local zones (hot spots) [1,2].
- The observed effects were explained by a fusion–fission reaction on the cathode; as a result of interaction between the palladium crystal lattice with Deuterium and by the subsequent decay into lighter elements.

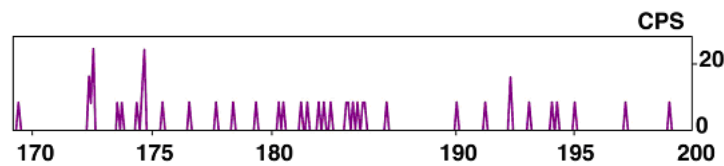


Figure 3. Mass spectra of original W in the 170-200 range of masses (CPS).

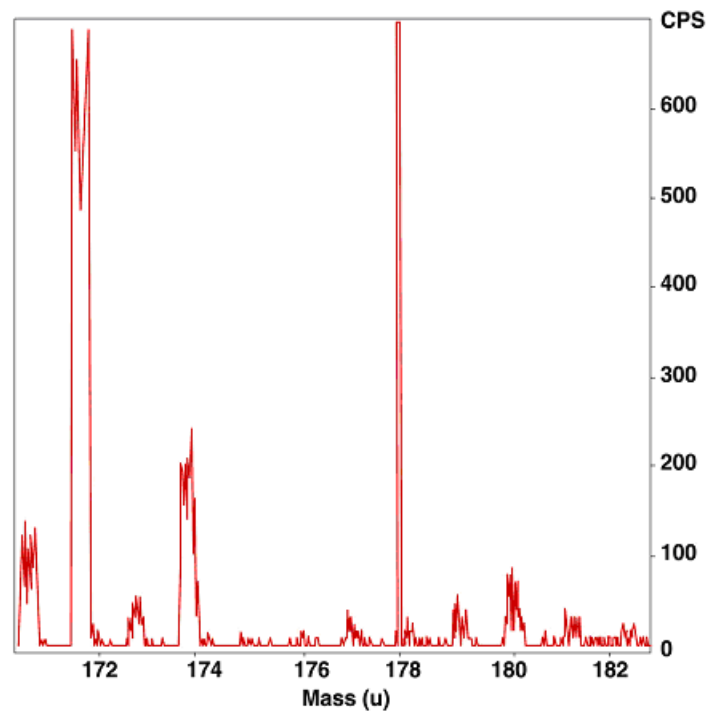


Figure 4. Tungsten mass spectra after deuterium discharge for the same foils (Mass: 172–700 cps).

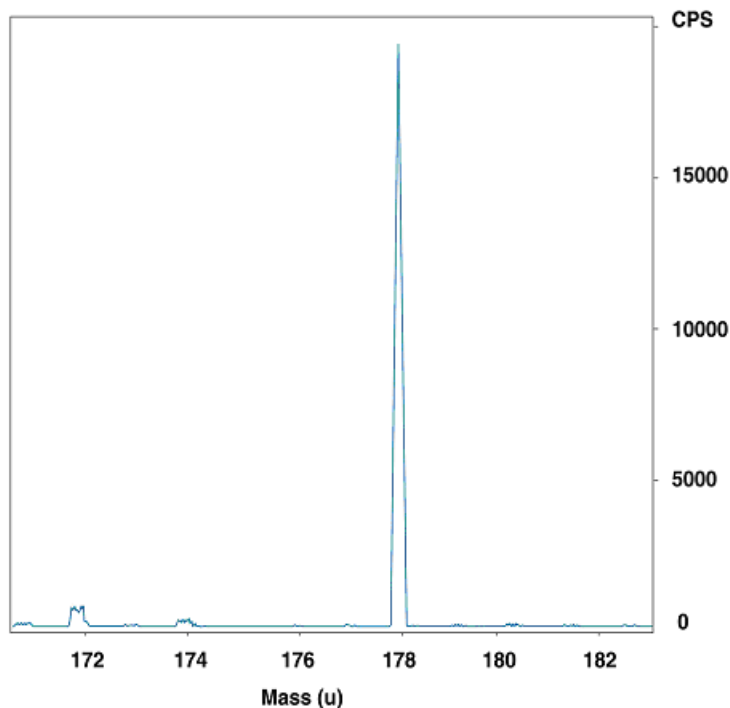


Figure 5. Tungsten mass spectra after deuterium discharge for the same foils (Mass: 178–20 000 cps).

3.4. Correlation of mass-spectrometry data with X-ray and gamma-emission [3,4]

Possible isotopes correlating to energy peaks in gamma/X-ray spectra were determined and compared to isotopic mass peaks intensity in mass-spectra.

Isotopes of lighter elements during and after the exposure in D GD were selected based upon the block of energy peaks for each isotope (Table of Radioactive isotopes) and upon the mass spectrometry data.

3.4.1. The change of isotopic composition in W after GD with TIMS [3]

Figures 2 and 3 show the calibration of TIMS spectra upon the Rhenium cathode. TIMS spectra measurements have good reproducibility. It can be seen for calibration spectrum on Re, performed before each investigation of new foil. The good reproducibility remained for short time intervals between scanned spectra practically always. An example of a precise definition of isotope mass is shown in the left spectrum, where we can see that 186.95 mass is ^{187}Re estimated very exactly. Peaks of ^{185}Re and of ^{187}Re isotopes are presented in the spectrum on the right.

The significant difference in isotopes intensity was found for the different conditions of experiments: especially, for dose of exposure and time interval after the experiment stopped. The spectra reproducibility is confirmed on the mass-spectra, observed through short time-interval, for example, through ~ 3 min. It was possible to estimate that the intensity of main isotopes is closed for the both spectra. The main isotopes and their intensity are proportional to each other.

As noted above, two series of experiments with W and Ta samples were performed: 15 min after irradiation

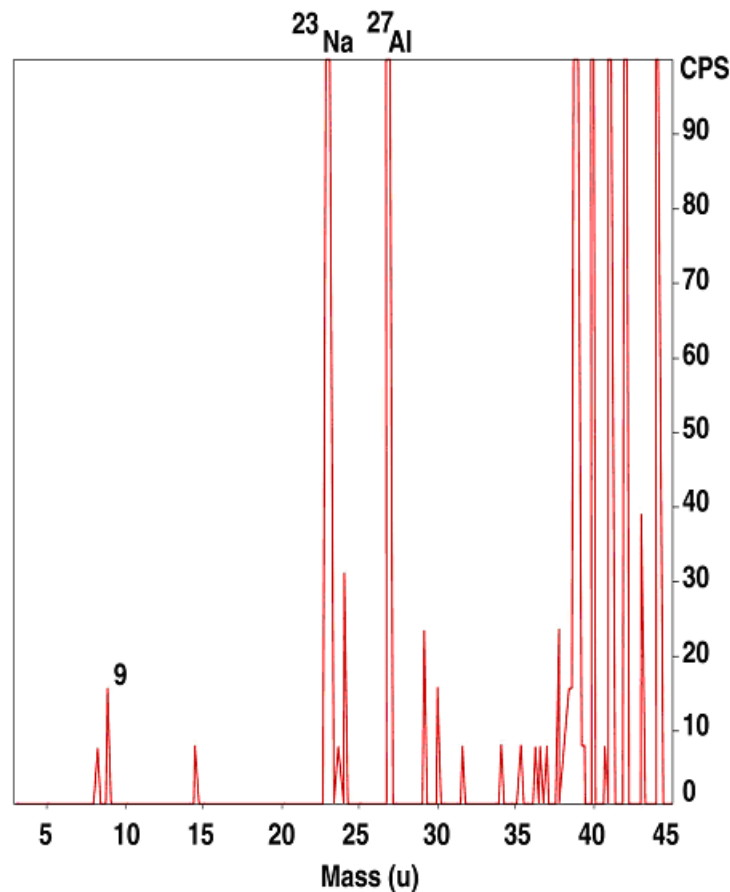


Figure 6. The intensity increasing of mass 9 in Ta after deuterium discharge (a).

(Table 8), and 3, 4 and 5 months after experiments (Table 9) both using TIMS.

Tables 8 and 9 compare mass spectra data from the original W and W after deuterium bombardment. The main isotopes changes in the different experiments with W and Ta foils for various time intervals were investigated in detail for the mass range 166–210. An increase in isotopes with masses lighter than tungsten by factors ranging from 5 to 400 was found. The analysis temperature was $\sim 1800^{\circ}\text{C}$. A mass spectrum in original W with 170–200 masses range shown in Fig. 4 the intensity of the separate isotopes from 10 to 30 cps.

A mass spectrum of the W after deuterium discharge for the mass region 170–182 for the same foil with two-minute intervals is shown in Figs. 5 and 6. Mass 172 is ~ 700 cps on the left spectrum, and mass 178 is $\sim 20\,000$ cps on the right spectrum. The intensity of these isotopes was 10–50 cps before experiments for similar scanning parameters. The increase of masses 172 and 178 intensity in the same tungsten foil was from 12 to 400 times, respectively.

The same result with increasing light mass 171 was observed for tantalum foil. The intensity of mass 171 was ~ 50 cps before the experiment, and after the experiment it reached 19 500 cps, increasing by a factor of ~ 390 . Ta has only single stable isotope ^{181}Ta .

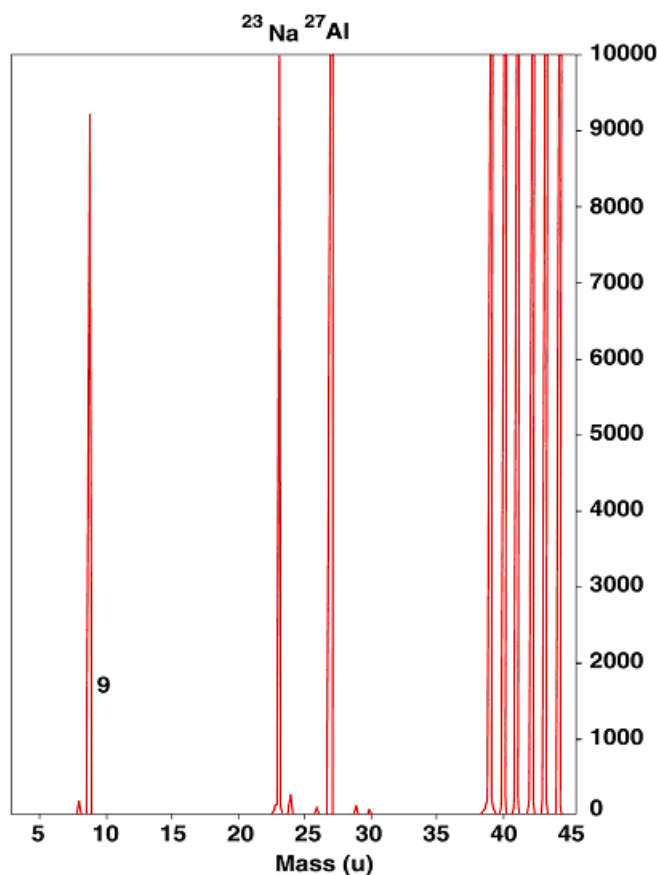


Figure 7. The intensity increasing of mass 9 in Ta after deuterium discharge (b).

Figures 7 and 8 show mass 9 in Ta before and after of the deuterium discharge. Mass 9 increased from 20 cps in original Ta foil to 9500 cps in post-experimental foil. The increase was a factor of ~ 475 .

Table 8 shows data from the first set of the experiments with W, showing that transmutation of heavier isotopes into lighter ones continues after the experiment is stopped. Increases from ~ 20 to ~ 200 times for different isotopes were found.

An analysis of tungsten foils irradiated with different doses of deuterium discharge performed 3, 4, and 5 months after irradiation is presented in Table 9.

The lighter masses appearance was observed after GD. Mass spectroscopy results include the following:

- Tungsten transmutation of heavy isotopes into lighter isotopes after exposure in deuterium discharge was confirmed.
- The group of lighter isotopes with mass numbers 169, 170, 171, 178, and 180 had high intensity after deuterium discharge soon after the experiment, and 3, 4, and 5 months later.
- Isotopes with lighter masses (in compare to W isotopes) continued forming for at least 3–5 months after the exposure in the deuterium discharge. The observed increase of different light isotopes was into 5–400 times

(from 5 to 50 cps in the original W into 100–20 000 cps after experiments).

- Experiment with tantalum was carried out to strengthen understanding of the possible reaction. Tantalum was

Table 8. Intensity of more light isotopes in tungsten foils after deuterium discharge with TIMS analysis in CPS (set 1)

Time (min*)	84*	101*	137*	1062*	1073*	1133*	1150*	**0, Original W
Mass								
168			40	30	60	2000	30	10 ± 10
170			40	55	50	1600	100	5 ± 5
171			60	95	100	100	70	5 ± 5
172			70	100	100	200	100	0
173			80	75	70	300	100	15 ± 15
174			30	55	60	200	100	5 ± 5
175			40	55	70	40	85	5 ± 5
176			40	55	40	95	75	5 ± 5
177			40	55	40	10	100	10 ± 10
180		70	10	45	100	20	30	25 ± 5
181		100	10	30	40	50		5 ± 5
189	70		20	30	10		50	5 ± 5
193	60		20	30	10		0	5 ± 5
194	70		40	65	0		10	10 ± 10

* First line shows the time in minutes after experiment.

** Last column is intensity of isotopes in the original W.

*** Set 1- The first analysis was carried out in 45 min after experiment stop. Farther the each analysis was fulfilled every 15 min during ~3 h and then analysis was made in ~10 h every 15 min during few hours.

Table 9. Intensity of isotopes with masses lighter than tungsten isotopes foils after deuterium GD, analyzed with TIMS (counts per second (CPS) Set No. 2)

No.	No. 1817				No. 1820					No. 1821	Original
Date Mass	16.03*	16.03*	19.03*	20.03*	21.04**	21.04**	23.04**	14.05***	14.05***	20.03***	****
1	2	3	4	5	6	7	8	9	10	11	12
168		0			235	200	75		130		30 ± 10
169		25			475	500	85		243		30 ± 10
170		70			600	600			243		30 ± 10
171	40	70	40	45	950	950	150	140	1670	25	35 ± 10
172	80	80	55	55	5000	6000	700	15	40	65	20 ± 10
173	400	400	300	300	200	200	50	40	488	200	25 ± 10
174	45	50	25	30	1600	1615	230	8	0	46	15 ± 10
175	125	170	75	80	15		15	35	300	70	20 ± 5
176*	8	8	8	8	30		15	50	0		20 ± 5
177	8	8	8	0	30		40	130	35		8 ± 1
178	15	8	0	8	50		19500	20	30		8 ± 1
179	0	8	0	8	70		60	220	100		30 ± 10
180	25	15	8	0			80	480	320		20 ± 5
181			0	120			40	1000			30 ± 5

*2–5, 11 present the date later tree months after experiments; **6–8 present the date later 4 months after experiments; ***9–10 present the date later 5 months after experiments; 12**** is average CPS for 3–5 original analyzed foils.

Table 10. Tungsten and tantalum energy peaks after deuterium glow discharge in contact with X-ray/gamma CdTe detector (for the one group of isotopes) [4].

W	W	W	Ta	Isotope	E_γ (keV)	Half-life	Decay mode	I_γ (%)	Mass according TIMS spectra
(1-4) 1817	1820	1818	1824						
Peaks energy of gamma spectra (keV)									
	20.7	20.7	20.7 ± 1	$^{170}_{72}\text{Yb}$	20.75	32d	ε	0.19	169
42 ± 1	43	42	42.18	$^{170}_{72}\text{Yb}$	42.76	32d	ε	0.25	169
50 ± 1	51.2	50.44	51	$^{170}_{72}\text{Yb}$	51.1	32d	ε	0.018	169
63 ± 1	63	62.83	63.5 ± 0.5	$^{170}_{72}\text{Yb}$	63.12	32d	ε	44.2	169
45 ± 1	45.10	44.46	46.46	$^{170}_{72}\text{Hf}$	44.52	16.01 h	$\varepsilon + \beta^+$	0.32	170
55.4	55.5	55.4	55.4	$^{170}_{72}\text{Hf}$	55.2	16.01 h	$\varepsilon + \beta^+$	1.1	170
99.9	99.0	100.8	100.8	$^{170}_{72}\text{Hf}$	99.93	16.01 h	$\varepsilon + \beta^+$	2	170
113.2	113.3	113.2	113.2	$^{170}_{72}\text{Hf}$	113.9	16.01 h	$\varepsilon + \beta^+$	0.18	170
115.6	115.0	115.7	115.6	$^{170}_{72}\text{Hf}$	115.5	16.01 h	$\varepsilon + \beta^+$	0.2	170
133.0	132.0	132.2	132.7	$^{170}_{72}\text{Hf}$	132.2	16.01 h	$\varepsilon + \beta^+$	0.044	170
138.81	138.5	138.0	138.8	$^{170}_{72}\text{Hf}$	139.2	16.01 h	$\varepsilon + \beta^+$	0.018	170
19 ± 1	19.89	19.06	19.1	$^{171m}_{72}\text{Yb}$	19.39	5.25 ms	IT	14.8	171
22.5 ± 1	23.19	23.19	23.2	$^{172}_{72}\text{Hf}$	23.4	1.87 y	ε		172
24 ± 1	24	24.02	24.84	$^{172}_{72}\text{Hf}$	23.93	1.87 y	ε	20.3	172
60 ± 1	60.5	60.35	60.5±0.5	$^{172}_{72}\text{Hf}$	60.65	1.87 y	ε	1.1	172
67 ± 1	63	62.35	67.5	$^{172}_{72}\text{Hf}$	67.3	1.87 y	ε	5.3	172
91 ± 1	91 ± 1	91.74	91	$^{172}_{72}\text{Hf}$	91.3	1.87 y	ε	0.11	172
115 ± 1	114	114.03	114.03	$^{172}_{72}\text{Hf}$	114.06	1.87 y	ε	2.6	172
115 ± 1		115	115.6	$^{172}_{72}\text{Hf}$	116.1	1.87 y	ε	0.034	172
119 ± 1	119	118.99	119.8	$^{172}_{72}\text{Hf}$	119	1.87 y	ε		172
129.03	129	127.25	127.5	$^{172}_{72}\text{Hf}$	127.9	1.87 y	ε	1.46	172
42 ± 1	43	42	42.18	$^{178}_{70}\text{Yb}$	42.4	74 m	β^-	6.7	178
13 ± 1	14.1	14.1	13.3	$^{180}_{70}\text{Yb}$	13.9	2.4 m	β^-		180
57 ± 1	58.7	57.05	57.88	$^{180m}_{72}\text{Hf}$	57.555	5.5h	IT	48.0	180m

selected because it has only one stable isotope, with mass number 181.

3.4.2. Observation of some isotopes in W after GD with CdTe gamma and X-ray detector [4]

Average intensity of gamma-emission with CdTe gamma and X-ray detector in usual configuration of glow discharge apparatus and original W as background was ~ 0.10 cps.

Calibration of CdTe detector was fulfilled according ^{133}Ba .

The presents of K_α series and K_β series lines of W (in energy regions 57, 58, 59 and 67–69 keV) is evidence of the reality of the identified with using series of pear energy on the observed gamma and X-ray spectra.

Masses in right coulomb were found with a thermal ionization mass spectrometer. It is possible $^{180m}_{72}\text{Hf}$ nine energy peaks of gamma-spectra correspond with $^{172}_{72}\text{Hf}$ isotope and seven $^{172}_{72}\text{Hf}$ peaks of gamma-spectra correspond with

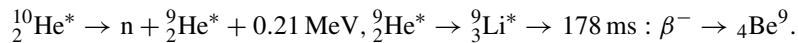
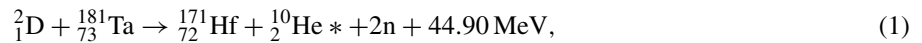
$^{170}_{72}\text{Hf}$ $^{180\text{m}}_{72}\text{Hf}$ isotope. The isotope $^{180\text{m}}_{72}\text{Hf}$ with IT 99.7%. β^- 0.3% and $T_{1/2} = 5.47$ h was assumed taking into account the maximal intensity of gamma-emission in 5.5 h time exposure.

The correlation of gamma and X-ray emission with mass-spectrometry data allows to have of opinion that the process of formation new isotopes are going during and after glow discharge [3,4].

Some variants of the way for isotope transformation under glow discharge was suggested early [1,4].

4. Discussion

Only one possible example of reaction taking into account the masses defect, spin and parity estimation is suggested below:



There are also alternative assumptions which may provide a better explanation of the details of this complex process, for example the poly-neutron theory of transmutation, suggested by John Fisher [15] or the stimulation of LENR by the electro-magnetic excitation of the crystal lattice in [5,9] and by Peter Hagelstein [16].

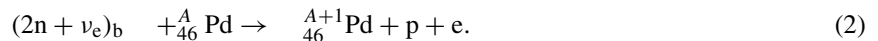
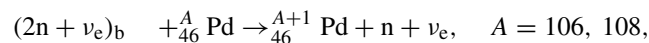
Presently, there are more than 150 theories and assumptions to explain low-energy nuclear reactions, some of them suggested by Russian researchers: the flux hypothesis by Boris Rodionov [17] based on the existence of cylindrical atoms, the idea of Vladimir Muromtsev about the cluster decay and neutrino–dineutron reactions, based on the neutrino interaction with elements and the resulting dineutrons formation [18], and the Unitary Quantum theory by Lev Sapogin [19].

The latest explanation of LENR phenomena in terms of classic nuclear physics was suggested by Ratis [20]. This explanation involves the reaction of nuclei-target with dineutroneum atoms, which represent a bound state of two neutrons and one neutrino generated by the inclusive electronic capture (EC) reaction $e^- + d \rightarrow (2n + \nu_e)_b + X$.

Ratis [20] suggests that the dineutroneum atoms are metastable particles with the life-time of $(2n + \nu_e)_b - 3 \times 10^{-3} \text{ s}$, by three orders more than the μ^- meson life-time. The size of the dineutroneum atom is commensurable with the size of the deuteron. The mass of the dineutroneum atom is equal to $M_{(2n+\nu_e)_b} = 2.014102236 \text{ e}^- = 1876.0965 \text{ MeV}$.

The metastability, electrical neutrality and the small sizes of the dineutroneum atoms allows them to take part in the fusion reaction with nuclei-targets.

In the deuterium plasma (in GD) may takes places generation of the dineutroneum atoms $(2n + \nu_e)_b$ (b- bound). These atoms collides with $^{106}_{46}\text{Pd}$ and $^{108}_{46}\text{Pd}$ nuclei in the Pd-cathode in the discharge chamber. As a result, one can observe reactions



Formula (2) gives us an answer to a question, why neutrons are registered so rarely in CF reactions. Neutrino is a very light particle, and palladium is a very heavy particle. In the neutron transfer reaction the $(n + \nu_e)_f$ –the rest does not practically interact with the Pd-nucleus. As a rule, the only open channel of the compound particle $(n + \nu_e)_f$ decay - the rest is $p + e^-$. We cannot observe a free neutron and neutrino in the exit channel of the $(n + \nu_e)_f$ -decay reaction,

because it is forbidden by conservation law (neutrino has a very large energy, and a very small momentum). Thus, the channel $(n + \nu_e)$ is closed. In contrast to the previous case, all particles in the $p+e^-$ channel have an electrical charge. Both particles – proton and electron – interact with a Pd-nucleus. The mass of electron is by many orders more than the mass of neutrino, and it carries away not only energy, but also momentum. As a result, the $p+e^-$ channel of the $(n+\nu_e)_f$ -decay opens up [20].

5. Conclusion

- (1) The presence of low-energy nuclear reactions was confirmed by the GD low-energy influence:
 - Significant increase in additional elements ranging 10 -1000 times was found.
 - Isotopic deviation in materials (Pd, Ti, W, and U) and the increase in the additional impurity elements from 2 up to 100 times was discovered.
 - The majority of the newly formed elements, found after the GD switch off were found in certain local zones (“hot” spots, micro melting points) on the cathode material surface.
 - Post-experimental isotopes with masses of 169, 170, 171, 178, and 181 (less than W and Ta isotopes) were found with the help of TIMS.
 - The isotopic changes continue to occur for at least 3–5 months after the GD exposure. Separate isotopes with masses less than W and Ta isotopes have grown by factors ranging 5–1000 times.
 - The same energy peaks in gamma-spectra occur during and after the GD current switch-off.
 - The change in alpha, beta, gamma radioactivity caused by the GD was observed.
 - Post experimental weak gamma, X-ray and beta- emissions were detected.
- (2) The correlation between the gamma and X-ray emission data and the thermal ionization mass-spectrometry data for the same isotopes is shown in the W foils.
 The comparison of the mass spectra and the gamma spectra points to the existence of the following isotopes:
 $^{169}_{70}\text{Yb}$, $^{170}_{72}\text{Hf}$, $^{171m}_{70}\text{Yb}$, $^{172}_{72}\text{Hf}$, $^{178}_{70}\text{Yb}$.
- (3) The collection of effects confirms availability of nuclear transformations under exposure to GD low-energy ions bombardment in materials and in other processes.
- (4) The GD low-energy influence can be used in new power engineering and new technologies (e.g., isotope production). The described effects should be paid more attention to.

References

- [1] I. Savvatimova and D. Gavritenkov, Results of analysis of Ti foil after glow discharge, *Proc. ICCF11*, World Scientific, France, 2004, pp. 438–458.
- [2] I. Savvatimova and D. Gavritenkov, Influence of the glow discharge parameters on the structure and isotope composition of cathode materials, *Proc. ICCF12, 2005*, World Scientific, Japan, pp. 231–252.
- [3] I. Savvatimova, Creation of more light elements in tungsten irradiated by low-energy deuterium ions, *ICCF13*, Russia, 2008, pp. 505–517.
- [4] I. Savvatimova, G. Savvatimov and A. Kornilova, Decay in tungsten irradiated by low energy deuterium ions, *ICCF13*, Russia, 2008, pp. 295–308.
- [5] I. Savvatimova, A. Senchukov and I. Chernov, Transmutation phenomena in the palladium cathode after ions irradiation at glow discharge. proceedings, *ICCF6*, Japan, 1996, pp. 575–579.
- [6] I. Savvatimova, Ya Kucherov and A. Karabut, Cathode material change after deuterium glow discharge experiments, *ICCF4*, Dec. 1993, *Trans. Fusion Technol.* **26** (4T) (1994) 389–394.
- [7] I.B. Savvatimova and A.B. Karabut, Nuclear Reaction Products Registration on the Cathode after Deuterium Glow Discharge, *Surface*, V. 1, Moscow: RAN, 1996, pp. 63–75.

- [8] I. Savvatimova, Transmutation in cathode materials exposed at glow discharge by low energy ions, Nuclear phenomena or ion irradiation result? *Proc. ICCF-7*, Canada, Vancouver, 1998, pp. 342–350.
- [9] A.B. Karabut, Ya.R. Kuchеров and I.B. Savvatimova, Nuclear product ratio for glow discharge in deuterium, *Phys. Lett. A* **170** (1992) 265–272.
- [10] A.B. Karabut, Ya.R. Kuchеров and I.B. Savvatimova, The investigation of deuterium nuclei fusion at glow discharge cathode, *Fusion Technol.* **20** (1991) 924–928.
- [11] I.B. Savvatimova, Reproducibility of experimental in glow discharge and process accompanying deuterium ions bombardment, *ICCF8*, Italian Phys. Soc, Italy, 2000, p. 277.
- [12] J. Dash, I. Savvatimova, S. Frantz, E. Weis and H. Kozima, Effects of glow discharge with hydrogen isotope plasmas on radioactivity, *Proc. ICENES*, 2002, p. 122.
- [13] J. Dash, I. Savvatimova, S. Frantz, *Proc. 11th Int. Conf. on Emerging Nuclear Energy Systems*, Univ New Mexico, Albuquerque, NM, 2002, pp. 122–127.
- [14] J. Dash and I. Savvatimova, Effects of glow discharge with hydrogen isotope plasmas on radioactivity of uranium, *Proc. American Nucl. Soc. Conf.*, San Diego, 6 June, 2003.
- [15] J. Fisher, Polyneutron theory of transmutation, *Proc. 12 Int. Conf. on Cold Fusion ICCF12*, Yokohama, Japan, 2005, pp. 516–520.
- [16] P. Hagelstein, *Proc. 6th Int. Conf. on Cold Fusion ICCF6*, Oct. 13–18, 1996, Japan, 1996.
- [17] B. Rodionov and I. Savvatimova, Unusual structures on the material surfaces irradiated by low energy ions, *ICCF12*, Japan, 2005.
- [18] V. Muromtzev, V. Platonov and I. Savvatimova, Neutrino-dineutron reactions, *Proc. the ICCF12*, Yokohama, Japan, 2005, pp. 571–576.
- [19] L. Sapogin, *Unitary Quantum Theory*, Moscow, Russia, 2005.
- [20] Yu. L. Ratis, *Controlled Hot fusion or Cold Fusion? Drama of Ideas*, 2009, Samara, Russia, 102 p.



Research Article

Experimental results on Excess Heat Power, Impurity Nuclides and X-ray Production in Experiments with a High-Voltage Electric Discharge System

A.B. Karabut *

Samar + COMPANY, Belay Dacha, 13, ap. 54, city Kotelnikiy, Moscow Region, 140055, Russia

E.A. Karabut

Moscow Power Engineering Institute (Technical University)

Abstract

We review results on low-energy nuclear reaction (LENR) processes in a high-voltage (1000–4000 V) electric discharge system. The experimental results are divided into three sets: excess heat measurements; yield of impurity nuclides (nuclear ash); x-ray measurements. Up to 8 W of excess power was observed, with a power gain of up to 170% was seen in glow discharge experiments. Up to 300 W of excess power, with a power gain up to 340% was observed in experiments using a high-voltage electrolysis cell. The impurity nuclide yield showing a shift of up to a few per cent from natural isotopic abundances was detected by spark mass spectrometry, by secondary ionic mass spectrometry, and by secondary neutral mass spectrometry. X-ray emission in the range of 0.6–6.0 keV, and up to 0.1 W/cm² has been observed. Based on these experimental results we propose a phenomenological model for LENR based on the interaction of an electric discharge with condensed matter (of the cathode).

© 2012 ISCMNS. All rights reserved.

Keywords: Excess heat power, Glow discharge device, High voltage electrolysis cell, Long-range (resonant) nuclear reactions, Transmutation, X-ray emission

1. Introduction

We have identified phenomena associated with the Fleischmann–Pons effect in the solid cathode of a high-voltage electrolysis cell and a high-voltage glow discharge system; including excess heat production, transmutation, and X-ray emission. In this work we will review experimental results on excess heat production in the glow discharge system (up to 8 W, and 170% power gain), and in the electrolysis cell (up to 300 W, and 340% power gain). We also describe the results of experiments which show transmutation products. Detailed experimental results on X-ray emission are

*E-mail: abkarab@mail.ru; Tel.: (495) 5508129, Fax: (495) 5508129

discussed in another paper in this proceedings. These include the observation of collimated X-ray emission from the cathode, which is a new fundamental effect that has not been reported prior to our experiments.

Based on these observations, we have developed some theoretical ideas that may be helpful in understanding the experimental results. We propose that long-lived metastable states are generated at solid density in the cathode with excitation energies in the keV range. In the glow discharge, a flux of ions with kinetic energies on the order of 500–2 keV is incident on the cathode; the appearance of X-rays in the 600–6 keV range implies that there is a physical mechanism capable of converting the incident ion energy into long-lived (up to tens of millisecond long) excitation of the electronic-nuclear system of the cathode. We observe characteristic X-ray emission of the cathode elements, suggesting that L and M excitation occurs in the cathode. Observations of excess power and transmutation products indicates that nuclear reactions occur, and it may be that these reactions occur as a consequence of the high effective temperature that might be associated with the strongly non-equilibrium conditions implied by the long-lived highly excited states. We propose that such reactions are responsible for LENR effects in our experiments.

2. Excess Power Measurements in Glow Discharge Experiments

The measurements were carried out using a glow discharge [5] consisting of a water-cooled vacuum chamber, cathode and anode assemblies as shown in Fig. 1(a). The cathode holder can accept cathodes made of different metals, and the discharge occurs between the cathode and anode in the low pressure gas inside the chamber. Periodic pulses are supplied by a high-voltage power source. We used flow calorimetry, with independent water cooling channels supplied to the cathode, the anode, and to the chamber. Each cooling channel included two thermal sensors differently turned on at the input and output and a cooling water flow meter. The excess power parameters (determined from input from the temperature sensors and the flow-meter), and the electric parameters (the glow discharge current and voltage), were recorded using a data acquisition board. The excess power P_{xs} was determined as the difference between the output thermal power and input electrical power.

The discharge current and voltage was measured with a two-channel data acquisition board. The use of 8-bit analog digital oscilloscope conversion (with 50 MHz clock frequency) allowed us to achieve about 1% measurement accuracy of electric parameters. Instantaneous current and voltage values were multiplied digitally and the resulting estimate for electric power was made; with the average electric power value obtained from

$$P_{el} = \frac{1}{T} \int_V(t) I(t) dt.$$

We used a numerical integration based on

$$P_{el} = \frac{1}{T} \sum_i \frac{1}{2} (I_i V_i + I_{i+1} V_{i+1}) (t_{i+1} - t_i).$$

Here T (the pulse-repetition period) is set by the power supply driving generator with accuracy no less than 0.1%; $I_i V_i$ and $I_{i+1} V_{i+1}$ represent electric power values for the different times t_i and t_{i+1} . The number of steps was determined by the condition that the electrical power must be linear over a time step.

The thermal power carried away by the anode, cathode and chamber cooling water channels, respectively, is determined by

$$P_A = C_w G_{WA} \Delta T_A,$$

$$P_C = C_w G_{WC} \Delta T_C,$$

$$P_{Ch} = C_w G_{WCh} \Delta T_{Ch}.$$

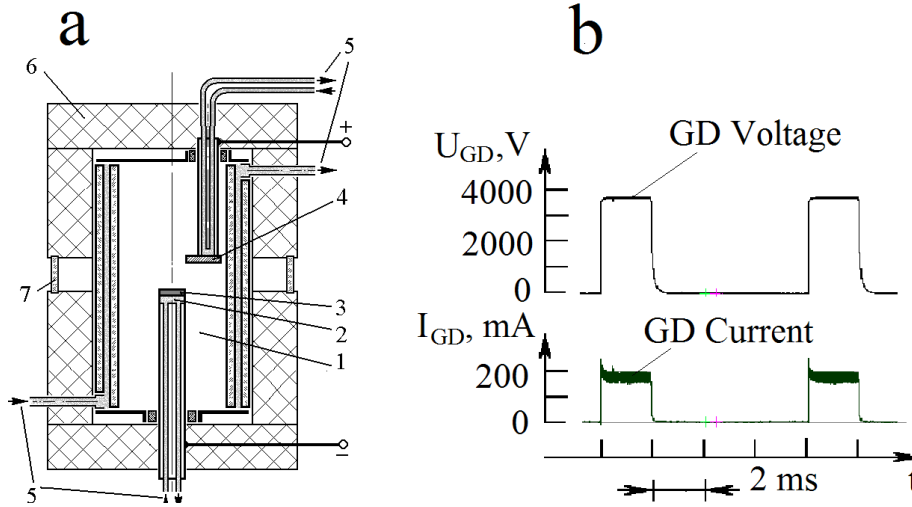


Figure 1. Schematic representation of the experiment: (a). Glow discharge device, 1 – discharge chamber, 2 – cathode holder, 3 – cathode sample, 4 – anode, 5 – cooling water; Be foil screens, 6 – heat insulation cover, 7 – windows in heat insulation cover. (b) Glow discharge voltage and current oscillograms.

Here C_w stands for the water specific heat; and G_{WA} , G_{WC} , and G_{WCh} are the anode, cathode and chamber cooling water flow rate, respectively. The temperature differences ΔT_A , ΔT_C , and ΔT_{Ch} denote the difference between the anode, cathode and chamber input and output cooling water temperature readings. The water flow rate is measured by volume flow meters with $\pm 0.2\%$ relative measurement error.

The actual error of the calorimetric system was determined in tests by a resistive heater. The resistance of the calibration heater was close to the glow discharge resistance (about $5 \text{ k}\Omega$); and was characterized by its own small specific heat and adequate thermal insulation. In test experiments the heater was powered by the periodic pulse power supply (similar to the power supplied to the glow discharge). The procedure used in processing of results was the same as that used in glow discharge experimentation. In so doing the electric power of calibration heaters was defined and measured. The temperature difference for calibration was determined by

$$\Delta T_A = \frac{P_{el,A}}{C_w G_{WA}},$$

$$\Delta T_C = \frac{P_{el,C}}{C_w G_{WC}},$$

$$\Delta T_{Ch} = \frac{P_{el,Ch}}{C_w G_{WCh}}.$$

Here $P_{el,A}$, $P_{el,C}$, and $P_{el,Ch}$ denote electric power (values) of calibration heaters in the anode, cathode and chamber water channels, respectively. The results of such calibration experiments show that the measurements actual error at rather high power levels did not exceed $\pm 1.0\%$.

If excess power is present, we can determine its value using

$$P_{xs} = (P_C + P_A + P_{Ch}) + P_{loss} - P_{el} \pm \Delta P_{error}.$$

The heat power losses into environment P_{loss} in the first approximation may be presented as being proportional to the magnitude (value) of the total thermal power:

$$P_{\Sigma} = P_C + P_A + P_{\text{Ch}}$$

in and it may be accounted for by introduction of the glow discharge efficiency coefficient η

$$\eta = \frac{P_A + P_C + P_{\text{ch}}}{P_A + P_C + P_{\text{ch}} + P_{\text{loss}}}.$$

The efficiency η is determined in experiments under operational regimes in which excess heat is not observed.

The Pd samples used in glow discharge calibration experiments with Xe and Kr were not pre-charged with deuterium, and relatively high values for the thermal efficiency were achieved. Following calibration, deuterium is loaded into the Pd. In these experiments the current density did not exceed 100 mA/cm². At such values of the discharge current density in D₂, a continuous loading of D₂ into Pd ran up to saturation. The amount of deuterium loaded into palladium was determined by the volume of the gas absorbed from the discharge chamber. When saturation was achieved, the value of the D/Pd ratio was close to 1. Then, experiments were carried out with Pd cathode samples in D₂, and also with deuterium pre-charged Pd cathode samples in Xe and Kr discharges. Relatively high values of excess power were achieved for deuterium pre-charged cathode samples in Xe and Kr discharges [6] (see Fig. 2(a)). No excess power was observed in the cathode samples made of pure Pd (not deuterium pre-charged) in Xe and Kr discharges, as can be seen in Fig. 2(b). The biggest values of power gain were observed under conditions when the glow discharge voltage ranged between 1000 and 1300 V (Fig. 2(b)).

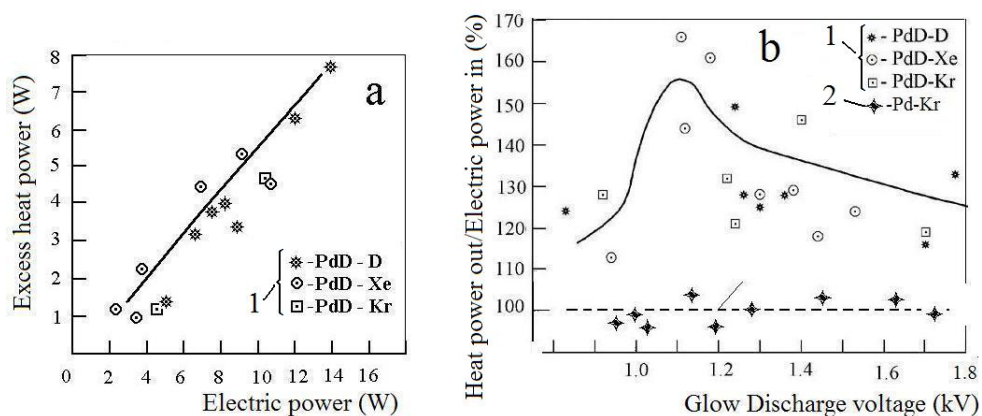


Figure 2. (a) Excess power as a function of input electric power for a Pd cathode sample, $d = 9$ mm, current is 50–100 mA. (b) Dependence of the ratio of thermal power to electrical input power as a function of the glow discharge voltage. 1 – deuterium pre-charged Pd cathode samples in D₂, Xe and Kr discharges, current is 50–100 mA, 2 – non deuterium pre-charged Pd cathode in Kr discharge.

We interpret this as showing two requirements for excess power generation: (1) deuterium should be loaded into the solid-state crystal lattice medium and (2) the crystal lattice should get an initial excitation, so that high-energy long-lived excited levels are created in the cathode sample solid. These excited conditions could be created by an additional source (for example by a flux of inert gas ions).

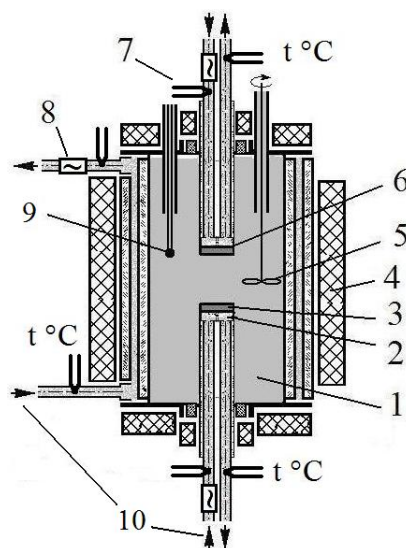


Figure 3. Schematic of a high-voltage electrolysis device, set up as a heat capacity and flow calorimeter; 1 – electrolyte chamber, 2 – cathode holder, 3 – cathode sample, 4 – thermal insulation cover, 5 – mixer, 6 – anode, 7 – temperature sensors, 8 – flow meter, 9 – thermocouple, and 10 – cooling water.

3. Excess Power Measurements In The High-Voltage Electrolysis Cell

The measurements were carried out using high-voltage electrolysis cell; which consists of two flanges made of stainless steel with fastening units for the anode and the cathode assembly as shown in Fig. 3. An electrolysis chamber (1) in the form of quartz glass tube is set between the flanges, and another cylindrical tube set co-axially serves as the chamber cooling jacket. The electrolysis chamber volume was 95 cm³. The cathode units were provided with changeable cathode holders (2) that allowed us to use different cathode samples (3) with associated fasteners to hold the samples.

The discharge chambers were wrapped up into a thermal insulation cover (4), that reduced thermal losses into the environment. The three units of the device (the cathode, anode and chamber) had independent channels of water cooling. Each cooling channel included two temperature sensors (at the input and output) and a volumetric counter of the cooling water flow. The stirrer (5) and the thermocouple (9) were fixed upon the anode (6) flange inside the chamber. A pulsed power supply was used in the experiments. The electrolysis voltage in different experiments ranged from 500 V to 2500 V, with the current in the range of 0.5–2.0 A. Pd, Ni and Pt cathode samples were used in the experiments; the cathode diameter was 11 mm.

The high-voltage electrolysis cell device was used in the two experimental runs:

- (1) Experiments based on heat capacity calorimetry. The cooling water (10) of the cathode, anode, and discharge chamber, was absent in these experiments.
- (2) Experiments based on continuous flow calorimetry.

Pre-deuterated Pd cathode samples and Ni cathode samples were used in high-voltage electrolysis cell experiments with excess power being measured.

3.1. Pre-deuterated Pd cathode sample preparation

Bombardment by D_2 ions in the glow discharge is viewed as the most effective procedure for loading deuterium into Pd [7]. The measurements were carried out using the glow discharge device consisting of a water-cooled vacuum chamber (1000 cm^3), and cathode and anode assemblies. The chamber design allowed the placement of cathode samples made of various materials on a water-cooled surface. The experiments were carried out using a high-current glow discharge in D_2 , with Pd samples. The power supply feeds the glow discharge with a periodic pulse direct current, and allows the generation of desired current forms (with various pulse length and pulse period) to obtain the required current voltage and current. We observed good D_2 loading into Pd cathodes with this approach. The glow discharge current was from 30 mA up to 300 mA, the voltage was from 500 to 1400 V, and the gas pressure in the chamber was between 1 and 25 torr.

The loading procedure can be summarized as:

- (1) First pump the gas out of the discharge chamber.
- (2) Bleed deuterium into the chamber until the pressure builds up to several torr.
- (3) Switch on the glow discharge and commence operation.

The D_2 pressure is observed to decrease steadily when loading into the cathode Pd. Then the glow discharge is switched off, with D_2 being pumped again into the chamber. The above procedure is repeated several times, the gas pressure being increased each time as shown in Fig. 4. During the experiment the D/Pd ratio was determined by summing up the pressure drops.

3.2. Heat capacity calorimetry in high-voltage electrolysis cell experiments

A variety of calorimetry experiments were carried out in the high-voltage electrolysis cell to study excess power generation. For control experiments, we used Pt cathodes (which do not load, and which produce no excess power). Excess power measurements were made on Pd cathodes that were pre-loaded with deuterium, and also with Ni cathodes. The electrolysis was done in light water.

In heat capacity calorimetry, estimation of the excess energy is made by comparing the temperature increase measured with deuterated Pd or Ni cathodes with the temperature rise of the Pt control. For the control experiment, a calibration of temperature versus electrical input energy is established as shown in Fig. 5. When a Pd cathode pre-loaded with deuterium is used, the temperature rise is much faster, also illustrated in Fig. 5. To estimate the excess energy, we begin with the observed temperature as a function of input electrical energy; for each observed temperature we determine how much input energy is needed to produce such a temperature in the Pt control experiment, and then determine the excess energy as the difference between the two (the estimated energy produced minus the input electrical energy). The electric discharge was switched off when the calorimeter temperature reached 57°C .

It is possible to develop estimates for the excess power produced from such measurements by determining the incremental excess energy produced during the time between successive temperature measurements. This approach was used for the estimated excess power in the different experiments of Figs. 6–10. We see from these measurements that the excess power produced reached 280 W, with a power gain (ratio of thermal output power to electrical input power) as high as 340%

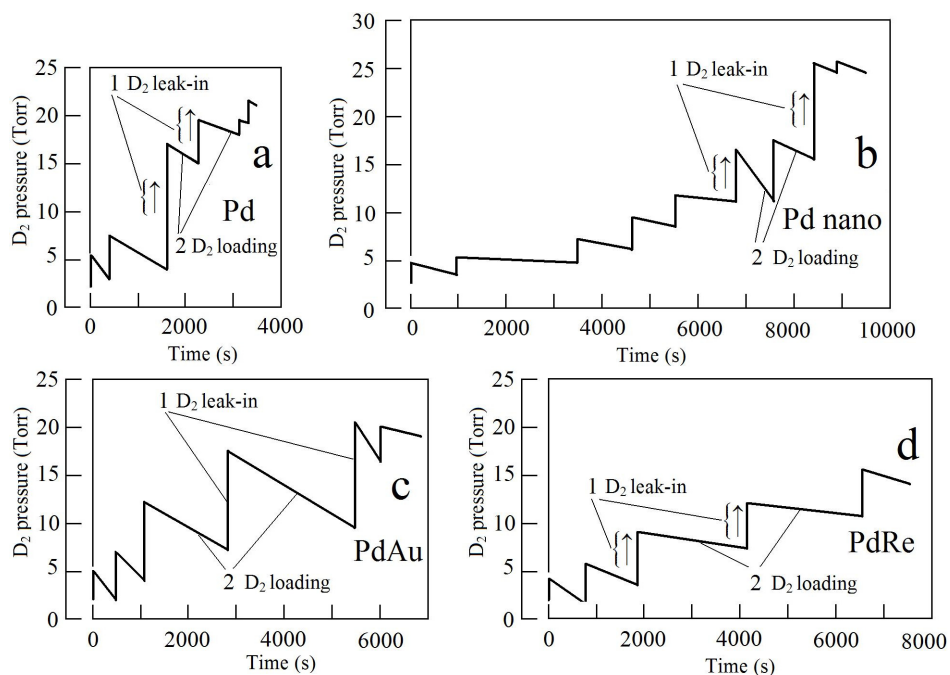


Figure 4. Time history of the D_2 pressure in the glow discharge chamber; (a) D_2 loading in Pd foil sample; (b) nanostructured Pd cathode sample, (c) Pd foil coated Au cathode sample, and (d) Pd foil coated Re cathode sample.

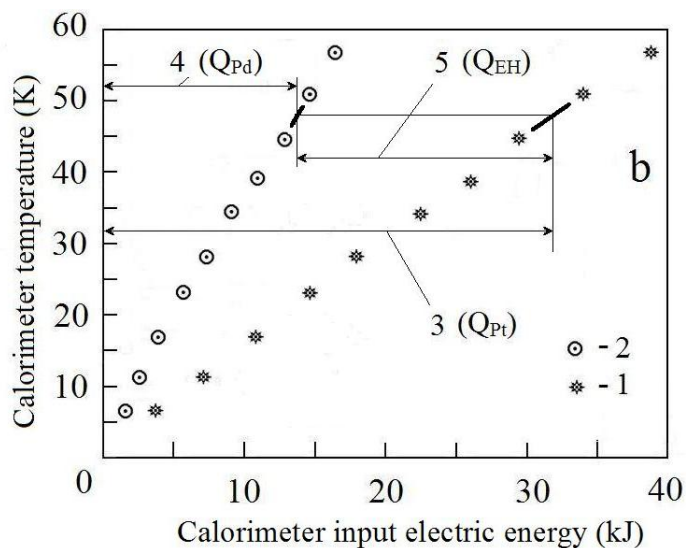


Figure 5. Dependence of the calorimeter temperature up input electric energy value; 1 – electrolysis in H_2O with the Pd cathode, 2 – electrolysis in H_2O with a Pt cathode, 3 – input electric energy in calorimeter with Pt cathode, 4 – input electric energy in calorimeter with Pd cathode, 5 – excess energy with pre-loaded Pd cathode.

3.3. Flow calorimetry in high-voltage electrolysis cell experiments

Our flow calorimetry in the high-voltage electrolysis cell is similar to the calorimetry described above for the glow discharge experiments. Independent cooling water flow was channeled to the cathode, anode and to the chamber. Measurements of the temperature difference between the input and output of the different channels was used to determine the thermal power associated with the cathode, anode and chamber individually, according to

$$\begin{aligned} P_A &= C_w G_{WA} \Delta T_A, \\ P_C &= C_w G_{WC} \Delta T_C, \\ P_{Ch} &= C_w G_{WCh} \Delta T_{Ch}, \end{aligned}$$

where P_A , P_C , and P_{Ch} are the thermal powers of the anode, cathode, and chamber; where C_w is the heat capacity of water, where the flow rates are denoted by G_{WA} , G_{WC} and G_{WCh} , and where the measured temperature differences are ΔT_A , ΔT_C , and ΔT_{Ch} .

The local average electrical power was determined from

$$P_{el} = \frac{1}{T} \int_T V(t) I(t) dt,$$

where $V(t)$ and $I(t)$ are the voltage and current associated with a pulse of length T . The excess power (P_{xs}) is determined from the difference between the total thermal output power and the electrical input power (P_{el})

$$P_{xs} = (P_C + P_A + P_{Ch}) - P_{el}.$$

In this case, we determined the calorimeter efficiency η according to

$$\eta = \frac{P_C + P_A + P_{Ch}}{P_{el}}.$$

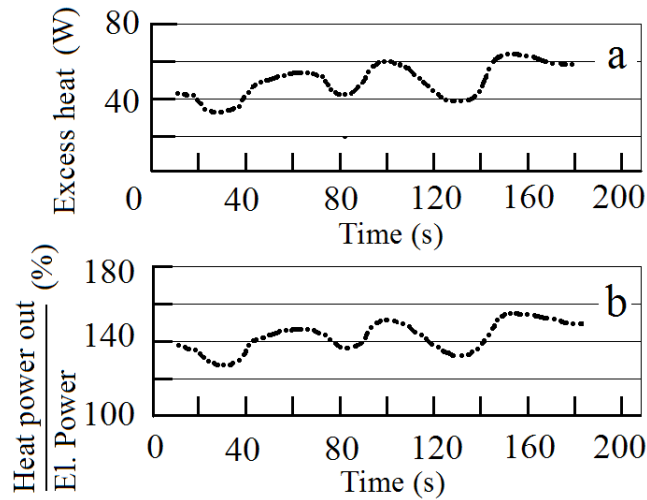


Figure 6. (a) Excess energy as a function of time. (b) Power gain as a function of time. Electrolysis in H_2O with a pre-loaded Pd foil cathode; cathode – anode voltage is 700 V, and current is 0.7 A.

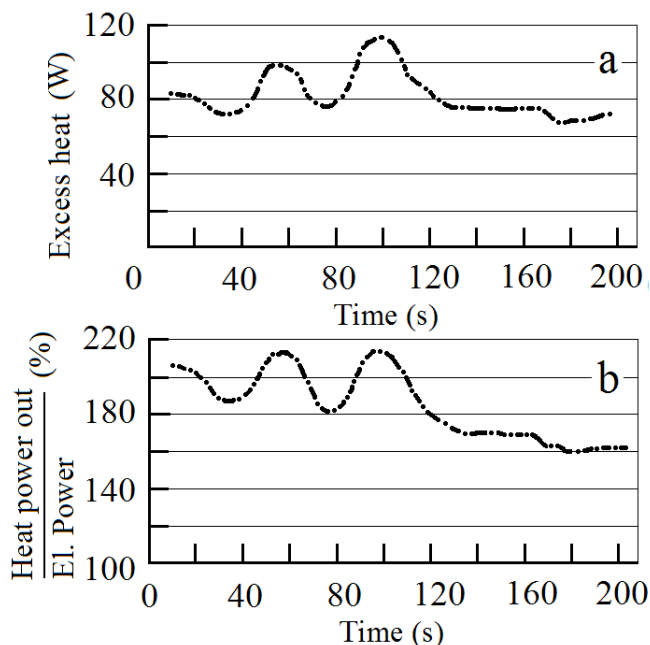


Figure 7. (a) Excess power as a function of time. (b) Power gain as a function of time. Electrolysis in H_2O with a D_2 pre-charged Pd foil coated Re cathode; cathode – anode voltage is 700 V, and current is 0.7 A.

Experimental results are tabulated in Table 1 for Pt control experiments, and for experiments with Ni cathodes. No excess power was observed with Pt cathodes, and the measured calorimeter efficiency was between 94 and 97%. Excess power gain was seen with Ni cathodes with good reproducibility; the largest excess power observed was 230 W with a power gain of 280%. The effect of the mixer (stirrer) can be seen in the greater proportion of power showing up in the chamber flow channel with the mixer on.

4. Nuclear Product Measurements

4.1. He measurements

There has been interest in the field in the issue of ^4He production in association with excess energy production. We reported measurements of ^4He in our early experimental results reported in [1]. We sent some of our Pd cathodes along with reference samples to be analyzed at the Rockwell International Laboratory (Oliver's group). A small increase in ^3He concentration, and a large increase in the ^4He concentration, were found in Pd samples from glow discharge experiments; results are indicated in Table 2.

4.2. Stable impurity nuclei measurements

We carried out elemental and isotopic assays of cathode sample before and after glow discharge experiments to search for possible nuclear reaction products. This was done using X-ray fluorescent spectrometry, spark mass spectrometry, secondary ionic mass spectrometry, and secondary neutral mass spectrometry. In the case of secondary ion mass spectrometry, the procedure that we used was

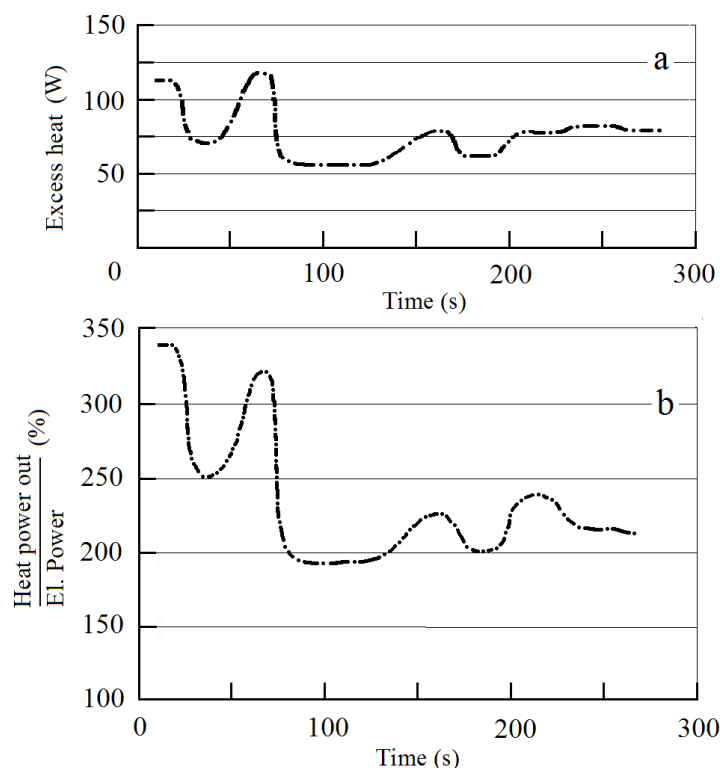


Figure 8. (a) Excess power as a function of time. (b) Power gain as a function of time. Electrolysis in H_2O with a D_2 pre-charged Pd cathode with nanostructure; cathode–anode voltage is 700 V, and current is 0.55 A.

- (1) removal the upper 1.5 nm-thick defect layer by plasma etching,
- (2) scanning the first and the second layers in 5 nm increments, while determining the content of the impurity nuclides,
- (3) removal of a layer with the thickness of 700 nm, and repeated scanning of the third and fourth layers in 5 nm increments while again determining the content of the impurity nuclides.

The initial impurity content was a few ten ppm. We measured impurity nuclei with masses both less than, and greater than, that of Pd as depicted in Fig. 11.

The primary impurity nuclei observed, with an abundance of more than 1%, include ^7Li , ^{12}C , ^{15}N , ^{20}Ne , ^{29}Si , ^{44}Ca , ^{48}Ca , ^{56}Fe , ^{57}Fe , ^{59}Co , ^{64}Zn , ^{66}Zn , ^{75}As , ^{107}Ag , ^{109}Ag , ^{110}Cd , ^{111}Cd , ^{112}Cd , and ^{114}Cd , as shown in Fig. 11. The total content of these impurities amounts to 10^{17} . The experiment duration in this case is up to 2×10^4 s. The deviation from the natural isotope ratio for these impurity nuclei is up to several tens of times. Interestingly, the following isotopes were absent: ^{58}Ni , ^{70}Ge , ^{73}Ge , ^{74}Ge , ^{113}Cd , and ^{116}Cd , as shown in Fig. 12. These peculiarities are also registered within 1 μm thick surface layer, the observed natural Pd isotopes ratio of the sample being changed (Fig. 13).

The main recovered impurity nuclides (with more than 1% content) are ^7Li , ^{12}C , ^{15}N , ^{20}Ne , ^{29}Si , ^{44}Ca , ^{48}Ca , ^{56}Fe , ^{57}Fe , ^{59}Co , ^{64}Zn , ^{66}Zn , ^{75}As , ^{107}Ag , ^{109}Ag , ^{110}Cd , ^{111}Cd , ^{112}Cd , and ^{114}Cd (Fig. 11.). The total content of these impurities amounts to 10^{17} , the experiment duration being up to 2×10^4 s. The observed change of natural isotope

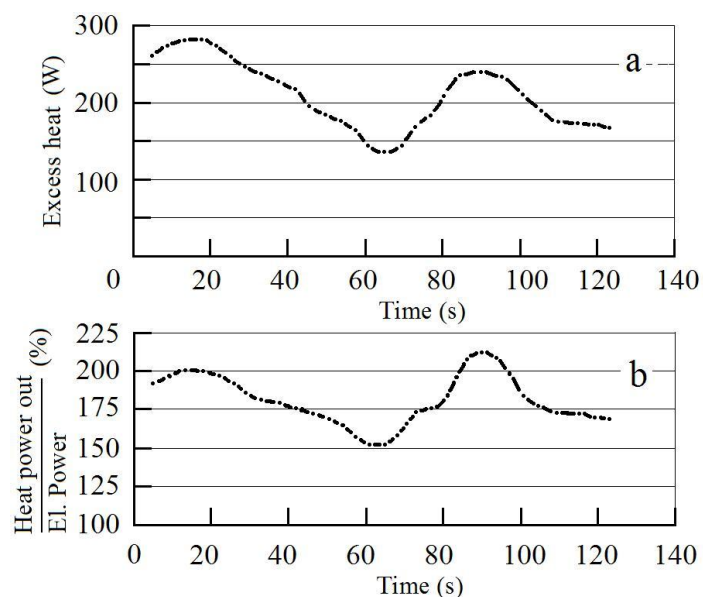


Figure 9. (a) Excess power as a function of time. (b) Power gain as a function of time. Electrolysis in H₂O with a D₂ pre-charged Pd cathode with nanostructure; cathode–anode voltage is 520 V, and current is 2.1 A.

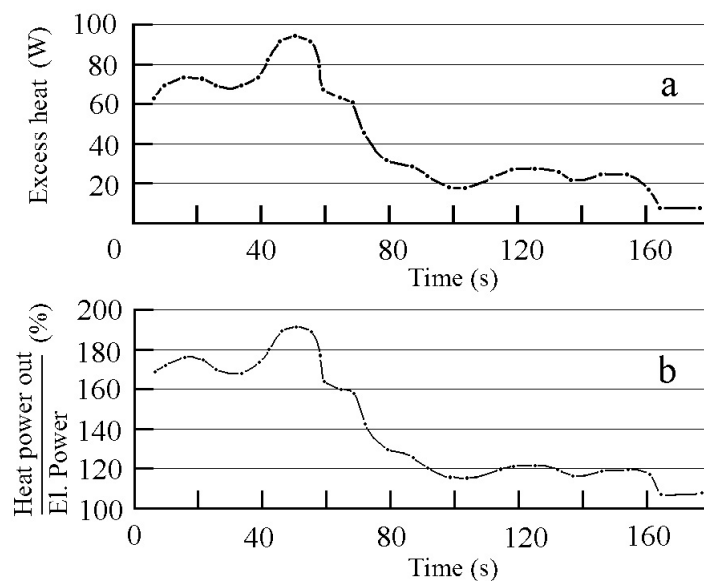


Figure 10. (a) Excess power as a function of time. (b) Power gain as a function of time. Electrolysis in H₂O with a Ni cathode; cathode–anode voltage is 600 V, and current is 0.7 A.

Table 1. Flow calorimetry results for high-voltage electrolysis cell calorimetry.

N Exp.	Current,	Voltage	Elec.	Heat power,	Heat power,	Heat power,	Total	Heat	Excess heat	Heat
	<i>I</i>	<i>U</i>	power	cathode	chamber	anode,	power,		power	efficiency
	(A)	(V)	(W)	(W)	(W)	(W)	(W)		(W)	(%)
Pt cathode, H ₂ O electrolyte with working mixer										
1	1.13	600	169	23.6	124	15.5	163		no	96
2	1.6	443	178	26.6	128.5	16.6	172		no	96
3	1.11	295	82	10.7	57	9.5	77.2		no	94
4	0.99	256	64	9.4	45	6	60.4		no	94
5	1.4	380	132	24	100	15.2	147		no	95
6	1.05	837	220	21	174	11	206		no	94
7	0.62	730	113	14.5	90.7	6.9	112		no	97
8	0.64	1525	245	15.1	145.4	74.3	234		no	96
Ni cathode, H ₂ O electrolyte without working mixer										
1	0.49	1506	183	93.2	128.3	57.4	279		88	148
2	0.54	1960	265	80.3	199	81	354		89	134
3	0.49	1700	207	94.2	198.3	30.6	323		116	156
4	0.84	840	178	27	163.5	41.7	232		54	131
5	0.63	1460	229	156.4	165.6	42.7	365		137	160
6	0.58	1770	212	128.8	127.6	63.5	320		108	151
Ni cathode, H ₂ O electrolyte with working mixer										
1	0.42	1110	109	15.8	113.5	21	150		40	136
2	0.68	1400	239	50	201	57.3	308		69	129
3	0.58	1070	151	28.2	162.5	17	207.6		56	137
4	0.25	1840	115	26.6	95.2	11.5	133		18.3	116
5	0.48	1530	184	45	188.5	13.2	247		63	134
6	0.4	620	62	16.7	93.8	7.9	118		56.3	190
7	0.84	654	138	60.7	286.5	20.9	368		230	280
8	0.88	634	139	42.7	268	20.8	332		180	240

ratio for these impurity nuclides is up to several tens of times, some main isotopes of impurity elements (with high natural abundance percentage) being absent. The following isotopes were registered as being absent: ⁵⁸Ni, ⁷⁰Ge, ⁷³Ge, ⁷⁴Ge, ¹¹³Cd, and ¹¹⁶Cd (Fig. 12). Modifications in the isotopic abundances of the Pd isotopes were seen in the surface layer (1 μm thick), as shown in Fig. 13. We observed ⁵⁷Fe production, which is a characteristic feature of low-energy reactions (Fig. 14).

Table 2. Relative content of ³He and ⁴He in Pd cathode samples from a glow discharge experiment. The cathode was Pd, the gas was D₂, the current was 35 mA, and the experimental run time was 4 h.

No.	³ He _{after discharge} / ³ He _{initial}	⁴ He _{after discharge} / ⁴ He _{initial}
1	Up to 10 times	Up to 100 times
2	Up to 2 times	Up to 35 times

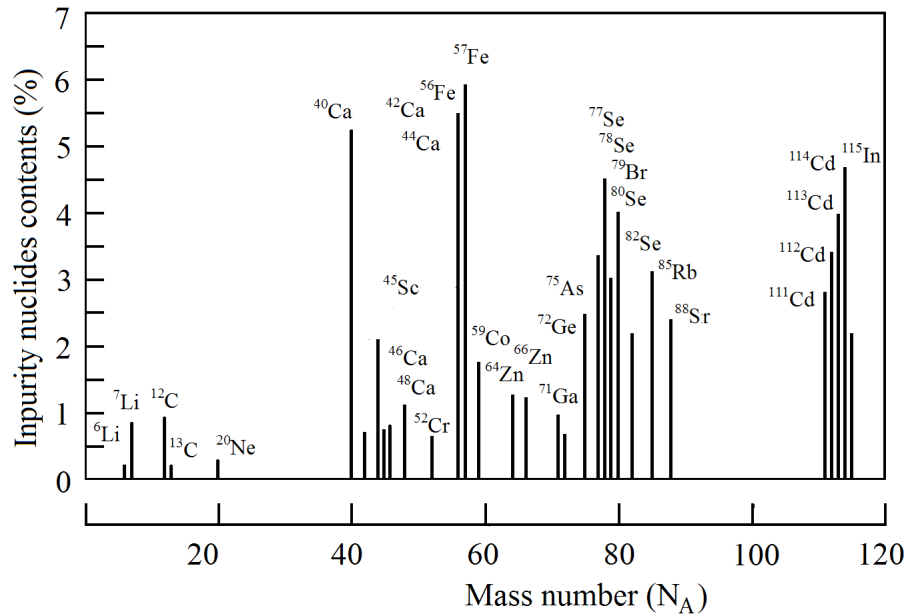


Figure 11. Impurity nuclei content in the surface layer of the cathode sample (with a thickness of $100\mu\text{m}$) after glow discharge; Pd cathode, D_2 gas, 100 mA current, and 22 h run time.

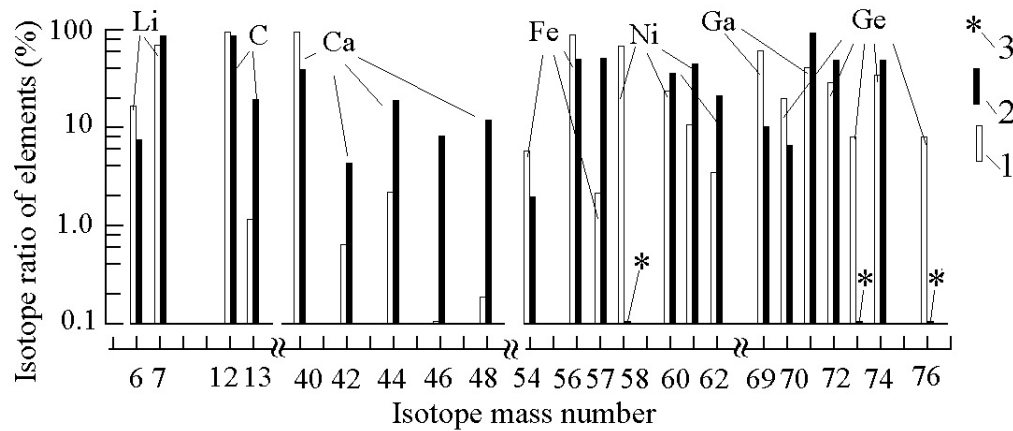


Figure 12. Impurity nuclei ratio change in the surface layer of the cathode sample (with thickness of $100\mu\text{m}$) after glow discharge run; Pd cathode, D_2 gas, 100 mA current, and 22 h run time. 1 – natural abundance, 2 – post-run ratio, 3 – absence of natural nuclei.

5. X-ray Measurements

We have observed both diffuse and collimated X-ray emission in the keV region in a large number of experiments carried out over the past decade; in this section we will provide a brief overview of some of our results. Experiments were carried out using a glow discharge system, with a variety of X-ray diagnostics; including an X-ray pinhole camera,

thermo-luminescent detectors with foils, scintillation detectors with a photomultiplier, and a curved mica spectrometer with X-ray film. Experiments were carried out on different metal cathode materials, including Al, Sc, Ti, Ni, Nb, Zr, Mo, Pd, Ta, and W. Different gasses were also used, including D₂, H₂, He, Kr and Xe. The power supply delivered a train of pulses, as illustrated in Fig. 1(b), with pulse durations between 0.1 and 2.0 ms, and periods between 0.3 ms and 100 ms. We used currents between 30 and 300 mA, and voltages between 1500 and 4300 V; the gas pressure in the chamber was 3–5 torr.

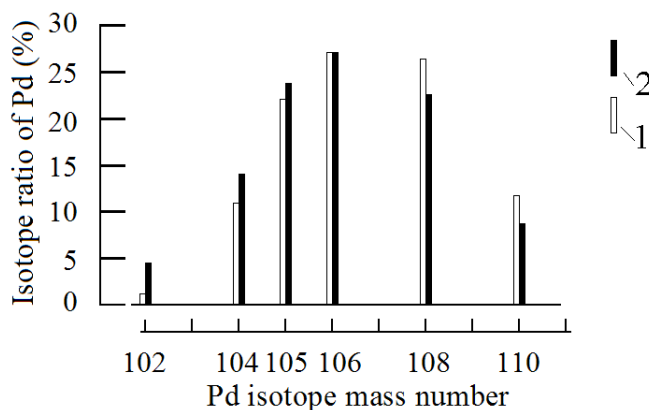


Figure 13. Pd isotope ratio change in the surface layer of the cathode sample (with thickness of 100 μm) following a glow discharge run; Pd cathode, D₂ gas, 100 mA current, and 22 h run time. 1 – natural ratio, 2 – ratio after glow discharge.

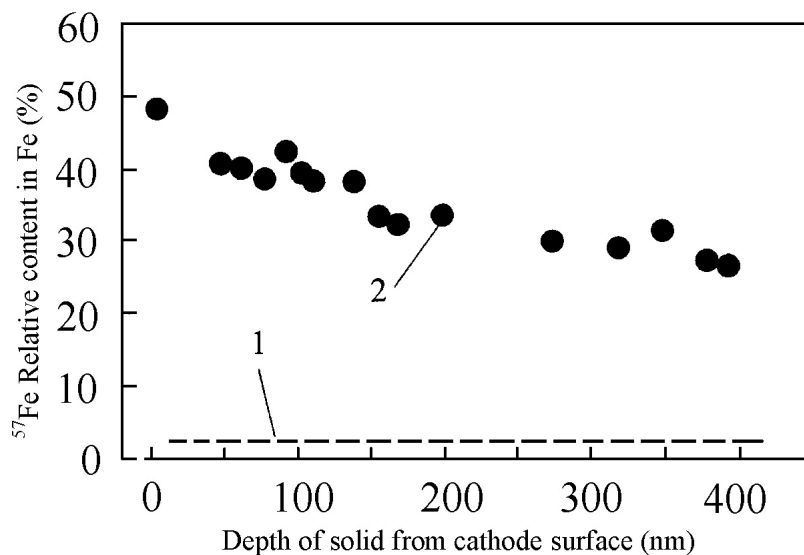


Figure 14. The relative abundance of ⁵⁷Fe nuclei in the surface layer of the Pd cathode.

5.1. Pinhole camera experiments

The X-ray emission was of sufficiently high intensity that it was possible to image the cathode using a pinhole camera. We used a transverse 0.3 T magnetic field to verify that the image was not due to charged particles [6]; it was observed that the image was nearly the same with and without the magnetic field.

5.2. Thermo-luminescent detector experiments

We used crystalline Al_2O_3 thermo-luminescent detectors covered with Be foils of different thicknesses in order to estimate the average energy of the X-ray emission [4]. We found that the main component was between 1.3 keV and 1.8 keV, with evidence of a higher energy component as well. These measurements showed that the X-ray intensity from the cathode surface increased exponentially with an increase in the discharge voltage, reaching as upper limit of 1 W.

5.3. Scintillator and photomultiplier experiments

We made use of PMMA scintillators with the optical scintillation detected using a photomultiplier and scope, to study the energy-dependence, spatial-dependence, and the time-dependence of the X-ray emission [6]. Tests with a transverse 0.3 T magnetic field again showed that the radiation was not composed of charged particles. We measured the transmission through 15–30 μm thick Be foils, and the difference in transmission was consistent with an average energy in the range of 1.0–2.5 keV. It was found that the average energy for different cathode materials in these measurements were in good agreement with the thermo-luminescent detector measurements discussed above. We also did time-resolved measurements which showed that the diffuse radiation was produced while the discharge was on, and collimated emission was observed in bursts that followed the switching off of the discharge with some delay.

5.4. Curved mica spectrometer experiments

Many experiments were carried out with the curved mica crystal spectrometer to give energy-resolved X-ray spectra on X-ray film [7]. A variety of spectral features were observed. We saw characteristic X-ray emission from Kr and Xe which showed up as strong spectral lines on the film. We also saw weaker characteristic X-ray emission from transitions in the host metal atoms. There was a continuum apparent that originated from the cathodes surface, centered roughly near 1.5 keV, with somewhat different widths depending on the discharge voltage, and with an intensity that was weakly correlated with the cathode material. An example of this continuum emission is shown in Fig. 15. Finally, we saw extremely strong micro-beam emission that was sufficiently intense to cause a bleaching (the proper technical term is solarization) of the film, and which appeared on the film as spots (instead of as spectral lines) and curves (consistent with a spot which moved during the emission).

6. Interpretation and Proposed Physical Mechanisms

Based on the experimental results reviewed in the previous sections, we can consider possible physical processes that might be involved. Presumably, some excited energetic levels are formed in the cathode solid when its surface is exposed to bombardment by the ions flux generated in plasma or electrolyte medium. It would follow that the observed X-ray emission occurs as a result of de-excitation of these energetic levels.

- Deuterium ion acceleration in the glow discharge near-cathode region produced ion energies from several hundred eV up to a few thousand eV.

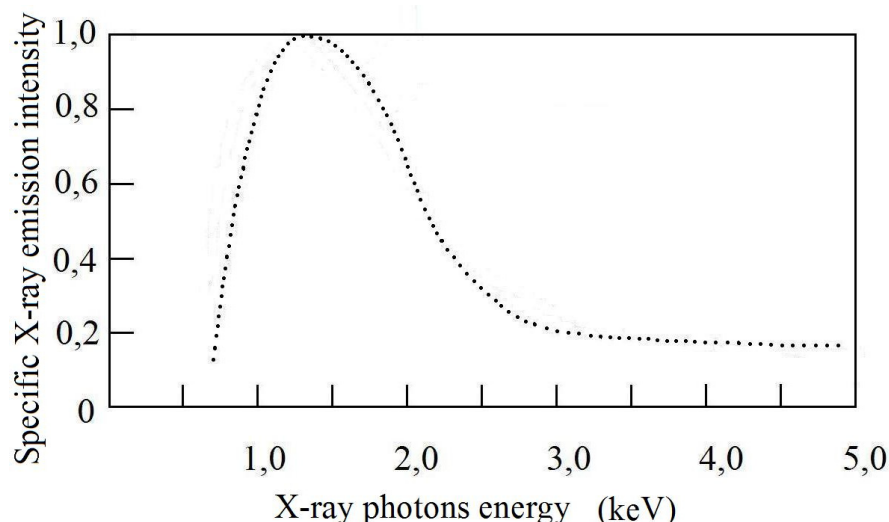


Figure 15. Continuum X-ray emission measured with the curved mica crystal spectrometer from a glow discharge experiment with a Pd cathode and D₂ gas.

- Deuterium ions collide with the atoms of the crystal lattice ions.

Presumably, some long-lived excited levels with energies up to several kilovolts are formed in the cathode solid. Under the resulting highly non-equilibrium conditions there exists an excited state population that can be characterized by an effective temperature on the order of 1–3 keV, which in our view are the conditions necessary for low-energy nuclear reactions to occur.

Within this framework, we can think about what kinds of reactions in particular might lead to the formation of stable transmutation products. The following reactions may be possible:

- (1) $\text{Pd} + m\text{D} \rightarrow [\text{PdmD}]^*$,
- (2) $[\text{PdmD}]^* \rightarrow \text{Pd}^* + {}^4\text{He} + \text{Heat}$,
- (3) $[\text{PdmD}]^* \rightarrow \text{A}^* + \text{B}^* \rightarrow \text{A} + \text{B} + \text{Heat}$,
- (4) $[\text{PdmD}]^* \rightarrow \text{C} + \text{Heat}$,

where $[\text{PdmD}]^*$ is a short-lived intermediate compound nucleus; where $m = 1, 2, 3, \dots$; where A^*, B^* denote nuclear isomers of nuclei with masses less than that of Pd; where A, B are stable nuclides; and where C stands for a nuclide with a mass more than that of Pd. The first step in the proposed process is the formation of an excited state compound-nucleus. Then one of three possible modes is realized:

- (1) The compound nucleus may lose its excitation and form an excited Pd nucleus and ${}^4\text{He}$.
- (2) The compound nucleus may split into two nuclear fragments with masses less than that of Pd. In so doing the two nuclei should be in excited isomer state (experiments show that the nuclear reactions energy is not produced as kinetic energy of nuclear fragments).
- (3) The compound nucleus may lose its excitation and form a stable nucleus of a heavier than Pd element.

To determine the specific physical mechanism for these reactions will require additional research.

One possible type of reaction for forming the impurity nuclides can be a long-range (resonant) nuclear reaction. The mechanism of such long-range reactions can be explained using as an example a specific transmutation reaction for Pd + D (Fig. 16(a)) and Pd + 2D (Fig. 16(b)) [4]. The formation of significant ^{13}C nuclei and ^{93}Nb nuclei was recorded in the experiments. In this case we assume that the reaction can proceed as

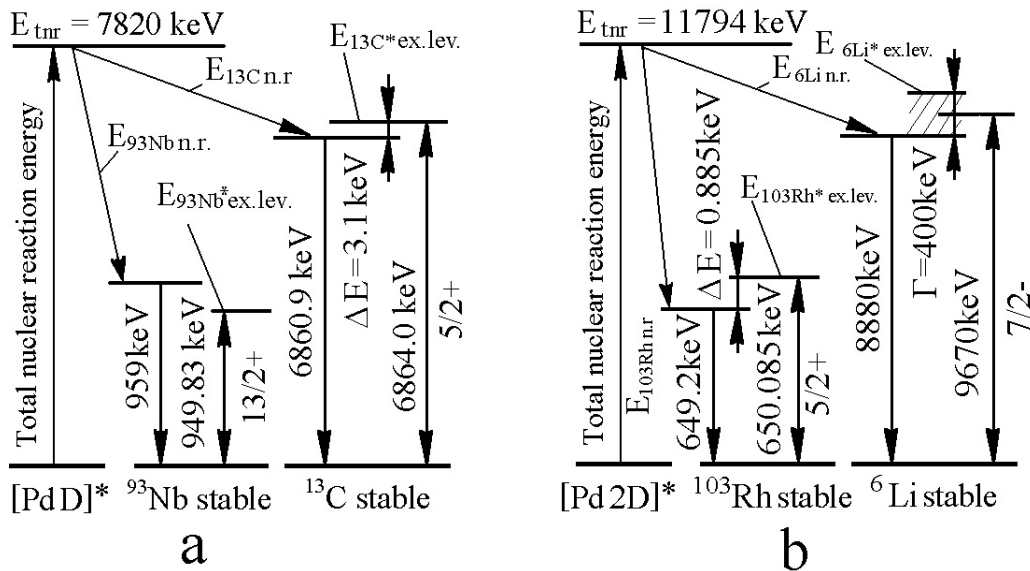
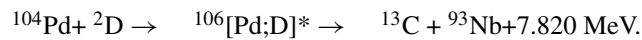
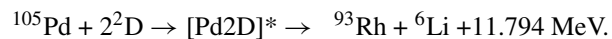


Figure 16. Schematic of proposed long-ranged (resonant) nuclear reactions; (a) for Pd + D transmutation reaction; (b) for Pd + 2D transmutation reaction.

Momentum and energy conservation dictates that the product nucleus ^{13}C should receive 6.8609 MeV, and that the product nucleus ^{93}Nb should receive 0.959 MeV (in connection with the reaction scheme of Fig. 16(a)). Note that a nuclear excited state (nuclear isomer) with an energy of 6.864 MeV (and excited level width of 6 keV) exists for ^{13}C , and that an excited level with an energy of 0.94983 MeV exists for ^{93}Nb . The difference between the energy received by nuclide ^{13}C and the energy of the excited level is 3.1 keV. If the crystalline lattice has available 1.5 keV, and given the 6 keV width of the excited energy level, one might expect that there should be a high probability for such a long-range (resonant) nuclear reaction to occur.

Consider the reaction (shown in Fig. 16(b))



Energy and momentum conservation again dictate that the product ^6Li nucleus should end up with an energy of 8.880 MeV. A nearby excited state is available, so a similar situation can occur as indicated in Fig. 16(b).

The totality of the experimental results allows us to assume that the energy of the excited nuclear levels of the product nuclei is converted into heat. The specific physical mechanism of such conversion will require additional research.

7. Conclusions

We have reviewed many results that we have obtained in glow discharge experiments and in high-voltage electrolysis experiments. We have observed excess power in glow discharge experiments up to 10 W/cm^2 , and with a power gain of up to 170%; in the high-voltage electrolysis experiments we have seen excess power up to 300 W, with a power gain as high as 340%. These experiments clearly demonstrate the presence of an interesting new source of thermal power and energy. We have reviewed results obtained in our search for nuclear products, where many new elements and isotopes appear to have been produced. We have observed both collimated and diffuse X-ray emission in the keV regime, which constitutes a new fundamental effect that we discovered. Finally, we have presented a discussion of our results in terms of conjectures and hypotheses concerning physical mechanisms and reactions that may be involved (but which will require further study in order to determine whether they are correct or not).

8. Acknowledgment

We are happy to express our thanks to: Professor R. Kuzmin (Moscow State University), Dr. V. Kushin (former employee Nobel prize winner Academician N. G. Basov, MEPI), employees of radiation measurements on the “MIR” space station and the ISS (IMBP), Dr. A. Lipson and employees (RAS Institute of Physical Chemistry), Dr. S. Pikuz and his staff (RAS Lebedev Physics Institute) for their help and participation in this work. Some rewriting of the manuscript was carried out by P. L. Hagelstein in order to help improve the English.

References

- [1] A. B. Karabut, Ya. R. Kucherov and I.B. Savvatimova, Nuclear product ratio for glow discharge in deuterium, *Phys. Lett. A*, **170** (1992) 265.
- [2] A.B. Karabut, Analysis of experimental results on excess heat power production, impurity nuclides yield in the cathode material and penetrating radiation in experiments with high current glow discharge, *Proc. 8th Int. Conf. Cold Fusion*, Italy 21–26 May 2000, p. 329.
- [3] A.B. Karabut, Experimental registration of a high current glow discharge of the excited long living atomic levels with the energy of 1–3 keV and nuclear products emission in the solid medium, *Proc. 11 Int. Conf. Emerging Nuclear Energy Systems (ICENES 2002)*, 29 September–4 October 2002, Albuquerque, New Mexico, USA, 1995, pp. 408–416.
- [4] A.B. Karabut, Production of excess heat, impurity elements and unnatural isotopic ratios formed at excited long-lived atomic levels with energy of more than 1 keV in a solid cathode medium during high-current glow discharge, *Proc. 10th Int. Conf. on Cold Fusion*, August 24–29, 2003, Cambridge, MA, USA.
- [5] A.B. Karabut, Excess heat production in Pd/D during periodic pulse discharge current in various condition, *Proc. 11th Int. Conf. Cold Fusion*, 31 October–5 November, 2004, France, pp. 178–193.
- [6] A.B. Karabut, Research into Low Energy Nuclear Reaction in Cathode Sample Solid with Production of Excess Heat, Stable and Radioactive Impurity Nuclides, *Proc. 12th Int. Conf. Cold Fusion*, December 2–7, 2006, Japan, pp. 214–230.
- [7] A.B. Karabut and E.A. Karabut, Study of Deuterium Loading into Pd Cathode Samples of Glow Discharge, *Proc. 9th Int. Workshop on Anomalies in Hydrogen/Deuterium Gas Loaded Metals*, 6–11 September 2010, Siena, Italy.



Research Article

Spectral and Temporal Characteristics of X-ray Emission from Metal Electrodes in a High-current Glow Discharge

A.B. Karabut*

Samar+ COMPANY, Belay Dacha, 13, ap. 54, city Kotelniky, Moscow Region, 140055, Russia

E.A. Karabut

Moscow Power Engineering Institute (Technical University)

P.L. Hagelstein

Massachusetts Institute of Technology, USA

Abstract

We have observed X-ray emission from metal cathodes in high-current (up to 500 mA) glow discharge experiments in the spectral range from 600 eV to 6 keV. The effect has been seen with a variety of different metal cathodes (including Al, Sc, Ti, V, Ni, Nb, Zr, Mo, Pd, Ta, W, and Pt), as well as with different gasses (including D₂, H₂, Kr, Ar, and Xe) at low pressure (10 torr). We have observed both diffuse and collimated X-ray emission. Diffuse emission occurs in bursts of X-rays; with up to 10⁵ bursts per second, with up to 10⁶ photons per burst. Collimated X-ray emission appears in the form of beamlets directed normal to the cathodes surface with a very small angular divergence; with up to 10⁴ bursts per second, and up to 10¹³ photons overall. Switching off the glow discharge current produces substantial X-ray bursts in these experiments; and we see some bursts during the discharge, and up to 20 h after switch off. We present results from a variety of diagnostics, including: pinhole camera imaging; thermo-luminescent detector measurements; time-resolved scintillator measurements; and a curved mica spectrometer to register X-ray spectra. The spectra of the collimated X-rays shows a strong broad emission feature that is centered near 1.5 keV in many experiments. Line emission is sometimes observed in addition along with the broad feature.

© 2012 ISCMNS. All rights reserved.

Keywords: Collimated X-ray, Diffuse X-ray emission, Excited phonon mode, Glow discharge device, X-ray spectra

1. Introduction

Our group has studied low energy nuclear reactions (LENR) in glow discharge experiments for many years. Glow discharges are relevant to such studies as deuterium (or hydrogen) can be loaded into Pd (or into other metals) by the

*E-mail: karab.ab@mail.ru; Tel.: (495) 5508129; Fax: (495) 5508129

discharge under low pressure and high current conditions. We have seen a variety of anomalies in our glow discharge experiments, including excess heat, charged particle emission, gamma emission, helium production, tritium, changes in the cathode composition, as well as residual radiation [1]. Some years ago we noticed a new effect in which collimated X-ray emission was observed in a beam normal to the cathode surface [2,3], and we have focused considerable effort on the effect subsequently [4–7]. This effect is interesting for a variety of reasons. In some experiments the X-ray emission is observed at higher energies (up to 10 keV) than would be expected given the discharge voltage (1–2 kV). The emission can be seen after the discharge has been turned off, under conditions where there is no discharge current. That the X-ray emission is collimated is significant, and we might expect that the effect itself can tell us something about the physical processes involved in LENR reactions.

In this work we review earlier collimated X-ray experimental results, including pinhole camera measurements, thermal luminescence detector measurements, and time-resolved scintillator/PMT measurements. Then we present our new results on the emission spectra, taken with a curved mica crystal spectrometer.

2. Glow Discharge Experiment

The measurements were carried out using a glow discharge device consisting of a water-cooled vacuum chamber, and cathode and anode assemblies as shown in Fig. 1(a). Cathode heating is an issue under high-current conditions, so we designed the cathode assembly so that cathode samples could be attached to a water-cooled surface. We studied cathode samples made out of a variety of different metals, including Al, Sc, Ti, Ni, Nb, Zr, Mo, Pd, Ta, W, Pb and Pt. Discharge experiments were run using different gasses as well, including D₂, H₂, He, Kr and Xe.

The power supply is designed to provide the glow discharge with periodic-pulse direct current, and permits the generation of desired current forms (of various pulse length and pulse period) to obtain the required current voltage operating conditions. The power supply consists of an autotransformer; a step-up transformer; a rectifier; a storage capacitor; a ballast resistor; and a high voltage transistor switch. The power supply produces direct pulse-periodic current of rectangular shape of pulse, illustrated in Fig. 1(b). In the experiments, we used pulse durations from 0.1 to 1.0 ms; and a period from 0.3 up to 100 ms. The glow discharge conditions were: current (amplitude), from 30 up to 300 mA; voltage, from 1500 to 4300 V; and gas pressure in the discharge chamber, from 3 to 5 Torr. As mentioned above, X-ray measurements were carried using an X-ray pinhole camera, thermo-luminescent detectors, and scintillation detectors with photomultiplier. The energy spectrum of the X-ray emission was obtained using a curved mica crystal spectrometer. The cathode samples made of Pd and other metals were placed on a cathode-holder above which a window for output penetrating radiation was provided. Various detectors were installed above the window to measure the output penetrating radiation.

3. Pinhole Camera and Results

Since the X-ray emission from the cathode was so intense, it was possible to use it to obtain an X-ray pinhole camera image of the cathode. The experimental set up is shown schematically in Fig. 2a. In order to check whether the emission is due to X-rays, a transverse 0.3 T magnetic field was used to deflect charged particles. The image of Fig. 2b shows the cathode (9 mm in diameter) and was taken with no magnetic field; the image of Fig. 2(c) was taken with a magnetic field. If the image were due to charged particles, such as electrons, then the image would have disappeared. One can see that the magnetic field does not change the cathode image qualitatively, so we conclude that the image is due to X-ray radiation.

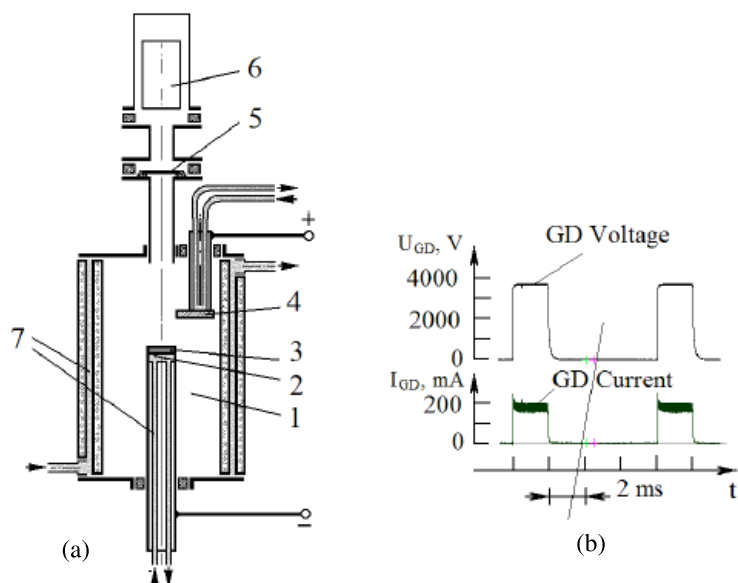


Figure 1. Schematic representation of the experiment. (a). Glow discharge device, 1 – discharge chamber, 2 – cathode holder, 3 – cathode sample, 4 – anode, 5 – Be foil screens, 6 – X-ray detectors different kind (pinhole, TLD detectors, scintillator- photomultiplier, spectrometer), objective, 7 –cooling water; (b) glow discharge voltage and current pulses.

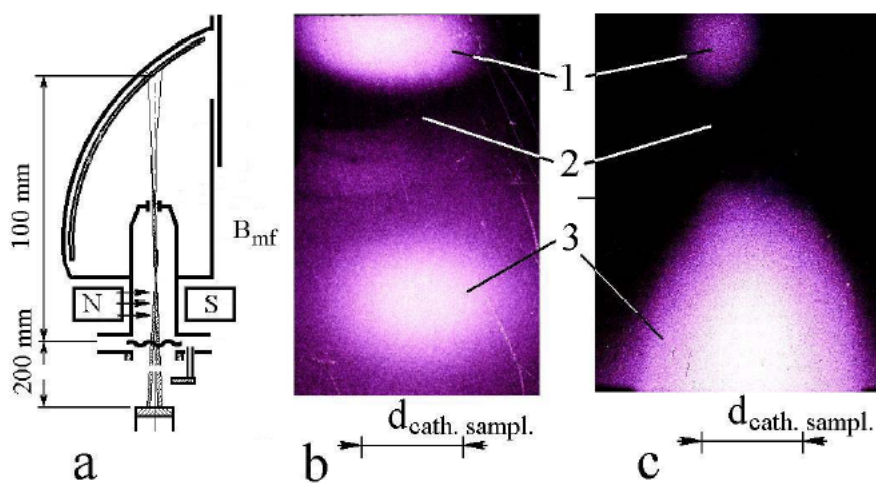


Figure 2. (a) Schematic of the X-ray pinhole camera experiment. The objective with 2.0 mm diameter closes by the $15 \mu\text{m}$ Be shield. Data is shown for a Pd cathode and D_2 gas, with a discharge current of 150 mA, a voltage of 1850 V, and with an exposure time of 10 000 s; (b) X-ray image without a cross magnetic field; (c) X-ray image with a cross magnetic field of 0.3 T. The image is positive, showing the anode (1), discharge plasma area (2) and cathode (3).

4. TLD Detector and Results

We used thermo-luminescent detectors (TLD) (based on crystalline Al_2O_3) to study the energy and intensity of the X-ray emission. Thermo-luminescence in Al_2O_3 is well known and has been studied in recent years in [8,9]. We used Al_2O_3 disk detectors that were 5 mm in diameter and 1 mm thick. Exposure with the 661.5 keV gamma line from a ^{137}Cs calibration source was used for calibration, assuming that the response to the total radiation energy would be similar for gamma radiation as for X-ray radiation. A Harshaw model 2080TL-PICOPROCESSOR was used for analysis of the exposed crystals. We built a seven channel TLD detector, with Be foils of different thicknesses (15, 30, 60, 105, 165, 225, 300 μm) in front of different TLD detectors. Additionally, two TLD detectors were arranged outside the camera for the registration of background value of the emission dose. The main component of the X-ray emission energy is in the range of 1.3–1.8 keV, but there is a component with a higher energy too (Fig. 3(b)). TLD measurements show that X-ray radiant intensity from the cathode surface increases exponentially with the increase in the glow discharge voltage (Fig. 3(c)).

5. Scintillation Detector and Results

We made use of scintillation detectors with photomultipliers to study the time-dependence of the X-ray emission, and also the X-ray energy and spatial dependence. We used organic scintillators based on polymethylmetacrylate (PMMA) with a de-excitation time of 3–5 ns. The optical signal from the PMMA was detected using a photomultiplier (PM); the signal from the PM was transferred to a fast preamplifier, and then to a two-channel computer digital oscilloscope with the frequency limit of 50 MHz per channel.

We used three variants of the discharge chamber (with different extensions of the vacuum chamber) for X-ray

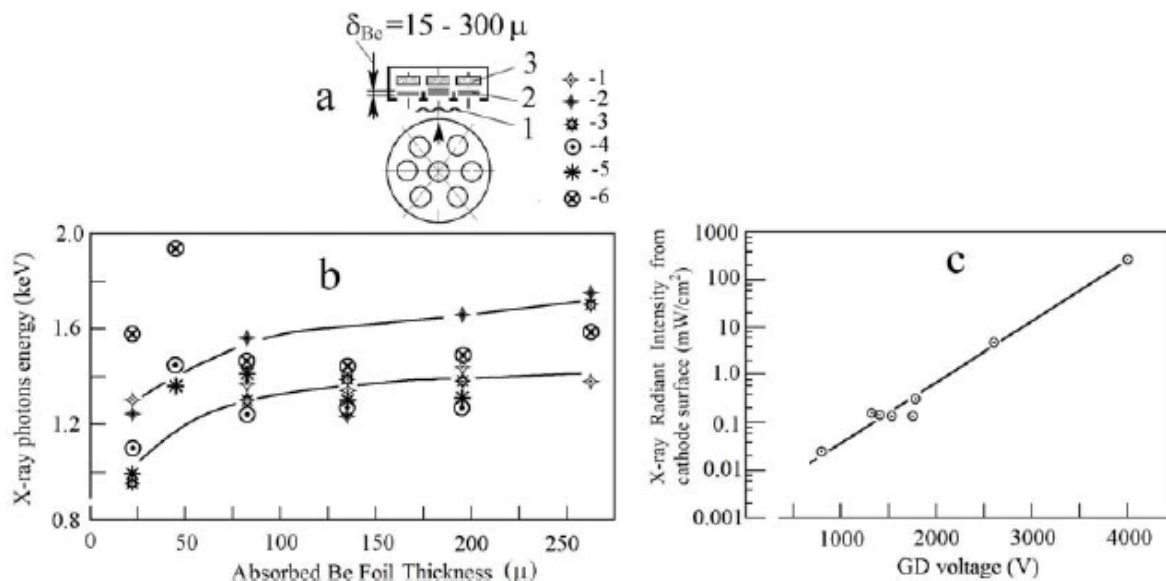


Figure 3. (a) The seven-channel TLD spectrometer; (b) the X-ray dose absorbed by TLD detectors covered with Be foil with the different thickness (where the discharge voltage for the different experiments is: 1 – 1750 V, 2 – 1770 V, 3 – 1650 V, 4 – 1530 V, 5 – 1400 V, 6 – 1250 V); (c) dependence of the X-ray emission energy on the discharge voltage from TLD measurements. These experiments were done with a Pd cathode, D_2 gas, with a current of 200 mA, and an exposure time of 6000 s.

detection (as described in [3]). In the first variant, the PMMA/PM detector was placed 21 cm from the cathode surface, and the diameter of the extension (for extracting the radiation) was 1.7 cm. In the second variant, the PMMA/PM detector was placed 70 cm from the cathode, and the extension diameter was 3.2 cm. For determining whether the radiation is charged particle or electromagnetic radiation, the third variant included a 0.3 T magnetic field 35 cm from the cathode oriented perpendicular to the beam. From the experiments with the magnetic field it was found that the collimated radiation is not charged particles.

We detected both diffuse and collimated X-rays in these experiments. Diffuse X-ray emission occurs mainly when the discharge is on (see Fig. 4(a)), and occurs in flashes some msec after switching off the current. The intensity of this diffuse radiation goes down as $1/r^2$ away from the cathode.

Collimated X-ray emission occurs during the discharge, and up to 100 ms after switching off the current. Under the certain parameters of discharge the generation of collimated X-rays occurs only some after turning off the discharge current (up to 20–30 beams after the each current pulse). The time-dependence of collimated X-ray emission correlated with the discharge switch off is illustrated in Fig. 4(b). Note that the bursts associated with the collimated X-rays are much more powerful than those associated with diffuse X-rays (the sensitivity of the PMMA/PM system was reduced by a factor of 2500 in the case of collimated X-rays). Collimated X-ray emission is also triggered by an increase in the value of discharge parameters, such as current, voltage, and the duration of the current pulse.

In Fig. 4(b) we denoted the delay time $\Delta\tau$ between the current switch off and the onset of a collimated X-ray burst. This delay time was studied in a series of experiments. Results for the delay time, and the associated number of bursts that occurred, are summarized in Fig. 5.

The average X-ray energy was determined in the PMMA/PM scintillator experiments by measuring the transmission through 15 and 30 μm Be foils, and matching the difference to the theoretical value. This was done by summing all pulses ($\Sigma A1_i$ and $\Sigma A2_i$) within a 1 s interval for the two cases (illustrated in Fig. 6). The average X-ray energy determined in this way for different cathode metals (between 1.2 and 2.0 keV) was found to be in good agreement with the average energy estimated from the TLD detector experiments, as indicated in Table 1. The number of photons was estimated as the energy of a burst divided by the average X-ray energy.

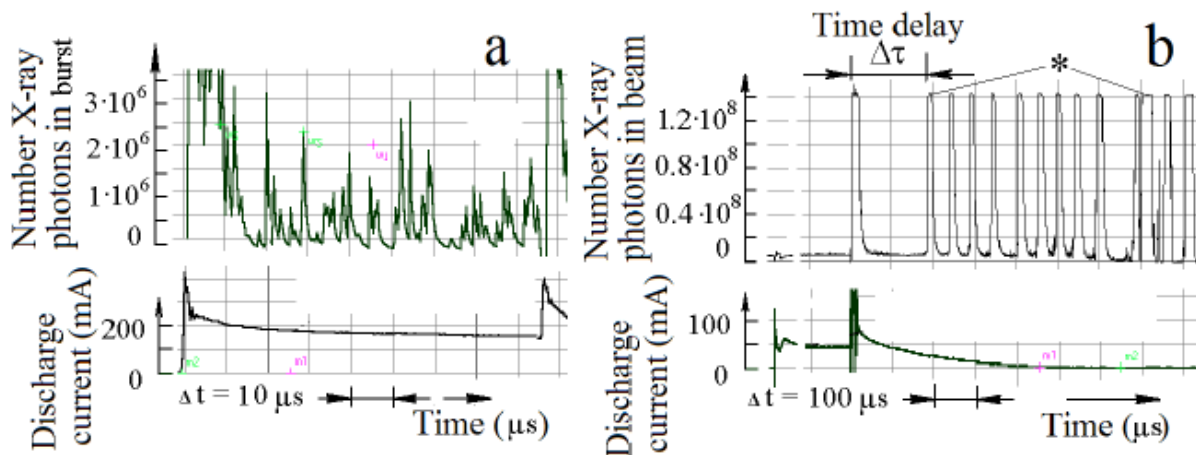


Figure 4. Typical oscillograms of the X-ray emission signal from the PMMA/PM scintillation detector. The cathode sample is Pd, run in a D_2 discharge; (a) diffuse radiation; (b) collimated radiation. The asterisk (*) signifies that the pulse peak was cut off by the amplifier discriminator.

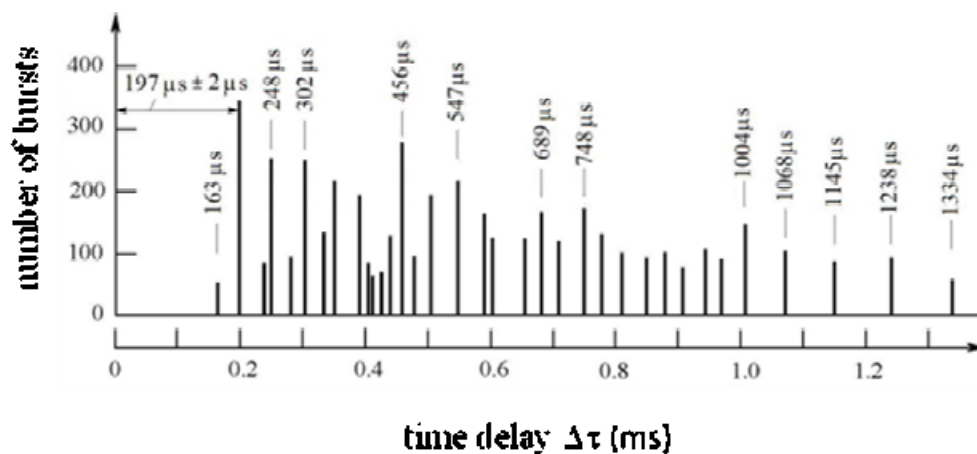


Figure 5. Results of a study of the number of bursts and their associated delay time from different experiments. The cathode for these experiments is Pd, the gas is D_2 , and the current when the discharge is on is 50 mA.

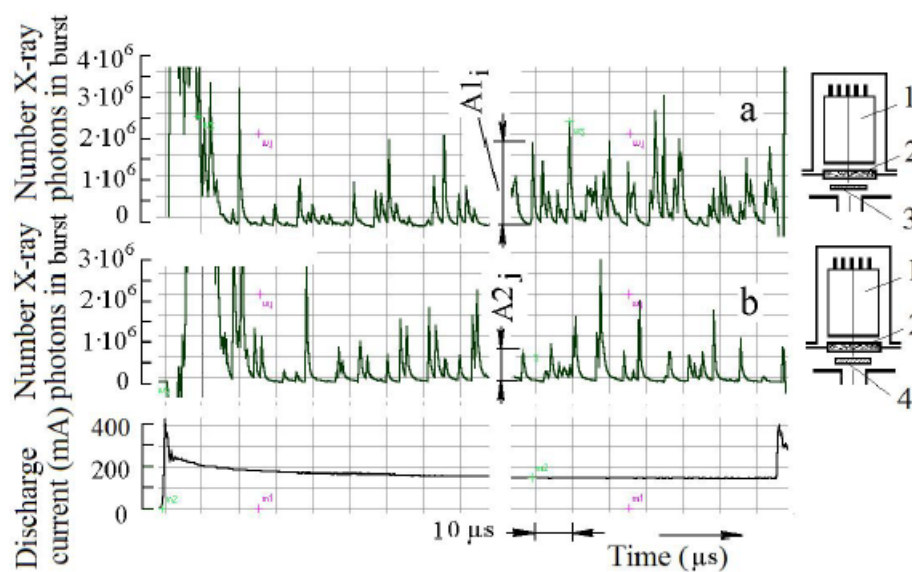


Figure 6. Typical oscillograms of X-ray emission from the PMMA/PM scintillator detector covered with Be foils with different thicknesses: (a) covered with a $15 \mu m$ Be foil; (b) covered with a $30 \mu m$ Be foil. In this case the cathode was Pd, the gas was D_2 , and the discharge current was 150 mA.

Table 1. Average X-ray energy for different cathode materials.

Material of Cathode	Al	Sc	Ti	Ni	Mo	Pd	Ta	Re	Pt	Pb
Glow discharge voltage (V)	1650	1540	1730	1650	1420	1650	1600	1520	1650	1610
Glow discharge current (mA)	130	130	170	150	210	138	138	125	138	138
X-ray photons energy (keV)	1.54	1.26	1.45	1.91	1.48	1.98	1.62	1.36	1.47	1.36

6. X-ray Spectrometer and Spectral Features

X-ray emission spectra were measured using a bent mica crystal spectrometer as illustrated in Fig. 7; the mica crystal holder has a diameter of 50 mm, and the spectra are registered on X-ray film. Because of the spectrometer set up, the film records some of the beam directly, a specular reflected image, the first-order diffracted spectrum, and higher-order diffracted spectra with less efficiency. The direct X-ray beam signal appears in the highest energy part of the diffracted spectrum, causing an interference with the diffracted spectrum.

To determine the wavelength and energy from the diffraction angle θ , we used the (normal incidence) grating equation

$$m\lambda = d \sin \theta$$

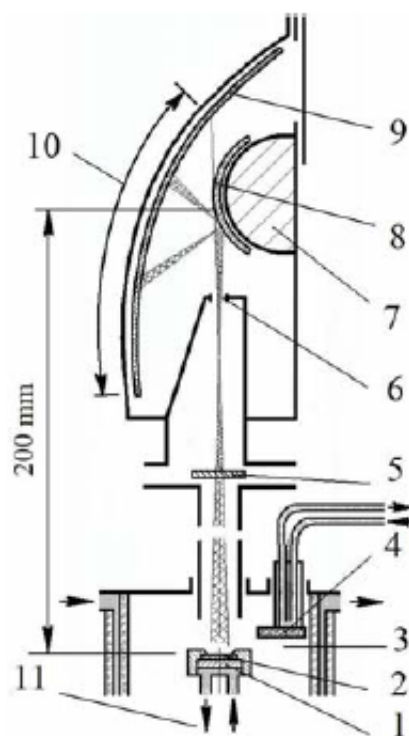


Figure 7. X-ray spectrometer; 1– cathode holder, 2– cathode sample, 3 – vacuum discharge chamber, 4 – anode, 5 –15 μ Be screen , 6 – input slit of spectrometer, 7 – crystals holder, 8 – curved mica crystal, 9 – X-ray film, 10 – area of reflection spectra , 11 – input and output cooling water.

where m is the spectrum order; λ stands for the X-ray wavelength; and d is the lattice constant of the mica crystal ($d = 2.0$ nm). (Note that the incident X-ray beam is not normal on the grating, so that this will introduce some error in the X-ray wavelengths and energies). The X-ray energy E is determined from

$$E(\text{keV}) = 1.235/\lambda(\text{nm}),$$

where E is in keV when the wavelength is expressed in nm.

The spectra were repeatedly recorded during the glow discharge operation with the exposure time 1–5 h, and some spectra were taken after the glow discharge current switch off (for up to 20 h). The X-ray negative films were scanned with 4800 dpi resolution points in color mode.

The spectra contains a variety of components, including a broad continuum, spectral lines, dark and light spots that are made up of multiple smaller spots, and finally separate dark and light spots. The collimated X-ray beams with small angular divergence were generally recorded as dark spots, but when the beam intensity was very high they appear white, (due to an effect known from the early days of photography as solarization). The continuum is diffuse, but originates from the cathode surface. Individual diffracted spectral lines are apparent in the spectra, and appear as conventional spectral lines since there is no source imaging in the spectrometer. Line emission from characteristic transitions in the heavy gas atoms (Ar, Kr and Xe) can be seen in some spectra. Line emission from characteristic transitions of the cathode metal atoms can be seen in some spectra.

The images of the spectra presented in what follows are negative.

6.1. Continuum spectra

We see a broad continuum signal between 0.6 and 6 keV (perhaps as high as 10 keV) which is diffuse (not collimated). The peak of this continuum appears between 1 and 2 keV, and is dependent on the cathode material. Examples are shown in Figs. 8–17. This emission is diffuse, and originates from the cathodes surface.

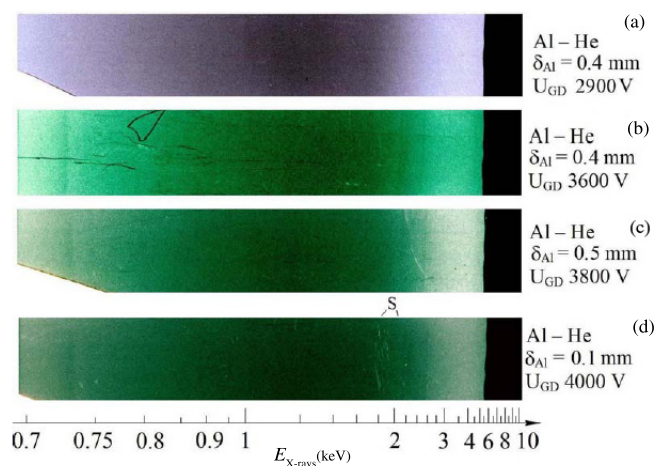


Figure 8. X-ray energy spectra from Al cathodes with different thickness (δ_{Al}) and different discharge voltages. The gas used in these experiments was He; U_{GD} is the glow discharge voltage; S denotes white solarization spots of photoemulsion from monenergetic X-ray beams with small angular divergence.

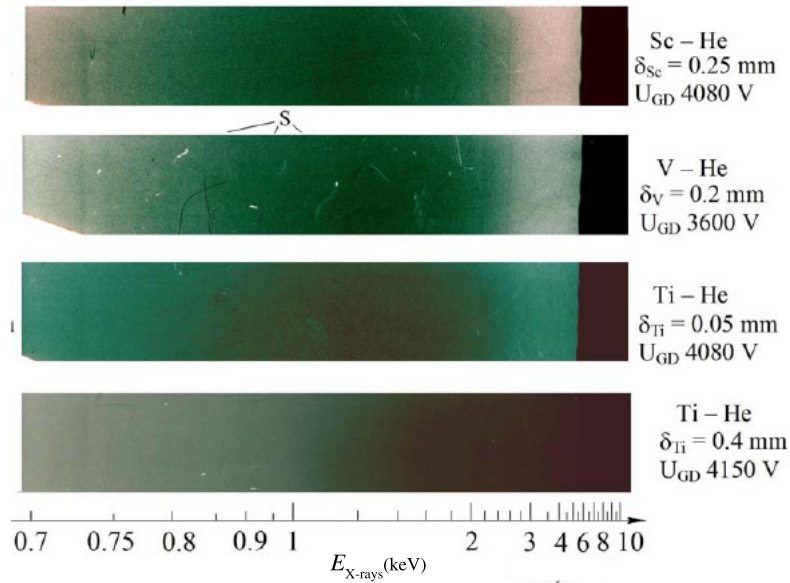


Figure 9. X-ray spectra from Sc, V and Ti cathodes with different thickness (δ) and different discharge voltages. The gas used in these experiments was He; U_{GD} is the glow discharge voltage; S denotes white solarization spots of photoemulsion from monenergetic X-ray beams with small angular divergence.

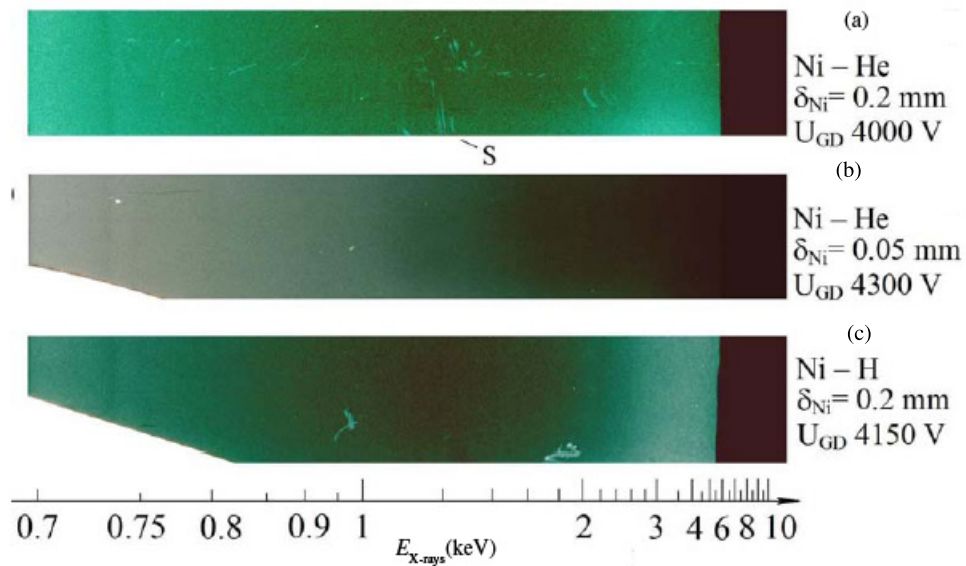


Figure 10. X-ray energy spectra from Ni cathodes with different thickness (δ_{Ni}) and different discharge voltages. The gas used in these experiments was He and H_2 as noted; U_{GD} is the glow discharge voltage; S denotes white solarization spots of photoemulsion from monenergetic X-ray beams with small angular divergence.

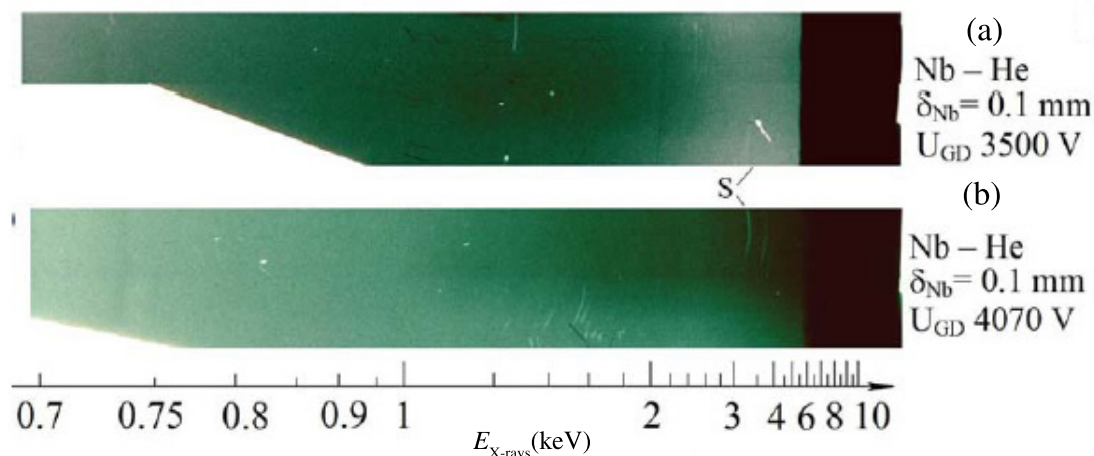


Figure 11. X-ray energy spectra from Nb cathodes at different discharge voltages. The gas used in these experiments was He; U_{GD} is the glow discharge voltage; S denotes white solarization spots of photoemulsion from monenergetic X-ray beams with small angular divergence.

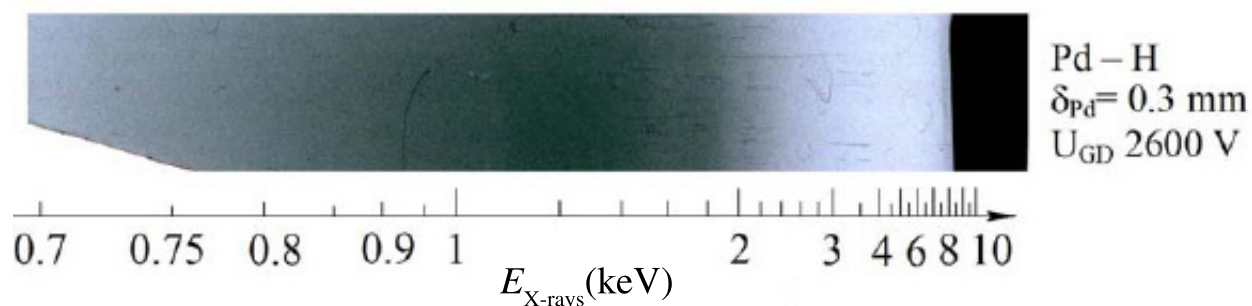


Figure 12. X-ray energy spectra from Pd cathode B H_2 discharge.

6.2. Spectra of collimated emission taken during discharge operation

Monoenergetic X-ray beams with small angular divergence were recorded as dark spots, and in case of very intense beams they turned white due to solarization of the photoemulsion. The term “solarization” comes from the early days of photography, and is an effect in which high intensity light produces a negative image (so that a dark spot become white) on the film. Examples of very bright X-ray beam emission taken during pulsed mode discharge operation are shown in Figs. 17–26.

A narrow beam with a fixed energy, direction, and origin will appear on the film after diffraction as a localized spot (see Fig. 20, and also Fig. 24, for examples). A change of direction during the emission, such as might be produced if the cathode surface moves, could result in a curve; if this slit were narrow, this would be expected to result in a vertical line (Fig. 23 shows a nearly vertical line, although the slit was not narrow); however, the slit used in these experiments was 6 mm wide, so that changes in the beam direction would alter the angle of incidence on the bent crystal causing what might look like a change in energy on the film.

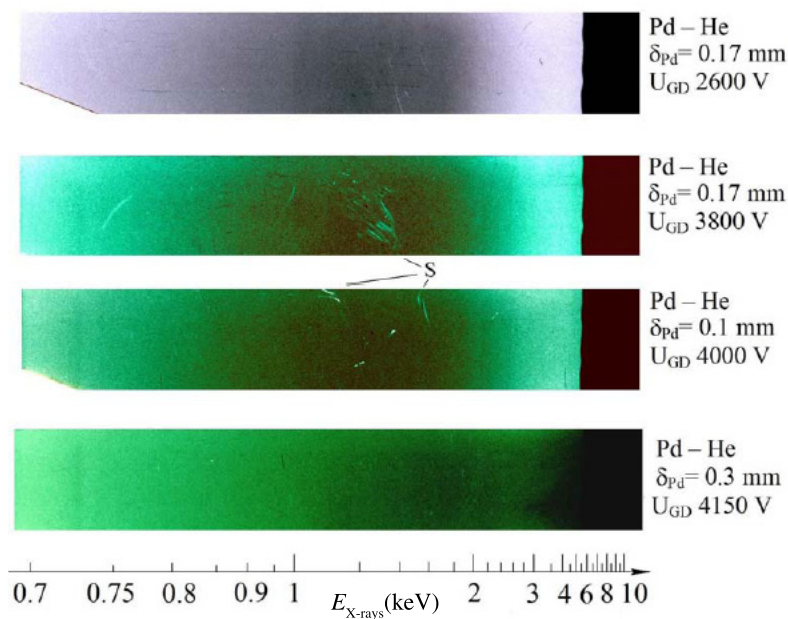


Figure 13. X-ray energy spectra from Pd cathodes with different thickness (δ_{Pd}) and different discharge voltages. The gas used in these experiments was He; U_{GD} is the glow discharge voltage; S denotes white solarization spots of photoemulsion from monenergetic X-ray beams with small angular divergence.

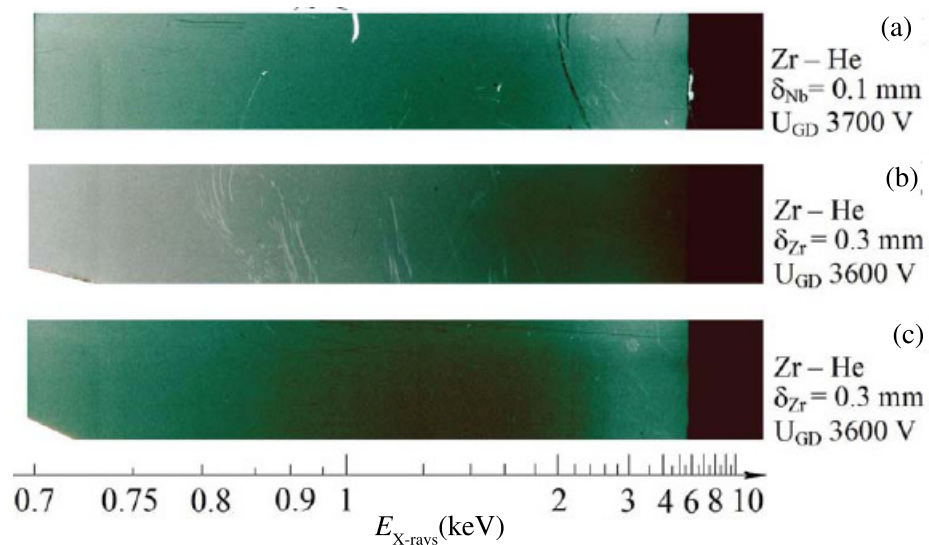


Figure 14. X-ray energy spectra from Zr cathodes with different thickness (δ_{Zr}) and different discharge voltages. The gas used in these experiments was He; U_{GD} is the glow discharge voltage; S denotes white solarization spots of photoemulsion from monenergetic X-ray beams with small angular divergence.

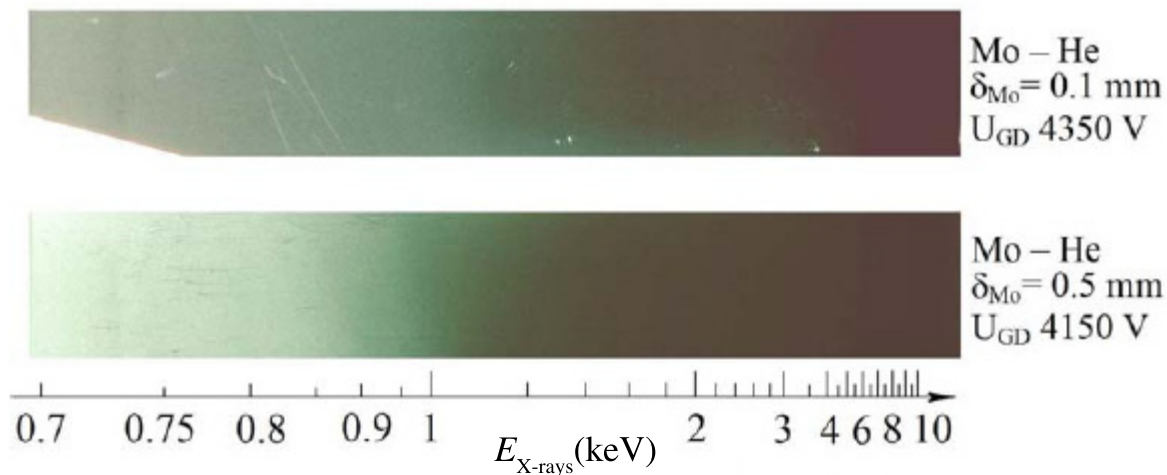


Figure 15. X-ray energy spectra from Mo cathodes with different thickness (δ_{Mo}) and different discharge voltages. The gas used in these experiments was He; U_{GD} is the glow discharge voltage; solarization spots of photoemulsion from monenergetic X-ray beams with small angular divergence are apparent.

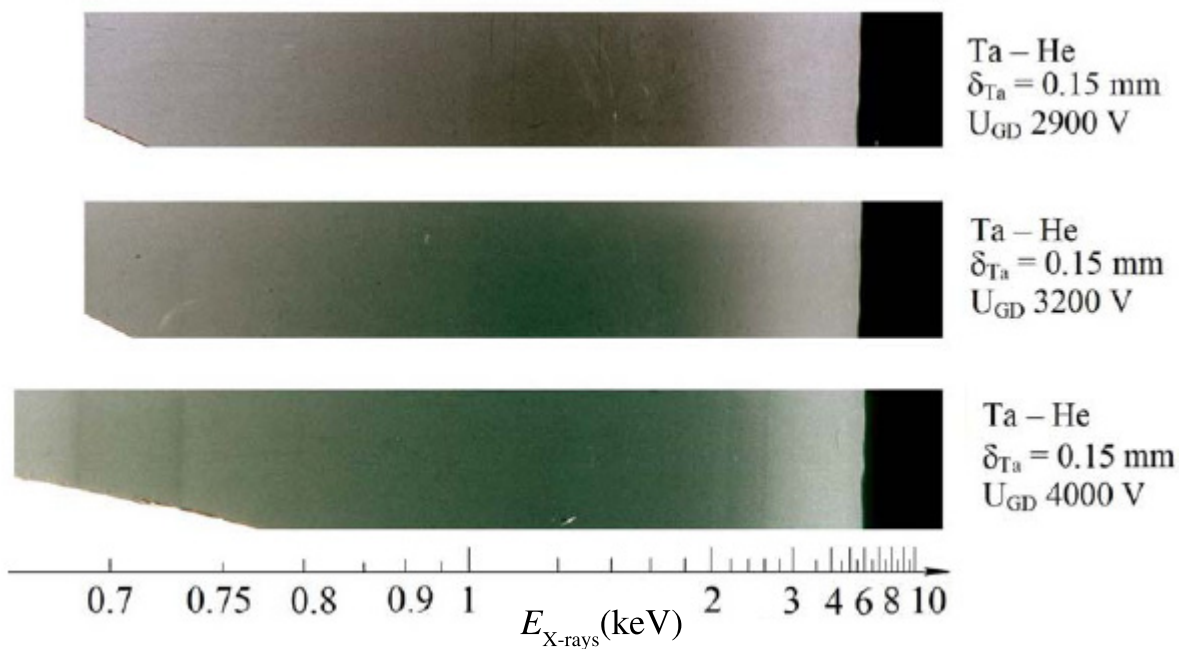


Figure 16. X-ray energy spectra from Ta cathodes at different voltages U_{GD} . He discharge.

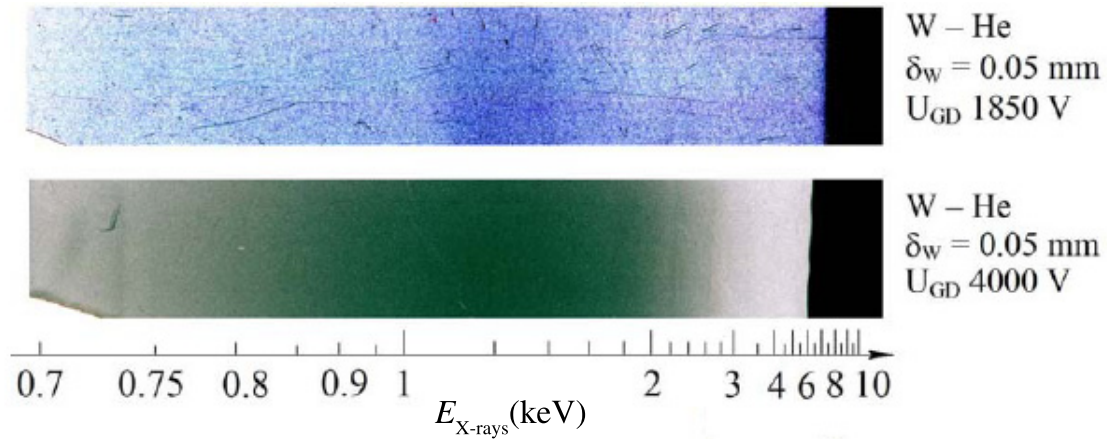


Figure 17. X-ray energy spectra from Mo cathodes at different voltages U_{GD} in He gas.

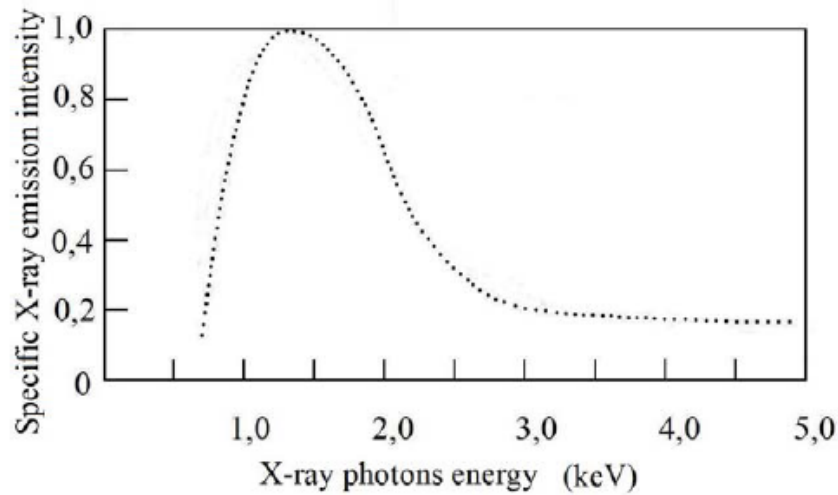


Figure 18. The X-ray continuum spectrum for a Pd cathode with D_2 gas, with a glow discharge voltage of 2600 V.

6.3. Spectra of collimated emission taken after discharge switch off

In the time resolved scintillator measurements, strong collimated emission occurs in bursts immediately following the switch off of the discharge. We noticed that emission can also occur an extended time after the discharge was turned off. In Figs. 27–32 we show examples of collimated monoenergetic X-ray beams that appeared after the discharge was switched off; data was collected for 20 h after switch off in the figures.

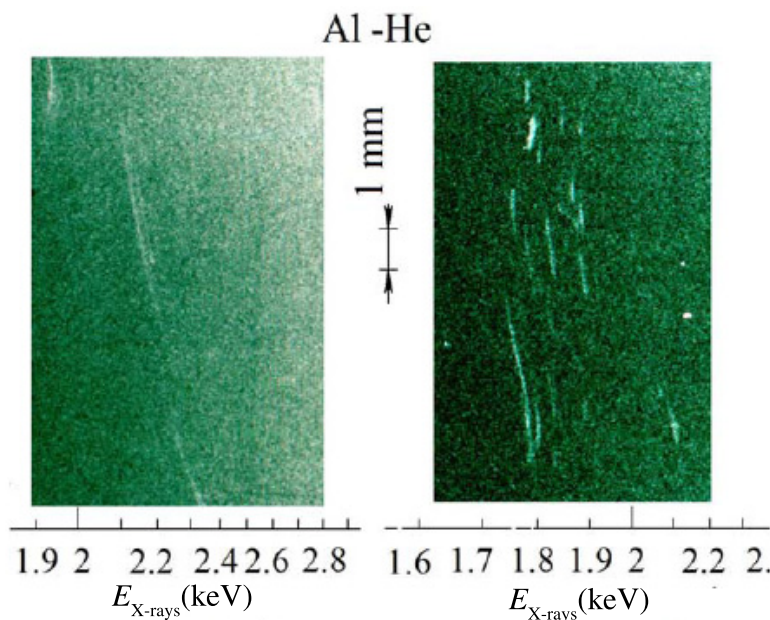


Figure 19. X-ray spectra showing collimated monoenergetic beams from Al cathodes with He gas.

6.4. X-ray spectra showing line emission taken during discharge operation

We observed characteristic X-ray K-shell line emission near 3 keV that could be associated with the gas in the case of Ar, as can be seen in Fig. 33. Electron beam excited Ar has been reported in the literature, and the K_{α} emission is dominant [10,11]. Similarly, when Kr gas is used we can see strong characteristic L-shell line emission in Fig. 34 (see [11] for the Kr line under electron beam excitation). In both cases this radiation appears to be sourced at or near the cathode surface, and not in the discharge. Characteristic L-shell emission from the cathode can be seen in the case of Zr and Mo cathodes (and perhaps the Pd cathode as well) in Fig. 35; theoretical and experimental spectra for electron beam bombardment of Mo is given in [12]. In all cases this diffuse radiation originates at (or near) the cathode surface.

7. Discussion and conclusion

Collimated X-ray emission in these glow discharge experiments constitutes a new and fundamental physical effect that has not been observed previously. Such an effect requires an explanation. In previous work we proposed that the collimated emission is due to X-ray lasing in the cathode. A problem with this proposal is that the creation of an X-ray laser requires a population inversion (or equivalent), which seems problematic since electronic lifetimes in the keV regime are very short, and since there seems to be no clear mechanism that could result in a population inversion.

There is an alternate approach, however, to the problem of developing a collimated beam in the X-ray regime. It is well known that a phased array of antennas (such as might be used for radar) can produce a collimated beam, and atoms and nuclei radiate individually as microscopic antennas. Hence, the experimental observation of collimated X-ray emission in these experiments suggests that there is some new mechanism which results in phase coherent excited states with keV energy (but no population inversion). This is a highly nontrivial accomplishment.

How might such phase coherent excitation be produced? Some colleagues have suggested that the electrons in the

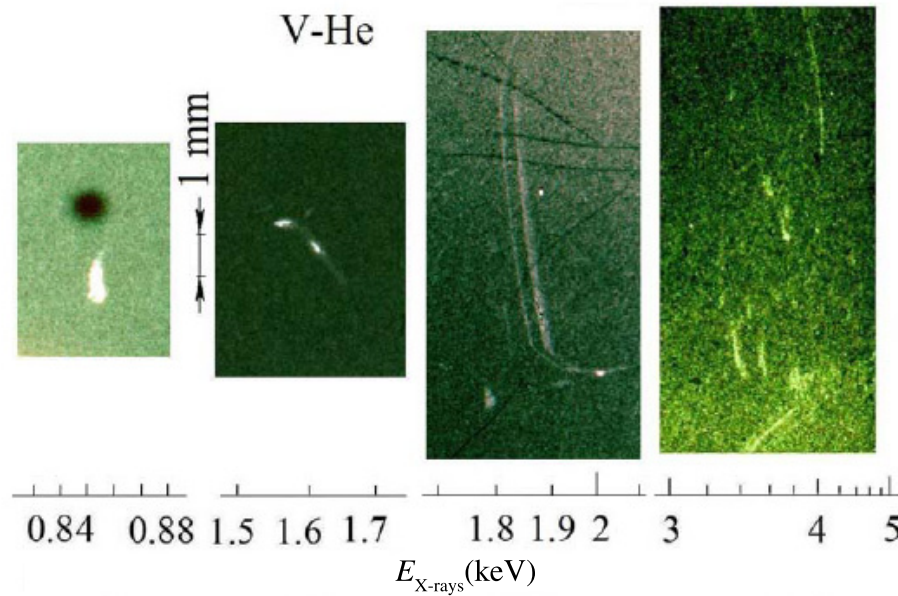


Figure 20. X-ray spectra showing collimated monoenergetic beams from V cathodes with He gas.

discharge will gain energy close to the applied voltage, which could cause excitation. While this is true in principle, collimated beams are seen after the discharge current is switched off (see Fig. 4), and also long after the discharge has been switched off (see Figs. 27–32). One would expect excitation caused by fast electrons to be strongest during the discharge. The collimated emission is sourced at the cathode surface, but energetic electrons impact the anode, and the corresponding radiation from the anode is blocked by the pinhole. Energetic ions impacting the anode could in principle cause electronic excitation (the energy is much too low for collisions producing nuclear excitation), but such an effect should be strongest during the discharge, not after.

There has been interest in the possibility that coherent energy exchange might be possible between a highly excited phonon mode, and an energetic nuclear transition [13,14]. If we consider such an approach as being relevant to collimated X-ray emission, then perhaps the first question might be whether there might exist a highly excited vibrational mode, preferably one that is uniform in the vicinity of the emitters. It can be noticed that a sharp current spike occurs when the current is switched off, which is likely to be associated with a local pressure spike on the cathode surface. The conjecture is that this can be effective in exciting the lowest compressional modes of the cathode.

It has been noted previously that ^{201}Hg has the lowest excitation energy from the ground state of all of the stable nuclei, with a transition energy of 1565 eV [15]. According to the models studied so far, it seems unlikely that coherent energy exchange can occur directly between this transition and the vibrational mode (since the coupling is far too weak). However, if there is another transition at higher energy that is strongly coupled, then we might expect energy exchange via a mechanism related to the model outlined in [16]. The stronger transition in this case would produce a mixing between the nuclear and phonon degrees of freedom, causing a spreading in the phonon distribution. Since the half life of the ^{201}Hg transition is short (about 81 ns according to [17]) we expect coherent energy exchange to occur while emission occurs, which would result in a broad line shape. This we might associate with the strong diffuse continuum feature seen in these experiments. Note that we would expect the least broadening to occur with the smallest phonon

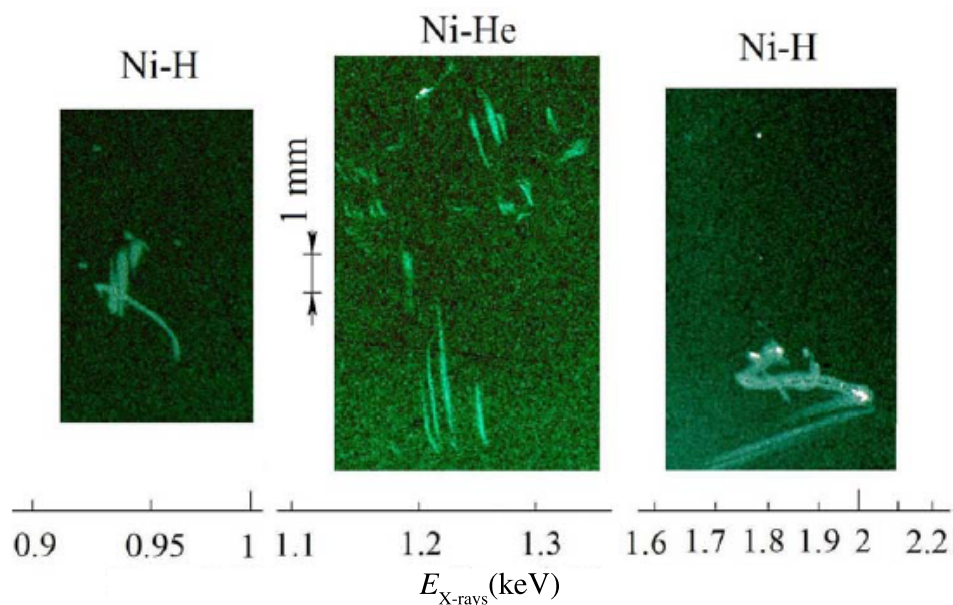


Figure 21. X-ray spectra showing collimated monoenergetic beams from Ni cathodes with H₂ and He gas.

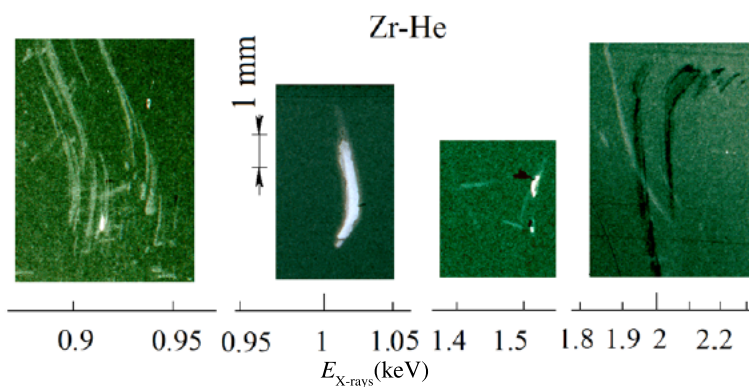


Figure 22. X-ray spectra showing collimated monoenergetic beams from Zr cathodes with He gas.

excitation; consequently our attention is drawn to the continuum in the lowest voltage example (1850 V) of Fig. 17, where the continuum seems narrower and more closely centered near about 1400 eV.

In this picture we would attribute the collimated X-ray beams to a phased array beam formation effect, in which ²⁰¹Hg nuclei are embedded randomly (but in phase) in the outer surface of the cathode. From preliminary simulation results, one observes that the phases can add up at sharp energy resonances (which can be different for different random samples) that fall within the broad emission line shape of the ²⁰¹Hg. If we include the effect of cathode photoabsorption

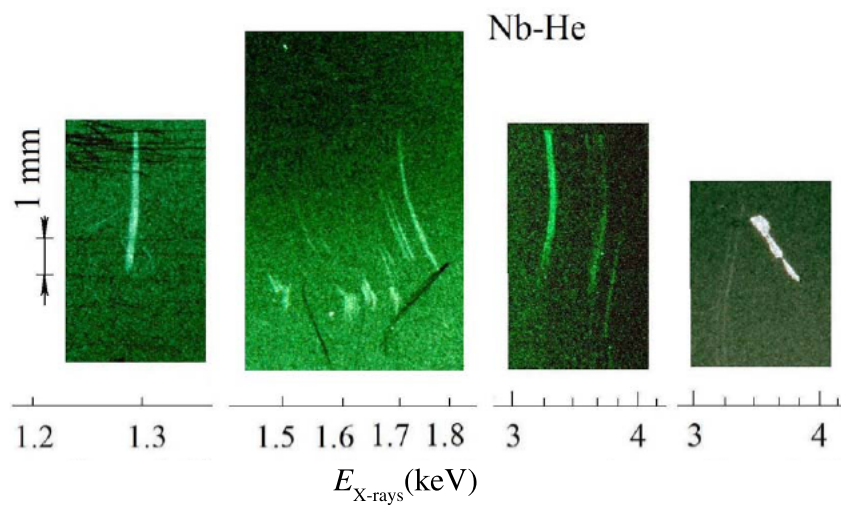


Figure 23. X-ray spectra showing collimated monoenergetic beams from Nb cathodes with He gas.

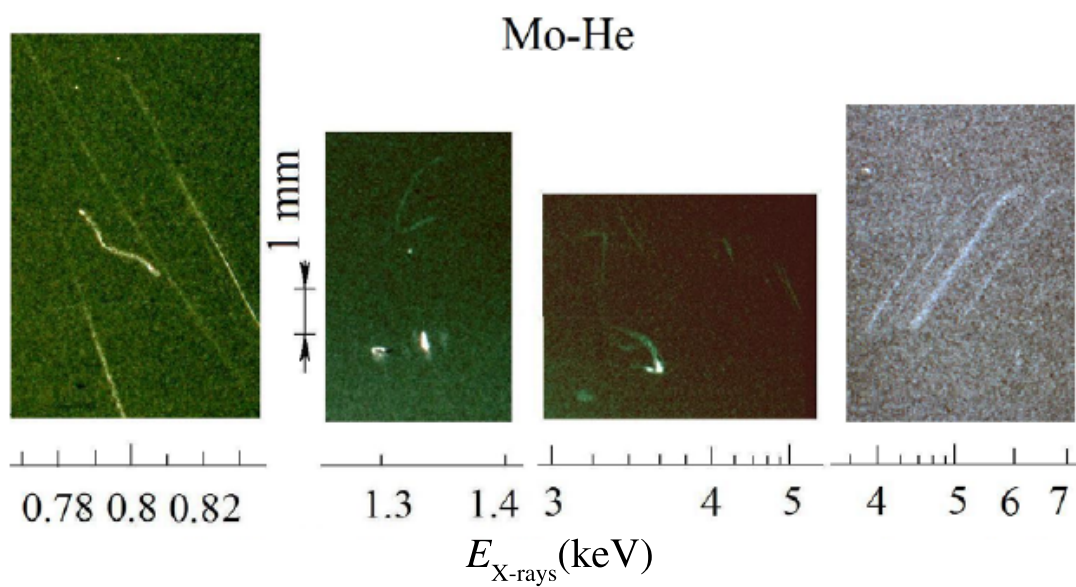


Figure 24. X-ray spectra showing collimated monoenergetic beams from Mo cathodes with He gas.

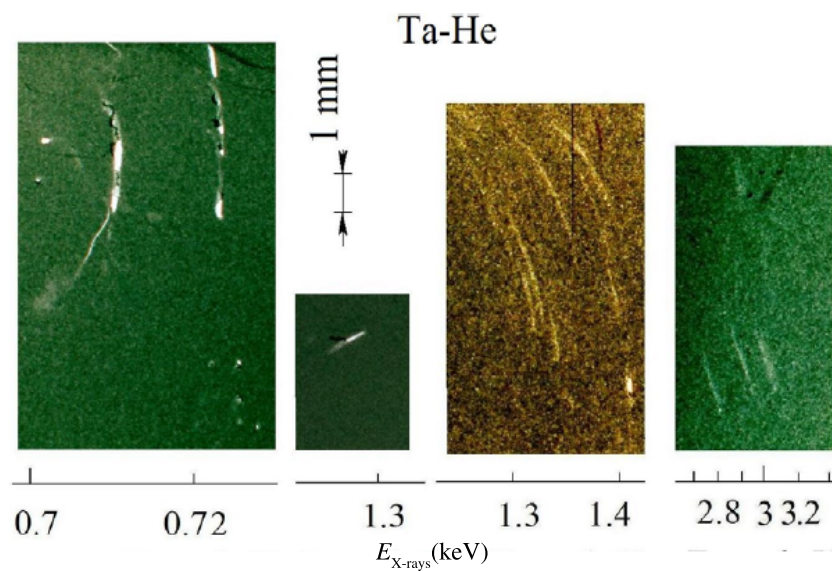


Figure 25. X-ray spectra showing collimated monoenergetic beams from Ta cathodes with He gas.

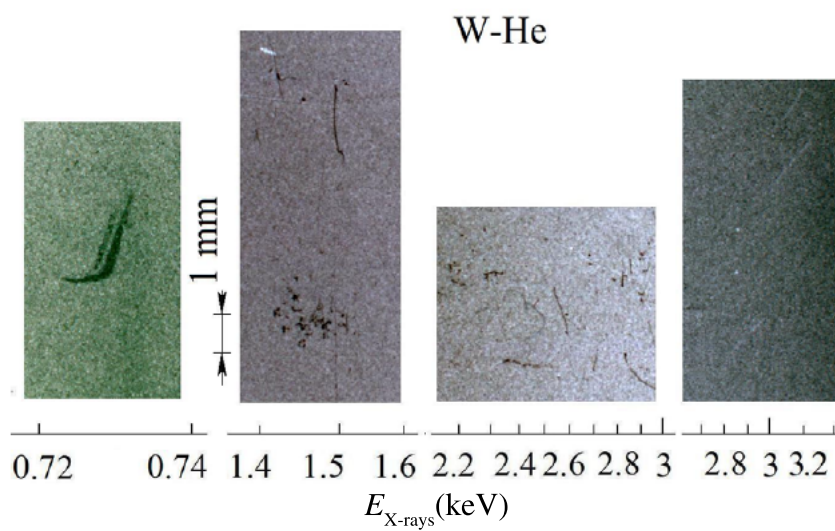


Figure 26. X-ray spectra showing collimated monoenergetic beams from W cathodes with He gas.

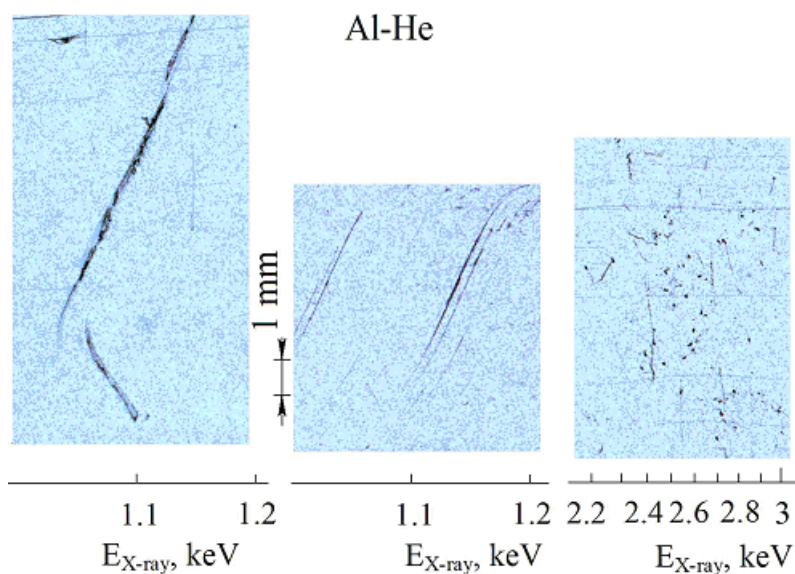


Figure 27. Collimated monoenergetic X-ray beam emission from Al cathodes in He taken after discharge switch off.

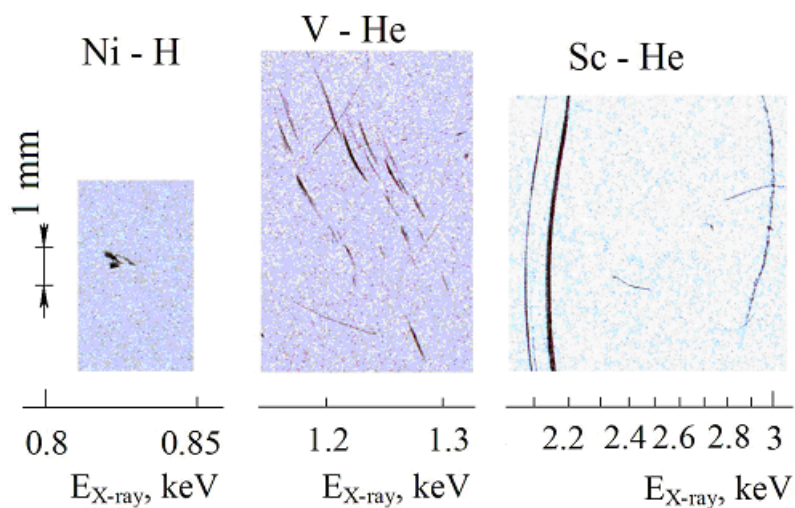


Figure 28. Collimated monoenergetic X-ray beam emission from Ni, V, and Sc cathodes in H₂ and He taken after discharge switch off.

in the modeling, we conclude that this emission is probably not from ^{201}Hg as an impurity in the bulk, but instead is deposited as an impurity from the gas. The coherent energy exchange models show a dynamics that involves a delay for the coherence to build up, and then a rapid energy exchange rate; it may be that the X-ray bursts observed after a delay following discharge switch off is a result of this kind of coherent energy exchange dynamics.

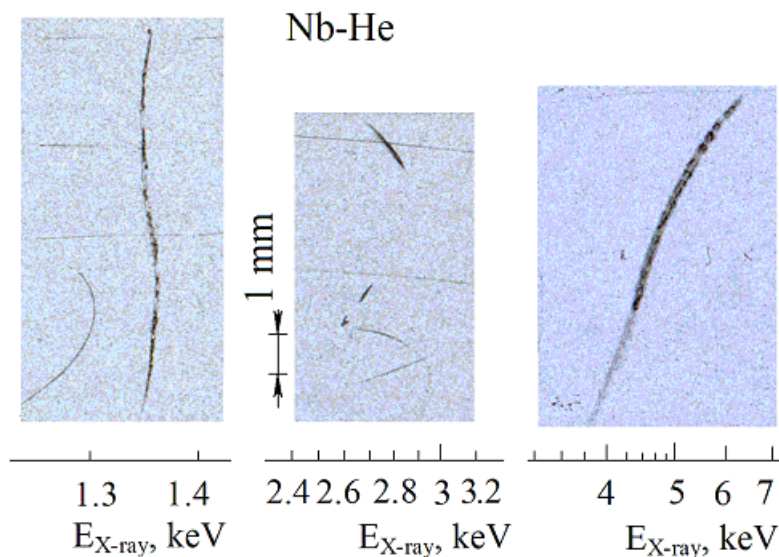


Figure 29. Collimated monoenergetic X-ray beam emission from Nb cathodes in He taken after discharge switch off.

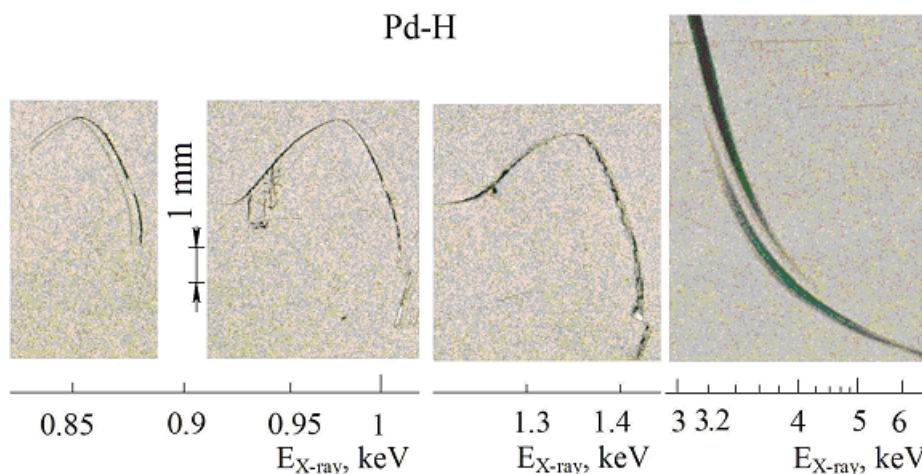


Figure 30. Collimated monoenergetic X-ray beam emission from Pd cathodes in H_2 taken after discharge switch off.

In the case of bursts that occur a long time after the discharge is shut off, it may be that mechanical stimulation of the cathode occurs in connection with the cooling and associated thermal and mechanical relaxation of the cathode assembly.

In the case of diffuse characteristic X-ray emission from gas atoms, the big issue is how excitation occurs. We would expect that the fast electrons should be able to cause inner shell ionization in Ar and Kr, resulting in characteristic X-rays emission. However, this emission in the experiments appears to be localized to the cathode surface or nearby,

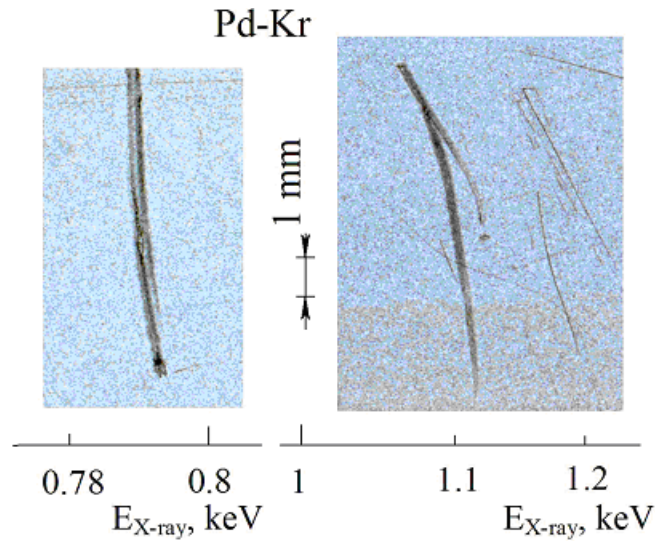


Figure 31. Collimated monoenergetic X-ray beam emission from Pd cathodes in Kr taken after discharge switch off.

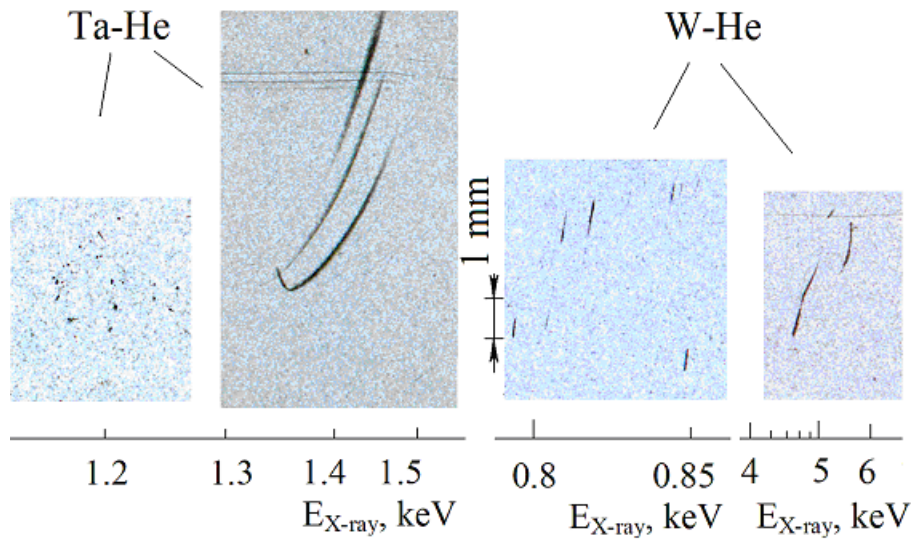


Figure 32. Collimated monoenergetic X-ray beam emission from Ta and W cathodes in He taken after discharge switch off.

while the fast electrons would be expected to produce excitation in an extended region between the cathode and anode. It may be that some Ar and Kr atoms are driven into the outer cathode surface, and are ionized as a result of energy exchange as a result of the spread in the phonon distribution (we have computed the matrix elements for dipole-dipole coupling involving the promotion of an inner shell electron to a phonon-sensitive outer shell orbital, and the coupling matrix elements can be large – in the eV range).

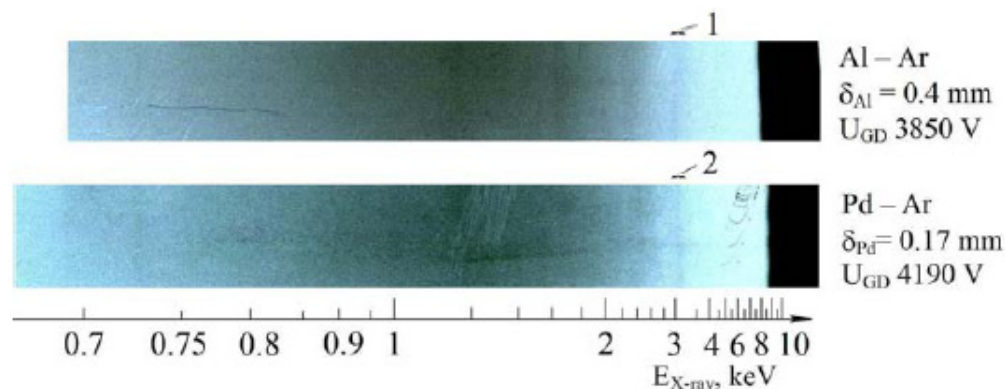


Figure 33. X-ray spectra for Pd and Al cathodes taken in Ar gas showing characteristic K-shell emission (denoted in the spectra as 1 and 2) near 3 keV (the $K_{\alpha 1}$ and $K_{\alpha 2}$ transitions are listed at 2.957 keV and at 2.955 keV). The difference between the observed energy and known energy may be due to the use of the normal incidence grating formula for data analysis.

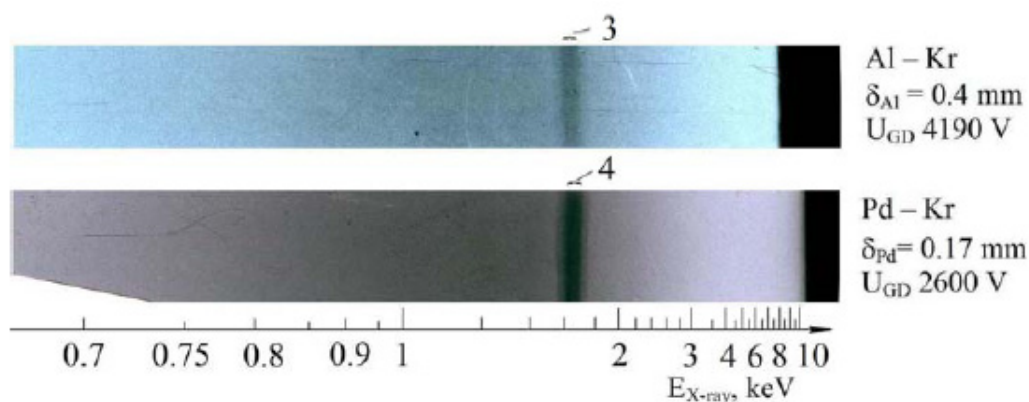


Figure 34. X-ray spectra for Pd and Al cathodes taken in Kr gas showing characteristic L-shell emission (denoted as 3 and 4 in the spectra) near 1.6 keV (the $L_{\alpha 1}$ and $L_{\alpha 2}$ transitions are listed at 1.581 keV and at 1.580 keV). Once again, minor differences between the observed and known energy may be due to the use of the normal incidence grating formula.

Further study is required in order to understand the effect better, and to clarify the connection between the experimental observations and the new models. In light of the X-ray results presented here and the coherent energy exchange models, such future studies might address different specific issues.

For example, collimated emission might be studied using something other than a glow discharge to drive vibrational excitation (such as piezoelectric or pulsed laser stimulation); ^{201}Hg could be ion deposited into the outer surface layer in controlled amounts and controlled depths; and control experiments could be carried out without ^{201}Hg . The emission as a function of vibrational frequency (which could be controlled by the sample thickness) could be investigated. Similar experiments could be carried out based on other low-energy transitions from ground state nuclei (such as the ^{181}Ta transition at 6.24 keV), and the dependence of the number of quanta exchanged could be studied as a function

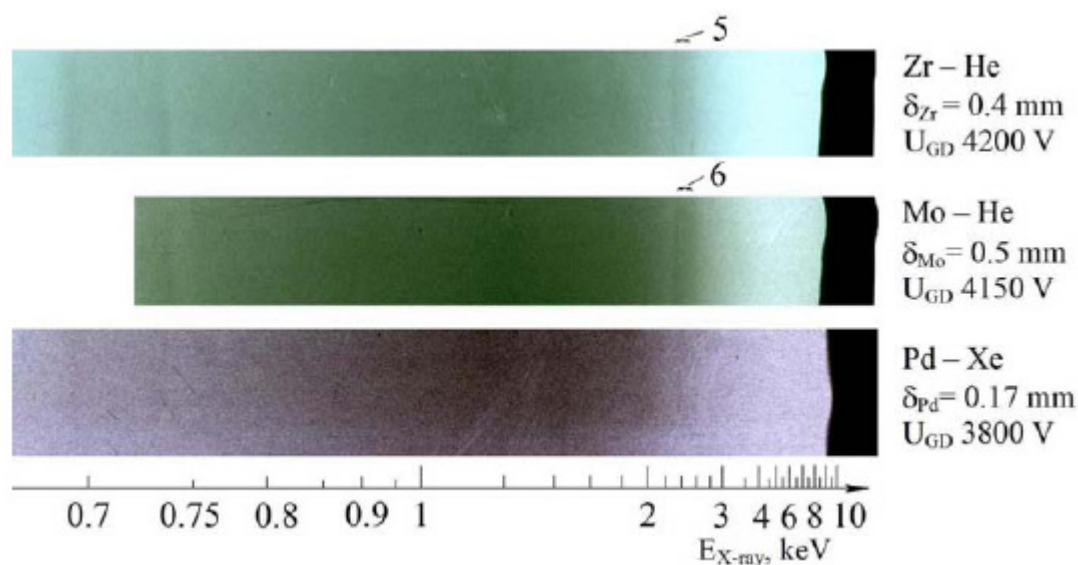


Figure 35. X-ray spectra for Zr, Mo and Pd cathodes taken in He and Xe gas showing characteristic L-shell emission (denoted as 5 and 6 in the spectra) above 2 keV. In the case of Zr, the $L_{\alpha 1}$ and $L_{\alpha 2}$ transitions are listed at 2.042 keV and at 2.040 keV; in the case of Mo, the $L_{\alpha 1}$ and $L_{\alpha 2}$ transitions are listed at 2.293 keV and at 2.290 keV. Once again, minor differences between the observed and known energies may be due to the use of the normal incidence grating formula.

of excitation strength. ^{201}Hg could be deposited in plane layers with a known separation in order to maximize the directional output at a particular energy.

Since the diffuse emission seems correlated with the discharge current, it may be that the vibrational modes being excited may be different. In this case, ion bombardment associated with the discharge is effective at driving strong incoherent excitation of very high frequency vibrational modes (in some ways similar to the excitation caused by fluxing hydrogen or deuterium through a metal). Coherent energy exchange with inner shell atomic transitions of impurity atoms could be pursued as a related effect (but one not dependent on, or requiring, ^{201}Hg). It should be possible to correlate the number of quanta exchanged to the level of excitation (presumably the exchange would occur through the most highly excited subset of modes, which would require a statistical analysis to understand); driving the system more strongly should allow higher energy transitions to be excited.

References

- [1] A.B. Karabut, Ya. R. Kuchеров and I.B. Savvatimova, *Phys. Lett. A*, **170** (1992) 265.
- [2] A.B. Karabut, Research into powerful solid X-ray laser (wave length is 0.8–1.2 nm) with excitation of high current glow discharge ions, *Proc. 11th Int. Conf. Emerging Nuclear Energy Systems*, 29 September– 4 October 2002, Albuquerque, New Mexico, USA, pp. 374–381.
- [3] A.B. Karabut, Experimental research into characteristics of X-ray emission from solid-state cathode medium of high-current glow discharge, *Proc. 10th Int. Conf. on Cold Fusion*, August 24–29, 2003, Cambridge, MA, USA.
- [4] A.B. Karabut, Research into characteristics of X-ray emission laser beams from solid-state cathode medium of high current glow discharge, *Proc. 11th Int. Conf. on Cold Fusion*, 31 October–5 November, 2004, France, pp. 253–257.
- [5] A.B. Karabut, Study of energetic and temporal characteristics of X-ray emission from solid state cathode medium of high current glow discharge, *Proc. 12th Int. Conf. on Cold Fusion*, December 2–7, 2006, JAPAN, pp. 344 - 350.

- [6] A.B. Karabut and E.A. Karabut, Research into energy spectra of X-ray emission from solid cathode medium during the high current glow discharge operation and after the glow discharge current switch off, *Proc. 14th Int. Conf. on Cold Fusion*, August 10–15, 2008, USA.
- [7] A.B. Karabut and E.A. Karabut, Study of deuterium loading into Pd cathode samples of glow discharge, *Proc. of 9th Int. Workshop on Anomalies in Hydrogen/Deuterium Gas Loaded Metals*, 6–11 September 2010, Siena, Italy.
- [8] D. Lapraz, P. Iaconi, Y. Sayandi, P. Keller, J. Barthe and G. Portal, *Phys. Stat. Sol. (A)* **108** (1988) 783.
- [9] P. Pokorny and A. Ibarra, *J. Appl. Phys.* **75** (1994) 1088.
- [10] M. Semaan and C. Quarles, *Phys. Rev. A* **24** (1981) 2280.
- [11] C. Quarles and M. Semaan, *Phys. Rev. A* **26** (1982) 3147.
- [12] D. Roet, C. Ceballos and P. Van Espen, *Nucl. Instr. and Methods Phys. Res. B* **251** (2006) 317.
- [13] P.L. Hagelstein and I.U. Chaudhary, *J. Cond. Mat. Nucl. Sci.* **5** (2011) 52.
- [14] P.L. Hagelstein and I.U. Chaudhary, *J. Cond. Mat. Nucl. Sci.* **5** (2011) 116.
- [15] P.L. Hagelstein, Bird's eye view of phonon models for excess heat in Fleischmann–Pons experiments, this proceedings.
- [16] P.L. Hagelstein and I.U. Chaudhary, *J. Cond. Mat. Nucl. Sci.* **5** (2011) 140.
- [17] V. Meot, J. Aupiais, P. Morel, G. Gosselin, F. Gobet, J.N. Scheurer, and M. Tarisien, *Phys. Rev. C* **75** (2007) 064306.



Research Article

First-principles Studies of Electronic and Ionic Transport in Palladium Hydrides/Deuterides

N. Luo and George H. Miley*

Department of Nuclear, Plasma and Radiological Engineering, University of Illinois, Urbana, IL 61801, USA

Abstract

We review first principles studies on some transport properties and ion dynamics of the palladium hydride/deuteride system. The review is not meant to be extensive, because it is aimed at understanding the abnormal and not-so-well-known part of the transport in the aforementioned compound that may be of particular importance to scientists studying Low-energy Nuclear Reactions (LENRs) as well as persons interested in hydrogen storage in metal hydrides. Many well-known properties of Pd/H, such as the steady-state electronic structure, have already been covered by numerous studies and reviews elsewhere. Many of the studies reviewed here were carried out at the University of Illinois. We focus on the three different but related topics: (1) The charge state of H in Pd, especially in the hopping process. (2) The electron–phonon interaction, and its role in the negative differential resistivity. (3) Defects and dislocations in Pd and their effects in the H state and its transport. The latter is of intellectual interest relative to our recent research on LENRs involving the conjectured formation of hydrogen/deuterium clusters in such defects.

© 2012 ISCMNS. All rights reserved.

Keywords: Electro-negativity, Electron–phonon interaction, Low-energy nuclear reaction, Palladium–hydride system

1. Introduction

The palladium–hydride system has been an interesting yet perplexing topic of multi-disciplinary research for many years [1–3]. This is a material system with many practical applications such as fuel cells, batteries, catalytic chemistry and nuclear chemistry. Also many controversies surround the particular palladium–deuteride system as for the possibility of low energy nuclear reactions. Unlike ordinary metal alloys, where a fairly good understanding is achieved through straightforward concepts, metal hydrides pose a number of complications. First, hydrogen is smaller and lighter than the host metals, and hence its motion in the host metals generates some unexpected effects, quantum ones included. Second, a hydrogen atom is a stronger attractor of electrons than most metal atoms. Therefore, the bonding nature between hydrogen and metals is different from that of a normal metal bond. Many other issues exist in the palladium–hydride system, which is finding increasing importance in various applications. For example, the unique hydrogen storage property of Pd plays an important role in fuel cells and storage battery development. The Pd alloys are often

*E-mail: nluo@illinois.edu; ghmiley@illinois.edu

utilized as a hydrogen permeation selector, which is important to both carbon sequestration of the green energy field and hydrogen/deuterium/tritium (H/D/T) separation of the nuclear industry. The latter will play an important role with future D–T nuclear fusion reactors' coming into the age. In the well-established domain, the phenomena of hydrogen adsorption and the resulting catalytic properties of hydrogenated Pd surfaces, on one hand, pose a fundamental issue for the theoretical understanding of basic surface physics and catalytic chemistry, while on the other hand, are significant for technical applications such as the hydrocarbon industry. More recently, various properties of highly loaded Pd have been of intense interest in low-energy nuclear reaction (LENR) research. In that case issues range from transport of deuterium in the Pd (or other materials such as PdO, Ti, U, and Ni), their localization to form “reactive sites” methods for triggering or catalyzing reactions in these sites, and subsequent reaction kinetics [4,5].

Yet despite extensive research carried out on Pd/H over the past 50 years, some of its fundamental properties are still not well understood. Such problems include the charge state of hydrogen and charge transport of both electron and H ion in the Pd lattice, which are addressed here.

Before we get into the details of Pd/H transport, first we need a few words on the major computational tools that were employed. The general feature of these methods is that they are from first-principles, i.e., their foundation is the simple mathematical formulation of quantum mechanics. This means that empirical data, like electron hopping matrix elements, force field of the atoms, for example that of Pd, extrapolated from experiment and so on, are *not* utilized in the calculation of electronic structures and simulation of atomic motion. Instead, all of the data are calculated from the simple fact that there are 46 electrons outside the Pd nucleus. Therefore, they are full quantum mechanical treatment of the condensed matter system. However, the many-body problem cannot be fully analytically solved. There must exist some simple approximations yet accurate enough so that a real-world calculation can be carried out. A broad range of approximations based on the Hohenberg–Kohn theorem [6] forms the density functional theory (DFT) approach to solving many-body problems. In this regard, most software tools employed in the study are first-principles (sometimes all termed *ab initio*) DFT packages for electronic structure and molecular dynamics. In solving the many-body problem, the total Hamiltonian can be projected to different Hilbert spaces to facilitate the computation, taking advantage of various symmetries that exist in the specific problem. Then we have DFT based on different basis sets: plane-wave pseudopotential, augmented plane wave, linear combination of atomic orbit, Gaussian orbitals and so on. Such terminology will be often encountered later in the review.

2. Charge Transport and the Charge State of Hydrogen in Pd

Charge transport in palladium hydride (and metallic hydrides in general) is complicated in that it involves both electrons and H ions. Electron transport in PdH is complex and not anticipated as is manifested by the unusual electric resistance change versus the H/Pd ratio, illustrated conceptually in Fig. 1. As shown, the normalized resistance as a function of loading x , i.e. H/Pd atomic ratio, first increases and then decreases [7]. Further, it was recently observed that the resistance, finally undergoes an oscillation at ultra high loadings [8]. As the mobility and the number of electrons in PdH are orders of magnitude higher than those of the H ion, electron transport dominates these resistance changes. The initial increase in the resistance (up until $x \sim 0.65$) is relatively easy to understand from an alloying point of view. Or, in other words, the added H in the lattice creates scattering centers, increasing the resistance. The subsequent drop for $x > 0.65$ is not completely understood, but is typically thought to be associated with the formation of new band states. The recently reported oscillation region shown in Fig. 1 has not yet been explained theoretically.

The instability is of particular interest since it could result in coherent oscillations that can accelerate the partially ionized hydrogen in the lattice like in a beat wave accelerator. The resulting high proton energy could well push the deuteron/palladium system far from the equilibrium, which in turn generates many unexpected phenomena.

In addition to resistivity studies, considerable research has been dedicated to probing the nature of H transport (e.g. diffusion and drift) in Pd. Original drift experiments [9,10] strongly suggest that H drifts in Pd in the form of a positive

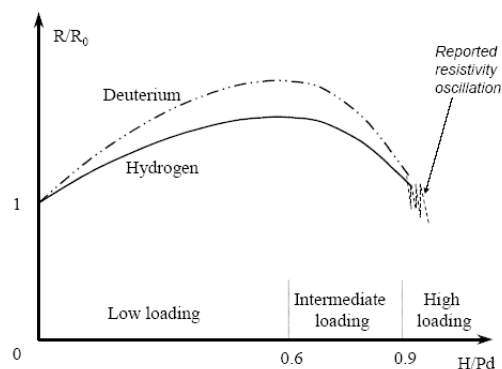


Figure 1. Normalized resistance R/R_0 vs. loading x , where R_0 is the initial resistance without loading. The solid curve is for hydrogen loading with the dot-dashed one for deuterium.

ion with a fractional charge number around +0.5, while a more recent study [11] gives +0.7. These observations, combined with the decrease of the paramagnetic susceptibility with H loading, strongly support the notion of a proton model in which the hydrogen is viewed as donating its electron to the unfilled Pd d-shell. However, such a proton model seems oversimplified in terms of experiments like the electronic specific heat [12]. As the electronic specific heat is directly proportional to the size of the Fermi surface, the proton model should predict a progressively smaller electronic specific heat as the H loading is increased. However, the contrary effect is found in the closely related nickel–hydride systems. Moreover, from a chemistry point of view, H can in principle acquire an electron from the host Pd because of its relatively large electro-negativity. Table 1 summarizes the relevant electronic properties of atomic Pd and H.

Some previous band structure calculations [12–18] have been carried out to elucidate the charge state of H in Pd. The studies include PdH and PdH_{0.25}, where unit cells can be easily defined. The general conclusion is that in these cases the H is slightly negatively charged in spite of the filling up of the Pd d-bands. Without further study, this result has appeared to contradict some of the observations made in H drifting experiments.

In [19], the authors provide improvements over previous band-structure calculations with more hydride compositions and proton locations considered. The authors also suggested how to reconcile the conflicting picture of a negative H ion inferred from electronic-structure calculations with the positive charge suggested by the hydrogen drift experiment.

3. Charge State of Hydrogen in Pd

Details of the calculation can be found in Ref. The explicit consideration of the so-called “bridging” site, designated in Fig. 2, was considered. This site, along with the two others, namely the “on-top” site and the “hollow” site, play an important role in the surface catalytic chemistry of Pd (1 0 0) surface.

The bridging site is considered here for one additional reason. The drift of hydrogen through interstitial hopping

Table 1. The work function of Pd metal and some related constants for atomic Pd and H.

	Electron affinity (eV)	Ionization energy (eV)	Electronegativity (Pauli scale)	Electronegativity (Allred–Rochow scale)
Pd Atom	0.518	7.76	2.2	1.35
H Atom	0.702	13.6	2.2	2.2
Work function of Pd metal (eV)			5.12	

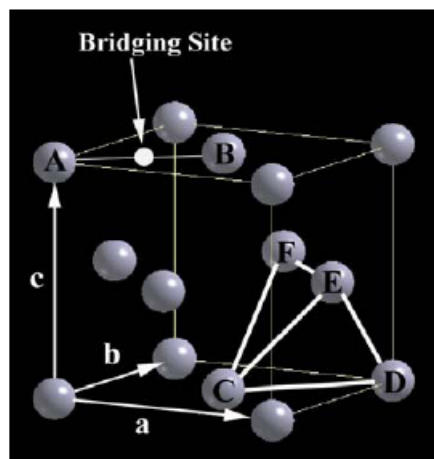


Figure 2. The so-called bridging site in the Pd face centered cubic lattice.

inside a Pd metal matrix is a dynamic process, and hydrogen atoms likely pass through one of two possible sites: the bulk tetrahedral site or the bridging site. Since the path through the bridging site is the shortest, it is of special interest to probe the electronic structure of H located at this site. Prior studies have generally assumed, without proof, that hopping mainly occurs through the tetrahedral site, even though the bridging site path is shorter. The charge state of H at the tetrahedral site was calculated for the first time too, because H is likely to hop through this site as well. Indeed, we will see later that compared with the bridging site, it is an energetically more favorable path. Also, PdH_x of three different compositions x , namely, $\text{PdH}_{0.25}$, $\text{PdH}_{0.5}$, PdH are studied when the H is at the octahedral site. This was done to investigate the change of charge density around H as the loading proceeds. A careful choice of super-cell was necessary for $\text{PdH}_{0.5}$ so as to maintain the inversion center. H atoms are added in the Pd lattice in such a way that the super-cell is kept as small as possible. The existence of the inversion center helps keep the calculation in real numbers and the convergence of the computation is much easier at a result.

We expect less charge around the H when the hydrogen fraction, x , decreases, because the electron around the H has to be shared by more Pd. From Table 2, this is indeed what happens. However, the magnitude of change is less than what is expected from a simple consideration of the work function, electron affinity and electro-negativity. As the electron affinity of a single H, 0.702 eV, is much smaller than the work function of a Pd metal, 5.12 eV, an electron tends to shift away from H when the H composition x is small. However, the DFT result for $\text{PdH}_{0.25}$ does not show much of this tendency. Our explanation is that in the calculation the H is always eight-coordinated in all three loadings, and intercepts roughly the same portion of Pd orbits. Therefore, the change in the charge state is quite small although the actual loading has been significantly altered.

The radius of the muffin-tin sphere is taken as 1.5 Bohr. For reference, previous calculations deal only with partial

Table 2. Charge and corresponding δ (defined by $\text{H}^{\delta-}$) in the H muffin-tin spheres in different compositions and locations.

Case	$\text{PdH}_{0.25}$	$\text{PdH}_{0.5}$	PdH	PdH (bridging)	PdH (tetrahedral)
Charge (e unit)	1.13	1.18	1.22	1.81	1.56
δ	0.13	0.18	0.22	0.81	0.56

charge from the lowest band and are, therefore, lower than the values shown here. Ref. [14] gives a partial charge of 0.67 for a radius of 1.35 Bohr while [15] has a partial charge of 0.68 at 1.6 Bohr.

The charge density distribution in one of the (1 0 0) planes is given in Fig. 3(a)–(c) for each of the three cases. The hydrogen is slightly negatively charged in all of these cases and the change with loading is hardly noticeable. To represent these cases, the charge state can be labeled as $H^{\delta-}$, where δ is often a small fraction. In the case of octahedral H, for example, δ ranges from 0.1 to 0.2. (see Table 2). This result qualitatively corroborates both the APW conclusion of [14] and the pseudopotential result of [15]. The results confirmed the formation of negatively charged H in Pd. A direct and quantitative comparison with their results is, however, not possible so far because both authors quoted the charge for the lowest band only, which underestimates the total charge around H.

In Fig. 3, the labeling of the horizontal axes is in percentage of the FCC cell lengths in (1 0 0) planes. The distance between the Pd atoms is about 2.8 Å. The scale for the vertical axis is electron charge per atomic unit volume. In Fig.

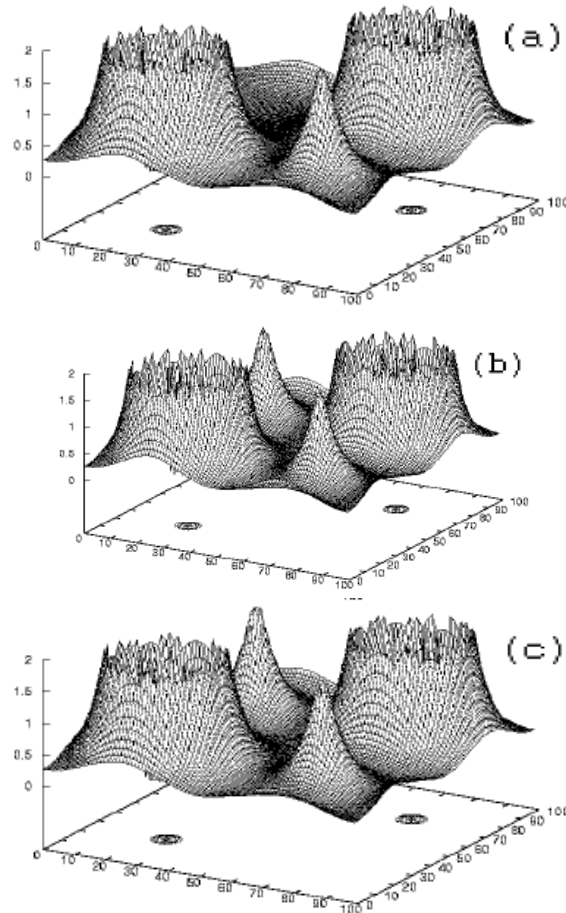


Figure 3. The charge distribution around octahedral H site, in one (1 0 0) plane of (a) $PdH_{0.25}$; (b) $PdH_{0.5}$; and (c) PdH .

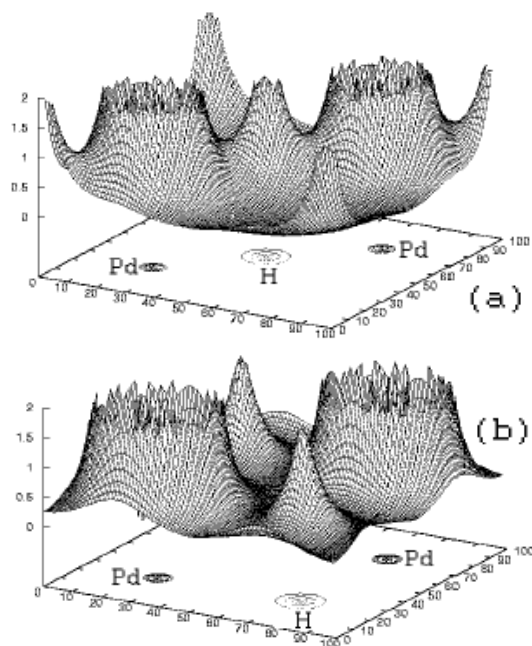


Figure 4. The charge distribution around: (a) bridging-site hydrogen and (b) tetrahedral-site hydrogen in one (1 0 0) plane of hypothetical PdH.

3(a), the H/Pd ratio in this particular (1 0 0) layer is 1:2, but that in the nearest-next neighbor layers is 0 and thus the bulk H/Pd ratio is 1:4. In Fig. 3(b), the H/Pd ratio in this particular (1 0 0) layer is 1:1, but that in the nearest-next neighbor layers is 0 and thus the bulk H/Pd ratio is 1:2.

This negatively charged H from a static band-structure calculation must be reconciled with the notion of a fractionally charged positive H ion found in drift experiments. This requires consideration of the dynamic nature of the proton hopping process. When an electric field is applied to the $H^{\delta-}$ at the octahedral site, the proton hopping (tunneling) process will be assisted in the direction of the field. Therefore, the hydrogen drift (or, in other words, an electric field assisted tunneling process) is characterized as that of a proton, i.e. a^{+1} charge, at the octahedral site. However, in hopping from one octahedral site to another, the proton likely follow a path through either the tetrahedral site or the bridging site, and the charge state at these two locations will also affect the path average charge of the hydrogen in a drift experiment. If the path is through the bridge site, there will be more negative (electron) charge around it as plotted in Fig. 4(a). Table 2 shows that the proton is roughly charged with 0.6 more electrons at the bridging site than at the octahedral site. This implies that the proton carries an effective electron cloud of -0.6 with it as it goes through the bridging region. Hence, the net proton charge manifested in this drift path is $1-0.6 \sim 0.4$. However, other possible paths all contribute. Therefore, the experimentally observed net charge Z^* should be a weighted average of paths through all possible sites.

The scales of axes in Fig. 4 are the same as those in Fig. 3. The horizontal locations of Pd and H atoms are, respectively, indicated with the corresponding labels. In Fig. 4(b), the H layer is roughly a quarter FCC Pd lattice constant from the (1 0 0) layers, and therefore, no Pd atom is shown in the plot.

The calculation of the effective charge in the drift experiments can be effected in a mathematical way. In the

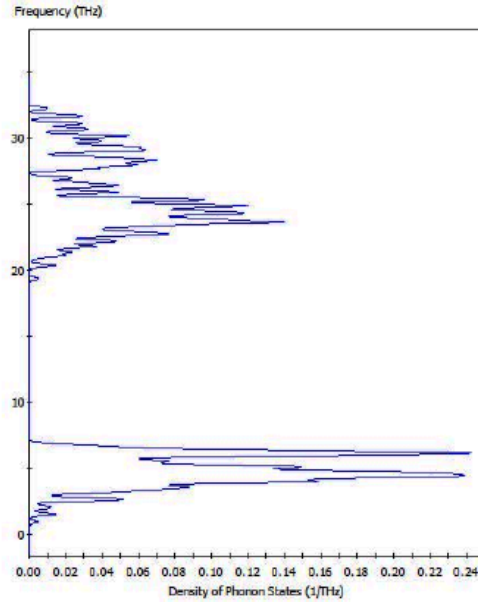


Figure 5. (a) The phonon density of states in PdH.

following explicit derivation, the weighted average is a sum as:

$$Z^* = \sum_i w_i [1 - (\delta_i - \delta_o)]. \quad (1)$$

Here, Z^* is the effective charge found in drift experiments, and i the site indices. δ_i is the fractional charge of H on sites, where the hopping must pass through, as given in Table 2, and δ_o the fractional charge at the octahedral sites. w_i , the statistical probability of taking a path through site i , is given by the following,

$$w_i = \frac{e^{-(E_i - E_o)/KT}}{\sum_i e^{-(E_i - E_o)/KT}}, \quad (2)$$

where K is the Boltzmann constant and T the temperature. E_o is the energy of H when it is at the octahedral site and E_i the energy at site i .

To find out the energy of H at different sites, the linearized augmented plane wave package WIEN2K [20] was used to carry out a total energy study for H at each of the three sites. The resulting energy shift, the difference in total energy between H at a specific site and the reference octahedral site, is given in Table 3.

E_t , E_b , and E_o are energies, respectively, for tetrahedral, bridging and octahedral sites. Ref. [21] gives $E_t - E_o \sim 0.1$ eV, to which our result closely matches. $E_b - E_o$ has not been studied before to the best of the authors' knowledge.

As hoppings are mainly through the bridging and the tetrahedral sites, the right-hand side of Eq. (1) has essentially two terms

$$Z^* = w_t [1 - (\delta_t - \delta_o)] + w_b [1 - (\delta_b - \delta_o)], \quad (3)$$

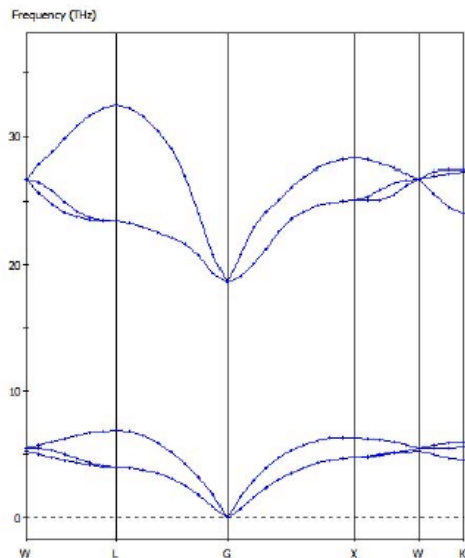


Figure 6. (a) The phonon dispersion (or band structure) along a few high-symmetry directions in the BZ.

where t and b are, respectively, indices for the tetrahedral and bridging sites. The tetrahedral δ_t is given by the last column of Table 2, and the general charge plot around the tetrahedral H is typified in Fig. 4(b). Because $E_b - E_o/KT$ is much larger than $E_t - E_o/KT$ at room temperature, the contribution from hopping via the bridging site is actually fairly small. Therefore, Eq. (3) simplifies to

$$Z^* = [1 - (\delta_t - \delta_o)] \quad (4)$$

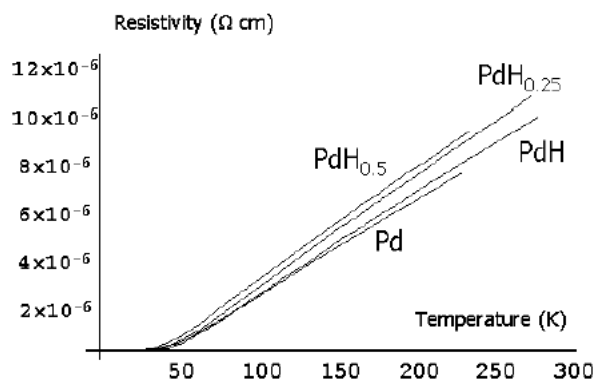


Figure 7. The temperature dependence of resistivity at different loadings.

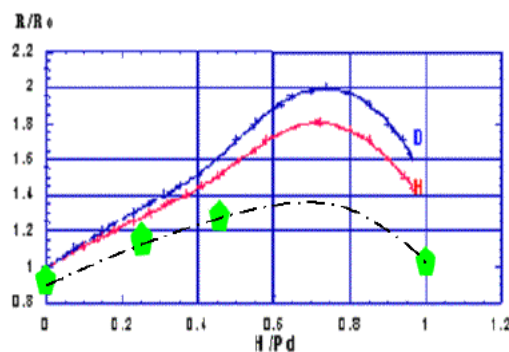


Figure 8. The normalized resistivity at different H loadings.

for ordinary experimental conditions. A simple calculation gives $Z^* \sim 0.7$, which is not far from the traditional average of 0.5 and closely matches the latest experiment results [10].

The negative charge of hydrogen found in the band-structure calculation is a *static* property in a condensed state, which is actually shared with all the coordinated Pd. On the other hand, the positive charge manifested in the proton drifting experiment is a dynamic property, because the proton obviously cannot carry all the negatively charged electrons and move around freely. Overall, the author's study served as a first step towards resolving certain problems involved in transport properties for the palladium–hydride system.

4. Resistivity from Electron–phonon Interaction

A significant part of the resistance of PdH is from the electron–phonon interaction. The first step in understanding the role of phonon in PdH is the phonon spectrum of the density of states. Because hydrogen or deuterium is the lightest

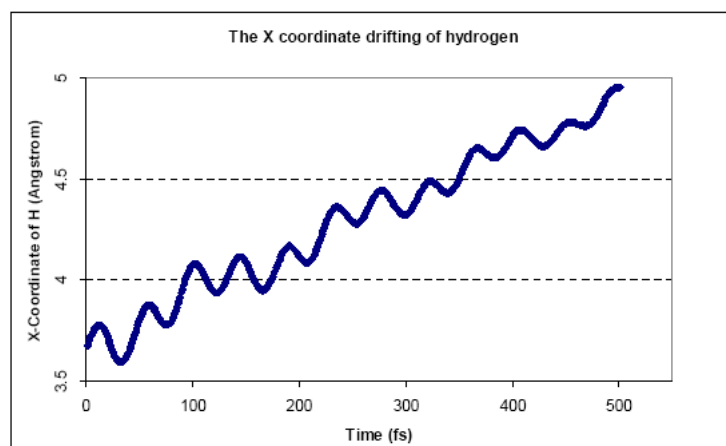


Figure 9. An exemplary coordinate change of H in Pd versus time. It is simulated in a micro-canonical ensemble, assuming an initial energy of 293 K for the H.

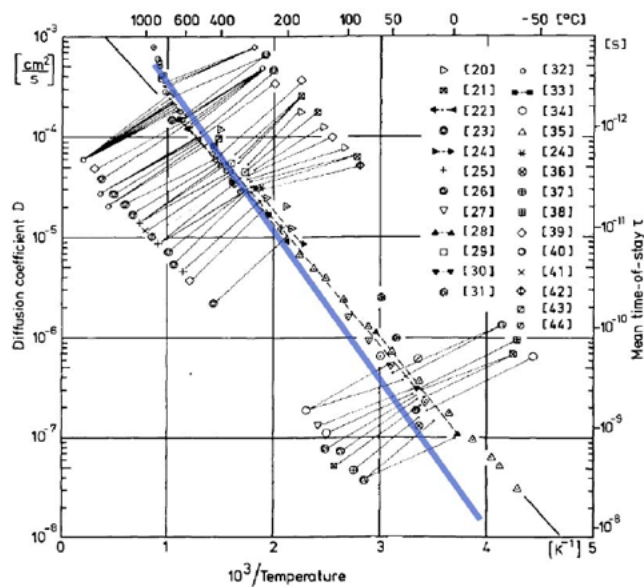


Figure 10. Calculated hydrogen diffusion constants with first-principles molecular dynamics. The *blue line* is obtained by connecting and extrapolating the calculated results at 0°C and 800°C . The width of the line roughly represents the statistical spread at different calculations.

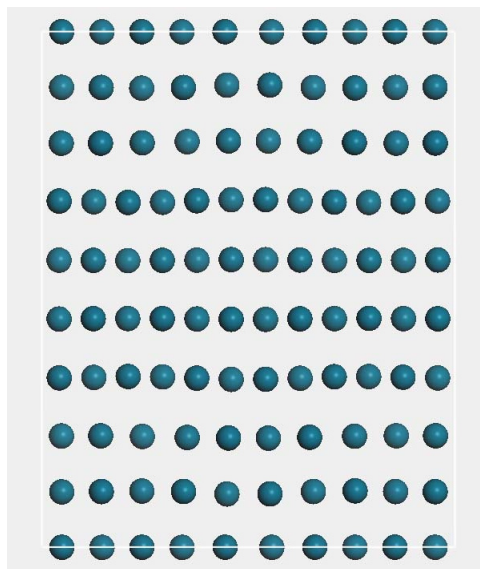


Figure 11. A dislocation along $[2\ 1\ 1]$ in the FCC lattice of Pd, structural-optimized with CASTEP.

among all elements one expects phonons of quite high energy play an important role. Also helpful is the phonon dispersion relation along the high symmetry directions in the Brillouin zone (BZ). Both properties can be calculated by the plane-wave pseudopotential method, with the results plotted in Fig. 5.

The results of Fig. 5 are calculated with CASTEP in the linear response regime by assuming PdH being essentially an insulator. Although this is quite far-fetched assumption, the general phonon band is qualitatively similar to more accurate methods, such as the finite displacement approach, which is nevertheless more time consuming.

With the previous studies investigating the phonon dispersion and density of state of Pd and PdH, we can proceed with one more step ahead with the electron–phonon coupling constant, at different loading x . Our objective is to explain the experimental ρ – x curve, through a first-principles study of the electron–phonon coupling strength.

4.1. Theoretical basis of electric resistivity

Without considering any interband e-e scattering, the resistivity of a metal is given by the Bloch–Gruneisen formula,

$$\rho(T) = \rho_0 + \lambda_{\text{tr}} \frac{4\pi}{\omega_{\text{p,D}}^2} \frac{128\pi (k_{\text{B}}T)^5}{(k_{\text{B}}\Theta_{\text{D}})^4} \int_0^{\Theta_{\text{D}}/2T} \frac{x^5}{\sinh^2 x} dx, \quad (5)$$

where λ_{tr} is the dimensionless electron–phonon coupling constant. ρ_0 is the residual resistivity at absolute temperature 0 K, attributed to scattering from lattice impurities. $\Theta_{\text{D}} \propto \sqrt{\text{bulk modulus/mass density}}$ is the Debye temperature, readily calculated if bulk modulus k is known.

$$\omega_{\text{p,D}}^2 = \frac{4\pi n e^2}{m}$$

the plasma frequency is actually the measurement of the number of band carriers n , including both electron and hole in the case of Pd. Note that in Eq. (5), n and m , the band mass of relevant carriers, can be calculated from the band structures at and near the Fermi surface, which is routinely available from a typical electronic-structure package. The bulk modulus k is, strictly speaking, a function of temperature, but here it can be simply approximated by $\partial U / \partial V$, where U is the total energy and V the crystal volume. Therefore, a straightforward volume-dependent total energy study using WIEN2K and other tools like CASTEP determine the value of k .

The electron–phonon coupling is one of most intensive parts of the computation. An often utilized method is the frozen-phonon approach. In this method, one has to find out the phonon normal modes of the relevant crystal. By distorting the lattice to the deformed types dictated by the normal modes, one can calculate the relevant energy change in the electronic band. The proportion between the band change and lattice change is directly related to the electron–phonon coupling. However, this approach is very time-consuming, sometimes prohibitive. The second and often-adopted means is the perturbative DFT, which is often faster at minimal sacrifice of accuracy. This is the method we adopted for this study.

Table 3. Energy shifts between different sites from total energy study.

Shifts	Energy (eV)
$E_{\text{t}} - E_{\text{o}}$	0.08
$E_{\text{t}} - E_{\text{o}}$	0.86

Table 4. Plasma frequency, Debye temperature and electron–phonon coupling constant at different H loadings.

	Pd	PdH _{0.25}	PdH _{0.5}	PdH
$\hbar\omega_{p,D}$ (eV)	7.68	7.34	7.03	7.80
Θ_D (K)	281	293	304	328
λ_{tr}	0.47	0.51	0.52	0.54

4.1.1. Calculation of electron–phonon coupling

For n and m , the eigenvalues of bands that cross the Fermi surface were calculated at 140 k points in the irreducible Brillouin zone (IBZ). The band mass tensor is then calculated by an interpolation scheme near the Fermi surface. The IBZ k points are then generalized to the whole BZ in order to find out the effective carrier number of the relevant bands. The resulting n and m are listed in the first two rows of Table 1.

The electron–phonon coupling is treated perturbatively using the Planewave Self-consistent Field (PWSCF) package. The norm-conserved pseudopotential (PP) of Pd used in the calculation is obtained from Paolo Giannozzi’s PP code. To ensure the transferability, the PP was tuned by calculating the band structure of Pd using PWSCF until a satisfactory comparison with the WIEN2K band is achieved. The result is given in the last row of Table 1.

The trend seen in electron–phonon coupling versus loading can be understood from other experimental facts. Pure Pd is not superconductive but a stoichiometric PdH has a critical temperature T_c of 9 K. This change indicates stronger electron–phonon interaction at higher H loading. Therefore, the theoretical λ_{tr} result given in Table 1 is confirmed by the trend in the superconducting transition temperature.

The plasma frequency Θ_D , or in other words, the total number of charge carriers keeps decreasing up to $x \sim 0.5$, then a rise is seen with x reaching 1. This can be understood from the band filling process with H is added in Pd. Palladium has three predominantly d-bands traversing the Fermi level. The fourth and fifth band have hole-like Fermi surface while that of the sixth is electron-like. At low loading, the added electrons from hydrogen mainly fills up the two hole bands, resulting in a decrease in the number of hole, which outpaces the increase in the electron number of the sixth band. Therefore, a reduction in the total number of current carrier happens, causing a decreasing plasma frequency with increasing loading. At $x = 0.6$, however, the two lower bands are now largely full, the increase in the electron number of the sixth band now more than offsets the loss in the hole number, and therefore Θ_D begins to increase.

Substituting the calculated parameters into Eq. (1), the temperature-dependent resistivity is then derived for various loadings as shown in Fig. 4. The linear temperature dependence is the characteristic of a phonon-induced resistivity when temperature is on the order of a few hundred degrees Kelvin.

Alternatively, the normalized loading-dependent resistance at the room temperature is given in Fig. 5. The absolute values of theoretical results are well below the experimental ones. It is not a surprise considering the additional scattering from the H-induced disorder and the inter-band electron–electron scattering not included in the calculation.

The resistivity (resistance) of Fig. 7 is normalized to that of pure Pd at 300 K. The red and blue curves are from experiments. Theoretical results are given as the four pentagons. The black dot-dashed line is the theoretical least-square fit.

5. Ionic Dynamics

The ionic or molecular dynamics of hydrogen and its isotopes in metal lattices is a very interesting topic and of practical importance. It has broad applications such as metal hydride hydrogen storage, carbon dioxide sequestration, catalytic chemistry and should play critical role in future nuclear fusion power plants. A clear understanding of various aspect of such a process is therefore highly desired.

The experimental data of hydrogen diffusion in metals, especially palladium, have long been in existence in the

literature. However, a theoretical and computational understanding of such experimental results is far from adequate. Here, we describe some of the authors' on-going studies as an effort to unravel the relevant physics in first principles.

The hopping or diffusion of H in solid-state lattices is a dynamic process, and belongs to the very broad domain of molecular dynamics. Note that H for the most of time transport in the metal lattice in a partial charged (ionic) form. Therefore, the more precise term might instead be “ionic dynamics”, when we are dealing with hydrogen in metals.

This problem can be addressed from first principles. In essence, a plain-wave pseudopotential method, CASTEP, based on the density functional theory can be utilized to find the electronic structure (energy eigenstates, charge density, etc.) of hydrogen in metals. The Car-Parrinello molecular dynamics method is resorted to in calculating the ionic force field. Afterwards, the statistic averages of a few correlation functions are calculated by the MDTEP package to yield important parameters such as diffusion coefficients. A typical MD simulation gives time-dependent variation of the H location as depicted in Fig. 8. The results can then be utilized to calculate the mean square displacement (MSD) of the hydrogen.

The MSD is related to the diffusion constant by a very simple relation

$$D = \frac{d(\text{MSD})}{dt}. \quad (6)$$

In other words, the time derivative of the MSD gives the diffusion constant of the relevant species. Then the first-principles MD can in this way compute the H diffusion coefficient at different temperatures.

Molecular dynamics is classified with different constraints. Because we are dealing with many statistical averages, the constraints often correspond to different statistical ensembles. For example, one often adopted constraint set is the NVT, meaning particle number (N), volume (V), and temperature (T) are held constant in the simulation. This corresponds to the well-known canonical ensemble often encountered in statistical physics.

An apparent feature of molecular dynamics computation is its statistical nature. This is due to the fact that a many-body system is being treated and therefore the result could be quite different due to a slight change of parameters and assumptions. Take the hopping the H in the metal lattice as an example. The hopping from one octahedral site to the next is a small-probability event. In real life it may take many, say 10^{10} , attempted bumps before a real jump can happen. Therefore, a variety of assumptions must be made to expedite the real simulation. Such assumptions cause a spread in the calculated results, sometimes could be fairly broad. Fortunately for many circumstances of MD, the mean objective is to obtain an order-of-magnitude estimate or a qualitative understanding. Hence, as long as the simulation can help us understand and predict, the MD study is then considered valuable. Figure 9 demonstrates some simulation results of H diffusion in Pd. The match with the experiment is better at higher temperature. At lower temperature, the MD results tend to underestimate the rate due to the fact that quantum tunneling brings additional hopping terms into the diffusion constant.

6. Dislocations Defects and their Effects

Linear defects or dislocations in a metal are known to generate a range of interesting phenomena. One possible consequence of have such a dislocation on H or D is to act as a potential trap so that the local effective density of very high localized H/D densities (terms “deuterium clusters”). However, so far there has not existed direct experimental evidence for such a trap of high H/D density, also very convincing circumstantial evidence reported in [4,5]. Theoretical studies of the condensation process for cluster formation have also been presented [22]. Because this is a small-scale phenomenon on the Angstrom level, existing spectroscopic and microscopic means are not powerful enough to observe it directly, deep inside the metal and often under high internal pressure.

Because of the limitation of the current experimental techniques, the first-principles MD is expected to play a critical role in understanding the effect of dislocations on hydrogen transport in metals. For example most of the metal hydrides utilized in modern batteries and fuel cells are high in the crystal defects. In essence, a perfect crystal of metal hydride

is for most time a rather poor hydrogen storage for rechargeable battery or fuel cell electrodes. This is because the hydrogen is then tightly bonded to the metal lattice, causing very slow diffusion. Meanwhile the high-power-density demand of modern electrochemical devices requires very fast ionics, which can only be furnished with a large amount of crystal defects in the hydride.

Due to the local trapping property of dislocations, it is natural to think about a high density accumulation of H/D, or cluster. We have attempted some preliminary MD simulation of such a situation. So far, the results have not been able to reproduce the conjectured structure that could be inferred from a variety of experiments. This work on density accumulation is continuing and will be reported later.

The first-principle simulations of defects are typically time-consuming. Because defects typically lack adequate periodicity at small scales, the simulation often involves large number of atoms and therefore is computational intensive. Nevertheless by proper choice of the structure one can simulate many properties with modest computational tools. Figure 10 is one example of dislocation along the FCC $[2\ 1\ 1]$ direction. The hydrogen diffusion in Pd is well known to be affected by the presence of dislocations [23–25]. However, the exact mechanism with which the mobility of H is affected still remains unclear and therefore consists of an interesting topic. It is intuitive to conjecture that the diffusion constant is significantly different normal and parallel to the dislocation direction. The authors have started some preliminary investigations of the defect properties and effects with MD simulations. The initial results are qualitatively matched to the experiments cited in [4]. The details will be published elsewhere.

7. Conclusions

Detailed FLAPW electronic structure calculations carried out for H at various sites and compositions of PdH_x provides the following insights of importance to the metal hydride and LENT communities. It is confirmed that H hopping through tetrahedral sites is energetically more favorable than through bridging sites. H drifting appears to involve a partially charged positive ion because the proton attracts extra negative charge in its hopping path, which partially screens out the unit positive charge carried by the proton. Charge accumulation around the bridging site is shown to be relatively large and thus must be considered in evaluating catalytic properties associated with PdH surfaces and reactive sites. Preliminary studies of dislocation defect trap sites for hydrogen and deuterium are also presented.

References

- [1] D.P. Smith, *Hydrogen in Metals*, The University of Chicago Press, Chicago, 1948.
- [2] F.A. Lewis, *The Palladium–Hydrogen System*, Academic Press, New York, 1967.
- [3] N.F. Mott and H. Jones, *Theory of the Properties of Metals and Alloys*, Dover, New York, 1958.
- [4] G. H. Miley and X. Yang, *Fusion Sci. Technol.* **56** (1), 395–400
- [5] L. Holmlid, H. Hora, G. Miley and X. Yang, *Laser and Particle Beams* **27**(3).
- [6] P. Hohenberg and W. Kohn, *Phys. Rev.* **136** (1964) B864.
- [7] P. Tripodi, M.C.H. McKubre, F.L. Tanzella, P.A. Honnor, D. Di Gioacchino, F. Celani and V. Violante, *Phys. Lett. A* **276** (2000) 122.
- [8] G.H. Miley, G. Selvaggi, A. Tate, M. Okuniewski, M. Williams, D. Chicea, H. Hora and J. Kelly, in *Proc.ICCF-8*, Villa Marigola, Lerici (La Spezia), Italy, 2000, p. 169.
- [9] C. Wagner and G. Heller, *Z. Phys. Chem. B* **46** (1940) 242.
- [10] H. Wipf, *Hydrogen in Metals* (Part II), in G. Alefeld and J. Volkl (Eds.), Springer-Verlag, Berlin, 1978, p. 273.
- [11] R. Pietrzak, R. Szatanik and M. Szuszkiewicz, *J. Alloys Comp.* **282** (1999) 130.
- [12] A.C. Switendick and Ber. Bunsenges, *Phys. Chem.* **76** (1972) 535.
- [13] D.A. Papaconstantopoulos, B.M. Klein, J.S. Faulkner and L.L. Boyer, *Phys. Rev. B* **18** (1978) 2784.
- [14] M. Gupta and A.J. Freeman, *Phys. Rev. B* **17** (1978) 3029.
- [15] C.T. Chan and S.G. Louie, *Phys. Rev. B* **27** (1983) 3325.

- [16] C. Elsasser, M. Fahnle, K.M. Ho and C.T. Chan, *Phys. B* **172** (1991) 217.
- [17] C. Elsasser, K.M. Ho, C.T. Chan and M. Fahnle, *J. Phys. Condens. Matter* **4** (1992) 5207.
- [18] Y. Wan, S.N. Sun and M.Y. Chou, *Phys. Rev. B* **53** (1996) 1.
- [19] N. Luo, G. H. Miley and A. G. Lipson, *Appl. Surface Sci.* **219** (2003) 167.
- [20] WIEN2K, <http://www.wien2k.at>.
- [21] C. Elsasser, K.M. Ho, C.T. Chan and M. Fahnle, *Phys. Rev. B* **44** (1991) 10377.
- [22] Yeong E. Kim, *Naturwissenschaften* **96** (2009) 803–811.
- [23] S.B. Gesari, M. E. Pronsato and A. Juan, *Int. J. Hydrogen Energy* **34** (2009) 3511.
- [24] B.J. Heuser and J.S. King, *Metall. Mater. Trans. A-Phys. Metall. Mater. Sci.* **29** (1998) 1593.
- [25] B.J. Heuser, T.J. Udovic and H. Ju, *Phys. Rev. B* **78** (2008) 214101.